Global Positioning System: Theory and Applications

Volume I

Edited by

Bradford W. Parkinson
Stanford University, Stanford, California
James J. Spilker Jr.
Stanford Telecom, Sunnyvale, California

Associated Editors:
Penina Axelrad
University of Colorado, Boulder, Colorado
Per Enge
Stanford University, Stanford, California

Volume 163
PROGRESS IN ASTRONAUTICS AND AERONAUTICS

Paul Zarchan, Editor-in-Chief
Charles Stark Draper Laboratory, Inc.
Cambridge, Massachusetts

Published by the
American Institute of Aeronautics and Astronautics, Inc.
370 L'Enfant Promenade, SW, Washington, DC 20024-2518

Third Printing

ISBN 1-56347-106-X

Preface

Overview and Purpose of These Volumes

Of all the *military* developments fostered by the recent cold war, the Global Positioning System (GPS) may prove to have the greatest positive impact on everyday life. One can imagine a 21st century world covered by an augmented GPS and laced with mobile digital communications in which aircraft and other vehicles travel through "virtual tunnels," imaginary tracks through space which are continuously optimized for weather, traffic, and other conditions. Robotic vehicles perform all sorts of construction, transportation, mining, and earth moving functions working day and night with no need for rest. Low-cost personal navigators are as commonplace as hand calculators, and every cellular telephone and personnel communicator includes a GPS navigator. These are some of the potential positive impacts of GPS for the future. Our purpose in creating this book is to increase that positive impact. That is, *to accelerate the understanding of the GPS system and encourage new and innovative applications.*

The intended readers and users of the volumes include all those who seek knowledge of GPS techniques, capabilities, and limitations:

- Students attending formal or informal courses
- Practicing GPS engineers
- Applications engineers
- Managers who wish to improve their understanding of the system

Our somewhat immodest hope is that this book will become a standard reference for the understanding of the GPS system.

Each chapter is authored by an individual or group of individuals who are recognized as world-class authorities in their area of GPS. Use of many authors has led to some overlap in the subject matter which we believe is positive. This variety of viewpoints can promote understanding and contributes to our overall purpose. Books written by several authors also must contend with variations in notation. The editors of the volume have developed common notations for the important subjects of GPS theory and analysis, and attempted to extend this, where possible, to other chapters. Where there are minor inconsistencies we ask for your understanding.

Organization of the Volumes

The two volumes are intended to be complementary. Volume I concentrates on fundamentals and Volume II on applications. Volume I is divided into two parts: the first deals with the operation and theory of basic GPS, the second section with GPS performance and errors. In Part I (GPS Fundamentals), a summary of GPS history leads to later chapters which promote an initial under-

standing of the three GPS segments: User, Satellite, and Control. Even the best of systems has its limitations, and GPS is no exception. Part II, GPS Performance and Error Effects, is introduced with an overview of the errors, followed by chapters devoted to each of the individual error sources.

Volume II concentrates on two aspects: augmentations to GPS and detailed descriptions of applications. It consists of Parts III to VI:

- III. Differential GPS and integrity Monitoring
- IV. Integrated Navigation Systems
- V. GPS Navigation Applications
- VI. Special Applications

Parts III and IV expand on GPS with explanations of supplements and augmentations to the system. The supplements enhance accuracy, availability, or integrity. Of special interest is differential GPS which has proven it can provide sub-meter (even centimeter) level accuracies in a dynamic environment. The last two sections (V and VI) are detailed descriptions of the major applications in current use. In the rapidly expanding world of GPS, new uses are being found all of the time. We sincerely hope that these volumes will accelerate such new discoveries.

Acknowledgments

Obviously this book is a group undertaking with many, many individuals deserving of our sincere thanks. In addition to the individual authors, we would especially like to thank Ms. Lee Gamma, Mr. Sam Pullen, and Ms. Denise Nunes. In addition, we would like to thank Mr. Gaylord Green, Dr. Nick Talbot, Dr. Gary Lennon, Ms. Penny Sorensen, Mr. Konstantin Gromov, Dr. Todd Walter, and Mr. Y. C. Chao.

Special Acknowledgment

We would like to give special acknowledgment to the members of the original GPS Joint Program Office, their supporting contractors and the original set of engineers and scientists at the Aerospace Corporation and at the Naval Research Laboratory. Without their tenacity, energy, and foresight GPS would not be.

B. W. Parkinson
J. J. Spilker Jr.
P. Axelrad
P. Enge

Table of Contents

Chapter 1

Introduction and Heritage of NAVSTAR, the Global Positioning System

Bradford W. Parkinson*
Stanford University, Stanford, California 94305

I. Background and History

FOR six thousand years, humans have been developing ingenious ways of navigating to remote destination. A fundamental technique developed by both ancient Polynesians and modern navies is the use of *angular measurements* of the natural stars. With the development of radios, another class of navigation aids was born. These included radio beacons, vhf omnidirectional radios (VORs), long-range radio navigation (LORAN), and OMEGA. With yet another technology—artificial satellites—more precise, *line-of-sight* radio navigation signals became possible. This promise was realized in the 1960s, when the U.S. Navy's Navigation Satellite System (known as Transit) opened a new era of navigation technology and capability. However, the best was yet to come.

Over a long Labor Day weekend in 1973, a small group of armed forces officers and civilians, sequestered in the Pentagon, were completing a plan that would truly revolutionize navigation. It was based on radio ranging (eventually with *millimeter precision*) to a constellation of artificial satellites called NAVSTARs. Instead of *angular measurements* to natural stars, greater accuracy was anticipated with *ranging measurements* to the artificial NAVSTARs.

Although it has taken over twenty years to establish that system and to realize its implications fully, it is now apparent that a new *navigation utility* has been created. For under a thousand dollars (price rapidly decreasing), anyone, anywhere in the world, can almost instantaneously determine his or her location in three dimensions to about the width of a street.

This book explains the technology, the performance, and the applications of this new utility—the Global Positioning System (GPS). "*With the quiet revolution of NAVSTAR, it can be seen that these potential uses are limited only by our imaginations.*"[1]

*Professor, Department of Aeronautics and Astronautics, and Director, GPS Program.

A. Predecessors

By 1972, the U.S. Air Force and Navy had for several years been competitively studying the possibility of improved navigation from space. These studies became the basis for a new synthesis known as NAVSTAR or the GPS. A brief discussion of the predecessor systems is followed by a description of the Air Force's development program and a summary of the technical design (which is expanded further in succeeding chapters).

1. Applied Physics Laboratory's Transit: Navy Navigation Satellite System

The first operational satellite-based navigation system was called NNSS (Navy Navigation Satellite System), or Transit. Developed by the Johns Hopkins Applied Physics Laboratory (APL) under Dr. Richard Kershner, Transit was based on a user measuring the Doppler shift of a tone broadcast at 400 MHz by polar orbiting satellites at altitudes of about 600 nautical miles (actually, two frequencies were transmitted to correct for ionospheric group delay).

The tone broadcast by Transit was continuous. The maximum rate of change in the Doppler shift of the received signal corresponded to the point of closest approach of the Transit satellite. The difference between "up" Doppler and "down" Doppler can be used to calculate the *range to the satellite at closest approach.* Users with known altitude (e.g. sea level) and the broadcast ephemeris of the satellite could use these Doppler measurements to calculate their positions to a few hundred meters. Of course, corrections had to be made for the user's velocity. Because of this velocity sensitivity and the *two*-dimensional nature, Transit was not very useful for air applications. Another limitation was the intermittent availability of the signals, because mutual interference restricted the number of satellites available worldwide to about five. This limited coverage had unavailability periods of 35 to 100 min.

Originally intended as a system to help U.S. submarines navigate, Transit was soon adopted extensively by commercial marine navigators. Although Transit is still operational, new satellites are no longer being launched, and the Federal Radionavigation Plan has announced the intent to phase it out.

Technology developed for Transit has proved to be extremely useful to GPS. Particularly important were the satellite prediction algorithms developed by the Naval Surface Warfare Center. Transit also proved that space systems could demonstrate excellent reliability. After initial "infant mortality" problems, an improved version exhibited operational lifetimes exceeding its specifications by two or three times. In fact, a number of these valuable spacecraft have lasted more than 15 years.

2. Naval Research Laboratory's Timation Satellites

By 1972, another Navy satellite system was extending the state of the art by orbiting very precise clocks. Known as *Timation,*[2] these satellites were developed under the direction of Roger Easton at the Naval Research Laboratory (NRL). They were used principally to provide very precise time and time transfer between various points on the Earth. In addition, they could provide navigation information. The ranging signals used a technique called *side-tone ranging,* which broadcast a variety of synchronized tones to resolve phase ambiguities.

Initially these spacecraft used very stable *quartz-crystal oscillators;* later models were to orbit the first *atomic frequency standards* (rubidium and cesium). The atomic clocks typically had a frequency stability of several parts in 10^{12} (per day) or better. This frequency stability greatly improves the prediction of satellite orbits (ephemerides) and also extends the time between required control segment updates to the GPS satellites. Timation satellites were flown in inclined orbits: the first two at altitudes of 500 nautical miles and the last in the series at 7500 nautical miles. The third satellite was also used as a technology demonstrator for GPS (see Fig. 1). This pioneering work in space-qualified time standards was an important foundation for GPS.

3. *U.S. Air Force Project 621B*

The third essential foundation for GPS was a U.S. Air Force program known as 621B. This program was directed by an office in the Advanced Plans group at the Air Force's Space and Missile Organization (SAMSO) in El Segundo, California. By 1972, this program had already demonstrated the operation of a new type of satellite-ranging signal based on pseudorandom noise (PRN). The signal modulation was essentially a repeated digital sequence of fairly random bits—ones or zeros—that possessed certain useful properties. The sequence could be easily generated by using a shift register or, for shorter codes, simply by storing the entire sequence of bits. A navigation user could detect the start

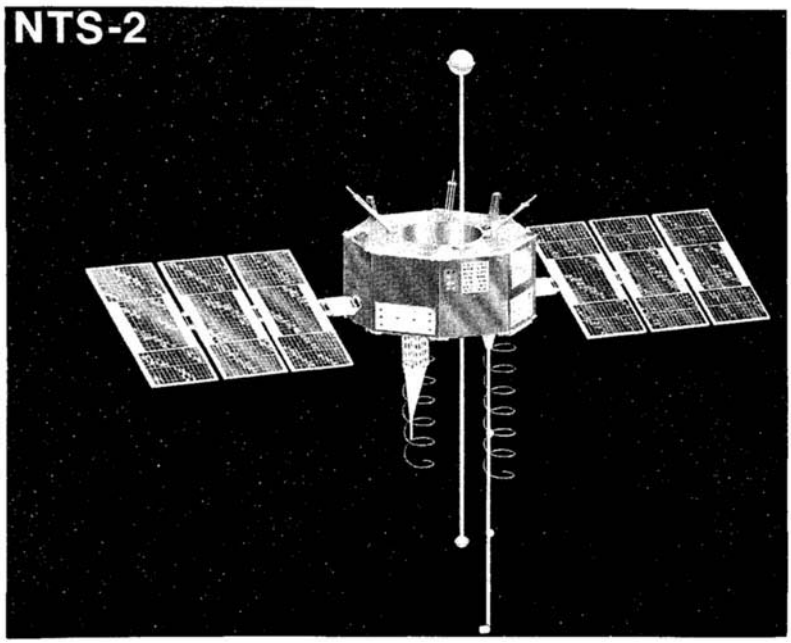

Fig. 1 Navigation technology Satellite II (NTS-II). This satellite was launched as part of the joint program effort to develop reliable spacecraft atomic clocks. NRL called this satellite Timation III (drawing courtesy of NRL).

("phase") of the repeated sequence and use this for determining the range to a satellite. The signals could be detected even when their power density was less than 1/100th that of ambient noise, and *all satellites could broadcast on the same nominal frequency* because properly selected PRN coding sequences were nearly orthogonal. Successful aircraft tests had been run at Holloman AFB to demonstrate the PRN technique. The tests used simulated satellite transmitters located on the floor of the New Mexican desert.

The ability to reject noise also implied a powerful ability to reject most forms of jamming or deliberate interference. In addition, a communication channel could be added by inverting the whole sequence at a slow rate and using these inversions to indicate the ones or zeros of digital data. This slow communication link (50 b/s) allowed the user to receive ephemeris (satellite location) and clock information.

The original Air Force concept visualized several constellations of highly eccentric satellite orbits with 24-h periods. Alternative constellations were nicknamed the *egg-beater, the rotating X and the rotating Y configurations* because of their resulting ground traces. Although these designs allowed the system to be deployed gradually (for example, North and South America first) they had high line-of-sight accelerations. Initially, the concept relied on continuous measurement from the ground to keep the signals time-synchronized. Later, the NRL clock concept was added because the synchronizing link would have been quite vulnerable. The GPS did substitute the Timation clocks later to remove any reliance on continuous ground contact.

B. Joint Program Office Formed, 1973

In the early 1970s, a number of changes in the systems acquisition process had begun to be adopted for the Department of Defense. These changes, recommended by David Packard, were to have a profound effect on NAVSTAR and other major DOD programs. To increase efficiency and reduce interservice bickering, "joint" programs were formed that forced the various services to work together. The GPS was one of the earliest examples. It was decreed to be a Joint Program, with a Joint Program Office (JPO) located at the Air Force's Space and Missile Organization and to have multiservice participation (with the Air Force as the lead service).

The first program director was Dr. (Col.) Bradford W. Parkinson (see Fig. 2), supported by Deputy Program directors—eventually from the Army, Navy, Marine Corps, Defense Mapping Agency, Coast Guard, Air Logistics Command, and NATO. Also continuing their support of 621B was a small cadre of engineers from the Aerospace Corporation under Mr. Walter Melton. Dr. Parkinson was directed to develop the initial concept as a joint development and to gain approval of the Department of Defense to proceed with full-scale demonstration and development.

There have been many speculations on the origin of the names Global Positioning System, and NAVSTAR. The GPS title originated with General Hank Stehling who was the Director of Space for the U.S. Air Force DCS Research and Development (R&D) in the early 1970s. He pointed out to Dr. Parkinson that "navigation" was an inadequate descriptor for the proposed concept. He suggested that "Global

Fig. 2 Joint program included deputy directors from all services. Dr. (Colonel) Parkinson is in discussions with his Navy Deputy, Cdr. Bill Huston of the U.S. Navy. Models of the NTS-II and Phase one GPS satellites are on the table. The civilian is Mr. Frank Butterfield of the Aerospace Corporation (photo courtesy of the U.S. Air Force).

Positioning System" would be a better name. The JPO enjoyed his sponsorship, and this insightful description was immediately adopted.

The title NAVSTAR came into being in a somewhat similar manner. Mr. John Walsh [an Associate Director of Defense Development, Research, and Engineering (DDR&E)] was a key decision maker when it came to the budget for strategic programs in general, including the proposed satellite navigation program. In the contention for funding, his support was not as fervent as the JPO would have liked. During a break in informal discussions between Mr. John Walsh and Col. Brent Brentnall (the program's representative at DOD), Mr. Walsh suggested that NAVSTAR would be a nice sounding name. Colonel Brentnall passed this along as a good idea to Dr. Parkinson, noting that if Mr. Walsh were to name it, he would undoubtedly feel more protective toward it. Dr. Parkinson seized the opportunity, and ever since the program has been known as NAVSTAR the Global Positioning System. Although some have assumed that NAVSTAR was an acronym, in fact, it was simply a nice sounding name* that enjoyed the support of a key DOD decision maker.

*We should note that TRW apparently had advocated a navigational system for which NAVSTAR was an acronym (*NAV*igation *S*ystem *T*iming *A*nd *R*anging). This may have been in Mr. Walsh's subliminal memory, but was not part of the process. It was never used as an acronym.

1. *Failed Defense System Acquisition and Review Council*

Fortunately, the first attempt to gain system approval failed in August 1973. The program that was brought before the Defense System Acquisition and Review Council (DSARC) at that time was not representative of a joint program. Instead it was packaged as the 621B system. Dr. Malcolm Currie,* then head of DDR&E, expressed strong support for the idea of a new satellite-based navigation system, but requested that the concept be broadened to embrace the views and requirements of all services.

2. *Synthesis of a New System*

With this philosophy, Dr. Parkinson and the Joint Program Office immediately went to work. Over the Labor Day weekend of 1973, he assembled about a dozen members of the JPO on the fifth floor of the Pentagon. He directed the development of a new design that employed the best of all available satellite navigation system concepts and technology. The result was a system proposal that was not exclusively the concept of any prior system but rather was a synthesis of them all. The details of the proposed GPS are outlined below. Its multiservice heritage precluded any factual basis for further bickering, because all contending parties now were part of the conception process. From that point forward, the JPO acted as a multiservice enterprise, with officers from all services attending reviews and meetings that had previously been "Air Force only."

3. *Approval to Proceed with GPS*

To gain approval for the new concept, Dr. Parkinson began to contact all those with some stake in the decision. After interminable rounds of briefings† on the new approach were given to offices in the Pentagon and to the operating armed forces, a successful DSARC was held on 17 December 1973. Approval to proceed was granted.

The first phase of the program included four satellites (one was the refurbished qualification model), the launch vehicles, three varieties of user equipment, a satellite control facility, and an extensive test program. By June of 1974, the

*Dr. Currie was appointed head of DDR&E in early 1973, as part of the incoming administration. He had been living in Los Angeles prior to his appointment and to complete his move he made numerous trips to Los Angeles in the initial months. One legitimate official purpose of these trips was to review programs at SAMSO. After a few trips, he had done all the high-level reviews that were available, so the head of SAMSO, General Schultz, suggested that he receive an indepth review by Dr. (Col.) Parkinson on the space-based navigation concept, then known as 621B. This resulted in a remarkable meeting with the number-three man in all of the U.S. DOD spending about three hours in a small office with a lowly Colonel, talking about engineering, technology, and the wide applications of the proposed system. With his doctorate in Physics, Mal Currie was a keen and quick study. He had a great deal of space experience from his years at Hughes Aircraft. The outcome was that the GPS program enjoyed his steadfast support. Without this key decision maker, the Air Force would have killed the program in favor of additional airplanes. The pivotal (and coincidental) meeting with Dr. Parkinson was destined to be an essential factor in gaining system approval.

†Lt. General Ken Schultz was particularly incensed with the endless presentations that had to be made in the Washington arena. The situation with any bureaucracy is that many can say no, and few (if any) can say yes. To bring the naysayers to neutral, the extended trips from Los Angeles to Washington were necessary for Dr. Parkinson.

satellite contractor, Rockwell International, had been selected, and the program was well underway. The initial types of user equipment included sequential and parallel military receivers, as well as a civil type set for utility use by the military. The development test and evaluation was extensive, with a laser-tracking range set up at the Army's Yuma Proving Ground. An independent evaluation was performed by the Air Force's Test and Evaluation Command.

To maintain the focus of the program the JPO adopted a motto:

> The mission of this Program is to:
> 1. Drop 5 bombs in the same hole, and
> 2. Build a cheap set that navigates (<$10,000),
> and don't you forget it!

The program developed rapidly; the first operational prototype satellite was launched in February of 1978 (44 months after contract start). By this time, the initial control segment was deployed and working, and five types of user equipment were undergoing preliminary testing at the Yuma Proving Ground. The initial user equipment types had been expanded to include a 5-channel set developed by Texas Instruments and a highly jam-resistant set developed by Rockwell Collins.

4. *Needed: A Few More Good Satellites*

As stated, only four satellites were initially approved by the DOD, including a refurbished qualification model (see Fig. 3). It became apparent that there was a need for additional satellites, because the minimum number for three-dimensional navigation is four. Any launch or operational failure would have gravely impacted the Phase I demonstration program. Authorization for spare GPS satellites was urgently needed.

The Navy's Transit program inadvertently solved this problem. The chain of events began when Transit requested funds for upgrading certain Transit satellites to a PRN code similar to that used by GPS. The purpose was to provide accurate tracking of the Trident (submarine launched missile) booster during test firings into the broad ocean areas. Dr. Bob Cooper of DDR&E requested a series of reviews to address whether GPS could fulfill this mission.

The GPS solution was to use a signal translator on the Trident missile bus that would relay the GPS modulations to the ground on another frequency. The central issues were whether the ionosphere could be adequately calibrated (because it was a single-frequency system, the ionosphere could not be directly measured), and whether the translated signal could be recorded with sufficient fidelity (it required digitizing at 60 MHz).

During the third and capstone review for Dr. Cooper, Dr. Parkinson (supported by Dr. Jim Spilker and Dr. Jack Klobuchar) was able to present convincing arguments that a GPS solution could solve the Trident problem *provided two additional satellites were authorized.* Dr. Cooper immediately made the decision to use GPS. He directed the transfer of $60M from the Navy to the Air Force, approving two additional satellites, and thereby greatly expanding the Phase one test time as well as significantly reducing the program risk. This little known

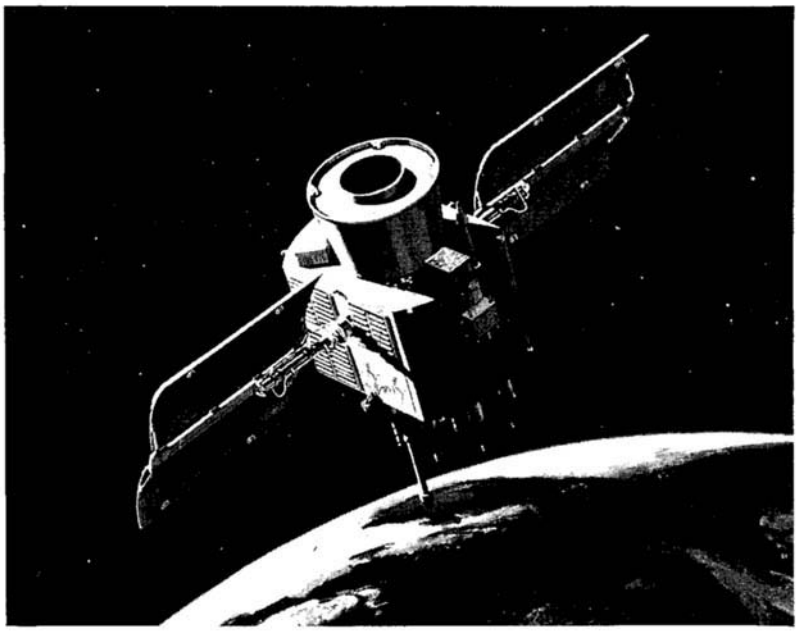

Fig. 3 Phase I GPS satellite. It is a three-axis stabilized design with double and triple redundancy where appropriate (drawing courtesy of the U.S. Air Force).

event also eliminated the possibility of an upgraded Transit program competing with the fledgling GPS.

III. Introductory GPS System Description and Technical Design

The operational GPS system of today is virtually identical to the one proposed in 1973. The satellites have expanded their functionality to support additional military capabilities; the orbits are slightly modified, but the equipment designed to work with the original four satellites would still perform that function today. The rest of this volume is devoted to detailed technical descriptions of the system and its applications; the following section provides an overview of the system design.

A. Principles of System Operation

The fundamental navigation technique for GPS is to use *one-way ranging* from the GPS satellites that are also broadcasting their estimated positions. *Ranges are measured to four satellites simultaneously in view by matching (correlating) the incoming signal with a user-generated replica signal and measuring the received phase against the user's (relatively crude) crystal clock.* With four satellites and appropriate geometry, four unknowns can be determined; typically, they are: latitude, longitude, altitude, and a correction to the user's clock. If

altitude or time are already known, a lesser number of satellites can be used (see Fig. 4).

Each satellite's future position is estimated from ranging measurements taken at worldwide monitoring stations.* These ranging measurements use the same signals that are employed by a typical user's receiver. Using sophisticated prediction algorithms, the master control station forms estimates of future satellite locations and future satellite clock corrections. For the uploads, which occur daily or (optionally) more frequently, the combined predictions for satellite clock and position have been measured to have an average rms error of 2–3 m. These estimates have demonstrated reasonable errors even after three days (24.3 m of expected ranging error).

B. GPS Ranging Signal

The GPS ranging signal is broadcast at two frequencies: a primary signal at 1575.42 MHz (L_1) and a secondary broadcast at 1227.6 MHz (L_2). These signals are generated synchronously, so that a user who receives both signals can directly calibrate the ionospheric group delay and apply appropriate corrections. However, most civilian users will only use the primary or L_1 frequency.

Potentially, both the signal at the L_1 frequency and the signal at L_2 can *each* have two modulations at the same time (called "phase quadrature"). Current

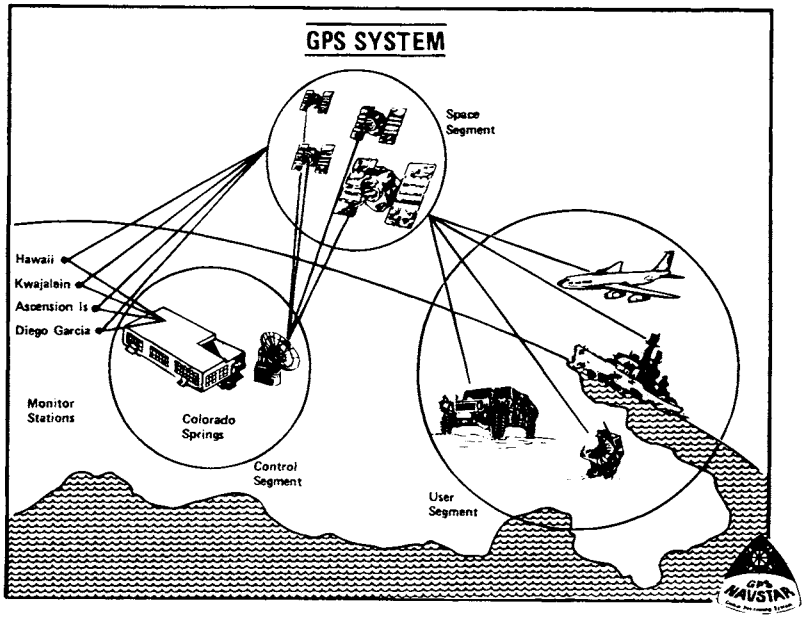

Fig. 4 System configuration of GPS showing the three fundamental segments: 1) user; 2) spacecraft; and 3) ground control (drawing courtesy of the U.S. Air Force).

*The Operational Control System (OCS) uses five monitor stations which are located at Colorado Springs, Ascension Island, Diego Garcia, Kwajalein, and Hawaii.

implementation has two modulations on the higher frequency (L_1), but only a single (protected) modulation (see below) on L_2 The two modulations are as follows:

1) C/A or Clear Acquisition Code: This is a short PRN code broadcast at a bit (or chipping) rate of 1.023 MHz. This is the principal civilian ranging signal, and it is always broadcast in the *clear* (unencrypted). It is also used to acquire the much longer P-code. The use of this signal is called the Standard Positioning Service or SPS. It is always available, although it may be somewhat degraded. At this time, and for the projected future, the C/A code is available only on L_1 (some civil users have requested C/A modulation on L_2 to allow ionospheric calibration).

2) P or Precise Code (sometimes called the Protected Code): A very long code (actually segments of a 200-day code) that is broadcast at ten times the rate of C/A, 10.23 MHz. Because of its higher modulation bandwidth, the code ranging signal is somewhat more precise. This reduces the noise in the received signal but will not improve the inaccuracies caused by biases. This signal provides the Precise Positioning Service or PPS. The military has encrypted this signal in such a way that renders it unavailable to the unauthorized user. This ensures that the unpredictable code (to the unauthorized user) cannot be spoofed. This feature is known as antispoof or AS. When encrypted, the P code becomes the Y code. Receivers that can decrypt the Y code are frequently called P/Y code receivers. As a result of the military intent, most civilian users should only rely on the C/A code or SPS.*

1. *Selective Availability*

In addition, the military operators of the system have the capability to degrade the accuracy of the C/A code intentionally by desynchronizing the satellite clock, or by incorporating small errors in the broadcast ephemeris. This degradation is called *Selective Availability, or S/A.* The magnitude of these *ranging* errors is typically 20 m, and results in rms *horizontal position* errors of about 50 m, one sigma. The official DOD position is that errors will be limited to 100 m, 2 drms, which is about the 97th percentile. A technique known as differential GPS (explained later) can overcome this limitation and potentially provide accuracies sufficient for precision approach of aircraft to landing fields.

2. *Data Modulation*

One additional feature of the ranging signal is a 50 b/s modulation used as a communications link. Through this link, each satellite transmits its location and the correction necessary to apply to the spaceborne clock.† Also communicated are the health of the satellite, the locations of other satellites, and the necessary information to lock on to the P code after acquiring the C/A code.

*There are provisions in the Federal Radionavigation Plan for civilian users with critical national needs to gain access to the P code.

†Although the atomic clocks are extremely stable, they are running in an uncorrected mode. The clock correction is an adjustment that synchronizes all clocks to GPS time.

C. Satellite Orbital Configuration

The orbital configuration approved at DSARC in 1973 was a total of 24 satellites—eight in each of three circular rings with inclinations of 63 deg. The rings were equally spaced around the equator, and the orbital altitudes were 10,980 n.mi. This altitude gave two orbital periods per sidereal day (known as *semisynchronous*) and produced repeating ground traces. The altitude was a compromise among: user visibility, the need to pass over the continental U.S. ground/upload stations periodically, and the cost of the spacecraft launch boosters. Three rings of satellites were initially selected because it would be easier to have orbital spares—only three such spares could easily replace any single failure in the whole constellation. This configuration provided a minimum of six satellites in view at any time, with a maximum of 11. As a result of this redundancy, the system was robust in the sense that it could tolerate occasional satellite outages (see Fig. 5).

Two changes have been made since the original constellation proposal. The inclinations have been reduced to 55 deg, and the number of orbital planes have been increased to six,* with four satellites in each. The number of satellites, including spares, remains 24.

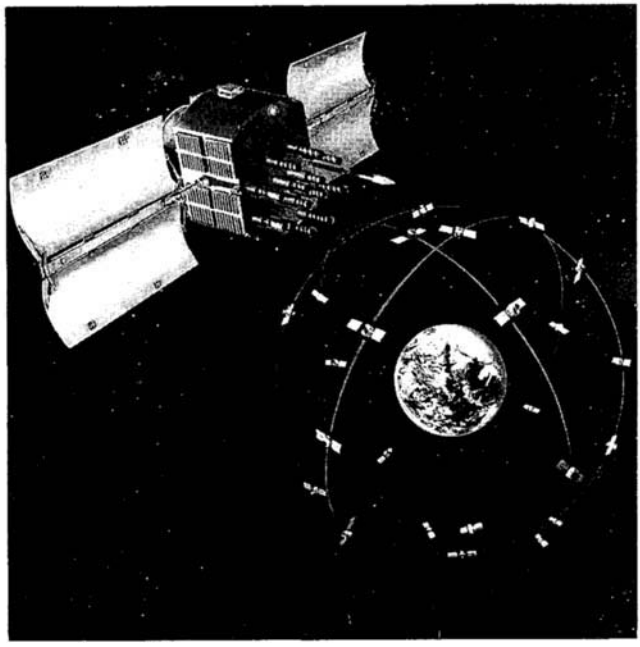

Fig. 5 Original GPS orbital configuration of three rings of eight satellites each. The final operational configuration has the same number of satellites, arranged in six rings of four satellites (drawing courtesy of the U.S. Air Force).

*For a number of reasons, the Department of Defense calls the configuration "21 satellites with three orbiting spares." We may find the system eventually having more satellites to increase robustness.

D. Satellite Design

The GPS satellites are attitude stabilized on all three axes and use solar panels for basic power (see Fig. 6). The ranging signal is radiated through a shaped beam antenna—by enhancing the received power at the limbs of the Earth, compensation is made for "space loss." The user, therefore, receives fairly constant power for all local elevation angles.* The satellite design is generally doubly or triply redundant, and the Phase I satellites demonstrated average lifetimes in excess of 5 years (and in some cases over 12).

E. Satellite Autonomy: Atomic Clocks

A key feature of the GPS design is that the satellites need not be continuously monitored and controlled. To achieve this autonomy, the satellites must be predictable in four dimensions: three of *position* and one of *time.* Predictability, in the orbital *position,* is aided because the high-altitude orbits are virtually unaffected by atmospheric drag. Many other factors which affect orbital position must also be considered. For example, variations in geopotential, solar pressure, and outgassing can all have significant effects.

When GPS was conceived, it was recognized that the most difficult technology problem facing the developers was probably the need to fly accurate timing

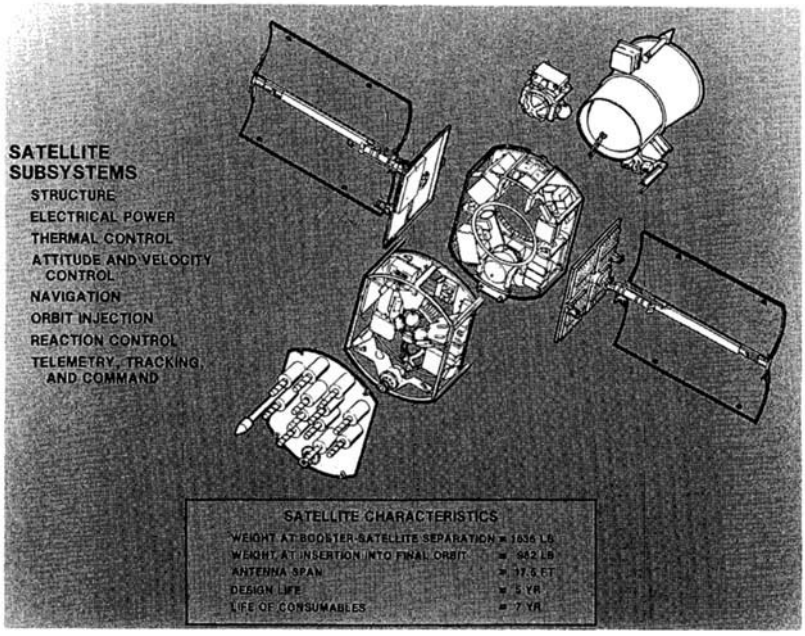

Fig. 6 Breakaway view of the GPS Phase I satellite design (drawing courtesy of the U.S. Air Force).

*The requirement for received power on L_1 is -163 dbw into an isotropic, circularly polarized antenna on the primary frequency.

standards, insuring that all satellites' clocks remained synchronized. As mentioned, NRL had been developing frequency standards for space, so this effort was continued and extended.

Payoff of a Good Clock

The basic arithmetic can be understood as follows: A day is about 100,000 s, or 10^5. Light travels about 1 ft per ns (10^{-9} s). If the system can tolerate an error buildup caused by the atomic clock of 5 ft, the stability must be 5 ns per upload (one-half a day). This is about $(5*10^9)/(5*10^4)$ sps, measured over 12 h. Therefore, this requirement is for a clock with about one part in 10^{13} stability,* which can only be met by an atomic standard. Note that there is a roughly constant frequency shift attributable to relativistic effects (both special and general) of about 4.5 parts in 10^{10}, which is compensated by a deliberate offset in the clock frequency.

GPS traditionally has used two types of atomic clocks: rubidium and cesium. Phase one test results for the rubidium cell standard are shown in Fig. 7. A key to outstanding satellite performance has been the stability of the space-qualified atomic clocks, which exceeded the specifications. They have measured stabilities of one part in 10^{13} over periods of 1–10 days.[3]

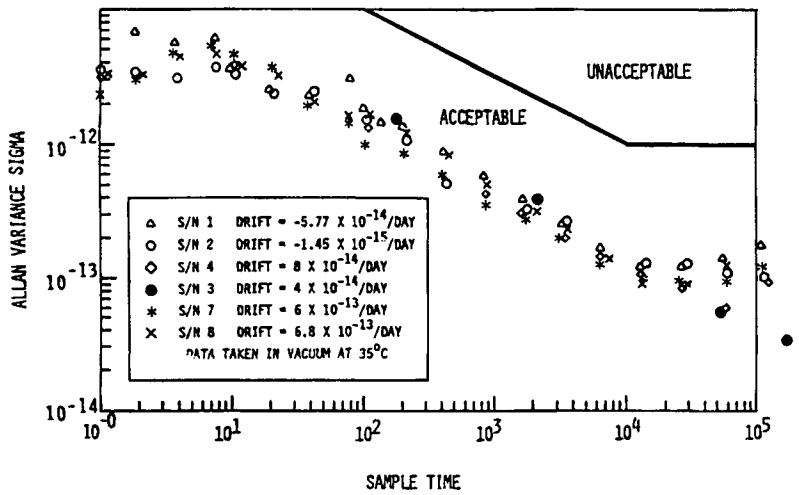

Fig. 7 Space qualified rubidium-cell frequency standard performance. These units were developed by Rockwell as a derivative of a clock designed by Efratom, Inc. (data courtesy of the U.S. Air Force).

*Clock stability is traditionally measured with the Allen variance, which shows stability versus averaging time. For short averaging times (1 s) virtually all clocks are dominated by the quartz oscillator, which acts as the short-term flywheel. In Phase one, the clocks were specified at 10^{-12}, measured over 1 day.

F. Ionospheric Errors and Corrections

The free electrons in the ionosphere create a delay in the modulation signal (PRN code). This delay is proportional to the integrated number of free electrons along the transmission path and inversely proportional to the square of the transmission frequency (to first order). The path delay at any elevation angle is often expressed as the product of a zenith delay (elevation equals 90 deg) and an *obliquity* factor that is a function of that elevation angle. This ratio ranges from 1.0 at the zenith (by definition) to about 3.0 at small elevation angles. Typical zenith (or vertical) delays range from a few meters at night to a maximum of ten or twenty meters at about 1400 hours (local solar time). Thus, it is not unusual to find delays of over 30 m at lower elevation angles. Fortunately, these delays are highly correlated between satellites, which helps reduce the calculated horizontal position errors.*

There are two techniques for correcting this error. The first is to use an ionosphere model. The 8-model parameters used to calculate the correction are broadcast as part of the GPS 50 b/s message. This model is typically accurate to a few meters of vertical error.

The second technique uses both broadcast frequencies and the inverse square law behavior to measure the delay directly. By differencing the code measurements on each frequency, the delay on L_1 is approximately 1.546*(difference in delays on L_1 and L_2). This technique is only available to a P/Y-code receiver (because the only L_2 modulation is the P code) or to a codeless (or cross-correlating) receiver.

G. Expected Navigation Performance

The performance capabilities of GPS are primarily affected by two things: 1) the *satellite geometry* (which causes *geometric dilution*); and 2) the *ranging errors*. Under the assumption of uniform, uncorrelated, zero-mean, ranging-error statistics, this can be expressed as follows:

RMS position error = (Geometric dilution)*(rms ranging error)

1. *Geometric Dilution*

The geometric dilution can be calculated for any instantaneous satellite configuration, as seen from a particular user's location. The details of this calculation are explained in Chapters 6 and 11, this volume. For a 21-satellite constellation and a three-dimensional fix, the world median value of the geometric dilution factor (for the nominal constellation) is about 2.7. This quantity is usually called PDOP or position dilution of precision. Typical dilution factors range from 1.5 to 8. The *variations* in this *dilution factor* are typically much greater than the variations in ranging errors.

*This correlation of errors due to the ionosphere will mostly show up as a user clock error. While this is not important for many navigation users, it is critical for the precise transfer of time. Such users must employ the dual frequency technique to eliminate this error.

2. *Ranging Errors*

Ranging errors are generally grouped into the following six major causes:

1) Satellite ephemeris
2) Satellite clock
3) Ionospheric group delay
4) Tropospheric group delay
5) Multipath
6) Receiver measurement errors, including software

Some of these errors tend to be correlated for the same satellite. For example, satellite clock and ephemeris errors tend to be negatively correlated; i.e. they tend to cancel each other somewhat. Other errors tend to be correlated between satellites. For example, the ionospheric and tropospheric group delays always have the same sign, because they are the result of signal paths penetrating the *same blanket of media* with different angles.

With S/A turned off, all errors for *single frequency* SPS are nearly *identical* in magnitude to those for *single-frequency PPS* except for receiver measurement errors (which decrease with increasing bandwidth). *Dual* frequency, which is only available on PPS, can reduce the third error (attributable to the ionosphere) to about 1 m.*

3. *Precise Positioning Service (PPS) Accuracy*

Ranging errors (including the effects of the satellite clock)[3] for the PPS have been *specified* to be better than 6 m. The product of the average PDOP and the ranging error is the specified three-dimensional accuracy of 16 m spherical error probable (SEP).†

Because each of the five worldwide monitoring stations is continuously measuring the ranging errors to all satellites in view, these measurements are a convenient statistic of the basic, static accuracy of GPS. Table 1 summarizes over 11,000 measurements taken from 15 January to 3 March 1991, during the "Desert Storm" operation of the Gulf War. The S/A feature was not activated during this period. Note that the PPS results presumably are not affected by S/A at all.

During this period, satellite (PRN 9) was ailing but is included in the solution, making the results somewhat worse than would be expected. By dividing the overall SEP by the rms PDOP, an estimate of the effective ranging error can be formed. The average of these results is 2.3 m.‡ This should be compared to the specification of 6 m. Because SEP is smaller than the RMS error, this estimate may be about 15% optimistic.

---

*Multipath errors are generally negligible for path delays that exceed one-and-one-half modulation chips, expressed as a range. Thus, P-code receivers reject reflected signals whose path delay exceeds 150 feet. For the C/A code, the number is 1500 feet, giving a slight advantage to the P code, although it is usually reflections from very close objects that are the main source of difficulty.

†SEP is the radius of the sphere that will contain 50% of the expected errors in three dimensions.

‡This number is probably somewhat better than an average receiver would measure for several reasons. Monitor station receivers are carefully sited to avoid multipath. The receivers are of excellent quality and are not moving. Also, since the monitor station measurements are used to update the ephemeris, there may be some tuning to make the predictions match any peculiarities (e.g. survey errors) at the monitor station locations. Nonetheless, an average ranging error of 2.3 m is an impressive result.

Table 1 PPS measured accuracies; SEP/CEP[a] navigation errors; PPS solutions for the OCS monitor stations during Desert Storm; S/A is off.[4]

Criteria	All	Colorado Springs	Ascension	Hawaii	Diego Garcia	Kwajalein
SEP three-dimensional, m	8.3	7.8	6.8	9.0	9.1	9.0
CEP two-dimensional, m	4.5	4.5	3.8	5.1	4.6	5.0
rms PDOP	3.6	3.9	3.4	3.9	3.4	3.3
Estimated range error, m[b]	2.3	2.0	2.0	2.3	2.7	2.7

[a] CEP is circular error probable, which equals the radius of a circle that would contain 50% of the errors. It is the two-dimensional analog of SEP.
[b] This row is formed by dividing the SEP by the rms PDOP.

Table 2 Expected accuracies for various operating conditions of GPS

	Precise positioning service (PPS)		Standard positioning, service (SPS), estimated capability	
	Specification	Measured, static	No S/A	With S/A
Ranging accuracy	6 m	2.3 m	6 m	20 m
CEP (horizontal)	——	4.6 m	12 m	40 m
SEP (three-dimensional)	——	8.3 m[a]	22 m	72 m

[a] The SEP reported for dynamic PPS users was less than 10 m. See Ref. 5.

a. SPS accuracy. Without the degradation of S/A, the SPS would provide solutions with about 50% greater error because of uncompensated ionospheric effects and somewhat greater receiver noise (because of the narrower band C/A code). *It is reasonable to expect that rms horizontal errors for SPS with S/A off would be less than 10 m.*

b. Accuracy summary for code-tracking receivers. Table 2 summarizes the expected accuracies for GPS.

H. High Accuracy/Carrier Tracking

A special feature of GPS, which initially was not generally understood, is the ability to create an extremely precise ranging signal by reproducing and tracking the rf carrier (1575.42 MHz). Because this signal has a wavelength of 19 centimeters (7.5 inches), tracking it to 1/100th of a wavelength provides a precision of about 2 mm. Modern receivers can attain these tracking precisions, but unfortunately, this is not *accuracy.* To provide equivalent accuracy, we must determine which carrier cycle is being tracked (relative to the start of modulation) and compare this with another carrier tracking receiver located at a known position.

Surveyors use a technique of double or triple differencing to resolve this *cycle ambiguity.* For dynamic users, the problem is a bit harder. Reflected signals (multipath) and distortions of the ionosphere can be significant errors.

Generally, the carrier-tracking techniques can be used in two ways. For normal use, the carrier tracking can smooth the code tracking and greatly reduce the noise content of the ranging measurement. The other use is in a differential mode for which there are several variations, including surveying, direct measurement of vehicle attitude (with multiple antennas), and various forms of dynamic differential. The GPS control segment uses accumulated delta range (ADR) as the measurement for the monitor stations. This is done with incremental counts of carrier cycles. Later chapters in this volume discuss these techniques in greater detail.

III. History of Satellites

Five groups (or blocks) of satellites have been developed for the GPS program. In chronological order they are: 1) Navigation technology satellites (NTS); 2) navigation development satellites—Block I or NDS; 3) block II satellites; 4) block IIA satellites; and 5) block IIR satellites. In addition, a follow-on group, called block IIF, is being planned.

A. Navigation Technology Satellites

The satellites of the first group were used to explore space technology. They were an extension of the Timation program of the NRL and were known as NTS, or, Navigation Technology Satellites. The first, NTS-1, had been planned as Timation II and was renamed when the JPO was formed. It was launched into a lower orbit than GPS (7500 n.mi.) on the 14th of July 1974. It was the first to fly atomic clocks: two rubidium oscillators were included. The second (and last) of the series, NTS-2, orbited a number of payload components that were identical to the development GPS satellites. This satellite included the first cesium clock in space, the PRN code generator used in the next block, and the first GPS spaceborne computer. The last two items were developed by Rockwell International under the JPO.

B. Navigation Development Satellites—Block I

These pioneering satellites were developed by Rockwell International for the JPO. The initial buy was for four, followed by two additional to support the Trident program. Later, six more were purchased as replacements. Of the 11 satellites that made it into orbit, all achieved initial operational capability. The sole premature failure in these satellites [in all, the satellites launched through the initial Operational capability (IOC)] was caused by the malfunction of a refurbished Atlas-F booster at Vandenberg. The first launch was on the 22nd of February 1978, 44 months after contract award. Designed for 3-year lifetimes, several operated for over 10 years.

C. Operational Satellites—Block II and IIA

In all, 29 satellites have been produced and are on orbit or ready to launch. The first satellite in this series was declared operational on the 10th of August

1989. These satellites were initially launched at a rate of about six per year. Initial operational capability was declared at the end of 1993, with full operational capability (FOC) attained by the end of 1994.

D. Replacement Operational Satellites—Block IIR

These are enhanced performance GPS satellites being developed by Martin Marietta (after buying out the division from GE, which bought it from RCA). The contract was awarded on 21 June 1989 for 20 satellites, with options for 6 more. The first delivery is planned for 1995. These satellites have enhanced autonomy, including the capability to meet a degraded range error specification of up to 180 days since the last ground control segment upload. They also have increased hardening against natural and man-made radiation.

IV. Launches

A. Launch Vehicles

The 12 original (Phase I) satellites were to be launched on refurbished Atlas-F ICBMs (see Fig. 8). The initial plan was to use the McDonnell-Douglas Delta for the next series of launches (Phase II). About 1979, this was changed, and the shuttle was decreed to be the booster of choice for Air Force missions. The

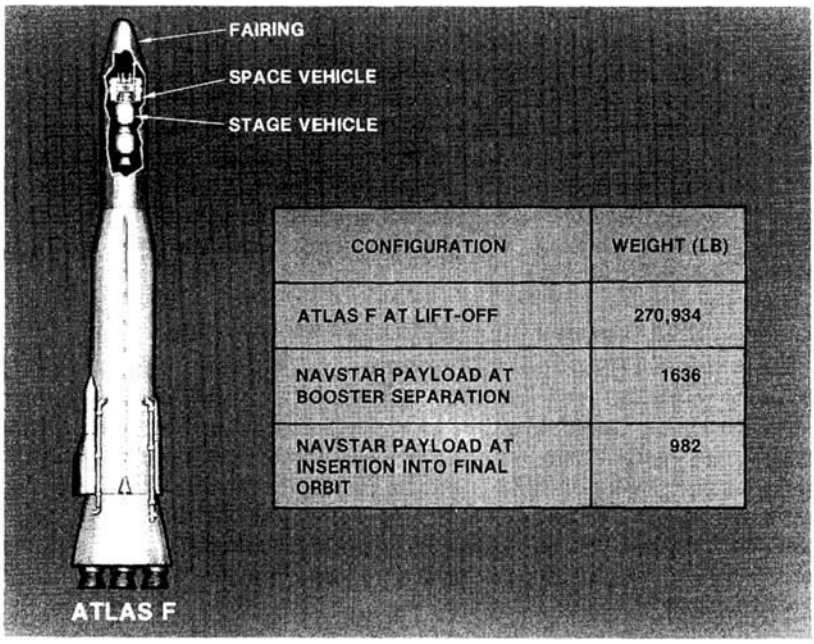

CONFIGURATION	WEIGHT (LB)
ATLAS F AT LIFT-OFF	270,934
NAVSTAR PAYLOAD AT BOOSTER SEPARATION	1636
NAVSTAR PAYLOAD AT INSERTION INTO FINAL ORBIT	982

Fig. 8 Refurbished Atlas F launch vehicle used for the first 12 launches. The stage vehicle was a tandem (stacked) solid rocket configuration (drawing courtesy of the U.S. Air Force).

Table 3 History of initial GPS launches through IOC

Block II seq.	SVN	PRN, code	Internat. ID	NASA catalog number[a]	Orbit plane pos'n.[b]	Launch date, UTC	Clock[c]	Available	Decommissioned
Block I									
——	01	04	1978-020A	10684	——	78-02-22	——	78-03-29	85-07-17
——	02	07	1978-047A	10893	——	78-05-13	——	78-07-14	81-07-16
——	03	06	1978-093A	11054	——	78-10-06	——	78-11-13	92-05-18
——	04	08	1978-112A	11141	——	78-12-10	——	79-01-08	89-10-14
——	05	05	1980-011A	11690	——	80-02-09	——	80-02-27	83-11-28
——	06	09	1980-032A	11783	——	80-04-26	——	80-05-16	91-03-06
——	07	——	——	——	——	81-12-18	Launch failure		——
——	08	11	1983-013A	14189	——	83-07-14	——	83-08-10	93-05-04
——	09	13	1984-059A	15039	C-1	84-06-13	Cs	84-07-19[d]	——
——	10	12	1984-097A	15271	A-1	84-09-08	Rb	84-10-03	——
——	11	03	1985-093A	16129	C-4	85-10-09	Rb[e]	85-10-30	——
——	——	——	——	——	——	——	——	——	——
Block II									
II-1	14	14	1989-013A	19802	E-1	89-02-14	Cs	89-04-15	——
II-2	13	02	1989-044A	20061	B-3	89-06-10	Cs	89-08-10	——
II-3	16	16	1989-064A	20185	E-3	89-08-18	Cs	89-10-14	——
II-4	19	19	1989-085A	20302	A-4	89-10-21	Cs	89-11-23	——
II-5	17	17	1989-097A	20361	D-3	89-12-11	Cs	90-01-06	——
II-6	18	18	1990-008A	20452	F-3	90-01-24	Cs	90-02-14	——
II-7	20	20	1990-025A	20533	B-2	90-03-26	Cs	90-04-18	——
II-8	21	21	1990-068A	20724	E-2	90-08-02	Cs	90-08-22	——
II-9	15	15	1990-088A	20830	D-2	90-10-01	Cs	90-10-15	——
——	——	——	——	——	——	——	——	——	——
Block IIA									
II-10	23	23	1990-103A	20959	E-4	90-11-26	Cs	90-12-10	——
II-11	24	24	1991-047A	21552	D-1	91-07-04	Cs	91-08-30	——
II-12	25	25	1992-009A	21890	A-2	92-02-23	Rb	92-03-24	——
II-13	28	28	1992-019A	21930	C-2	92-04-10	Cs	92-04-25	——
II-14	26	26	1992-039A	22014	F-2	92-07-07	Cs	92-07-23	——
II-15	27	27	1992-058A	22108	A-3	92-09-09	Cs	92-09-30	——
II-16	32	01[f]	1992-079A	22231	F-1	92-11-22	Cs	92-12-11	——
II-17	29	29	1992-089A	22275	F-4	92-12-18	Cs	93-01-05	——
II-18	22	22	1993-007A	22446	B-1	93-02-03	Cs	93-04-04	——
II-19	31	31	1993-017A	22581	C-3	93-03-30	Cs	93-04-13[g]	——
II-20	37	07	1993-032A	22657	C-4	93-05-13	Cs	93-06-12	——
II-21	39	09	1993-042A	22700	A-1	93-06-26	Cs	93-07-20	——
II-22	35	05	1993-054A	22779	B-4	93-08-30	Cs	93-09-28	——
II-23	34	04	1993-068A	22877	D-4	93-10-26	Cs	93-11-22	——
II-24	——	——	——	——	——	——	——	——	——

[a] NASA Catalog Number is also know as NORAD or U.S. Space Command object number.
[b] No orbital plane position listed = satellite no longer operational.
[c] Clock: Rb = rubidium; Cs = cesium
[d] The power supply of PRN 13 has insufficient capacity to maintain L_1/L_2 transmissions during eclipse season. During this period, the L_1/L_2 transmissions of PRN 13 may be turned off for up to 12 h a day.
[e] PRN 03 is operating on Rb clock without temperature control.
[f] The PRN number of SVN 32 was changed from 32 to 01 on 93-01-28.
[g] Corrective maintenance performed on PRN 31 on 93-06-16 seems to have fixed the L_2 intermittent-lock problem.

Block II satellites were designed to that interface. After the Challenger accident, this decision was reconsidered, and the Delta II has since been used as the GPS launch vehicle. The history and recent status of launches is shown Table 3.

V. Initial Testing

The objective of the Phase I approval of GPS was to validate the total system concept. A major stumbling block in obtaining Phase I approval was a classic bureaucratic "catch 22." The issues raised were the following: 1) How could user equipment development be approved when it wasn't clear they would work with the satellites? but ... 2) How could the satellites be launched without ensuring they would work with the user equipment? Pursued to a superficial conclusion, nothing could be done at all. The solution was adapted from the 621B program. A system of solar-powered GPS transmitters was deployed on the desert floor at the Yuma test ground. These transmitters all radiated one of the unique orthogonal GPS codes (at the approved frequencies), which were synchronized to each other and to the satellites as they were launched. These transmitters were called pseudolites (from pseudosatellites). They provided a geometry that approximated that of the satellites, although the signals were coming from negative elevation angles. The user equipment could be verified to work with satellite transmitters prior to launch.* As satellites were launched, psuedolites could be dropped from the test system; when four satellites were on orbit, the equipment was completely debugged and able to verify the claims that had been made at DSARC. This approach solved the logical impasse. The pseudolite concept was later expanded as a technique to improve accuracy and integrity for civil landing of aircraft.

This approach satisfied the doubters, and in fact significantly strengthened the program. By 1978, when the first NDS satellite was launched, the main varieties of user equipment had been validated quantitatively and qualitatively.

A. Test Results

Initial testing of user equipment included seven different types that were integrated into 11 types of land, sea, and air vehicles plus manpack testing. Literally hundreds of tests were run. Two results are presented here. Figure 9 shows the summary of integrated tests. Values of SEP† range from 6 to 16 m. The later testing in the A-6 is probably more representative of total system performance.

The blind bombing results, Fig. 10, reflect a substantial improvement because of the GPS. Radar bombing is the usual alternative in poor visibility. The results are particularly significant because the probability of a hit is usually inversely

*In fact a further cross check had been conceived and implemented by (then Major) Gaylord Green who initially ran the satellite development for the JPO. The satellite transmitter was activated during ground testing and shown to allow lock up by the phase one user equipment. Col. Green later returned to the JPO and completed a distinguished career as the Director of the GPS program.

†Spherical error probable is the radius of the sphere that contains 50% of the measured errors. The A-6, B-52, and F-16 are aircraft. The SSN is a submarine, the CV is an Aircraft Carrier. The UH-60 is a helicopter, and MV is the manpack/vehicular set test. Data for these two sets of results come from the JPO publication YEE-82-009B of September 1986, titled "User's Overview" (unclassified).

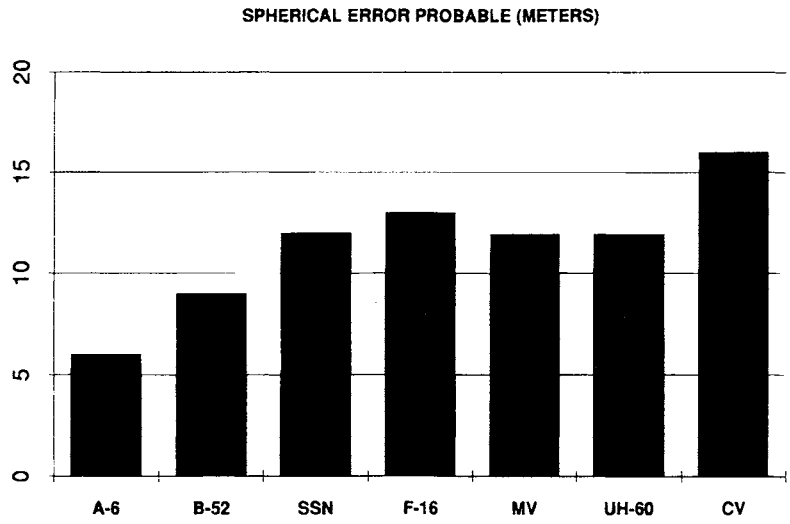

Fig. 9 Test results for seven vehicles using integrated GPS. The earliest tests are on the right and the later on the left. The improved accuracy, in part, reflects system maturity (data courtesy of the U.S. Air Force).

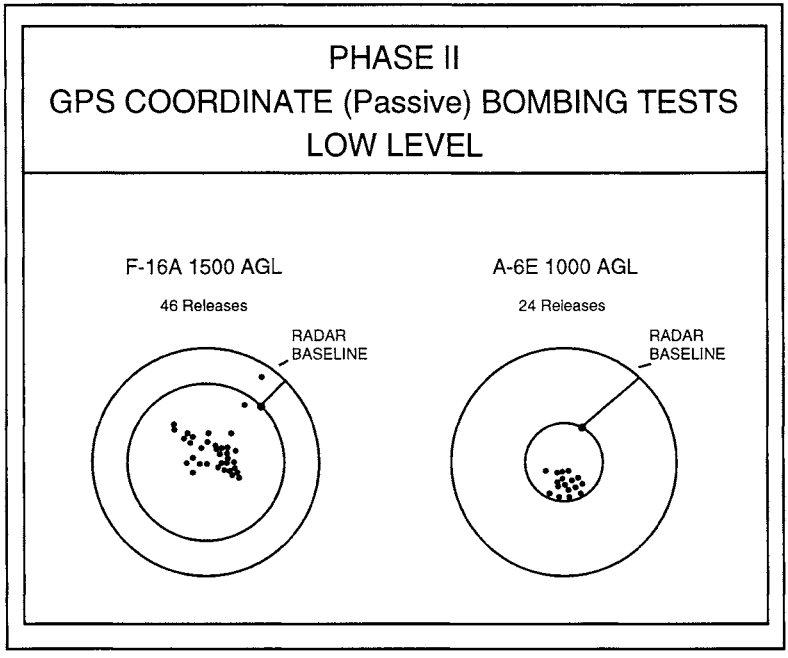

Fig. 10 GPS blind bombing results compared to radar bombing baselines (data courtesy of the U.S. Air Force).

proportional to the *square of the miss radius.* Indeed these results more than satisfied the original part of the motto that called for "five bombs in the same hole."

B. Conclusions

During its initial tests, the Global Positioning System more than met the original design objectives. The impact was not fully appreciated by the operational forces of the military until the Desert Storm battles showed the value of GPS as a force multiplier. The second half of the motto "build a cheap set ($10,000 1973 dollars) that navigates has been overtaken by the civil rush to build integrated chip sets that have driven the costs of GPS down to less than $300 in 1973 dollars. The decision to use a digitally formatted signal has also been vindicated.

VI. Applications

A. Military

The DOD's primary purposes in developing GPS were as follows: 1) its use in precision weapon delivery; and 2) providing a capability that would help reverse the proliferation of navigation systems in the military. Military applications include mine sweeping, aircraft landing, and infantry operations (to name just a few). The Desert Storm campaign was almost a boutique war to demonstrate the effectiveness of GPS. The tactical commanders were finally able to experience the power that comes from precise knowledge of position in a common coordinate frame. It was ironic that the majority of receivers being used were developed by civil companies, with no help from military sponsorship.

B. Dual Use: The Civil Problem

From the beginning of the GPS, it was recognized that the proposed GPS system would provide utility for many more users than the U.S. military. The code structure was arranged to have a precise, protected modulation (the P code), which could be encrypted, and a clear acquisition modulation (the C/A code), which could be exploited by civil users. The earliest presentations always included descriptions of the usefulness to the worldwide civil community. The applications of the GPS for the civilian community are extensive. Initially the GPS was used for accurate time transfer and survey, because these applications could accept the limited initial coverage. Later uses span marine, air, land, and even space. Civil sets currently outnumber military by more than ten to one. That ratio will probably increase as civil set cost decreases. Other chapters discuss in detail many of these applications for these civil receivers.

Table 4 summarizes some of these major civil applications.

This proliferation has led to legitimate fears that the GPS system would be used against its builders, the U.S. Military. Initially it was felt that the P code would demonstrate accuracies about seven times better than C/A.* Therefore, civil receivers would be inherently less accurate. Technology invalidated that assumption. By using carrier aiding, the noise in the C/A receivers could be

*The P code has a chip rate ten times higher, but the C/A code has approximately twice as much power.

Table 4 Some civil applications of GPS

Air navigation	Nonprecision approach and landing
	Domestic en route
	Oceanic en route
	Terminal
	Remote areas
	Helicopter operations
	Aircraft attitude
	Collision avoidance
	Air traffic control
Land navigation	Vehicle monitoring
	Schedule improvement
	Minimal routing
	Law enforcement
Marine navigation	Oceanic
	Coastal
	Harbor/approach
	Inland waterways
Static positioning and timing	Offshore resource exploration
	Hydrographic surveying
	Aids to navigation
	Time transfer
	Land surveying
	Geographical information systems
Space	Launch
	In-flight/orbit
	Reentry/landing
	Attitude measurement
Search and Rescue	Position reporting and monitoring
	Rendezvous
	Coordinated search
	Collision avoidance

smoothed to the point that receiver measurement was an insignificant error source. Anticipating the need to withhold full accuracy from an enemy, the system design had included the ability to degrade the accuracy of the satellite clock or the broadcast satellite location. This so-called selective availability is an important feature for the potential protection of the free world. However, Dr. Parkinson had argued that this capability should not be used all the time, because it could be defeated by various forms of differential (locally corrected) GPS. Degrading the signal continuously would lead to rapid introduction of improved differential techniques. It was felt to be better if S/A were only used when an urgent need was determined.

Alleviating fears of enemy use, any civil differential technique could also be countered in time of hostility by using local area jamming of the more susceptible C/A code. The military would continue to rely on the more jam resistant P code for combat operations.

This civil problem is only partially resolved. The international and civil communities have been pushing for less restrictive civil use. The U.S. government has

now agreed to provide the signal worldwide, for the foreseeable future, at the 50 m (one sigma) error level. In addition, they have agreed to give 10 years notice, should they not be able to continue to meet the commitment. Moreover, there is now a joint *military/civil* task force overseeing the operation of GPS with representatives from the departments of defense and transportation.

VII. Pioneers of the GPS

The GPS owes its existence to many foresighted and self-sacrificing people. The following list is not complete; it is hoped that those not mentioned will not feel offended. As is often the case, the engineers who took a concept and made it a reality tend to be forgotten. The writer would like to personally thank the outstanding, and dedicated men and women of the initial JPO who truly made GPS possible with their heroic efforts.

A. Defense Development, Research, and Engineering—Malcolm Currie and David Packard

A staunch and essential supporter from early 1973 was Dr. Malcolm Currie, then Deputy Secretary of Defense for Research and Engineering. In the early years, the GPS suffered because it did not have a single operational Armed Forces command that felt space-based navigation was an operational necessity. Most of the affected commands felt it was desirable, but hoped it would be sponsored (and funded) by someone else. Dr. Currie could visualize the value and threw his support into the bureaucratic fray. Without his intercession, the GPS would have been canceled before the first satellites flew.

Another pioneer—although he may not have been aware of his impact on the GPS program—was David Packard (previously Deputy Secretary of Defense for Research and Engineering). Mr. Packard had brought significant reforms to the DOD decision-making process. This streamlining included brief (7-page) decision coordinating papers (DCP) and crisp decisions after a meeting of the DSARC. Without these reforms, gaining program approval would have been a much longer and more arduous task.

B. Commander of SAMSO, General Ken Schultz

As Program Director, Dr. Parkinson was extremely fortunate to work for a general who also had been a Program Director. Lt. General Kenneth Schultz was tough and fair and knew how difficult it was to run a large program. He laid down the objectives but did not attempt to control the process totally. Along the way, he taught the JPO many essential things about keeping a program on track, from procurement to personnel.

C. Contractors

The principal Phase I hardware contractors are listed in Table 5. Literally hundreds of hardworking, capable engineers and managers produced the Phase I success.

Table 5 Principal contractors

Contractor	Development effort	Comments
Rockwell International	Development satellites	Initially three plus a flying Qual model; two more added later
General Dynamics	Control segment and direction of Magnavox	Also developed the inverted range for testing
Magnavox	User equipment	Included monitor receivers for the control segment
Texas Instruments	User equipment	An alternate, competitive receiver source
Collins Radio of Rockwell International	Jam resistant user equipment	Actually under contract to the U.S. Air Force Flight Dynamics Lab
Stanford Telecommunications	Signal structure	Also instrumental in obtaining extra satellites

D. Joint Program Office Development Team

It was members of this team who synthesized the design of GPS in 1973, prior to signing contracts with any of the support contractors. From the beginning, a conscious decision was made *not* to use an integrating contractor. The overall integration was to be handled by the Joint Program Office in cooperation with various contractors. For this to work, the JPO had to manage the technical tradeoffs and all major systems interfaces.

Fortunately, Dr. Parkinson had been given strong support in directing the effort. This included careful selection of the Air Force officers who had to make the management and technical approach succeed. Of the approximately 35 military officers involved, 6 held Ph.D.s in engineering, and virtually all the others held Master's degrees. Many had experience in running large programs, and some (who had been at the Air Force's Central Inertial Guidance Test Facility) were extremely skilled in devising and running test programs for navigation systems. With the extensive travel demands, it was essential that Dr. Parkinson had a strong and effective deputy to smooth administration of the complex program. That role was filled effectively by then Lt. Col. Steve Gilbert during the initial phase of development and later by Lt. Col. Don Henderson. In addition, the JPO was supported by a small, but effective, cadre of engineers from the Aerospace Corp., which was initially headed by Walt Melton, who had done much of the pioneering work on 621B.

E. Predecessors

The Air Force 621B program had been developed in the Plans Directorate of the Air Force's Space and Missile Systems Organization with strong support from the Aerospace Corp. Two individuals who pioneered the most essential pieces of other GPS technology were Roger Easton of the NRL, who developed the initial clock technology, and Dr. Richard Kirschner of the ARL, who had developed Transit.

VIII. Future

The quiet revolution of NAVSTAR GPS has just begun. Given that the number of active satellites in the constellation now has reached 24, the use of GPS surely will expand. As that expansion continues, the demand will be for greater integrity, which will lead to a modest increase in the number of satellites. The major issues awaiting resolution are the following:

1) Sufficiency of the number of satellites
2) Expansion of the backup control segment capability
3) Resolution of the international request for some civilian control of the system

An expanded dialogue between the military operators and civilian users has begun. The next great wave of progress will be *differential* GPS systems, which squeeze the expected dynamic errors down to less than 1 m. All users will benefit as this new "navigation utility" comes into full operation and usefulness over the next 20 years.

References

[1]Parkinson, B. W., "Overview," *Global Positioning System,* Vol. I, Institute of Navigation, Washington, DC, 1980, p. 1.

[2]Easton, R. L., "The Navigation Technology Program," *Global Positioning System,* Vol. I, Institute of Navigation, Washington, DC, 1980, pp. 15–20.

[3]Bowen, R. et al., "GPS Control System Accuracies," *Global Positioning System,* Vol. III, Institute of Navigation, Washington, DC, 1986, p. 250.

[4]Sharrett, Wysocki, Freeland, Brown, and Netherland, "GPS Performance: An Initial Assessment," *Proceedings of ION GPS-91,* Institute of Navigation, Washington, DC, 1991.

[5]Anon., *Proceedings of ION-89,* Institute of Navigation, Washington, DC, 1989, p. 19.

Chapter 2

Overview of GPS Operation and Design

J. J. Spilker Jr.*
Stanford Telecom, Sunnyvale, California 94089
and
Bradford W. Parkinson†
Stanford University, Stanford, California 94305

I. Introduction to GPS

THE Global Positioning System (GPS) consists of three segments: the space segment, the control segment, and the user segment, as shown in Fig. 1. The *control segment* tracks each satellite and periodically uploads to the satellite its prediction of future satellite positions and satellite clock time corrections. These predictions are then continuously transmitted by the satellite to the user as a part of the navigation message. The *space segment* consists of 24 satellites, each of which continuously transmits a ranging signal that includes the navigation message stating current position and time correction. The *user receiver* tracks the ranging signals of selected satellites and calculates three-dimensional position and local time.

This chapter is designed to provide a summary discussion of the GPS. Later chapters develop the details. All segments of the system, along with a detailed discussion of the signal and the multiple applications of the GPS, are covered in separate chapters.

II. Performance Objectives and Quantitative Requirements on the GPS Signal

The key performance objectives of the GPS system can be summarized as follows:

1) High-accuracy, real-time position, velocity, and time for *military users* on a variety of platforms, some of which have high dynamics; e.g., a high-performance

*Ph.D., Chairman of the Board.

†Professor, Department of Aeronautics and Astronautics, and Director, GPS Program.

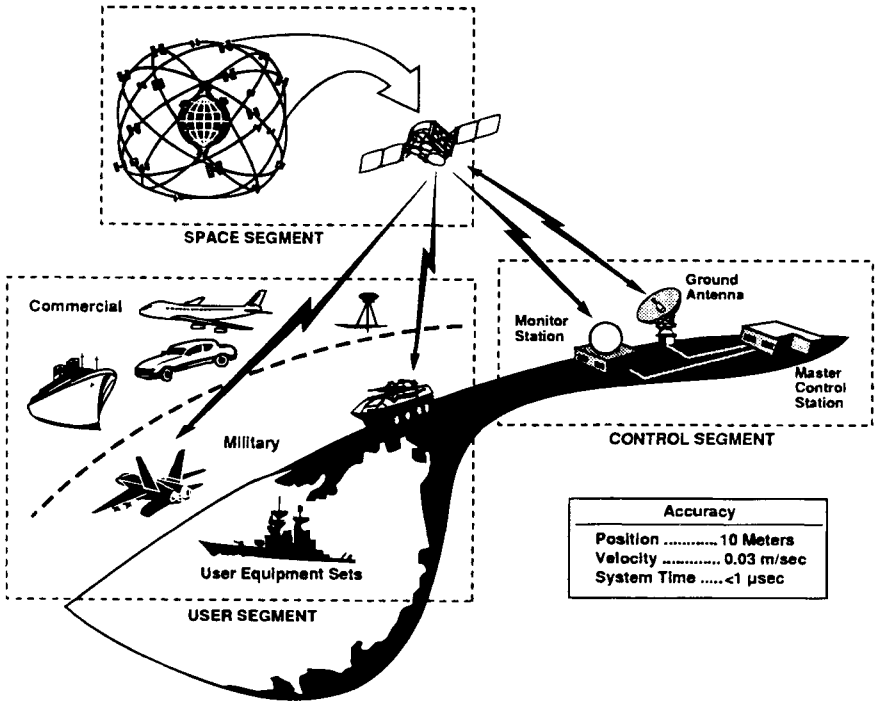

Fig. 1 GPS consists of three segments: space, control, and user; the user segment contains both civil and military users.

aircraft—high accuracy translates into 10-m three-dimensional rms position accuracy or better; velocity accuracy < 0.1 m/s.

2) Good accuracy for *civil users*—the real-time civil user accuracy objective is considered to be 100 m (at about the 95th percentile) or better in three dimensions. In the future, this accuracy may be improved by reducing or eliminating the deliberate degradation of the ranging signal.

3) Worldwide, all weather operation, 24 h a day.

4) Resistance to intentional (jamming) or unintentional interference for all users—enhanced resistance to jamming for military users.

5) Capability for highly accurate geodetic survey to centimeter levels using radio frequency carrier measurements—capability for high-accuracy time transfer to 100 ns or better.

6) Affordable, reliable user equipment—users cannot be required to carry high-accuracy clocks; e.g., atomic frequency standards, or sophisticated arrays of directional antennas that must be pointed at the satellites.

In addition to these performance requirements for the user, the GPS must also employ a cost-efficient space segment, must live within constraints of available bandwidth and frequency allocations, and have a control segment capable of measuring the satellite orbits, clocks, and uploading data to the spacecraft for retransmission to the users.

This chapter provides a summary of the GPS and describes how these accuracy and other performance requirements translate into requirements on the GPS signal. For example, user position accuracy translates into accuracy requirements for the time measurement performed by the GPS user receiver. These requirements also affect the radio frequency frequency selection. Because the satellites must be limited in transmit power, and there are many perturbing physical phenomena and geometrical considerations as discussed later, all of these selections have been made with care.

A. Satellite Navigation Concepts, Position Accuracy, and Requirement Signal Time Estimate Accuracy

As an elementary step in discussing the use of satellites for real-time navigation, consider the single idealized navigation satellite and a single user, as shown in Fig. 2. Assume that the user is fixed in inertial space on a nonrotating Earth. Assume also that the satellite has information as to its precise position vs. time and contains a perfect clock. Imagine that both position and time are displayed in lights on the side of the spacecraft so that they are observable to the user who has a telescope and camera. For this example of the principal of satellite ranging, the satellite and user coordinates are both expressed in an Earth–centered-inertial (ECI) nonrotating coordinate system with the origin at the Earth's center (see Fig. 3) and we neglect atmospheric and relativistic effects.

In this example, the user camera periodically photographs the satellite clock and position indicator and compares the satellite clock reading t_s with a simultaneous

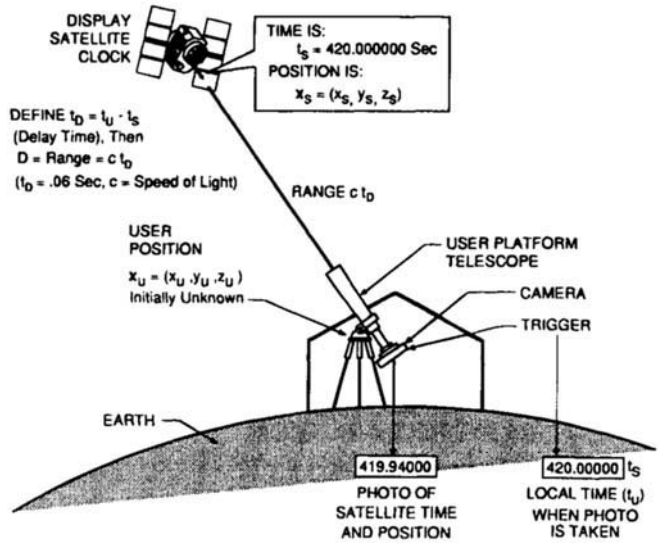

Fig. 2 Satellite and user clock timing concepts—photographs of the satellite clock are taken by the user. Coordinates are expressed in an Earth–centered-inertial (ECI) coordinate system. The true system time is t_u at the time of reception. A perfect user clock is assumed. The satellite position can be alternately denoted by x_s in Cartesian coordinates or r_s in radius vector coordinates.

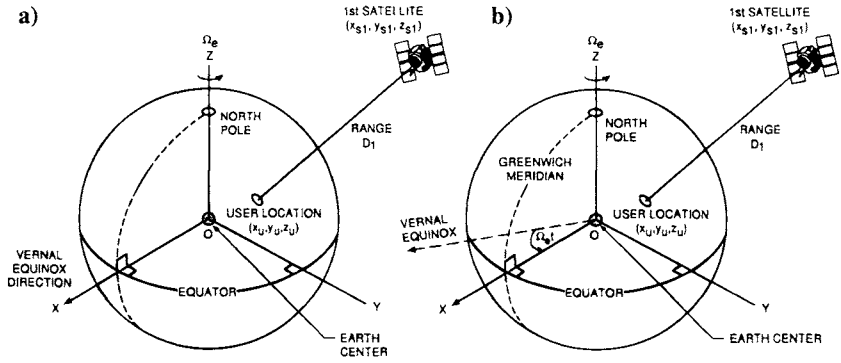

Fig. 3 Earth–centered-inertial and Earth-centered, Earth-fixed (ECEF) coordinates: a) the ECI coordinates are nonrotating with the x-axis aligned with a vector from the Sun to the Earth position at the vernal equinox (the first day of autumn); b) ECEF coordinates rotate with the Earth with the x-axis on the Greenwich meridian.

reading of the local user clock t_u. Also for this example, both clocks are assumed to be exactly synchronized to system time, and the user is assumed to be stationary. The photograph reveals that, at the receive time instant when the user clock shows $t_u = 420.00000$ s, the image received at the camera from the satellite showed the satellite position at $\boldsymbol{x}_s(t_s)$ [or $\boldsymbol{r}_s(t_s)$ in radius vector coordinates] and $t_s = 419.94000$; i.e., it shows the satellite clock and position 0.060 s earlier. Thus, there is a measured delay caused by the finite speed of light c of $t_D = t_u - t_s = 0.06$ s and a range to the satellite $D = c\,t_D$ measured at time $t = t_u$. Therefore, the receiver's location at time t_u is somewhere on a sphere of radius D centered at $\boldsymbol{x}_s(t_s)$. This simple example does not address the impact of the satellite's velocity nor the possibility of a dynamic user. Note also that in order to convert this result to meaningful user coordinates; e.g., Earth-centered, Earth-fixed (ECEF) coordinates, we must account for the fact that the Earth is rotating through 360 deg in inertial space per sidereal day. (A sidereal day is approximately 23 h 56 min 4 s of mean solar time.)

Clearly, if we were able to perform the same type of measurement with three satellites simultaneously, we could locate the user position in three dimensions at the intersection of three spheres and perform the desired real-time navigation. However, doing so requires accurate, synchronized time at the user terminal. Assume now that the user clock has an unknown bias error b_u and thus the user clock reads $t'_u = t_u + b_u$, where t_u is the "true" system time at the user's time of reception. By adding a ranging measurement to a fourth satellite, the solution can be found for both $\boldsymbol{x}(t_u)$ and true user clock time t_u (or user clock error Δt_u), at the time at which the measurement is taken (see Fig. 4).

The difference between satellite clock time and user clock time when the user clock is not precise is termed *"pseudorange."* For the ith satellite, this range difference is denoted as ρ_{iT} where subscript T denotes true pseudorange. The *true pseudorange* ρ_{iT} to satellite i, in the idealized error-free condition, is the true range plus the user clock bias correction b_u expressed in seconds and is expressed as $\rho_{iT} = c(t_u - t_{si}) + c\,b_u$. However, in the real measurement, there are random

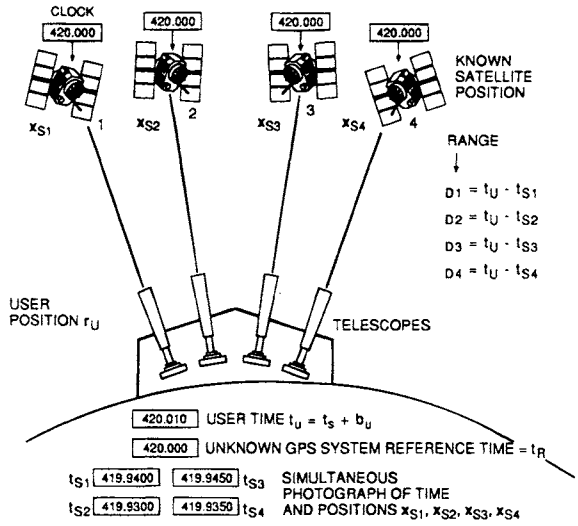

Fig. 4 Three-dimensional user position and clock bias measurement for a user with an accurate user clock. Four pseudorange equations are needed to solve for the four unknowns, user *x*, *y*, and *z* coordinates and user clock bias b_u. Note that the satellite positions are all observed by the user at slightly different times t_{si}.

noise effects, various other bias errors, propagation errors (and relativistic effects) so that the *measured pseudorange* ρ_i is $\rho_i = \rho_{iT} + \Delta D_i - c\,\Delta b_i + c\,(\Delta T_i + \Delta I_i + v_i + \Delta v_i)$ where Δb_i is the satellite bias clock error (s); ΔD_i is the satellite position error effect on range; v_i is the receiver measurement noise error for satellite i (s); ΔI_i is the ionospheric delay error (s); ΔT_i is the tropospheric delay error (s); and Δv_i is the relativistic time correction (s). Thus, the actual user clock reads $t'_u = t_u + b_u$, and the actual clock of satellite i reads $t'_{si} = t_{si} + \Delta b_i$, where t_u and t_{si} are the true system times at the user at the time of reception and at satellite i at the time of its signal transmission, respectively.

We define *true pseudorange* $\rho_{iT} = |\boldsymbol{x}_{si} - \boldsymbol{x}_u| + cb_u = |\boldsymbol{r}_{si} - \boldsymbol{r}_u| + cb_u = D_i + cb_u$. Note that pseudorange defined in this manner is not directly an observable, and each of these quantities may vary with time. Note also that the techniques discussed here permit real-time satellite navigation and position measurement. This technique is distinct from systems that must observe the changes in satellite Doppler shift over some period of time as the satellite passes overhead to determine position. Techniques of this latter type clearly cannot autonomously determine the position of a rapidly moving vehicle.

Although the preceding examples of Figs. 2 and 4 used optical measurements, exactly the same process can be performed using microwave signaling with coded signals. Examination of the fine detail of the received signal code provides exactly the same information as a photograph of a clock, because the structure of the code can be interpreted as time counts of a clock. One simple radio frequency analogy to the optical clock display is a signal that is modulated by a 10-stage binary counter that counts the number of precisely timed 1 μs clock cycles up to $2^{10} = 1024$ and then repeats. Examination of the last 10 bits of the binary

waveform then gives coarse time analogous to hours and minutes, and examination of the exact timing of the clock transition gives the finer resolution of time. As compared to a system that simply monitors periodic sequences of identical 1 μs pulses, the counter, in effect, reduces the level of ambiguity in the measurement from 1 to 1024 μs, etc.

The preceding simplified description of the GPS positioning calculations briefly introduces a number of significant effects, which are treated in detail in later chapters of this volume. These include the following:

1) *User motion*—The user is generally moving in inertial space, and we must account for the user motion between the time the signal is transmitted from the satellite and the time when the signal is received.

2) *Atmospheric effects*—Excess delay caused by the wave traveling through the atmosphere (troposphere and ionosphere) must be estimated or measured.

3) *Relativistic effects*—There are a number of effects caused by satellite and user motion, Earth rotation, and the Earth's gravitational field, all of which can be significant.

1. *User Receiver Measurements—Pseudorange and Carrier Phase*

Next we examine how a receiver makes the measurements on the signal waveform or the radio frequency carrier to form an accurate estimate of the pseudorange ρ_i. Figure 5 illustrates some of the range measurements that can be

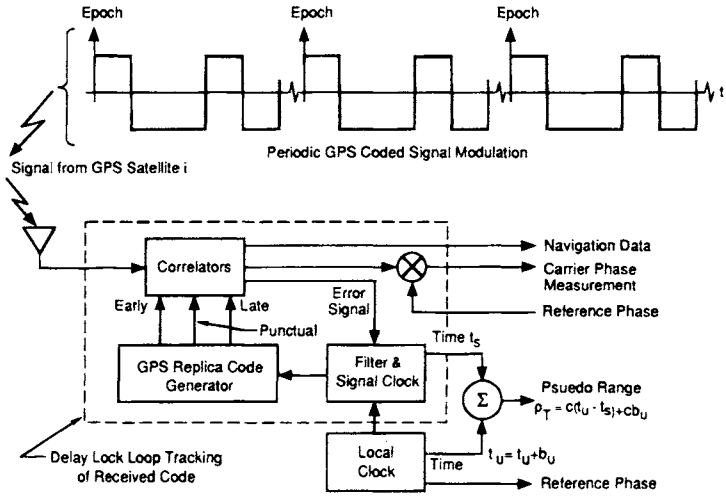

Fig. 5 Pseudorange measurement using a delay–lock-loop (DLL). The GPS replica code generates early and late reference signals that are both fed to a correlation device that produces an estimate of whether the early or late signal provides the best match. The resulting error signal is then used to control the signal clock in a tracking mode. The differences between the two clocks t'_u–t_s is then multiplied by c to form pseudorange $c(t'_u - t_s)$. Similar measurements are made on the received carrier phase. The user receiver has a clock bias offset b_u in seconds. (Satellite clock error is ignored here.)

made on a signal waveform. Pulses of radio frequency energy can be modulated with a special pulse code sequence that has a distinct beginning (or epoch). The GPS civilian [coarse acquisition (C/A)] signal repeats such a sequence every millisecond. The C/A code is a random-like or pseudonoise (PN) binary sequence of 1023 chips. The pseudorange $t_u - t_s$ can then be recovered in a special delay lock loop receiver designed to track and to detect the code from that satellite, as shown in Fig. 5. The measurement relies on the unique code properties of each satellite signal. These properties enable the receiver to measure pseudorange to each satellite separately. The delay lock technique creates an internal replica of the known modulation sequence and adjusts the internal epoch until it exactly matches the received signal in delay. This matching is performed by cross-correlating the received and internal signals and finding the start time that maximizes the correlator output. The satellite clock time at the time of transmission is then subtracted from the user clock time to recover the measured pseudorange.

If the user receiver clock t_U and the satellite clock are both synchronized to GPS reference time,* then range $= D = c(t_u - t_s)$. For purposes of this discussion, atmospheric and other propagation path delay perturbations are neglected. Pseudorange is the same measurement when the user receiver clock t_U has an unknown and possibly time varying clock bias b_u expressed in seconds. The pseudorange is then $\rho = D + cb_u$, as shown in Fig. 5. This technique is known as *code ranging* to distinguish it from carrier phase measurements.

Most GPS receivers can also reconstruct the GPS radio frequency carrier at 1575.42 MHz and use this sinusoid as a ranging signal. This measurement is very precise (typically subcentimeter or a fraction of the 19-cm wavelength), but its *accuracy* is limited by the difficulty of resolving which cycle is being received (called the cycle ambiguity or $n\lambda$ problem). Carrier phase accuracy corresponds to the equivalent carrier phase noise expressed in distance which would be on the order of 2 mm if the carrier phase could be measured to 1% of the wavelength. However, the initial value of the carrier phase is completely ambiguous, and we must resort to the use of various phase differencing techniques. Nonetheless, it is possible to measure changes in phase both very precisely and without significant cycle slipping over many seconds. This carrier phase measurement can then allow us to make very precise position measurements. The use of carrier phase measurements for various surveying and aircraft landing applications is discussed in later chapters in this volume. Table 1 gives a rough estimate of the measurement accuracy, bias, and precision for GPS carrier and code measurements.

a. Relating pseudorange accuracy and positioning accuracy—dilution of precision (DOP). Positioning accuracy reflects the final capability of most GPS receivers. Although it is related to *ranging* accuracy, they are not the same. The relationship between them is a function of the geometry of the selected satellites; that is, the directions of arrival of the satellite signals. To achieve a positioning accuracy requirement of 10 m, the ranging accuracy and geometry must both combine to acceptable values. For example, if each individual pseudorange measurement has a statistically independent error of zero mean with the same rms

*All time intervals can be expressed in equivalent distance in meters by multiplying by the speed of light c.

Table 1 Rough order of magnitude estimates of GPS code and carrier phase measurements in meters[a]

	Rough measurement accuracy	
Measurement	Bias	Precision
Code	≈ 5 m	≈ 2 m
Carrier phase	$n\lambda$	≈ 0.002 m

[a]There is assumed to be no selective availability (SA) degradation. The value of n in the carrier phase ambiguity must be determined.

value of σ (caused by all effects), then the rms position errors are given by the following:

Position error = DOP $*$ σ, where DOP is a multiplier determined by the geometry and is typically between 1 and 100.

The quantity DOP is calculated from the unit vectors to each of the satellites, as shown in Chapters 5 and 11, this volume. Generally, if the DOP rises above six, the satellite geometry is not very good. There are several measures of positioning accuracy. For the current nominal constellation, the worldwide median position dilution of precision (PDOP) (50th percentile) is approximately 2.5. As another example, the horizontal error (in the x and y coordinates) is given by rms error horizontal = HDOP (horizontal dilution of precision) $*$ σ, where rms denotes the root mean square error. The vertical error (in the z coordinate) is found from rms error vertical = VDOP (vertical dilution of precision) $*$ σ.

The speed of light is approximately $< \cong 3$ m/ns and l/c $\cong 3.3$ ns/m. If the satellite geometry produces an HDOP of 3 (and a horizontal error less than 10 m is required), then HDOP $*$ $\sigma = 3\sigma \leq 10$ m $*$ 3.3 ns/m. Thus, the required ranging accuracy is then $\sigma \leq 11$ ns. In a similar manner, the rms position error (in three dimensions x, y, and z) is estimated by the relationship rms position error = PDOP $*$ σ.

Table 2 summarizes some of the key definitions of parameters in the GPS user position calculations and error sources.

III. GPS Space Segment

A. GPS Orbit Configuration and Multiple Access

The discussions of the basic concepts for GPS and analysis of the geometric dilution of precision have shown that the user must make measurements on four or more satellites simultaneously to provide real-time three-dimensional navigation. Thus, the satellite orbital constellation must provide a user anywhere in the world simultaneous access to measure pseudorange to four or more satellites at any time, 24 h a day. Furthermore, as shown later in the DOP analysis, the satellites should be widely spaced in angle. Measurements on each of the four or more satellites must be made simultaneously or nearly simultaneously without mutual interference if we are to solve for position. This capability is termed

Table 2 Summary of notation for GPS position and pseudorange parameters

Parameter	Description
$\boldsymbol{x}_{si}$ or $\boldsymbol{r}_{si}$	Position of satellite i in either x, y, z or radius vector coordinates, respectively. The position of the satellites at the time of transmission is $\boldsymbol{x}_{si}\ (t_{si})$ or $\boldsymbol{r}_{si}\ (t_{si})$.
$\boldsymbol{x}_u$ or $\boldsymbol{r}_u$	User position in either x, y, z or radius vector coordinates. User position may also vary with time. User position at time of reception is $\boldsymbol{x}_{ui}\ (t_{Ri})$ or $\boldsymbol{r}_{ui}\ (t_{Ri})$.
t_{si}	True time of transmission from satellite i. This parameter is the true time of transmission and may not be exactly the same as indicated by the satellite.
t'_{si}	Actual satellite clock reading $t'_{si} = t_{si} + \Delta b_i$
Δb_i	Satellite bias clock error (expressed in s)
t	GPS system time
t'_u	Actual user clock time at time of reception of signal $t'_u = t_u + b_u$
t_u	True user time at time of reception
b_u	User clock bias—can vary with time
ρ_{iT}	True value of pseudorange $\rho_{iT} = \lvert\boldsymbol{x}_{si} - \boldsymbol{x}_u\rvert + b_u = \lvert\boldsymbol{r}_{si} - \boldsymbol{r}_u\rvert + b_u$
ρ_i	Measured pseudorange with various error contributors
$n(t)$	Receiver thermal noise
Δb_i	Satellite bias clock error (expressed in s)
ΔD_i	Satellite position bias error effect on range
v_i	Receiver pseudorange measurement noise error for satellite i, s
ΔI_i	Ionospheric delay (expressed in s)
ΔT_i	Tropospheric delay (expressed in s)
Δv_i	Relativistic time correction (expressed in s)
c	Velocity of light
DOP	Dilution of precession
VDOP, HDOP, PDOP	Vertical, horizontal, and position geometric dilutions of precession
GDOP	Geometric dilution of precession includes both position and time error effects
ϕ_i	Measured carrier phase offset as received from satellite i
ϕ_{iT}	True received carrier phase offset $\phi_{iT} = \omega_o(t_{si} - t_u)$ at frequency ω_o
λ	Wavelength of GPS carriers can have value λ_{L_1} or λ_{L_2} for GPS L_1 or L_2 frequencies.
n	Carrier phase cycle count ambiguity
D_i	True range from satellite i to user $\lvert\boldsymbol{x}_{si} - \boldsymbol{x}_u\rvert = \lvert\boldsymbol{r}_{si} - \boldsymbol{r}_u\rvert = c(t_u - t_{si})$

multiple access. Multiple access signaling permits measurements to be made on a signal from one satellite without signals from other satellites interfering with that measurement.

From a user performance standpoint, satellite orbit altitude selection has several effects:

1) The higher the orbit altitude, the greater the fraction of the Earth visible by a single satellite

2) Within limits, power flux density on the Earth is nearly independent of orbit altitude because the satellite antenna beamwidth can be selected (widened or narrowed) to provide full Earth coverage.

3) A low-orbit altitude with its corresponding short visibility time leads to a larger number of signal acquisitions and satellite–satellite handovers by the user receiver, and larger Doppler shift must be tolerated in the receiver.

The selected satellite orbital constellation contains 24 satellites, the GPS-24, in six orbit planes. There are four satellites in each of the six planes, as shown in Fig. 6. The satellites have a period of 12 hours sidereal time* and a semimajor axis of 26,561.75 km. A satellite with an orbit period of 12-h sidereal time produces a ground track (projection on the Earth's surface) which repeats over and over. For GPS the longitude crossing at the equator is kept fixed to within $\pm$ 2° by the GPS Control Segment. This orbit has 63% of the radius of a geostationary satellite orbit with a 24-h period. The GPS semimajor axis is the orbit radius of the circular GPS orbits, and thus the GPS satellites have an altitude of 20,162.61 km above the Earth's equatorial radius[1] of 6378.137 km. The altitude of the GPS orbit obviously is well above the atmosphere and not subject to atmospheric drag. Other perturbations such as solar pressure and lunar and solar gravitational orbit perturbations can be significant. The satellites are inclined with respect to the equator by 55 deg (the initial GPS satellites had a 63-deg inclination). Table 3 summarizes the approximate parameters of the GPS orbit. The satellite orbital constellation is described in detail in Chapter 5, this volume.

B. GPS Satellite Payload

The key role of the satellites is to transmit precisely timed GPS signals at two *L*-band frequencies† 1.57542 GHz and 1.2276 GHz. These signals must have embedded in them, in the form of navigation data, both the precise satellite clock time as well as satellite position so that a user receiver can determine both satellite time t_{si} and satellite position $\boldsymbol{r}_{si}$ at the time of transmission. These navigation data are uploaded from the GPS control segment (CS) to each satellite and then stored in memory in the satellite for readout in the satellite navigation data stream. Figure 7 shows a simplified view of the GPS satellite payload. The GPS upload station sends the satellite the ephemeris information regarding the satellite orbit

*A sidereal day is defined as the time for the Earth to complete one revolution on its axis in ECI space and consists of 24 mean sidereal hours where 1 mean sidereal day is slightly shorter than a mean solar day. One sidereal day is 23 h, 56 min, 4.009054 s or 86,164.09054 s of mean solar time. One mean sidereal day is equal to 0.997269566 mean solar day or one mean solar day is equal to 1.002737909 mean sidereal day.

†These signals, as well as the L_3 signal at 1381.05 MHz, are all selected and filtered so as to minimize interference with the radio astronomy bands (see Chapter 3, this volume).

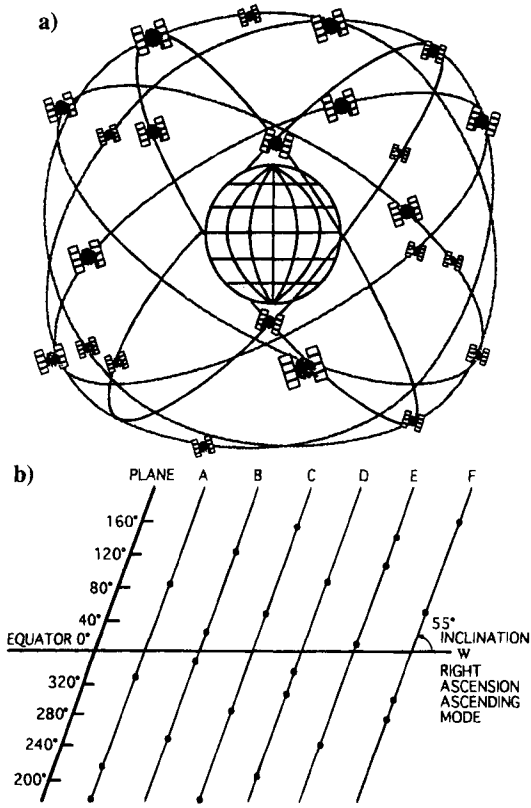

Fig. 6 GPS satellite constellation: a) the six orbit planes shown in ECI coordinates; and b) satellite positions on each of the six orbit planes. The GPS constellation has satellites in six equally spaced orbit planes. The present GPS-24 satellites constellation shown in b) contains 24 satellites. The uneven satellite phasing in each plane is designed to minimize the effect of satellite outage.

and the exact position in that orbit vs. time. Included is a satellite clock correction that calibrates the offset of the satellite clock relative to GPS system time. These data are uploaded to the satellite through an S-band telemetry and command system.

One of the keys to GPS satellite performance is the stability of the GPS satellite clocks. Each satellite carries redundant atomic oscillators of high stability. These atomic clocks are stabilized using either rubidium or cesium atoms in gaseous form.

The atomic clocks along with appropriate frequency synthesizers then synchronize the GPS signal generators and also control the radio frequency center frequencies of the two *L*-band frequencies. The signals are then amplified and filtered to remove signal power outside the allocated frequency bandwidth of 20 MHz for each of the two *L*-band signals. The signals also are modulated by the navigation data that carry the satellite position and time information to the user.

Table 3 Approximate GPS satellite parameters

Orbit plane	Six equally spaced ascending nodes at 120 deg
Orbit radius r_{cs}	26,561.75 km semimajor axis
Orbit velocity (circular) (ECI)	$= \sqrt{\frac{\mu}{r_{cs}}} = 3.8704$ km/s
Eccentricity	Nominally zero, but generally less than $e = 0.02$
ω_s angular velocity	1.454×10^{-4} rad/s
Period[a]	12 h mean sidereal time
Inclination	$i = 55$ deg nominal

[a]The period of an orbit in seconds of mean solar time is $T_p = (2\pi/\sqrt{\mu})a^{3/2}$ where a is the semimajor axis in meters and μ is the Earth's gravitational parameter $\mu = 3.986005 \times 10^{14}$ m^3/s^2. For 12-h mean sidereal time period, $a = 26561.75$ km including a minor correction for a nonspherical Earth. A new model, Joint Gravity Model #2, is being proposed by NASA and the University of Texas, which gives $\mu = 3.986004415 \times 10^{14}$ m^3/s^2, and $R_e = 6378.1363$ km for the Earth's mean equatorial radius.

(The reader is referred to Chapter 6, this volume on the GPS satellite payloads for a more thorough description.) One of the limitations on GPS clock accuracy is selective availability. Selective availability is a clock dither that can be imposed on the GPS signals to restrict unauthorized (nonmilitary) access to the full accuracy of the system.* Chapter 1 of the companion volume describes differential GPS that can be used to improve civil accuracy.

C. Augmentation of GPS

As discussed in later chapters in this volume and the companion volume, we can augment the GPS satellite system with other ranging signal sources:

1) Ground transmitters or pseudolites that transmit GPS signals and other information to support GPS—a special form is the integrity beacon used for aircraft landing

2) Additional satellites can either carry transponders that can relay GPS-type signals from synchronized ground transmitter uplinks or have navigation payloads similar to the basic GPS satellites. The Federal Aviation Administraton's Wide Area Augmentation System (WAAS) is an example of an augmentation of GPS. This system adds geostationary relay satellites.

3) Differential and wide area differential ground stations. These ground stations transmit correction information to appropriately equipped GPS receivers to improve the accuracy of the receivers.

IV. GPS Control Segment

The GPS CS has several objectives:

1) Maintain each of the satellites in its proper orbit through infrequent small commanded maneuvers.

*It is expected that selective availability effects will eventually be eliminated. A recent report of the National Research Council[5] has recommended that selective availability be turned to zero.

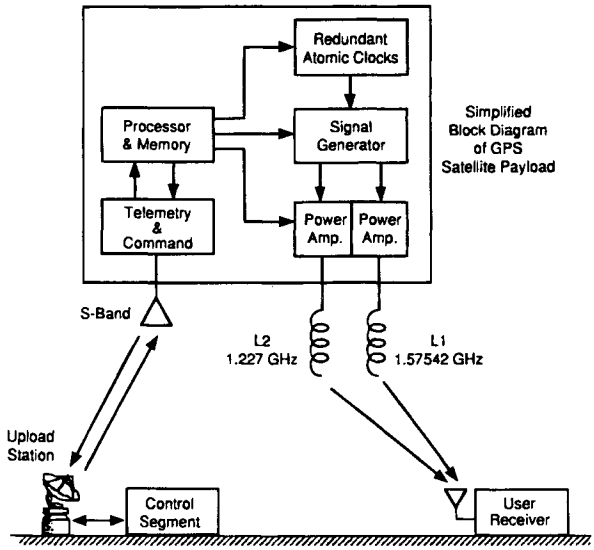

Fig. 7 Simplified GPS satellite payload functional diagram.

2) Make corrections and adjustments to the satellite clocks and payload as needed.

3) Track the GPS satellites and generate and upload the navigation data to each of the GPS satellites.

4) Command major relocations in the event of satellite failure to minimize the impact.

Although each of these objectives is important, this discussion concentrates on the third objective.

The Operational Control Segment began operation in 1985 and consists of five monitor stations, four ground antenna upload stations, and the Operational Control Center. Each of these facilities is shown in Fig. 8. The sites have been selected to provide a significant separation in longitude between each of the monitor stations. Each of these sites, except the site in Hawaii, also contains a ground antenna upload station.

A. Monitor Stations and Ground Antennas

Each of the five monitor stations contains multiple GPS tracking receivers designed to track both the L_1 and L_2 codes and carriers for each of the satellites in view. The monitor stations also contain redundant cesium standard clocks for the GPS receivers to use as a reference oscillator and also to time tag each of the measurements. The measurements of code clock delay and carrier phase for each satellite in view are then sampled, time tagged, and multiplexed in a data-stream to send back to the operational control center. Each of the four ground antenna (GA) upload stations has the capability of uploading navigation data to the satellites on an *S*-band T T&C link. As discussed earlier, the visibility region around each GA extends approximately ± 72 deg in Earth angle about the GA.

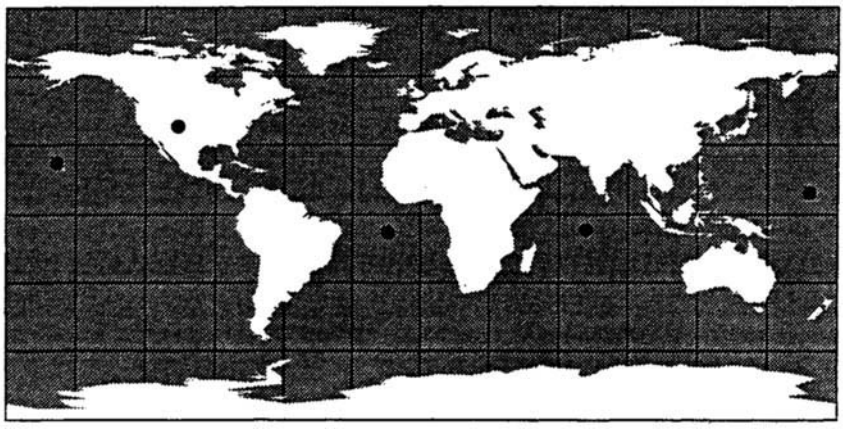

Fig. 8 GPS control segment. There are monitor stations at Hawaii, Colorado Springs, Ascension Island, Diego Garcia in the Indian Ocean, and at Kwajalein Island in the West Pacific.

B. Operational Control Center

The operational control center receives the multiplexed pseudorange measurements and carrier measurements from each satellite in the L_1 and L_2 carriers. The Kalman filter processor in the OCS then estimates the ephemerides, clock error, and other navigation data parameters; e.g., satellite health, for each satellite. The objective of the OCS is to format navigation data for a minimum of 14 days of updates. Navigation data are then transmitted to the upload ground antennas. Each satellite can be given a fresh upload three times a day, approximately eight hours apart. However, normally there is only one upload per day. (See Chapter 16, this volume.) Each upload contains many pages of navigation data that are then fed to the GPS spacecraft processor. The GPS satellite processor then reads out the appropriate set of navigation data for the specific time period appropriate to the time of transmission.

Satellite clock errors in the navigation data are the dominant source of user range error (URE) when the time since the last upload reaches several hours.* Even with three uploads per day, computer simulations run in 1985 show that satellite clock predictability based on clock specification values can limit the GPS user range accuracy to 3m (1σ) 10 h after the satellite ephemeris and clock prediction upload using the specified Allan variance for the satellite clock (2×10^{-13} at $\tau \geq 61{,}200$ s and 7×10^{-12} at $\tau \leq 50$ s).[2] However, actual satellite clocks perform better than the specification. The specified URE is computed as the following rms sum: URE = [(radial perturbation)^2 + 0.0192 (in-track perturbation)^2 + 0.0192 (crosstalk perturbation)^2]$^{1/2}$, which is a representative error projection to the user.

The simulations showed the total URE had an rms value for 10-h updates of 4.2m (1σ), which was dominated by the clock error component for the specified

*This statement assumes that both L_1 and L_2 are available. If not, ionospheric modeling errors are often the largest.

clock and is well within the specified 6m maximum. By way of comparison, the simulated URE for 0 h, 3 h, 6 h, and 24 h predictions were 1.4m, 2.4m, 3.2m, and 8.4m (1σ), respectively. Most (95%) of the URE at 10 h is a result of the accumulated clock noise. When the simulated clock stability was reduced to the typical observed value (rather than specified levels) of 1×10^{-13}, the URE at 10 h decreased to 2.3m (1σ). For further information on expected errors see Chapters 11 and 16, this volume. A discussion of the GPS control segment is found in Chapter 10, this volume.

V. GPS User Segment

There are a great many applications for the GPS system. New applications seem bounded only by the imagination. This section lists some of the more common modes of operation. All of these are discussed in more detail elsewhere in this volume. Although the primary purpose of GPS was a military application, civil users are already more prevalent. The section begins however by describing the fundamental user system architecture.

A. GPS User Receiver Architecture

A generalized view of a typical GPS user system is depicted in Fig. 9. This section discusses the basic configuration of each of these elements. Although most receivers employ only a single GPS antenna, the generalized GPS receiver begins with one or more antenna/low noise amplifiers. More than one antenna/amplifier may be employed in order to achieve the following:

1) Accommodate maneuvering of the user platform; e.g., an aircraft banking

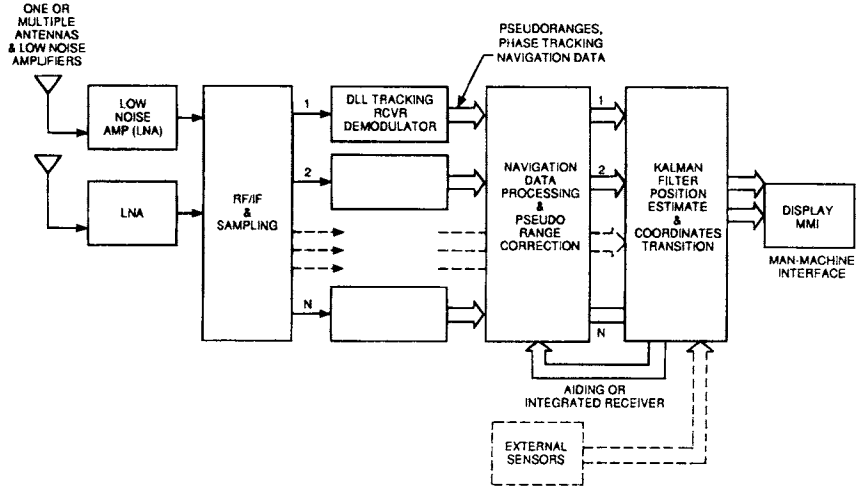

Fig. 9 Generalized GPS user system configuration with separate receiver and position estimating functions.

and thereby avoid blocking some of the satellites with a wing

2) Increase the antenna gain

3) Discriminate against interfering jammers through the use of multiple narrow beam antennas or adaptive antennas

4) Measure attitude

The antenna beams can be steered electronically or mechanically, if necessary. The most common GPS receivers employ only a single omnidirectional (really hemispherical antenna). The output of the antenna is then fed to a radio frequency filter/low-noise amplifier combination in order to amplify the signal and to filter out potential high-level interfering signals in adjacent frequency bands that might either saturate the amplifier or drive it into a nonlinear region of operation. The filters must be selected with low loss and sufficient bandwidth and phase linearity to minimize the distortion of the desired C/A- or P(Y)-code (precise nonstandard code) signals. The signal then passes through serial stages of radio frequency amplification, downconversion, and intermediate frequency (IF) amplification and sampling/quantizing. The sampling and quantizing of the signal can either be performed at IF or at baseband. In either case, in-phase and quadrature (I, Q) samples are taken of the received signals plus noise. At the present state-of-the-art, the functions of radio frequency amplification, downconversion, IF amplification, and A/D sampling can be implemented with a single MMIC (monolithic microwave integrated circuit) chip.

The I, Q samples are then fed to a parallel set of DLLs each of which tracks a different satellite signal and recovers the carrier, which is bi-phase modulated with both the GPS codes and the GPS navigation data. The DLL[2-4] and associated demodulators provide estimates of the pseudorange, carrier phase, and navigation data for each satellite. Typically, the number of parallel tracking DLL varies from 2 to 16 and can possibly track all of the satellites in view at both L_1 and L_2 frequencies simultaneously (see Chapters 7 and 8, this volume). Generally, at least five satellites are tracked as a minimum, either in parallel or in time sequence. At the present state of the art, a 10-channel receiver with 10 parallel DLLs can be implemented on one CMOS chip.

The parallel measurements of pseudoranges and carrier phase along with the navigation data for each satellite are then sent to the navigation data processor where the position of each satellite is calculated from the navigation data in subframes 2,3 at the time of each pseudorange measurement (see Chapters 3 and 4, this volume, for detailed discussion of the GPS signal and navigation data). The pseudorange and phase data are then corrected for the various perturbations, including satellite clock errors, Earth rotation, ionosphere delay, troposphere delay, relativistic effects, and equipment delays. The corrected pseudorange data, phase or accumulated phase [accumulated delta range ADR] measurements along with other sensor data are then processed by the Kalman filter, which estimates user position and velocity state vector. As discussed in Chapter 9, this volume, it is also possible to integrate the Kalman filter with the DLL instead of performing these operations independently. The output of the Kalman filter estimator provides position, velocity, and time estimates relative to the user antenna phase center. These coordinates are usually computed in ECEF coordinates and are then trans-

ferred by appropriate geodetic transformation to a local coordinate set convenient to the user.

The Kalman filter may also receive inputs from various other sensors; e.g., barometric altimeters, dead-reckoning estimates of attitude, heading, speed, inertial navigation ring laser gyros, or other navigation aids. This Kalman filter estimate of user position can also be used in a differential mode or kinematic survey mode with other GPS units where at least one unit is at a known reference point, in order to provide precision geodetic survey, more accurate airborne or shipborne navigation, or a common view mode, precision differential time transfer (see Chapter 9, this volume and Chapter 1 of the companion volume). The position, velocity, and time information can then be used with other user-provided information to provide tracks of user positions vs. time, display position on a map, to show way-points to a desired destination, or to satisfy a wide variety of other applications.

B. Uses of GPS

A partial listing of the uses of GPS includes the following:

1) Aircraft navigation—GPS and differential GPS, commercial and general aviation aircraft
2) Land mobile navigation—automobiles, trucks, and buses
3) Marine vessel navigation—GPS and differential GPS
4) Time transfer between clocks
5) Spacecraft orbit determination
6) Attitude determination using multiple antennas
7) Kinematic survey
8) Ionospheric measurement

See the companion volume for in-depth discussions of many of these applications.

1. Various Applications of GPS Receivers

a. Airborne GPS receivers. Airborne GPS receivers provide three-dimensional real-time navigation. These receivers must receive GPS signals from a minimum of four satellites to solve for four unknowns (x,y,z,T) because the airborne receiver clock generally is imprecise. A fifth satellite is needed for satellite handover because periodically new satellites are coming into view while another satellite is going out of view. In addition, the receivers also generally provide three-dimensional velocity estimates and clock drift estimates by making Doppler measurements on the carrier. The GPS receiver may process these satellite signals either in parallel or in time sequence. Aircraft in banked turns may suffer blockage of one or more satellites because of wing or other obstructions. Generally, receivers operate by tracking many more than the minimum four or five satellites in parallel; e.g., 8 to 12, and the clock stability may be sufficient to flywheel through momentary satellite blockage. The GPS receiver may be augmented by inertial navigation systems and/or other navigation aids to provide a hybrid GPS/inertial solution. For higher accuracy, the GPS receiver may operate in a differential mode wherein a GPS receiver at an appropriate known site; e.g., an airport, transmits differential corrections for GPS errors. In the Wide Area

Augmentation System (WAAS), corrections are transmitted to users in the form of satellite clock and position corrections, and ionospheric delay estimates which are valid over a wider geographic region. Further applications are covered in Chapters 12–15 of the companion volume.

b. Land mobile navigation. Land vehicles may require either two- or three-dimensional positioning. Generally, the altitude is varying, but typically, its variation is at a much slower relative rate compared to its horizontal motion in contrast to an aircraft. In principle, land vehicles can operate at least for a time with only two or three satellites because of the slowly varying vertical component. A fourth satellite could provide less frequent periodic updates of the altitude. However, land vehicles also are subject to blockage or shadowing of one or more satellites by trees, hills, or man-made obstructions. Another augmentation is the use of a magnetic or gyroscopic heading indicator and a wheel counter (see Chapter 10 of the companion volume).

c. Marine navigation. Navigation on the ocean or large bodies of water is usually at an altitude that varies only with the tides and any roll, pitch, and yaw-induced motion of the GPS antenna aboard the ship. For most purposes, only two dimensions are unknown. Thus, three satellites are adequate to solve for position and two satellites can suffice if a third is employed for periodic updates of the ship receiver clock. Again, however, typical receivers may operate on all satellites in view, and differential navigation can be employed for greater accuracy in harbors. This application is discussed in Chapter 11 of the companion volume.

d. Time transfer using GPS. Time can be transferred from a reference station to a clock of known location with a single satellite. Four or more satellites can be used initially if the exact location of the remote clock is unknown initially. Greater accuracy can be obtained with the civil signal using "common view" time transfer wherein two clocks at different locations are both within line of sight of the same GPS satellite. In this instance, receivers at each site are tracking the same GPS satellite simultaneously. Satellite clock errors along with any clock dither caused by SA cancel in this mode. Some fraction of the satellite position and ionospheric errors also cancel, depending on the relative separation between the two locations. This cancellation has a residual that depends (approximately) on the size of the angle between the two locations (see Chapter 17 of the companion volume).

e. Spacecraft GPS receivers. The position/orbit of a near-Earth satellite can be determined by placing a GPS receiver onboard. If the user satellite is below the altitude of GPS, then the satellite can receive the GPS signals from satellites in view above and to the sides where not shadowed by the Earth. If the user satellite is above the altitude of GPS, for example, at geostationary orbit, the user satellite can still receive the GPS signal as it passes on either side of the Earth's shadow. The GPS satellite signals are transmitted to Earth by an antenna pattern slightly greater than the Earth angle, and therefore they extend beyond the Earth's limb. The range to the GPS satellite is, of course, approximately

equal to the sum of the GPS altitude and the synchronous satellite altitude, and the GPS signal is accordingly weaker. Furthermore, the GDOPs usually will not be as good as for an Earth-based user. The weaker signal can be compensated by the gain of a directional antenna (at some cost). This approach is discussed in Chapter 21 of the companion volume.

f. Differential GPS (DGPS). If two GPS receivers operate in relatively close proximity, many of the errors inherent in two GPS position solutions are common to both solutions. For example, satellite clock time errors and a significant fraction of the satellite ephemeris, ionospheric, and other errors cancel when we seek a differential or relative position solution. Thus, if one receiver is at a known, fixed position it can transmit pseudorange correction information to other receivers in the area so they can achieve higher relative position accuracy. In the future, it is expected that many GPS receivers will operate in the differential mode as differential corrections become more available. A simplified version of DGPS operation is shown in Fig. 10. The DGPS reference station transmits pseudorange correction information (≈250 bps) for each satellite in view on a separate radio frequency carrier. Because there may be a number of DGPS stations in a network, the data would typically include an almanac giving the location of other DGPS reference stations so the user can use the closest station. Differential GPS is discussed in Chapter 1 of the companion volume.

Differential GPS normally is limited to separations between users and reference stations to approximately 100 km. To carry out a similar differential GPS operation over a wider region a concept known as wide area differential GPS (WADGPS) or wide area augmentation system (WAAS) has evolved. Wide area differential GPS employs a set of monitor stations spread out geographically and a central control or monitor station in somewhat the same mold as the GPS control segment, but simpler. The WADGPS upload station then would relay GPS satellite position and clock and atmosphere corrections via separate geostationary relay satellites.

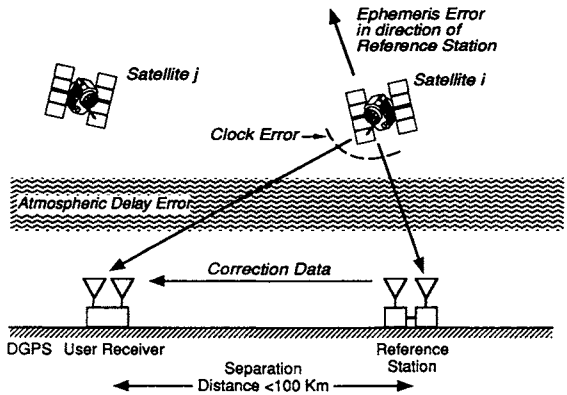

Fig. 10 Simplified view of differential GPS. This correction can completely eliminate satellite clock error offsets but ephemeris and atmospheric corrections differ for the user from the reference station by an amount that depends on the separation distance.

The corrections would be in real time with delays of less than 30 s. Wide area DGPS is discussed in Chapters 3 and 4 of the companion volume.

g. GPS survey. Global positioning system survey operates with double differencing operations similar to those described above, but carrier measurements are employed to get resolutions on the order of a fraction of the carrier wavelength. For example, the GPS carrier wavelength at 1.57542 GHz is approximately 19 cm. If a carrier phase cycle can be measured to 1%, the differential range error is only 2 mm. Certainly there are ambiguities in the carrier phase measurements, and these must be resolved with various double-differencing techniques.

The basic concept of double differencing is illustrated in simplified form is Fig. 11 where carrier phase measurements are differenced for a single satellite and the double differenced for two (or more) satellites. Obviously, this difference can be carried out at multiple time intervals to resolve the ambiguity. Survey is discussed in detail in Chapters 18 and 20 in the companion volume.

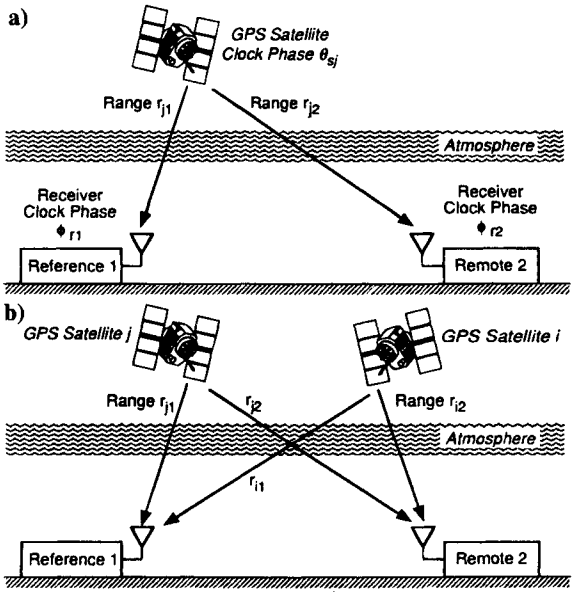

Fig. 11 Single and double carrier phase differencing for GPS and GPS-kinematic survey: a) *Single-difference receiver.* The phase received in receiver 1 is the satellite phase θ_{sj} minus the range delay effect $\omega_o r_{j1}/c$ minus the receiver reference clock phase ϕ_{r1}; namely, $\phi_{1j}(t) = \theta_{sj} - \omega_o r_{j1}/c - \phi_{r1}$. The first difference is then $\phi_{2j}(t) - \phi_{1j} = \Delta_j(t) = \omega_o(r_{j1} - r_{j2})/c + \phi_{r1} - \phi_{r2}$ where the first difference cancels out the satellite clock phase. Also, most of the atmospheric effects cancel if the separation distance is sufficiently small; b) *double-difference receiver.* The second difference is the difference between two first differences for satellite i and j; namely, $\delta_{ij}(t) = \Delta_j(t) - \Delta_i(t) = \omega_o[(r_{j1} - r_{j2}) - (r_{i1} - r_{i2})]/c$ where both the receiver carrier phase offsets cancel.

h. Attitude Determination. In addition to position measurement, GPS can also be employed in an interferometric mode with multiple user antennas to determine vehicle attitude orientation. The GPS codes can isolate each satellite signal, which can then be employed in a differential phase measurement mode with two antennas to measure angular offset for the axis of the rotation of each antenna pair and the direction of the satellite signal. Usually this technique employs carrier phase measurements. Because the baselines are short, simplified techniques to resolve the $n\lambda$ uncertainty can be used. Attitude determination is further explored in Chapter 19 of the companion volume.

i. Hybrid GPS receivers. In many applications, it makes sense to integrate GPS receiver measurements with inertial measurement systems or other navigation aids. The two sets of measurements can provide better capability than either could alone. For example, temporary shadowing or other interruption of the GPS satellite signals by a momentary obstruction or interference can be accommodated by an inertial system that can allow the navigation systems to continue to operate without interruption. (See Chapters 6–9 of the companion volume.)

VI. GPS Signal Perturbations—Atmospheric/Ionospheric/Tropospheric Multipath Effects

The GPS signal frequencies L_1 and L_2 at 1.57542 GHz and 1.2276 GHz are sufficiently high to keep the ionospheric delay effects relatively small, yet not so high as to cause too large a path loss with the use of small omnidirectional antennas (which do not require pointing). In addition, the signal frequency is not so high as to cause any significant path loss attributable to rainfall attenuation. Nonetheless, the atmosphere does cause small but nonnegligible effects. As the GPS signal passes through the atmosphere from the satellite to the user, the signal encounters a number of propagation effects, the magnitude of which depends on the elevation angle of the signal path and the atmospheric environment where the user is located. These effects include the following:

1) Ionospheric group delay and scintillation
2) Group delay caused by wet and dry atmosphere—the troposphere and stratosphere
3) Atmospheric attenuation in the troposphere and stratosphere

There are also effects caused by multipath signals from reflective surfaces and scattering. These effects are discussed fully in Chapters 12, 13, and 14, this volume; the discussion below simply introduces the key principles.

A. Ionospheric Effects

The ionosphere is a region of ionized gases that varies widely from day to day and with solar conditions and also has a large diurnal fluctuation. The presence of the ionosphere changes the velocity of propagation v according to the refractive index $n = c/v$. The cumulative effect also depends on the angle of penetration through the ionosphere as shown in Fig. 12. The refractive index $n(r)$, in turn, varies along the propagation path r. The lower extent of the ionosphere is above 75–100 km, and the ionosphere peak electron content is somewhere in

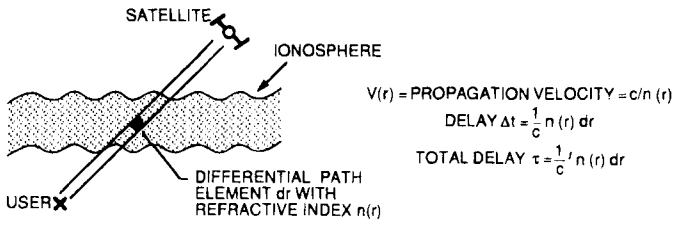

Fig. 12 Ionospheric delay along path through the medium.

the vicinity of 200–400 km. The peak ionospheric electron content can vary by as much as two orders of magnitude between day and night. A fundamental difference between the refractive index for the ionosphere and that for the troposphere is that the refractive index for the ionosphere varies with frequency because of the ionized gases.

The ionosphere can cause two primary effects on the GPS signal. The first is a combination of *group delay* and *carrier phase advance,* which varies with the exact paths and the electron density through which the satellite to user signal traverses the ionosphere. The second effect is ionospheric *scintillation,* which can at some latitudes cause the received signal amplitude and phase to fluctuate rapidly with time. Both effects depend the on the radio frequency and influence the GPS signal design. There are other effects, Faraday rotation and ray bending changing the angle of arrival, but these effects are not significant for purposes here.

At GPS frequencies in the 1.6 GHz frequency region, the ionospheric zenith path delay tends to vary with time in a diurnal fashion, as shown in Fig. 13 and might vary from 2 to 50 ns. As can be seen, however, the diurnal variation fluctuates quite markedly from day to day in a manner that seems difficult to predict. To first order, the ionospheric delay $\Delta\tau$ varies inversely with frequency squared $\Delta\tau \cong A/f^2$. As shown later, this relationship permits us to make dual frequency measurements at L_1 and L_2 to estimate the ionospheric delay. Note that because the lower extent of the ionosphere is typically well above the Earth's surface (see Fig. 14), the angles ϕ of entrance and exit of a satellite observed at 0 deg elevation angle by a user on the ground are well above 0 deg.

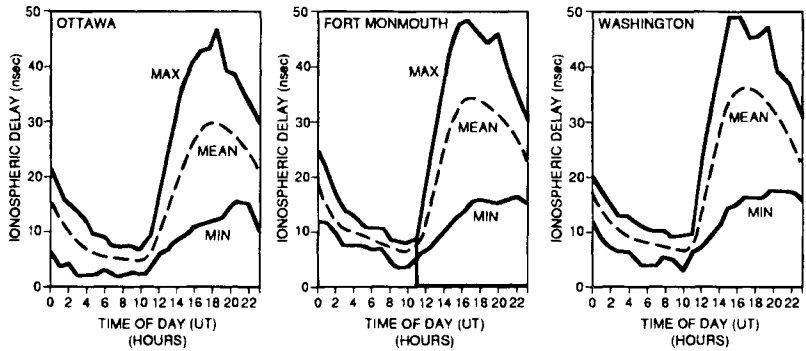

Fig. 13 Typical mean ionospheric delay and envelope of delay variation vs time of day during March 1958. Satellite at zenith f = 1.6 GHz.[5]

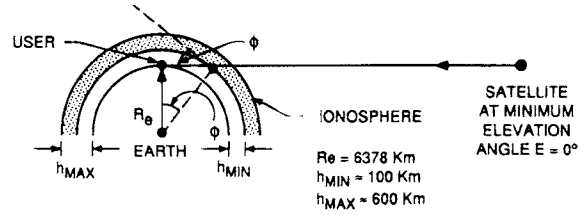

Fig. 14 Angle of incidence and exit of the ionosphere ϕ.

Thus, at lower elevation angles, the signal path transits through a larger extent of the ionosphere as shown in Fig 14. The delay at any elevation angle can be described as the ratio of actual delay to the vertical delay at $E = 90$ deg. This ratio is defined as the obliquity factor Q as shown in Fig. 15.

Note that the obliquity factor can be as high as three for low elevation angles. Because the ionosphere extends over moderate altitudes, 0.1–0.3 Earth radii, the satellite user signal path does not penetrate the ionosphere at very low elevation angles. This ionospheric effect is unlike the troposphere effects where the troposphere extends down to the Earth's surface. For an upper limit of the ionosphere of 600 km, the minimum angle of entrance to the ionosphere from the satellite is 24 deg. If the lower limit of the ionosphere is at $h = 100$ km, then the angle of exit is 10 deg. Height differences of 160–220 NM (160 NM $\cong$ 296 km) do not cause the obliquity factor to vary greatly at low elevation angles, as shown in Fig. 15. If the zenith ionospheric delay is 50 ns, then for an obliquity factor of three, the ionospheric delay at the lower elevation angles can be as much as 150 ns or approximately 45 m at 1.6 GHz. Clearly, this amount of unknown excess propagation delay is not consistent with a 15-m position accuracy objective for GPS and must be compensated for in some manner, either by modeling, measurement, or operation in a differential mode. Intuitively common ranging errors tend to affect the clock much more than horizontal position.

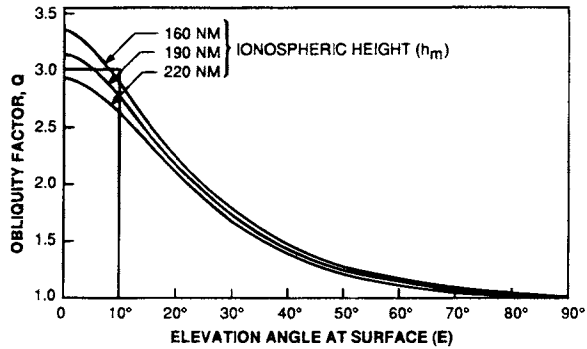

Fig. 15 Ionospheric group delay obliquity factor as a function of the relationship surface elevation angle.[5] The obliquity factor Q is the ratio of the ionospheric path delay for a satellite at elevation angle E to the delay function satellite at zenith (note 1 NM = 1.852 km).

B. Tropospheric Effects

The troposphere/stratosphere can produce a variety of propagation effects on radio waves from the satellite including the following:

1) Atmospheric attenuation
2) Tropospheric scintillation
3) Tropospheric refraction caused by the wet and dry atmosphere that produce excess delay in the signal

1. Tropospheric Group Delay

The troposphere is a region of dry gases and water vapor that extends up to approximately 50 km. This region has an index of refraction, $n(h) = 1 + N(h) \times 10^{-6}$, that varies with altitude. The index of refraction is slightly greater than unity, and hence, causes an excess group delay in the signal waveform beyond that of free space. This region is not ionized and is not frequency dispersive because the excess group delay $\Delta\tau$ is constant with frequency for frequencies below 15 GHz and is approximately equal to the following:

$$\Delta\tau = \int_{\text{path}} N(h)dh \times 10^{-6}$$

The excess group delay is normally on the order of 2.6 m for a satellite at zenith, and it can exceed 20 m at elevation angles below 10 deg. Thus, it must be modeled and removed if high accuracy positioning and time transfer are to be achieved. Dry atmospheric effects that are relatively easily modeled account for approximately 90% of the tropospheric excess delay. The wet atmosphere, although only about 10% of the total, is highly variable and very difficult to model. Detailed discussions of the ionospheric and tropospheric effects on GPS are given in Chapters 12 and 13, this volume.

C. Multipath Effects

1. Multipath

Some of the most difficult navigation problems are for aircraft. Aircraft navigation and three-dimensional navigation in general are also prime motivations for the GPS system. It is important to examine potential multipath effects that can be present in aircraft navigation. An aircraft flying at altitude h has a multipath environment with ground or sea surface reflections, as shown in Fig. 16. If the satellite elevation angle is E, the reflected ray is delayed with respect to the direct ray by $\Delta R = c\Delta\tau = 2h \sin E$. If, as an example, $h = 1$ km and $E = 10$ deg, then the delay difference in the reflected signal is $\Delta\tau = 1.16$ μs. The sea surface reflection cannot be avoided easily by antenna design if we must operate with satellites at low or moderate elevation angles. (The antenna pattern must allow for aircraft banking.) Furthermore, the reflected signal amplitude from the sea surface can at times be nearly as large or sometimes even larger than the direct ray. As shown later in Chapters 3 and 7, the GPS receiver can effectively reject most of the multipath signal if the differential delay $\Delta\tau > 1.5$ μs for the C/A code and 0.15 μs for the P(Y)-code. Note the region of potential

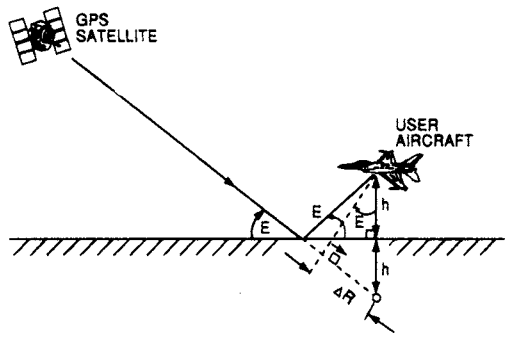

Fig. 16 Multipath effects. Multipath delay varies with elevation angle E and user altitude h. Delay = $\Delta R = 2h \sin E$.

mutipath delay problems for the C/A code is then

$$1.5\ \mu s > \frac{2b}{c} \sin E = \Delta\tau$$

or

$$h \sin E < (1.5\ \mu s)c = 448.5\ \text{m}.$$

Because the satellite is moving, the multipath will, in general, be time varying. A reflected multipath signal has the following Doppler shift

$$\Delta f = \Delta\dot{\phi} = \frac{2\dot{h} \sin E + 2h\dot{E} \cos E}{\lambda}$$

for the example shown in Fig. 16. More generally, the multipath may consist of a whole array of scatterers/reflectors, as shown in the impulse response of Fig. 17b. If the number of reflectors is sufficiently large and they are modeled as

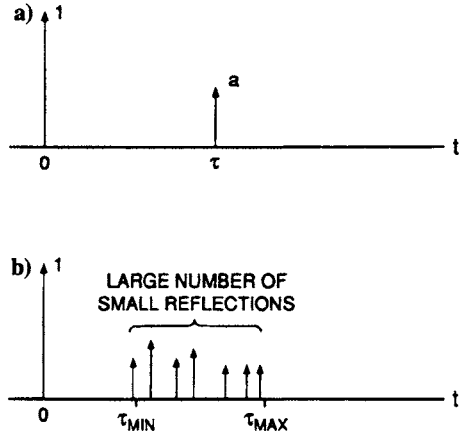

Fig. 17 Multipath channel impulse response with a) a single specular reflection; and b) a large number of smaller reflections.

independent random reflections, then the summed multipath reflection is approximately Gaussian and has a Rayleigh distribution in amplitude.

Within the constraints of available bandwidth (≈2 MHz per channel for the usual civilian receivers) and limitations on receiver complexity, the GPS signal is designed to resist the interference from multipath signals for delay differences that exceed 1 μs. Of special importance are multipath signals with a delay difference corresponding to the aircraft sea surface reflections described above. The capability for multipath discrimination of the selected GPS signal is examined in Chapter 14, this volume. We should recognize however, that there can also be reflections from nearby metallic or conducting surfaces (e.g., aircraft wings or stabilizers) that cannot be discriminated against by choice of signal within the bandwidth constraint because the delay difference is too small.

D. Other Perturbing Effects

In addition to the satellite clock and ephemeris errors of the GPS control segment and the atmospheric effects of the ionosphere, troposphere, and multipath, there are several other effects that are important for at least some users. Each of these is briefly discussed below.

1. Relativistic Effects

The Global Positioning System is perhaps the first widely used system where relativistic effects are not negligible. For example, referring back to Figs. 2 and 4, the position and time were all discussed in gravity-free inertial space with stationary users and a nonrotating Earth. In fact, there are several relativistic effects that are nonnegligible. These effects include the following: 1) gravitational field of the Earth and Earth rotation; and 2) velocities of satellite and user. The major effects cause an average increase in the satellite clock frequency as observed by a user on Earth. These effects are partially accommodated by purposely setting the satellite clock slightly low in frequency prior to launch. This topic is discussed in Chapter 18, this volume.

2. Foliage Attenuation

One of the major classes of users for GPS are ground mobile users. If these users are traveling along a road or highway, there is the possibility of obstructions or tree foliage attenuations of the GPS segments. This topic is discussed in Chapter 15, this volume.

3. Selective Availability

To reduce the potential for GPS to be used in hostilities toward the United States, the accuracy of the GPS signal for civil users can be purposely reduced by a capability called selective availability, which is discussed in Chapter 17, this volume.

References

[1]Kaplan, G. H., "The IAU Resolutions on Astronomical Constants, Time Scales, and the Fundamental Reference Frame," U.S. Naval Observatory Circular 163, Washington, DC, Dec. 1981.

[2]Spilker, J. J., Jr., and Magill, D. T., "The Delay Lock Loop—An Optimum Tracking Device," *Proceedings of the IRE,* Vol. 49, Sept. 1961.

[3]Spilker, J. J., Jr., *Digital Communications by Satellite,* Prentice-Hall, Englewood Cliffs, NJ, 1977, 1995.

[4]Spilker, J. J., Jr., "GPS Signal Structure and Performance Characteristics," *Navigation,* Summer 1978, pp. 121–146; also published in *Global Positioning System Papers,* Institute of Navigation, Washington, DC.

[5]National Research Council, *The Global Positioning System—A Shared National Asset,* National Academy Press, Washington, DC, 1995.

Chapter 3

GPS Signal Structure and Theoretical Performance

J. J. Spilker Jr.*
Stanford Telecom, Sunnyvale, California 94089

I. Introduction

THIS chapter discusses the details of the Global Positioning System (GPS) signal structure, its specifications, and general properties. The chapter begins with a review of the general performance objectives and quantitative requirements of the signal. Because the GPS signal falls into a broad category of signals known as spread spectrum signaling, the fundamentals of spread spectrum signaling are introduced. The chapter continues with a detailed description of the GPS signal structure for both the precision (P code) and civil coarse/acquisition (C/A code) signals. The various minor distortions and imperfections permitted by the GPS satellite–user interface specification are also discussed. Although the general format of the navigation data is summarized, details of the navigation message are given in the next chapter. The radio frequency signal levels and relevant signal-to-noise ratios are discussed next. The chapter concludes with a discussion of the signal performance characteristics including: 1) C/A- and P-code cross-correlation properties for multiple access, and 2) performance bounds on the C/A- and P-code pseudorange tracking accuracy for the optimal delay–lock-loop tracking receivers.

A brief summary of Galois fields that are the mathematical basis for maximal length and Gold sequences is given in the Appendix.

A. Summary of Desired GPS Navigation Signal Properties

Based on the navigation accuracy and system requirements and the relevant physics/communication theory discussed in the previous chapter, the system level accuracy requirements can now be stated and translated into signal measurement accuracy requirements. User position and velocity accuracy objectives translate into requirements on pseudorange and other GPS signal measurements and infor-

*Ph.D., Chairman of the Board.

mation on satellite position and clock time at the time of transmission that must be available to the user receiver. This required information is summarized in Fig. 1.

The accuracy of the pseudorange measurements can be related to the desired accuracy of position by the various **dilutions of precision** (DOP); e.g., position dilution of precision (PDOP), and horizontal dilution of precision (HDOP). If it is assumed that PDOP ≈ 3 then a 10-m rms user position error translates into a pseudorange accuracy* of ≤ 10 m/3 = 3.33 m or 11 ns. Likewise, a civil user needing 100-m real-time accuracy translates to a pseudorange accuracy of roughly 110 ns. In addition, the GPS signal should also possess the following properties:

1) Tolerance to signals from other GPS satellites sharing the same frequency band; i.e., multiple access capability

2) Tolerance to some level of multipath interference—there are many potential sources of multipath reflection; e.g., man-made or natural objects or the sea surface for an aircraft flying over water

3) Tolerance to reasonable levels of unintentional or intentional interference, jamming, or spoofing by a signal designed to mimic a GPS signal

4) Ability to provide ionosphere delay measurements—dual frequency measurements made at L_1, L_2 frequencies must permit accurate estimation of the slowly changing ionosphere

1. *Flux Density Constraints*

In addition to the requirements stated above for the GPS signal, there are requirements that the GPS signal received on the Earth be sufficiently low in power spectral density so as to avoid interference with terrestrial microwave line-of-sight communication. For example, a line-of-sight microwave terminal carrying a large number of 4-kHz voice channels potentially can receive interference from a GPS satellite signal that might be observed within the antenna pattern of the receive microwave antenna. Thus, the power flux density of the GPS

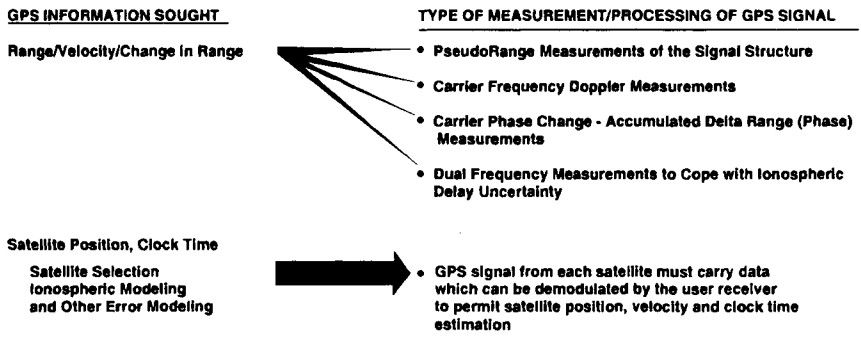

Fig. 1 GPS information sought and measurement/signal processing by the user receiver.

*This statement assumes that there are no other error effects besides pseudorange. There are other errors; e.g., satellite position and clock time errors, but at the moment only the GPS pseudorange error effects are considered.

satellite signal in a 4-kHz band is constrained so as to remain below a certain level, thus eliminating the possibility of interference on one or more voice channels. Because the 24 GPS satellites orbit the Earth in 12-h orbits, many microwave radio locations will observe GPS satellites at low-elevation angles at one time or another. For this reason, the International Telecommunication Union (ITU) has set flux density regulations on the power that can be generated by a satellite-to-Earth link. In the 1.525–2.500 GHz band, the flux density limit for low-elevation angles is -154 dBW/m^2 for any 4/kHz frequency band[1]. Because the constraint is on power flux spectral density rather than total radiated power, a satellite can radiate more total power and stay within the flux density limit if the signal energy is spread out fairly uniformly over a wider spectral band. The Global Positioning System uses spread spectrum signals to achieve this goal wherein the signal spectra are spread out over a much wider bandwidth than their information content in order to permit use of higher power levels and, of course, to achieve sufficiently precise ranging accuracy. For a unity (0 dB) gain antenna, the aperture area is $A = \lambda^2/4\pi$, and for GPS L_1 at 1.57542 GHz, where the wavelength is $\lambda = 0.1904$ m and $A = 2.886 \times 10^{-3}$ m^2 or -25.4 dB relative to 1 m^2. Thus, this flux density limit transblates to a power level to a unit gain antenna at 1.54542 GHz of $-154 - 25.4 = -179.4$ dBW in any 4-kHz frequency band.

In addition to constraints for line-of-sight microwave radio, there are also constraints to protect radio astronomy. Radio astronomy makes use of the 1420.4 MHz spectral line of neutral atomic hydrogen (the 1400–1427 MHz band is assigned for radio astronomy) and the OH radical molecule with lines at 1612.232, 1665.402, 1667.359, 1720.530 MHz.[2] Thus, the GPS satellite signal is specially filtered to avoid interference with these bands.

B. Fundamentals of Spread Spectrum Signaling

Spread spectrum signaling in its most fundamental form is a method of taking a data signal $D(t)$ of bandwidth B_d that is modulated on a sinusoidal carrier to form $d(t)$, and then spreading its bandwidth to a much larger value B_s where $B_s >> B_d$. The bandwidth spreading can be accomplished by multiplying the data-modulated carrier by a wide bandwidth-spreading waveform $s(t)$. A simplified spread spectrum system is shown in Fig. 2. The figure shows a conventional biphase modulated transmitter* on the far left, followed by a spectrum-spreading operation, an additive noise and interference transmission channel, and the spread spectrum receiver processor. A binary data bit stream $D(t)$ with values $D = \pm 1$ and clock rate f_d is first modulated on a carrier of power P_d to form the narrow bandwidth signal:

$$d(t) = D(t)\sqrt{2P_d}\cos \omega_o t \tag{1}$$

This narrow bandwidth signal of bandwidth B_d is then spread in bandwidth by a binary pseudorandom signal $s(t)$ where $s(t) = \pm 1$ and has a clock rate f_c that greatly exceeds the data bit rate; i.e., $f_c >> f_d$. For random data and spreading

*In general the data signal $D(t)$ can be multilevel and complex. However, this discussion is restricted to binary real $D(t) = \pm 1$.

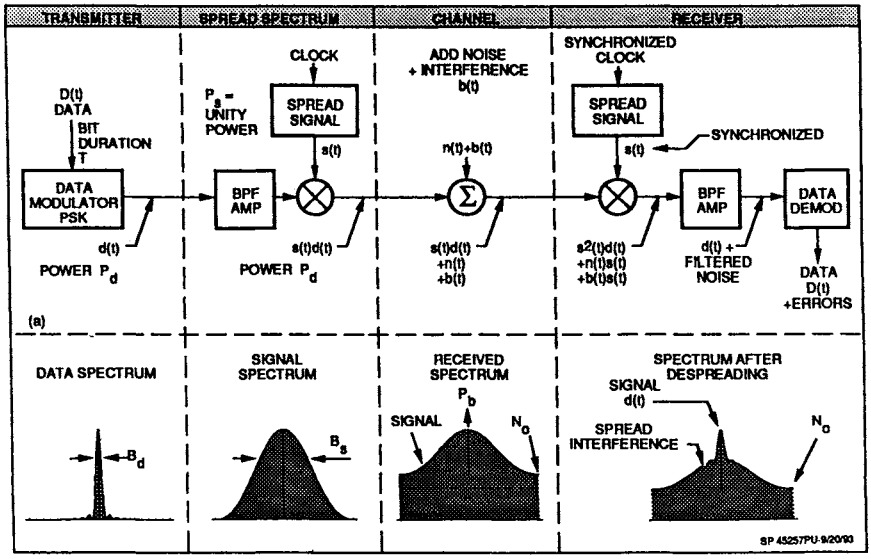

Fig. 2 Simplified spread spectrum link.

codes, the data $D(t)$ and spreading waveforms $s(t)$ have the following power spectral densities, respectively, as shown in Fig. 2.

$$G_d(f) = \frac{1}{f_d}[(\sin \pi f/f_d)/(\pi f_d)]^2 \quad \text{and} \quad G_s(f) = \frac{1}{f_c}[(\sin \pi f/f_c)/(\pi f/f_c)]^2$$

Because the timing of the data and clock transitions are synchronous, the spread spectrum product $D(t)\ s(t)$ has exactly the same spectrum as that of $s(t)$ alone. The spread spectrum signal then has the following form:

$$s_o(t) = s(t)d(t) = s(t)D(t)\sqrt{2P_d}\cos \omega_o t \tag{2}$$

where the spreading signal is as follows:

$$s(t) = \sum_{n=-\infty}^{\infty} S_n p(t - nT_c) \tag{3}$$

and $p(t)$ is a rectangular unit pulse over the interval $\{0, T_c = 1/f_c\}$ and S_n is a random or pseudorandom sequence $S_n = \pm 1$. In general, $p(t)$ can represent a filtered pulse, and different spreading waveforms $s_i(t)$ with coefficients S_{in} in Eq. (3) can separately modulate in-phase and quadrature carrier components. For this example, we restrict the discussion to rectangular pulses and biphase modulation.

This form of spread spectrum is termed **direct sequence-spread spectrum** (DS-SS), and it is one of many different forms of spread spectrum. Other forms* include spreading by pseudorandom frequency hopping, termed frequency hop-

*There are other means for bandwidth spreading, such as low rate error correction coding, that do not employ an independent spreading waveform.[3]

spread spectrum (FH-SS), and various hybrid forms of DS-SS and FH-SS. We restrict our discussion here to DS-SS because it provides a means to recover precise timing, and at the same time, it permits recovery of the pure rf carrier. The ability to recover pure carrier is key to precision differential delay and Doppler measurements that provide accuracies on the order of 1% of a carrier wavelength.

The DS-SS signal in Fig. 2 next passes through a channel (with zero channel delay for simplicity and without loss of generality) with additive white noise $n(t)$ of power spectral density N_0 and interference $b(t)$ to form the received signal $r(t) = s(t)\,d(t) + n(t) + b(t)$ where $b(t)$ is a pure tone interference of power P_b. In the receiver, an identical and precisely time-synchronized replica spreading signal $s(t)$ is generated and correlated (multiply and filter) with the received noisy signal. The fact that the received replica must be accurately time synchronized is shown later to be the exact property that enables the system to extract accurate timing and ranging information. That is, the signal has a narrow autocorrelation envelope of width inversely proportional to the clock rate f_c. The receiver multiplier converts the desired signal $d(t)\,s(t)$ to $d(t)\,s^2(t) = d(t)$ because $s^2(t) = 1$; that is, it compresses the spread spectrum signal to its original narrow bandwidth with only the data modulation remaining. The noise spectral density is still N_0 because convolving white thermal noise with a continuous constant envelope spread spectrum signal is still white Gaussian noise. The narrowband interference $b(t)$ has now been spread to look like $s(t)$ and has bandwidth B_s, similar to the manner in which the narrowband signal $d(t)$ was spread in the transmitter. Filtering this multiplier output through a bandpass filter passes the narrowband signal $d(t)$ relatively undistorted, however only a fraction of the noise and interference power passes through the bandpass filter with power $N_0\,B_d$ and $P_b\,(B_d/B_s)$, respectively.

Demodulation of this filtered output then produces a bit error rate that is determined by this noise and interference level. Note that if there is only thermal noise and no other interference is present, then the receiver output is exactly the same in terms of signal power and noise density as if there had been no spectral spreading at all. That is, the effects of the spreading and despreading by the binary pseudorandom code $s(t)$ in the transmitter and receiver cancel. Thus, the use of properly synchronized spread spectrum signaling neither improves nor degrades the signal performance against a thermal noise background.

However, the performance against a tone interference of fixed power is greatly improved because the interference power level is reduced by the ratio of the clock rates f_c/f_d. The ratio, f_c/f_d, of the PN chip rate f_c to the data bit rate f_d is termed the *processing gain of* the spread spectrum system and is a key parameter because it determines what fraction (f_d/f_c) of the interference power passes through to the output. Whereas the thermal noise power increases in direct proportion to radio frequency bandwidth, the interference power is fixed and independent of bandwidth. In fact, spread spectrum signaling is effective against a much broader class of interference than simple tone interference.

1. Direct Sequence-Spread Spectrum Signals—Autocorrelation Function and Spectrum

A noise-like pseudorandom binary spreading sequence $s(t)$ bears a close resemblance to a random sequence. A purely random binary sequence is generated by

a coin-flipping operation where the outcome is equally probable ± 1. This sequence at clock rate f_c can generate the waveform $s(t)$ of (3), which is shown in Fig. 3a, and it has a triangular autocorrelation function and $(\sin \pi\tau f/\pi\tau f)^2$ shaped power spectral density as shown in Fig. 3b,c. As is shown in a later paragraph, a close approximation (pseudorandom) to a random sequence can be generated by using suitable feedback shift registers. Thus, we can generate a replica waveform at the receiver and suitably time synchronize this replica to the received signal.

2. *Multiple Access Performance of Spread Spectrum Signaling*

It is often desired to provide a method by which multiple signals can simultaneously access exactly the same frequency channel with minimal interference between them. Spread spectrum signaling has the capability to provide a form of multiple access signaling called code division multiple access (CDMA) wherein multiple signals can be transmitted in exactly the same frequency channel with limited interference between users, if the total number of user signals M is not too large. This multiple access capability is important for GPS because a user receiver may receive simultaneously 10 GPS signals from 10 different satellites, wherein all signals occupy the same frequency channel and are continuous (i.e., not time gated). For example, assume that there are M signals, all of exactly the same power P_s received at a receiver antenna. If all M signals are received with exactly the same code clock delay, it is possible to select a certain number of signals that are completely orthogonal, and thus cause no multiple access interference provided $M \leq f_c T_d$ where $f_d = 1/T_d$ is the data bit rate. However, in many communication/ranging tasks orthogonal signaling is not possible because the signal sources—the GPS satellites in our example—cannot possibly all be equally distant from each user. Good multiple access performance is still possible, however, by selecting the different GPS spread spectrum pseudorandom codes to be nearly uncorrelated for all possible time offsets.

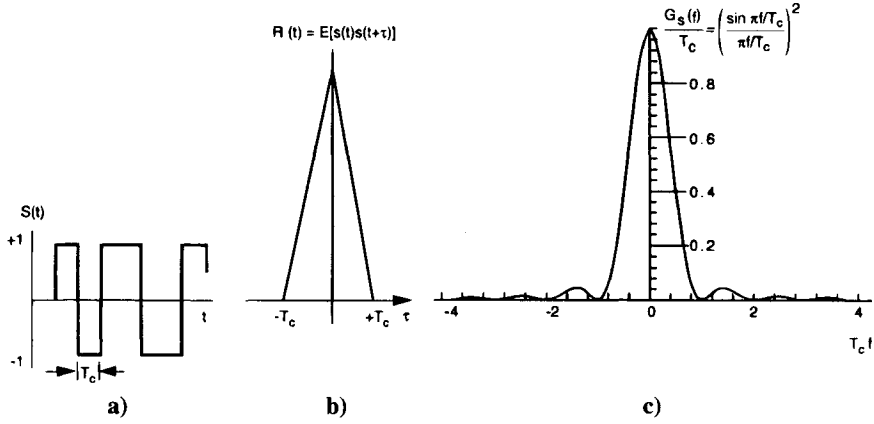

Fig. 3 Random binary sequence, autocorrelation function, and power spectral density—a) waveform, b) autocorrelation function, and c) power spectral density. The clock rate is $f_c = 1/T_c$.

Examine two multiple access signals $s_i(t)$ and $s_j(t)$, which are both uncorrelated pseudorandom codes with identical spectra $G_s(f)$ and are both transmitted on the same frequency channel and received with independent random timing. The receiver of Fig. 2 for the first signal; e.g., $s_i(t)$, cross-correlates the received additive signals with the desired reference signal code $s_i(t)$. Ignoring the data modulation, carriers, and noise for the moment, the correlator output is then $s_i(t - \tau_1)\,[s_i(t - \tau_1) + s_j(t - \tau_2)] = 1 + s_i(t - \tau_1)\, s_j(t - \tau_2)$. The unity term is the desired component, and the spread spectrum multiple access interference term is $s_i(t - \tau_1)\, s_j(t - \tau_2)$. For random time offsets between the two signals and power level P_s, the multiple access interference spectrum is defined as $G_{ma}(t)$ and is obtained by convolving the individual spectra (see Fig. 4):

$$G_{ma}(f) = P_s \int G_s(\nu) G_s(\nu - f)\, d\nu \quad \text{and} \quad G_{ma}(0) = P_s \int G_s^2(\nu)\, d\nu$$

Assume that the processing gain is large; i.e., $f_c/f_d >> 1$. Then only the multiple access interference spectrum near $f = 0$ is significant because the correlation filters can have a bandwidth on the order of f_d. The convolved spectrum at $f = 0$ can be computed to be:

$$G_{ma}(0) = P_s \int_0^{\infty} \left(\frac{\sin \pi f/f_c}{\pi f/f_c} \right)^4 df$$

$$G_{ma}(0) = \left(\frac{2}{3} \right) (P_s/f_c)$$

Note that if the multiple access signal has transitions coincident with the reference signal; that is, a nonrandom time offset, the multiple access interference

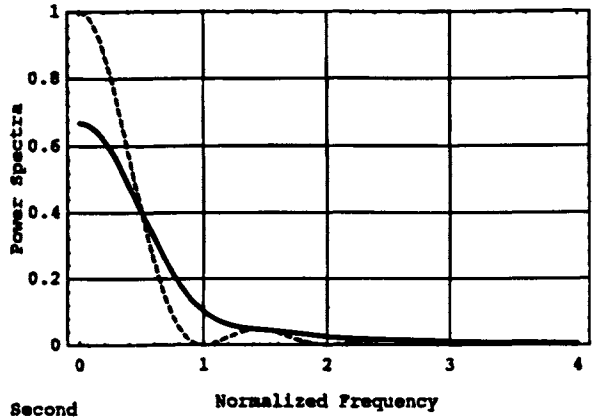

Fig. 4 Original spectrum (sin $\pi/\tau f)^2$ (dashed line) and the convolved spectrum G_{ma} (f) (solid line) at the correlator output, for a normalized clock rate $f_c = 1$ for an unfiltered pseudorandom signal. Note that the multiple access power spectral density at $f = 0$ decreases to 2/3.

is not spread, and the factor of 2/3 does not appear. Note also, that this result (Fig. 4) assumes that the $[(\sin \pi f/f_c)/\pi f/f_c]^2$ spectrum includes all of its sidelobes and is not filtered. If the signal is filtered to include only the main lobe the factor of 2/3 increases to approximately 0.815. If the signal spectrum is rectangular the factor is unity. As shown later, the transmitted GPS C/A code is nearly unfiltered and contains sidelobes out to the 10th. The GPS P code has the same bandwidth but 10 times the clock rate, and thus only contains the mainlobe.

Because there are M-1 interfering multiple access signals, and there is only one desired signal for each tracking receiver, the net effect of the M-1 multiple access signals is to increase the effective noise spectrum in the vicinity of the desired data modulation from a value N_o with no multiple access interferences to an equivalent noise density:

$$N_{oeq} = N_o + \frac{2}{3}\left(M - 1\right)P_s/f_c = N_o[1 + \frac{2}{3}(M - 1)P_s/f_cN_o] \tag{4}$$

Table 1 summarizes the equivalent noise density relationships for spread spectrum multiple access signals for the complete $(\sin x/x)^2$ spectrum, $(\sin x/x)^2$ mainlobe only, and rectangular spectra.

Thus, if all sidelobes are included, the effective noise density is increased by the factor $1 + (2/3)(M - 1)P_s/f_c$, and the effective energy per bit E_b to equivalent noise density ratio decreases to the following:

$$\frac{E_b}{N_{oeq}} = \frac{P_sT_d}{N_o\left[1 + \frac{2}{3}(M - 1)P_s/f_cN_o\right]} = \frac{P_s}{N_of_d}\frac{1}{\left[1 + \frac{2}{3}(M - 1)P_s/f_cN_o\right]} \tag{5}$$

The quantity E_b is the energy per bit $E_b = P_s/f_d$. The quantity E_b/N_{oeq} determines the output error rate. For biphase modulated (antipodal) signaling the E_b/N_{oeq} needs to be on the order of 10 if no error correction coding is employed.* If the performance of the system is not to be degraded by more than 3 dB relative to thermal noise performance, then from (5) the number of equal power multiple access signals is limited by the following:

$$M < \frac{3}{2}\left(\frac{N_of_c}{P_s}\right) + 1 = \frac{3}{2}\left(\frac{N_of_c}{E_sf_d}\right) + 1 = \frac{3}{20}\left(\frac{f_c}{f_d}\right) + 1 \quad \text{for} \quad \frac{E_b}{N_{oeq}} = 10 \tag{6}$$

the limit on M increases as the spread spectrum clock rate of f_c increases.† Again, it is pointed out that the factor of 3/2 applies only for the unfiltered $(\sin x/x)^2$ spectrum.[4] Note that for GPS there are often $M = 9$, 10 GPS signals in view. See the later chapter on the GPS constellation. Furthermore, note that if the

*Although GPS does not employ error correction coding, it should be pointed out that the use of spread spectrum signaling generally does permit the use of low rate error correction codes that can allow operation at low values of E_b/N_o without suffering from bandwidth expansion because the spread spectrum signaling is already broadening the spectrum by itself.

†For example, with $f_c = 10^6$ and $f_d = 50$, this result, (6), becomes:

$$M < (3/20)(10^6/50) + 1$$
$$M < 3 \times 10^3 + 1$$

Table 1 Equivalent noise density for M equal power spread spectrum signals of different power spectral densities[a]

Spread spectrum signal spectra	Multiple access equivalent noise density at $F = 0$
$G_s(f)$, $-\infty < f < \infty$	$N_o\left[1 + \frac{(M-1)P_s}{N_o}\right]\int_{-\infty}^{\infty} G_s^2(f)\,df$
$\frac{1}{f_c}\left[\frac{\sin \pi f/f_c}{\pi f/f_c}\right]^2$, $-\infty < f < \infty$	$N_o\left[1 + \left(\frac{2}{3}\right)\frac{(M-1)P_s}{f_c N_o}\right]$
All sidelobes	
$\frac{1}{f_c}\left[\frac{\sin \pi f/f_c}{\pi f/f_c}\right]^2\left(\frac{\pi}{2 \text{ sin integral}(2\pi)}\right)$, $-f_c < f < f_c$	$N_o\left[1 + \frac{\pi(M-1)P_s}{3f_o N_o}\cdot\left(\frac{2 \text{ sin integral}(4\pi) - \text{sin integral}(2\pi)}{(2 \text{ sin integral}(2\pi))^2}\right)\right]$
Mainlobe only	$= N_o\left[1 + \frac{(M-1)P_s}{f_o N_o}(0.815497)\right]$
Rectangular spectrum $\frac{P_s}{2f_o}$, $-f_o < f < f_o$	$N_o\left[1 + \frac{(M-1)P_s}{f_o N_o}\right]$

[a]The reference signal spectra $G_s(f)$ are all normalized to unity signal power. Each of M received signals has power P_s.

desired signal is 1/10th of the power of the other signals, the value of M permitted decreases approximately by a factor of 10. As shown later, in some instances the DS-SS code has a relatively short period (e.g., the GPS C/A code), the spectrum of the spreading code has line components spaced at the epoch rate, and the performance is not quite as good as indicated above.

3. *Generation of the Spreading Signal Using Linear Feedback Shift Registers*

Figure 5 shows a simple four-stage linear feedback shift register with taps after stages 1 and 4, which are modulo-2 added to form a short period maximal length pseudorandom or pseudonoise PN sequence. The sequence of shift register state vectors is shown in Fig. 5b, where the initial state vector is as follows:

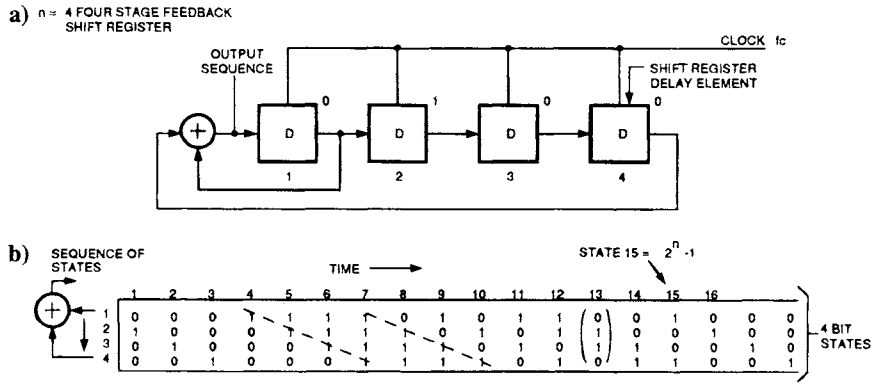

Fig. 5 Generation of a PN sequence using a maximal length feedback shift register and the $2^4 - 1 = 15$ sequence of code generator states. The state vectors each have four binary components, as shown in b.

$$\mathbf{s}_1 = \begin{pmatrix} 0 \\ 1 \\ 1 \\ 1 \end{pmatrix}$$

The state vector components are defined by the state of each of the four binary shift register delay elements. As long as this shift register is not set to the "all zero" state, it will cycle through all $2^4 - 1 = 15$ state vectors in a periodic manner. Only specific tap combinations produce a sequence of length $2^4 - 1 = 15$. In general, an n stage linear feedback shift register (LFSR) with proper taps generates all 2^n of the n-bit states except the all-zero state, thus it cycles through each of the possible state vectors. The use of the word "linear" refers to the restriction on the logic to modulo-2 adders. Thus, there are $2^n - 1$ states in the period of the sequence, and the sequence has a period $2^n - 1$.

Figure 6 shows the PN sequence at the output of a selected stage. The autocorrelation of the PN sequence where $s(t) = \pm 1$ is the following:

$$R(i) = (1/15) \int_0^{15} s(t)s(t + i)\mathrm{d}t$$

and for rectangular pulses has the form shown in Fig. 6c when expressed as a function of continuous time.

The maximal length sequence can be designed to have an arbitrarily long period $2^n - 1$ by increasing the number of stages n. As n increases, the maximal length sequence becomes more random in appearance or pseudorandom, and its spectrum approximates the $(\sin x/x)^2$ spectrum of Fig. 3. Because of the sharp (narrow in time) peak of the autocorrelation function for a high clock rate signal, the waveform also can be used for very accurate measurements of time and range or pseudorange. Obviously, this characteristic is key for GPS. An introduction

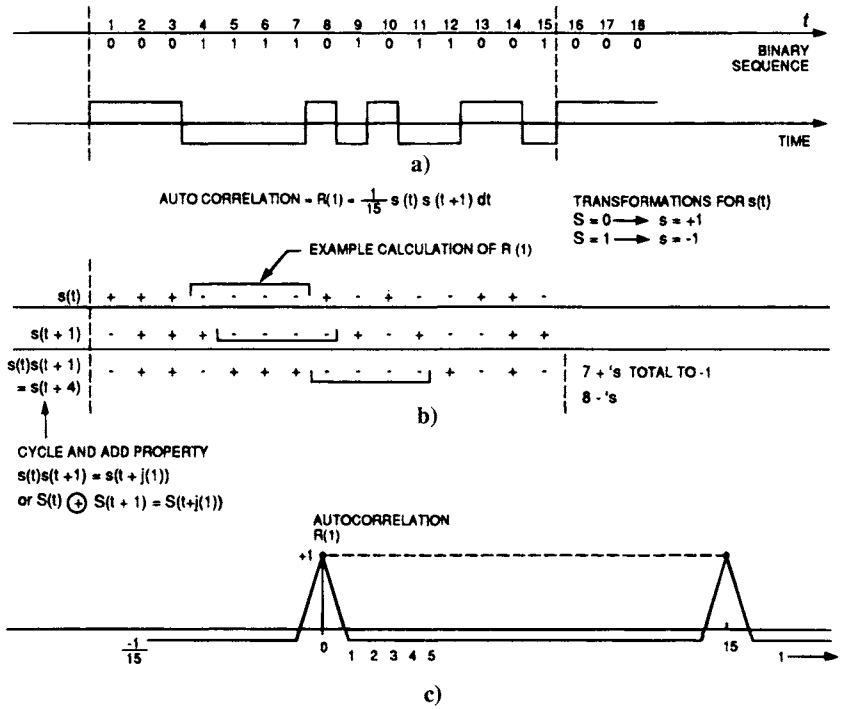

Fig. 6 Autocorrelation function of a PN sequence with $P = 2^n - 1 = 15$ states.

to the more detailed analysis of PN codes and Galois field algebra for PN codes is given later in the chapter as an appendix.

II. GPS Signal Structure

In this section, the structure of the GPS signal is described in detail. The general properties of the civil and precision direct sequence spread spectrum signals and codes are discussed and related to many of the system requirements. Detailed analyses of the performance of the signal are given in the next section.

As stated earlier, the GPS system must provide authorized users with a 10-m or less rms position error, which for a PDOP ≈ 3 translates to a required accuracy of pseudorange measurement on the order of 11 ns. The Global Positioning System chose to accomplish this required accuracy with a 10.23-Mcps precision P code. Two other GPS objectives, rapid acquisition of the P-code and providing a lesser but still revolutionary three-dimensional accuracy for the civil user are achieved by the use of the civil coarse/acquisition (C/A)-code, which has a 1.023-Mcps chip rate and a code period of 1023 chips. Civil users do not have access to the P(Y) code when the P code is in the antispoof (AS) Y-code mode. The somewhat unusual code rates of 1.023 Mcps and 10.23 Mcps are selected so that the period of the C/A code corresponds exactly to 1 ms for time-keeping purposes.

A. Multiplexing Two GPS Spread Spectrum Signals on a Single Carrier and Multiple Access of Multiple Satellite Signals

Two important questions to deal with are how to multiplex the two codes, C/A and P, on a single carrier and how to provide the multiple access of the various GPS signals that are to be received from the different satellites within the available frequency band.

The GPS L_1 signal has two spread spectrum signals, civil, C/A, and precision, P, multiplexed onto a single radio frequency carrier. In addition, the signals from multiple satellites must share the same frequency channel. The Global Positioning System multiplexes the civil and precision code on a single carrier in phase quadrature and then employs CDMA so that the different satellite signals can share the identical frequency band. Each satellite P signal occupies the entire available bandwidth to maximize timing accuracy. Table 2 shows the multiplexing and multiple access alternatives considered during the original design of the GPS signal.

Time multiplexing of the two signals, civil (coarse) and precision on one carrier; i.e., transmitting a portion or all of the period of the civil signal followed by a portion of the long military signal, was a possible choice for GPS. However, a time multiplexed signal would not have permitted continuous phase measurement of the carrier because the civil user does not have access to the military precision signal. The ability to perform precision carrier phase measurements was always considered to be of key value to the GPS system. Time gating of the shorter C/A civil signal would also change its autocorrelation characteristics and results in a less desirable cross-correlation performance.

The alternative selected for GPS is to modulate the civil C/A signal on the in-phase component of the L_1 carrier and modulate the precision P signal on a quadrature phase (90 deg rotated), thus providing a constant envelope modulated carrier even if the two signals have different power levels. The GPS signal then has the form (neglecting data modulation) $XP_i(t) \cos \omega_o t + XG_i(t) \sin \omega_o t$ where XP_i represents the P-code and XG_i represents the C/A code. Data biphase modulates both inphase quadrature components identically.

The selected multiple access technique for GPS is CDMA wherein the signals are separated through the use of codes with good cross-correlation properties. Code division multiple access in some systems has a so-called "near–far" problem when substantial differences exist in the received signal levels from different

Table 2 Alternative multiplexing and multiple access techniques considered for the global positioning system

Methods of multiplexing onto a single carrier	Time multiplex civil and military codes		In phase and quadrature multiplex
Multiple access methods	Frequency division multiple access	Time division multiple access	Code division multiple access

transmitters. However, with GPS, the satellites are all at roughly the same range, and the received signal levels normally do not vary greatly. (Exceptions occur when the signal from a given satellite is blocked momentarily by an aircraft wing tip, or, if on the ground, by tree foliage.) The choice of a specific family of codes for GPS that provide the desired code division multiple access performance is discussed in detail in later paragraphs.

An alternative multiple access technique considered was frequency division multiple access (FDMA). Frequency division multiple access of the satellite signals, which was subsequently selected for the GLONASS navigation satellites, has the advantage that the civil signals can be truly uncorrelated by offsetting the carriers in frequency by the bandwidth of the civil PN code. However, this approach occupies a larger bandwidth for a given code bandwidth, a disadvantage that the GLONASS developers diminished by operating the civil signal at roughly half the clock rate of the GPS signal. The GLONASS civil signal operates with a single 511-bit length PN code at 511 kbps, and spaces the carriers in frequency by 562.5 kHz.*[5] GLONASS is discussed more extensively in a later chapter. Decreasing the C/A-code clock rate for the same power flux density on the ground would provide a somewhat lesser accuracy. The other aspect of the frequency division approach felt to be a disadvantage was that the user receiver would have to operate with several frequency offsets if many satellites were to be tracked simultaneously. It was believed that the frequency division multiple access operation had a cost implementation disadvantage for the state of the art at that time (1973–1974).

B. GPS Radio Frequency Selection and Signal Characteristics

During the design phase of the GPS system, various frequency bands were considered for the GPS signal. Although a strict optimization of the frequency is not meaningful because only certain frequency bands could be made available, several considerations were important in selecting the GPS frequency band. Some of these are noted in Table 3.

The use of *L*-band gives acceptable received signal power with reasonable satellite transmit power levels and Earth coverage satellite antenna patterns, whereas the *C*-band path loss is roughly 10 dB higher because the path loss is proportional to f^2 for an omnidirectional receive antenna and fixed transmit antenna beamwidth and range. The large ionospheric delay and fluctuation in delay weighs against uhf as does the difficulty in obtaining two large (≈20 MHz) bandwidth frequency assignments in the uhf band (two frequency bands are necessary for ionospheric correction). Thus, *L*-band was selected, and dual frequencies permit ionospheric group delay measurements. The signal bandwidths at both center frequencies are 20 MHz.

1. Global Positioning System Signal Characteristics

Thus, the GPS signal consists of two components, Link 1 or L_1, at a center frequency of 1575.42 MHz and Link 2, L_2, at a center frequency of 1227.6 MHz.

*The center frequencies of the channels are $1602 + 0.5625\,n$ MHz, where $n = 0, 1, 2, \ldots, 24$. See Chapter 9 in the companion volume.

Table 3 Global positioning system transmission frequency band selection considerations

Performance parameter	uhf ≈400 MHz	*L*-band (1–2 GHz)	*C*-band (4–6 GHz)
Path loss for omnidirectional receive antenna-loss $\sim f^2$	Path loss lowest of the three	Acceptable	Path loss ≈ 10 dB larger than at *L*-band
Ionospheric group delay, $\Delta R \sim 1/f^2$	Large group delay, 20–1500 ns	Group delay 2–150 ns at 1.5 GHz	Group delay ≈ 0–15 ns
Other considerations	Galactic noise ≈ 150°K at 400 MHz	—	Rainfall/atmospheric attenuation can be significant in 4–6 GHz band 0.1 to 1 dB/km at 100 mm of rain/hour

Each of the center frequencies is a coherently selected multiple of a 10.23 MHz master clock. In particular the link frequencies are the following:

$$\begin{aligned} L_1 &= 1575.42 \text{ MHz} = 154 \times 10.23 \text{ MHz} \\ L_2 &= 1227.6 \text{ MHz} = 120 \times 10.23 \text{ MHz} \end{aligned} \tag{7}$$

Similarly, all of the signal clock rates for the codes, radio frequency carriers, and a 50 bps navigation data stream are coherently related.

The frequency separation between L_1 and L_2 is 347.82 MHz or 28.3%, and it is sufficient to permit accurate dual-frequency estimation of the ionospheric group delay. (The ratio of $L_1/L_2 = 77/60 = 1.2833$.) The ionospheric group delay varies approximately as the inverse square of frequency, and thus measurement at two frequencies permits calculation of the ionospheric delay. The ionospheric group delay correction is obtained by subtracting the total L_1 group delay τ_{GDL_1} from the total L_2 group delay τ_{GDL_2} in order to cancel the true pseudorange delay. This difference $\Delta\tau$ is then (neglecting random noise for the moment) the following:

$$\Delta\tau = \tau_{GDL_2} - \tau_{GDL_1} = \frac{A}{f_{L_2}^2} - \frac{A}{f_{L_1}^2} = \frac{A}{f_{L_1}^2}\frac{1}{1.54573} = \frac{\tau_{iono}}{1.54573} \tag{8}$$

or

$$\tau_{iono} = A/f_{L_1}^2 = 1.54573\ \Delta\tau$$

where τ_{iono} is the ionospheric group delay at L_1, and $\Delta\tau$ is the measurable difference between total propagation delays at L_1 and L_2. Thus, the frequencies L_1 and L_2 are separated far enough in frequency so that the ratio is only a factor 1.54573. Ionospheric effects and models are discussed both in Chapter 4 and in considerable detail in Chapter 12, this volume.

As discussed in Chapter 18, the relativistic effects are not negligible in GPS but are partially compensated for in the satellite by offsetting the 10.23 MHz master clock rate to a slightly lower number before launch. As the signal approaches the Earth from the satellite, the frequency increases slightly because of relativity by approximately the same factor as the offset, and for a stationary user on the Earth's surface, the GPS signal clock appears to have a frequency very close to the desired 10.23 MHz. Henceforth, when reference is made to the desired 10.23 MHz, the frequency will always be this slightly offset frequency as far as the satellite clocks are concerned when observed prior to launch. The actual frequency of the satellite clocks before launch is 10,229,999.995453 MHz or an offset of $\Delta f = 4.57$ mHz below 10.23 MHz. The fractional frequency offset is -4.46×10^{-10}(see Ref. 6).

The L_1 signal is modulated by both a 10.23 MHz clock rate precision P signal and by a 1.023 MHz civil C/A signal to be used by the civil user. The transmitted signal spectra for both L_1 and L_2 are shown in Fig. 7. The binary modulating signals are formed by a P code or a C/A code that is modulo-2 added to the 50 bps binary data D, to form* P⊕D and C/A ⊕ D, respectively. The P code also can be converted to a secure antispoof Y code at the same clock rate, and is labeled the P(Y) code. The L_1 signal has an in-phase component of its carrier that is modulated by the P signal, P⊕D, and a quadrature (within ±100 m rad) carrier component that is modulated by C/A⊕D. The peak power spectral density of the C/A signal exceeds that of the P code at L_1 by approximately 13 dB because it is nominally 3 dB stronger and has 1/10 the chip rate and bandwidth. The in-phase and quadrature waveforms and phasor diagram of the L_1 signal are shown in Fig. 8.

The L_2 signal is biphase-modulated by either the P code or the C/A code. Normal operation would provide P- or Y-code [labeled P(Y)] modulation on the L_2 signal. There may or may not be data modulation on L_2 dependent on ground command.

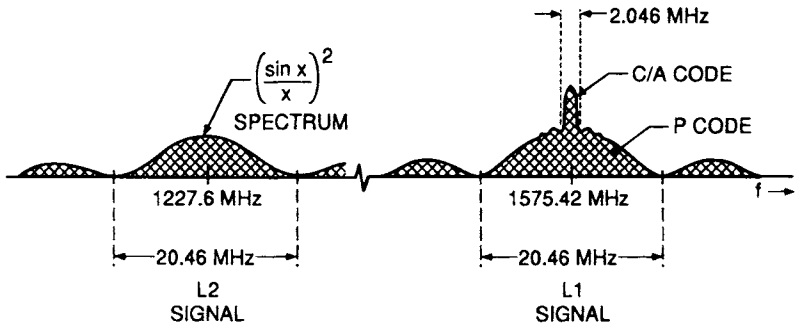

Fig. 7 GPS power spectral density.

*The symbol ⊕ stands for modulo-2 addition of 0, 1 numbers, which is equivalent to multiplication of +1, −1 numbers, respectively.

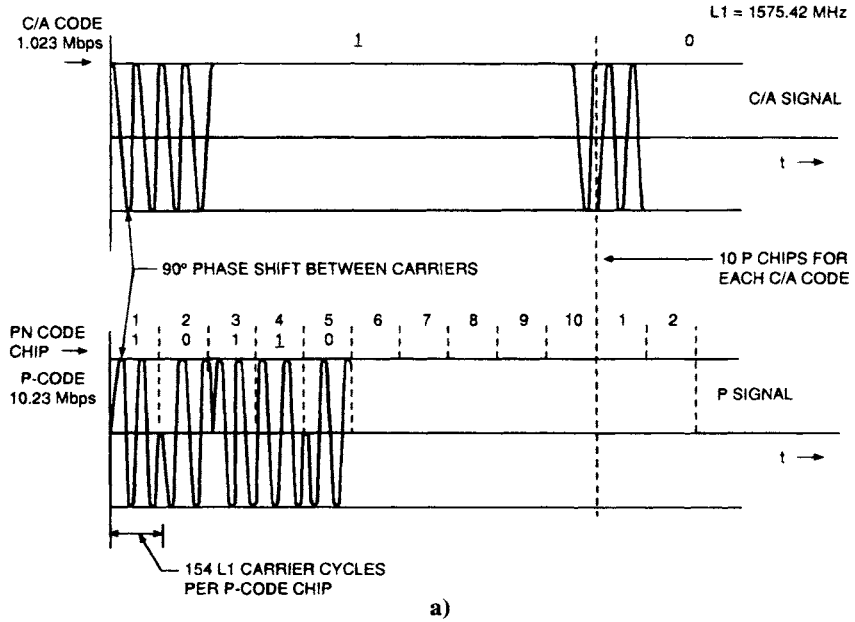

a)

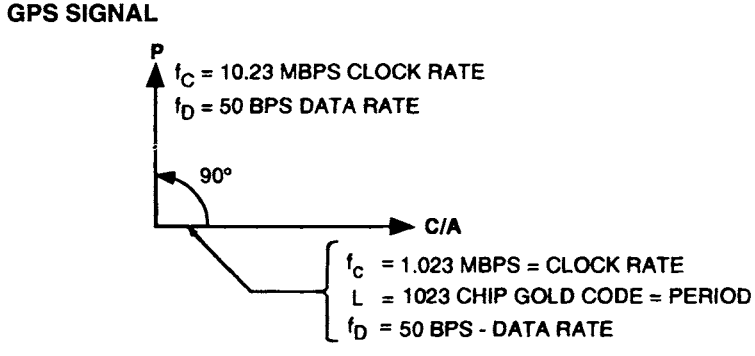

b)

Fig. 8 GPS L_1 signal waveform and phasor diagram. The P code for satellite i is labeled XP_i, and the C/A code for satellite i is labeled XG_i. a) Radio frequency waveforms for the P signal and C/A signal (carrier not to scale). b) Phasor diagram.

The GPS satellite can also transmit a third L-band carrier modulated by the C/A code at an L_3 frequency of 1381.05 MHz = 135 × 10.23 MHz. This signal is utilized only in a time-gated mode for a Nudet (Nuclear Detonation) Detection System (NDS) and is not used in the GPS navigation receiver.

C. Detailed Signal Structure

The L_1 signal contains both in-phase and quadrature signals. The signal transmitted (see Fig. 8) by the satellite i is then as follows:

$$S_{L_{1i}}(t) = \sqrt{2P_c}XG_i(t)D_i(t)\cos(\omega_1 t + \phi) + \sqrt{2P_p}XP_i(t)D_i(t)\sin(\omega_1 t + \phi) \quad (9)$$

where ω_1 is the L_1 frequency as defined above, ϕ represents a small phase noise and oscillator drift component and P_c and P_p are the C/A and P signal powers, respectively. Oscillator frequency stability is obtained using redundant cesium and rubidium atomic frequency standards. (The first satellite in the GPS series NTS-2, had a long-term clock stability better than 2×10^{-13} and later satellites have improved stability $\approx 3 \times 10^{-14}$). The P code $XP_i(t)$, is a ± 1 pseudorandom sequence with a clock rate of 10.23 Mbps, and a period of exactly 1 week. Each satellite i transmits unique C/A and P codes. The binary data $D_i(t)$, also has amplitude ± 1 at 50 bps and has a 6 s subframe and a 30 s frame period. The C/A code XG_i is a unique Gold code of period 1023 bits and has a clock rate of 1.023 Mbps. Thus, the C/A code has a period of 1 ms.

In GPS, the C/A-code strength is nominally 3 dB stronger than the P code on L_1. As already mentioned above, the code clocks and transmitted radio frequencies are all coherently derived from the same on-board satellite frequency standard. The rms clock transition time difference between the C/A and P code clocks is required to be less than 5 ns. Both C/A and P codes are of a class called product codes; i.e., each is the product of two different code generators clocked at the same rate where the delay between the two code generators defines the satellite code i (see Fig. 9). The specific component codes forming the product code for P and C/A are quite different, but the principle is similar. The clock interval for the C/A code $T_{cc} = 10T_c$ where T_c is the P-code clock interval in the figure.

1. *P Code—Precision Code*

The P code for satellite i is the product of 2 PN codes, $X1(t)$ and $X2(t + n_iT)$, where $X1$ has a period of 1.5 s or 15,345,000 chips, and $X2$ has a period of 15,345,037 or 37 chips longer. Both sequences are reset to begin the week at the same epoch time. Both $X1$ and $X2$ are clocked in phase at a chip rate $f_c = 1/T_c = 10.23$ MHz. Thus, the P-code is a product code of the following form:

$$XP_i(t) = X1(t)X2(t + n_iT), \quad 0 \le n_i \le 36 \quad (10)$$

where $X1(t)$ and $X2(t)$ are binary codes of value ± 1 and $XP_i(t)$ is reset at the beginning of the week. The delay between $X1(t)$ and $X2(t)$ is n_i code clock intervals of T_c s each (see Fig. 10). The $X1$ and $X2$ codes are each generated as the products of two different pairs of 12-stage linear feedback shift registers)

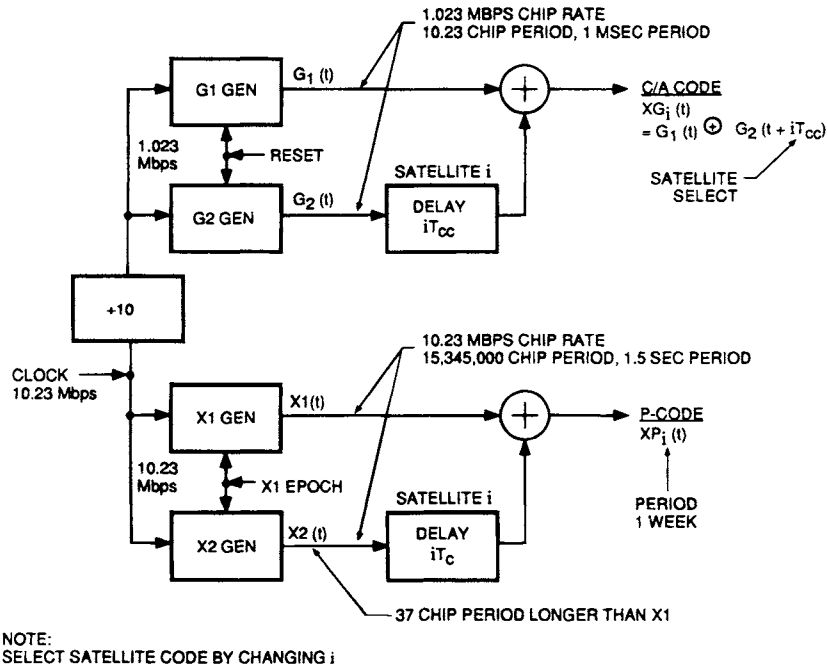

Fig. 9 GPS code generators for satellite *i*. Both the C/A- and P-codes are product codes.

X1A and *X1B* and *X2A* and *X2B* with polynomials specified in the GPS-ICD-200[6] as follows:

$$\begin{aligned} &X1A\colon 1 + X^6 + X^8 + X^{11} + X^{12} \\ &X1B\colon 1 + X + X^2 + X^5 + X^8 + X^9 + X^{10} + X^{11} + X^{12} \\ &X2A\colon 1 + X + X^3 + X^4 + X^5 + X^7 + X^8 + X^9 + X^{10} + X^{11} + X^{12} \\ &X2B\colon 1 + X + X^3 + X^4 + X^8 + X^9 + X^{12} \end{aligned} \tag{11}$$

See the Appendix for a discussion of code polynomials, Galois fields, and shift registers.

For now, suffice it to say that these polynomials give the feedback tap positions of the 12-stage shift registers, *X1A*, *X2A*, *X1B*, *X2B*, of Fig. 10. Recall the introductory discussion of Fig. 5. The *X1A* and *X1B* codes have different relatively prime periods as do the *X2A* and *X2B* codes. A 12-stage maximal length shift register produces a code period of $2^{12} - 1 = 4095$. If two code generators are short cycled to give relatively prime periods less than or equal to 4095, then the product code can have a period in the vicinity of 1.6×10^7, the product of the two periods. For GPS, the two product codes have been short cycled to relatively prime periods of 15,345,000 and 15,345,037 for the *X1* and *X2* respectively. Likewise, the product of *X1* and *X2* codes generates a new code that has a period that is the product of the periods, unless it is short cycled.

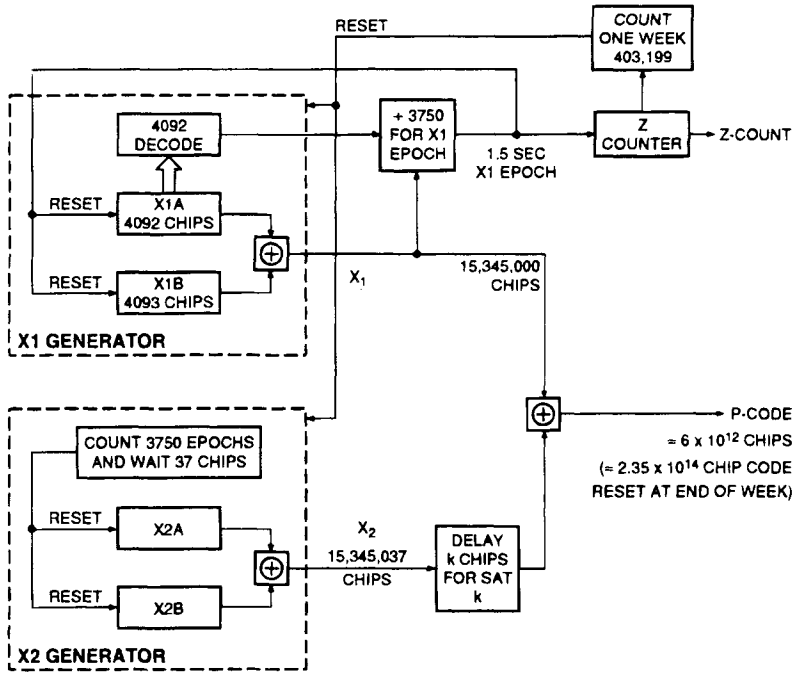

Fig. 10 Simplified P-code generator block diagram.

The product of $X1$ and $X2$ codes clocked together act somewhat like two gears with a number of teeth on each gear corresponding to the periods of $X1$ and $X2$ as shown in Fig. 11. If we imagine that the teeth of both gears are coded in black and white according to the respective binary chips in the PN sequence, then for relatively prime code lengths for $X1$ and $X2$ the period of this product code is equal to the product of the two individual codes periods (the number of teeth on each gear wheel). Each satellite has a unique code offset n_iT between code $X1$ and code $X2$, which makes the P-code unique as well. The increase in code period for $X2$ by 37 relative to $X1$ allows the values of n_i to range over 0–36 without having any significant segment of a P code of one satellite match that of another. Thus, we have 37 different pseudorandom P codes.

For a different view of the P code, note that the period of a product of $X1$ and $X2$ codes, each of which has a relatively prime period, is the product of the periods; i.e. $(15{,}345{,}000) \times (15{,}345{,}037) = 2.35469592765 \times 10^{14}$. Thus, if the P-code were allowed to continue without being reset, each P code would continue without repetition for slightly more than 38 weeks. In effect, this overall period has been subdivided so that each of 37 possible GPS satellites or ground transmitters (pseudolites) gets a 1-week period code, which is nonoverlapping with that of any other satellite.

A long period code such as the P code is difficult to acquire without acquisition aids. For example, a receiver correlator must be timed to within roughly one P-code chip or roughly 0.1 μs and clocked in synchronism in order to correlate at

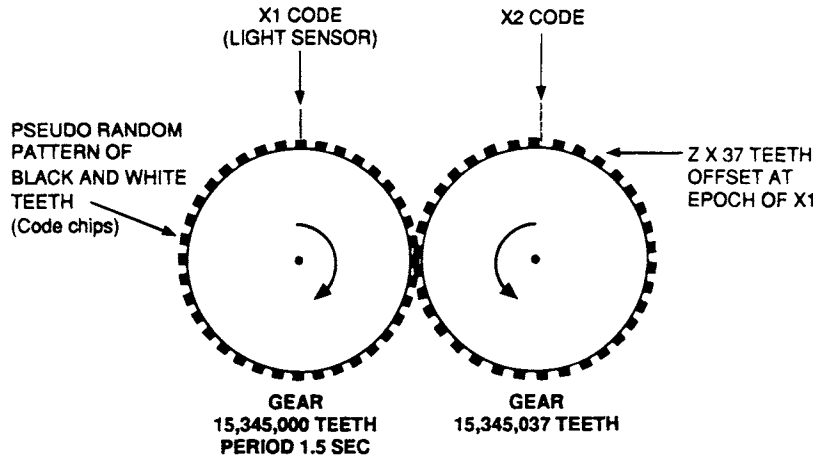

Fig. 11 P-code–subcode characteristics as represented pictorially by two gear wheels with light sensors for both gear wheels.

all. Note that the period of the $X1$ code is exactly 1.5 s, i.e., $1.5 \times 10.23 \times 10^6 = 15{,}345{,}000$, and there are this same number of code chip time bins to search.

A timing Z-count is defined in Fig. 12 as the number of 1.5 s $X1$ epochs since the beginning of the week. There are four $X1$ epochs per data subframe of 6 s. To help the receiver to acquire the long period P code, the 50 bps datastream contains an updated handover-word (HOW) for each 6-s subframe. The HOW when multiplied by 4, equals the Z-count at the beginning of the next 6-s subframe. Thus, if we have acquired timing from the relatively short C/A code and know the subframe epoch times and the HOW words, we can instantly acquire the P-code at the next subframe epoch. Figure 13 summarizes the timing relationships between $X1$, $X2$ epochs, and the Z-count and HOW words.

2. *Antispoof P(Y) Code, Nonstandard Codes, and Selective Availability*

The P code is a long, 1-week period code; however, it is published in GPS-ICD[6] and is available to potential spoofers or jammers. (A spoofer generates a signal that mimics the GPS signal and attempts to cause the receiver to track the wrong signal.) For this reason, the GPS system has the option to replace the P code with a secure Y code available only to authorized U.S. Government users. The Y code is employed when the "antispoof" or AS mode of operation is activated. The Y code is a secure version of the published P code that operates at the same clock rate as the P code, but has a code available only to authorized users. The main purpose of the Y code is to assure that an opponent cannot spoof the Y-code signal by generating a Y-code replica.

Nonstandard C/A and Y codes (NSC and NSY codes) are used in place of the C/A and P(Y) codes to protect the user from a malfunction in the spacecraft. They are only used for a malfunctioning satellite. These codes are not used in navigation receivers.

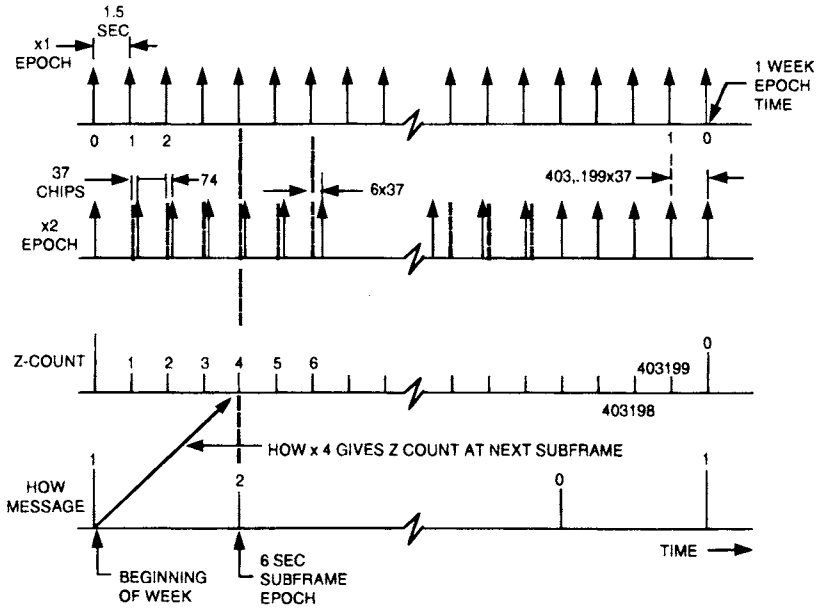

Fig. 12 Timing diagram for the P-code components X_1, X_2, and the Z-count and HOW message relationship (not to scale). The HOW message is carried in the 50-bps datastream.

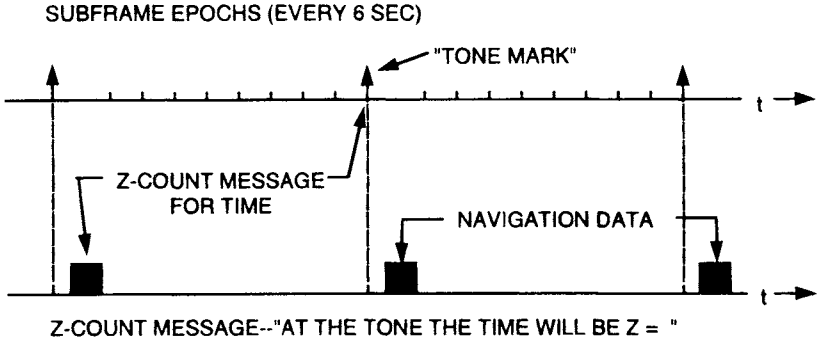

Fig. 13 GPS received signal time and the Z-count navigation data that are used to help acquire the P-code once the C/A code is acquired. The Z-count also aids in time ambiguity resolution for the C/A code.

Selective availability is a purposeful degradation of the GPS signal by the U.S. Government that can be imposed to restrict the full accuracy of the GPS system to authorized military users. Selective Availability (SA) is discussed in a later chapter in this volume. RMS position accuracy with SA is less than or equal to 100 m. SA purposely dithers the GPS clock in a pseudorandom manner. The clock dither has been reported by Allan and Dewey[7] to have a decorrelation time of 300–400 s. For observation times shorter than 300 s the clock dither can be modeled as a random walk phase modulation; for longer observation times it can be modeled as white noise phase modulation. As discussed in Chapter 2, this volume, recommendations have been made to turn selective availability to zero.

3. *Coarse/Acquisition (C/A) Code—Civil GPS Signal*

The C/A code for the civil user is a relatively short code with a period $2^{10} - 1 = 1023$ bits or 1-ms duration at a 1.023 Mbps bit rate. The code period is purposely selected to be relatively short so as to permit rapid acquisition. That is, there are only 1023 code chip time bins to search. The C/A codes are selected to provide good multiple access properties for their period. The C/A codes for the various satellites are taken from a family of codes known as Gold codes that are formed by the product of two equal period 1023 bit PN codes $G1(t)$ and $G2(t)$ (see Appendix and Ref. 8). Thus, this product code is also of 1023 bit period and is represented as follows:

$$XG(t) = G1(t)G2[t + N_i(10T_c)] \tag{12}$$

where N_i determines the phase offset in chips between $G1$ and $G2$. Note that C/A-code chip has duration $10T_c$ s where T_c is the P-code chip interval. There are 1023 different offsets N_i, and hence 1023 different codes of this form.* Each code $G1$, $G2$ is generated by a maximal-length linear shift register of 10 stages. The $G1$ and $G2$ shift registers, are set to the "all ones" state in synchronism with the $X1$ epoch. The tap positions are specified by the generator polynomial for the two codes:

$$\begin{aligned} G1&: G_1(X) = 1 + X^3 + X^{10} \\ G2&: G_2(X) = 1 + X^2 + X^3 + X^6 + X^8 + X^9 + X^{10} \end{aligned} \tag{13}$$

Because each Gold code has a 1-ms period, there are 20 C/A-code epochs for every databit. The 50-bps data clock is synchronous with both the C/A epochs and the 1.5 *s* $X1$ epochs of the P code. Figure 14 shows a simplified block diagram of the C/A-code generator. The unit is comprised of two 10-stage feedback shift registers clocked at 1.023 Mbps having feedback taps at stages 3 and 10 for $G1$ and at 2, 3, 6, 8, 9, 10 for $G2$, as indicated by the polynomials of (13). The various delay offsets are generated by tapping off at appropriate points on the $G2$ register and modulo-2 adding the two sequences together to get the desired delayed version of the $G2$ sequence using the so-called "cycle-and-add" property of the linear maximal length shift register (LMLSR). Maximal length shift register codes have the property that the addition of two time offset ("cycled") versions of the same code gives a shifted

*There actually are 1025 different Gold codes of this period and family. The codes, $G1(t)$ and $G2(t)$, by themselves, are the other two codes.

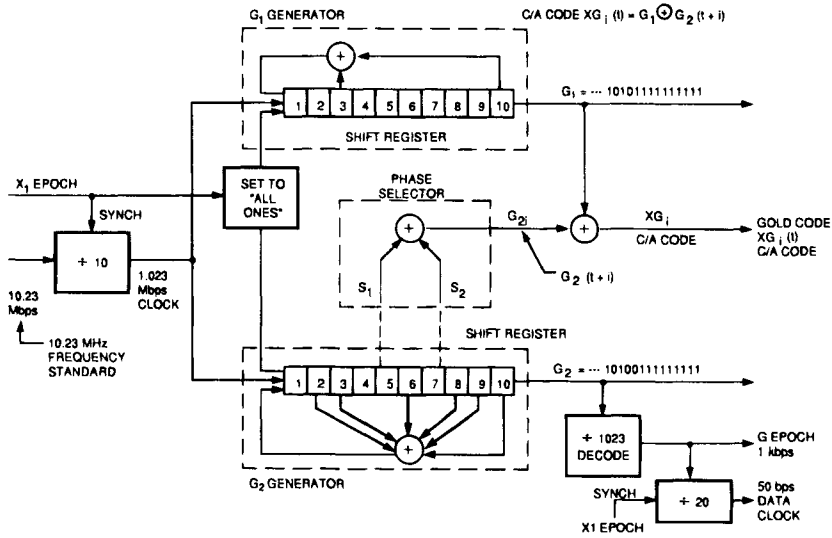

Fig. 14 C/A-code generator block diagram showing the 1-ms G epoch and data clock generators that are all in synchronism.

version of the same code; hence the name "cycle and add" property. This property is discussed later in the chapter. The code tap positions for various codes are given in Table 4. Note that there are 45 possible tap positions in Fig. 14, but as shown in Table 4, only 37 codes are defined in GPS-ICD-200.[6] The general relationship between code taps and code phase is analyzed in the Appendix. Epochs of G code occur at 1 Kbps and are divided down by 20 to get the 50 bps data clock. All clocks are in phase synchronism with the $X1$ clock, as shown in Fig. 14.

The recursive equations for the $G1$ and $G2$ sequences that correspond to the $G1$, $G2$ polynomials of (2–8) are as follows:

$$\begin{aligned} G1(i) &= G1(i-10) \oplus G1(i-3) \\ G2(i) &= G2(i-10) \oplus G2(i-9) \oplus G2(i-8) \\ &\quad \oplus G2(i-6) \oplus G2(i-3) \oplus G2(i-2) \end{aligned} \tag{14}$$

Table 4 gives the first bits of each of the 37 C/A codes in octal form. For reference, the first 31 bits of the first Gold code for SV#1 are {1, 1, 0, 0, 1, 0, 0, 0, 0, 0, 1, 1, 1, 0, 0, 1, 0, 1, 0, 0, 1, 0, 0, 1, 1, 1, 1, 0, 0, 1, 0, 1}.

Notice that the first 10 bits of this code match exactly those shown in Table 4.

It is also possible to generate each Gold code with a single 20-stage shift register (not maximal length) by simply using a code generator that corresponds to a polynomial that is the product of the $G1(x)$ and $G2(x)$ polynomials (modulo-2). This code generator still produces codes of length 1023. Different codes are formed by starting the shift register in the correct state. However, that form does not allow one generator to generate all codes easily. It is also possible simply to delay one code generator, the $G2$ generator, relative to $G1$ simply by changing the starting state of $G2$.

Table 4 GPS code phase assignments for various spacecraft ID numbers (taken from GPS-ICD-200)

SV ID No.	GPS PRN signal No.	Code phase selection, C/A, ($G2_i$)	$X2_i$	Code delay chips C/A	P	First 10 chips octal[a] C/A	First twelve chips octal P
1	1	2⊕6	1	5	1	1440	4444
2	2	3⊕7	2	6	2	1620	4000
3	3	4⊕8	3	7	3	1710	4222
4	4	5⊕9	4	8	4	1744	4333
5	5	1⊕9	5	17	5	1133	4377
6	6	2⊕10	6	18	6	1455	4355
7	7	1⊕8	7	139	7	1131	4344
8	8	2⊕9	8	140	8	1454	4340
9	9	3⊕10	9	141	9	1626	4342
10	10	2⊕3	10	251	10	1504	4343
11	11	3⊕4	11	252	11	1642	4343
12	12	5⊕6	12	254	12	1750	4343
13	13	6⊕7	13	255	13	1764	4343
14	14	7⊕8	14	256	14	1772	4343
15	15	8⊕9	15	257	15	1775	4343
16	16	9⊕10	16	258	16	1776	4343
17	17	1⊕4	17	469	17	1156	4343
18	18	2⊕5	18	470	18	1467	4343
19	19	3⊕6	19	471	19	1633	4343
20	20	4⊕7	20	472	20	1715	4343
21	21	5⊕8	21	473	21	1746	4343
22	22	6⊕9	22	474	22	1763	4343
23	23	1⊕3	23	509	23	1063	4343
24	24	4⊕6	24	512	24	1706	4343
25	25	5⊕7	25	513	25	1743	4343
26	26	6⊕8	26	514	26	1761	4343
27	27	7⊕9	27	515	27	1770	4343
28	28	8⊕10	28	516	28	1774	4343
29	29	1⊕6	29	859	29	1127	4343
30	30	2⊕7	30	860	30	1453	4343
31	31	3⊕8	31	861	31	1625	4343
32	32	4⊕9	32	862	32	1712	4343
——[c]	33	5⊕10	33	863	33	1745	4343
——[c]	34[b]	4⊕10	34	950	34	1713	4343
——[c]	35	1⊕7	35	947	35	1134	4343
——[c]	36	2⊕8	36	948	36	1456	4343
——[c]	37[b]	4⊕10	37	950	37	1713	4343

[a] In the octal notation for the first 10 chips of the C/A code as shown in this column the first digit (1) represents a "1" for the first chip and the last three digits are the conventional octal representation of the remaining 9 chips. (For example, the first 10 chips of the C/A code for PRN Signal Assembly No. 1 are: 1100100000).

[b] C/A codes 34 and 37 are common

[c] PRN sequences 33 through 37 are reserved for other uses (e.g. ground transmitters).

⊕ = "exclusive or"

We might ask why not simply take 37 different maximal length shift register codes and use them in place of the Gold codes? After all, 2 of the Gold codes of this family of length 1023 are the maximal length codes themselves. The answer is that the other maximal length codes of length 1023 would not guarantee uniformly low cross-correlation sidelobes for all other needed satellite codes and all possible delay offsets.

4. L_2 Signal

The L_2 signal is biphase-modulated by either the P code or the C/A code, as selected by ground command. The same 50 bps datastream modulates the L_2 carrier as transmitted on L_1. Thus, the L_2 signal is represented in the normal P format as follows:

$$S_{L_{2_i}}(t) = \sqrt{2P_2}XP_i(t)D_i(t)\cos(\omega_2 t + \phi_2) \tag{15}$$

where $\sqrt{2P_2}$ represents the L_2 signal amplitude at the satellite, $XP_i(t)$ is the P code for the ith satellite, which is clocked in synchronism with the L_1 codes. As with the L_1 signal, both L_2 carrier and code are synchronous with one another. The L_2 signal can also be modulated with the P-code without the data. This feature permits the precision receiver tracking loops to be reduced further in IF bandwidth, and thereby can improve the noise/interference performance.

Because the L_2 signal is biphase-modulated, it is possible to recover the L_2 carrier without knowledge of the P code by simply squaring the signal or cross-correlating L_1 with L_2 with a delay offset that matches the L_1 to L_2 ionospheric delay difference. These types of codeless recovery of the L_2 carrier can then be used in estimating the ionosphere delay (see Chapter 4, this volume). There is added noise degradation in this codeless carrier recovery because of the nonlinear squaring operation or noisy cross-correlation operation. However, the information bandwidth of the ionosphere is sufficiently small that if we have already tracked the L_1 code, the noise bandwidth required to track the L_2–L_1 ionospheric difference is also very small, and noise effects can be kept small by narrow bandwidth filtering.

5. GPS Data Format

Table 5 summarizes the signal and data characteristics just discussed. There are five subframes of 6 s each for a total frame period of 30 s. One of the key points to be made in the signal structure discussion is that acquisition by a receiver of the relatively short period C/A code plus the recovery of a single full subframe of data permits us to acquire the P code with minimal or zero search. Knowledge of the C/A epoch plus the data subframe epoch and the HOW word gives the exact phasing of the P(Y) code. Navigation solutions require, as a minimum, reception of data subframes 1, 2, 3 containing clock-correction and ephemeris data and, in general, require reception of a full 30- s frame of data. The navigation data are discussed in detail in the next chapter.

6. Codes for GPS Augmentation

The GPS satellites are augmented at times by pseudolites or ground transmitters that may transmit frequency offset or a low-duty factor pulsed GPS-type signal

Table 5 Summary of GPS signal parameters and data formats

Parameter	C/A Signal	P Signal
Code clock (chip) rate	1.023 Mbps	10.23 Mbps
Code period	1023	$= 6 \times 10^{12}$; 1 week
Data rate	50 bps	50 bps
Transmission frequency	L_1	L_1, L_2

Data formal—frame and subframe structure

Subframe No.	Ten, 30-bit words, 6-s subframe			
1	TLM	HOW	Block 1—Clock correction + satellite quality	1-Frame 30 s 1500 bits
2	TLM	HOW	Block 2—Ephemeris	
3	TLM	HOW	Block 3—Ephemeris continued	
4	TLM	HOW	Block 4—Almanac + ionosphere + UTC correction	
5	TLM	HOW	Block 5—Almanac—(25 frames for complete almanac)	

Each Telemetry (TLM) word contains an 8-bit Barker word for synchronization. The Handover Word (HOW) contains a 17-bit Z-count for handover from the C/A code to the P code.

and use codes different from those employed in the GPS satellites to avoid confusion. GPS pseudolites are discussed in detail in a later chapter.

Also planned is the augmentation of the GPS satellites with geostationary overlay satellites using different Gold codes. These signals might be generated either by the satellite or generated and synchronized on the ground and broadcast to the GPS users via geostationary satellite transponders. Table 6 lists the Gold codes selected by INMARSAT for future transmission by the INMARSAT satellites.[9] Table 6a lists the codes for the Wide Area Augmentation System (WAAS) of the Federal Aviation Administration. GPS augmentation is also discussed in later chapters on the GPS wide area differential GPS (WADGPS) and Wide Area Augmentation System in Volume II.

III. GPS Radio Frequency Receive GPS Power Levels and Signal-to-Noise Ratios

A. GPS Radio Frequency Signal Levels and Power Spectra

The minimum specified received signal strength for a user receiver employing a 0 dBIC antenna is given below in Table 7 for a satellite at elevation angles above 5 deg. As shown in the next subsection, the actual minimum varies with elevation angle to the satellite because of the shaped satellite antenna pattern. The signal power spectral densities for the P and C/A signal components are shown in Fig. 15. Figure 15 also shows the measured radiofrequency power spectral density of the L_1 signal. Note the narrowband high-power density C/A signal in the center of the signal spectrum. Note that these spectra are

Table 6 Final INMARSAT C/A-code selection

Order	PRN	Delay	Initial *G*2 state (octal)
1	201	145	1106
2	205	235	1617
3	208	657	717
4	206	235	1076
5	202	175	1241
6	207	886	1764
7	209	634	1532
8	211	355	341

Table 6a Wide Area Augmentation System (WAAS) PRN ranging C/A codes (Note that these codes include the INMARSAT codes of Table 6)

PRN Code #	Display (Chips)	First 10 WAAS Chips (Octal)[a]
115	145	0671
116	175	0536
117	52	1510
118	21	1545
119	237	0160
120	235	0701
121	886	0013
122	657	1060
123	634	0245
124	762	0527
125	355	1436
126	1012	1226
127	176	1257
128	603	0046
129	130	1071
130	359	0561
131	595	1037
132	68	0770
133	386	1327

[a] The first digit represents a 0 or 1 in the first chip. The next three digits are the octal representation of the remaining nine chips.

Table 7 GPS minimum received signal power levels at output of a 0 dBIC antenna with right-hand circular polarization[a]

	GPS signal component (minimum strength) specified		Expected maximum does not exceed this level with 0.6 dB atmospheric loss	
Link	P	C/A	P	C/A
L_1	−163 dBW	−160 dBW	−155 dBW	−153 dBW
L_2	−166 dBW	−166 dBW	−158 dBW	−158 dBW

[a] The satellite is assumed to be at an elevation angle ≥ 5 deg.

the transmitted spectra. In normal operation, the thermal white noise of the receiver significantly exceeds the signal spectral density, and the signal is not visible using a spectrum analyzer. Recall that the maximum power spectral density for a pseudonoise signal with a continuous $[(\sin \pi f/f_c)/\pi f/f_c)]^2$ shaped spectrum is P_s/f_c. Thus, if $P_s = -160$ dBW, the maximum power density is -160 dBW $- 60.1$ dB $= -220.1$ dBW/Hz.

It is useful to compare this number with the recommended power flux density limit of the CCIR[1] cited earlier in this chapter in Sec. I.A. If an effective antenna aperture area* of $A = \lambda^2/4\pi = 2.8856 \times 10^{-3}$m^2 or -25.4 dBm^2 at 1.57542 GHz is assumed for a unity gain antenna, then the power flux density per Hz is $P_s/f_sA = -194.7$ dBW/Hz-m^2. The total flux density in a 4-kHz band is then $4 \times 10^3\ P_s/f_sA = -158.7$ dBW/m^2, which is within the level recommended by the CCIR[1] of -154 dBW/m^2.

B. Satellite Antenna Pattern

The radio frequency received signal levels are transmitted from the satellite by shaped pattern antennas (see Fig. 16) to compensate partially for the increased path loss to the user at low-elevation angles. The GPS Block II satellite antenna is an array of helices on the face of the satellite. The edge of Earth is approximately 13.87 deg off the satellite antenna boresight, i.e., the Earth subtends an angle of approximately 27.74 deg from the GPS satellite altitude. The satellite antenna pattern extends somewhat beyond the edge of the Earth, as shown in Fig. 16. Thus, even a GPS receiver in another satellite can receive signals from GPS satellites to perform satellite positioning, provided that it is not blocked by the Earth's shadow and is not too far off the main lobe of the satellite antenna pattern (see Fig. 17).

The transmitted signal from the satellite is right-hand circularly polarized with an ellipticity (offset from perfectly circular) no worse than 1.2 dB for L_1 and 3.2 dB for L_2 within an angle of ±14.3 deg from boresight.† Because the user antenna can be at various orientations with respect to the satellites, the satellite received power is specified under the following conditions; a) the signal is measured at the output of a 3 dBIC (isotropic) linearly polarized receiving antenna; b) the space

*The relationship between antenna gain G and effective aperture area A for an ideal lossless antenna is $G = 4\pi A/\lambda^2$.[10]

†NAVSTAR GPS Space Segment/Navigation User Segment Interface Control Document, ICD-GPS-200, IRN-200B-005, Dec. 16, 1991.

a)

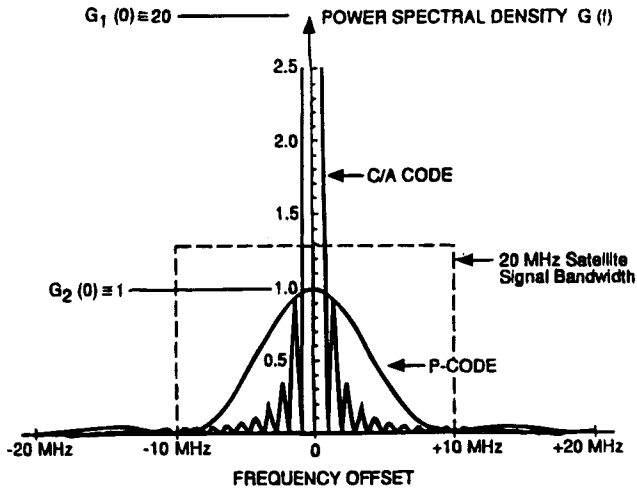

b)

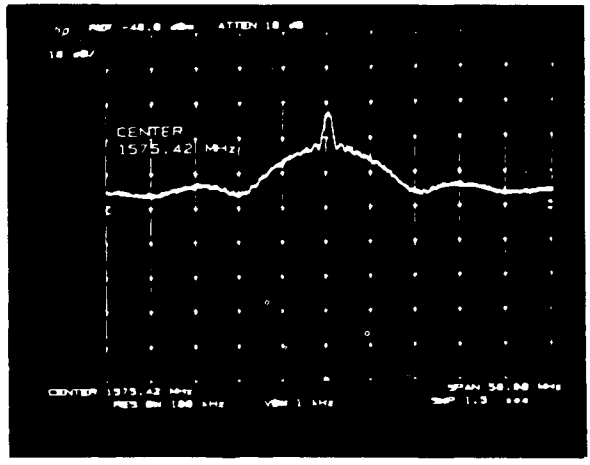

Fig. 15 Radio frequency spectrum plot and photograph of received L_1 carrier with C/A and P QPSK modulation; a) Power spectra of carriers with bit rates of 1.023 Mb/s and 10.23 mb/s. The ratio of C/A power to P-code signal power is 3 dB in this figure, b) Photograph of signal generated by Stanford Telecom GPS signal simulator 7200. Spectrum scales: horizontal, 5 MHz/division; vertical, 10 dB/division (courtesy Stanford Telecom).

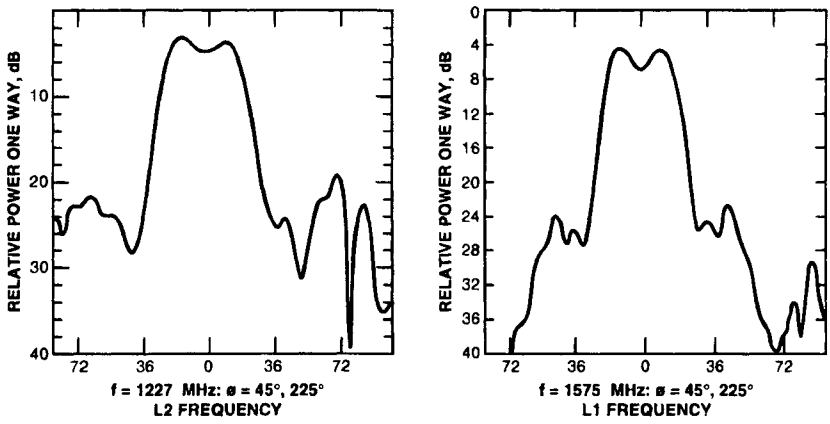

Fig. 16 Typical GPS satellite system transmit antenna patterns for the Block II satellites.

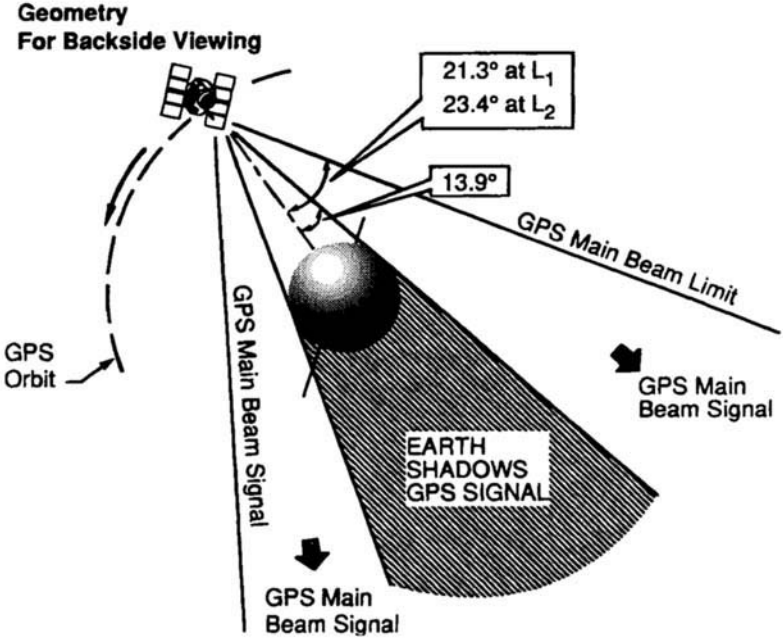

Fig. 17 GPS satellite main beam relative to Earth (not to scale). User satellites can navigate using GPS provided they are in the main beam of the GPS antenna but outside the Earth's shadow.

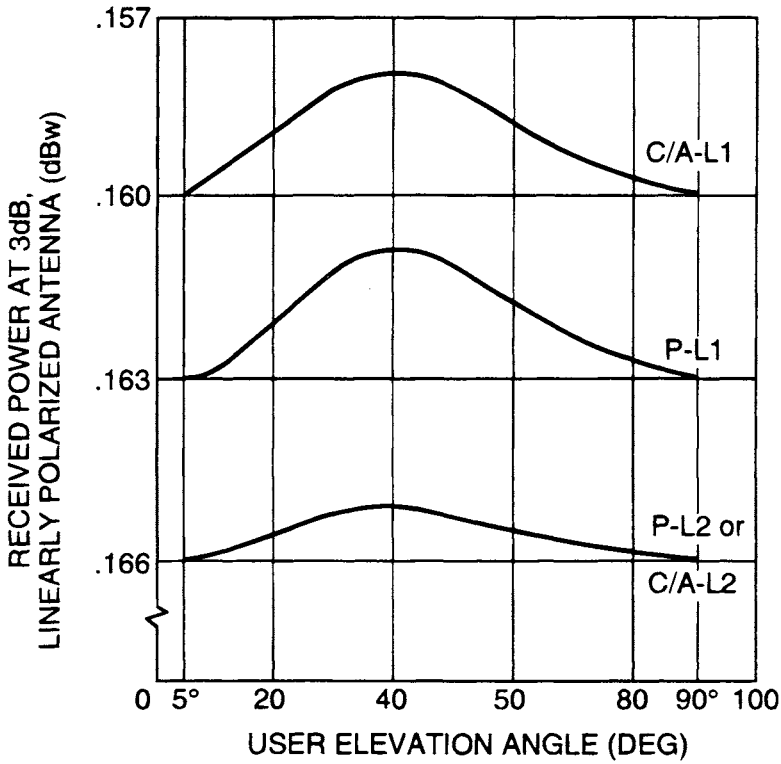

Fig. 18 GPS user received minimum signal levels vs elevation angle as stated in the GPS document GPS-ICD-200.[6]

vehicle is above a 5 deg elevation angle; c) the received signal levels are observed within the 20 MHz frequency allocation; d) the atmospheric path loss is 2.0 dB; and e) the space vehicle's attitude error is 0.5 deg (toward reducing signal level). The specified minimum received signal power vs. elevation angle for these conditions is shown in Fig. 18. Note that the specified received signal level peaks at 40 deg elevation angle at a level that is approximately 2 dB above the nominal −160 dBW level for the C/A code on L_1. As shown in Chapter 13 this volume, atmospheric path loss is generally less than 2 dB, except at low-elevation angles. In addition, the satellites are designed so that these numbers are met at the end of the satellite's life. Beginning-of-life power levels are generally higher. Thus, these numbers are somewhat conservative.

C. Signal Specifications

1. Signal Correlation Loss

The GPS C/A and P(Y) signals are filtered to a bandwidth of 20.46 MHz. There are two such 20.46 MHz frequency bands centered at L_1 and L_2. The GPS space segment GPS-ICD-200[6] defines a maximum correlation loss of 1.0 dB

Chapter 4

GPS Navigation Data

J. J. Spilker Jr.*
Stanford Telecom, Sunnyvale, California 94089

I. Introduction

GPS signal carries with it data from the satellite that the user receiver needs to solve for position, velocity, and time. This chapter describes these GPS navigation data in some detail and gives the background analysis useful in understanding their functions. The data formats correspond to the ICD-GPS-200.[1] The first section gives a complete overview of the entire navigation data format and overall frame structure. The second section describes in some detail the format and algorithms of ICD-GPS-200 for each of the subframes. The final sections present some of the physical and mathematical bases for the algorithms of Sec. II. Detailed discussion of the effects of relativity, the ionosphere, and troposphere is reserved for later chapters. A table of physical constants used in this chapter and elsewhere is given in the Appendix.

A. Overall Message Content of the Navigation Data

The 50 bits/s datastream provides the user with several key sets of data required to obtain a satisfactory navigation, geodetic survey, or time transfer solution. These navigation data are uploaded to each satellite by the GPS Control Segment (CS) for later broadcast to the user. Uploads occur once per day, or more often, if needed to keep the user range error (URE) within specification. The navigation data provide the information shown in Table 1. The form of the information is also described in the table.

1. Perturbing Factors in the Navigation Measurements

Various perturbations affect the relationship between measurements made on the received signal and the true range to the satellite from the user. Some of these are discussed in the preceding chapter. The remaining effects are discussed here and in the next chapter. Let us begin by defining (refer to Chapter 2, this volume) the "true" geometric pseudorange $\rho_{it}(t)$, which assumes perfect

*Ph.D., Chairman of the Board.

Table 1 Requirements and characteristics of GPS navigation data

Requirement	Information provided by GPS navigation data
Precise satellite position at time of transmission	Satellite ephemeris using a modified Kepler model (sinusoidal perturbations) in an Earth–centered-inertial (ECI) coordinate frame with transformation to Earth-centered, Earth-fixed (ECEF) coordinates
Precise satellite time at time of transmission	Satellite clock error models and relativistic correction
P(Y) code[a] acquisition from C/A code[b]	A handover word (HOW) is transmitted that keeps track of the number of P(Y) code 1.5-s (*X*1 subsequence) periods thus far in the week. These data can aid in P(Y) code acquisition.
Select the best set of satellites for lowest appropriate GDOP[c] within elevation angle constraints (requires approximate knowledge of satellite position)	Moderate accuracy almanac that gives approximate position, time, and satellite health for the entire GPS constellation
Time transfer information	GPS time to universal coordinated time (UTC) time conversion data
Ionospheric corrections for single-frequency users	Approximate model of ionosphere vs time and user location
Quality of satellite signals/data	User range accuracy (URA)—a URA index N is transmitted that gives a quantized measure of space vehicle accuracy available to the civil (unauthorized) user

[a]P(Y) code, precise, antispoof code.
[b]C/A code, coarse/acquisition code.
[c]GDOP, Geometric Dilution of Precision.

knowledge of satellite clock time and position, assumes further the absence of any atmospheric propagation delay or relativistic effects, and uses a nonrotating ECI coordinate system. The "true" geometric pseudorange $\rho_{iT}(t)$ at time t for satellite i is then defined as follows:

$$\rho_{iT}(t) \triangleq = c(t_u - t_{si}) + cb_u = |\boldsymbol{x}_{si} - \boldsymbol{x}_u| + cb_u = |\boldsymbol{r}_{si} - \boldsymbol{r}_u| + cb_u = D_i + cb_u \tag{1}$$

where c is the speed of light, $\boldsymbol{x}_{si}(t - D_i(t)/c)$ is the true satellite position at the true time of transmission, $t - D_i(t)/c$, in ECI coordinates $\boldsymbol{x}_u(t)$ is the unknown user position also in ECI coordinates where t is the time of reception, and $t_u(t)/c$ is the user clock reading at the time of reception. Pseudorange is expressed in meters. User position is expressed either in Cartesian coordinates as $\boldsymbol{x}_u$ or in spherical coordinates as $\boldsymbol{r}_u$. The received satellite signal indicates the satellite

clock time at the time of transmission* $t_{si}(t - D_i(t)/c)$, and $b_u(t)$ is the user clock time offset $b_u(t) = [t_u(t) - t_{GPS}(t)]$ expressed in seconds. The geometric transit time of the signal is $D_i(t)$ expressed in meters. The coordinates can be rotated to ECEF coordinates, but the rotation of the Earth during the transit time $D_i(t)$ must also be taken into account.

The true pseudorange $\rho_{iT}(t)$ is not directly an observable, but instead must be observed with various perturbations. The measured pseudorange $\rho_i(t)$ is equal to the true pseudorange plus various perturbing factors, as shown below [refer again to Chapter 2, Eq. (2)].

$$\rho_i = \rho_{iT} + \Delta D_i - c\Delta b_i + c(\Delta T_i + \Delta I_i + \nu_i + \Delta \nu_i) \tag{1}$$

where

Δb_i = satellite bias clock error, s
ΔD_i = satellite position bias error effect on range, m
ν_i = receiver measurement noise error for satellite i, s
ΔI_i = ionospheric excess delay, s
ΔT_i = tropospheric excess delay, s
$\Delta \nu_i$ = relativistic time correction, s

To be precise one also must account for small second-order effects caused by motion of the satellite during the time interval caused by ionospheric and tropospheric excess delay when computing the satellite position at time of transmission.

Each of the perturbations in the pseudorange measurement equation above must be either estimated, measured, or computed using the navigation datastream or other information. Satellite position information itself, of course, must be estimated from the navigation datastream. Table 2 identifies which type of data is involved for each perturbing parameter. Figure 1 (modified from ICD-GPS-200)[1] illustrates in specific terms how each of the corrections is applied to the pseudorange measurements. Each of these parameters is discussed either in this chapter or in other chapters of this book. Note that the tropospheric corrections are not discussed in ICD-GPS-200.[1] However, tropospheric correction models are discussed in detail in Chapter 13, this volume.

B. Navigation Data Subframe, Frame, and Superframe

The navigation data are transmitted in a 50 bits/s stream that is modulo-2 added to the C/A and P(Y) codes on the L_1 frequency and may or may not be carried on the L_2 P(Y) code, depending on the satellite mode. The data bit stream is synchronous with the 1-kHz C/A code epochs. The databits are formatted into 30-bit words, and the words are grouped into subframes of 10 words that are 300 bits in length and 6 s in duration. Frames (or pages) consist of 5 subframes of 1500 bits and 30 s in duration, and a superframe consists of 25 frames and has a duration 12.5 min. The general frame and subframe format is shown in Fig. 2. Much of the data repeat every frame and some data; e.g. the 8-bit preamble repeat every subframe. Periodically, the navigation dataframes are updated. New navigation data set (4-h curve fit for normal operations) cutovers occur only on

*The time indicated is the "proper" time indicated by the satellite clock at the time of transmission.

Table 2 Relationship between measured pseudorange and other parameters

	Parameters	Source of information for parameter
True pseudorange	$\rho_{iT} = \lvert \boldsymbol{x}_{si} - \boldsymbol{x}_u \rvert + cb_u$	Estimated by the GPS receiver
Pseudorange measurement	$\rho_i(t)$	Measured by GPS navigation receiver
Satellite position for satellite i	$\boldsymbol{x}_{si}(t)$	Satellite position, calculated from the navigation data
User position	$\boldsymbol{x}_u(t)$	Unknown user position, to be estimated
Ionospheric excess path delay	$\Delta I_i(t)$	Measured using dual-frequency measurements, or for single-frequency user, modeled using navigation data
Tropospheric excess path delay	$\Delta T_i(t)$	Estimated using approximate equations of various levels of accuracy, some of which rely on pressure and humidity measurements.
Satellite clock error	$\Delta b_i(t)$	Computed using navigation data. There can remain a residual error caused by selective availability for unauthorized users or users without differential GPS connection
User clock bias	b_u	Unknown user clock bias, to be estimated. Once estimated, it may vary only slowly depending on quality of user clock
Satellite position error bias error effect on range	$\Delta D_i(t)$	Unknown bias error cause by errors in GPS control segment estimate

one hour boundaries except for the first data set after a new upload, which may be cut in at any time during the hour. Block II satellite data sets for subframes 1, 2, and 3 are transmitted for periods of two hours before update. Block I satellite subframes 1, 2, and 3 are transmitted for periods of one hour before update.

Words 1 and 2 of each subframe are used for synchronization (preamble), handover word, and C/A code time ambiguity removal. The remaining words, 3–10, of subframe 1 provide clock correction information for the space vehicle clock and space vehicle health and user range accuracy (URA) measures. Subframes 2 and 3 contain ephemeris data that allow estimation of the transmitting satellite's position. Subframes 1, 2, and 3 have the same format from frame to frame, however, subframe 4 and 5 have 25 pages or different sets of data and contain the almanac that gives the approximate satellite ephemeris, clock correction, and space vehicle status for all of the satellites. The almanac data permit the user to select the best set of satellites or simply to determine which satellites are in view. Subframe 4 also contains ionospheric modeling and UTC-GPS clock correction information. A detailed view of the frame structure is shown in Fig. 3. Note that each 30-bit word includes six parity check bits that permit the user receiver to check for errors in the received datastream. A detailed discussion of each of these subframes in Fig. 3 can be found in Sec. II of this chapter, and their mathematical bases are given in the later sections.

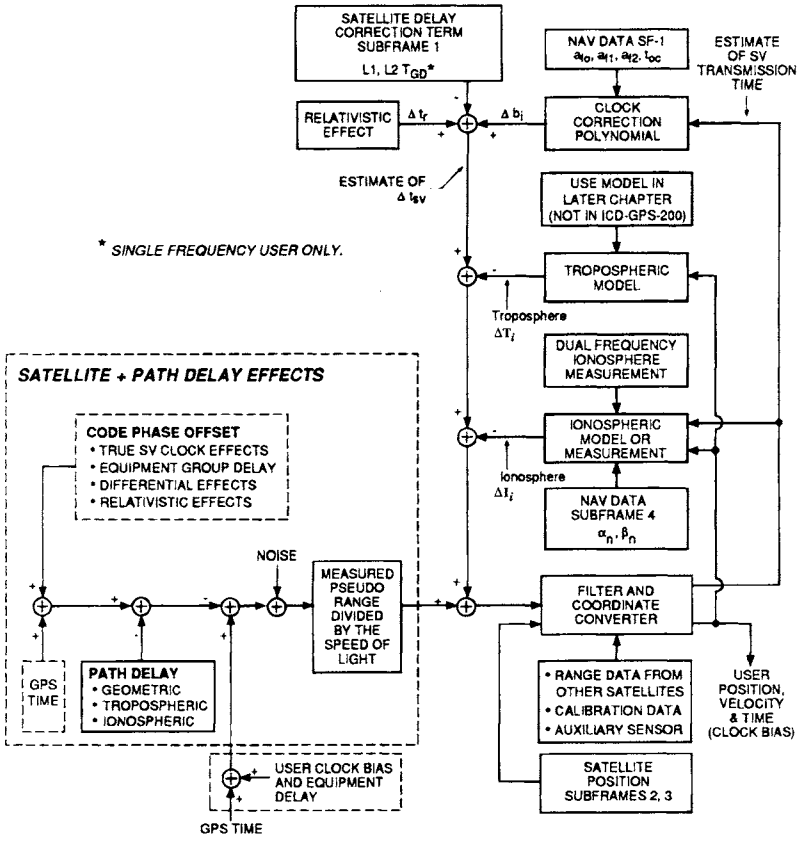

Fig. 1 Navigation data and correction parameters for pseudorange estimate from the pseudorange measurement. This diagram is a modified version of that contained in ICD-GPS-200.[1] The notation *SF* represents the navigation data subframe.

The subframes, frames, and 25-frame superframes are all synchronous with the 1.5-s, *X*1 epochs of the P code. Recall that the full P code has a 1-week period. The superframe also begins at the beginning of each week. Subframes begin at the beginning of the week and are numbered consecutively from the beginning of the week to aid in C/A to P(Y) code acquisition/handover. The timing relationships, shown in Fig. 4 and Fig. 5, illustrate the relationships between *X*1 epochs, time of week (TOW), handover word, *Z*-count, data bits, frames, and the chip durations.

The timing starts at the beginning of each week, defined as midnight Saturday night–Sunday morning in GPS time, which is referenced to UTC time kept by the U.S. Naval Observatory. GPS zero time point is defined as midnight on the night of January 5, 1980/morning of January 6, 1980. Note that the *Z*-count rolls over 1024 weeks later every 19+ years. UTC time is nominally referenced to time at the Greenwich meridian. GPS time differs from UTC in that GPS time does not exhibit the leap second that is sometimes inserted in UTC. GPS time,

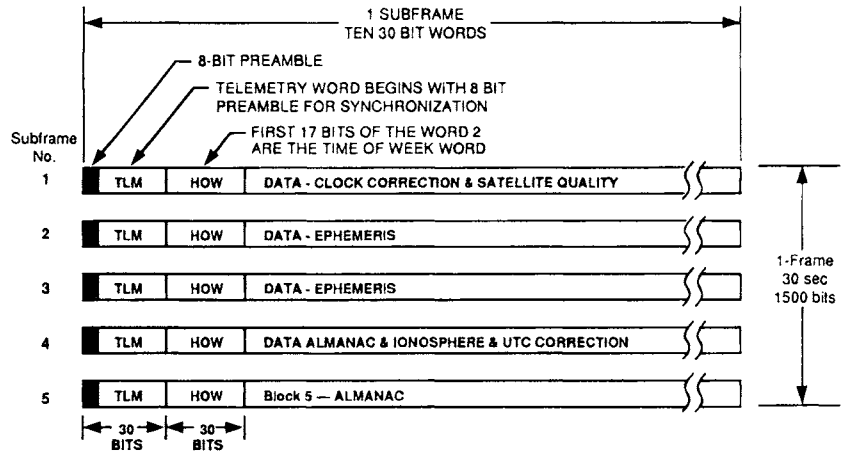

Fig. 2 Simplified GPS frame and subframe format. A superframe consists of 25 frames of 30 s each or 750 s or 12.5 min, and provides a complete almanac.

however, is kept to within 1 μs of UTC (modulo-1 s) by the GPS Control Segment. As years pass, the GPS time will differ from UTC by an integer number of seconds.

The number of *X*1 epochs (1.5 s each) since the GPS zero time point modulo-1024 weeks is a 29-bit number called the *Z*-count. The 19 least significant bits of the *Z*-count are referred to as the *time of week* (TOW) count, which is defined as the number of *X*1 epochs (1.5 s each) since the transition from the previous week. A truncated version, the 17 most significant bits of the TOW word is defined as the handover word, which ranges from 0 to 100,799, corresponds to the number of 6-s subframes since the beginning of the week, and is contained in the *L*-band downlink datastream. The HOW removes any timing ambiguity caused by the 1-ms C/A-code period and aids in C/A- to P-code handover/acquisition. The ten most significant digits of the 29-bit *Z*-count represent the number of weeks since the GPS zero time point.

As shown in Fig. 6, each 10-word subframe begins with a telemetry (TLM) word, which in turn begins with an 8-bit preamble, as shown for synchronization (a modified Barker sequence). Other parts of the TLM contain data needed by authorized users, as defined in GPS-ICD-205 and/or GPS-ICD-207.

1. Subframe Synchronization

The 8-bit modified Barker word at the beginning of the TLM word (or the 8-bit modified Barker word plus the two zeros in positions 29 and 30 of the HOW word) provides a synchronization pattern for subframe synchronization by the GPS receiver. However, random data patterns elsewhere in the frame can provide an identical pattern. Furthermore, there is a ± 1 sign ambiguity in demodulating any biphase modulated data signal. Thus, the 8-bit or the 8-bit plus 2-bit pattern still has a probability of a "false alarm" or random bit pattern match with the sync pattern of 2×2^{-8} or 2×2^{-10} for 1/128 or 1/512, respectively. Thus,

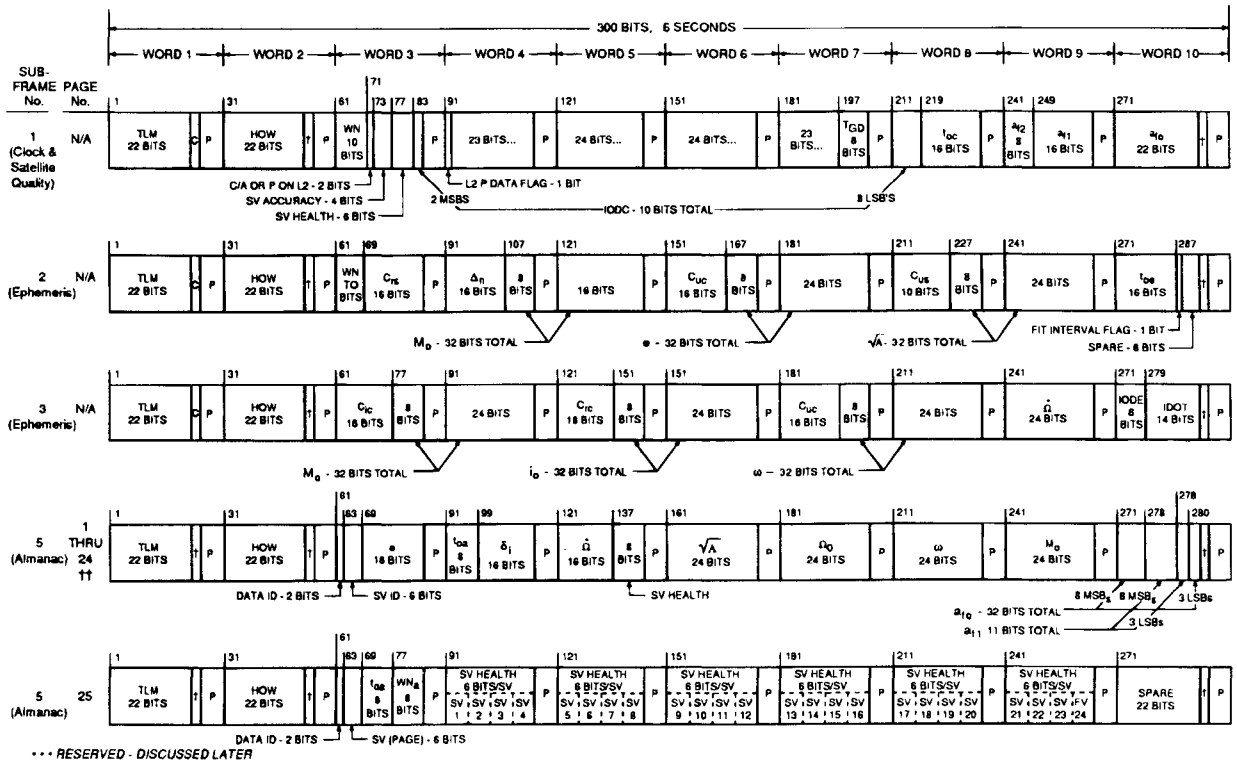

Figure 3 GPS data format from ICD-GPS-200.[1] Bit 1 is transmitted first. Within each word the most significant bits are transmitted first.

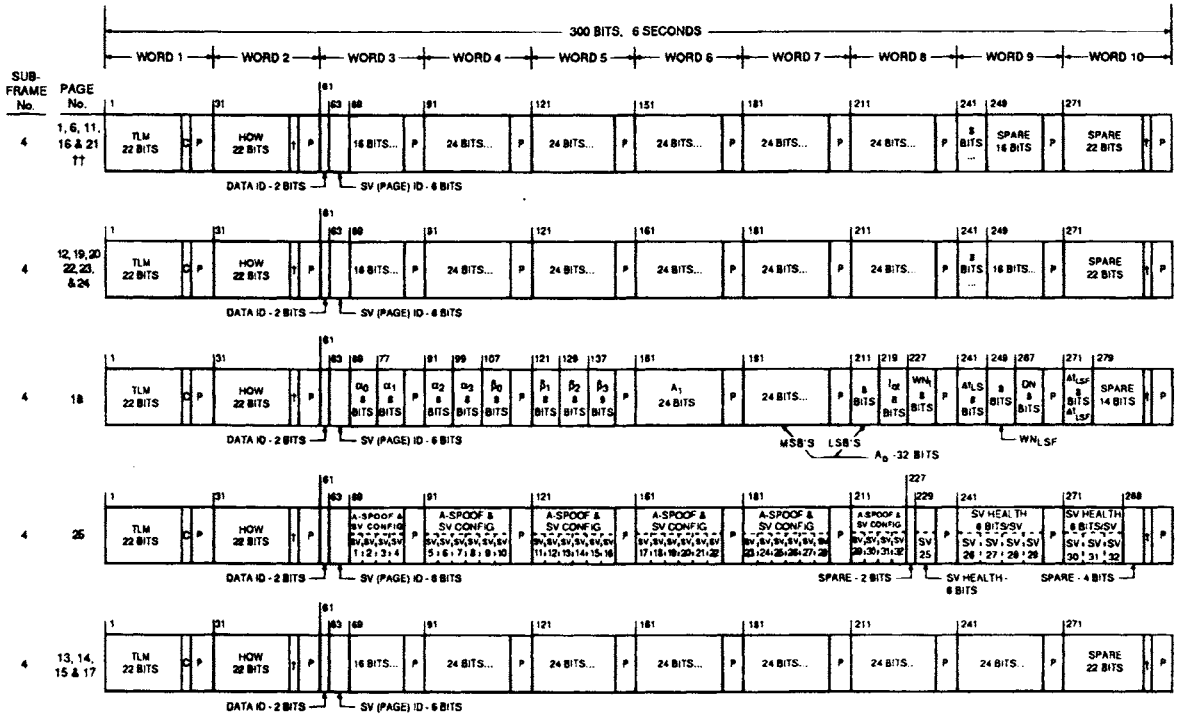

*** RESERVED - DISCUSSED LATER

† = TWO NONINFORMATION BEARING BITS USED FOR PARITY COMPUTATION (SEE PARITY CHECK ALGORITHM)

†† = PAGES 2, 3, 4, 5, 7, 8, 9, AND 10 OF SUBFRAME 4 HAVE SAME FORMAT AS PAGES 1 THROUGH 24 OF SUBFRAME 5

P = SIX PARITY BITS

C = TLM BITS 23 AND 24 WHICH ARE RESERVED

Figure 3 (continued) GPS data format from ICD-GPS-200.[1] Bit 1 is transmitted first. Within each word the most significant bits are transmitted first.

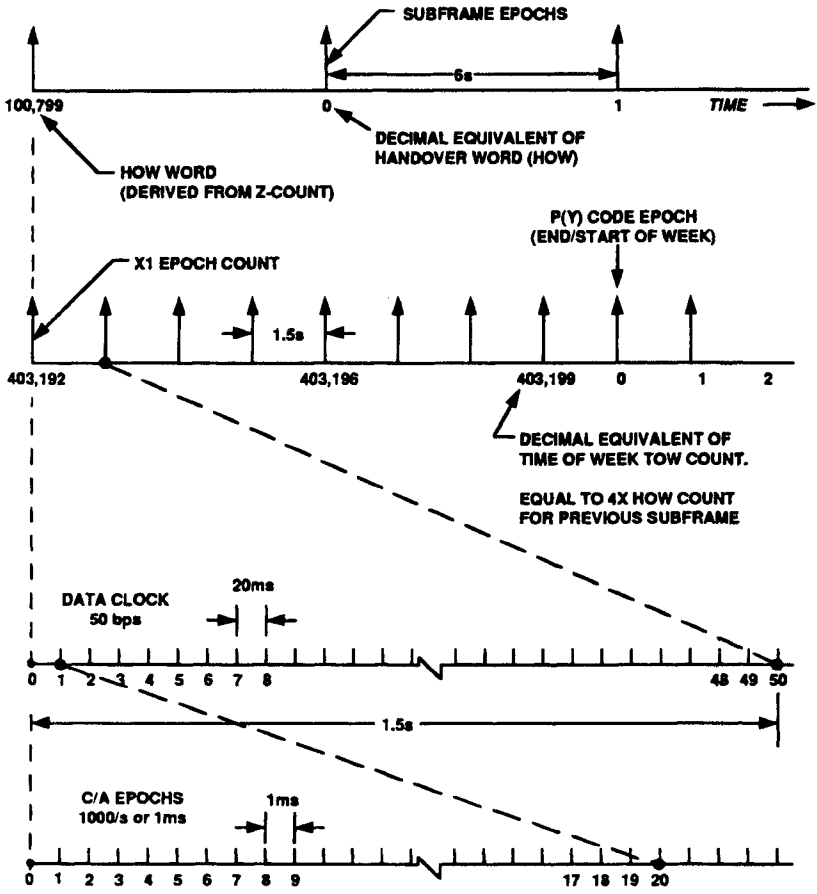

Fig. 4 Timing relationships between C/A-code epochs, P-code epochs, and navigation data.

the modified Barker word by itself yields too high a false alarm rate to be acceptable. However, we can also check the 17-bit truncated TOW message at the beginning of the HOW word to see that it increments by one and only one from subframe to subframe as a means for confirming the subframe synchronization.

2. *Parity Check Algorithm*

Although the navigation data are normally received at a relatively high signal-to-noise ratio and correspondingly low bit error rates $P_b < 10^{-5}$, it is important to have a parity check algorithm to reject words with any errors in them. Each 30-bit word plus the last two bits of the previous word is encoded into an extended Hamming (32,26) block code of $n = 32$ symbols and $k = 26$ "information" bits, where only 24 of the bits are true information bits d_i, $i \leq 24$.

If the parity transmission bits D_i (computed from the equation below and the $\boldsymbol{H}$ matrix of Fig. 7 or Table 3) do not match the six received parity bits D_i for

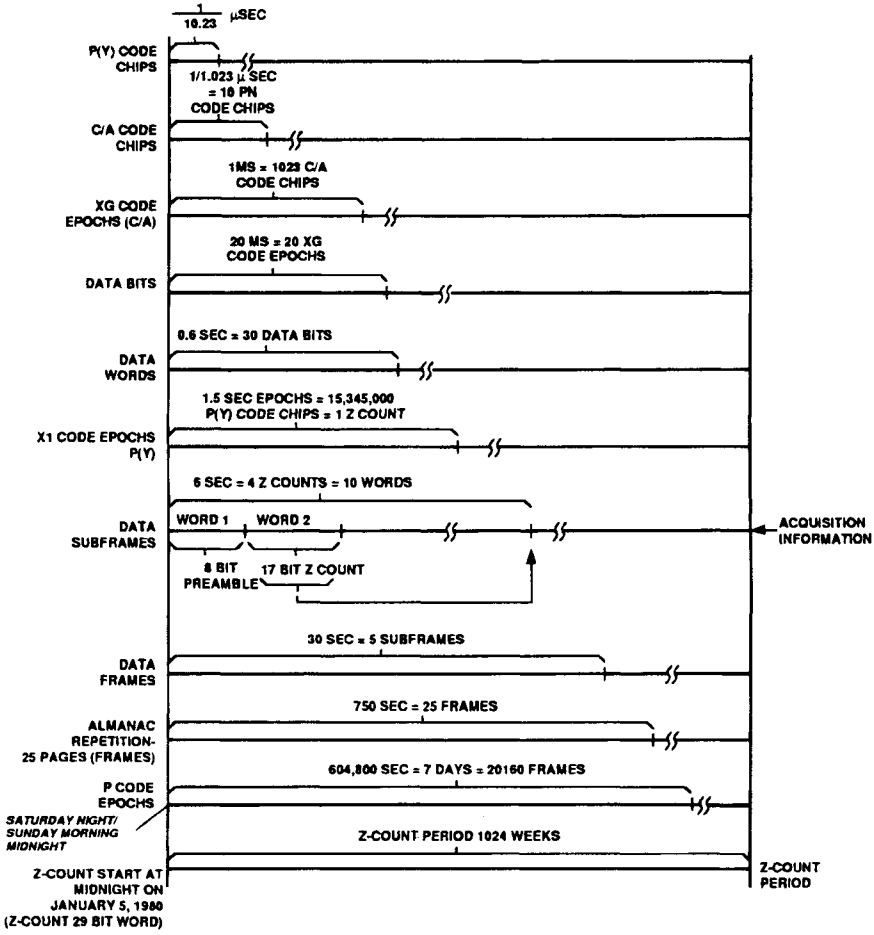

Fig. 5 Timing relationships of C/A codes, and data to Z-count.

D_{25}, D_{26}, D_{27}, D_{28}, D_{29}, D_{30}, then the information bits d_i for $i \leq 24$ are rejected. The parity check equation for the six parity check bits is $\boldsymbol{p} = \boldsymbol{Hd}$ where $\boldsymbol{H}$ is the (24×6) matrix of Fig. 7 and $D_i = d_i + D_{30}^*$ for $i \leq 24$, the received databit vector is $\boldsymbol{d} = (D_{29}^*, D_{30}^*, d_1, d_2, \ldots, d_{24})$, and $\boldsymbol{p}$ represents the vector $(D_{25}, D_{26}, D_{27}, D_{28}, D_{29}, D_{30})$.

In making this calculation, the $d_i = D_i \oplus D_{30}^*$, $i \leq 24$ are computed first, then the parity check bits D_i, for $25 \leq i \leq 30$ are computed and checked. In Fig. 7, note that each row in the parity matrix is a cyclic shift of the previous row, except for the last row. The last row is a check of all the previous rows. Note that the sum of all of the row vectors in the matrix is the all "1" row vector.

The Hamming code of length n with parameter m is of the form $(2^m - 1, 2^m - m - 1, 3) = (n, k, 3)$ is of minimum weight 3 for all m. For $m = 5$, the code is (31, 26, 3). The number of information bits in the code word is k. The

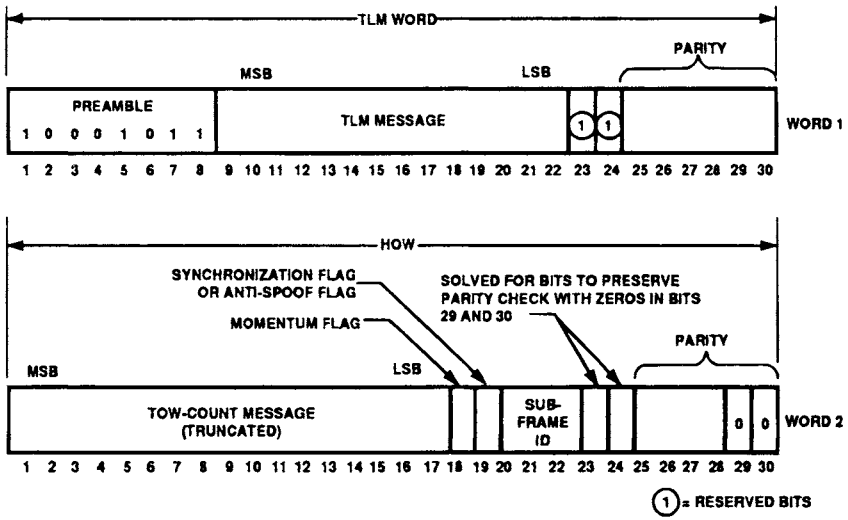

Fig. 6 Telemetry and handover words formats referenced from ICD-GPS-200.[1]

normal Hamming code (31,26) is a perfect code, which means that $2^{n-k} = 1 + n$, that is, $2^{31-26} = 2^5 = 1 + 31$ and has distance 3 for double error detection capability. It takes a minimum of three errors to cause an undetected error.

For GPS the distance 3 Hamming code is converted to a minimum distance 4 code by appending an added parity bit (the 32nd bit) that checks all of the other symbol bits including the other parity bits. In effect, this change adds the last row to the parity check matrix shown in Fig. 7. The code is then shortened to 30 bits by deleting two of the databits.

The GPS parity check code is an extended Hamming code (32,26) and has distance 4. Therefore, it takes certain patterns of four errors to cause an undetectable error.[2-4] If the error probability is p, then the probability of an undetectable error is approximately equal to $p_u \cong 1085\,p^4 - 29295\,p^5 + 403403\,p^6 + 0\,(p^7)$, and it is negligibly small for moderately low error probabilities $p < 10^{-3}$.

$$H = \begin{array}{c} \begin{array}{cccccccccccccccccccccccc} 1 & 2 & 3 & 4 & 5 & 6 & 7 & 8 & 9 & 10 & 11 & 12 & 13 & 14 & 15 & 16 & 17 & 18 & 19 & 20 & 21 & 22 & 23 & 24 \end{array} \\ \left[\begin{array}{cccccccccccccccccccccccc} 1 & 1 & 1 & 0 & 1 & 1 & 0 & 0 & 0 & 1 & 1 & 1 & 1 & 1 & 0 & 0 & 1 & 1 & 0 & 1 & 0 & 0 & 1 & 0 \\ 0 & 1 & 1 & 1 & 0 & 1 & 1 & 0 & 0 & 0 & 1 & 1 & 1 & 1 & 1 & 0 & 0 & 1 & 1 & 0 & 1 & 0 & 0 & 1 \\ 1 & 0 & 1 & 1 & 1 & 0 & 1 & 1 & 0 & 0 & 0 & 1 & 1 & 1 & 1 & 1 & 0 & 0 & 1 & 1 & 0 & 1 & 0 & 0 \\ 0 & 1 & 0 & 1 & 1 & 1 & 0 & 1 & 1 & 0 & 0 & 0 & 1 & 1 & 1 & 1 & 1 & 0 & 0 & 1 & 1 & 0 & 1 & 0 \\ 1 & 0 & 1 & 0 & 1 & 1 & 1 & 0 & 1 & 1 & 0 & 0 & 0 & 1 & 1 & 1 & 1 & 1 & 0 & 0 & 1 & 1 & 0 & 1 \\ 0 & 0 & 1 & 0 & 1 & 1 & 0 & 1 & 1 & 1 & 1 & 0 & 1 & 0 & 1 & 0 & 0 & 0 & 1 & 0 & 0 & 1 & 1 & 1 \end{array}\right] \end{array}$$

Fig. 7 Parity matrix H for the extended Hamming (32,26) code where $d_1, d_2, \ldots d_{24}$ are the source databits and $D_1, D_2, \ldots D_{30}$ are the bits transmitted by the global positioning system satellite. The notation D_{29}*, D_{30}* represents the last 2 bits transmitted in the previous 30-bit word. Note that each row in H is simply a cyclic shift of the previous row except for the row D_{30}.

Table 3 Parity encoding equations for each 30-bit word (from GPS-ICD-200)[1]

$D_1 = d_1 \oplus D_{30}^*$
$D_2 = d_2 \oplus D_{30}^*$
$D_3 = d_3 \oplus D_{30}^*$
. .
. .
. .
$D_{24} = d_{24} \oplus D_{30}^*$
$D_{25} = D_{29}^* \oplus d_1 \oplus d_2 \oplus d_3 \oplus d_5 \oplus d_6 \oplus d_{10} \oplus d_{11} \oplus d_{12} \oplus d_{13} \oplus d_{14} \oplus d_{17} \oplus d_{18} \oplus d_{20} \oplus d_{23}$
$D_{26} = D_{30}^* \oplus d_2 \oplus d_3 \oplus d_4 \oplus d_6 \oplus d_7 \oplus d_{11} \oplus d_{12} \oplus d_{13} \oplus d_{14} \oplus d_{15} \oplus d_{18} \oplus d_{19} \oplus d_{21} \oplus d_{24}$
$D_{27} = D_{29}^* \oplus d_1 \oplus d_3 \oplus d_4 \oplus d_5 \oplus d_7 \oplus d_8 \oplus d_{12} \oplus d_{13} \oplus d_{14} \oplus d_{15} \oplus d_{16} \oplus d_{19} \oplus d_{20} \oplus d_{22}$
$D_{28} = D_{30}^* \oplus d_2 \oplus d_4 \oplus d_5 \oplus d_6 \oplus d_8 \oplus d_9 \oplus d_{13} \oplus d_{14} \oplus d_{15} \oplus d_{16} \oplus d_{17} \oplus d_{20} \oplus d_{21} \oplus d_{23}$
$D_{29} = D_{30}^* \oplus d_1 \oplus d_3 \oplus d_5 \oplus d_6 \oplus d_7 \oplus d_9 \oplus d_{10} \oplus d_{14} \oplus d_{15} \oplus d_{16} \oplus d_{17} \oplus d_{18} \oplus d_{21} \oplus d_{22} \oplus d_{24}$
$D_{30} = D_{29}^* \oplus d_3 \oplus d_5 \oplus d_6 \oplus d_8 \oplus d_9 \oplus d_{10} \oplus d_{11} \oplus d_{13} \oplus d_{15} \oplus d_{19} \oplus d_{22} \oplus d_{23} \oplus d_{24}$

where $d_1, d_2, \ldots d_{24}$, are the source data bits;
the symbol (*) is used to identify the last 2 bits of the previous word of the subframe;
$D_{25}, \ldots D_{30}$ are the computed parity bits;
$D_1, D_2, D_3, \ldots D_{29}, D_{30}$, are the bits transmitted by the space vehicle (SV); and $\oplus$ is the modulo-2 or "exclusive-or" operation.

II. Detailed Description of the Navigation Data Subframes

The previous section defined the overall format of the 50-bs navigation data. This section describes in detail each of the elements of the navigation data for each of the five subframes. The next section provides some of the analytical background for the satellite clock and ephemeris calculations.

A. Subframe 1—GPS Clock Correction and Space Vehicle Accuracy Measure

Subframe 1 contains the data to be used in the algorithms described below to provide the space vehicle clock correction. It also contains data to give an estimate of the effect of space vehicle accuracy on user range accuracy (URA).

1. GPS Clock Correction Data Formats—Subframe 1

The user receiver needs to correct the GPS satellite clock errors. The user receiver must have an accurate representation of GPS system time t at the time of transmission for the GPS signal it now is receiving from satellite i. The satellite clock correction Δt_{sv} is obtained using coefficients broadcast from the satellite after being uploaded by the GPS control segment. The control segment actually uploads several different sets of coefficients to the satellite, of which each set is valid over a given time period. The data sets are then transmitted in the downlink datastream to the users in the appropriate time intervals. Subframe 1, words 8, 9, 10, shown previously in Fig. 3, contain the data needed by the users to perform corrections of the space vehicle clock. These corrections represent a second-order polynomial in time. Specifically, bits 9–24 of word 8, bits 1–24 of word

9, and bits 1–22 of word 10 provide four clock correction parameters, t_{oc}, a_{f2}, a_{f1}, a_{f0}, which are described in the following paragraphs.

The GPS time t (the space vehicle SV clock time) needed to solve for user position is $t = t_{SV} - \Delta t_{SV}$, where t_{SV} is the SV pseudorandom noise (PRN) code phase time at the time of transmission and is easily determined by the GPS receiver. The satellite clock correction term is approximated by a polynomial $\Delta t_{SV} = a_{f0} + a_{f1}(t - t_{oc}) + a_{f2}(t - t_{oc})^2 + \Delta t_R$, where a_{f0}, a_{f1}, and a_{f2} are the polynomial correction coefficients corresponding to phase error, frequency error, and rate of change of frequency error; the relativistic correction is Δt_R; and t_{oc} is a reference time (in s) for clock correction. Table 4 describes the parameters in number of bits, scale factors, and units.

The relativistic correction must be computed by the user. A first-order effect described in the GPS ICD[1] gives the relativistic correction for an Earth-centered, Earth-fixed (ECEF) observer and a GPS satellite of orbit eccentricity e. This relativistic correction varies as the sine of the satellite eccentric anomaly E_k as follows:

$$\Delta t_R = Fe\sqrt{A}\sin E_k = 2\boldsymbol{R}\cdot\boldsymbol{V}/c^2$$

where

$F = -2\sqrt{\mu}/c^2 = -4.442807633 \times 10^{-10}\ s/m^{1/2}$
$\mu = 3.986005 \times 10^{14}\ m^3/s^2$ value of Earth universal gravitational parameter
$c = 2.99792458 \times 10^8$ m/s
$\boldsymbol{R}$ = instantaneous position vector of the space vehicle
$\boldsymbol{V}$ = instantaneous velocity vector of the space vehicle
e = space vehicle orbit eccentricity

Table 4 Subframe 1 parameters for clock correction and other data

Parameter	No. of bits	Scale factor, LSB[a]	Effective range[b]	Units
Code on L_2	2	1	——	N/A
Week no.	10	1	——	Week
L_2 P data flag	1	1	——	Discretes
SV accuracy	4	——	——	(see text)
SV health	6	1	——	N/A
T_{GD}	8[c]	2^{-31}	——	s
Issue of data clock (IODC)	10	——	——	(see text)
t_{OC}	16	2^4	604,784	s
a_{f2}	8[c]	2^{-55}	——	s/s^2
a_{f1}	16[c]	2^{-43}	——	s/s
a_{f0}	22[c]	2^{-31}	——	s

[a]Least significant bits.
[b]Unless otherwise indicated in this column, effective range is the maximum range attainable with indicated bit allocation and scale factor.
[c]Parameters so indicated shall be two's complement, with the sign bit (+ or −) occupying the most significant bits (MSB).

E_k = eccentric anomaly of the satellite orbit
A = semimajor axis of the satellite orbit

R and V are expressed in the same inertial coordinate system. Chapter 18, this volume, discusses the relativistic effects and the derivation of this equation in more detail.

In addition, as discussed in Chapter 18, the other relativistic effects are as follows:

1) Increase in the received clock frequency by a fixed user on the surface of the Earth's geoid by a fraction $\Delta f/f = +4.46 \times 10^{-10}$. This effect is compensated by purposely setting the 10.23 MHz satelite clock low by $\Delta f = +4.56 \times 10^{-3}$ Hz. Thus, the satellite clock is set to 10,229,999.99543 Hz before launch to ensure that the received GPS signals arrive at the Earth geoid at the correct frequencies.

2) We may also have to account for any significant velocity of the user relative to the Earth or displacement in altitude (gravitational potential) from the surface of the geoid. For example, if the user is at an altitude above the geoid, the fractional increase in the received satellite frequency is not as large. Some of these effects simply may be accounted for by a modification in the user clock bias offset and may not significantly affect user position estimates, because they are approximately the same for all satellites.

We must also account for the rotation of the Earth during the time of transit of the GPS signals from satellite to user. It has already been pointed out that the satellite position has been computed at the time of transmission, whereas the user receiver is computing position at a slightly later time. The Earth has rotated during this transit time, and this rotation must be taken into account. Note that these times of transit for different satellites are not all identical. This effect is a simple effect of the finite velocity of light.

2. $L_1 - L_2$ Correction—Single-Frequency Users

The $L_1 - L_2$ delay correction term is calculated by the GPS Control Segment (CS) to account for the group delay difference in the space vehicle transmission between L_1 and L_2 signals based on measurements made on the SV prior to launch in the factory test. The GPS CS uses a two-frequency ionospheric correction and estimates the a_{fo} satellite clock correction term based on the dual-frequency measurement. Thus, the user employing both L_1 and L_2 in the ionospheric correction need make no further correction. However, the user who employs only L_1 must modify the space vehicle clock correction by $(\Delta t_{sv})_{L_1} = \Delta t_{sv} - T_{GD}$, where T_{GD} is provided in the subframe 1 data by bits 17–24 of word 7 (see Table 4). For the user who employs only L_2 the space vehicle clock correction is $(\Delta t_{sv})_{L_2} = \Delta t_{sv} - \Gamma T_{GD}$ where $\Gamma = (f_{L_1}/f_{L_2})^2 = (1575.42/1227.6)^2 = (77/60)^2$.

The value of the correction term T_{GD} is not equal to the SV group delay differential but rather $T_{GD} = (t_{L_1} - t_{L_2})/(1 - \Gamma)$, where $t_{L_1} - t_{L_2}$ is the SV differential group delay for the satellite. Thus, the value of T_{GD} is not equal to the mean SV group delay differential but to that delay multiplied by $1/(1 - \Gamma)$.

3. Subframe 1—Space Vehicle Accuracy—User Range Accuracy Index

Bits 13 through 16 of word 3 subframe 1 give the user range accuracy (URA) index, of the SV for the user who does not have access to the full accuracy of

Table 5 Table of user range accuracy index *N*, vs the user range accuracy interval in meters

URA index	URA, m
0	0.0–2.4
1	2.4–3.4
2	3.4–4.85
3	4.85–6.85
4	6.85–9.65
5	9.65–13.65
6	13.65–24.0
7	24.0–48.0
8	48.0–96.0
9	96.0–192.0
10	192.0–384.0
11	384.0–768.0
12	768.0–1536.0
13	1536.0–3072.0
14	3072.0–6144.0
15	>6144.0[a]

[a](No accuracy prediction is available. Unauthorized users are advised to use the SV at their own risk.)

Table 6 Ephemeris data definitions[1]

Symbol	Definition
M_0	Mean anomaly at reference time
Δ_n	Mean motion difference from computed value
e	Eccentricity of the orbit
$(A)^{1/2}$	Square root of the semimajor axis
$(\text{OMEGA})_0$	Longitude of ascending node of orbit plane at reference time
I_0	Inclination angle at reference time
ω	Argument of perigee
OMEGADOT	Rate of right ascension
IDOT	Rate of inclination angle
C_{uc}	Amplitude of the cosine harmonic correction term to the argument of latitude
C_{us}	Amplitude of the sine harmonic correction term to the argument of latitude
C_{rc}	Amplitude of the cosine harmonic correction term to the orbit radius
C_{rs}	Amplitude of the sine harmonic correction term to the orbit radius
C_{ic}	Amplitude of the cosine harmonic correction term to the angle of inclination
C_{is}	Amplitude of the sine harmonic correction term to the angle of inclination
T_{oe}	Reference time for ephemeris
IODE	Issue of data (ephemeris)

GPS. (These nonmilitary users are termed the unauthorized users in ICD-GPS-200.[1]) The URA itself (as opposed to the index) is given in meters. The URA index N is an integer in the range of 0–15 and has the relationship to the URA of the SV shown in Table 5.

4. *Issue of Data-Clock*

The issue of data clock (IODC) indicates the issue number of the data set for clock correction, which provides a means for detecting any change in the clock correction parameters. This information is carried in bits 23 and 24 of word 3 MSB and bits 1–8 of word 8 in subframe 1.

B. GPS Ephemeris Parameters—Subframes 2 and 3

The purely elliptical Kepler orbit is precise only for a simple two-body problem where the mutual gravitational attraction between the two bodies is the only force involved. In the actual GPS satellite orbit, there are many perturbations to the ideal orbit, including nonspherical Earth gravitational harmonics; lunar, solar gravitational attraction; and solar flux. Thus, the GPS orbit is modeled as a modified elliptical orbit with correction terms to account for these perturbations: 1) sin, cos perturbations to the a) argument of latitude, b) orbit radius, and c) angle of inclination; and 2) rate of change of a) right ascension, and b) inclination angle.

Furthermore, the parameters for this model are changed periodically to give a best fit to the actual satellite orbit. In normal operations, the fit interval is 4 hours. Subframes 2 and 3 provide 375 bits of information for the modified Keplerian model. Table 6 shows ephemeris model parameters including the sinusoidal perturbations to the orbit radius, the angle of inclination and argument of latitude; the rate of change of inclination angle, angular rate of change of the right ascension; and the basic Keplerian parameters. The scale factors for these parameters are given in Table 7.

1. *Calculation of Satellite Position*

By demodulating and extracting the navigation data in subframes 2 and 3, the user can calculate the satellite position vs. time. The issue of data-ephemeris IODE is a number provided in both subframes 2 and 3 for purposes of comparison and for comparison with the 8 LSB of the IODC term in subframe 1. It should be pointed out that the two IODE numbers in subframes 2 and 3 must match and should also correspond to the IODC for the clock in subframe 1; otherwise, a data set cutover has occurred, and the user must collect new data.

2. *Curve Fit Intervals for the Ephemeris Data*

Bit 17 in word 10 of subframe 2 is a fit interval flag that indicates whether the GPS CS used a least squares fit over a 4-h period or a longer 6-h period; a "0" bit is transmitted for fit periods greater than 4 h. For data sets with a 4-h fit interval (transmitted during the first approximately 1-day period after upload), the curve fit procedures provide a URE contribution for the predicted SV ephemeris of

Table 7 Ephemeris parameters[1]

Parameter	Number of bits[a]	Scale factor, LSB	Effective range[b]	Units
IODE	8	——	——	(See text)
C_{rs}	16[c]	2^{-5}	——	m
Δn	16[c]	2^{-43}	——	Semicircles
M_0	32[c]	2^{-31}	——	Semicircles
C_{uc}	16[c]	2^{-29}	——	rad
e	32	2^{-33}	0.03	Dimensionless
C_{us}	16[c]	2^{-29}	——	rad
$(A)^{1/2}$	32	2^{-19}	——	$m^{1/2}$
t_{oe}	16	2^{4}	604,784	s
C_{ic}	16[c]	2^{-29}	——	rad
$(OMEGA)_0$	32[c]	2^{-31}	——	Semicircles
C_{is}	16[c]	2^{-29}	——	rad
i_0	32[c]	2^{-31}	——	Semicircles
C_{rc}	16[c]	2^{-5}	——	m
ω	32[c]	2^{-31}	——	Semicircles
OMEGADOT	24[c]	2^{-43}	——	Semicircles/s
IDOT	14[c]	2^{-43}	——	Semicircles/s

[a]See Fig. 3 for complete bit allocation in subframe.
[b]Unless otherwise indicated in this column, effective range is the maximum range attainable with indicated bit allocation and scale factor.
[c]Parameters so indicated shall be two's complement, with the sign bit (+ or −) occupying the MSB.

less than 0.35 m, one sigma. These URE component values apply when the data set is transmitted, as well as for a period of 3 h thereafter. The longer, less accurate, 6-h fit interval normally is not used. It is employed if the upload does not occur daily, and the same uploaded data set must apply for a 2nd day through the 14th day after upload. For data sets with a 6-h fit interval, the curve fit provides a URE of less than 1.5 m, one sigma. These URE values apply during transmission and for 2 h thereafter.

The equations in Table 8 give the space vehicle antenna phase center position in WGS-84[5] Earth-centered, Earth-fixed reference frame (including correction for the Earth's rotation with the x_k' to x_k matrix transformation). The ECEF coordinate system is defined as follows:

Origin = Earth center of mass (Geometric center of the WGS-84[5] ellipsoid)
z axis = Parallel to the direction of the Conventional International Origin (CIO) for polar motion as defined by the Bureau International de l'Heure (BIH) on the basis of the latitudes adopted for the BIH stations (Rotation axis of the WGS-84[5] ellipsoid)
x axis = Intersection of the WGS-84[5] reference meridian plane and the plane of the mean astronomic equator, the reference meridian being parallel to the zero meridian defined by the Bureau International de l'Heure on the basis of the longitudes adopted for the BIH stations
y axis = Completes a right-handed, Earth-centered, Earth-fixed orthogonal coordinate system measured in the plane of the mean astronomic equator 90° east of the x axis (x, y axis of the WGS-84[5] ellipsoid)

Table 8 Elements of ephemeris model equations[1]

$\mu = 3.986005 \times 10^{14}$ m^3/s^2	WGS-84[5] value of the Earth's universal gravitational parameter
$\dot{\Omega}_e = 7.2921151467 \times 10^{-5}$ rad/s	WGS-84[5] value of the Earth's rotation rate
$A = (\sqrt{A})^2$	Semimajor axis
$n_0 = \sqrt{\mu/A^3}$	Computed mean motion–rad/s
$t_k = t - t_{oe}$[a]	Time from ephemeris reference epoch
$n = n_0 + \Delta n$	Corrected mean motion
$M_k = M_o + nt_k$	Mean anomaly
$\pi = 3.1415926535898$	GPS standard value for π
$M_k = E_k - e \sin E_k$	Kepler's equation for the eccentric anomaly E_k (may be solved by iteration), rad
$\nu_k = \tan^{-1}\left\{\frac{\sin \nu_k}{\cos \nu_k}\right\} = \tan^{-1}\left\{\frac{\sqrt{1-e^2}\sin E_k/(1-e\cos E_k)}{(\cos E_k - e)/(1-e\cos E_k)}\right\}$	True anomaly ν_k as a function of the eccentric anomaly
$E_k = \cos^{-1}\left\{\frac{e + \cos \nu_k}{1 + e\cos \nu_k}\right\}$	Eccentric anomaly
$\Phi_k = \nu_k + \omega$	Argument of latitude
$\delta u_k = C_{us}\sin 2\Phi_k + C_{uc}\cos 2\Phi_k$	Argument of latitude correction — Second harmonic perturbations
$\delta r_k = C_{rs}\sin 2\Phi_k + C_{rc}\cos 2\Phi_k$	Radius correction — Second harmonic perturbations
$\delta i_k = C_{is}\sin 2\Phi_k + C_{ic}\cos 2\Phi_k$	Inclination correction — Second harmonic perturbations
$u_k = \Phi_k + \delta u_k$	Corrected argument of latitude
$r_k = A(1 - e\cos E_k) + \delta r_k$	Corrected radius
$i_k = i_0 + \delta i_k + (\text{IDOT})\, t_k$	Corrected inclination
$x_k' = r_k \cos u_k$ $y_k' = r_k \sin u_k$	Satellite position in orbital plane
$\Omega_k = \Omega_0 + (\dot{\Omega} - \dot{\Omega}_e)\, t_k - \dot{\Omega}_e\, t_{oe}$	Corrected longitude of ascending node
$x_k = x_k' \cos \Omega_k - y_k' \cos i_k \sin \Omega_k$ $y_k = y_k' \sin \Omega_k + y_k' \cos i_k \cos \Omega_k$ $z_k = y_k' \sin i_k$	Satellite position in Earth-centered, Earth-fixed coordinates

[a]t is GPS system time at time of transmission; i.e., GPS time corrected for transit time (range/speed of light). Furthermore, t_k shall be the actual total time difference between the time t and the epoch time t_{oe} and must account for beginning or end of week crossovers. That is, if t_k is greater than 302,400 s, subtract 604,800 s from t_k. If t_k is less than 302,400 s, add 604,800 s to t_k.

From Table 8 note that it is the mean anomaly $M_k = M_0 + nt_k$ that varies linearly with the time interval t_k. However, the solution of the satellite position requires knowledge of the eccentric anomaly E_k, which does not vary linearly with time unless the eccentricity $e = 0$.

The eccentric anomaly E_k must be solved for by iterative calculations not given in Table 8. However, some of these techniques are briefly discussed in Sec. III of this chapter. Note again, that the model of Table 8 is not merely a simple elliptical orbit. Second harmonic (sinusoidal) corrections are made for the argument of latitude, radius, and inclination of the Kepler model for satellite position. These corrections are then introduced to provide the corrected position for the

satellite in the orbital plane, the corrected radius, argument of latitude, and inclination. Finally, the x, y, z coordinates for the satellite position are transferred to Earth-centered, Earth-fixed coordinates to be used in the final computations of the user position.

3. *Geometric Range*

The ICD-GPS-200[1] also states "The user must also account for the effects due to Earth rotation during the time of signal propagation so as to evaluate the path delay in an inertially stable system." This effect is discussed later in Chapter 18 on relativistic effects.

C. Subframes 4 and 5—Almanac, Space Vehicle Health, and Ionosphere Models

1. *Almanac Data*

Almanac data are used for satellite selection purposes and as aids to acquisition; the almanac can also be used to give approximate Doppler and delay information. Almanac data are used by P(Y) code users in order to perform direct P(Y) code acquisition (if they choose not to acquire the C/A signal first and then handover to the P(Y) code). The almanac data provides a truncated, reduced precision set of the ephemeris parameters described earlier in Table 6. Almanac data provide approximate ephemeris information for up to 32 satellites along with the associated health data for each satellite. Almanacs are provided only for valid satellites or perhaps for a satellite that is about to become active. Where there is no satellite data to fill an almanac data slot, dummy alternating "0s" and "1s" are transmitted to aid in synchronization.

Subframes 4 and 5 each carry 25 pages of information, one new page per frame repetition. We term a 25-frame segment a superframe. Thus, a GPS receiver must demodulate 25 frames over a period of 25 × 30 s or 12.5 min in order to receive all 25 pages of the subframe 4 and 5 almanac data. Of particular interest are the pages shown in Table 9.

Table 9 Key elements of pages in subframes 4 and 5

Pages	Subframe 4	Pages	Subframe 5
2,3,4,5,7,8,9,10	Almanac data for SV 25 through 32	1–24	Almanac data for SV 1–24
18	Ionosphere and UTC data	25	SV health for SV 1–24, almanac reference time and reference week number
25	Anti-spoof flag SV configuration for 32 SV, SV health for SV 25–32	——	——
Other pages	Reserved + special messages, spares	——	——

Table 10a Almanac parameters and accuracy

Age of data time since transmission	Almanac accuracy
1 day	900 m
1 week	1200 m
2 weeks	3600 m

The almanac data are much less accurate than the detailed ephemeris data of subframes 2 and 3. However, the almanac data are valid for longer periods of time and do not require frequent updates. Approximate one sigma almanac accuracy varies as a function of the time since the time of transmission approximately as shown in Table 10a.

The almanac parameters and their scale factors are shown in Table 10b. The algorithm for these parameters is the same ephemeris algorithm as discussed for subframes 2 and 3. Where the almanac does not include a parameter; e.g., sinusoidal corrections, these parameters are set to zero. For the inclination angle, a nominal value of 0.30 semicircles is implicit, and only a parameter δ_i, the correction to the inclination, is transmitted.

In addition, the almanac provides truncated clock correction a_{f0}, a_{f1} parameters for the algorithm discussed in subframe 1. The Almanac time correction provides time to within 2 μs of GPS time using the first order polynomial $t = t_{SV} - \Delta t_{SV}$ where t is GPS time, t_{SV} is the space vehicle clock time (PRN code phase at message transmission time) and $\Delta t_{SV} = a_{f0} + a_{f1} t_k$, where t_k is the time from epoch.

The almanac data occupy almost all bits of words 3–10 of each page of subframe 5 (pages 1–24) and subframe 4 (pages 2–5 and 7–10). The exceptions are the first 8 bits of word 3 (data ID and SVID), bits 17–24 of word 5 (SV health), and the 50 bits of parity. The "0" SVID, binary all zeroes, is used to

Table 10b Almanac parameters

Parameter	Number of bits	Scale factor LSB	Effective range	Units
ϵ	16	2^{-21}		dimensionless
t_{oa}	8	2^{12}	602,112	s
δ_i	16[a]	2^{-19}	——	semicircles
OMEGADOT	16[a]	2^{-38}	——	semicircles/s
$(A)^{1/2}$	24	2^{-11}	——	$m^{1/2}$
(OMEGA)0	24[a]	2^{-11}	——	semicircles
ω	24[a]	2^{-23}	——	semicircles
M_0	24[a]	2^{-23}	——	semicircles
a_{f0}	11[a]	2^{-20}	——	s
a_{f1}	11[a]	2^{-38}	——	s/s

[a]Parameters so indicated shall be two's complement, with the sign bit (+ or −) occupying the MSB.

identify a dummy satellite. When not all satellite slots are needed for different satellites, the same satellite almanac data may be repeated in more than one page. Space vehicle ID is given by bits 3–8 of word 3.

3. *Space Vehicle Health*

Subframes 4 and 5 also contain two types of space vehicle health data: 1) each of the 32 pages that contain satellite clock/ephemeris data also provide an 8-bit SV health status for that particular satellite; and 2) the 25th page of subframe 4 and 5 jointly contain a satellite summary consisting of 6-bit health status words for up to 32 space vehicles.

The first three most significant bits of the 8-bit health words give the health of the navigation data for that space vehicle; e.g., an indication that the Z-count in the HOW word is good or bad. The five LSB of the 8-bit words and the 6-bit words give the health of the space vehicle signal components, as described in Table 11.

4. *Translation of GPS Time to UTC Time*

GPS time is based on atomic standard time, and the time broadcast from the satellite is continuous (modulo-1 week) without the leap seconds of UTC, because the introduction of leap seconds would throw the P-code receivers out of lock at the time when they are introduced. Nonetheless, GPS time is maintained by the GPS CS to be within 1 μs of UTC (USNO) time (modulo-1 s) and provides correction parameters in the GPS navigation message. Thus, the GPS provides an important time transfer function. The UTC–GPS translation parameters are shown in Table 12.

The correction parameters to convert GPS time broadcast by the satellite to UTC are contained in the 24 MSB of words 6–9 plus the 8 MSB of word 10 in page 18 of subframe 4. The bit length scale factors are shown in Table 12.

The information contains the parameters required to relate GPS time to UTC and provides notice to the user of any delta time in the recent past or the near future due to leap seconds Δt_{LS} and the week number WN_{LSF} at which that leap second becomes effective. The above relationships apply for the vast majority of the time. However, when the user is operating at a time near the time for a leap second change, special adjustments are required.

The algorithm defining the relationship between GPS time and UTC using the navigation data in subframe 4 is as follows:[1]

$$t_{UTC} = (t_E - \Delta t_{UTC}) \text{ [modulo-86,400 s]}$$

where t_{UTC} is in ss and

$$\Delta t_{UTC} = \Delta t_{LS} + A_0 + A_1(t_E - t_{ot} + 604{,}800\ (WN - WN_t)), \text{ s}$$

t_E = GPS time as estimated by the user on the basis of correcting t_{SV} for factors given in the Subframe 1 clock correction discussion as well as for ionospheric and SA (dither) effects

Δt_{LS} = delta time due to leap seconds

$A_{0\text{ and }}A_1$ = constant and first-order terms of polynomial

t_{ot} = reference time for UTC data (see Table 13)

Table 11 Codes for health of space vehicle signal components

MSB				LSB	Definition
0	0	0	0	0	All signals OK
0	0	0	0	1	All signals weak[a]
0	0	0	1	0	All signals dead
0	0	0	1	1	All signals have no data modulation
0	0	1	1	0	L_1 P signal weak
0	0	1	0	1	L_1 P signal dead
0	0	1	1	0	L_1 P signal has no data modulation
0	0	1	1	1	L_2 P signal weak
0	1	0	0	0	L_2 P signal dead
0	1	0	0	1	L_2 P signal has no data modulation
0	1	0	1	0	L_1 C signal weak
0	1	0	1	1	L_1 C signal dead
0	1	1	0	0	L_1 C signal has no data modulation
0	1	1	0	1	L_2 C signal weak
0	1	1	1	0	L_2 C signal dead
0	1	1	1	1	L_2 C signal has no data modulation
1	0	0	0	0	L_1 and L_2 P signal weak
1	0	0	0	1	L_1 and L_2 P signal dead
1	0	0	1	0	L_1 and L_2 P signal has no data modulation
1	0	0	1	1	L_1 and L_2 C signal weak
1	0	1	0	0	L_1 and L_2 C signal dead
1	0	1	0	1	L_1 and L_2 C signal has no data modulation
1	0	1	1	0	L_1 signal weak[a]
1	0	1	1	1	L_1 signal dead
1	1	0	0	0	L_1 signal has no data modulation
1	1	0	0	1	L_2 signal weak[a]
1	1	0	1	0	L_2 signal dead
1	1	0	1	1	L_2 signal has no data modulation
1	1	1	0	0	SV *Is* temporarily out (do not use this SV during current pass[a])
1	1	1	0	1	SV *Will Be* temporarily out (use with caution[a])
1	1	1	1	0	Spare
1	1	1	1	1	More than one combination would be required to describe anomalies (except those marked by[a])

[a]Three to six-dB below specified power level due to reduced power output, excess phase noise, SV attitude, etc.

WN = current week number (derived from subframe 1)
WN_t = UTC reference week number

Note that the number of seconds in a day is 86,400.

The estimated GPS time is in seconds relative to end/start of week. The reference time for UTC data t_{ot} is referenced to the start of that week whose number is given in word 8 of page 18 in subframe 4, which represents the 8 LSB of the week number. The user must account for the truncated nature of the week number (see ICD-GPS-200[1]).

When the effectivity time of the leap second event is in the past relative to the user's current time, the relationship presented above is valid except that Δt_{LSF}

Table 12 GPS-UTC clock correction parameters from subframe 4, page 18[a]

Parameter	Number of bits	Scale factor LSB	Effective range	Units
A_0	32[b]	2^{-30}	——	s
A_1	24[b]	2^{-50}	——	s/s
Δt_{LS}	8[b]	1	——	s
t_{ot}	8	2^{12}	602,112	s
WN_t	8	1	——	weeks
WN_{LSF}	8	1	——	weeks
DN	8[c]	1	7	days
Δt_{LSF}	8[b]	1	——	s

[a]The notations DN and WN stand for day number and week number, respectively.
[b]Parameters so indicated shall be two's complement, with the sign bit (+ or −) occupying the MSB.
[c]Right justified.

Table 13 Reference times for block II satellite vehicles to be used for various clock, ephemeris, almanac, and UTC correction polynomials.[a]

		Hours after first valid transmission time			
Fit interval, h	Transmission interval, h	t_{oc} clock	t_{oe} ephemeris	t_{oa} almanac	t_{ot} UTC
4	2	2	2	——	——
6	4	3	3	——	——
8	6	4	4	——	——
14	12	7	7	——	——
26	24	13	13	——	——
50	48	25	25	——	——
74	72	37	37	——	——
98	96	49	49	——	——
122	120	61	61	——	——
146	144	73	73	——	——
——	——	——	——	——	——
144 (6 days)	144	——	——	84	84
144 (6 days)	4080	——	——	84	84

[a]This table describes the nominal selection that is expressed modulo-604,800 s in the navigation message.

is substituted for Δt_{LS}. The exception to the above algorithm occurs whenever the user's current time falls within the timespan of $DN + 3/4$ to $DN + 5/4$ where DN is the day number. In this time interval, proper accommodation of the leap second event with a possible week number transition is provided by the following expression for UTC: $t_{UTC} = W[\text{modulo-}(86400 + \Delta t_{LSF} - \Delta t_{LS})]$, s, where $W = (t_E - \Delta t_{UTC} - 43200)$ [modulo-86400] + 43200, s; and the definition of Δt_{UTC} (as given in the paragraph above) applies throughout the transition period. Note that when a leap second is added, unconventional time values of the form 23:59:60.xxx are encountered. Some user equipment may be designed to approxi-

mate UTC by decrementing the running count of time within several seconds after the event, thereby promptly returning to a proper time indication. Whenever a leap second event is encountered, the user equipment must consistently implement carries or borrows into any year/week/day counts.

5. *Subframe 4 Ionospheric Delay Corrections*

Ionospheric group delay can cause a significant error in the measured pseudorange group delay by perhaps as much as 300 ns during the daytime at low elevation angles and a lesser error, perhaps 5–15 ns, delay at nighttime and varies in roughly a diurnal pattern. Ionospheric delay effects are discussed in detail in Chapter 12, this volume. The two-frequency user with access to the P(Y) code can correct for most of this delay error by measurement.

The single-frequency user has several alternatives:

1) Ignore the ionosphere and accept the ionospheric error,
2) Use a model of the ionosphere,
3) Use a single-frequency carrier/code differential ionospheric measurement scheme,
4) Use a dual-frequency codeless technique either by cross-correlating L_1 and L_2 channels or by squaring the L_2 P(Y) code to recover the pure carrier as shown at the end of this chapter. (Carrier frequency estimates from L_1 and the almanac can be used to reject the multiple access interference caused by other carriers in the estimation process.)

The single-frequency user can get an approximate correction by using a model of the ionosphere with model parameters transmitted in the downlink datastream. However, the user should be advised that the ionosphere varies in a manner that is difficult to predict, hence the model provides only an approximate correction (for perhaps 70% of the ionosphere delay). In addition, the single-frequency user must correct for the L_1–L_2 delay differential T_{GD} in the satellite that is not needed by the two-frequency user.

The ionospheric group delay model developed for GPS by Klobuchar (see Chapter 12, this volume) essentially employs a half cosine approximation, as shown in Fig. 8. The ionospheric group delay is modeled essentially as follows:

$$\begin{aligned} I(t) &= F(E)\left[5 \times 10^{-9} + \text{AMP(L)} \cos[2\pi(t - 50{,}400)/\text{PER(L)}] \text{ for day}\right] \\ &= F(E)(5 \times 10^{-9}) \text{ for night} \end{aligned} \tag{3}$$

where $F(E)$ is the obliquity factor that gives a larger I for lower elevation angles E. The parameter AMP(L) is the amplitude of the half cosine for daytime, which is a function of the geomagnetic latitude L of the Earth projection of the ionosphere contact point and PER(L) is the period of the half cosine.

The small constant level of delay equal to 7 ns in this example of Fig. 8 is meant to represent the delay at night. As the sun rises and sets, the ionospheric model gives rise to the cosine-shaped pulse for daytime.

The half-cosine model in the actual GPS ionospheric group delay model is represented by the first three terms in the series expansion $\cos x \cong 1 - (x^2/2) + (x^4/24)$, $|x| < 1.57 \approx \pi/2$, as shown in the algorithm of Table 14.

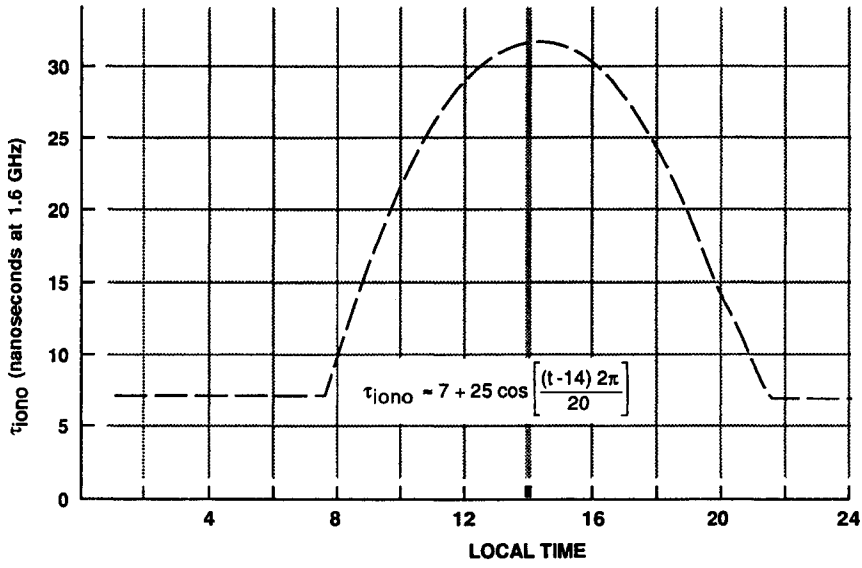

Fig. 8 Example ionospheric group delay cosine fit model.

The specific ionospheric parameters for GPS are given by subframe 4, page 18 for the single-frequency L_1 (or L_2 user) for use in the algorithm given below. These data occupy bits 9–24 of word three plus the 24 MSB of words four and five. The scale factors are shown in Table 15.

Notice that with this definition of the obliquity factor F at elevation angle E = 0-deg gives $F = 3.382032$. Thus, the obliquity factor is slightly greater than three at low elevation angles, and $F = 1.0004$ for $E = 0.50$ semicircles (90 deg).

The GPS ionospheric obliquity factor from the model is plotted in Fig. 9. The obliquity factor of 3.382 at 0-deg elevation angle does not become as great at low elevation angles as the tropospheric obliquity factor, because the ionosphere occupies an altitude range of approximately 50–500 km, and as a consequence of this altitude, even a ray path at 0 deg elevation angle on Earth enters the ionosphere at a steeper elevation angle than 0 deg, whereas the troposphere has maximum effect right at the Earth's surface (see Chapter 13, this volume).

The approximate behavior of the variation of ionospheric delay vs. elevation angle can be estimated by referring to Fig. 10, which shows a uniform spherical shell of ionosphere extending from one altitude h_{min} to an upper altitude h_{max}. The upper and lower limits shown are only examples, the ionosphere is in reality not uniform, and in any event, the upper and lower extent of any model would vary with time. In contrast to the troposphere, the ionosphere does not extend to the Earth's surface. Thus, even if the user elevation angle at the Earth's surface is $E = 0$ deg, the angle of incidence ϕ to the ionosphere for this simple model is greater than zero and for this example: $\phi = \cos^{-1}\{[1/(1 + \delta)]\cos E\} = 13.455$ deg for $E = 0$ deg, where $\delta = (h_{min}/R)$, and for this example $h_{min} = 180$ km and $\delta = 0.02822$. The length L_I through the ionosphere for this simple model is easily determined to be as follows:

Table 14 Ionospheric model

The ionospheric correction model is given by the following:

$$I = T_{\text{iono}} = \left\{ \begin{array}{ll} F^* [(5.0 * 10^{-9}) + (\text{AMP})(1 - (x^2/2) + (x^4/4))], & |x| < 1.57 \text{ day} \\ F^* (5.0 * 10^{-9}), & |x| \geq 1.57 \text{ night} \end{array} \right\}$$

where $I = T_{\text{iono}}$ is referred to the L_1 frequency; if the user is operating on the L_2 frequency, the correction term must be multiplied by $\gamma = 1.646944444$. (T_{iono} is the notation of ICD-GPS-200.)[1]

$$\text{AMP} = \left\{ \begin{array}{l} \sum_{n=0}^{3} \alpha_n \phi_m^n, \quad \text{AMP} \geq 0 \\ \\ \text{if AMP} < 0, \text{ set AMP} = 0 \end{array} \right\} \text{(s)} \qquad \text{Amplitude}$$

$$x = \frac{2\pi (t - 50400)}{\text{PER}}, \text{ (rad)}$$

$$\text{PER} = \left\{ \begin{array}{l} \sum_{n=0}^{3} \beta_n \phi_m^n, \qquad \text{PER} \geq 72000 \\ \text{if} \qquad \text{PER} < 72{,}000, \text{ set PER} = 72{,}000 \end{array} \right\} \text{(s)} \qquad \text{Period}$$

$F = 1.0 + 16.0\,[0.53 - E]^3$, the obliquity factor
α_n and β_n are the satellite transmitted data words with $n = 0$, 1, 2, and 3.

Other equations that must be solved are as follows:

$$\phi_m = \phi_i + 0.064 \cos(\lambda_i - 1.617) \text{ (semicircles)},$$

$$\lambda_i = \lambda_u + \frac{\Psi \sin A}{\cos \phi_i} \text{ (semicircles)},$$

$$\phi_i = \left\{ \begin{array}{c} \phi_u + \Psi \cos A \text{ (semicircles)}, |\phi_i| \leq 0.416 \\ \text{if } \phi_i > 0.416, \text{ then } \phi_i = +0.416 \\ \text{if } \phi_i < -0.416, \text{ then } \phi_i = -0.416 \end{array} \right\} \text{(semicircles)},$$

$$\Psi = \frac{0.0137}{E + 0.11} - 0.022 \text{ (semicircles)},$$

$t = 4.32 * 10^4 \lambda_i + \text{GPS time (s)}$, t = local solar time (s)

where $0 \leq t < 86{,}400$, therefore: if $t \geq 86{,}400$ seconds, subtract 86,400 seconds;
if $t < 0$ seconds, add 86,400 seconds.

The terms used in computation of ionospheric delay are as follows:

Satellite Transmitted Terms

α_n = the coefficients of a cubic equation representing the amplitude of the vertical delay, 4 coefficients—8 bits each

β_n = the coefficients of a cubic equation representing the period of the model, four coefficients—8 bits each

(Table 14 continues on next page.)

Table 14 Ionospheric model (continued)

Receiver Generated Terms

E = elevation angle between the user and satellite, semicircles
A = azimuth angle between the user and satellite, measured clockwise positive from the true north, semicircles
ϕ_u = user geodetic latitude, semicircles, WGS-84[5]
λ_u = user geodetic longitude, semicircles, WGS-84[5]

GPS time receiver computed system time

Computed Terms

x = phase, rad
F = obliquity factor, dimensionless
t = local time, s
ϕ_m = geomagnetic latitude of the Earth projection of the ionospheric intersection point, mean ionospheric height assumed 350 km, semicircles
λ_i = geodetic longitude of the Earth projection of the ionospheric intersection point, semicircles
ϕ_i = geodetic latitude of the Earth projection of the ionospheric intersection point, semicircles
Ψ = Earth's central angle between user position and Earth projection of ionospheric intersection point, semicircles

Table 15 Ionospheric parameters from subframe 4, page 18

Parameter	Number of bits	Scale factor, LSB	Effective range[a]	Units
α_0	8[b]	2^{-30}	——	s
α_1	8[b]	2^{-27}	——	s per semicircle
α_2	8[b]	2^{-24}	——	s per semicircle^2
α_3	8[b]	2^{-24}	——	s per semicircle^3
β_0	8[b]	2^{11}	——	s
β_1	8[b]	2^{14}	——	s per semicircle
β_2	8[b]	2^{16}	——	s per semicircle^2
β_3	8[b]	2^{16}	——	s per semicircle^3

[a]Effective range is the maximum range indicated by the bit allocation and scale factor.
[b]Parameters so indicated shall be two's complement, with the sign bit (+ or −) occupying the MSB.

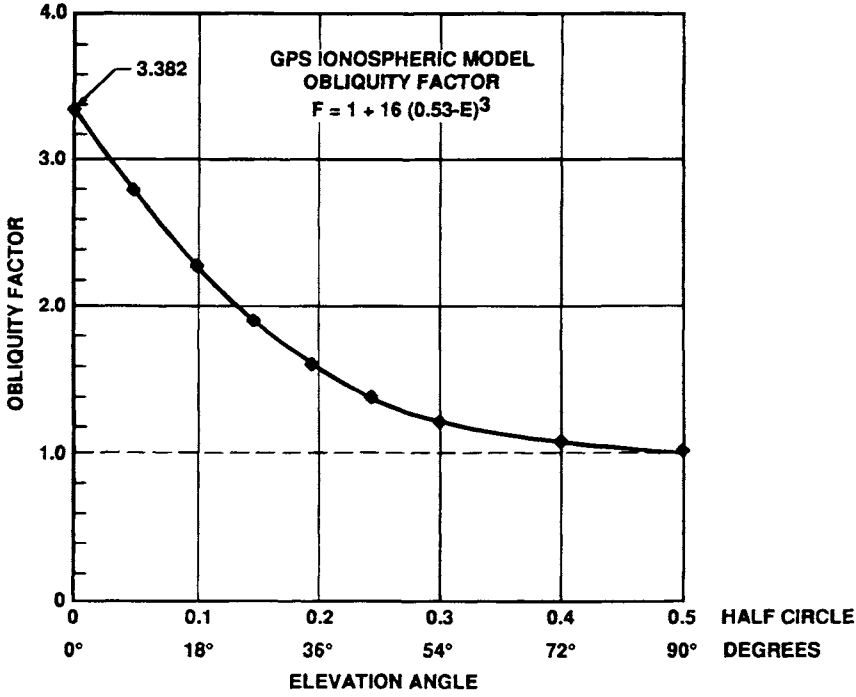

Fig. 9 GPS ionospheric model obliquity factor.

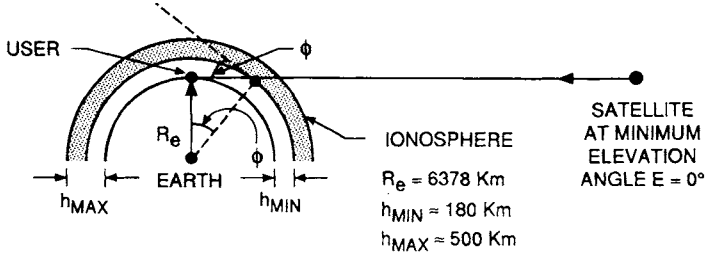

Fig. 10 Approximate representation of the ionosphere by a spherical shell of width $h = h_{max} - h_{min}$. The angle of incidence of the ionosphere d relative to the elevation angle E is given by $\phi = \cos^{-1}[(\cos E)/(1 + \delta)]$ where $\delta = h_{min}/R_e$.

Chapter 5

Satellite Constellation and Geometric Dilution of Precision

J. J. Spilker Jr.*
Stanford Telecom, Sunnyvale, California 94089

I. Introduction

THE GPS satellite constellation is selected to satisfy many different conditions to provide worldwide three-dimensional navigation. The satellite constellation has been placed in an inclined orbit at 55 deg (formerly 63-deg inclination for earlier Block I satellites) to provide full Earth coverage, whereas a purely equatorial orbit cannot provide coverage above approximately 72° latitude at the GPS orbit altitude. The requirement for a minimum of four simultaneous pseudorange measurements with good geometry directly leads to a constellation of many satellites. A nongeosynchronous orbit was selected to permit the use of carrier phase/Doppler measurement profiles in addition to pseudorange measurements of code phase/delay. This objective was one of the reasons for the selection of the 12 sidereal hour orbit.

This chapter discusses the operational satellite constellation of 24 satellites termed the GPS-24 (closely related to the previous Primary 21) constellation. The specific characteristics of this constellation are discussed in terms of the statistics of the numbers of satellites visible at different user latitudes and various elevation angles, the satellite ground tracks, and the signal Doppler shifts. The potential for the future augmentation of this GPS constellation by adding satellites in either the same planes or as geostationary satellites is also discussed.

The chapter then continues with an analysis of the *geometric dilution of precision* (GDOP) and the related DOPs: PDOP, HDOP, VDOP, TDOP for position, horizontal, vertical, and time dilutions of precision. The bounds on the minimum value of these DOPs are analyzed for various numbers of satellites for both two- and three-dimensional problems with various constraints on elevation angle and user clock stability. Further discussion and development of the DOP concept is found in Chapter 11, this volume. The chapter concludes by describing the GDOP for the GPS-24 satellite constellation with a single satellite outage.

*Ph.D., Chairman of the Board.

II. GPS Orbit Configuration, GPS-24

As mentioned earlier, the operational constellation is defined as GPS-24. The selected satellite orbital constellation contains 24 satellites in six orbit planes. There are four satellites in each of the six planes, which are shown in Fig. 1. The satellites have a period of 12 h *sidereal time** and a semimajor axis of 26,561.75 km.† A sidereal day is defined as the time for the Earth to complete one revolution on its axis in Earth–Centered-Inertial (ECI) space and consists of 24 sidereal hours where 1 sidereal day is slightly shorter than a mean solar day (see Chapter 4, this volume). One sidereal day is 23 h, 56 min, 4.009054 s or 86,164.09054 s of mean solar time. One mean sidereal day is equal to 0.997269566 mean solar day. The satellites are inclined with respect to the equatorial plane by 55 deg. Table 1 summarizes the nominal parameters of the GPS orbit.

A. GPS Orbit-Semi-Major Axis

The nominal period T_{po} of an orbit around the Earth is as follows:

$$T_{po} = \frac{2\pi}{\sqrt{\mu}} a_o^{3/2} \quad \text{and} \quad a_o = (T_{po}^2 \mu/(2\pi)^2)^{1/3} \tag{1}$$

where a_o is the semimajor axis in m, and μ and π are defined for GPS using

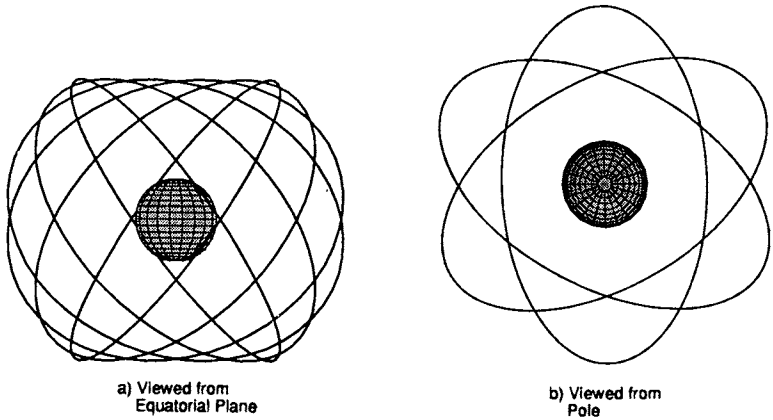

Fig. 1 GPS-24 satellite constellation: a) the six orbit planes inclined at 55 deg shown in Earth–centered-inertial (ECI) coordinates viewed from the equatorial plane. The GPS constellation has four satellites in six equally spaced orbit planes. Note that the symmetrical satellite orbit planes are superimposed in part b. The present GPS-24 satellite constellation contains four nonequally spaced satellites in six orbit planes. The satellite phasing is designed to minimize the effect of satellite outage. The satellite phasing is shown in Fig. 2.

*A satellite with a 12-h orbit in sidereal time rotates once in inertial space in 12 h of sidereal time. The semimajor axis for a 12-h sidereal orbit is 26,561.75 km and has an altitude above the Earth equatorial radius of 6378.137 km of 20,183.6 km.

†Strictly speaking, the GPS satellites have a 12-h orbit (sidereal time) wherein the ground tracks repeat to within ± 2° in longitude. If the ground track drifts off from its nominal value by more than 2°, the GPS control segment makes a minor orbit correction.

Table 1 Approximate GPS satellite parameters and physical constants

Parameter	Value	
Orbit plane spacing	6 equally spaced ascending nodes at 120 deg	
Orbit radius r_{cs}	26,561.75 km semimajor axis	
Orbit velocity (circular) (ECI)	$\cong \sqrt{\mu/r_{cs}} = 3.8704$ km/s	
Eccentricity	Nominally zero but generally less than $e = 0.02$	
ω_s angular velocity	$2 \times 7.29211 \times 10^{-5}$ rad/s	
Period	12-h mean sidereal time	
Inclination	$i = 55$ deg nominal	
Velocity of light c	2.99792458×10^8 m/s	GPS-ICD-200[a]
Earth's gravitational parameter μ	3.986005×10^{14} m^3/s^2	GPS-ICD-200 WGS-84 value[b]
Pi, π	3.141592653898	GPS ICD-200
Earth's rotation rate Ω_e in inertial space	$7.2921151467 \times 10^{-5}$ rad/s	ICD-200 WGS-84 value
One sidereal day $2\pi/\Omega_e$	86164.0989038 s	WGS-84 (calculated from $\dot{\Omega}_e$)
One solar day	86400 s	
J_2 harmonic	1.08268×10^{-3}	

[a] GPS-ICD 200, GPS Interface Control Document.
[b] WGS-84, 1984 World Geodetic System.

WGS-84 and GPS-ICD-200 values as shown in Table 1. The values of a_o and T_{po} neglect the effect of Earth oblateness. If the period of the orbit is set as 1/2 of a sidereal day, (12 h sidereal time), then the nominal value of the semimajor axis a_o is 26,561.765 km. However, because of Earth oblateness, the orbit period must be corrected slightly.*

The orbit mean motion (angular) of the satellite with the J_2 correction for Earth oblateness is as follows[1]:

$$\bar{n} = \sqrt{\frac{\mu}{a^3}}\left[1 + \frac{3}{2}\frac{J_2 R_e^2}{p^2}\left(1 - \frac{3}{2}\sin^2 i\right)(1 - e^2)^{1/2}\right] \tag{2}$$

where a is the corrected semimajor axis at epoch; e = eccentricity; $p = a(1 - e^2)$; R_e is the Earth equatorial radius; i is the orbit inclination; and $J_2 \cong 1082.68 \times 10^{-6}$. For $e \cong 0$, this equation reduces to the following:

$$\bar{n} \cong \sqrt{\frac{\mu}{a^3}}\left[1 + \frac{3}{2}\frac{J_2 R_e^2}{a^2}\left(1 - \frac{3}{2}\sin^2 i\right)\right]\Bigg\} \quad \text{for} \quad e \cong 0$$

$$\cong \sqrt{\frac{\mu}{a^3}}(1 + \Delta) \tag{2a}$$

where $\Delta = (3/2)\, J_2[R_e/a)^2[1 - (3/2)\sin^2 i]$ for $e \cong 0$.

*There is also a correction for solar pressure, which is dependent on the spacecraft size and shape, that is neglected here.

The period of the orbit corresponds to $\bar{n}T_p = 2\pi$, and then is given by the following:

$$\bar{n}T_p = 2\pi, \quad \text{or} \quad T_p = 2\pi/\bar{n} \cong 2\pi\sqrt{\left(\frac{a^3}{\mu}\right)/[1+\Delta]} \tag{3}$$

for T_p = 12 h sidereal time, and $\Delta << 1$. Solve Eq. (3) for the semimajor axis a to obtain the following:

$$a \cong \left[\mu\left(\frac{T_p}{2\pi}\right)^2(1+\Delta)^2\right]^{1/3} \tag{4}$$

noting that Δ is inversely proportional to a^2.

For the GPS orbit with an orbit inclination of 55 deg and zero eccentricity, $\Delta \cong -6.098 \times 10^{-7}$. Thus, the second-order effect on Δ by the variation of a can be neglected, and the corrected value of the semimajor axis is as follows:

$$a \cong \left[\frac{(1+\Delta)^2}{(2\pi)^2}\mu T_p^2\right]^{1/3} = \left[\frac{\mu T_p^2}{(2\pi)^2}\right]^{1/3}(1+\Delta)^{2/3}$$

$$\cong \left[\frac{\mu T_p^2}{(2\pi)^2}\right]^{1/3}\left(1+\frac{2}{3}\Delta\right) \quad \text{for} \quad \Delta << 1 \tag{5}$$

For GPS, the J_2 correction is relatively small and only corresponds to a 0.0108 = km reduction in the semimajor axis.*

Thus, the corrected value of a is 26561.754 km.

B. GPS Orbit–Satellite Phasing

Table 2 lists the orbital parameters for the GPS-24 satellite constellation. The satellites all have a design eccentricity of $e = 0$ and an inclination $i = 55$ deg. The angle Ω is the right ascension of the ascending node measured in inertial coordinates from the vernal equinox. The *lan* is the longitude of the ascending node in ECEF coordinates at the epoch time 7,1,0,0,0 of year 1993. The quantity M is the mean anomaly, which is the satellite phase for a circular orbit. If the 24 satellites were equally spaced in each orbit plane, there would be a 360 deg/4 = 90 deg separation in M.

In Table 2, note that the longitude of the ascending node *lan* is expressed in Earth-centered, Earth-fixed (ECEF) rotating coordinates. The right ascension of ascending node Ω for each of the six planes *A, B, C, D, E,* and *F* as expressed in ECI coordinates is the same for all four satellites in each individual plane and are offset by 60 deg from one another. All of the phase angles and longitudes of the ascending node *lans* (expressed in ECEF coordinates) are different. Thus, there are 24 different ground tracks. Units are in km and deg. The satellite phases in each of the planes are shown in Fig. 2. Notice that in inertial space, the satellite planes are equally spaced in longitude relative to the vernal equinox, but the

*Note that at the earlier Block I satellite inclination of 63 deg, the semimajor axis reduction is 29.29 times as large.

Table 2 GPS-24 satellite constellation

	ID	a	i	Ω	M	ΔM	lan
1	A3	26561.75	55.0	272.847	11.676	103.55	179.63
2	A4	26561.75	55.0	272.847	41.806	31.13	14.69
3	A2	26561.75	55.0	272.847	161.786	119.98	74.68
4	A1	26561.75	55.0	272.847	268.126	106.34	127.85
5	B1	26561.75	55.0	332.847	80.956	130.98	94.27
6	B2	26561.75	55.0	332.847	173.336	92.38	140.46
7	B4	26561.75	55.0	332.847	204.376	31.04	155.98
8	B3	26561.75	55.0	332.847	309.976	105.6	28.78
9	C1	26561.75	55.0	32.847	111.876	100.08	169.73
10	C4	26561.75	55.0	32.847	241.556	129.68	54.57
11	C3	26561.75	55.0	32.847	339.666	98.11	103.62
12	C2	26561.75	55.0	32.847	11.796	32.13	119.69
13	D1	26561.75	55.0	92.847	135.226	100.07	61.40
14	D4	26561.75	55.0	92.847	167.356	32.13	77.47
15	D2	26561.75	55.0	92.847	265.446	98.09	126.51
16	D3	26561.75	55.0	92.847	35.156	129.71	11.37
17	E1	26561.75	55.0	152.847	197.046	130.98	152.31
18	E2	26561.75	55.0	152.847	302.596	105.55	25.09
19	E4	26561.75	55.0	152.847	333.686	31.09	40.63
20	E3	26561.75	55.0	152.847	66.066	92.38	86.82
21	F1	26561.75	55.0	212.847	238.886	103.54	53.23
22	F2	26561.75	55.0	212.847	345.226	106.34	106.40
23	F3	26561.75	55.0	212.847	105.206	119.98	166.39
24	F4	26561.75	55.0	212.847	135.346	30.00	1.46

Units are in km for a, and degrees elsewhere, identification ID = Plane/slot; a = Semimajor axis, size in km; i = Inclination, deg; Ω = Right ascension of ascending node, deg; M = Mean anomaly, deg; lan = Longitude of ascending node, deg; ΔM = Phase difference in mean anomaly to adjacent satellite in the same plane.

satellites themselves in each plane are not equally spaced. In fact, two of the satellites in each plane are spaced by between 30.0 and 32.1 deg. If the remaining two satellites were equally spaced in the remaining 330 deg, that would put the spacing of the other satellites at approximately 330 deg/3 = 110 deg. The actual separation varies from 92.38 to 130.98 deg. The spacing has been optimized to minimize the effects of a single satellite failure on system degradation. As discussed later in the chapter, even with a single satellite failure, the PDOP does not exceed six for more than 25 min/day for a user constraint on satellite elevation angles of 5 deg or more.

II. GPS Satellite Visibility and Doppler Shift

Some important characteristics of the GPS satellite constellation as they relate to user receiver navigation performance are the number of satellites in view and the range of Doppler shifts. It is critical that at least four satellites be in view, but it is highly desirable that five or more be in view at all times. When one

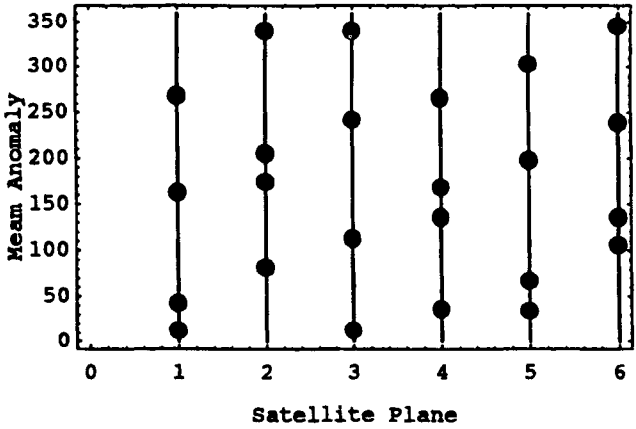

Fig. 2 GPS-24 satellite mean anomaly (satellite phase) in each of the six planes at the epoch 7,1,0,0,0 in 1993 (ECI space). Time is in universal clock time (UTC).

satellite is going out of view, the user receiver must begin to transition to another satellite as its replacement. Furthermore, four satellites by themselves may not provide a sufficiently low GDOP because of poor geometry at certain times.

A. Bound on Level of Coverage for 24 Satellites

A general class of circular orbit satellite constellations with equally spaced satellites and orbit planes has been defined by Walker.[2] In this family of constellations, there are T total satellites in P uniformly spaced planes of circular satellites, each plane at inclination angle i with respect to the equatorial plane. There are T/P uniformly spaced satellites in each plane. The relative phasing between satellites in adjacent planes is given by F, which is in units of 360 deg/T; i.e., if a satellite in one plane is just crossing through the equatorial plane in the northerly direction, the adjacent plane satellite is offset by an angle (360 deg/T)F below the equatorial plane. Thus, the constellation can be described by the notation (T/P/F), and the inclination angle by i. For example, if there are $T = 18$ satellites, and the relative phasing between satellites is $F = 2$, then the relative phasing between satellites in adjacent planes as they pass through the equator is (360 deg/T)F = (360/18)2 = 40 deg.

The degree of worldwide multiple satellite coverage can be determined by computing the maximum Earth angle separation between satellites for a cone that contains N satellites. That is, in any conical section of the sphere of satellites there must be N satellites in view for a conical angular separation of 2β deg where β deg is determined by the minimum allowed user elevation angle E (see Fig. 3). This N-satellite visibility must be maintained at all user coordinates and at all times.

Walker[2] has shown that continuous worldwide coverage with at least six satellites in view everywhere is possible with 24 satellites in six planes using a 24/6/1 constellation at an inclination angle of 57 deg for users with a minimum elevation angle of 7 deg. The maximum Earth angle separation between satellites of $\beta = 69.9$ deg for this constellation corresponds to $E \approx 7$ deg minimum elevation

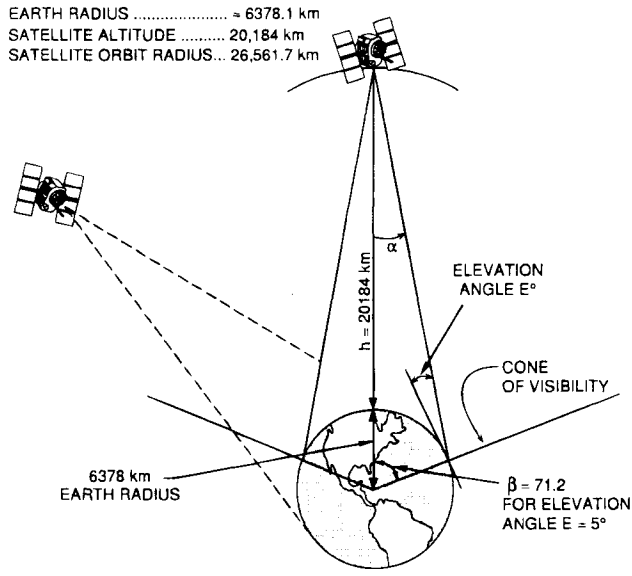

Fig. 3 Ground coverage by GPS satellites. The user is restricted to receiving satellites above a minimum elevation angle *E*.

angle (see Fig. 4a). Sevenfold coverage is achievable with a (24/8/4) constellation with a smaller minimum elevation angle of 3 deg is too low for normal operation. However, this constellation's seven-satellite minimum coverage is obtained with the maximum Earth angle separation between satellites of $\beta = 75.8$ deg and the corresponding minimum elevation angle of 3 deg which is too low for normal operation. It should also be noted that the maximum satellite visibility does not necessarily correspond to the smallest GDOP nor to the best performance.

The selected GPS-24 satellite constellation is shown later to give fivefold visibility. Although it does not have as good a full constellation satellite visibility as the (24/6/1) constellation, the GPS-24 satellite constellation has instead been selected on the basis of best coverage if a single satellite becomes inoperative.

B. GPS Satellite Visibility Angle and Doppler Shift

The half angle subtended by the users as viewed from the satellite is termed α as shown earlier in Fig. 3. Each GPS satellite broadcasts to the Earth with an antenna coverage pattern that somewhat exceeds the angle $\alpha = 13.87$ deg subtended by the Earth, as shown in Fig. 3. That is, the satellite antenna pattern extends beyond the edge of the Earth, in order to provide coverage to user satellites not shadowed by the Earth. Each satellite covers users within $\pm\beta$ deg of the subsatellite point, where β is determined by the minimum elevation angle. The subsatellite point can be defined by: A line drawn between the Earth's center, and the satellite intersects the Earth's surface at the subsatellite point. (For a spherical Earth, the satellite is at the zenith of a user at the subsatellite point.) Thus, the fraction of the Earth covered

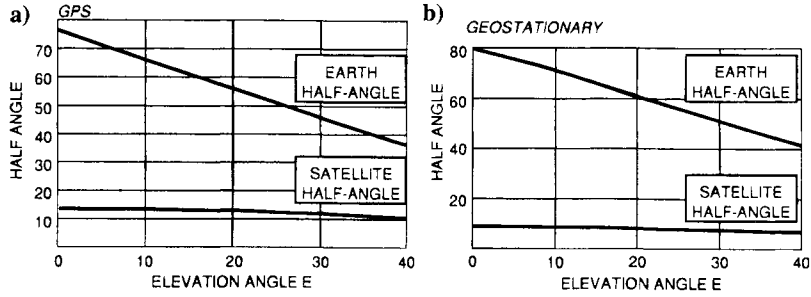

Fig. 4 Half-angles subtended from Earth center β and from the satellite α as a function of the elevation angle *E*. The half-angles are given both for the GPS 12-h orbit (a), and for the 24-h geostationary orbit (b).

depends on the constraint on the minimum elevation angle from the user to the satellite. Within this elevation angle constraint E, the value of α is as follows:

$$\alpha = \sin^{-1}\left[\left(\frac{R_e}{R_e + h_s}\right)\cos E\right], \qquad \begin{cases}\alpha = 13.87 \text{ for } E = 0 \text{ deg} \\ \alpha = 13.82 \text{ for } E = 5 \text{ deg}\end{cases} \tag{6}$$

where R_e is the Earth radius; h_s is the satellite altitude; $h_s + R_e = a$; and a is the orbit radius or semimajor axis because we have assumed a circular orbit and spherical Earth.

The Earth half-angle $\beta = 90 \text{ deg} - \alpha - E = 71.2 \text{ deg}$ for $E = 5$ deg, and β is termed the visibility half-angle. Figure 4a shows the visibility half-angles β as a function of elevation angle E for GPS altitude orbits. For completeness, the visibility half-angles are shown in Fig. 4b for geostationary 24-h orbits, because there is a consideration of augmenting the GPS orbit satellites with one or more geostationary orbit satellites. The fraction of the spherical shell of satellites visible to the user is $(1/2)(1 - \cos\beta)$. On the average, if all 24 satellites were always equally spaced on a sphere (which they cannot be), we would expect to see a fraction of the satellites corresponding to the fraction of the sphere subtended by the β deg cone; namely, $24(1/2)(1 - \cos\beta) = 8.1$ satellites for $E = 5$ deg of the total 24 satellites.

An example of the actual GPS satellite visibility region for a user at a fixed point on Earth is shown* on a Mercator projection map in Fig. 5. The visibility region is defined by the subsatellite points above the dashed line on the figure.

C. GPS-24 Satellite Visibility

A set of satellite visibility statistics for the operational GPS-24 satellite constellation is shown in Figs. 6 and 7 for various user latitudes. The results have been

*The parametric equation for the locus of latitude and longitude at the edge of satellite visibility (subsatellite point) for a user at latitude ϕ and longitude θ is as follows:

$$\text{latitude} = \sin^{-1}[\sin(71 \text{ deg}) \sin b \cos\phi + \cos(71 \text{ deg}) \sin\phi];$$
$$\text{longitude} = \tan^{-1}[\sin(71 \text{ deg}) \cos\phi/(\cos(71 \text{ deg}) \cos\phi - \sin(71 \text{ deg}) \sin b \sin\phi)] + \theta,$$

where b is the parametric angle $b = (-\pi, \pi)$ and 71 deg is the assumed coverage half-angle from the Earth's center.

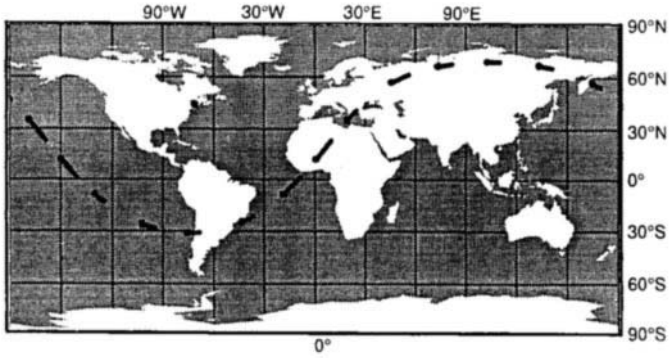

Fig. 5 Example GPS satellite visibility region for a user in the northeastern United States at latitude 40.1°N, longitude 74.5°W (see the dot) with an Earth visibility half-angle of 71 deg. Satellites with a subsatellite point above the dashed curve are in view of the user.

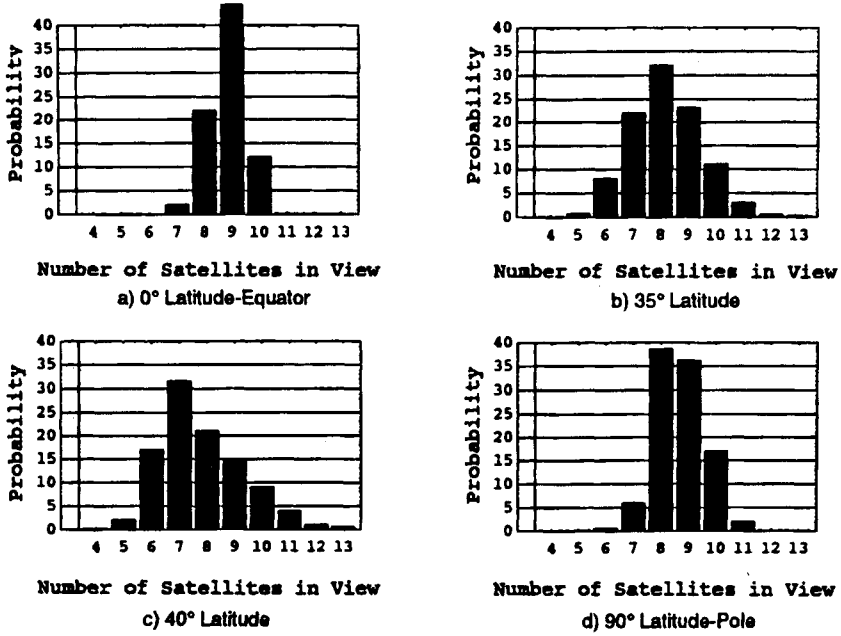

Fig. 6 GPS satellite visibility for the GPS-24 satellite constellation for a 5-deg elevation mask angle. The bar charts correspond to user latitudes as indicated. Note that there are always at least five satellites in view and at least seven more than 80% of the time.

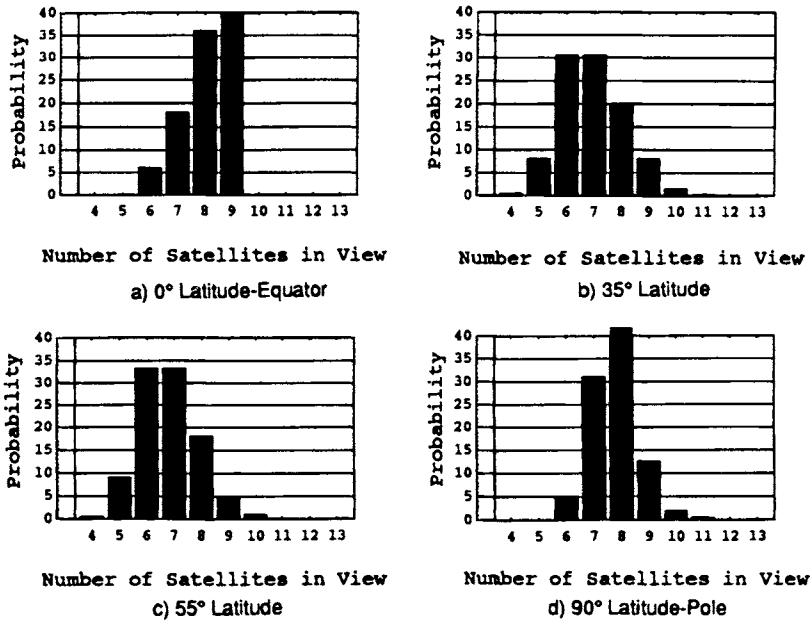

Fig. 7 GPS-24 satellite visibility in percent at various latitudes, averaged over longitude and a 24-h time span. The 35° user latitude corresponds to the approximate worst latitude where momentarily there are only four satellites in view (approximately 0.4% of the time) at this high elevation angle.

averaged over all user position longitudes at that latitude. Figure 6 shows the satellite visibility for a 5-deg elevation mask angle. The majority of the time there are at least seven satellites in view. Compare this result with the previously presented result for equally spaced satellites on a sphere where the average number of satellites on a sphere is 8.1. There are a minimum of five satellites visible for this 5-deg elevation mask angle. Note that a moderately high altitude aircraft can view satellites down to 0-deg elevation angle, and hence have even better satellite visibility. Both sets of results are based on 100 time samples over 24 h and 16 longitude samples at each latitude. It should also be pointed out that a uniform spacing of GPS satellites in an orbit such as the (24/6/1) constellation would lead to better visibility statistics, but greater sensitivity to a satellite outage.

In Fig. 7, a 10-deg elevation mask angle has been used, and satellite visibility has again been averaged over 24 h in time and a set of longitudes at 11.25-deg increments. Note that at both very high and very low latitudes, a minimum of six satellites are always in view and as many as 9–11. However, for a 10-deg elevation mask angle in the vicinity of 35 to 55° latitude, only four satellites are in view a small fraction, $<0.5\%$, of the time. Clearly whenever only four satellites are in view, a failure of one of these satellites would cause an outage. Furthermore, even if four satellites are in view, the satellite/user geometry might correspond to a high GDOP. Thus, although these outages are not very likely and only

occur at certain short intervals of time, methods of augmentation of the GPS-24 constellation are of interest.

A word of caution is in order for users at high latitudes. Note that the maximum satellite elevation angle for a user at the pole is

$$E = \tan^{-1}(a \cos (55 \text{ deg})/a \sin (55 \text{ deg}) - R_e) = 44.7 \text{ deg}$$

because the satellite inclination angle is 55 deg. Thus, there are no satellites anywhere at or near the zenith, and the GDOP is degraded, although satellite visibility is good. If the minimum elevation angle is 5 deg, then the usable range of satellite elevation angles is only 39.7 deg.

D. Augmentation of the GPS-24 Constellation

A number of methods can be used to increase the minimum number of satellites in view by adding satellites to the constellation:

1) Add another satellite to each plane to create a (30/6/*X*) constellation with five satellites in each plane instead of four.

2) Add a ring of GPS satellites at the same altitude but in the equatorial plane. Because the GPS visibility outage regions appear most likely at the midlatitude range 30–50°, a ring of three evenly spaced GPS satellites can add another satellite in view for users anywhere in the midlatitudes. However, sparing is made more difficult by adding yet another plane of satellites.

3) Add several geostationary satellites. These satellites also cover the midlatitude region, and because they are of higher altitude than the GPS satellites, fewer are required for the same degree of coverage. Second, we may be able to put GPS-like payloads on host geostationary communications or weather satellites.

4) Another augmentation being considered is the use of satellites with inclined planes on lower altitude 6-h orbits.

E. Constellation of 30 GPS Satellites

As an example of 30-satellite visibility, the coverage statistics for the (30/6/1) constellation are computed (not necessarily the optimum 30-satellite constellation) and shown in Fig. 8, which illustrates the visibility statistics for a 5-deg elevation mask angle. *Note that here there are a minimum of eight satellites in view at all tested user latitudes.* (55° latitude also showed a minimum of eight satellites in view.) Thus, there seem to be several real advantages in a 30-satellite constellation; namely, visibility is markedly improved; single-satellite outages are easily tolerated; and as is shown later in the chapter on signal-tracking theory, the added power of the other satellites in view can improve receiver performance.

III. Coverage Swath for an Equatorial Plane of Satellites

One of the methods for augmenting GPS is to add an equatorial plane of satellites at either GPS altitude of geostationary altitude. A plane of n equally spaced satellites with separation angle $2\phi = 360/n$ between subsatellite points generates a swath of continuous coverage, as shown in Fig. 9. If the coverage region half-angle for a single satellite for the desired minimum elevation angle

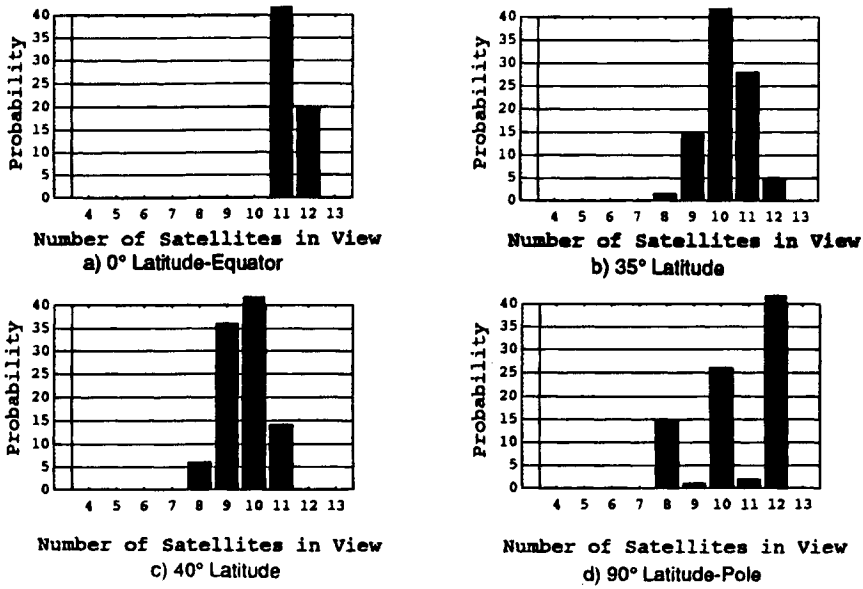

Fig. 8 Visibility statistics for 30 uniformly spaced satellites (30/6/1) constellation vs latitude for a 5-deg elevation mask angle. The user latitudes are as indicated.

E is β as measured from Earth's center, then the coverage swath angle λ in latitude is given by $\lambda = \cos^{-1}[\cos \beta/\cos \phi]$ for satellites in the equatorial plane. If the satellites are at GPS altitude and $\beta = 71$ deg for $E = 5$ deg, then the coverage swath latitudes are as shown in Table 3. Table 3 also gives the "swath for a geosynchronous orbit" at radius 42,162 km.

Thus, it is clear that 3, 4, or 5 satellites in the equatorial plane at GPS altitude produce a continuous coverage swaths of ± 49.3, ± 62.6, ± 66.3 deg, respectively, in latitude about the equator. The operational GPS satellite constellation already has a high degree of redundancy in satellite visibility at the higher latitudes

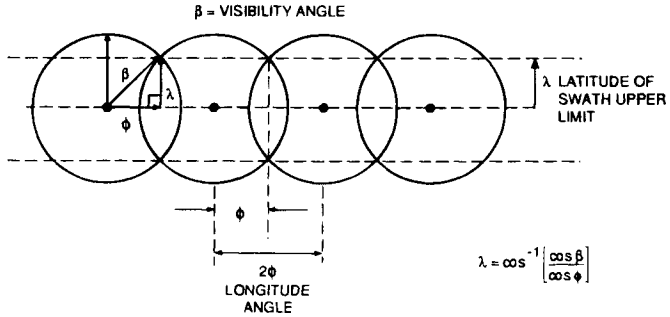

Fig. 9 Visibility coverage swath for n satellites in a single plane (equatorial) on a spherical Earth.

Table 3 Coverage swath width latitude λ for n = 3,4,5 satellites in an equatorial plane at GPS altitude and geosynchronous altitude (separation $2\phi = 360°/n$)

Number of satellites n	Separation 2ϕ	GPS		Geosynchronous	
		Coverage β	Swath λ	Coverage β	Swath λ
3	120 deg	71 deg	49.4 deg	77 deg	63.3 deg
4	90 deg	71 deg	62.6 deg	77 deg	71.5 deg
5	72 deg	71 deg	66.3 deg	77 deg	73.9 deg
6	60 deg	71 deg	67.9 deg	77 deg	74.9 deg

because the GPS orbits are inclined at 55 deg (see Fig. 6). Momentary periods of low satellite visibility that might occur in the event of a catastrophic satellite failure tend to occur at the midlatitudes, as shown earlier. Thus, it is clear that an equatorial ring of satellites at either GPS or geostationary altitudes with GPS-like payloads could provide an extra degree of redundancy for the GPS system. More specifically, the GPS-24 constellation has momentary periods of only four-satellite visibility for user elevation angle constraints at 10-deg elevation angle and user latitudes in the 30–60-deg region. These regions could be easily covered by three equatorial satellites at either geostationary or GPS altitudes to provide a minimum of five satellite visibility at 10-deg elevation angle or six-satellite visibility at 5-deg elevation angle. Even better would be an additional six satellites in either the (30/6/1) constellation at 55-deg inclination or a set of six equatorial satellites.

A. Satellite Ground Traces

From a user's standpoint, it is sometimes useful to show the ground trace that each of these satellites makes as its subsatellite point moves with time. The ground trace is the line generated on the Earth's surface by the line joining the satellite and the Earth's center as both the satellite moves in its orbit and the Earth rotates. Because the satellites have precisely a 12-h (sidereal time) orbit, each satellite traces out exactly the same track on the Earth's surface each sidereal day.* The Earth, of course, rotates once in inertial space each sidereal day underneath the satellite orbit. Thus the satellite produces a ground track (the locus of points directly below the satellite on the surface of the Earth), which exactly repeats every day. If we stand on a ground track of a satellite, we see the same satellite appear overhead at the zenith every day. In fact, a user at any fixed point sees exactly the same pattern of satellites every day. However, because the user's clock time is mean solar time rather than sidereal time of the satellite period, the user sees this satellite pattern appear approximately four minutes earlier each day (235.9 s).

Define a reference GPS satellite in a circular orbit at inclination i which crosses the equator at $t = 0$ at longitude θ_j. If another satellite of interest is in the same

*As pointed out earlier, the GPS satellite ground tracks are held to within ±2° in longitude by the GPS Control Segment at the time of the writing.

plane but offset in phase (the mean anomaly) by ϕ_i, then it can be shown that this satellite ground track has latitude that varies with time as follows:

$$\text{Lat} = \sin^{-1}[\sin i \sin(\omega t + \phi_i)] \tag{7a}$$

where the period of the orbit $T = 2\pi/\omega$.

The longitude likewise varies with time as follows:

$$\text{Long} = \phi_j - \Omega_e t + \tan^{-1}[\tan(\omega t + \phi_i)\cos I] \tag{7b}$$

where Ω_e is the Earth rotation rate.*

As a simple example, if there were four equally spaced satellites, and one of these crossed the equator at 0° longitude, the ground traces would appear as shown in Fig. 10. Notice that each satellite ground track repeats and makes two complete cycles as it moves from −180 to +180° in longitude, as we would expect from the 12-h period. It can be shown that a satellite in another plane, but offset in phase, can have exactly the same ground track. For example, if one satellite crosses the equator in a positive direction at $t = 0$, another satellite crossing the equator in a negative direction at the same time but 180° offset in longitude would have exactly the same ground track. In general, two satellites have the same ground track if $\Delta\phi = 2\Delta\theta(\text{mod } 2\pi)$. That is, the offset in satellite phase is equal to twice the offset in longitude of their planes modulo 2π. Thus, it is possible for satellites in different orbit planes in inertial space to have the same ground track if the phasing is selected accordingly.

Clearly, with the GPS-24 constellation the satellites do not all have the same ground tracks because the longitude of the ascending nodes (measured in the rotating Earth coordinates) are different (mod π or 180°). Thus, there are 24 separate ground tracks, one for each satellite. However, each of their ground traces have exactly the same shape as those shown here except for the position of the longitude of the ascending node.

IV. Geometric Dilution of Precision Performance Bounds and GPS-24 Performance

The previous section discussed satellite orbits and visibility, and previous and later chapters discuss the pseudorange measurement accuracy. However, it is really user position that is of greatest interest, and as described earlier, the general relationship between the errors in the pseudorange measurements by the user to the user position accuracy is described by the GDOP. The GDOP generally assumes that the measured pseudorange errors are independent with zero mean, and all *measurement errors* have the same rms value σ. (GDOP is also discussed in Chapter 11, this volume, wherein a different approach is taken but leads, of course, to the same result.) The following are the GDOP parameters:

$$\text{GDOP} = \frac{1}{\sigma}\sqrt{\sigma_x^2 + \sigma_y^2 + \sigma_z^2 + \sigma_b^2} \text{ for three dimensions plus time}$$

$$= \text{Geometric Dilution of Precision}$$

*For computational purposes, it is sometimes useful to approximate the $\tan^{-1}(\ )$ relationship for $I = 55$ deg of Eq. (6b) by $\text{Long}(t,\phi,\theta) \cong 2\pi t/12 + \phi - 0.271 \sin 2(2\pi t/12 + \phi) + 0.0367 \sin 4(2\pi t/12 + \phi) - 0.00663 \sin 6(2\pi t/12 + \phi) + 0.00135 \sin 8(2\pi t/12 + \phi) - 2\pi t/2y + \theta)$.

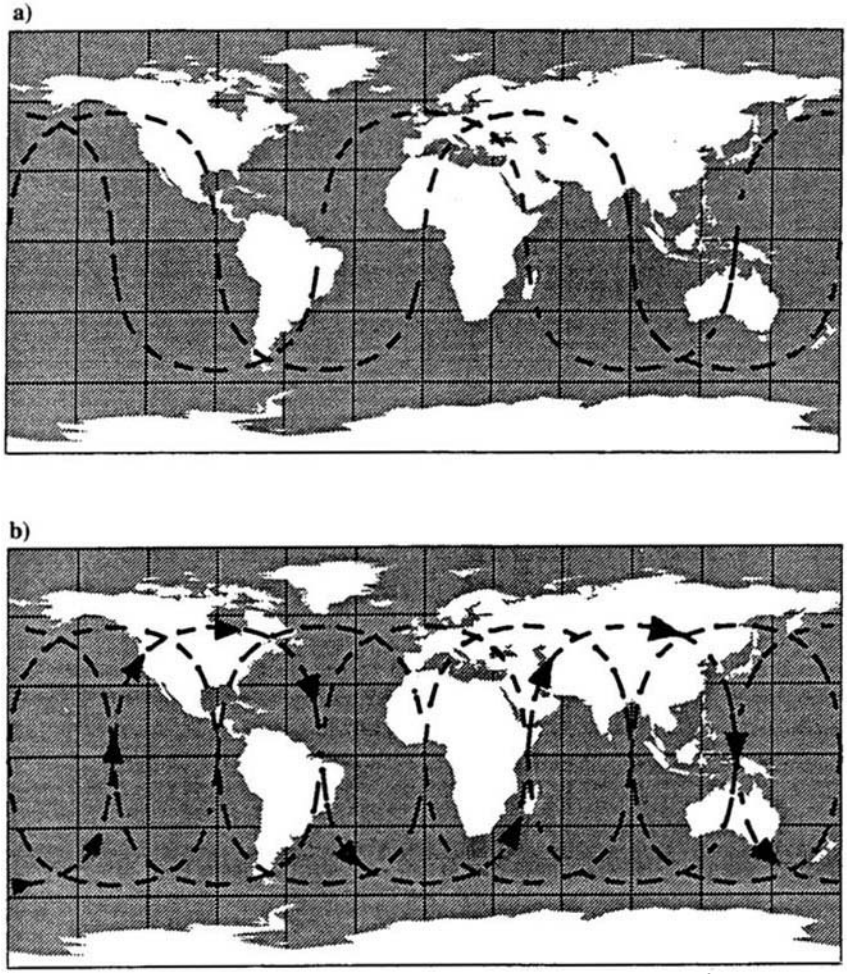

Fig. 10 Example of ground traces for four equally spaced satellites at 55-deg inclination in a single orbit plane at inclination 55 deg where one of the satellites crosses the equator at longitude 0°. Each satellite travels from west to east along its ground track: a) ground traces for two satellites, one of which crosses the equator at 0° longitude (longitude of ascending node is 0°), and the second is in the same orbit plane but spaced by 90 deg; b) ground traces for all four equally spaced satellites. Each satellite follows the ground trace moving from west to east. Note that the GPS satellites are not equally spaced in the GPS-24 constellation.

Chapter 6

GPS Satellite and Payload

M. Aparicio, P. Brodie, L. Doyle, J. Rajan, and P. Torrione*
ITT, Nutley, New Jersey 07110

I. Spacecraft and Navigation Payload Heritage

A. Concept

THE launch of Sputnik I by the USSR in October 1957 was the beginning of the age of navigational satellites. That event was the culmination of centuries of navigation based on the known position of natural heavenly bodies and ever-improving clock accuracy. Observations of the signals transmitted by Sputnik I established the idea that accurate timing signals coming from artificial satellites of known position could aid navigators substantially. In effect, the artificial satellite replaced the functions of the sun and star tables with the known ephemeris of the satellite. In addition, the satellite's accurate timing signals replaced the ship's chronometer. The satellite-based system could provide continuous, worldwide coverage with few satellites; it could be an all-weather system, and it could provide extraordinary position location accuracy.

B. Relation to Earlier Non-GPS Satellites

The challenge of Sputnik I led to the U.S. satellite system Transit I. Begun in December 1958, its goal was continuous, worldwide, all-weather coverage. Transit was placed in operation January 1964. During the late 1960s, the growing need for accurate navigation among the U.S. strategic and tactical forces, combined with the rapid reduction in the cost of computers and processors (user equipment) established the need for, and potential feasibility of, a highly accurate tri-service navigational satellite system. The Air Force and Navy began independent programs called, respectively, 621B and TIMATION. NAVSTAR/GPS is the program that combined features of 621B and TIMATION. The Air Force's signal structure and frequencies were used, while the Navy's orbital configuration was chosen.

C. Overview of Payload Evolution

Two prime contractors under the management of the U.S. Air Force have taken the responsibility of taking the GPS satellite from concept into practice. Rockwell

*Aerospace/Communications Division.

International was the developer of the initial or Block I spacecraft and the Production Block II and IIA spacecraft, and Martin Marietta is the current developer of the GPS Block IIR (replenishment) spacecraft. ITT Corporation developed the critical navigational payload elements on all these satellites. The pseudorandom noise signal assembly (PRNSA), which constitutes the navigation payload on the original eight GPS development spacecraft consists of the following components: baseband processor; L_1/L_2 synthesizer; L_1 modulator; L_2 modulator; L_1 high-power amplifier; L_2 high-power amplifier; and diplexer. It also included delivery of GPS peculiar support equipment (GPSE) for ground station and prelaunch testing. Four more PRNSAs were subsequently added for a total of 12 GPS Block I deliveries.

The development Block I program resulted in 10 GPS spacecraft that were successfully launched from 1978 through 1985. One Block I spacecraft was destroyed because of launch failure. The 12th Block I was a qualification unit that was not flown. The Block II production spacecraft launches began in 1989. The Block II changes to the basic navigation service of the Block I spacecraft consisted of a gradually degrading navigation service for a period of 14 days, if the Control Segment (GPS CS) became inoperable. Block IIA spacecraft added an autonomous momentum management capability that functioned for a period of 180 days without ground contact.

The navigation message uploads to the Block II/IIA spacecraft are performed on a daily basis by the GPS CS. Block IIR satellites incorporate a ranging capability in the satellite crosslink. This ranging capability, combined with an onboard Kalman filter, gives the Block IIR autonomous navigation Autonov capability. Using the crosslink range measurements, the Block IIR spacecraft estimates the error in the Kepler orbital parameters. This enables the Block IIR satellites to support full navigation accuracy of 16-m spherical error probable (SEP), without CS contact for periods of up to 180 days. The comparable error of a Block IIA at the end of 180 days is of the order of kilometers.

D. On-Orbit Performance History

Figure 1 summarizes the historical development of the GPS space segment. Block IIR spacecraft are presently in development and will replace the Block I, II, and IIA satellites as they are declared nonfunctional. There are two basic ways in which satellites become nonfunctional. The first is unplanned and involves an on-orbit failure causing loss of the spacecraft, "caused by," "and" failure of two or more redundant components. The second is depletion of such life-limiting items as thruster fuel and degradaton of the solar arrays or batteries.

The GPS achieved a major milestone in December 1993 when it established initial operational capability or IOC. At IOC, the Air Force Space Command achieved operation of a full constellation of 24 GPS satellites. Shortly thereafter in February 1994, the Federal Aviation Agency (FAA) declared GPS operational for aviation use.

Figure 2 summarizes the launch and on-orbit performance history of the Block's I, II, and IIA space vehicles (SV). The last Block IIA SV is expected to be launched in the first quarter of 1996. Block IIR satellites will begin launches in

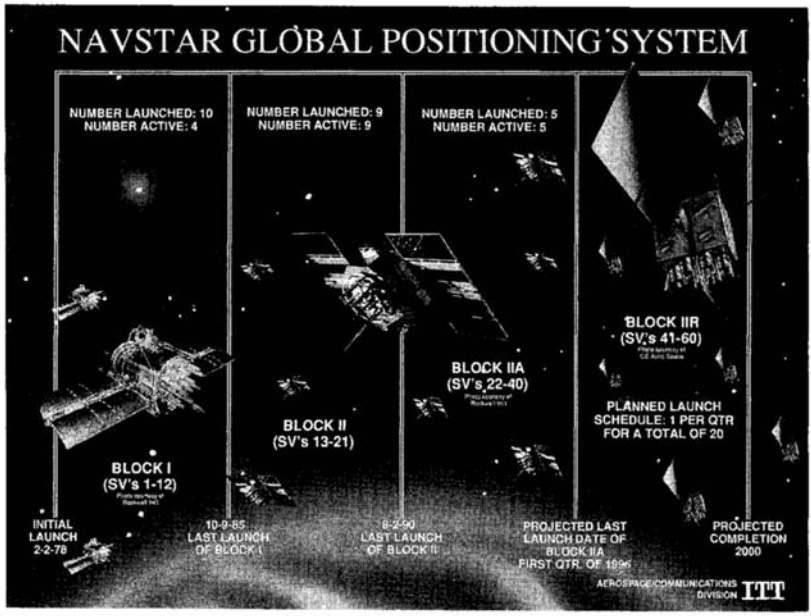

Fig. 1 Historical development of the space segment.

1996. The Air Force plans to begin the Block IIF (Follow-on) program in 1995 with expected launches beginning in 2001.

II. Navigation Payload Requirements

A. GPS System

GPS is a highly accurate, passive, all-weather, 24-h, worldwide, common-grid navigation system. The navigation payload must supply a continuous, precision, high-integrity signal to support this requirement.

The GPS has also enabled specialized users to enhance system accuracy, availability, and integrity with augmentation and sensor integration. The augmentations include differential stations providing differential corrections to GPS measurements; the GPS integrity channel (GIC) providing faster integrity information via geostationary satellites and pseudolites, enabling faster cycle ambiguity resolution and precise localized navigation. The sensor integrations include GPS integrations with inertial navigation systems (INS) and low-cost multisensors to provide accurate navigation comparable to INS at much lower cost. These combined systems provide superior short-term accuracy of GPS and control the error growth during GPS signal outage (caused by masking and aircraft maneuver) by utilizing the long-term stability of an INS.

B. GPS Performance

The GPS is designed to provide a precision positioning service with a 16-m SEP. This performance is achievable by a dual-frequency precision code user

Data is current as of 06-Sep-94

SV/ PRN No.	GPS Block	Launch Date	On-Orbit Available Date	Nav Load Date	Deactivation Date	Total Months Available	Mission Life Rqmt (Months)	Exceeded Life by (Months)	Failure Mechanism
1/4	I	22-Feb-78	29-Mar-78	25-Jan-80	17-Jul-85	22	48	-26	Clock
2/7	I	13-May-78	14-Jul-78	30-Jul-80	16-Jul-81	24	48	-24	Clock
3/6	I	06-Oct-78	09-Nov-78	19-Apr-92	25-Apr-92	161	48	113	Clock
4/8	I	11-Dec-78	08-Jan-79	27-Oct-86	14-Oct-89	93	48	45	Clock
5/5	I	09-Feb-80	27-Feb-80	28-Nov-83	28-Nov-83	45	48	-3	Wheel
6/9	I	26-Apr-80	16-May-80	10-Dec-90	06-Mar-91	127	48	79	Wheel
7/	I	*18-Dec-81 - Satellite destroyed during launch (booster failure)*							
8/11	I	14-Jul-83	10-Aug-83	04-May-93	04-May-93	117	48	69	EPS Degr.
9/13	I	13-Jun-84	19-Jul-84	28-Feb-94	28-Feb-94	115	48	67	Clock
10/12	I	08-Sep-84	03-Oct-84			119	48	71	
11/3	I	09-Oct-85	30-Oct-85	27-Feb-94	27-Feb-94	100	48	52	Not ID'd
12/	II	*Qual Unit - will not be launched*							
13/2	II	10-Jun-89	11-Jul-89			62	60	2	
14/14	II	14-Feb-89	15-Apr-89			65	60	5	
15/15	II	01-Oct-90	15-Oct-90			47	60		
16/16	II	18-Aug-89	14-Oct-89			59	60		
17/17	II	11-Dec-89	06-Jan-90			56	60		
18/18	II	24-Jan-90	16-Feb-90			55	60		
19/19	II	21-Oct-89	26-Nov-89			58	60		
20/20	II	24-Mar-90	18-Apr-90			53	60		
21/21	II	02-Aug-90	22-Aug-90			49	60		
22/22	IIA	03-Feb-93	30-Mar-93			18	60		
23/23	IIA	26-Nov-90	10-Dec-90			45	60		
24/24	IIA	04-Jul-91	30-Aug-91			37	60		
25/25	IIA	23-Feb-92	24-Mar-92			30	60		
26/26	IIA	07-Jul-92	23-Jul-92			26	60		
27/27	IIA	09-Sep-92	30-Sep-92			24	60		
28/28	IIA	10-Apr-92	25-Apr-92			29	60		
29/29	IIA	18-Dec-92	05-Jan-93			20	60		
30	IIA	FY 96					60		
31/31	IIA	04-Apr-93	13-Apr-93			17	60		
32/1	IIA	22-Nov-92	11-Dec-92			21	60		
33	IIA	FY 95					60		
34/4	IIA	26-Oct-93	29-Nov-93			10	60		
35/5	IIA	30-Aug-93	28-Sep-93			12	60		
36/6	IIA	10-Mar-94	28-Mar-94			6	60		
37/7	IIA	13-May-93	12-Jun-93			15	60		
38	IIA	FY 96					60		
39/9	IIA	26-Jun-93	20-Jul-93			14	60		
40	IIA	FY 97					60		

Total On-Orbit Availability (to Date): 1,751 months
145.9 years

On-Orbit Mission Life above Program Rqmts (to Date): 37.5 years

Fig. 2 The GPS satellite on-orbit performance history.

under dynamic environment. The current policy is to encrypt the precision code so that it is available only to authorized users. The user ranging error (URE) is derived from the Block II requirement that the system meet a navigational accuracy of 16-m SEP. The derived user ranging error (URE) is 6.6 m (one sigma). The URE budget is shown in Table 1. The velocity accuracy achievable by the system in a dynamic environment is 0.1 m/s. The time transfer accuracy that can be achieved by the system is at least 100 ns. The system also provides a standard positioning service (SPS) of 100-m 2d rms for unauthorized users. The C/A code by itself can provide an accuracy of about 25-m SEP. However, the accuracy is degraded to a 100-m level by man-made degradation of the navigation signal and parameters.

The total root-sum-square errors (rss) allowed for the space segment is approximately 3.5 m (one sigma). An rss is taken, because these errors are uncorrelated

Table 1 System error budget (Block II)

Error sources	User range error (1σ), m
Space segment	
Clock and navigation subsystem stability	3.0
L-Band phase uncertainty	1.5
Predictability of SV parameters	1.0
Other	0.5
Control segment	
Ephemeris prediction and model implementation	4.2
Other	0.9
User segment	
Ionospheric delay compensation	2.3
Tropospheric delay compensation	2.0
Receiver noise and resolution	1.5
Multipath	1.2
Other	0.5
Total (root-sum-square) rss URE	6.6

or statistically independent. Achieved performance for the satellite is 2.2 m (one-sigma) using the rubidium atomic frequency standard (AFS), and 2.9 m (one-sigma) for the cesium AFS. Both performance measures are taken 24 h after the last update from the ground. For normal operations, the ground updates the satellite every 24 h.

C. GPS Signal Structure

The GPS satellites provide precise ranging signals at two frequencies, L_1 and L_2. The satellite transmits precise ranging information using precision (P) code and transmits coarse range using the coarse/acquisition (C/A) code. The C/A code is a Gold code of register size 10, which has a sequence length of 1023. The clock rate of the C/A code is 1.023 MHz, and the code period is 1 ms. The P code is clocked at 10.23 MHz. Each satellite uses a different member of the C/A Gold code family. The P code is over 37 weeks long but is short-cycled on a weekly basis. Different satellites use a different 1-week segment of the P code. The short length of the C/A code allows user equipment that has a low-cost clock with time uncertainty of the order of seconds to search the entire code phase of the C/A code quickly and acquire and track the C/A signal. Tracking the C/A code enables the receiver to demodulate the navigation data. The navigation message is a 50 b/s datastream arranged in 25 pages, each page containing 5 subframes, with each subframe containing 10 words of 30 bits each. The navigation datawords are encoded with (32, 24) Hamming parity providing single error correction and double error detection capabilities. The navigation data on the C/A code has, in addition to the ephemeris and satellite clock correction and double error detection information, the hand-over information that enables the receiver to acquire and track the P code. Specialized receivers with direct time transfer capability can directly search, acquire, and track the P code.

Dual-frequency transmission of ranging signals by the GPS satellite enables user equipment with dual-frequency capability to measure ranges at the L_1 and

L_2 frequencies. These measurements allow the user equipment to accurately compensate for the propagation delay through the ionosphere.

The signal levels guaranteed to the users near the surface of Earth are shown in Table 6-2 for various signal components. The C/A-code power level is 3 dB higher than that of P code to enable fast initial acquisition of the C/A code. The L_2 power is considerable lower, because it typically is not used for initial acquisition. The receivers in general search, acquire, and track the L_1 C/A signal. Based on range measurements made while tracking L_1 C/A, a limited and somewhat slower search is made on the L_2 signal to enable L_2 acquisition and subsequent tracking.

D. Payload Requirements

The link budget covers the three segments of the system and satisfies the power density levels guaranteed to the users. The obvious trade-off in the link budget is the antenna gain vs payload transmit power. This trade-off is made by evaluating the cost, size, power, and weight.

Key requirements are derived from the receive bands of the receivers onboard the satellites and from such specialized frequency bands as a radio astronomy band. An additional requirement minimizes the phase noise of the space-borne *L*-band transmitters.

Other key performance parameters include: group delay variation on the *L*-band transmitter chain, which has an impact on the payload URE; the uncertainty in the differential group delay between L_1 and L_2, which has an impact on the accuracy to which the ionospheric corrections can be made; and gain flatness, which influences the symmetry of the code autocorrelation function at the receiver.

As in most complex systems, high reliability is an important factor in the GPS payload design. High reliability provides an assurance that the system is providing an accurate signal to meet the user's navigational needs.

The design of the spacecraft incorporates subassembly and component redundancy; environmental controls; the use of flight-proven, high-reliability piece parts (e.g., transistors, integrated circuits, relays); and proven manufacturing and test procedures and practices. Particular design and test emphasis is placed on ensuring that a failure within a component will neither degrade the performance of the components within the spacecraft nor propagate throughout the system.

Single point failures have been absolutely minimized. Detailed reliability analyses have been performed on all spacecraft elements to determine the effectiveness of design trade-offs. Failure modes, effects, and criticality analyses (FMECA)

Table 2 *L*-band rf power

	L_1		L_2
	I	*Q*	*I*
	C/A	P(Y)	P(Y)/C/A
Output power at the antenna input, dbw	+14.3	+11.3	+8.1
Power near the Earth's surface	−160.0	−163.0	−166.0

have been performed on all elements of the SV. The analyses are performed concurrently with the design efforts, thus producing designs that reflect the analyses conclusions and recommendations. The GPS spacecraft is required to meet a 7.5-year life and is designed for a 10-year life.

III. Block IIR Space Vehicle Configuration

As noted earlier, the Block IIR spacecraft will replace the Block II and IIA spacecraft as they become nonoperational. The contract to develop the Block IIR system was awarded to Martin Marietta (then General Electric Astro Space) and to ITT Aerospace/Communications Division (then ITT Defense Communications Division) in 1987. The team consists of more than 20 subcontractors nationwide. The launch of the first Block IIR spacecraft is planned for the last quarter of 1996. An exploded view of the Block IIR SV is shown in Fig. 3.

The GPS navigation signal is generated and transmitted by the total navigation payload (TNP). The AFS is the heart of the TNP. It provides the precision timing needed to achieve GPS accuracy. The TNP includes two rubidium atomic frequency standards and a cesium atomic frequency standard.

The L-band system consists of the three transmitter chains for three radio frequencies denoted as L_1, L_2, and L_3. The L_1 and L_2 frequencies are used for the navigation mission of the GPS, and the L_3 frequency is used by the nuclear detonation detection system (NDS or Nudet), also located onboard the GPS SV.

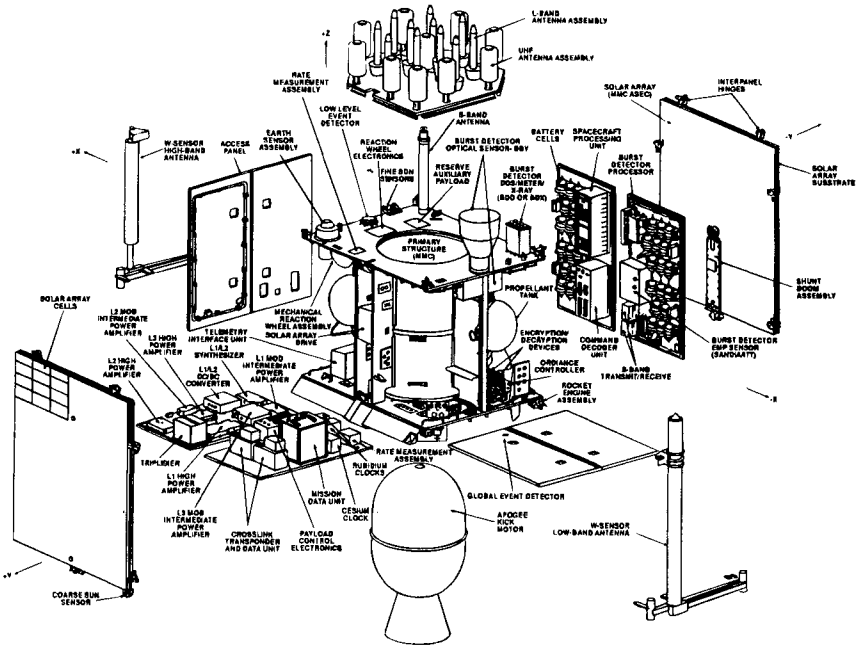

Fig. 3 The GPS Block IIR space vehicle.

Within the TNP, are two major functional capabilities that provide the Block IIR with a giant leap in mission capabilities as compared to Block II/IIA. These are referred to as the time-keeping system (TKS) and the autonomous navigation (AutoNav) capability.

The subsystems of TNP, TKS, and the AutoNav capabilities are explored in detail in the following sections.

The central body of the Block IIR SV is a cube of approximately 6 ft on each side. The span of the solar panel is about 30 ft. The lift-off weight of the spacecraft is 4480 lb and the on-orbit weight is about 2370 lb. The Block IIR spacecraft will be launched by the Delta launch vehicle. The spacecraft has 16 thrusters and a standard set of bus equipment such as telemetry, tracking, and command (TT&C), payload control electronics (PCE), a spacecraft processing unit (SPU), and an attitude reference system. The Block IIR spacecraft are designed to meet 10-year mission life and 4-year storage life. They are designed to be ready to launch with 60-days notice. The SV is designed to operate autonomously for at least 180 days without ground intervention; whereas, the Block I and II satellites' accuracy degrades without ground contact.

A. Navigation Payload Architecture

The TNP components are shown mounted on the two payload panels of the spacecraft shown on the lower left of Figure 6-3. This assembly consists of all the components needed to generate the signals that provide the navigational capability of the GPS. The antennas that radiate the signals to Earth are shown on the top face in the figure. This face is always accurately pointed toward the Earth to ensure uniform and stable illumination of the Earth by the navigational signals. Placing the TNP on two adjacent and stand-alone panels allows easy integration and testing of the spacecraft.

The mission data unit (MDU), atomic frequency assembly, and *L*-band subsystem produce the navigational signals. The crosslink transponder and data unit (CTDU) provides direct satellite-to-satellite communication and ranging. This allows the satellites to operate autonomously (i.e., without ground control segment time and ephemeris updates) at full accuracy for at least 180 days.

The MDU is the brains of the TNP. It integrates all mission functions, such as ephemeris calculations, encryption, NDS data, pseudorandom code generation, and autoNav, as well as monitoring the health of specific TNP components. The MDU software consists of approximately 25,000 lines of code written in Ada running on a MIL-STD 1750A radiation-hard processor at 16 MHz. A block diagram of the TNP is shown in Fig. 4.

IV. Block IIR Payload Design

A. Payload Subsystems

The *L*-band subsystem also includes bi- and quadriphase shift keyed modulators, (BPSK and QPSK) which place the MDU information with the pseudorandom C/A and P codes (1.023 Mbs and 10.23 Mbs, respectively) on the three *L*-band carriers. These three carriers are at 1227.60 MHz (L_2), 1381.05 MHz (L_3), and 1575.42 MHz (L_1). The three carriers are amplified by bipolar transistor

MISSION DATA UNIT

- 1750A Central Processor
- ADA HOL Used Throughout
- Clock Frequency Synthesis from Multiple Standards
- Integral Baseband Processor
- Full Message Encoding and Message Processing
- Real Time Kalman Filter Navigation and Clock State Estimation

CROSSLINK TRANSPONDER DATA LINK

- RF Receive Transmit of Digital Data
- Precision Inter Satellite Ranging
- Frequency Hopped TDMA
- Full Frame Modulation and Mode Control

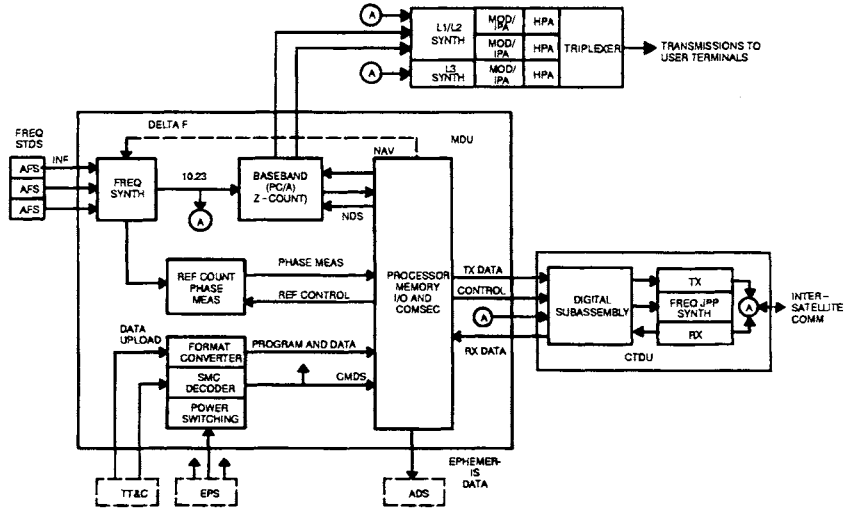

TIME STANDARD ASSEMBLY

- Multiple Atomic Frequency Standards for Reliability
- Accommodates Various Clock Types (Cs, Rb)
- RAD-Hard Upset Proof Design
- Synthesized High Stability GPS Timing Signals
- Automated Integrity Monitoring

L-BAND SUBSYSTEM

- 25–50 Watt Transmitter
- Bandwidth 20 MHz
- Radiation Hardened
- L_1 : 1 or 10 MChip/s Quadraphase L_2, L_3 : 1 or 10 MChip/s Biphase
- Space Proven Design Operational on Block I and Block II

Fig. 4 Complete system from atomic reference clocks through transmitted navigation messages to users.

amplifiers using microwave integrated circuits technology and sent to the triplexer, which combines them and delivers them to the spacecraft antennas for radiating to users on the Earth. The L_3 signal is filtered through an L_3 astronomy filter.

A principal element of the spacecraft is the atomic frequency standard or atomic clocks. The key requirement is to maintain an accuracy of 6 ns with respect to GPS time. To do this, cesium and rubidium atomic frequency standards are integrated into the TKS of the navigation payload. To ensure operation if one of these critical components fails, two rubidium standards and one cesium standard provide redundancy for the time standard assembly (TSA). The Block

IIR TNP unit is shown in Fig. 5 undergoing prequalification tests at the ITT A/CD facility in Clifton, New Jersey.

The following sections discuss the key design issues associated with each element. Table 3 summarizes the functions of each payload element. Each of these is described in detail in the following sections.

1. Atomic Frequency Standards

a. Introduction. Placing a very stable time reference in a position where maximum user access can be achieved is the basis for modern satellite navigation. At the speed of propagation of electromagnetic signals in the atmosphere, 1 ns of phase uncertainty of the signal, as measured at the user, is roughly equivalent to 1 ft or 1/3 m in position uncertainty. The only instruments that can maintain the phase uncertainty within the required limits for GPS; i.e., 9 ns, one sigma for 24, are atomic frequency standards. This phase stability is equivalent to an uncertainty of 1 mm out of the distance from the Sun to the Earth.

Atomic frequency standards* are amazingly accurate and stable devices. The history of frequency standards and clocks spans the spectrum from sand and water clocks to the modern chronometer and present day AFS. The fundamental problem of clock use has remained the same: "How do we measure the time

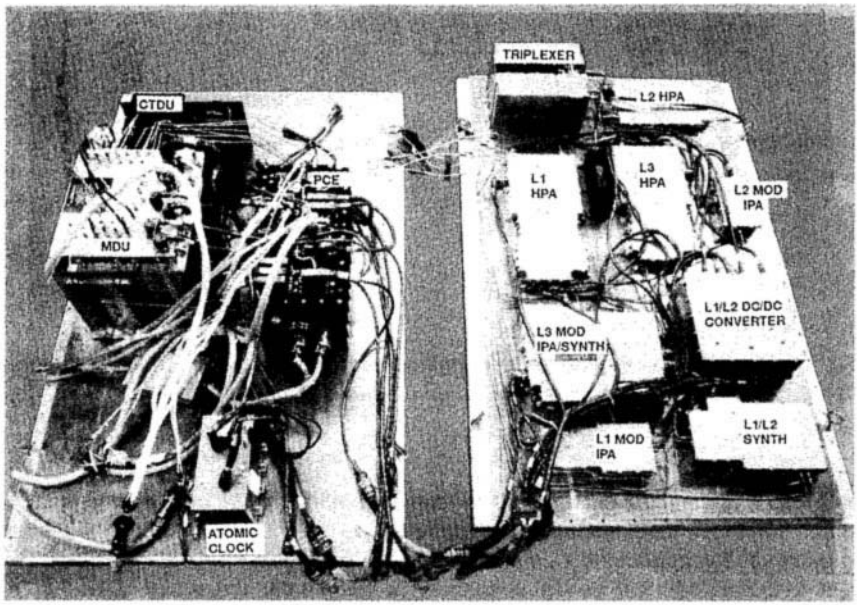

Fig. 5 The GPS Block IIR total navigation payload under test.

*The primary difference between clocks and frequency standards is that clocks keep a record of how many repetitions of a periodic phenomenon have occurred since an event; whereas, frequency standards provide only the periodic phenomenon to the external world.

Table 3 GPS Block IIR payload element functionality

Element	Function
Atomic frequency standards	Provide accurate, stable and reliable timing for all GPS signals. (This is the most important function, because accurate navigation depends primarily upon accurate time.)
Onboard processing	Generate navigational messages, perform ephemeris calculations, and data encryption, generate P and C/A code, monitor health of payload, provide clock error corrections
Software	Implement onboard processing functions. Reprogrammable from ground stations
L-band system	Generate and modulate the L_1, L_2, and L_3 signals and combine them for transmission to Earth
Crosslinks	Provide satellite-to-satellite communications and ranging
Auto navigation	Provide accurate autonomous operation without regular communications from Earth

interval between two events?" The answer has also remained the same; "Count periods of a stable phenomenon." The technological history of clocks and frequency standards is a search for more accurate and stable phenomena and implementation of the measuring device, ranging from the rising and setting of the sun, through mechanical pendulums, to transitions of electrons between energy bands.

The principle of operation of atomic frequency standards[12,14,15] in its most fundamental form is: "The coupling of the output frequency to a periodic natural phenomenon whose period (time to complete a cycle) is essentially invariant." The natural phenomenon used is the change in energy of the outermost electron of an atom of a given element or compound. When this change in energy occurs, the atoms release or absorb the energy at a precisely determined frequency, hence the term atomic frequency standard.

There are different types of AFS, classified by the element or compounds they use for the electron energy transition and the way they couple this information to external devices. Among the most successful AFS types are: hydrogen masers; ammonia frequency standard; cesium frequency standard; rubidium frequency standard and maser; beryllium frequency standard; and mercury electromagnetic ion trap frequency standard.

All AFS types have three common functions: 1) preparation of the outermost electron population into a known state; 2) injection of an electromagnetic signal that causes the energy transition, (higher precision of the frequency of the injected signal causes more atoms to transition); and 3) interrogation and sorting of the resulting energy state of the resulting outermost electron atomic or molecular population. The last step generates an error signal that is used to tune a voltage control oscillator (VCXO) to that natural frequency. The VCXO provides the clock signal with the correct output frequency. Specific examples of this process are the rubidium and cesium AFS. These two types of AFS are of significant importance and are the only types in use in the GPS space segment. The diagrams

shown (Fig. 6 and 7) are of the resonator sections of the cesium and rubidium AFS. They are those elements of the AFS that perform the three operations described above.

b. Operation of the cesium AFS. For the GPS cesium AFS, cesium atoms are emitted from a heated cesium reservoir (Fig. 6). Then the three operations are performed. The first is the preparation or sorting of the energy states of the electron in the atomic or molecular population of the cesium atoms. This is accomplished using a magnetic field tuned to the natural frequency of the magnetic dipole of the atoms that contain the electrons in the ground state. This field is produced by a magnet known as the "A" magnet that deflects atoms into the cavity only if they contain electrons in the ground state. This operation creates a relatively pure population of atoms that have their outermost electrons in the ground state.

The second operation is the electromagnetic stimulation of the outermost electron of the cesium atoms. The electrons are shifted from the ground energy state to the next energy state or hyperfine state. This stimulation takes place, if and only if, the electromagnetic field is oscillating extremely close to the specific frequency. That frequency is 9, 192, 631, 770 Hz. If the electromagnetic stimulus is not very close to the oscillating frequency, few transitions to the hyperfine energy state take place, and most electrons remain in the ground energy state. If the electromagnetic stimulus is at the right frequency, many electrons will make the hyperfine transition. This transition changes the properties of the atoms that contain the electrons. In particular, this transition changes the magnetic dipole of the host atoms and allows sorting of the atoms.

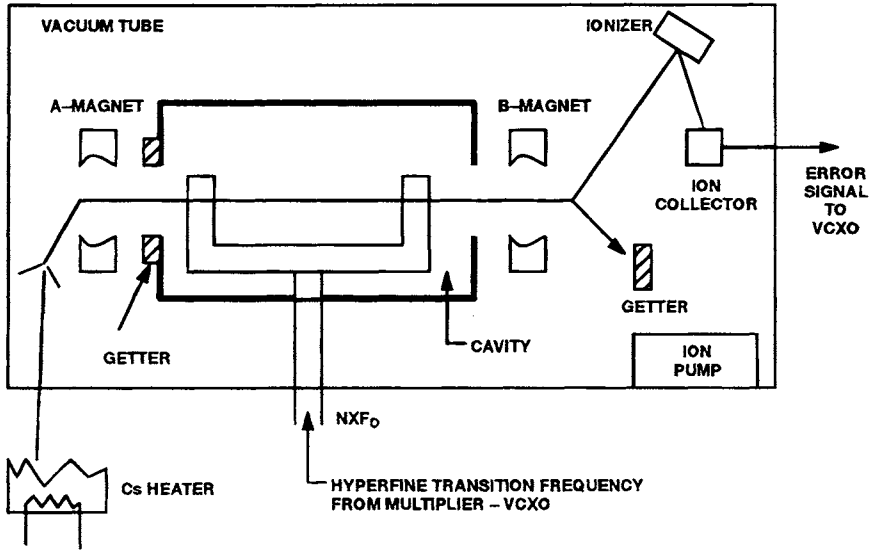

Fig. 6 Cesium beam frequency standard resonator.

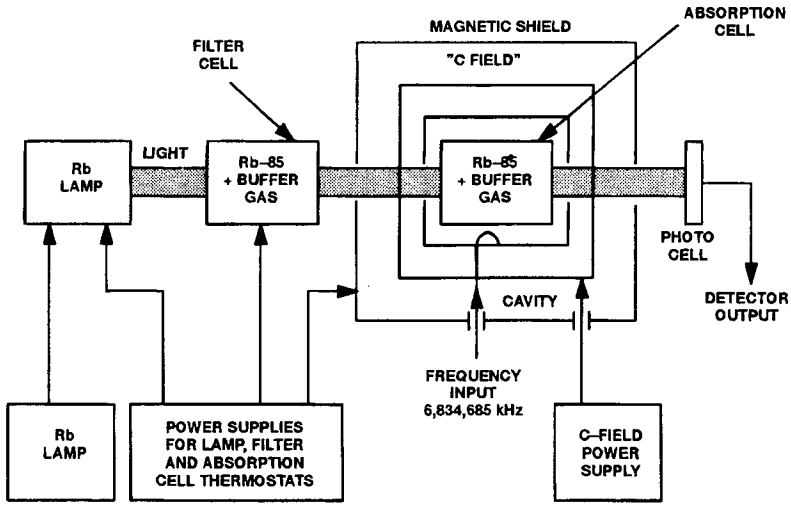

Fig. 7 Rubidium atomic resonator.

The third operation, which is the interrogation and sorting of the atomic population, is performed with the magnet placed at the other end of the cavity. This magnet, the "B" magnet, is tuned so that it deflects atoms that contain electrons in the hyperfine energy state. If the atoms coming out of the cavity contain electrons in the hyperfine energy state, those are then deflected. This means that the electromagnetic stimulus is precisely on frequency if it is successfully causing many energy transitions. The deflected atoms are sent in a path that causes them to strike an ionizer rod. The ionizer rod very efficiently converts the neutral atoms into ions. The ions continue their trajectory into an electron multiplier that turns the ion flow into a current flow proportional to the number of atoms that have been deflected. The current is an indication of the frequency of the electromagnetic stimulus that was injected in the cavity. From the electron multiplier detector output, an error signal is derived, which corrects the VCXO in a control loop. The VCXO oscillation frequency is the actual clock output frequency of the device.

c. Operation of the rubidium AFS. For the rubidium AFS, three similar operations are performed (see Fig. 7). Initially, electrons are in the ground energy state. There will always be a fraction of the total population of atoms that naturally contain outermost electrons in the ground state. In a working standard, this is normally 0.1% of the total population.

The outermost electrons are then excited to the hyperfine energy state. This excitation is carried out by injecting an electromagnetic signal into the cavity that contains the rubidium vapor (the so-called absorption cell). If this stimulus is oscillating at precisely the right frequency 6, 834, 682, 608 Hz (for a zero magnetic field), many electrons in the ground energy state in the atomic population change into the hyperfine energy state. This transition in energy state changes the optical absorption properties of the host atoms.

The third operation is interrogation of the atomic population for energy changes. This optical interrogation process begins at the lamp. The lamp is a discharge device filled with the rubidium isotope 87 and excited by an rf source at about 100 MHz. The lamp emits a spectrum of electromagnetic frequencies, the majority in the visible range. The electromagnetic emissions are passed through a filter cell filled with the rubidium isotope 85. The filter cell stops all but two visible frequencies from reaching the absorption cell. Atoms containing the outermost electrons that have made the hyperfine energy state transition from the ground state will absorb the light. The absorption of the light by the host atoms creates a minimum current output at the optical detector located at the other end of the absorption cell. The minimum occurs only if the electrons in the population of host atoms make the hyperfine energy transition. The optical detector or photodetector generates a current proportional to the amount of light that reaches it. The current is used to shift the VCXO oscillation frequency to the desired clock output frequency.

d. Performance. The most important requirements for operating an AFS in a space-borne platform for a navigational application are: phase stability; reliability; low power; low weight; low volume; and high tolerance to the space environment. To meet these requirements, special space-qualified units are used in the GPS satellites. The most difficult requirements to meet are phase stability and reliability. Although the AFS units used by the National Bureau of Standards exhibit excellent performance, they are too large and heavy for spacecraft applicaton. The reliability of AFS has traditionally been low because of the nature of their high sensitivity to the environment and their complexity. Balancing these unique requirements and constraints to produce units accurate and reliable enough for space poses unique technological challenges.

Phase stability is measured in terms of the time-averaged integral of the fractional frequency stability ($\sigma_y(\tau)$). The fractional frequency stability is measured by the Allan variance $\sigma^2_y(\tau)$, which is the square of the Allan deviation $\sigma_y(\tau)$. The Allan variance is defined by the following equation:

$$\sigma_y^2(\tau) = \frac{1}{2N-1} \sum_{i=0}^{N-1} (Y_{i+1} - Y_i)^2$$

where Y_i = fractional frequency at time interval i (actual frequency/nominal desired frequency, and N = number of fractional frequency samples.

The Allan deviation is a measure or statistical estimate of the noise contribution to the frequency instability of frequency standards. The noise processes that have experimentally been found to have significant effects in precision frequency standards are: white phase modulation noise (PM); white frequency modulation noise; flicker phase modulation noise; flicker frequency modulation noise; and random walk of phase noise.

Table 4 is a comparison of some of the critical parameters for the GPS Blocks I, II, IIA, and IIR.[15] As mentioned previously, reliability, power, weight, volume, and tolerance to the space environment are the critical parameters for AFS in the GPS context.

Table 4 GPS Blocks I, II, IIA, and IIR atomic frequency standards specifications

AFS type	Reliability requirement	Size, in.	Weight, lb	Power consumption, W
Rb GPS Block I	0.763 for 5.5 years	L = 5.00 W = 6.00 H = 7.50	13	24.75
Cs GPS Block I[a]	0.663 for 5.5 years	L = 5.30 W = 15.10 H = 7.80	28	22.00
Rb GPS Block II	0.763 for 5.5 years	L = 5.00 W = 6.00 H = 7.50	13	24.75
Cs GPS Block II	0.663 for 5.5 years	L = 5.30 W = 15.10 H = 7.80	28	22.00
Rb GPS Block IIA	0.763 for 5.5 years	L = 5.00 W = 6.00 H = 7.50	13	24.75
CS GPS Block IIA	0.663 for 5.5 years	L = 5.30 W = 15.10 H = 7.80	28	22.00
CS GPS Block IIA second source	0.750 for 5.5 years	L = 5.30 W = 15.10 H = 7.80	28	22.00
Rb GPS Block IIR	0.763 for 7.5 years	L = 8.50 W = 5.60 H = 6.20	14	15
Cs GPS Block IIR	0.775 for 7.5 years	L = 16.50 W = 5.50 H = 5.25	22	26

[a]Only the last four satellites of Block I carry cesium atomic frequency standards.

Table 4 shows that the greatest improvements from Block I, II, and IIA to IIR are the reliability, weight, and power consumption of the rubidium standards. Of these parameters, the most relevant change is the power consumption from 24.75 W to 15 W. Predicted reliability has been increased significantly for both standards. The reliability parameter is of extreme importance in the space mission environment, where the life of components and subsystems limit the mission's life.

B. Mission Data Unit

1. Onboard Processing

Onboard processing is performed in the MDU. The MDU and the frequency synthesizer unit (FSU) are housed together in one physical package. The MDU provides storage of navigation data as uploaded by the CS via the TT&C subsystem of the SV. The MDU combines these data with internally generated ranging codes and sends the resulting navigation message to the *L*-band system (LBS) for transmission to the ground. The MDU also is capable of altering these

navigation signals when necessary to deny full GPS navigation accuracy to unauthorized users [i.e., it provides selective availability (SA)]. The FSU plays a role in both the generation of the navigation signals and selective availability, and it is controlled by the MDU processor. The MDU has the capability of autonomously operating for 180 days without receiving navigation data updates from the CS. When the MDU operates in this mode, it computes the SV ephemeris and clock correction data by processing rf ranging performed between spacecraft. The MDU then updates the contents of the navigation message sent to the users.

In addition to the function of providing navigation data to GPS users, the MDU receives data from the NDS. These data are encoded by the MDU and transferred to the ground with navigation data via the LBS. The data are also transmitted via the uhf crosslink to other in-view satellites for retransmission to the ground via the *L*-band. The MDU/FSU operates in the space radiation environment and can operate through or recover from specified transient nuclear events without a permanent impact on navigation functional accuracy or the NDS data-processing function.

The following is a summary of MDU/FSU functions:

1) provide storage of messages uploaded by the CS;
2) process, format, and generate navigation data;
3) provide precise timing for other payload components;
4) generate pseudorandom noise (PRN) codes for navigation;
5) provide SA; i.e., alter the navigation downlink when necessary to deny full GPS navigation accuracy to unauthorized users;
6) perform antispoof (AS); i.e., alter the navigation downlink on CS command to allow the authorized user full GPS accuracy through hostile environments;
7) operate through certain specific transient nuclear events without a permanent impact on the navigation functional accuracy;
8) recover from nuclear radiation transient including logic upset without assistance;
9) autonomously operate for 180 days without update from the CS; i.e., modify navigation data on a periodic basis by processing ranging data from other in-view satellites and exchange navigation data with other SVs and enable autonomous determination of ephemeris and clock corrections;
10) operate for 14 days, with at least the same navigation accuracy as the Block II vehicles are required to meet, without updates from the CS or other satellites;
11) encode NDS data received from the burst detection processor (BDP).
12) insert current SA data and SV ephemeris data into the NDS datamessage for transmission to other GPS satellites and the nuclear detonation user segment (NDUS).
13) update the SA data element (rapid turn-on) via the CTDU upon ground command.
14) perform a graceful turn-on and turn-off function to a known acceptable condition.
15) provide telemetry, diagnostics, and self-check capabilities.

2. *Software*

The computer program in the Block IIR navigation payload is large and complicated, as compared to those used in other spacecraft. This program is

referred to as the mission processor (MP) software. The requirement to function autonomously for 180 days dictates that the spacecraft will have to perform many functions currently performed by the CS. In addition to ephemeris and clock parameters estimation, this includes integrity monitoring, curve fitting of the navigation parameters, user range accuracy (URA) estimation, formatting the navigation message, selective availability, universal coordinated time (UTC) steering, and unassisted recovery from upsets.

Another factor contributing to the complexity of the software is the variety of hardware and software interfaces that the processor must deal with concurrently. These interfaces are shown in Fig. 8. Abbreviations for the interfaces that connect directly to the MP are defined in Table 5. Each of these corresponds to one or more I/O ports.

The interfaces connect the MP to the other subsystems shown in Fig. 8, including the SPU; reserve auxiliary payload (RAP); TT&C; CTDU; BDP; FSU; LBS; AFS; hop sequence generator (HSG); COMSEC; watchdog monitor; and error detection and correction (EADC).

The MP is programmed entirely in Ada. This affected the overall approach to developing the software. The Ada tasking model is used to accommodate the wide variety of processing deadlines. Ada portability and modularity are exploited to allow testing of the code in a variety of test environments.

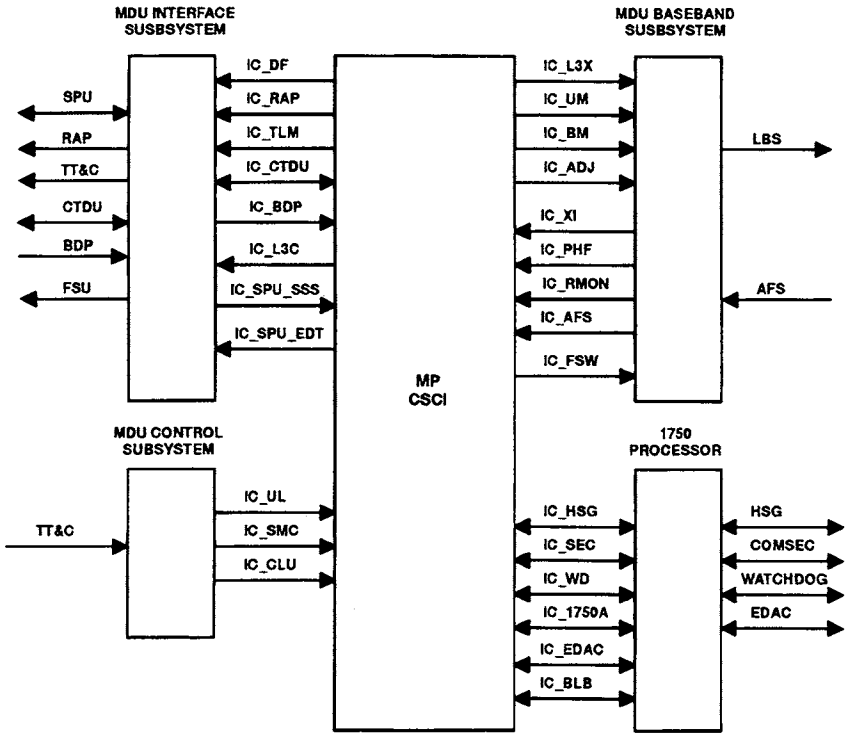

Fig. 8 CSCI–HWCI interfaces.

Table 5 Mission processor CSCI external Interfaces

PUID	Name
IC-UL	Upload data interface
IC-SMC	Serial magnitude command interface
IC-CLU	Clear upload interface
IC-TLM	Telemetry interface
IC-CTDU	CTDU interface
IC-BDP	BDP data interface
IC-L3X	L3 transmit data interface
IC-L3C	L3 on/off command interface
IC-BM	Baseband modulation interface
IC-UM	User message interface
IC-ADJ	Adjustment interface
IC-XI	X1/Z-count interface
IC-PHF	Phase feedback interface
IC-RMON	Reference monitor interface
IC-DF	Delta F command interface
IC-AFS	Atomic frequency standards interface
IC-FSW	AFS switch interface
IC-BLB	Blind bus interface
IC-WD	Watchdog monitor interface
IC-HSG	Hop sequence generator interface
IC-SEC	Comsec interface
IC-1750A	MIL-STD-1750A processor interface
IC-SPU-SSS	Spacecraft subsystem status interface
IC-SPU-EDT	Ephemeris data/time interface
IC-RAP	RAP interface
IC-EDAC	Error detector and correction interface
IC-LLED	Low-level event detector interface

3. *In-Space Reprogrammability*

The operational flight code can be completely reprogrammed from the ground. Upon cold start, the processor executes a program that is resident in PROM (programmable read-only memory). This program then uplinks the operational program over the S-band datalink. The PROM program has sufficient diagnostic capability to verify proper operation of the processor, memory, and data interfaces needed to upload and execute the flight program.

In addition to the capability to upload the entire program, partial uploads are possible. Certain parts of the program have been segmented so that they can be modified without uploading the entire program.

4. *Software Partitioning Facilitates Test*

An important feature of the onboard software is its ability to test certain components in accelerated time. This feature is most significant for AutoNav. A special test bed, the autonomous navigation emulator (ANE), has been developed by ITT to support this testing both before and after launch.

Chapter 7

Fundamentals of Signal Tracking Theory

J. J. Spilker Jr.*
Stanford Telecom, Sunnyvale, California 94089

I. Introduction

A. GPS User Equipment

THE GPS basic concepts, signal structure, navigation data, satellite constellation, satellite payload, and geometric dilution of precision (GDOP) concepts have all been introduced in previous chapters. This chapter and the next two discuss the user equipment. These chapters provide the foundation for much of the material in the companion volume on GPS applications.

Figure 1 illustrates the basic configuration of a GPS user equipment in its typical form. Generally, the user equipment performs two functions: the first, track the received signals, usually with some form of delay lock loop (DLL) so as to measure the pseudorange and usually the pseudorange-rate or accumulated delta range (ADR), a carrier measurement, as well. This chapter discusses the fundamentals of signal tracking theory as applied to the GPS signals. The next chapter, Chapter 8, discusses means for implementation of the GPS receiver functions. The following chapter, Chapter 9, discusses the navigation algorithm used to convert these receiver measurements into the desired output; namely, user position, velocity, and user clock bias error. This present chapter on signal tracking theory also describes a technique for combining the two functions, receiver tracking and navigation algorithm into one combined integrated tracking system.

In this chapter, the received signals are assumed to be received with stationary additive white Gaussian noise (AWGN) that is representative of the thermal noise at the receiver frontend. For most of this chapter, the received radio frequency signal-to-noise ratio is small, typical of most GPS receiver applications. Thus, the effects of self-noise or multiple access noise caused by the other GPS signals is generally small and is usually neglected. However, in the last section on the vector delay lock loop (VDLL), it is shown that the quasioptimal detector that tracks all signals is designed to remove much of this multiple access noise.

*Ph.D., Chairman of the Board.

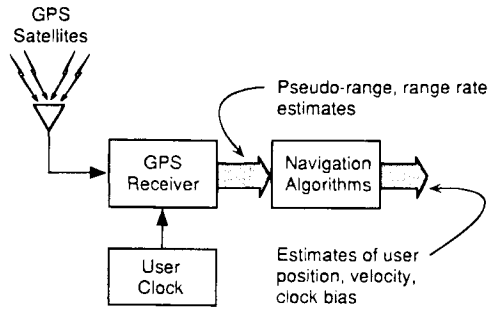

Fig. 1 Simplified configuration of the GPS user equipment.

B. GPS User Equipment-System Architecture

A generalized view of a basic GPS user equipment system is depicted in Fig. 2. The satellite signals are received by one or more antennas/low-noise amplifiers.* The output of the antenna is fed to a radio frequency bandpass filter/low-noise amplifier combination in order to amplify the signal and to filter out potential high-level interfering signals in adjacent frequency bands. Otherwise, these potential interfering signals might either saturate the amplifier or drive it into a nonlinear region of operation. The radio frequency filters must be selected with low loss in order to maintain a low noise temperature and also must have sufficient bandwidth and phase linearity to minimize the distortion of the desired C/A- or P(Y)-code signals. The signal then passes through serial stages of radio frequency amplification, downconversion, IF amplification and filtering, and sampling/quantizing. The sampling and quantizing of the signal can be performed either at intermediate frequency (IF) or at baseband. In either approach, in-phase and quadrature (I, Q) samples are taken of the received signals plus noise. At the present state of the art, we can implement the functions of radio frequency amplification, downconversion, IF amplification, and A/D sampling with a single monolithic microwave integrated circuit chip (MMIC). Filtering and reference frequency generation may require additional circuitry.

The I, Q samples are then fed to a parallel set of DLLs each of which tracks a different satellite, measures pseudorange, and recovers the carrier which is bi-phase modulated with the GPS navigation data.† The DLL 1–3 and associated

*Although most receivers employ only one antenna, some use more than one antenna/amplifier in order to:

- Accommodate maneuvering of the user platform; e.g., an aircraft banking and thereby avoid blocking some of the satellites with a wing. For example, one antenna can be at the top of the aircraft and others can be at the sides.
- Provide increased antenna gain. Each higher gain antenna can be pointed at single or clustered groups of satellites. The antenna beams can be steered electronically or mechanically, if necessary.
- Discriminate against interfering signals or multipath. Multiple narrow beam antennas or adaptive antennas can be employed. Some antennas use special ground planes to reduce multipath. Null steering antennas can be employed.

†An alternative time sequencing approach can be employed in which a DLL is sequenced over several satellites, dwelling on each satellite for a short period of time. There is, however, some performance degradation with this sequencing approach.

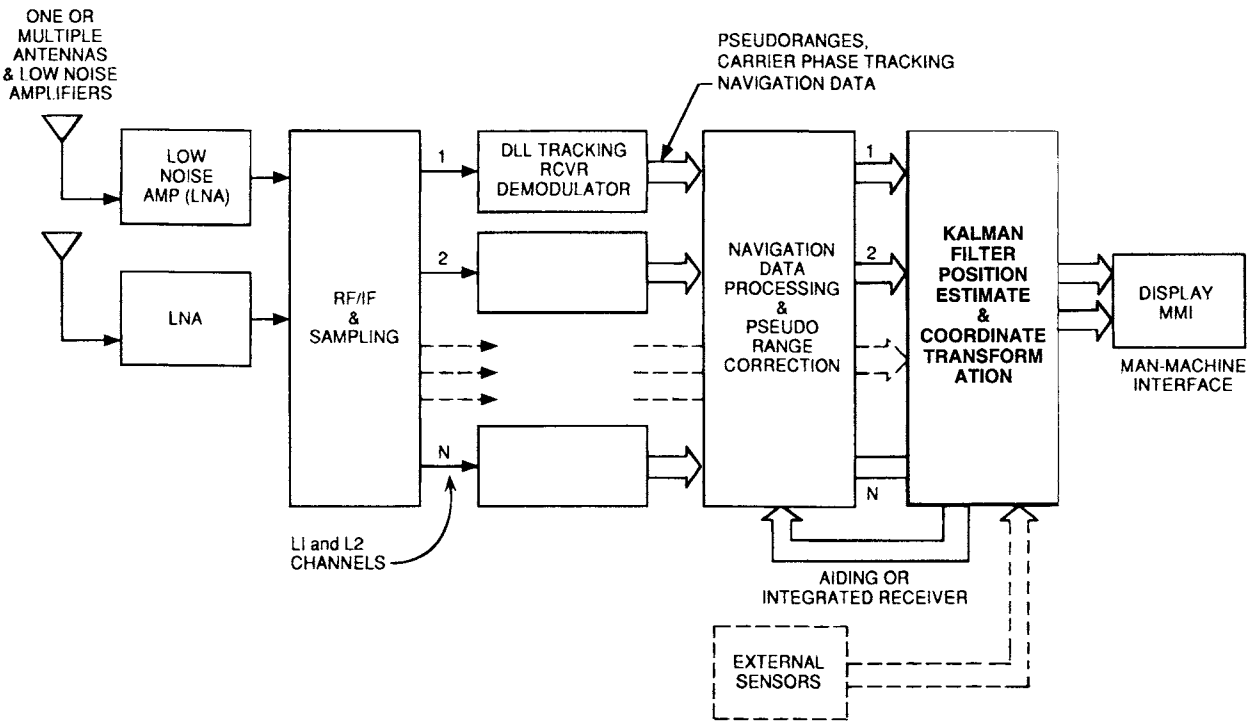

Fig. 2 Generalized GPS user system configuration with separate delay estimating receiver and position-estimating functions. There are N satellite signals tracked by the parallel DLL ($2N$ signals if both L_1 and L_2 channels are used).

demodulators provide estimates of the pseudorange, carrier phase, and navigation data for each satellite and are usually implemented using digital processing. As discussed in Chapter 5, this volume, on the GPS satellite constellation, there may be as many as ten satellites in view at one time. Typically the number of parallel tracking DLL varies from 2 to 16, and it is possible to track all of the satellites in view at both L_1 and L_2 frequencies. Generally, at least five satellites are tracked as a minimum, either in parallel or in time sequence. At the present state of the art, an L_1 10-channel receiver with 10 parallel DLLs can be implemented in digital form on one CMOS chip. Semiconductor technology is increasing significantly every 18 months, and the processing power available for GPS receivers is expanding in the same manner.

The receiver system with its parallel signal DLL and computer processors must carry out the operations of satellite selection, signal search, tracking, and data demodulation, as shown in Table 1.

This chapter concentrates on the signal-tracking task. The other tasks are described in detail in Chapter 8, this volume. The parallel pseudoranges, navigation data, and, in the more sophisticated receivers, the carrier phase measurements are fed to the navigation data processor where the position of each satellite is calculated, and pseudorange and clock corrections are made. As a first step in this operation, the pseudorange and carrier phase measurements are corrected for the various perturbations, including satellite clock errors, Earth rotation effects, ionosphere delay, troposphere delay, relativistic effects, and equipment delays.

The corrected pseudorange, phase, or accumulated phase (ADR) measurements along with other sensor data are then fed to the extended Kalman filter (EKF) or similar filter. The output of the EKF estimator provides position, velocity, and time estimates relative to the user antenna phase center (see Chapter 9, this volume.) There may or may not be information from additional sensors; e.g., altimeters, inertial measurement units (IMUs), or dead-reckoning instruments. If so, these measurements are also fed to the EKF. Data from carrier tracking and some of these sensors can also be used to aid the DLL tracking operation itself. As discussed in the companion volume, this Kalman filter estimate of user position can also be used in a differential mode with other GPS receivers where at least one receiver is at a known reference point for geodetic sensing, more accurate airborne or shipborne navigation, or in common-view mode for precision differential time transfer. The user position is usually computed in Earth-centered, Earth-fixed (ECEF) coordinates and are then transferred by appropriate geodetic

Table 1 Simplified sequence of operations in a GPS receiver system

1) Select the satellites to be tracked among those in view. Approximate satellite position can be determined using the Almanac, and the selection criteria can be based on GDOP.
2) Search and acquire each of the GPS satellite signals selected.
3) Recover navigation data for each satellite.
4) Track the satellites under whatever conditions of user dynamics are present and measure pseudorange and range-rate and/or ADR.

transformation to a desired local coordinate set or map display convenient to the user. As pointed out in a previous paragraph and discussed in more detail later, it is also possible to integrate the EKF with the DLL instead of performing these operations independently. The author has termed the integrated system the vector delay lock loop (VDLL) because it processes the signals in parallel as a vector operation. The VDLL can be interpreted as a further extension of the EKF.

C. Alternate Forms of Generalized Position Estimators

Figure 3 shows the received GPS signals from N satellites, each with delay $\tau_i(\boldsymbol{x})$ and signal amplitude a_i. The user position is $\boldsymbol{x}$. The C/A or P received signal is expressed as follows;

$$r(t, \boldsymbol{x}) = \sum_{i=1}^{N} a_i d_i(t) s_i[t - \tau_i(\mathbf{x})]\cos[\omega_o(t - \tau_i) + \phi_i] + n(t) \tag{1}$$

where $s_i(t)$ represents the radio frequency signal* transmitted by satellite i with amplitude a_i, delay τ_i, and phase ϕ_i, and d_i is the binary data modulation. Both the delay and phase vary with time in accord with user dynamics relative to the satellite i. The signal s_i can represent either the C/A or P codes at either L_1 or L_2 frequencies†. The noise $n(t)$ is assumed to be stationary AWGN.‡ The delay

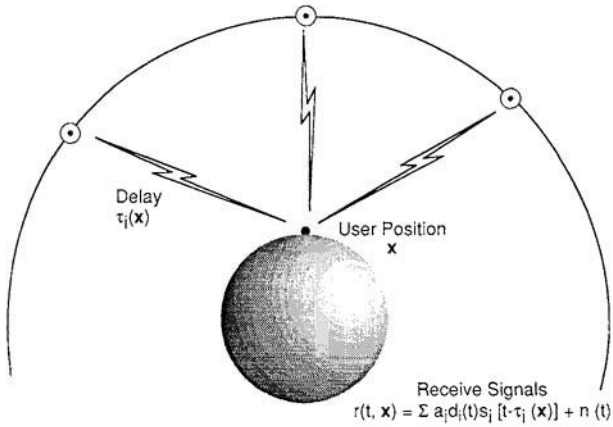

Fig. 3 Simplified representation of received GPS signals for a user at position x and path delays $\tau_i(x)$. The signals are received in the presence of white Gaussian noise $n(t)$.

*In reality, of course, the signal has both a C/A code and a P code in-phase quadrature. Both of these pseudonoise (PN) signals can be used simultaneously in delay estimation by a simple generalization of these results.

†More precisely, of course both C/A and P codes should be shown in phase quadrature, and both signals can be tracked in one receiver.

‡Although $n(t)$ is generally white Gaussian thermal noise, there clearly can be signal level fluctuations caused by multipath, attenuation caused by blockage from physical obstruction, and satellite-user motion/geometry. The delay $\tau_i(x)$ is also perturbed by atmospheric delay effects, selective availability, and multipath, which are separate colored noise effects discussed later.

τ_i and phase ϕ_i are functions of the user position vector $\boldsymbol{x}$. In general, the position vector $\boldsymbol{x}(t)$ is a function of time and is assumed to have some limited set of dynamics governed by a process model.

There are at least two general forms of position estimators that can be configured for the GPS system and many types within each of those forms. The most general estimator, shown in Fig. 4a, shows a single estimator that produces in one step an estimate of the user position vector $\boldsymbol{x}$. The second more restricted form of Fig. 4b first processes the received signal so as to estimate each of the satellite pseudoranges τ_i (and range-rate, etc.) and then generates an estimate of position $\hat{\boldsymbol{x}}$ based on the $\hat{\tau}_i$. Each of the estimates of τ_i are performed completely independently in this second form.

Assume for the moment that the user position is an unknown constant vector and that the received signal samples at discrete times t_k are $r(t_k,\boldsymbol{x})$ and are represented over the time interval $t_1, t_2, \ldots t_k$ as the following received vector:

$$\boldsymbol{r}(\boldsymbol{x}) = [r(t_1, \boldsymbol{x}), r(t_2, \boldsymbol{x}), \ldots, r(t_K, \boldsymbol{x})] \tag{2}$$

Then the estimate in Fig. one 4a can be represented as follows:

$$\hat{\boldsymbol{x}}_a = F_a[\boldsymbol{r}(\boldsymbol{x})] \tag{3}$$

The estimate of Fig. 4b is the following more restricted type of estimate;

$$\hat{\boldsymbol{x}}_b = F_b[\boldsymbol{r}(\boldsymbol{x})] = F_{bx}\{\hat{\tau}[\boldsymbol{r}(x)]\} \tag{4}$$

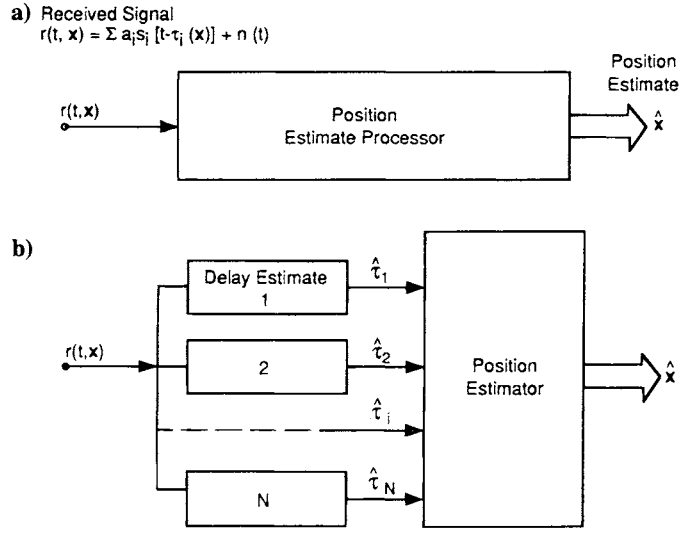

Fig. 4 Two forms of generalized GPS position estimate processors. The first form of processor a) estimates the position directly without an independent intermediate delay estimate. This estimator may also produce an estimate of delay, because with GPS a delay estimate is needed for recovery of the navigation data. The second form b) first estimates the delay using independent parallel estimators for each τ_i and then estimates position as a separate process.

where each of these τ_i delay (pseudorange) estimates in (b) are made independently. That is, no use is made of the fact that the delays τ_i may be correlated by the geometry of the transmission paths. Most present GPS receivers fall into this latter more restricted class.

An obvious potential disadvantage of the two-step approach of Fig. 4b can be illustrated by a hypothetical example where there are a large number of equal power satellite signals, say $N = 100$, and only one coordinate, a scalar x, to be estimated. Further assume that the satellite path delays are simple offsets of one another, namely, $\tau_i(x) = x + C_i$, where the C_i are known delay offsets. This signal model obviously represents an extreme example of an overdetermined estimation problem. Clearly, an estimate of x, based on the totality of 100 equal power received signals can, in general, produce a better estimate by making use of the linear relationship of the 100 different τ_i and the full power of the 100 signals than would an estimate based on processing each individual signal independently, and then combining the 100 independent estimates of delay. For example, a receiver could offset each of the signals by the known delays C_i add the signals coherently,* and estimate the delay using the composite signal that now has a signal-to-noise ratio 100 times as large. We can envision a situation where the signal-to-noise ratio of each individual signal is too small to process independently (i.e., below threshold); whereas, the delay in the composite signal is easily measured.

Section II of this chapter discusses receivers of the form of Fig. 4b wherein each delay estimate is made independently. Quasioptimum forms of the receivers (scalar delay lock loops) are discussed and related to more conventional delay lock loop tracking systems. The chapter concludes (Sec. III) with a discussion of quasioptimum forms of receivers of the more general form of Fig. 4a, which the author has defined as the vector delay lock loop (VDLL).[4]

D. Maximum Likelihood Estimates of Delay and Position

As shown in Appendices A and B, the DLL is a quasioptimal iterative form of two different statistically optimum delay estimators, the maximum likelihood estimator and the least mean square error estimator. In this subsection, we review a class of estimates termed the maximum likelihood estimate.[5-10] The parameter to be estimated can represent either delay or user position, is assumed to be constant over some time interval of interest, and slowly varies from interval to interval. When cast in an iterative approximation form, these estimators take the configuration of the DLL or the VDLL.

Assume that we make independent observations of a set of scalar random variables r_i, each of which depends on an unknown vector parameter $\boldsymbol{x}$ that we want to estimate. Define $\boldsymbol{r}$ as a vector representing a set of K random variables r_i, where the vector has a probability density $p(\boldsymbol{r})$. The conditional probability density of $\boldsymbol{r}$ is conditioned on a certain value for the unknown vector parameter $\boldsymbol{x}$, and is defined as $p(\boldsymbol{r}|\boldsymbol{x})$. The conditional density, $p(\boldsymbol{r}|\boldsymbol{x})$, is termed the likelihood function when the variable $\boldsymbol{x}$ is assumed to be the unknown random variable (rather than the opposite). In particular, suppose that we make K independent

*The noise also adds for each signal, but not coherently.

observations of the random variables r_i at discrete times t_k to form an observation vector $\boldsymbol{r} = (r_1, r_2, \ldots r_K)$, where the observations include additive Gaussian noise. The unknown $\boldsymbol{x}$ is assumed to be constant over this K sample interval. We define the maximum likelihood estimate as that estimate $\hat{\boldsymbol{x}}$, which maximizes $p(\boldsymbol{r}|\boldsymbol{x})$; namely,* the following:

$$p(\mathbf{r}\,|\,\hat{\mathbf{x}}) \geq p(\mathbf{r}\,|\,\mathbf{x}_o) \tag{5}$$

where $\boldsymbol{x}_o$ is any other estimate of $\boldsymbol{x}$.

Appendix A derives the maximum likelihood estimates for (1) delay $\tau(t_k)$; (2) a scalar position variable $x(t_k)$ where delay is a nonlinear function of x; and (3) a vector position variable $\boldsymbol{x}(t_k)$, where all signals are received in the presence of white Gaussian noise.

Figure 5 shows the block diagrams of the estimators (delay lock loops) that provide iterative closed-loop approximations to maximum likelihood for the two forms of estimators of Fig. 4 with time compared to the noise effects. Thus, the effective bandwidth of the closed-loop tracking filters can be small because it need only track the dynamics of user motion rather than the wide bandwidth of the signal itself. The estimator of Fig. 5a is configured as a closed loop operation in a form similar to what has been called the delay lock loop in earlier papers by the author and has the same form as the delay estimator of Fig. 4b.† The estimator of Fig. 5c is in a form that corresponds to Fig. 4a and is termed a vector delay lock loop.

The reader is referred to Appendix A for details. Suffice it to say here that each of these forms of delay lock loops serves to track the variable to be estimated by generating a correction term that is directly proportional to the error in the estimate. Furthermore, each tracking loop begins by forming the product of the received signal with a differentiated version of the signal component; namely, $s_i'(t)$.

A third closely related estimate is the least mean square error estimate for the AWGN channel. As shown in Appendix B, the least-mean-square estimate of a parameter for signals received is produced by a receiver that can also be configured in an iterative closed-loop form very similar to that for the maximum likelihood estimate when certain linearizing assumptions are made in both estimators. Thus, both estimators configured in iterative form are versions of delay lock loops.

E. Overall Perspective on GPS Receiver Noise Performance

Although this chapter discusses only the fundamentals of GPS signal tracking, it is important to place the noise performance that is discussed here in perspective with the noise effects on the other operations that must be performed in the GPS

*Another type of optimal estimate is the maximum a posteriori estimator (MAP),[11] which maximizes $p(\boldsymbol{x}|\boldsymbol{r})$; i.e., the most probable value of $\boldsymbol{x}$ given the observation vector $\boldsymbol{r}$. The MAP can be written $p(\boldsymbol{x}|\boldsymbol{r}) = \dfrac{p(\boldsymbol{r}|\boldsymbol{x})\,p(\boldsymbol{x})}{\int p(\boldsymbol{r}|\boldsymbol{x})\,p(\boldsymbol{x})\,d\boldsymbol{x}}$. Thus, use of the MAP estimate requires knowledge of the a priori probability density $p(\boldsymbol{x})$ as well as $p(\boldsymbol{r}|\boldsymbol{x})$. However, in many problems, the a priori probability $p(\boldsymbol{x})$ is assumed to be unknown.

†For a pure sinusoidal signal, Viterbi[12] showed that the MAP estimator for a Gaussian phase variable can be configured in the form of a phase locked loop. For a pure sinusoidal signal, the delay lock loop reduces to a phase locked loop. See also Ref. 10.

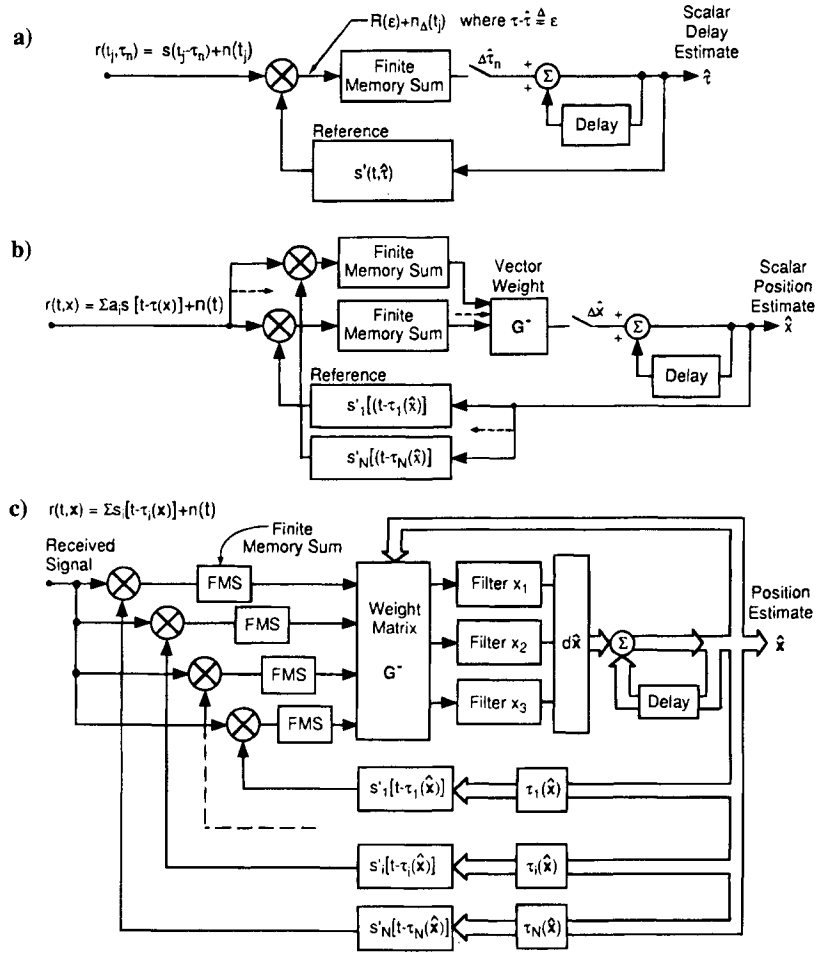

Fig. 5 These various forms of the delay-lock tracking loop provide estimates are iterative closed-loop approximations to the maximum likelihood estimates of τ or x provided that the changes in x occur in steps every K samples and are sufficiently small. Also assume that the loop begins with an initial estimate $\hat{\tau}$ or $\hat{x}$, which is close to the true value of τ or x. Three different generalizations of the delay lock estimator are shown for various levels of complexity of the estimation task. In part a, only a single received signal is present, and the parameter to be estimated is a scalar τ. In part b, multiple signals are received, and the quantity estimated is a scalar position variable x. In part c, multiple signals are received, and the parameter to be estimated is a position vector $x = (x_1,x_2,x_3, \ldots x_m)$. The G^- matrix is the generalized inverse that gives the minimum mean square error estimate of dx given $d\tau$. Different loop filters process each of the position variable components.

receiver; namely, GPS signal search and acquisition, and navigation data demodulation.

It is also important to illustrate some contrasts in the multiple access performance of GPS used for signal tracking with the multiple access performance of code division multiple access (CDMA) used for communications. The primary differences are twofold. First, the GPS signals are transmitted with only moderate power and are generally received with low gain, nearly omnidirectional antennas. Consequently the received radio frequency signal-to-noise ratios that result are low. Thus multiple access and self-noise are generally (although not always) of secondary importance to thermal noise effects. Second, with GPS, the primary objective is to estimate the user position and velocity, rather than transmit and receive a multiplicity of communications signals. Thus, as the number of satellites increases, the information sought does not increase significantly.* Contrast that objective with that of a CDMA communications network wherein each user signal carries with it digitized information at a substantial datarate, the transmission of which is the key objective of the communications system. In a CDMA system, maximum channel capacity is achieved when the signal-to-thermal noise ratio is large, thus multiple access noise effects dominate and limit the number of signals that can be transmitted (because each signal carries additional, rather than redundant, information).

Search and acquisition of the GPS signal is discussed in the next chapter. However, since this chapter on signal tracking assumes that the initial value of delay error has been reduced to a small value, it is well to spend a moment to make plausible that that assumption is realistic. The required C/N_o must be reasonable.

GPS signal search and acquisition is often accomplished by sequencing a reference C/A code over each of the 1023 chips of the C/A code in fractional chip (often in 1/2 chip) steps, in each of several Doppler frequency offset increments. This time-frequency search is completed when the signal component is detected by a noncoherent square law detector. The noncoherent detector operates using a relatively narrow IF bandwidth W, and acquisition occurs when the detector produces an output that exceeds some threshold level. The threshold level is set, in turn, to produce some acceptable level of false alarms, perhaps on the order of 5 in 10^3. If threshold is exceeded several times; e.g., three times out of five, "lock" is declared. If each time-frequency cell is examined for T_r s; i.e., the search rate is $S_r = 1/T_r$. For a false alarm probability $P_{FA} = 5 \cdot 10^{-3}$, and a probability of detection $P_d = 0.9$, the required ratio of carrier power $C = P_s$ to noise density, N_o (one-sided) is approximately $C/N_oS_r \cong 22$ or 13.4 dB if the IF signal-to-noise ratio is unity or more.[3,13] Thus if† $C/N_o = 33$ dB-Hz, and the IF bandwidth is 2000 Hz, then the maximum search rate is $S_r < 90$ or 45 chips/s if 1/2 chip steps are used. If the maximum residual Doppler phase oscillator drift is $\pm$ 1 kHz, then only one IF channel of 2 kHz must be searched.

*There is, of course, more navigation data to be recovered but these data are at a very low datarate of 50 bps.

†Typical GPS C/N_o are larger; $C/N_o > 40$ dB-Hz. The rule of thumb $C/N_oS_R = 22$ for signal search can also be written $E_R/N_o = 22$ where $E_R = C/S_R$ is the energy per search time interval $1/S_R$. Note the similarity in form with the bit error rate constraint $E_b/N_o = 10$ where E_b is the energy per bit.

Thus search and acquisition do not pose any severe constraints on C/N_o for these search rates. Search and acquisition are discussed more fully in the next chapter.

The navigation data demodulation places a similar requirement on C/N_o. Coherent demodulation of the binary phase-shift keyed (BPSK) waveform produces a theoretical bit error probability $P_E = \text{erfc}\sqrt{2E_b/N_o} = \text{erfc}\sqrt{2C/N_o f_d}$ where E_b is the energy per bit $= P_s T_d = CT_d$, where $T_d = 1/f_d$, and f_d is the 50 bps datarate. If $C/N_o f_d = 10$, then the output error probability is approximately 10^{-5}, which is quite satisfactory for good receiver performance. This ratio corresponds to a $C/N_o = 500$ or 27 dB, which is less than the 33 dB-Hz just cited in the search and acquisition example.

Thus, we can proceed with the discussion of tracking knowing that the C/N_o requirement for acquisition in a reasonable time is consistant with available GPS signal levels (see Chapter 3, this volume), and data can be demodulated at sufficiently low error rate.

F. Interaction of Signal Tracking and Navigation Data Demodulation

As described above, the complete GPS receiver has two closely related and interacting tasks; the receiver must track the delay of each of the received signals and must also coherently (or differentially coherently) detect the 50 bps navigation databit stream, as shown in Fig. 6. Each of these tasks can support the other. For example, the extraction of the navigation data relies on a reasonably accurate delay estimate of each signal so that a reference waveform properly aligned in time; i.e., punctual, can be used to remove the GPS spread spectrum PN code and recover the BPSK signal. The BPSK signal itself can be coherently demodulated by recovering an estimate carrier phase $\phi_i(t)$ and then extracting the navigation data $d_i(t + \tau)$. The recovered carrier phase and navigation data estimates can, in turn, be used as a coherent reference to eliminate the carrier and data in the

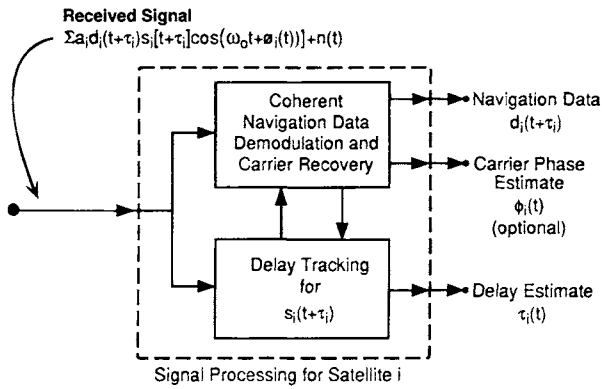

Fig. 6 Two separable, but interacting, signal processing tasks in the GPS receiver, navigation data demodulation, and signal delay tracking. The outputs of each of these tasks can aid the operation of the other.

received signal to permit coherent tracking. Alternatively, this carrier frequency estimate can be used as an aid in removing Doppler shift from the received signal prior to the delay tracking operation, or as an aid in code tracking.

II. Delay Lock Loop Receivers for GPS Signal Tracking

This section describes several alternate methods for tracking the GPS signal. Both code tracking and, to a lesser extent, carrier tracking are described. The signal is generally assumed to be received in the presence of stationary additive white Gaussian noise (AWGN). In this chapter, the signals $s_i(t)$ are always assumed to be bandlimited finite rise time signals with a continuous autocorrelation function $R(\epsilon)$ and continuous, finite, differentiated autocorrelation function $R'(\epsilon) \Delta \partial R(\epsilon)/\partial\epsilon$. The discussion begins with the quasioptimal delay lock loop that employs a differentiated signal as the reference.[1,3] This delay lock loop is then related to the early-late gate delay lock loop.[2,3,14] It is shown that for a signal represented by a PN trapezoidal pulse sequence with finite rise-time, the two forms are identical. Although some of the discussion of tracking systems is expressed in terms of continuous time systems, the reader should be aware that implementations are generally performed in discrete time digital operations. Thus, read $s(t_k)$ for $s(t)$ where the samples are taken at discrete times t_k with independent samples taken at the Nyquist rate.

A. Coherent Delay Lock Tracking of Bandlimited Pseudonoise Sequences

Consider a coherent tracking receiver as shown in Fig. 7 where for the moment we focus on a single received PN signal of power $P_s = A^2/2$ plus bandpass AWGN of spectral density N_o (one-sided).* The coherent receiver downconverts the signal and removes the data modulation using information and control signals from a yet to be described coherent demodulation channel (see Sec. I.F and II.C). The output of the coherent downconverter is then passed through a low-pass

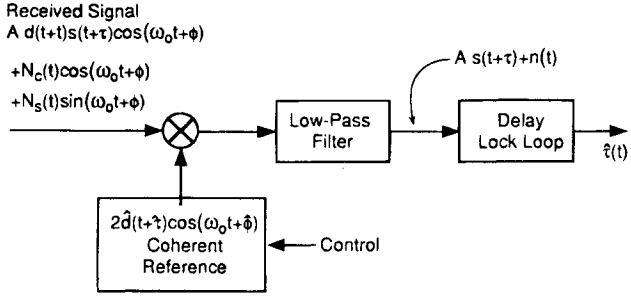

Fig. 7 General form of the coherent delay lock loop receiver system.

*Throughout much of this section, the functions are often expressed in continuous time t. The reader should be aware that these results are easily translated to complex discrete time functions at sample time t_k sampled at the Nyquist rate.

filter that maintains the signal spectrum but removes the components at frequency $2f_o$. The output of the coherent downconverter, assuming sufficiently accurate estimates of carrier phase ϕ and data d, is then a pure PN signal plus white Gaussian noise $n(t)$. It should be pointed out that coherent tracking loops of this form have definite practical limitations in that a carrier tracking cycle slip can cause the code tracking loop to lose lock. Nonetheless, the coherent tracking loop serves a useful purpose as a bound on performance and as an introduction to the other forms of the DLL.

The output of the multiplier low-pass filter combination in Fig. 7 for perfect data demodulation and carrier phase recover, namely, $\hat{d}(t) = d(t)$ and $\phi = \hat{\phi}$, is then $A\ s(t + \tau) + N_c(t)$. The radio frequency signal power is $P_s = (A^2/2)$ for constant envelope signals and somewhat less than that for finite rise time trapezoidal waveforms. The ratio of the signal power in the multiplier output $A^2 = 2P_s$ to the noise density* $2N_o$ of the $n(t) = N_c(t)$ term is then $A^2/2N_o = P_s/N_o$, the same as at the radio frequency input. The baseband pseudonoise PN signal is represented by the following:

$$s(t) = \sum_i P_i p(t - iT)$$

where P_i is a random or pseudorandom binary sequence of numbers ± 1, and $p(t)$ is a bandlimited finite rise time pulse waveform of approximate pulse width T. The PN clock rate is $f_c = 1/T$.

The original paper on the "Delay-Lock Discriminator"[1] pointed out that the optimal tracking system for tracking the delay of a signal $s(t + \tau)$ can be approximated by a tracking loop that first multiplies the received signal plus noise by the differentiated signal, as shown in Fig. 8. The true delay τ and

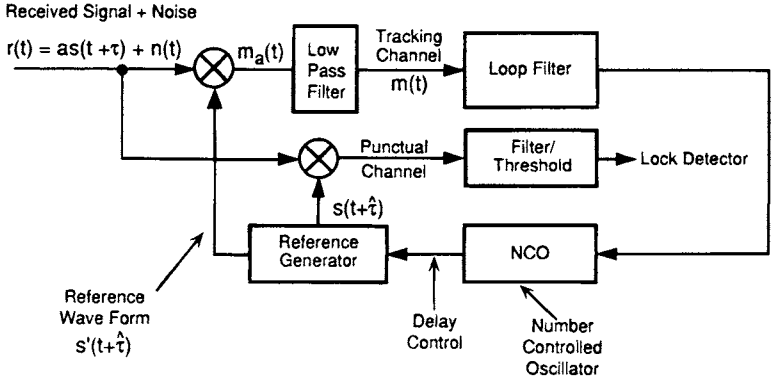

Fig. 8 Delay lock tracking of signal $s(t + \tau)$ where τ varies with time. The punctual channel reference $s(t + \hat{\tau})$ is used to detect that the receiver is locked-on. The bandwidth of the closed-loop tracking must match the dynamics of the delay variation.

*The power of the radio frequency finite bandwidth AWGN, $N_c(t)\cos\omega_o(t) + N_s(t)\cos\omega_o(t)$ with center frequency ω_0 is $P_n = (1/2)E[N_c^2(t) + N_s^2(t)] = E[N_c^2(t)]$. If the one-sided spectral density of the radio frequency noise is N_o, then the one-sided spectral density of $N_c(t)$ is $2N_o$, noting that $N_c(t)$ has half the bandwidth of the radio frequency noise.

the delay estimate $\hat{\tau}$ are assumed to be sufficiently close that first-order linear approximations are accurate; i.e., the delay error $\epsilon \Delta \tau - \hat{\tau}$ is sufficiently small relative to the width of the autocorrelation function. The received signal, $s(t + \tau)$, can then be expanded in a Taylor series referenced to the signal with a delay estimate $\hat{\tau}$ as follows:

$$s(t + \tau) \cong s(t + \hat{\tau}) + \epsilon s'(t + \hat{\tau}) + \frac{\epsilon^2}{2} s''(t + \hat{\tau}) +, \ldots, \text{for small } \epsilon \quad (6)$$

where the partial derivative of the signal waveform with respect to time is $s' \Delta (\partial/\partial t)\, s$, etc.

The output of the upper multiplier, the tracking channel, in Fig. 8 is $m_a(t)$, which can be expanded using Eq. (6) as follows:

$$m_a(t) = s'(t + \hat{\tau})[As(t + \tau) + n(t)] \quad (7a)$$

$$m_a(t) \cong As(t + \hat{\tau})s'(t + \hat{\tau}) + A\epsilon(t)s'(t + \hat{\tau})^2 + (A\epsilon^2(t)/2)s''(t + \hat{\tau})s(t + \hat{\tau}) +, \ldots, + n(t)s'(t + \hat{\tau}) \quad (7b)$$

As before, $n(t)$ is assumed to be stationary AWGN is independent of $s(t)$. The signal is also assumed to be stationary. Define $R(\epsilon) = E[s(t + \epsilon)s(t)]$ as the autocorrelation function of the signal $s(t)$. Note that the expected value of the multiplier output is as follows:

$$E[m_a(t)] = E(s(t + \tau)s'(t + \hat{\tau})] = E[s(t + \hat{\tau} + \epsilon)s'(t + \hat{\tau})] = R'(\epsilon) = D(\epsilon) \quad (8)$$

where $R'(\epsilon) = D(\epsilon)$ is the differentiated autocorrelation function where $R'(\epsilon) = (\partial/\partial\epsilon)R(\epsilon)$, and $D(\epsilon)$ is termed the delay lock loop discriminator characteristic. The slope of the discriminator characteristic at $\epsilon = 0$ is $D'(0)$ and defines the loop gain of the DLL. Define $P_d = E[s'(t)]^2 = -R_s''(0) = -D'(0)$ as the power of the differented signal,* and assume that the clock-rate f_c of the signal $s(t)$ is large compared to the closed-loop noise bandwidth† B_n of the linearized equivalent tracking loop, which is defined later. We can represent the product $s(t)s'(t + \epsilon)$ by its expected value plus a "self-noise" term‡; namely,

$$s(t + \tau)\, s'(t + \hat{\tau}) = D(\epsilon) + [s(t + \tau)\, s'(t + \hat{\tau}) - D(\epsilon)] = D(\epsilon) + n_{sn}(t)$$

where $n_{sn}(t)$ is a wide bandwidth self-noise term

$$n_{sn}(t) \Delta [s'(t + \hat{\tau})s(t + \tau) - D(\epsilon)],$$

*The slope of the discriminator characteristic is $D'(0) = R_s''(0)$ and is negative. Note that the dimension of $s'(t)$ is s^{-1} and the dimension of $(s')^2$, and hence, P_d is s^{-2}.

†If the closed-loop transfer function is $H(j\omega)$ then the closed-loop noise bandwidth is

$$B_n = \frac{1}{2\pi} \int_0^\infty |H(j\omega)|^2 \, d\omega / |H(0)|^2$$

‡Self-noise is defined as the difference between the expected value of the product $s(t + \tau)$ $s'(t + \hat{\tau})$ and its actual value. The self-noise is a broadband noise-like waveform.[3,4]

most of which is removed by the low-pass and tracking loop filters, and thus, can often be neglected.

The output of the upper multiplier $m_a(t)$ in Fig. 8 is next filtered with a low-pass filter. This filter has bandwidth that is small compared to f_c but large compared to the dynamics of the delay. Thus, it performs a limited amount of averaging. Hence, it is useful to represent the low-pass filtered multiplier output $m(t)$ of Eq. (7) as follows:

$$
\begin{aligned}
m(t) &= AD(\epsilon) + [n(t)s'(t + \hat{\tau}) + An_{sn}(t)|_{\text{low pass}}] = AD(\epsilon) + n_s(t) \\
m(t) &\cong -A\epsilon(t)P_d + [n(t)s'(t + \hat{\tau}) + An_{sn}(t)] \\
&\quad + (\epsilon^2, \epsilon^3 \text{ terms})|_{\text{low pass}} \\
&\cong -A\epsilon(t)P_d + n_s(t) \qquad \text{for small } \epsilon \text{ and } B_n << B
\end{aligned} \tag{9}
$$

where $D(\epsilon) \approx D'(0)\epsilon = -P_d\epsilon$ for small ϵ, self-noise effects are neglected, and it is assumed that the ϵ^2 and higher-order ϵ terms are negligible for small ϵ and $n_s(t) = n(t)s'(t + \hat{\tau})|_{\text{low pass}}$. Thus, the last form of Eq. (9) represents the first two terms in the Taylors' series of Eqs. (6) and (7b). The first component of $m(t)$ in Eq. (9) represents the delay lock loop discriminator characteristic* $D(\epsilon)$.

Thus, for small ϵ, the output of the low-pass filter of Fig. 8 produces a correction term directly proportioned to delay error ϵ, and thereby, enables the loop to track the delay $\tau(t)$. To begin the tracking operation we must initialize (lock up) the DLL with a moderately accurate initial estimate of τ obtained by some search procedure (see Chapter 8, this volume). Note also that for a pure sine wave signal $s(t) = \sin \omega t$, the differentiated signal $s'(t) = \omega \cos \omega t$, and the delay lock loop for this special case simplifies to a conventional phase lock loop. In this case, the filtered product $s(t + \tau)s'(t + \hat{\tau}) = \omega \sin \omega\epsilon \cong \omega^2\epsilon$ for $\omega\epsilon << 1$ (neglecting the 2ω terms), and the discriminator characteristic is $D(\epsilon) = \omega \sin(\omega\epsilon)$. Digital phase lock loops are employed in the carrier-tracking operation.

1. *Trapezoidal Pseudonoise Waveform*

It is useful to approximate the finite rise time PN waveform by a symmetrical trapezoidal waveform† $s(t)$ of zero mean (equiprobable zero and ones) and rise time δT, as shown in Fig. 9. This finite rise time PN waveform is a more realistic representation of the GPS signal than the ideal rectangular shape. Thus, the DLL reference waveform $s'(t)$ is a ternary waveform that is a sequence of narrow pseudorandom pulses with pulse width equal to the rise time δT. It can be seen that the synchronized product $s(t)s'(t)$ with zero delay offset has zero long-term average ($D(0) = 0$), as we would expect. For a finite rise time pseudorandom

*Note that with this definition of $D(\epsilon)$, the slope at $\epsilon = 0$ is negative, and we must put a sign reversal in the loop in order to track the delay variable.

†To be consistent with the assumption of a bandlimited waveform with a continuous derivative, assume that the corners of the trapezoid are slightly rounded.

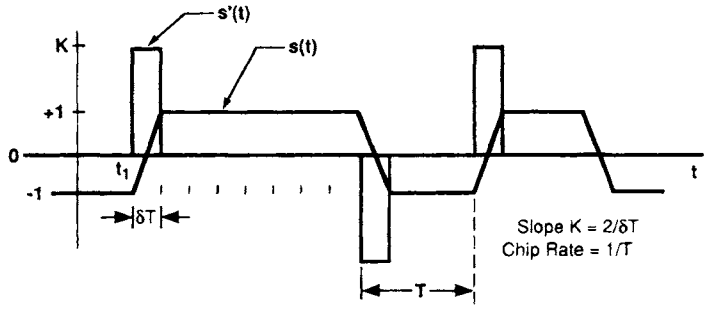

Fig. 9 Plot of PN sequence with a trapezoidal waveform and finite rise time $\delta T < T/2$. The differentiated waveform $s'(t)$ is also shown. The peak value of $s'(t)$ is $K = 2/\delta T$. Where there is no transition $s'(t) = 0$. Because there are transitions half the time, the duty factor of $s'(t)$ is $\delta T/2T$.

sequence of chip duration T, the multiplier output integrated over one chip interval T with zero delay error also is zero; namely

$$\int_{NT}^{NT+T} s(t)s'(t)\mathrm{d}t = 0$$

Note that for the trapezoidal waveform, the only portion of the waveform useful for time delay measurement is during the transient rise time δT of the waveform, which occurs at the beginning of the chips 50% of the time. This characteristic is in marked contrast to a communication channel where essentially all of the waveform is useful. Thus, the noise is time-gated to a duty factor of $\delta T/2T$ without significant loss of tracking information.

Thus, the multiplier output of Eq. (9) can be approximated as follows:

$$\begin{aligned} m(t) &\cong AD[\epsilon(t)] + n(t)s'(t)\,|_{\text{low pass}} \\ &\cong -AP_d\epsilon(t) + n(t)s'(t)\,|_{\text{low pass}} \qquad \text{for small } \epsilon \end{aligned} \tag{10}$$

where the multiplier output noise is time-gated by $s'(t)$, which has a duty factor* of $\delta T/2T$. The discriminator function for this trapezoidal PN sequence is quasilinear $D(\epsilon) \cong -[2\epsilon/\delta T - (\epsilon/\delta T)^2]$ for $|\epsilon| < \delta T/2$. Figure 10 shows a plot of example trapezoidal pulse waveforms, their autocorrelation functions $R(\epsilon)$, and differentiated autocorrelation functions $R'(\epsilon) = D(\epsilon)$ for unit amplitude triangular and trapezoidal pulse waveforms. The power in the differentiated signal is as follows:

$$-D'(0) = P_d = E[s'(t)^2] = K^2\frac{\delta T}{2T} = \left(\frac{2}{\delta T}\right)^2\frac{\delta T}{2T} = \frac{2}{T(\delta T)} \tag{11}$$

where $D'(0) = -P_d$, and $K = 2/\delta T$ is the slope of $s(t)$ at a transition, and it is assumed that the PN signal has transitions one-half the time. The rise time δT is inversely related to the one-sided 3-dB bandwidth of the baseband wave-

*The duty factor of each pulse is $\delta T/T$, but its pulses occur only in half of the chip intervals.

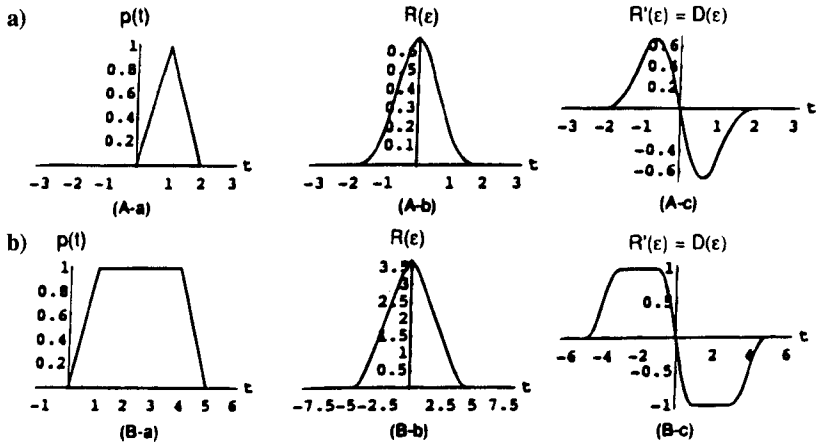

Fig. 10 Triangular- and trapezoidal-shaped pulses with the same normalized δT = 1, their autocorrelation functions and the quasioptimal delay lock discriminator functions $D(\epsilon) = R'(\epsilon)$. In part a, the PN sequence chip rate is normalized to 1.0, and the rise time of the PN pulse is also 1.0 leading to a triangular waveform shown in A-a with $\delta T/T$ = 1.0. The autocorrelation function $R(\epsilon)$ is shown in A-b, and the differentiated waveform or quasioptimal delay lock loop discriminator characteristic $R'(\epsilon)$ is shown in A-c. Figure 10b shows the trapezoidal waveform B-a, autocorrelation function B-b, and discriminator characteristic $R'(\epsilon)$) in B-c, for a PN pulse where the rise time δT = 1.0 is 25% of the pulse width T = 4.0; i.e., $\delta T/T$ = 0.25.

shaping filter B by the approximation* $\delta T \cong 0.44/B$. If, for example, the bandwidth $B = 1/T$, then $\delta T = 0.44T$. If, on the other hand, the bandwidth is considerably larger and B = 10/T, as is approximately the situation for the transmitted C/A code on the GPS L_1 channel, then $\delta T = 0.044T$. Thus, the pulse width of the quasioptimum reference waveform is very narrow for short rise-time pulses. Even for the P code, the rise time is significantly less than T.

2. *Delay Lock Loop Discriminator Curve*

Assume again that the signal waveform is the trapezoidal shaped PN sequence. The reference waveform is then a PN sequence of finite width pair of rectangular pulses shown in Fig. 11a where $T = 4$, $\delta T = 1$. The coherent delay lock loop with a differentiated reference has a discriminator curve $D(\epsilon) = R'(\epsilon)$, as shown in Fig. 11b (and also Fig. 10B-c).

Thus, for small values of $\delta T/T$, this delay lock loop operates approximately as a piecewise-linear "bang-bang" servo system, and the discriminator curve

*The trapezoidal waveform can result by filtering a rectangular shaped PN sequence with a finite memory integrator filter with impulse response $h(t) = 1/\delta T$ for $0 \le t \le \delta T$, and $h(t) = 0$ otherwise. This filter has a frequency transfer function $|H(j\omega)| = \sin(\pi f \delta T)/\pi f \delta T$. This signal spectrum has a first zero in the frequency response at $f = 1/\delta T$. At frequency $f = 0.44/\delta T$, the spectral response is down 2.97 dB. Thus, we define the bandwidth measure $B = 0.44/\delta T$. Clearly, the actual relationship between δT and bandwidth of the waveshaping filter is dependent on the exact signal waveform and the definitions of bandwidth and rise time.

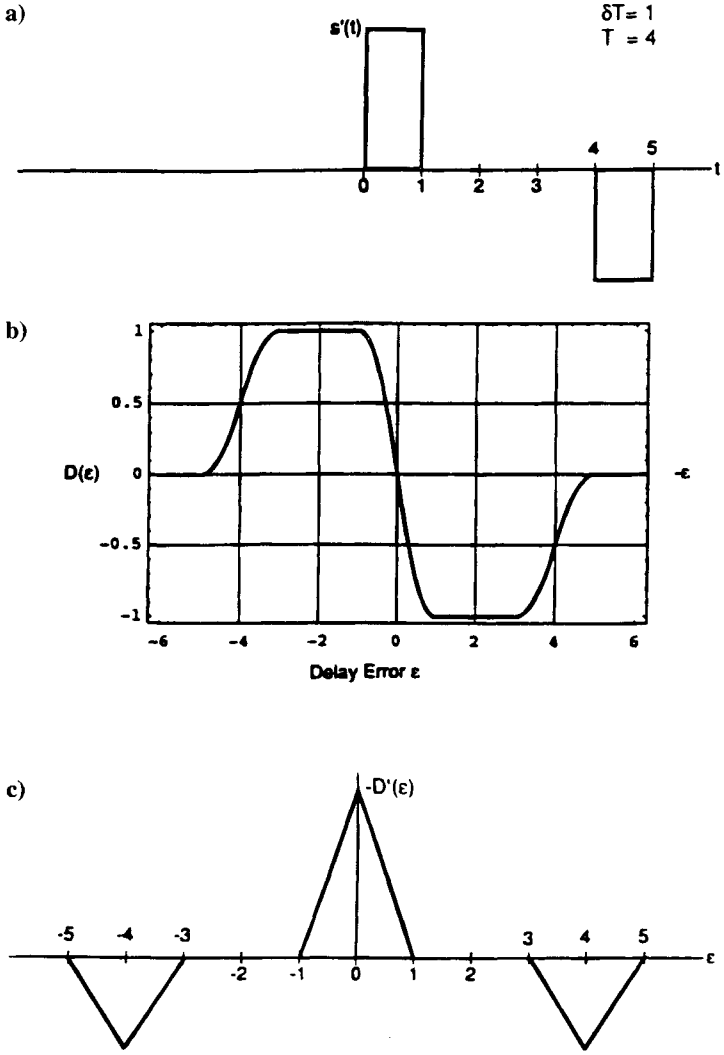

Fig. 11 Coherent delay lock loop discriminator curve $D(\epsilon)$ for a finite rise-time PN signal with a trapezoidal waveform for the optimal delay lock loop. The slope of $D(\epsilon)$," namely, $D'(\epsilon)$, is also shown. The differentiated reference s' is shown in part a. The discriminator curve $D(\epsilon)$ is shown in part b, and the derivative of the discriminator curve (loop gain) $D'(\epsilon)$ is shown in part c. The rise time $\delta T = 1$ and the pulse period $T = 4$ in this example. Thus, the normalized rise time is $\delta T/T = 0.25$. The slope $-D'(0) = 2/(T\delta T)$.

approximates a square wave "doublet." The slope $D'(\epsilon)$ of the discriminator function is as follows:

$$D'(\epsilon) = \frac{\partial}{\partial \epsilon} D(\epsilon) = -\frac{\partial}{\partial \epsilon} \int s(t+\epsilon)s'(t)\mathrm{d}t = -\int s'(t+\epsilon)s'(t)\mathrm{d}t \qquad (12)$$

and is zero for $|\epsilon/T| > 1 + \delta T/T$. If $s'(t)$ is a quasirectangular-shaped "doublet" of Fig. 11a then the slope of $D(\epsilon)$ is a triangular-shaped "triplet," as shown in Fig. 11c.

3. *Coherent Early-Late Gate Delay Lock Loops*

The earliest published delay lock loop specifically for binary PN signals used two reference signals, an early reference and a late reference signal, each binary PN signal with nearly rectangular shape[2] (see Fig. 12a).* Often the difference between the early signal and the late signal is set equal to a chip width T s. The low-pass filters in the two legs of Fig. 12a simply remove broadband noise and self-noise, as discussed in the previous section. Define the (nearly) zero rise-time binary PN reference waveform as $s_o(t)$. Clearly, the difference between the early and late binary reference signals shown in Fig. 13 is identical to the ternary signal at the bottom of Fig. 13 if the waveforms $s_o(t)$ are rectangular with zero rise-time.

The low-pass filtered output $m(t)$ for the early-late version of the DLL can be written from Fig. 12 as follows:

$$\begin{aligned} m(t) &= [As(t+\hat{\tau}) + n(t)][s_o(t+\hat{\tau}-\Delta/2) - s_o(t+\hat{\tau}+\Delta/2)]\,|_{\text{low pass}} \\ &\cong A[R_s(\epsilon-\Delta/2) - R_s(\epsilon+\Delta/2)] + n(t)s_\Delta(t+\hat{\tau})\,|_{\text{low pass}} = AD_\Delta(\epsilon) \\ &\quad + n(t)s_\Delta(t+\hat{\tau})\,|_{\text{low pass}} \\ &\cong AD'_\Delta(0)\epsilon + n(t)s_\Delta(t+\hat{\tau})\,|_{\text{low pass}} \end{aligned} \qquad (13)$$

where $R_s(\epsilon) = E[s(t+\epsilon)(s_o(t))]$ is the crosscorrelation between the reference $s_o(t)$ and the finite rise-time received waveform $s(t)$, $s_\Delta(t) = s_o(t+\Delta/2) - s_o(t-\Delta/2)$ and the DLL discriminator function is $D_\Delta(\epsilon) = R_s(\epsilon+\Delta/2) - R_s(\epsilon-\Delta/2)$. Note that this early-late DLL multiplier output, Eq. (13), is in exactly the same form as that for the quasioptimal DLL and is identical if $s_\Delta(t) = s'(t)$.

Thus, for the trapezoidal PN waveform, the $s'(t)$ ternary pulse sequence of Fig. 11 is exactly equivalent to the properly scaled difference between two time displaced zero rise-time PN sequences, as shown in Fig. 13. Thus, the differentiated delay lock loop of Fig. 12b is also equivalent to an early-late gate delay lock loop with delay offsets of $\pm\delta T/2$, as shown in Fig. 12a. In this chapter, the difference in delay between the early and late reference signals is defined as Δ.

For a signal with bandwidth $B = 10/T$ then if rise time is related to bandwidth by $\delta T = 0.44/B$, the quasioptimal delay differences $\Delta = \delta T = 0.044T$. This offset is significantly smaller than the commonly used delay difference $\Delta = T$.

*The original delay lock loop paper in 1961 defined the differentiated reference that gives an early-late spacing equal to the rise-time for a trapezoidal waveform. However, at that time, the state of the art made a longer delay spacing more practical.

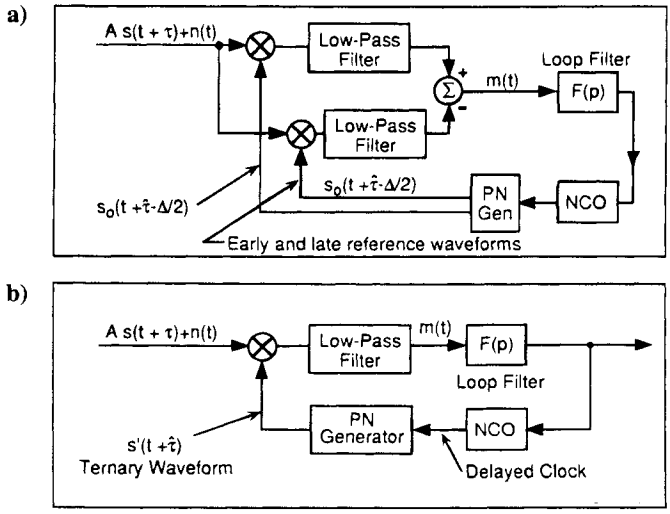

Fig. 12 The early-late delay lock loop with a delay difference between early and late reference signals of δT (part a). For a trapezoidal PN waveform, this loop is mathematically equivalent to the loop shown in part b, the optimal delay lock loop. The early-late delay difference Δ is set at $\Delta = \delta T$, where δT is the pulse rise-time. The NCO is a number-controlled oscillator used to control the clock phase of the PN generator. Part b shows the optimal delay lock loop for the trapezoidal or ternary waveforms of Fig. 9 utilizes a differentiated reference that is a ternary waveform.

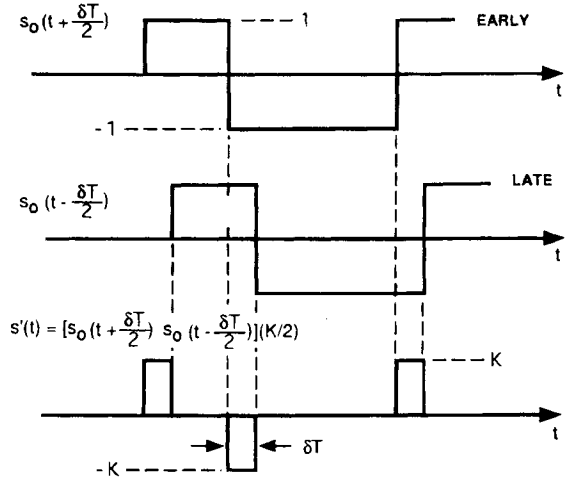

Fig. 13 The pulse sequence representing $s'(t)$ for a trapezoidal finite rise-time δT waveform of Fig. 11 is equal to the difference between two zero rise-time reference PN sequences; namely, $s'(t) = [s_o(t + \Delta/2) - s_o(t - \Delta/2)](K/2)$ with only a scale factor $K/2$ difference if the delay difference is $\Delta = \delta T$.

The smaller delay offset gives a higher accuracy but a slightly smaller threshold acquisition range and a substantially smaller quasilinear region. As discussed later in the subsection on transient performance of the DLL, there are certain disadvantages if the early-late spacing Δ becomes too small.* Note, however, that if the rise-time of the PN signal δT is equal to the chip interval; i.e., $\delta T = T$, then the signal becomes the triangular wave of Fig. 10, and the quasioptimal early-late gate delay lock loop delay offset is the commonly used plus or minus half-chip setting.[2] Thus, the commonly used delay lock loop for an early-late spacing of $T/2$ is optimum only for the triangular wave PN signal.†

If the received signal has an ideal rectangular pulse shape, the discriminator characteristic $D(\epsilon)$ for the early-late reference signal with early–late offsets of $\pm T/2$; i.e., $\Delta = T$ is piecewise linear, as shown in Fig. 14, and has a normalized one-sided width $(\epsilon/T) = 1.5$, and thus, gives a nearly 50% wider acquisition range than the DLL with narrow correlator spacing for $\delta T/T << 1$. However, as shown later, the noise performance of the DLL that uses an approximation to the differentiated reference, a PN sequence of narrow pulses or equivalently a narrow early-late spacing close to the rise-time of δT, gives better noise performance than that for the early-late gate DLL with the wide early-late spacing, $\Delta = T$.

It is informative to compare the noise performance of two different delay lock loop discriminator characteristics that can be used for the same received trapezoidal pulse waveform of Fig. 9. Consider a pulse of width $T = 4$ for this waveform with a rise-time $\delta T = 1$ for a ratio $\delta T/T = 0.25$. The two different reference waveforms are shown in Fig. 15. Figure 16 shows the discriminator characteristic for the quasioptimal reference waveform $s'(t)$ as the solid curve where its discriminator characteristic $D(\epsilon) = R'(\epsilon)$. The dashed curve is the discriminator characteristic for an early-late gate delay lock loop with an early-late separation of $\Delta = T$. Note that both discriminator curves have the same slope at $\epsilon = 0$. However, the effective noise spectral density is four times as large for the loop with the $\Delta = T$ separation because the effective noise is time gated by the duty factor. Thus, the noise performance of the quasioptimal loop is superior for this trapezoidal signal for small delay error.

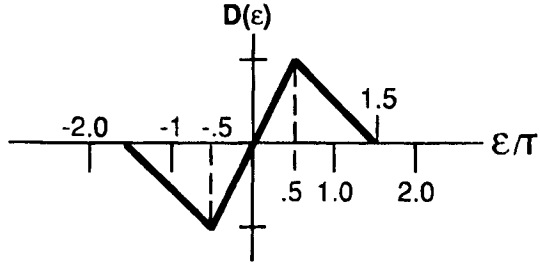

Fig. 14 Delay lock loop discriminator curves for offset reference signals $s(t \pm T/2)$; i.e., $\Delta = 1$, and an ideal rectangular received PN signal.

*During acquisition, we may have to increase the loop gain to improve the pull-in performance.

†Note that there are more recent papers that discuss the use of narrower time separations between the early and late gate signals. See also the next chapter.[15,16]

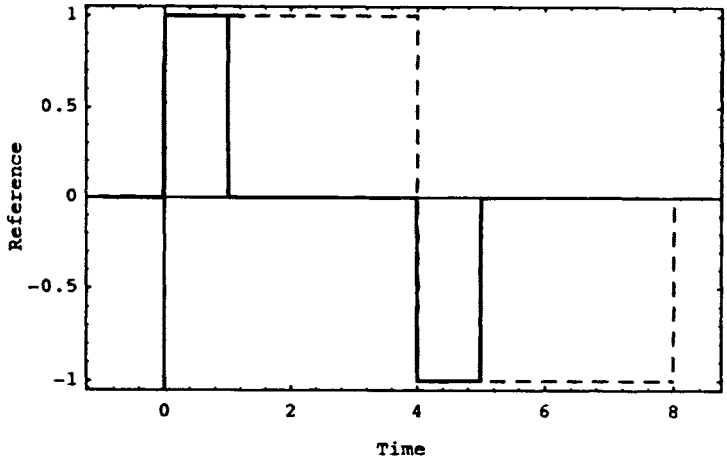

Fig. 15 Quasioptimal reference waveform $s'(t)$ for the trapezoidal shaped PN pulse waveform, $\Delta = \delta T = T/4$ (solid curve), and a reference with an early-late separation of T. The received Trapezoidal pulse waveform has a pulse duration of $T = 4$ and a $\delta T = 1$ rise-time. The dashed curve shows the commonly used early-late reference waveform with an early-late separation of $\Delta = T$ s.

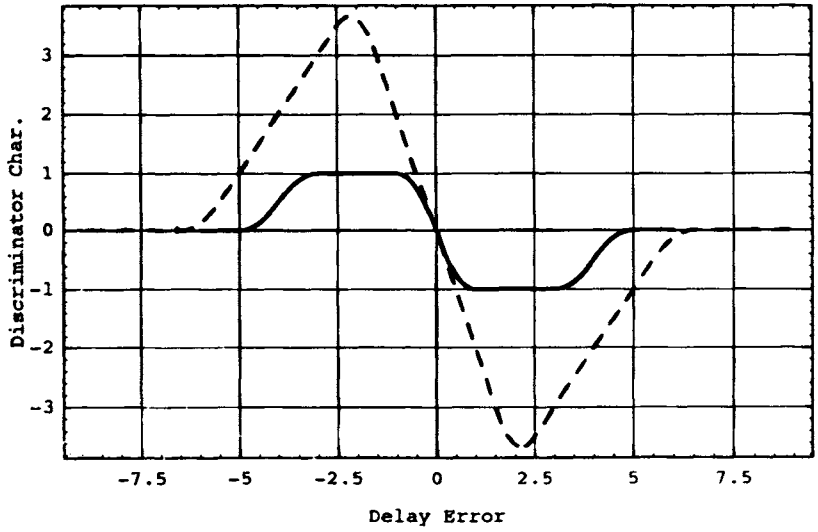

Fig. 16 Quasioptimal and early-late gate discriminator characteristics for the trapezoidal waveform of Fig. 10b with $T = 4$ and $\delta T = 1$ for a rise-time ratio $\delta T/T = 0.25$. The solid curve, quasioptimal, is obtained using the differentiated reference $s'(t)$. The dashed curve is obtained using an early-late gate rectangular reference with an early-late separation of T. Note that the slope of both discriminator characteristics at the origin is approximately equal to $D(0) \cong -2$.

Chapter 8

GPS Receivers

A. J. Van Dierendonck
AJ Systems, Los Altos, CA 94024

I. Generic Receiver Description

A. Generic Receiver System Level Functions

A SYSTEM level functional block diagram of a generic GPS receiver is shown in Fig. 1. The generic receiver consists of the following functions: 1) antenna; 2) preamplifier; 3) reference oscillator; 4) frequency synthesizer; 5) downconverter; 6) an intermediate frequency (IF) section; 7) signal processing; and; 8) applications processing.

In a general sense, not all GPS receivers perform navigation processing. Many perform time transfer or differential surveying, or simply collect measurement data. Thus, the last function is more appropriately called applications processing, thus covering a broad set of applications.

The antenna may consist of one or more elements and associated control electronics, and may be passive or active, depending upon its performance requirements. Its function is to receive the GPS satellite signals while rejecting multipath and, if so designed, interference signals. The preamplifier generally consists of burnout protection, filtering, and a low-noise amplifier (LNA). Its primary function is to set the receiver's noise figure and to reject out-of-band interference.

The reference oscillator provides the time and frequency reference for the receiver. Because GPS receiver measurements are based on the time-of-arrival of pseudorandom noise (PRN) code phase and received carrier phase and frequency information, the reference oscillator is a key function of the receiver. The reference oscillator output is used in the frequency synthesizer, from which it derives local oscillators (LOs) and clocks used by the receiver. One or more of these LOs are used by the downconverter to convert the radio frequency (rf) inputs to intermediate frequencies (IFs) that are easier to process in the IF section of the receiver.

The purpose of the IF section is to provide further filtering of out-of-band noise and interference and to increase the amplitude of the signal-plus-noise to a workable signal-processing level. The IF section may also contain automatic

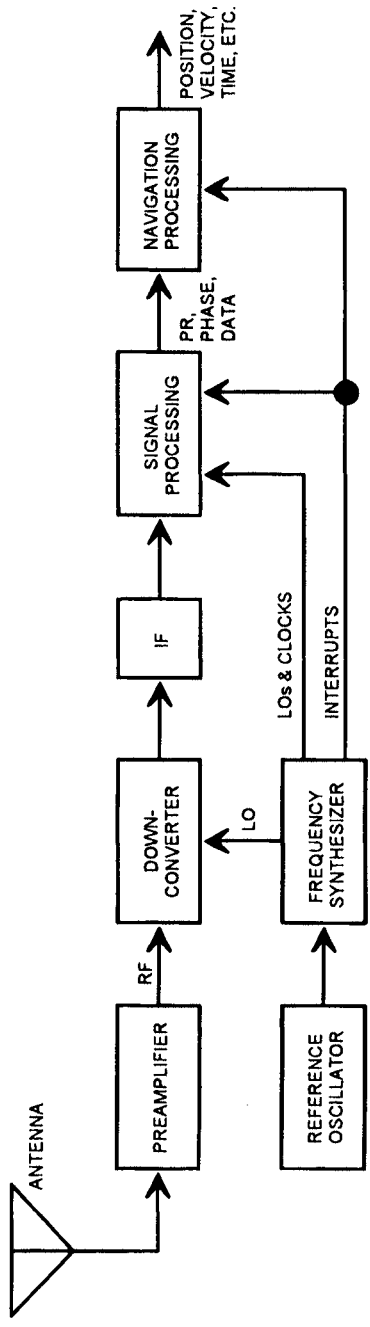

Fig. 1 Generic GPS receiver functional block diagram.

gain control (AGC) circuits to control that workable level, to provide adequate dynamic range, and to suppress pulse-type interference.

The signal-processing function of the receiver is the core of a GPS receiver, performing the following functions:

1) splitting the signal-plus-noise into multiple signal-processing channels for signal-processing of multiple satellites simultaneously;
2) generating the reference PRN codes of the signals;
3) acquiring the satellite signals;
4) tracking the code and the carrier of the satellite signals;
5) demodulating the system data from the satellite signals;
6) extracting code phase (pseudorange) measurements from the PRN code of the satellite signals;
7) extracting carrier frequency (pseudorange rate) and carrier-phase (delta pseudorange) measurements from the carrier of the satellite signals;
8) extracting signal-to-noise ratio (SNR) information from the satellite signals; and
9) estimating a relationship to GPS system time.

The outputs of the signal-processing function are pseudoranges, pseudorange rates and/or delta pseudoranges, signal-to-noise ratios, local receiver time tags, and GPS system data for each of the GPS satellites being tracked, all of which are used by the applications-processing function. Most of this chapter is devoted to the details of the signal-processing function.

The applications-processing function controls the signal-processing function and uses its outputs to satisfy application requirements. These requirements vary with application. Although GPS is primarily a satellite navigation system, the applications of a GPS receiver are diverse. Some of the other applications with significantly differing processing requirements are as follows:

1) time and frequency transfer;
2) static and kinematic surveying;
3) ionospheric total electron content (TEC) and amplitude and phase scintillation monitoring;
4) differential GPS (DGPS) reference station receivers; and
5) GPS satellite signal integrity monitoring.

The common link between these diverse applications is that they all use the same signal-processing measurements in one form or another. However, because of bandwidth and accuracy requirements imposed by these various applications, the requirements on signal-processing function also differ. In general, GPS receivers do not meet the signal-processing and applications-processing requirements for all the applications. Special processing is required for some of the applications.

B. Design Requirements Summary

In addition to the variation in signal- and applications-processing requirements with application, the receiver front-end functions will also have varying design requirements with application. In the following, these variations are noted by function, with details provided later in the chapter.

1. *Antenna*

The parameters that dictate the antenna requirements are as follows: gain vs azimuth and elevation, multipath rejection, interference rejection, phase stability and repeatability, profile, size, and environmental conditions. The gain requirements are a function of satellite visibility requirements and are closely related to multipath rejection, and somewhat related to interference rejection. The goal is to have near uniform gain toward all satellites above a specified elevation angle, but, at the same time, reject multipath signals and interference typically present at low elevation angles. These are usually conflicting requirements. Some multipath rejection can also be achieved by reducing the left-hand, circularly polarized (LHCP) gain of the antenna without reducing the right-hand, circularly polarized (RHCP) gain. This is because the satellite signals are RHCP signals; whereas, reflected multipath signals usually tend to be either linearly polarized (LP) or even LHCP, depending upon the dielectric constant of the reflecting surface.

Interference rejection can also be achieved using a phased-array antenna, where the relative phase received from each antenna is controlled to "null" out the interference in the combined reception. This type of antenna is called a controlled-reception pattern antenna (CRPA), which is usually used only for military applications.

Phase stability and repeatability are important in differential surveying applications when differential carrier-phase accuracy is important. In this case, orientation of the antenna is important, taking advantage of phase repeatability.

Antenna profile is important in dynamic applications, such as for aircraft and missiles. Normally, requiring a low profile for those applications must be traded off against a desired gain pattern or other desired parameter.

Environmental conditions dictate the type of material used for the antenna and whether or not a radome is required. Some materials change their dielectric properties as a function of temperature.

2. *Preamplifier*

The preamplifier generally consists of burnout protection, filtering, and an LNA. The parameters that dictate the preamplifier requirements are as follows: the unwanted rf environment as received through the antenna, losses that precede and follow the preamplifier, and desired system noise figure (or noise temperature) as derived from overall receiver performance requirements. The gain of the preamplifier is not a system-level requirement, per se, but a derived requirement that satisfies that system level requirement.

The unwanted rf environment as received through the antenna affects the preamplifier in two ways. Either it could cause damage to the preamplifier electronics, or cause saturation of the preamplifier and circuitry that follows. Of course, except for damage prevention, we can do nothing to suppress the rf environment, as passed by the antenna, at frequencies that are in the bandwidth of the desired GPS signal. (Actually, there are techniques such as adaptive equalizers, usually applied at IF. These techniques are not discussed in this chapter.) That environment is considered to be either jamming or unintentional interference. However, suppression of the rf environment out of the desired GPS

signal band can be accomplished by filtering, either before, during, and/or after amplification. When it is accomplished, it is based upon a trade-off between system noise figure requirements and filter insertion loss and bandwidth efficiency. Suppression of in-band and out-of-band damaging interference is usually accomplished with diodes that provide a ground path for strong signals. In the case of lightning protection, more complex lightning arrestors are sometimes used.

The system noise figure is set using an LNA that provides enough gain to cause any losses inserted after the LNA to have a negligible effect. Losses inserted prior to the LNA add directly to the system noise figure and are not affected by the LNA.

3. *Reference Oscillator*

The requirements on reference oscillators for GPS receivers have changed considerably over the years, mainly because of their expense. A high-quality oscillator can be the most significant cost item of a modern receiver. Thus, there have been compromises made on oscillator performance. Also, the oscillator's performance is not as critical in the modern multichannel receivers, especially in most commercial applications. However, there are some commercial and military applications where reference oscillator performance is critical. Typical requirements applied to reference oscillators are as follows:

1. *Size*—Stable oven-controlled crystal oscillators (OCXOs) and rubidium oscillators can be relatively large. Temperature-compensated crystal oscillators (TCXOs) are relatively small. Larger oscillators have more temperature inertia.
2. *Power*—Oven-controlled crystal and rubidium oscillators consume significant power.
3. *Short-term stability* caused by temperature, power supply, and natural characteristics. Short-term stability affects the ability to estimate and predict time and frequency in the receiver.
4. *Long-term stability* caused by natural characteristics, including crystal aging
5. *Sensitivity to acceleration*—g force and vibration sensitivity. Vibration causes phase noise, and dynamic g forces affect the ability to estimate time and frequency in the receiver.
6. *Phase noise*—high-frequency stability. Phase noise degrades the signal-processing performance of the receiver.

4. *Frequency Synthesizer*

Mostly, the requirements placed on the frequency synthesizer are derived requirements and the receiver designer's choice. Its design is based on the designer's *frequency plan,* which defines the receiver's IF frequencies, sampling clocks, signal processing clocks, etc. The frequency plan requires careful analysis to ensure adequate rejection of mixer harmonics, LO feed-through, unwanted sidebands and images. A key design parameter for the synthesizer is the minimization of phase noise generated in the synthesizer. Phase noise generated at the reference oscillator frequency is multiplied by the ratio of the rf frequency to its frequency through the synthesis process. Thus, the design of the synthesizer is critical to the performance of the GPS receiver.

The frequency synthesizer may also be required to generate local clocks for signal processing and interrupts for applications processing. This requirement might be assigned to signal processing. These local clocks comprise the receiver's time base.

5. *Downconverter*

The downconverter mixes LOs generated by the frequency synthesizer with the amplified rf input to IF frequencies, and, if so designed, IF frequencies to lower IF frequencies. This process implements the frequency plan, which, again, is the receiver designer's choice. The outputs of the mixers include both the lower and upper sideband of the mixing process, either of which can be used as an IF frequency. The unwanted sideband, LO feed-through, and harmonics are rejected by filtering at the IF. The unwanted image is filtered at rf before the mixing process. Because all of these processes are a function of the frequency plan, the requirements placed upon the downconverter are also derived requirements.

6. *Intermediate Frequency Section*

The requirements on the IF section are as follows:

1) Final rejection of out-of-band interference, unwanted sidebands, LO feed-through, and harmonics. The bandwidth of this rejection is a trade-off against correlation loss caused by filtering. In addition, the rejection of wide-band noise is required to minimize aliasing in a sampling receiver.

2) Increase the amplitude of the signal-plus-noise to workable levels for signal processing and control that amplitude as required for signal processing (AGC).

3) Suppress pulse-type interference.

4) Depending upon design, convert the IF signal to a baseband signal composed of in-phase (I) and quadraphase (Q) signals.

7. *Signal Processing*

As previously stated, signal processing may include the generation of the local clocks and interrupts. However, its prime requirement is to provide the GPS measurements and system data from selected satellites required to perform the navigation or other applications function. How this requirement is met constitutes the signal–processing-derived requirements and is based upon the receiver designer's choice. The functions of the signal processing are listed in the beginning of this section.

8. *Applications Processing*

The requirements for applications processing are to control the signal processing to provide the necessary measurements and system data and to use those measurements and system data to perform one or more of a variety of GPS applications. The processing requirements for these applications are covered elsewhere in this volume.

II. Technology Evolution

A. Historical Evolution of Design Implementation

In this section, the historical evolution of GPS receiver design implementation is described, dating back to the mid-1970s, the start of GPS Phase I concept validation. This does not include the development effort during the 621B program, predecessor to the GPS.

The first seven GPS receivers were mostly developed concurrently. These were the Phase I sets—the X Set, the Y Set, the Z Set, the Manpack developed by Magnavox, the High Dynamic User Equipment (HDUE) developed by Texas Instruments, the Advanced Development Model (ADM) developed by Collins Radio, and a satellite-monitoring receiver developed by Stanford Telecommunications, Inc. Three of these receivers, the Z Set, Manpack, and the satellite-monitoring receiver, had analog baseband signal processing and used processors only for the applications-processing function. The other three used microprocessors of one form or another to perform some of the signal processing. Needless to say, these receivers were all quite large, except for the medium sized Z Set and the Manpack. However, these two receivers had only one channel with one correlator, using this channel in a sequencing mode.

The rf sections of these receivers used discrete components, such as transistors, including large cavity filters. Circuit isolation was difficult. Consequently, there were a number of IF stages (three or four or more) to distribute the gain over a number of frequencies. This made the frequency synthesizers very complicated. Furthermore, the high-frequency LOs were generated using cavity multipliers.

The lower-frequency analog signal-processing sections were made up of operational amplifiers and other discrete components. The digital portions, such as the code generators and clocks, consisted of medium-scale integrated (MSI) circuits, at best. CMOS circuitry was in its infancy at that time, so higher-power consumption circuitry was used. The X Set used a bit-slice process controller for its baseband signal processing, which was state of the art at that time. Computers ranged from Hewlett Packard minicomputers to DEC large-scale integrated (LSI) computers. A structured version of Fortran was used by Magnavox as the applications-processing language; whereas, assembler language was used for the baseband signal processing.

The evolution into the Phase II GPS receivers was not that dramatic, although analog baseband signal processing was completely replaced with microprocessors and some MSI gave way to LSI. The evolution into the Phase III GPS receivers included some digital gate arrays and more powerful microprocessors. However, multiple IF stages and complicated frequency plans were still common. Signal processing was still not accomplished digitally, and the receivers were generally still quite large and expensive. Some of these receivers are still being produced today (the RCVR-3A airborne set and the RCVR-3S shipboard set). The operational control segment (OCS) monitor stations still use large hybrid analog/digital baseband receivers. However, these receivers are no longer in production.

B. Current Day Design Implementation

Except for the RCVR-3A and the RCVR-3S, all GPS receivers in production today are *probably* all true digital signal-processing receivers. I use the word

probably because there are so many different GPS receivers in existence today, that one could never know. However, the consensus is that, in order to produce inexpensive receivers, they have to perform true digital signal processing. One reason for this is because almost all new GPS receivers have at least 4 full tracking channels; whereas, some have up to 24 to 36 channels for dual-frequency processing. Even the new military receivers, which usually lag in technology, have up to six tracking channels. The evolution of CMOS very-large scale integration (VLSI) technology has caused an explosion in the capabilities of new GPS receivers. The two technologies were made for each other. The processing speed of the new CMOS matches the signal-processing requirements for GPS receivers. Five or more channels on a chip are the norm in new GPS receivers.

The front-end electronics of GPS receivers have also experienced a dramatic evolution with the introduction of monolithic microwave integrated circuits (MMIC), stripline filter techniques, chip capacitors and resistors, high-speed digital integrated circuits, surface acoustic wave (SAW) filters, and surface mount printed circuit boards (PCBs).

1. Radio Frequency Electronics

The use of gallium arsenide (GaAs) MMIC for GPS receivers has been attempted and used on occasion, but with limited success. Most modern receivers use silicon bipolar technology because of efficiency and cost. Although the Defense Advanced Research Projects Agency (DARPA) sponsored Rockwell Collins on a program for the development of gallium arsenide (GaAs) MMIC for GPS receivers, Rockwell abandoned its use in favor of silicon bipolar in their miniature airborne GPS receiver (MAGR) design for those very reasons.[11] The GPS frequencies are not high enough to warrant the use of highly integrated GaAs circuitry. Most rf designers agree that the use of GaAs is usually limited to a front-end FET, and little more than a marketing "buzz word." Any advantage gained in using GaAs with respect to noise figure and power dissipation is lost because of circuit-matching problems at the GPS frequencies.

To an extent, the same is true for large-scale MMIC, even if silicon bipolar is used. However, in this case, the use of large-scale MMIC is a trade-off between size and circuit efficiency. Large-scale MMIC is certainly smaller, but may not be as efficient as smaller-scale MMIC in terms of power dissipation, cost, and out-of-band rejection. That is because the large-scale MMIC is designed for a wide range of applications, not just for a GPS receiver. Furthermore, in the rf and IF sections of a receiver, filters must be injected between stages of amplification and mixing for out-of-band rejection and gain stability. Efficient filtering cannot be accomplished in the MMIC chips.

Times are changing, however. GEC Plessey has introduced a silicon bipolar MMIC chip, the GP1010, that was developed specifically for GPS receivers.[2] Its input is at rf at the GPS L_1 frequency, although already amplified and filtered via a preamplifier. Intermediate frequency filtering is not included on the chip. Its output is a stream of 1.5-bit samples for input to digital signal processing. The chip also contains the frequency synthesizer and AGC, but not the loop filters.

2. Frequency Synthesizer Electronics

The use of cavity multipliers has been replaced with phase–lock-loops (PLLs) using voltage-controlled oscillators (VCOs) and high-speed digital divider circuits (prescalers). Chips are commercially available that contain programmable prescalers. However, because of the clocking speeds required for the first LO provided by these frequency synthesizers, sometimes the frequency of the VCO and clocking speed of the prescaler are half what is required, and a frequency doubler or a second-harmonic mixer is used to achieve the *L*-band LO. However, these components are still small and quite simple. In the end, we have small, efficient frequency synthesizer electronics that are significantly smaller and lower power than technology used 5–10 years ago. As described above, the GEC Plessey GP1010 chip contains the VCO and prescalers, but it is not programmable.[2]

3. Down Conversion and Intermediate Frequency Electronics

The conversion from rf to IF has generally become a silicon bipolar MMIC implementation, where the MMIC includes mixing and a stage or two of amplification. The VCO for the LO may also be included. Once at IF, surface acoustic wave (SAW) filters provide a small, efficient means of final filtering to minimize unwanted out-of-band signals and noise.

4. Reference Oscillators

Unfortunately, the development of good, stable reference oscillators has not kept up with the pace of the development of the other sections of a GPS receiver. There have been improvements, but, depending upon the ultimate stability required, the oscillator can be the most expensive and largest component in the receiver. For example, for very good stability, not including that achieved with relatively large and expensive atomic oscillators, a crystal oscillator must be ovenized to minimize frequency excursions that are the main cause of frequency instability. Unfortunately, to have temperature inertia, mass is required. Thus, although the sizes of these oscillators have been reduced over the years, they are still relatively large. In fact, these smaller oscillators are not usually as stable as the older, larger, oscillators.

The advancement of digital signal processing and multiple receiver channels has allowed the use of TCXOs in most commercial applications. This has prompted some improvement in TCXO performance over what had been the norm in the past. However, that improvement has not been dramatic, although the size and cost of the TCXOs have been reduced significantly.

III. System Design Details

In this section, the block diagram of Fig. 1 is expanded, and design details are presented, starting with the hardware and following with the software part of the digital signal processing. Only the implementation of modern digital receivers is presented along with some trade-offs between different modern implementations. Specifically, two receiver designs that are familiar to the author are used as examples—the Rockwell Collins miniature airborne GPS receiver

(MAGR), an example of a military receiver, and the NovAtel GPSCard™, an example of a commercial receiver. A functional overview of the MAGR is shown in Fig. 2.[1] Details of these functions may vary from receiver to receiver, but they exist in one form or another in all modern receivers. Although the MAGR is a dual-frequency receiver that receives both L_1 and L_2 signals and both the C/A- and P-codes, processing that is common for those signals is presented only once.

A. Signal and Noise Representation

Before describing the remainder of the receiver operations, it is appropriate to provide a representation of the received signal and noise in both the time domain and the frequency domain. The signal is represented as follows:

$$s(t) = AC(t)D(t)\cos[(\omega_0 + \Delta\omega)t + \phi_0] \tag{1}$$

where A = signal amplitude; $C(t)$ = PRN code modulation (± 1); $D(t)$ = 50 bps data modulation (± 1); $\omega_0 = 2\pi f_0$ = carrier frequency (L_1 or L_2); $\Delta\omega = 2\pi\Delta f$ = frequency offset (Doppler, etc.); and ϕ_0 = nominal (but ambiguous) carrier phase.

For the purpose of the processing described herein, it is necessary to represent only one component of the L_1 signal, because one of the two components (in-phase or quadrature) does not correlate with the receiver channel's reference code in channel tracking the desired code. L_2 processing is identical to that of the L_1 signal except that L_2 acquisition and tracking are usually aided with information obtained by tracking the more powerful L_1 signal.

In the frequency domain, the spectral density of the signal is the spectral density of the PRN code centered at $\pm(\omega + \Delta\omega)$. At baseband, this spectral density is as follows:

$$S_s(\omega) = \frac{A^2 T_c}{2} \frac{\sin^2(\omega T_c/2)}{(\omega T_c 2)^2} \tag{2}$$

where T_c is the PRN code chip width, or the inverse of the PRN code chipping rate. Although the C/A-code spectrum is a line spectrum, this representation suffices for most of the processing described herein. Exceptions are noted as they arise.

Signal power in a $2B$ Hz two-sided bandwidth is given by the following:

$$P_s = \frac{1}{2\pi} \int_{-2\pi B}^{2\pi B} S_s(\omega)\mathrm{d}\omega \tag{3}$$

If $B = \infty$, $P_s = A^2/2$. If $B = 1/T_c$, $P_s = 0.9\,A^2/2$, resulting in a 0.45 dB signal loss.

Ambient noise is represented in the frequency domain as white noise with a constant spectral density $N_0/2$. If passed through a unity-gain bandpass filter with a two-sided noise bandwidth $2B$ Hz centered at frequency ω_0, the spectral density appears as illustrated in Fig. 3. The resulting noise power in the two-sided bandwidth is as follows:

$$P_n = 2N_0 B \tag{4}$$

and a signal-to-noise ratio in a $2B$ two-sided noise bandwidth of

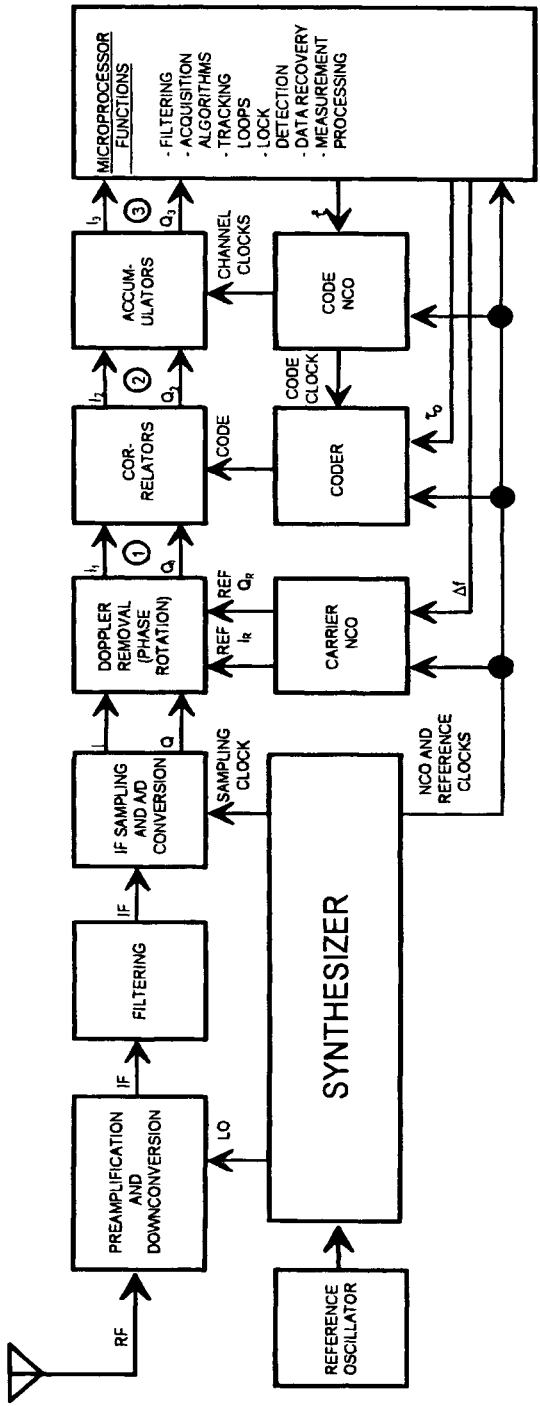

Fig. 2 Functional block diagram of the MAGR.

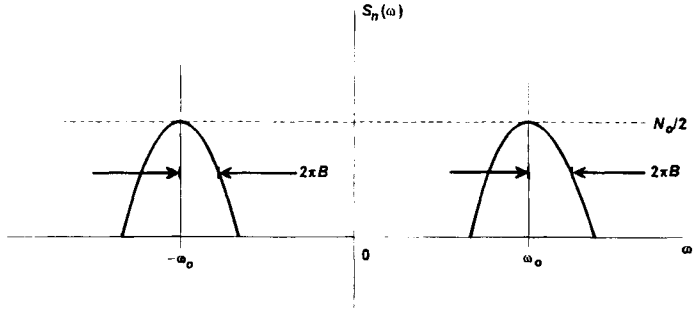

Fig. 3 Spectral representation of ambient noise.

$$\frac{P_s}{P_n} = \frac{A^2}{4N_0B} \tag{5}$$

The output of the bandpass filter has two equivalent time domain representations[3]:

$$n(t) = x(t)\cos\omega_0 t - y(t)\sin\omega_0 t \tag{6}$$

$$n(t) = r(t)\cos[\omega_0 t + \varphi(t)] \tag{7}$$

where $x(t)$ and $y(t)$, the in-phase and quadraphase components, respectively, are bandlimited Gaussian processes with the properties defined as follows:

$$\begin{aligned} E[x(t)] &= E[y(t)] = 0 \\ E[x^2(t)] &= E[y^2(t)] = E[n^2(t)] = P_n \\ E[x(t)y(t)] &= 0 \end{aligned} \tag{8}$$

Furthermore, $r^2(t) = x^2(t) + y^2(t)$ has a chi-squared (or Rayleigh) distribution with two DOF, and

$$\varphi(t) = \tan^{-1}\left[\frac{x(t)}{y(t)}\right] \tag{9}$$

is uniformly distributed between 0 and 2π radians.

B. Front-End Hardware

The hardware is comprised of the front-end electronics and part of the digital signal processing. The other part of the digital signal processing is implemented in software.

1. Antenna

The following requirements were placed upon the Fixed Reception Pattern Antenna (FRPA3) for Rockwell's military receivers[4]:

1) *rf:* "The GPS antenna shall accept the GPS navigation signals at both the L_1 and L_2 frequencies and output them to the GPS antenna electronics."[4] This implies either a wide-band antenna that accepts both frequencies and all frequencies between them, or implies two antennas packaged in a single unit. Both types of antennae are available, because some are naturally narrow band while others are wide band.

2) *Antenna gain:* "The GPS antenna shall provide a minimum gain of −2.5 dBic to a RHCP signal over a 160° solid angle cone of coverage (above 10° elevation angle) for signals in both the L1 and L2 bandwidths. Gain shall be measured at the L1 and L2 carrier frequencies at the prevailing ambient temperature using a standard gain horn for comparison. The combined effects of environmental temperature range and bandwidth . . . shall not cause the gain to be less than −3.3 dBic. These gain requirements apply when using a test ground plane."[4] (This ground plane matches the housing of the antenna electronics for shipboard installation.)

3) *Other antenna specifications:* Other FRPA3 specifications are as follows:

a) *Voltage standing wave ratio (VSWR):* ≤2:1 (referenced to 50 ohms over L_1 and L_2 bands)

b) *dc impedance @ signal interface:* 0 ohms

c) *Connector:* Single TNC female receptacle

d) *Size:* Less than 6 in. in diameter and 1.75 in. in height, including connector

The dc impedance of 0 ohms provides lightning protection. More than one vendor supplies the antenna and not necessarily through Rockwell Collins. Typical gain patterns from one vendor (Sensor Systems, Inc. S67-1575-14) are shown in Fig. 4. This model has two narrowband antennas packaged in a single unit. The Sensor Systems antenna has a diameter of 3.5 in. and a height of 0.565 in.[5]

The following technical specifications are given for a Sensor Systems' commercial aeronautical antenna (S67-1575-16), which was designed to meet ARINC 743A characteristics[5,6]:

1) *rf:* 1575 ±2 Mhz with a VSWR ≤ 1.5:1 or 1575 ±10 MHz with a VSWR ≤2:1.

2) *antenna gain:* The gain pattern is specified as follows:

> −1 dBic to 75 deg from vertical
> −2.5 dBic to 80 deg from vertical
> −4.5 dBic to 85 deg from vertical
> −7.5 dBic at 90 deg from vertical

The RHCP gain pattern is shown in Fig. 5.

2. *Receiver Front End*

The receiver front end consists of filtering and limiting, an LNA, a frequency synthesizer, downconversion, and conversion to baseband. Initial filtering, limiting, and LNA can be housed with the antenna to comprise an integrated antenna electronics. This is an optional configuration of the MAGR and is usually the case in commercial receivers. In the case of the MAGR, the following requirements are imposed:[7]

1. *Preselector filtering:* The preselector filtering is required to reject out-of-band interference and to limit the noise bandwidth of the antenna electronics.

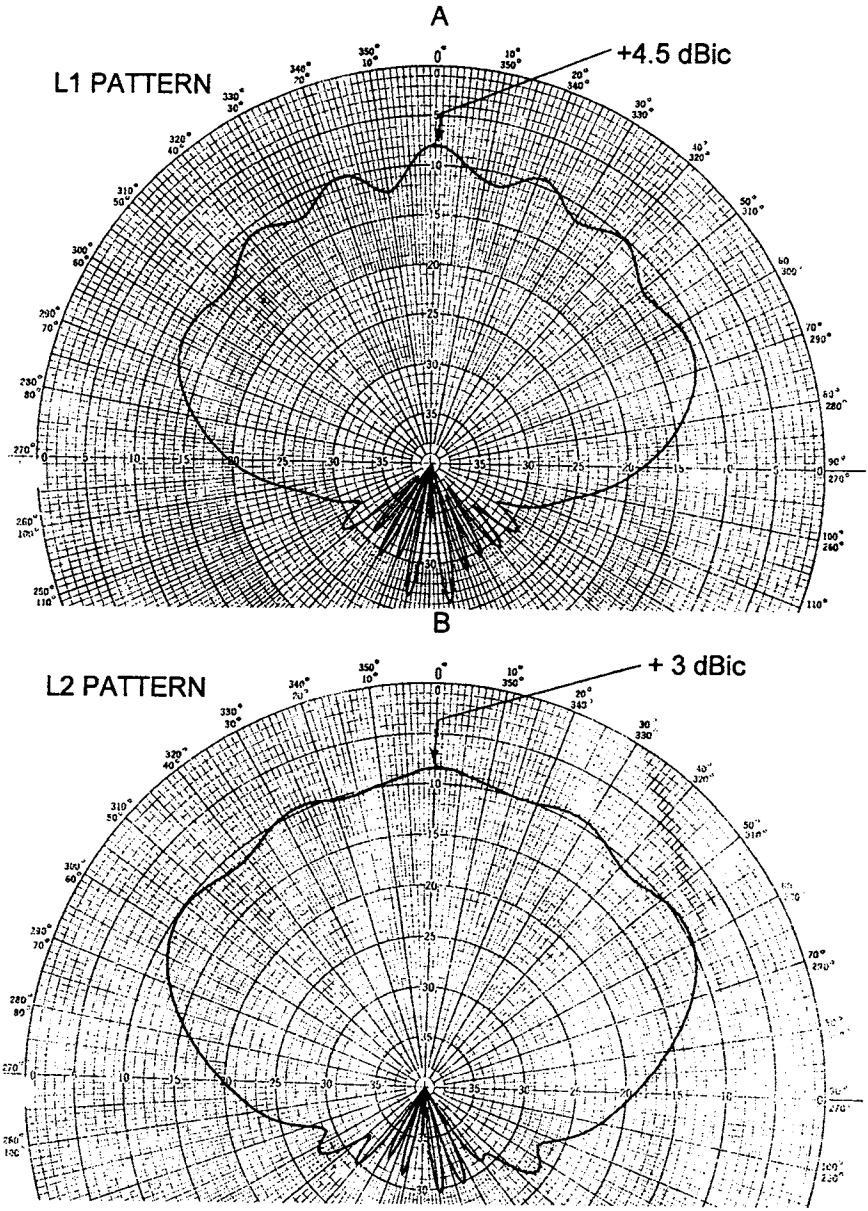

Fig. 4 Fixed Reception Pattern Antenna 3 antenna gain patterns (courtesy of Sensor Systems, Inc.).

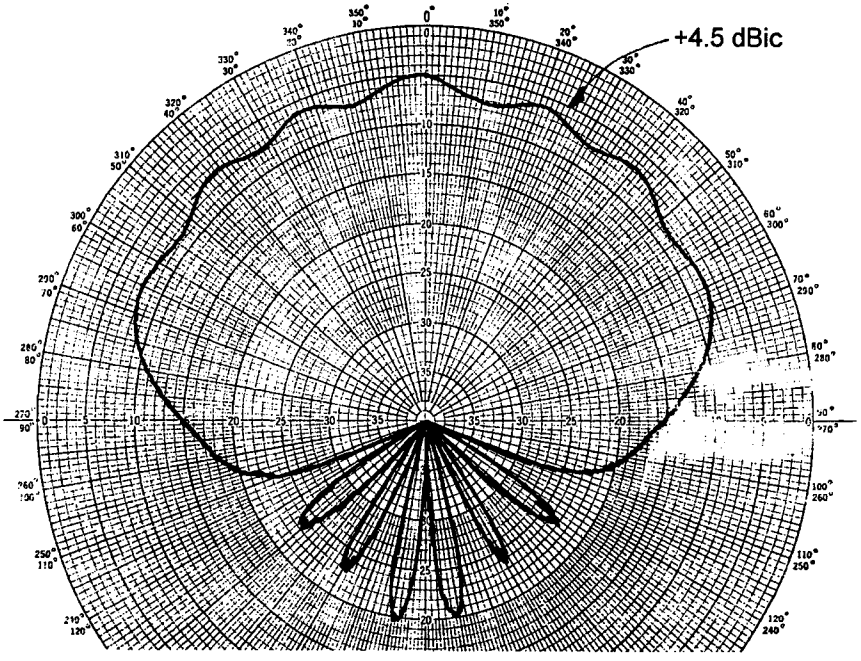

Fig. 5 Commercial L_1 Antenna Gain Patterns (courtesy of Sensor Systems, Inc.).

The filtering shall be dual-band centered at L_1 and L_2, with a noise bandwidth of 80 MHz in each band. The insertion loss shall be sufficiently low to meet overall gain and noise figure requirements.

2. *Burnout protection:* The antenna electronics shall not incur damage or performance degradation after being subject to a peak signal power density of 69 kW/m^2 for not more than 10 μs, or a continuous signal power density of 348 W/m^2 in either band of frequencies.

3) *Gain and noise figure:* The antenna electronics, including interconnecting cabling, preselector, and protection circuitry, shall have a minimum overall gain of 23 dB, with a noise figure of 4 dB at the input to the MAGR receiver.[8] The maximum overall gain shall be 33 dB.

The Sensor Systems' commercial ARINC 743A antenna described is also available with an internal preamplifier with 26 ±3 dB gain with an internal interference rejection filter and an LNA (S67-1575-52). A single TNC connector carries both the L_1 signal and dc power to the LNA (+4 to +24 VDC at 25 mA, maximum). Out-of-band rejection is 35 dB at 1625 MHz.

3. *Noise Figure Computations*

Figure 6 provides a model of a receiver front end for the purposes of computing the receiver and system noise figure and noise temperature. In general, the system noise figure (in dB) is related to system noise temperature (in Kelvin) as follows[9]:

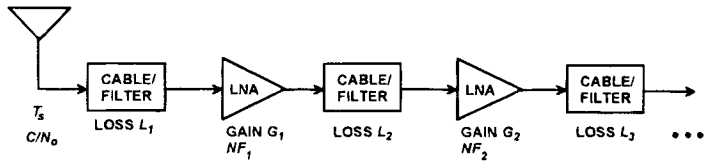

Fig. 6 Noise figure computation model.

$$\mathrm{NF} = 10 \log_{10}\left(1 + \frac{T_{\mathrm{sys}}}{T_0}\right) \tag{10}$$

where $T_0 = 290\ \mathrm{K} = 24.6\ \mathrm{dB{-}K}$.

The corresponding noise density, in W/Hz, is $N_0 = K_B T_{\mathrm{sys}}$; where $K_B = -228.6$ dBW/K−Hz $= 1.380 \times 10^{-23}$W/K−Hz, is the Boltzmann constant.[9] Based upon the model given in Fig. 6, the system noise temperature is computed as follows:[10,11]

$$\begin{aligned} T_{\mathrm{sys}} &= T_s + T_R \\ &= T_s + T_0[L_1 - 1 + L_1[\mathrm{NF}_1 - 1 + G_1^{-1}[L_2 - 1 \\ &\quad + L_2\,[\mathrm{NF}_2 - 1 + G_2^{-1}[L_3 - 1 + \cdots]]]]] \end{aligned} \tag{11}$$

where T_s is the source (antenna) temperature; T_R is the receiver noise temperature; and the L_i, NF_i, and G_i are loss, amplifier noise figure, and amplifier gain of each stage i, respectively, all given in ratio. This formula is known as the *Friis Formula.* Note that the loss and noise figure of the first stage affects the system noise figure directly; whereas, any losses after the first amplification are reduced proportional to that gain. Thus, the first stage is said to *set* the system noise figure or noise temperature.

Note, also, that the source temperature adds directly to the system noise temperature. Normally, this is the antenna sky temperature, which is relatively low with respect to the ambient noise temperature T_0. One exception is when the receiver is connected directly to a GPS signal generator or simulator, in which the source temperature is the ambient noise temperature (290 K), which is a worst-case situation. Normally, adjustments to the signal power must be made to compensate for this. Note that in this case, if the first stage gain is high enough, the noise density is simply as follows:

$$\begin{aligned} N_0 &= K_B T_0 \mathrm{NF}_1 \\ &= -228.6 + 24.6 + \mathrm{NF}_1(\mathrm{dB}) \\ &= -204\ \mathrm{dBW/Hz} + \mathrm{NF}_1(\mathrm{dB}) \end{aligned} \tag{12}$$

Sometimes this equation is erroneously used for "real-world" computations, providing pessimistic analysis results. A source temperature of 75–100 K is typical, depending upon the antenna pattern and the amount of ground temperature observed.[9,12]

4. *Synthesizers and Frequency Plans*

Figure 7 presents the block diagram of two of the MAGR's custom silicon bipolar chips that make up its synthesizer.[1] One chip (*L*-band chip) also includes

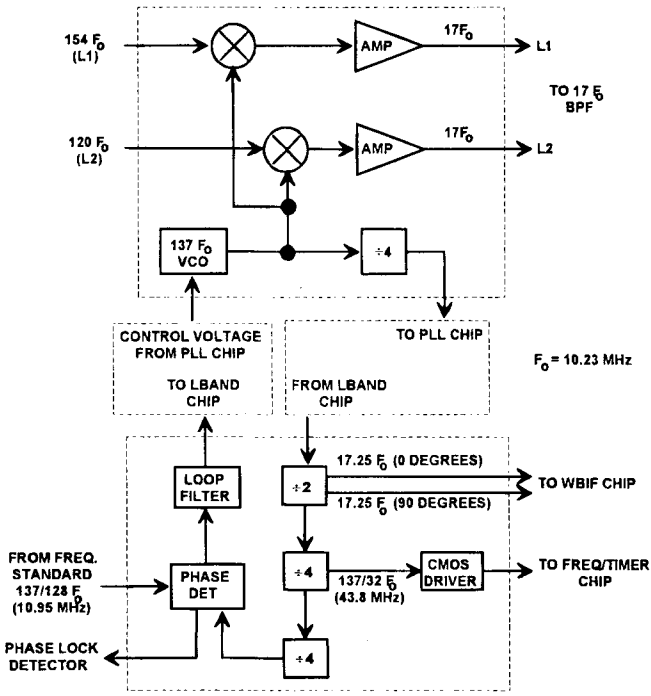

Fig. 7 Miniature airborne GPS receiver *L*-band/phase-lock-loop chips and frequency plan.

the downconverter function of the receiver. This synthesizer design reflects the concept used in modern GPS receivers, where a nonstandard reference oscillator frequency is used. Older receivers used such frequencies as 5 or 10 MHz, or 5.115 or 10.23 MHz, which also became standards because of GPS. Note that the MAGR uses 10.949296875 MHz as its reference.

The MAGR synthesizer generates a common local oscillator at $137F_0$ (1401.51 MHz) for both the L_1 and L_2 frequencies by phase-locking the LO voltage controlled oscillator, divided by 128, to the 10.95 MHz reference ($F_0 = 10.23$ MHz). It also generates common in-phase and quadraphase LOs for conversion of the IF frequencies to baseband at 17.25 F_0 (176.4675 MHz) and a CMOS clock at 43.7971875 MHz, which is used for clocking the digital signal-processing circuitry. Note that the baseband LOs do not match the IF frequecies at 17 F_0. This leaves a residual frequency offset at baseband, which is part of the frequency planning scheme. The overall effects of this residual offset is treated as Doppler. These effects are described later. However, along with the nonstandard reference frequency, allowing for such an offset also simplifies the frequency plan and the synthesizer design.

The GPSCard™ uses the same concept for its frequency plan and synthesizer as illustrated in Fig. 8. Its reference frequency is 20.473 MHz, which is also its digital signal-processing clock. The GPSCard™ utilizes a commercial synthesizer

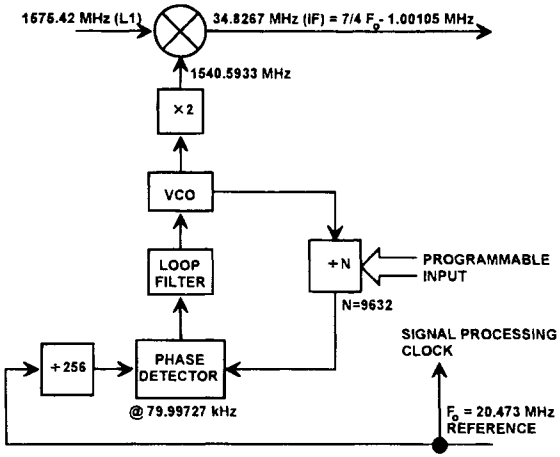

Fig. 8 GPSCard™ synthesizer and frequency plan.

chip with a programmable divider (prescaler) rather than custom chips. The key difference between this frequency plan and that of the MAGR is that the GPSCard™ uses IF sampling for its conversion to baseband, which is described later. Note that there is also a residual frequency offset.

5. *Mixing Operations and Intermediate Frequency Filtering*

Downconversion from rf to IF, and, in the case of the MAGR, conversion from IF to baseband, are accomplished by mixing the incoming signal and noise (rf or IF) with an LO. This process is illustrated in Fig. 9.

If the local oscillator is represented as $LO_1(t) = 2\cos\omega_1 t$ with power of two units, then the output of the mixer is this LO multiplied by the sum of Eq. (1) and Eq. (7), or $s_{IF}(t) + n_{IF}(t) = 2[s(t) + n(t)]\cos\omega_1 t$ + harmonics + LO feedthrough + image noise. Ignoring for the moment the harmonics, LO feedthrough, and image noise and using the product of cosines, for the signal we have $s_{IF}(t) = AC(t)D(t)\{\cos[(\omega_0 + \omega_1 + \Delta\omega)t + \phi_0] + \cos[(\omega_0 - \omega_1 + \Delta\omega)t + \phi_0]\}$ consisting of upper and lower sideband components, each with a power of

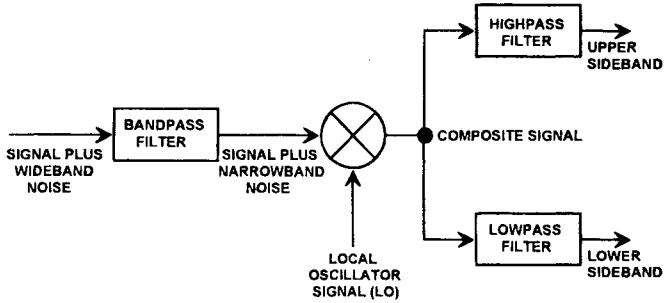

Fig. 9 Mixing operations.

$A^2/2$. Only the lower sideband is wanted. Therefore, the upper sideband is eliminated via a low-pass filter, resulting in the IF frequency $\omega_{IF} = \omega_0 - \omega_1$. Similarly, for the noise, in terms of Eq. 7, $n_{IF}(t) = r(t) \cos[\omega_{IF}t + \varphi(t)]$.

Harmonics and LO feedthrough are removed via a well-designed frequency plan and the use of bandpass filters at IF. Harmonics are generated by the mixer, because it is a nonlinear device. LO feedthrough (at ω_1) is the LO leaking through the mixer. In addition, these filters also provide the final rejection of out-of-band interference and image noise, primarily because it is easier to obtain narrowband filtering at the lower IF frequencies.

In-band image noise is either at the frequency $\omega_0 - 2\omega_1$ (upper sideband component at the lower sideband), or at the frequency $\omega_0 - 2\omega_{IF}$ (mixes to the negative of the lower sideband). Both would mix to the IF frequency and, thus, would not be filtered at IF. It is necessary to filter noise at these frequencies prior to mixing at rf so that they do not exist. In order to avoid the use of narrowband filters at rf for this purpose, the frequency plan should be designed to prevent image noise close to the IF frequency.

6. *Conversion to Baseband*

Conversion to baseband is the process of converting the IF signal to that of in-phase and quadraphase components of the signal envelope, but still modulated with residual Doppler. However, as pointed out in the discussions of synthesizers and frequency plans, in most modern receivers, an intentional residual frequency offset may still exist. There are two methods for achieving this conversion—by analog mixing or by a technique known as IF (or pass-band) sampling. Because the latter (used in the GPSCard™) is a sampling process, its description is delayed to the next section.

The MAGR uses the former method, and does so in its wide-band IF chip (silicon bipolar), which is shown in Fig. 10.[1] Also shown are the AGC and the analog-to-digital (A/D) converters. This conversion to baseband is realized by mixing the IF signal with two LOs, one of which is shifted 90° in phase with respect to the other (in quadrature). The low-pass filters reject the upper sidebands. The in-phase and quadraphase combined unity power LOs are, respectively,

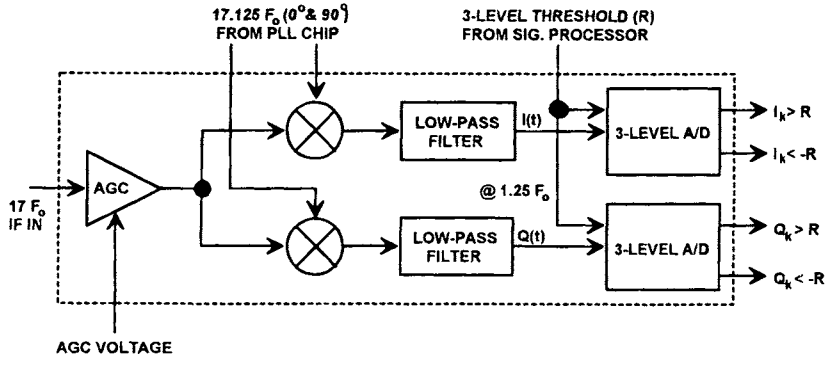

Fig. 10 Miniature airborne GPS receiver wideband intermediate frequency chip.

as follows:

$$\mathrm{LO}_{2I}(t) = \sqrt{2}\cos\omega_2 t \tag{13}$$

$$\mathrm{LO}_{2Q}(t) = \sqrt{2}\cos\left(\omega_2 t + \frac{\pi}{2}\right) = -\sqrt{2}\sin\omega_2 t \tag{14}$$

The resulting analog in-phase and quadraphase baseband signal components are then as follows:

$$I_s(t) = \frac{A}{\sqrt{2}}C(t)D(t)\cos(\Delta\omega_B t + \phi_0) \tag{15}$$

$$Q_s(t) = \frac{A}{\sqrt{2}}C(t)D(t)\sin(\Delta\omega_B t + \phi_0) \tag{16}$$

where the residual frequency offset is

$$\Delta\omega_B = \omega_{\mathrm{IF}} - \omega_2 + \Delta\omega \tag{17}$$

The relationship of these I and Q levels at this point and the signal power, related to that defined in Eq. (3), is $P_s = E[I_s^2(t) + Q_s^2(t)] = A^2/2$.

Under the assumption that this residual frequency offset is quite small with respect to the bandwidth of the low-pass filters, and that their single-sided bandwidths are essentially B Hz, the baseband noise components are simply $I_n(t) = x(t)/\sqrt{2}$ and $Q_n(t) = y(t)/\sqrt{2}$, and the noise power, in terms of Eqs. (4) and (8), is $P_n = E[I_n^2(t) + Q_n^2(t)] = 2N_oB$. The MAGR AGC shown in Fig. 10 does not operate on signal power, because the signal is still below the noise level at this point in the receiver. It is a very wideband AGC whose time constant is such that it suppresses pulse interference (time constant < 1 μs).

C. Digital Signal Processing

Digital signal processing consists of precorrelation sampling, Doppler removal, PRN coders, correlators, number-controlled oscillators (NCOs), postcorrelation filtering, and various receiver clocks.

1. Precorrelation Sampling

As is evident for the MAGR in Fig. 10, modern GPS receivers all become digital prior to correlation and Doppler removal. However, this is where the commonality ends. They differ in sample rates, sample quantization, and, as discussed previously, some receivers convert to baseband as part of the sampling process, known as IF sampling.

Intermediate frequency sampling is illustrated in Fig. 11. The concept is to sample the IF signal at a rate at which the I and Q samples are obtained directly. Suppose the sample rate is as follows:

$$\mathrm{SR} = \frac{4f_{\mathrm{IF}}}{N} \tag{18}$$

where f_{IF} is the IF frequency being sampled, and N is an odd number. Then, the samples would be taken at

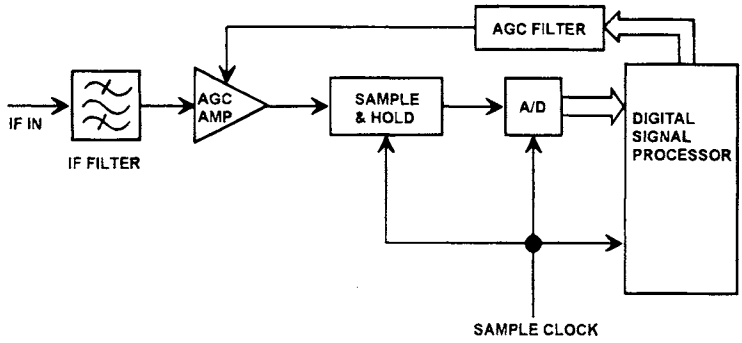

Fig. 11 Intermediate frequency sampling process.

$$t_k = \frac{kN}{4f_{\text{IF}}} \text{ sec}; \; k = 0, 1, \ldots \tag{19}$$

Sampling the IF signal at these times yields the following:

$$s_k = s_{\text{IF}}(t_k) = AC(t_k)D(t_k)\cos\left[2\pi(f_{\text{IF}} + \Delta f)\frac{kN}{4f_{\text{IF}}} + \phi_0\right]$$

$$= AC_kD_k\cos\left[\frac{\pi kN}{2}\left(1 + \frac{\Delta f}{f_{\text{IF}}}\right) + \phi_0\right]$$

$$= AC_kD_k\cos\left[\frac{\pi kN}{2} + \phi_k\right] \tag{20}$$

where Δf is an intentional frequency offset plus that attributable to Doppler, C_k and D_k are the code and data at time t_k, and

$$\phi_k = \phi_0 + \frac{\pi kN\Delta f}{2f_{\text{IF}}} = \phi_0 + \Delta\omega t_k = \phi_0 + \Delta\phi_k \tag{21}$$

is the baseband phase of the sample attributable to the nominal phase and frequency offset at time t_k. If the sample rate is offset from that of Eq. (18), $\Delta\omega$ in Eq. (21) simply becomes $\Delta\omega_B$, analogous to Eq. (17). If we ignore the Δf of Eq. (20) for the moment, note that the IF signal is sampled at exactly successive 90 deg phases, producing the following sequence of samples:

$$\sqrt{2}[I_{sk}, Q_{sk}, -I_{sk}, -Q_{sk}, I_{sk}, Q_{sk}, -I_{sk}, -Q_{sk}, \ldots] \tag{22}$$

or

$$\sqrt{2}[I_{sk}, -Q_{sk}, -I_{sk}, Q_{sk}, I_{sk}, -Q_{sk}, -I_{sk}, Q_{sk}, \ldots] \tag{23}$$

depending upon the value of N. The Δf results in a time-varying $\Delta\phi_k = \Delta\omega t_k$, causing a phase rotation of the samples that is removed after the sampling process.

This IF sampling process is sometimes called *pseudo sampling,* because the I and Q samples do not occur at the same time. For large frequency offsets with

respect to the sampling rate, but still within the Nyquist rate, this will induce an additional phase shift in the Q samples causing aliasing to a negative frequency offset. However, this is not a problem for this GPS receiver application for reasonable Δf values.

The digital signal-processor can simply invert the sign on half the samples and sort them into in-phase and quadraphase samples. This sign inversion is actually an advantage in that, if there are any dc biases present in the sampling process, they will eventually cancel in subsequent signal processing. Also, because the I and Q samples are generated in the same circuitry, there are no gain and phase imbalances between them, except as noted above. This can occur in the analog baseband conversion process. Also, only one A/D converter is required, although it must sample at twice the rate.

There are disadvantages, however, other than the double sample rate. First, the aperture time of the sampling process must be small with respect to the period of the IF frequency. That is why a sample-and-hold circuit is shown in Fig. 11. If the A/D is flash, and the IF frequency is low enough, this circuit is not required. For IF frequencies as high as they are in the MAGR, certainly a silicon bipolar flash A/D would be required for this process. How quick the sample must be is debatable, other than it must be fast with respect to the IF frequency. $\mathrm{Sin}(x)/x$, where x is proportional to the product of the frequency and the aperture time, attenuation occurs if the aperture time is too long, but then this attenuation also occurs on the noise, which is also at the IF frequency. Thus, there would be no loss in signal-to-noise ratio to a point.

The second disadvantage is minor. That is, as described above, the sample rate must be high enough so that there is no significant delay between the I and Q samples. This delay should be small with respect to a pseudonoise (PN) chip so that most of the time the I and Q samples do not straddle chip transitions. Thus, there is some loss associated with sampling right at twice the Nyquist frequency (four times the code chipping rate), but it is minimal. It has an effect similar to filter phase distortion.

This delay between the I and Q also has an effect on interference that may be present in the IF bandwidth. For example, consider an interference signal that is offset in frequency from the center of the IF band by a large amount, but is still in band. The sampling process also generates I and Q of the interference. The delay between these I and Q can be significant if the frequency offset is large, but, for normal receiver processing, this is acceptable. The effect is that some of the interference energy is folded over to the other side of center. Energy cannot be created, so this is of no consequence. Both sides of the center frequency are spread by the code correlation process.

As previously stated, the GPSCard™ uses IF sampling. Note from Fig. 8 that its IF frequency and sample frequency are such that N is 7 with a frequency offset of -1.00105 MHz. There are also at least 10 individual I and Q samples per chip, so the loss caused by the second disadvantage is negligible. Furthermore, the sample rate is not an integer multiple of the chipping rate, so that the I and Q sample times will never stay synchronous with the chip transitions. Because the IF frequency is relative low with a period of approximately 30 ns, the CMOS A/D aperture time poses no problem. Five levels of the A/D are used for a 2.5-bit quantization.

The MAGR performs baseband sampling, as shown in Fig. 10 using two 1.5-bit quantization (three levels: −L, 0, and +L) A/D converters. The result is the same as IF sampling, where

$$I_{sk} = \frac{A}{\sqrt{2}} C_k D_k \cos \phi_k \tag{24}$$

$$Q_{sk} = \frac{A}{\sqrt{2}} C_k D_k \sin \phi_k \tag{25}$$

with the exception that the Q sample is one sample later in the case of IF sampling. For the reasons stated above, we neglect that fact in the following discussions, although, in some applications, it is important.

The noise samples are simply as follows:

$$I_{nk} = x(t_k)/\sqrt{2} = x_k/\sqrt{2} \tag{26}$$

$$Q_{nk} = y(t_k)/\sqrt{2} = y_k/\sqrt{2} \tag{27}$$

The MAGR samples at a frequency at one-half of the 43.8 MHz clock from the PLL chip shown in Fig. 7, or 21.9 MHz. Given that this sampling is done at baseband, it is slightly more than the Nyquist sampling frequency, with at least two samples per P-code chip. Note that this sample rate is also not an integer multiple of the chipping rate, thus the sampling will never be synchronized with the chip transition times. The A/D threshold control is for CW interference suppression. This is a topic of discussion in Chapter 10, this volume.

2. *Precorrelation Filtering*

Precorrelation filtering (low-pass filters in Fig. 10 and bandpass filter in Fig. 11) is necessary to prevent aliasing while sampling in a digital receiver. However, this filtering also causes correlation losses, because the sidelobes of the PRN code spectrum are eliminated. Figure 12 illustrates this loss for a sharp cutoff,

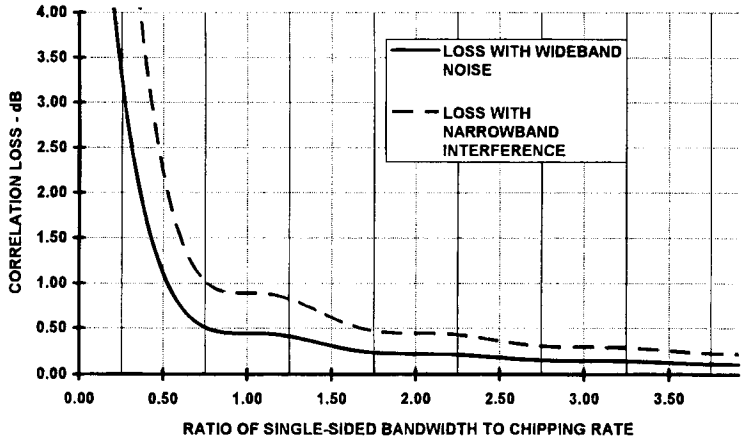

Fig. 12 Correlation loss caused by filtering.

Chapter 9

GPS Navigation Algorithms

P. Axelrad*
University of Colorado, Boulder, Colorado 80309
and
R. G. Brown†
Iowa State University, Ames, Iowa 50010

I. Introduction

THE previous chapters described the hardware and software needed to make GPS observations in the receiver. This chapter focuses on how these observations are processed to form a navigation solution. Fundamentally, a navigation solution is an estimate of the user position plus any other required parameters. The term "state" is used to describe all the parameters to be determined. The typical states in a GPS navigation estimator are three components of position, clock offset, and clock drift. In a moving application, three components of velocity are added. There are many applications described in the companion volume in which GPS is integrated with one or more other sensors, such as an altimeter or an inertial navigation system (INS). In such configurations, the state may be expanded to include specific sensor error states; however, in this chapter, we restrict ourselves to stand-alone GPS navigation estimation.

A navigation algorithm embedded in the GPS receiver combines raw measurements from the signal processor with GPS satellite orbit data to estimate the observer state. This process requires two sets of models—a measurement model and a dynamics or process model. The dynamics model describes the evolution of the system state. The measurement model relates the state to the GPS observations.

Section II describes the GPS measurements and Sec. III shows how they may be combined into a single point navigation estimate. Section IV provides various dynamic models used in GPS. The Kalman filter and some variations are described in Sec. V, and specific numerical examples are given in Sec. VI. For further information on filtering, the reader is advised to refer to Ref. 1, which specifically addresses GPS navigation filters, or more generally, Refs. 2, 3, or 4.

*Assistant Professor, Department of Aerospace Engineering Sciences.
†Distinguished Professor Emeritus, Department of Electrical and Computer Engineering.

II. Measurement Models

We consider three types of GPS measurements—pseudorange, Doppler, and accumulated delta range (ADR). The specifics of how a receiver actually forms these measurements is discussed in Chapters 7 and 8, this volume. Here we concentrate on the mathematical models of how the observations relate to the state of the vehicle.

A. Pseudorange

When the signal processor delay lock loop (DLL) finds the point of maximum correlation with a given GPS satellite signal, it produces an observation of the code phase, or equivalently, signal transmit time t_T for the current local receive time t_R. (In most cases, the observation is not a function of the filter navigation solution; however, the vector delay lock loop described in Chapter 8 of this volume provides a means to integrate the DLL and filter functions for improved performance.) The observed signal propagation delay is $(t_R - t_T)$. The pseudorange observable is merely this time interval scaled by the speed of light in a vacuum: $\rho = c\,(t_R - t_T)$.

The pseudorange observation between a user and satellite i can be related to the user position and clock states as follows:

$$\rho_i = |\boldsymbol{r}_i - \boldsymbol{r}_u| + c \cdot b_u + \epsilon_{\rho_i} \tag{1}$$

Where $\boldsymbol{r}_i$ is the satellite position at transmit time; $\boldsymbol{r}_u$ is the receiver position at receive time; b_u is the bias in the receiver clock (in s), and ϵ_ρ is the composite of errors produced by atmospheric delays, satellite ephemeris mismodeling, selective availability (SA), receiver noise, etc. (in m). Chapter 11, this volume provides an error budget for ϵ_ρ under various conditions.

The state to be estimated, consisting of $\boldsymbol{r}_u$ and $c \cdot b_u$ is embedded in this measurement equation. To extract it we must linearize the measurement equation about some nominal value, for example, about our current best estimate.

Given an a priori estimate of the state $\hat{\boldsymbol{x}} = [\hat{\boldsymbol{r}}_u{}^T \; c \cdot \hat{b}_u]^T$ and an estimate of the bias contributions caused by ionospheric and tropospheric delay, relativistic effects, satellite clock errors $\hat{\epsilon}_{\rho_i}$, we can predict what the pseudorange measurement should be as follows:

$$\hat{\rho}_i = |\boldsymbol{r}_i - \hat{\boldsymbol{r}}_u| + c \cdot \hat{b}_u + \hat{\epsilon}_{\rho_i} \tag{2}$$

The measurement residual $\Delta\rho$, which is the difference between the predicted and actual measurement, can be modeled as linearly related to the error in the state estimate, $\Delta x \equiv [\Delta r^T \; c \cdot \Delta b]^T$, by performing a Taylor expansion about the current state estimate. The linearized result is given by the following:

$$\Delta\rho_i = \hat{\rho}_i - \rho_i = [-\hat{\mathbf{1}}_i^T \quad 1] \begin{bmatrix} \Delta \boldsymbol{r} \\ c \cdot \Delta b \end{bmatrix} + \Delta\epsilon_{\rho_i} \tag{3}$$

where

$$\hat{\mathbf{1}}_i \equiv \frac{\boldsymbol{r}_i - \hat{\boldsymbol{r}}_u}{|\boldsymbol{r}_i - \hat{\boldsymbol{r}}_u|}, \qquad \Delta\boldsymbol{r} \equiv \hat{\boldsymbol{r}}_u - \boldsymbol{r}_u, \qquad \Delta b \equiv \hat{b}_u - b_u, \qquad \Delta\epsilon_{\rho_i} \equiv \hat{\epsilon}_{\rho_i} - \epsilon_{\rho_i}$$

$\hat{\mathbf{1}}_i$ is the estimated line of sight unit vector from the user to the satellite; and

$\Delta\epsilon_{\rho_i}$ is the residual error after the known biases have been removed. This linearized model is the fundamental GPS pseudorange measurement equation.

The residual measurement error $\Delta\epsilon_{\rho_i}$ is generally composed of a slowly varying term, usually dominated by SA in civilian receivers, plus random or white noise. The expected variance of the error is required for any weighted navigation solution algorithm. An order of magnitude estimate of the slow terms can be obtained from the user equivalent range error (URE) reported in the Navigation message (see Chapter 4, this volume). The high-frequency error is produced primarily by receiver noise and quantization. For a typical receiver, the standard deviation is about 1/100 of the code chip, or about 3 m for C/A code and 0.3 m for P code. A more precise estimate can be based on the signal-to-noise ratio calculation in the channel, as described in Chapter 8, this volume.

B. Doppler

The numerically controlled oscillator (NCO), which controls the carrier-tracking loop, provides an indication of the observed frequency shift of the received signal. This observed frequency differs from the nominal L_1 or L_2 frequency because of Doppler shifts produced by the satellite and user motion, as well as the frequency error or drift of the satellite and user clocks. The Doppler shift caused by satellite and user motion is the projection of the relative velocities onto the line of sight scaled by the transmitted frequency $L_1 = 1575.42$ MHz divided by the speed of light, as follows:

$$D_i = -\left(\frac{\boldsymbol{v}_i - \boldsymbol{v}_u}{c} \cdot \mathbf{1}_i\right) L_1 \tag{4}$$

The Doppler can be converted to a pseudorange rate observation given by the following:

$$\dot{\rho}_i = (\boldsymbol{v}_i - \boldsymbol{v}_u) \cdot \frac{\boldsymbol{r}_i - \boldsymbol{r}_u}{|\boldsymbol{r}_i - \boldsymbol{r}_u|} + f + \epsilon_{\dot{\rho}_i} \tag{5}$$

where f is the receiver clock drift in m/s; and $\epsilon_{\dot{\rho}_i}$ is the error in the observation in m/s. Again, this effect can be predicted, based upon the current estimates of the velocity $\hat{\boldsymbol{v}}_u$; line of sight vector $\hat{\mathbf{1}}_i$, the clock drift estimate in m/s $\hat{f}$; and the known error rates $\hat{\epsilon}_{\dot{\rho}_i}$ as follows:

$$\hat{\dot{\rho}}_i = (\boldsymbol{v}_i - \boldsymbol{v}_u) \cdot \hat{\mathbf{1}}_i + \hat{f} + \hat{\epsilon}_{\dot{\rho}_i} \tag{6}$$

The linearized Doppler measurement equation is then as follows:

$$\Delta\dot{\rho}_i \equiv \hat{\dot{\rho}}_i - \dot{\rho}_i = [-\hat{\mathbf{1}}_i^T \quad 1] \begin{bmatrix} \Delta\boldsymbol{v} \\ \Delta f \end{bmatrix} + \Delta\epsilon_{\dot{\rho}_i} \tag{7}$$

Note that the Doppler does depend on the observer position through the line-of-sight unit vector. This dependence can be exploited to perform "Doppler positioning" in which the position is solved for using the Doppler observations and, sometimes, the rate of change of Doppler. This is the positioning method

employed with the Navy's Transit satellites. The observation geometry for Doppler positioning is substantially weaker than ranging; thus, it is not used much in GPS, except to set an a priori position estimate.

C. Accumulated Delta Range

The ADR is produced by the signal processor by accumulating the commanded values to the NCO required to maintain lock on the signal. In other words, it keeps track of changes in the observed range to the satellite. Thus, both terms "accumulated delta range" or "integrated Doppler" are appropriate. In the literature (cf. Ref. 5) this measurement has also been called "carrier beat phase," referring to the output of a mixing process between a nominal L_1 carrier signal generated in the receiver, and the received Doppler-shifted version.

The distinction between the ADR and a code-based pseudorange is that the ADR has an ambiguous starting value. Once the phase–lock-loop (PLL) begins to follow the carrier signal, it can keep track of the total change in range; however, there is no way to know the whole number of carrier cycles between the satellite and the user antenna. Thus, for stand-alone navigation it is not possible to use the ADR for absolute estimation of position. (The ADR initial condition problem is similar to that encountered in inertial navigation systems.) However, for differential GPS or attitude determination, it is possible to determine the difference in the ambiguities between two nearby stations and/or two GPS satellites. Thus, for these applications, the precision of the ADR can be fully exploited.

A common use of the ADR in stand-alone navigation is to smooth the noisy pseudorange measurements. A number of techniques are available for doing this. A commonly used technique forms a weighted average of the code and carrier-based measurements.[6] Reference 7 has also suggested an integration scheme where the ADR provides the reference trajectory (in much the same manner as an INS), and then the pseudorange data is used at a slower rate to update the reference trajectory via a Kalman filter. Other ad hoc methods have also been successfully employed for real-time, stand-alone applications. The ADR measurements play only a minor role in many GPS stand-alone navigation applications; however, they are pivotal to kinematic differential operations and surveying, as described in Chapters 15 and 18 in the companion volume.

D. Navigation Data Inputs

To compute the predicted pseudorange and Doppler, the navigation algorithm must have information on the position and velocity of the GPS satellite, as well as error models to correct the satellite clock offset and atmospheric delays. This information is provided via the Navigation message. The satellite positions are computed as described in Chapter 4, this volume; the atmospheric delay models are described in Chapter 8, this volume; and the clock corrections are described in Chapter 4, this volume. This information is also contained in Ref. 8.

III. Single-Point Solution

The physical measurements and equations provided in the previous section are all that is required for a single-point solution or kinematic solution. In this

method, the navigation estimate is the least squares solution to the measurement equations made at a single time. For each satellite tracked by the receiver, the predicted pseudorange is formed using Eq. (2), and the linearized observation Eq. (3) is formed. All the measurements are then combined into a set of normal equations:

$$\Delta\rho = G\Delta x + \Delta\epsilon_\rho \tag{8}$$

where

$$\Delta\rho \equiv \begin{bmatrix} \Delta\rho_1 \\ \Delta\rho_2 \\ \vdots \\ \Delta\rho_n \end{bmatrix}, \quad G \equiv \begin{bmatrix} -\hat{\mathbf{l}}_1^T & 1 \\ -\hat{\mathbf{l}}_2^T & 1 \\ \vdots & \vdots \\ -\hat{\mathbf{l}}_n^T & 1 \end{bmatrix}, \quad \Delta x \equiv \begin{bmatrix} \Delta r_u \\ c \cdot \Delta b_u \end{bmatrix}, \quad \Delta\epsilon_\rho \equiv \begin{bmatrix} \Delta\epsilon_{\rho_1} \\ \Delta\epsilon_{\rho_2} \\ \vdots \\ \Delta\epsilon_{\rho_n} \end{bmatrix}$$

which is to be solved for a correction, Δx to the a priori state estimate. To improve the state estimate subtract Δx from the a priori values. In GPS, "G" is frequently referred to as the geometry matrix, and corresponds to the measurement connection matrix, commonly named "H" in the more general literature on filtering.

The $\Delta\epsilon_\rho$ are assumed to be zero mean, so that the least squares solution to the set of normal equations is given by the following:

$$\Delta\hat{x} \equiv (G^TG)^{-1}G^T\Delta\rho \tag{9}$$

or, if a weight R_i^{-1} is assigned to each observation, the weighted least squares estimate is as follows:

$$\Delta\hat{x} \equiv (G^TR^{-1}G)^{-1}G^TR^{-1}\Delta\rho \tag{10}$$

If the a priori estimate used to construct G, is off by a lot (typically more than a few km), the least squares solution may be iterated until the change in the estimate is sufficiently small. Because G only depends upon the line-of-sight unit vector, it is not very sensitive to errors in the observer position. Numerically efficient methods for solving Eqs. (8–10) are well known (c.f. Ref. 9).

A. Solution Accuracy and Dilution of Precision

How accurate is the single-point, least squares solution? The accuracy is decided by two factors, the measurement quality and the user-to-satellite geometry. [Chapter 11, this volume, on errors in GPS details the contributions of both measurement errors and geometry, and Chapter 5, this volume, provides an extensive discussion of geometric dilution of precision (GDOP).] The measurement quality is described by the variance of the measurement error, which for a typical pseudorange is in the range of 0.3 to 30 m, depending on the error conditions. The geometry is described by the "G" matrix, which is composed of line-of-sight vectors and "1s" for the clock states.

The solution error covariance can be expressed as follows:

$$E[\Delta\hat{\boldsymbol{x}} \quad \Delta\hat{\boldsymbol{x}}^T] = E[(G^TG)^{-1}G^T\Delta\rho \quad \Delta\rho^TG(G^TG)^{-1}]$$
$$= (G^TG)^{-1}G^TRG(G^TG)^{-1} \tag{11}$$

where R is the pseudorange measurement covariance. If we assume (somewhat incorrectly, as described later) that the measurement errors are uncorrelated and have equal variance σ^2 then $R = \sigma^2 I$, and the point solution error covariance reduces to the following:

$$E[\Delta\hat{\boldsymbol{x}} \quad \Delta\hat{\boldsymbol{x}}^T] = \sigma^2(G^TG)^{-1} \tag{12}$$

If the state is parameterized so that $\Delta\boldsymbol{x} = [\Delta E \ \Delta N \ \Delta U \ c \cdot \Delta b]^T$, where ΔE, ΔN, and ΔU, are the east, north, and up position errors, respectively; and $c \cdot \Delta b$ is the clock bias error, then the variance of the state estimates is given by the following:

$$E[\Delta\hat{\boldsymbol{x}} \ \Delta\hat{\boldsymbol{x}}^T] = \begin{bmatrix} E[\Delta E^2] & E[\Delta E\Delta N] & E[\Delta E\Delta U] & E[\Delta Ec\cdot\Delta b] \\ E[\Delta N\Delta E] & E[\Delta N^2] & E[\Delta N\Delta U] & E[\Delta Nc\cdot\Delta b] \\ E[\Delta U\Delta E] & E[\Delta U\Delta N] & E[\Delta U^2] & E[\Delta Uc\cdot\Delta b] \\ E[c\cdot\Delta b\Delta E] & E[c\cdot\Delta b\Delta N] & E[c\cdot\Delta b\Delta U] & E[c\cdot\Delta b^2] \end{bmatrix} \tag{13}$$

Most of the time, we are primarily interested in the diagonal elements. The following DOPs summarize the contribution of the geometry:

$$A \equiv (G^TG)^{-1}$$

$$\begin{aligned} \text{GDOP} &\equiv \sqrt{\text{trace}(A)} && \text{geometrical DOP} \\ \text{PDOP} &\equiv \sqrt{A_{11} + A_{22} + A_{33}} && \text{position DOP} \\ \text{HDOP} &\equiv \sqrt{A_{11} + A_{22}} && \text{horizontal DOP} \\ \text{VDOP} &\equiv \sqrt{A_{33}} && \text{vertical DOP} \\ \text{TDOP} &\equiv \sqrt{A_{44}} && \text{time DOP} \end{aligned} \tag{14}$$

Thus, the total position error magnitude can be estimated by $\sigma \times$ PDOP, and the vertical position error by $\sigma \times$ VDOP, etc. However, keep in mind that this is only an approximation, because of the assumption that all satellite pseudorange measurements errors are independent and have the same statistics. The equations for a single-point velocity solution are identical with the pseudorange measurements replaced by pseudorange rates.

Typical modern receivers track 5–12 satellites simultaneously. More satellites produce improved geometry, generally leading to a more accurate single-point navigation solution. (An exception can occur if the ranging error to the additional satellite is exceptionally poor.) ADR smoothing can reduce the receiver-induced measurement noise in each observation; however, it cannot eliminate the effects of SA or atmospheric effects. To improve the navigation estimate further, we

must tie together measurements over time by including knowledge of the vehicle dynamics in a solution filter.

B. Point Solution Example

As an example of the least squares solution method, assume an observer is actually located on the surface of the Earth at 0° latitude, 0° longitude, and has a clock error from GPS time equivalent to 85,491.5 m. If the observer state is comprised of the WGS-84 (1984 Word Geodetic System) position components x, y, z, and the clock bias in meters, the true state is as follows:

$$\boldsymbol{x} = [6{,}378{,}137.0\text{ m} \quad 0.0\text{ m} \quad 0.0\text{ m} \quad 85{,}000.0\text{ m}]^T$$

At a certain time there are seven satellites visible above an elevation of 10 deg at the positions shown in Table 1.

If the a priori position and clock estimate is given by

$$\hat{\boldsymbol{x}} = [6{,}377{,}000.0\text{ m} \quad 3{,}000.0\text{ m} \quad 4{,}000.0\text{ m} \quad 0.0\text{ m}]^T$$

then the computed range and line-of-sight unit vector to each satellite are as shown in Table 2.

Table 1 Satellite positions for point solution example

Satellite	X position, m	Y position, m	Z position, m
SV 01	22,808,160.9	−12,005,866.6	−6,609,526.5
SV 02	21,141,179.5	−2,355,056.3	−15,985,716.1
SV 08	20,438,959.3	−4,238,967.1	16,502,090.2
SV 14	18,432,296.2	−18,613,382.5	−4,672,400.8
SV 17	21,772,117.8	13,773,269.7	6,656,636.4
SV 23	15,561,523.9	3,469,098.6	−21,303,596.2
SV 24	13,773,316.6	15,929,331.4	−16,266,254.4

Table 2 Computed pseudorange and line-of-sight vectors

Satellite	Computed pseudorange, m	Line-of-sight X	Line-of-sight Y	Line-of-sight Z
SV 01	21,399,408.0	0.767832	−0.561178	−0.309052
SV 02	21,890,921.6	0.674443	−0.107718	−0.730427
SV 08	22,088,910.4	0.636607	−0.192041	0.746895
SV 14	22,666,464.0	0.531856	−0.821318	−0.206314
SV 17	21,699,943.6	0.709454	0.634576	0.306574
SV 23	23,460,242.4	0.391493	0.147744	−0.908243
SV 24	23,938,978.9	0.308965	0.665289	−0.679655

The computed geometry matrix is as follows:

$$G = \begin{bmatrix} -0.767832 & 0.561178 & 0.309052 & 1 \\ -0.674443 & 0.107718 & 0.730427 & 1 \\ -0.636607 & 0.192041 & -0.746895 & 1 \\ -0.531856 & 0.821318 & 0.206314 & 1 \\ -0.709454 & -0.634576 & -0.306574 & 1 \\ -0.391493 & -0.147744 & 0.908243 & 1 \\ -0.308965 & -0.665289 & 0.679655 & 1 \end{bmatrix}$$

Table 3 provides the simulated measured pseudorange (already corrected for known errors such as ionospheric delay, satellite clock, etc.) and the pseudorange residual $\Delta\rho_i \equiv \hat{\rho}_i - \rho_i$. The standard deviation of the pseudorange errors is 6 m. Note that the pseudorange residuals are dominated by the large error in the estimate of the receiver clock.

Solving the normal equations for a correction to the state estimate gives $\Delta x = [-1{,}131.8 \quad 2{,}996.8 \quad 3{,}993.1 \quad -84{,}996.4]^T$ m. Subtracting this from the a priori estimate gives the improved estimate $\hat{x} = [6{,}378{,}131.8 \quad 3.2 \quad 6.9 \quad 84{,}996.4]^T$ m. This new estimate is closer to the true value of the state; however, it contains errors produced by the pseudorange measurement error as well asthe approximation in the line-of-sight vectors caused by the incorrect a priori guess. To see how large the latter effect is, we can redo the least squares solution using the improved estimate to compute the elements of the G matrix. The resulting correction to the state estimate is $\Delta x = [0.3 \quad -0.1 \quad -0.2 \quad 0.6]^T$ m, and the "improved" state estimate (actually worse than the last estimate) is $\hat{x} = [6{,}378{,}131.5 \quad 3.3 \quad 7.1 \quad 84{,}995.8]^T$ m. Thus, it is apparent that the approximation made in computing the G matrix was quite good, and to get a solution at the 1-m level, it is not necessary to iterate if the solution is already known to within a few kilometers.

The final error in the state estimate is $\Delta x = [-5.5 \quad 3.2 \quad 7.1 \quad -4.2]^T$ m. Now let us compare this to the error bound predicted by the GDOP approximation. The A matrix can be computed from the G matrix given in Eq. (14). The DOPS for each of the state components are computed as the square roots of the diagonal elements of A. The measurement standard deviation $\sigma = 6$ m.
Thus, the DOP approximations seem to be valid for this example.

Table 3 Simulated pseudorange and residual

Satellite	Measured pseudorange, m	Pseudorange residual, m
SV 01	21,480,623.2	−81,215.3
SV 02	21,971,919.2	−80,997.6
SV 08	22,175,603.9	−86,693.4
SV 14	22,747,561.5	−81,097.6
SV 17	21,787,252.3	−87,308.8
SV 23	23,541,613.4	−81,371.0
SV 24	24,022,907.4	−83,928.6

Table 4 Actual point solution errors compared to DOP predictions

State component	DOP value	Expected $1-\sigma$ error, $\sigma \times$ DOP	Actual error
X position	3.0	18.0 m	−5.5 m
Y position	0.8	4.8 m	3.2 m
Z position	0.8	4.8 m	7.1 m
Clock bias	1.9	11.4 m	−4.2 m
Total error	3.7	22.2 m	10.4 m

IV. User Process Models

In anticipation of employing Kalman filter methods in the GPS solution (Sec. V), we now look at user "process models." The vehicle dynamics are summarized in the filter process model. The GPS has the capability to provide real-time three-dimensional position, velocity, and time information to any user. However, there are times when all this information is not required or valuable. The degree to which the user dynamics are constrained or predictable dictates the type of process model used.

A. Clock Model

Two states required in any GPS-based navigation estimator are the user clock bias and drift, which represent the phase and frequency errors in the atomic frequency standard or crystal oscillator in the receiver. Within the navigation algorithm the two-state model shown in Fig. 1 is commonly employed.

This model says that we expect both the frequency and phase to random walk over a short period of time. The discrete process equations are given by Ref. 1.

$$\boldsymbol{x}_c(k) = \Phi_c(\Delta t)\boldsymbol{x}_c(k-1) + \boldsymbol{w}_c(k-1) \tag{15}$$

where

$$\boldsymbol{x}_c \equiv \begin{bmatrix} b \\ f \end{bmatrix}, \qquad \Phi_c(\Delta t) = \begin{bmatrix} 1 & \Delta t \\ 0 & 1 \end{bmatrix}$$

$$Q_c \equiv E[\boldsymbol{w}_c \boldsymbol{w}_c^T] = \begin{bmatrix} s_b \Delta t + S_f \dfrac{\Delta t^3}{3} & S_f \dfrac{\Delta t^2}{2} \\ S_f \dfrac{\Delta t^2}{2} & S_f \Delta t \end{bmatrix}$$

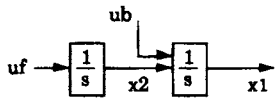

Fig. 1 Dynamic model for GPS clock states.

The white noise spectral amplitudes S_b and S_f can be related to the classical Allan variance parameters. The approximate relation given in Ref. 1 (p. 427) is $S_f = 2\ h_0$, and $S_g = 8\ \pi^2\ h_{-2}$ (see also Ref. 10). Figure 2 shows simulated clock states for a crystal oscillator with $h_0 = 2 \times 10^{-19}$, and $h_{-2} = 2 \times 10^{-20}$ (Ref. 1, Chapter 10).

Two clock states of this type must be included for all types of GPS users. In a time transfer receiver, which is described in greater detail in Chapter 16 of the companion volume, these two clock states are the ones of primary interest. In this case, the receiver position is generally known to at least the level of accuracy of timing information desired (1 m ~ 3 ns). For highest accuracy, the position is held fixed and only the two clock parameters are estimated.

B. Stationary User or Vehicle

If the user antenna is known to be stationary at an unknown location, three position coordinate states may be added to the clock model to form a 5-element state vector. It is assumed that the velocity is zero, thus, the dynamic model for

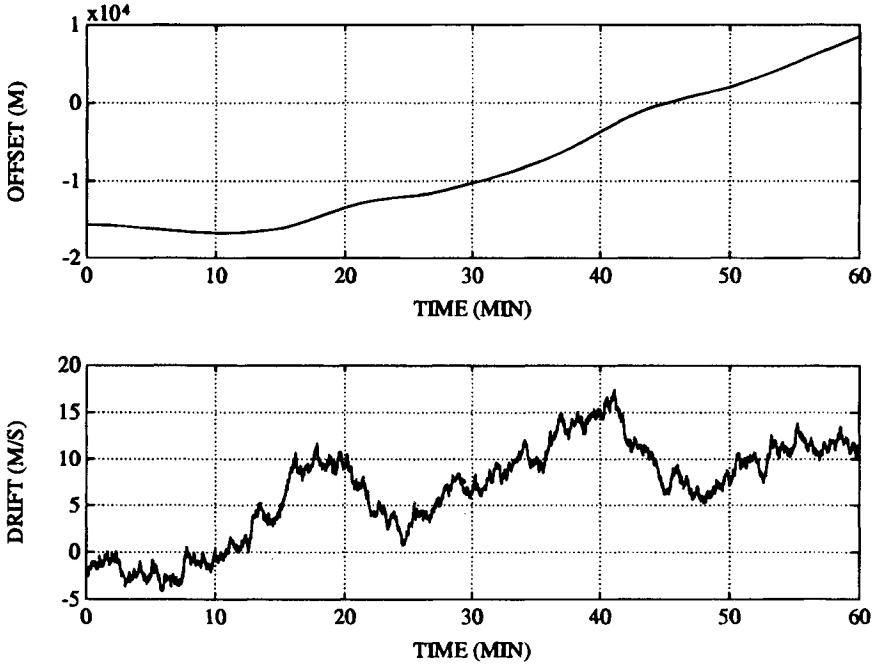

Fig. 2 Simulated GPS clock errors. The bottom graph shows an example of clock frequency drift measured in m/s. The top graph shows the corresponding clock offset in meters. Note, the receiver clock errors can be very large, in this case more than 10 km, and must be estimated along with the position solution.

the stationary user is given by the following:

$$\boldsymbol{x}_s(k) = \Phi_s(\Delta t)\boldsymbol{x}_s(k-1) + \boldsymbol{w}_s(k-1) \tag{16}$$

where

$$\boldsymbol{x}_s \equiv [x \quad y \quad z \mid b \quad f]^T$$

$$\Phi_s(\Delta t) = \begin{bmatrix} I & \vdots & 0 \\ \cdots & \vdots & \cdots \\ 0 & \vdots & \Phi_c(\Delta t) \end{bmatrix}, \qquad \text{and } I \text{ is a } 3 \times 3 \text{ identity matrix}$$

$$Q_s \equiv E[\boldsymbol{w}_s \boldsymbol{w}_s^T] = \begin{bmatrix} Q_p & \vdots & 0 \\ \cdots & \vdots & \cdots \\ 0 & \vdots & Q_c \end{bmatrix}$$

There are two important things to note. First, it cannot be assumed that the clock state is constant; thus, the frequency error state is required as well as the bias. Second, even for a stationary result, we model the dynamics by a random walk to prevent numerical problems in the navigation algorithm. The process noise covariance Q_p represents the uncertainty in the dynamic model. Thus, for a stationary observer, we would think that it could be set to zero. This is not generally done because it can lead to numerical problems or cause the filter to "go to sleep." In this situation, the estimation error covariance has decreased so far that the estimator gain for new measurements goes to zero—essentially the filter begins to ignore new information. As long as this situation is avoided, Q_p can be set to a small value to maximize the smoothing that will occur.

C. Low Dynamics

The next step up in user dynamics is a low dynamic vehicle, such as a boat or car. In these cases, the position, velocity, and clock terms must be estimated, leading to an 8-element state representation. The discrete model for such a user is shown in Fig. 3. The corresponding dynamic model is given by the following:

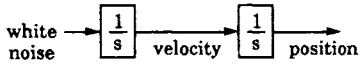

Fig. 3 Integrated random-walk model for a dynamic observer.

$$\boldsymbol{x}_L(k) = \Phi_L(\Delta t)\boldsymbol{x}_L(k-1) + \boldsymbol{w}_L(k-1) \tag{17}$$

where

$$\boldsymbol{x}_L \equiv [x \quad y \quad z \mid \dot{x} \quad \dot{y} \quad \dot{z} \mid b \quad f]^T$$

$$\Phi_L(\Delta t) = \left[\begin{array}{cc:c} I & \Delta t I & 0 \\ 0 & I & 0 \\ \hdashline 0 & 0 & \Phi_c(\Delta t) \end{array}\right]$$

$$Q_L \equiv E[\boldsymbol{w}_L \boldsymbol{w}_L^T] = \left[\begin{array}{cc:c} Q_p & Q_{pv} & 0 \\ Q_{pv} & Q_v & 0 \\ \hdashline 0 & 0 & Q_c \end{array}\right]$$

The effect of unknown random accelerations between measurement updates is represented by Q_v. Often, different values are used for horizontal and vertical components; i.e., a car cannot change its vertical velocity substantially; whereas, it can accelerate or decelerate rapidly. If the dynamical uncertainty of the vehicle is large, filtering will not improve the navigation solution.

D. High Dynamics

When the vehicle, such as a fighter aircraft or missile, has the potential for significant accelerations, it is usually necessary to measure and account for the deterministic changes in velocity. This leads to the integrated GPS/INS system, which is discussed in detail in Chapter 2 of the companion volume. A less accurate way of handling the high dynamics problem is to add three acceleration states to the process model and let the stand-alone GPS system estimate the vehicle acceleration in addition to position and velocity. The acceleration states are usually modeled as either random walk or Markov processes. This method of coping with high dynamics is not as good as a full-fledged integrated GPS/INS system, but it is better than treating acceleration as white noise, which is what has to be done if the acceleration states are omitted.

V. Kalman Filter and Alternatives

As mentioned previously, one disadvantage of the point solution approach is that it does not carry any information from one measurement epoch to the next; i.e. it does not include any of the known user dynamics. A second problem is

that the solution accuracy is extremely dependent on the instantaneous satellite geometry. Employing a Kalman filter addresses both of these issues (Ref. 1).

A. Discrete Extended Kalman Filter Formulation

For use with stand-alone GPS, a discrete, extended Kalman filter (EKF) is generally used. This means that measurements are incorporated at discrete intervals, and the measurement models are linearized about the current best estimate of the state. The updated state estimate is formed as a linear blend of the previous estimate (projected forward to the current time) and the current measurement information. The relative weighting in the blend is determined by the a priori error covariance and the measurement error covariance. After updating, the state estimate and its error covariance matrix are projected ahead to the next measurement time via the assumed process dynamics.

The state x includes the two clock components, three position components, and possibly three velocity components, depending on the type of dynamic model used. Associated with the state are four key matrices that must be specified in the discrete EKF:

G—the measurement connection matrix, the elements of which are the partials of the measurement model with respect to each of the states (In most literature on filtering, this matrix is refered to as H; we use G for geometry matrix to be consistent with the GPS literature.)

R—the measurement noise covariance matrix

Φ—the state transition matrix, which is a linearized representation of the process model

Q—the process noise covariance matrix

The selection of R and Q has a significant effect on the convergence and accuracy of the filter solutions. The adjustment of these parameters is refered to as "filter tuning." Tuning is often performed to achieve the best possible performance while avoiding filter divergence in the face of unmodeled errors.

In addition to specifying the four matrices, we must also establish an initial estimate of the state $\hat{x}_0^-$ and the state covariance matrix (P_0^-). The filter proceeds by processing all available measurements at each epoch (the measurement update) and then propagating the state estimate and covariance ahead to the next epoch (the time update). Estimates of the state and covariance after the measurement update are indicated by a superscript "+"; estimates and covariances propagated ahead are indicated by a superscript "−".

The measurement update is summarized as follows:

1) Compute the expected pseudorange $\hat{\rho}_k$ according to Eq. (2) based on the GPS satellite position and the a priori state estimate $\hat{\boldsymbol{x}}_k^-$.

$$\hat{\rho}_k = h(\hat{\boldsymbol{x}}_k^-)$$

2) Construct the measurement connection matrix as follows:

$$G_k(\hat{\boldsymbol{x}}_k^-) \equiv \frac{\partial h(\hat{\boldsymbol{x}}_k^-)}{\partial \boldsymbol{x}}$$

3) Compute the gain matrix K_k according to the following:

$$K_k = P_k^- G_k^T (G_k P_k^- G_k^T + R_k)^{-1} \tag{18}$$

4) Update the state as follows:

$$\hat{\boldsymbol{x}}_k^+ = \hat{\boldsymbol{x}}_k^- + K_k(\rho_{k-\text{measured}} - \hat{\rho}_k) \tag{19}$$

(Note that the quantity in parenthesis is opposite in sign to the measurement residual $\Delta\rho = \hat{\rho}_k - \rho_k$ defined earlier.)

5) and the following covariance matrix*:

$$P_k^+ = (I - K_kG_k)P_k^-(I - K_kG_k)^T + K_kR_kK_k^T \tag{20}$$

The projection steps are as follows:

1) Propagate the covariance matrix to the next measurement epoch as follows:

$$P_{k+1}^- = \Phi_kP_k^+\Phi_k^T + Q_k \tag{21}$$

2) Propagate the state estimate to the next measurement epoch using the assumed process dynamics. If the dynamic model is linear, the propagation is given by the following:

$$\hat{\boldsymbol{x}}_{k+1}^- = \Phi_k\hat{\boldsymbol{x}}_k^+ \tag{22}$$

In the more general case where the zero-noise dynamic model is given by the following:

$$\frac{\mathrm{d}}{\mathrm{d}t}\boldsymbol{x} = f(\boldsymbol{x}, t) \tag{23}$$

$\hat{\boldsymbol{x}}_k^+$ is projected forward by numerically integrating the nonlinear dynamic model. These steps are illustrated in Fig. 4.

The standard EKF assumes that the measurement and process noise are not correlated with each other and that each is uncorrelated between time epochs. For GPS, the former assumption is largely valid, but the latter is not. In the next section, methods for dealing with correlated measurement noise are discussed.

B. Steady-State Filter Performance

A key feature of the Kalman filter is that, under many conditions, it quickly converges to a quasi-steady-state condition. In GPS navigation, for example, the geometry matrix G changes rather slowly, and in all of the models considered here, the state transition matrix is only a function of the measurement time interval. Thus, after a short time, the increase in the error covariance caused by state propagation and dynamic uncertainty is matched by the decrease in error covariance caused by the measurement update. The discrete, steady-state Kalman filter can be derived by assuming that both P^+ and P^- are constants in Eqs. (18), (20), and (21). Substitution results in a discrete time Riccati equation that does converge but in general does not afford a closed form solution. This is described in further detail in Refs. 11 and 12. An interesting point is that in GPS, it frequently takes only a few measurement epochs to achieve this steady-state value.

* The form of the expression given in Eq. (20) for the covariance measurement update ensures that if P^- is symetric, P^+ will also be symetric. The more commonly used form $P_k^+ = (I - K_kH_k)P_k^-$, does not have this property. In this form, numerical difficulties can result, for example, if the initial covariance is very large and the measurements are very accurate.

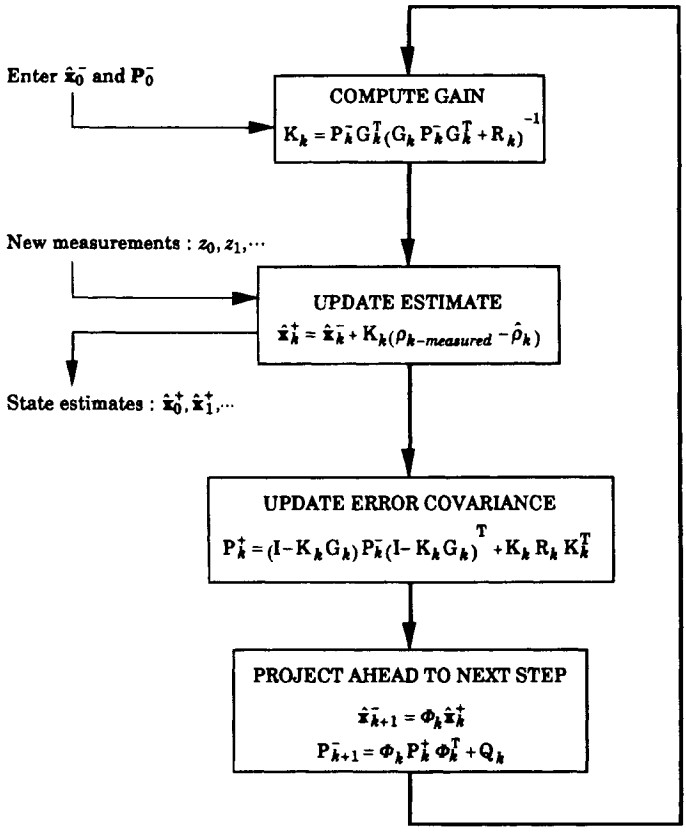

Fig. 4 Flow chart of the discrete Kalman filter solution.

C. Alternate Forms of the Kalman Filter

Under special conditions, there may be computational difficulties with the standard Kalman filter formulation shown above. These include numerical instability and divergence produced by round-off errors even when high precision arithmetic is employed. Square-root filters can mitigate these problems to some extent. Perhaps the most widely used square-root filter in GPS is the *U-D* filter. This is described in detail in Ref. 13, and in less detail in Refs. 1 and 4.

In the U-D filter, the covariance matrix P is decomposed into the factored form $P = UDU^T$. The measurement and time updates are formulated directly in terms of the U and D matrices, and conversion to the covariance form is only required for input and output purposes. In brief, the divergence problems encountered in propagating the U and D separately are less severe than they would be if P were propagated in unfactored form.

D. Dual-Rate Filter

A second implementation issue relates to the rate at which the various filter matrices are updated. The computational load of updating the measurement

connection matrix, the covariance, and the Kalman gain at each measurement epoch may be a severe burden on the receiver processor. In reality, the measurement geometry changes rather slowly, and once the filter has converged, the covariance matrix tends to a steady value until there is a change in the satellites tracked. Thus, some GPS receivers employ a dual rate or background scheme for updating some of these parameters. This approach may have benefit in reducing the real-time processing load, but also has the potential to increase the software complexity.

E. Correlated Measurement Noise

One of the major difficulties for GPS navigation filters in civilian receivers is selective availability. Recall that the Kalman filter assumes that successive measurement errors are uncorrelated to each other; however, when SA is present, there is an unknown, slowly varying error associated with each satellite, as described in Chapter 16, this volume. Even without SA, measurement errors produced by orbit errors, ionosphere, troposphere, and multipath have time-correlated statistics. This clearly violates one of the basic filter assumptions; thus, even if the measurement noise as described by the R matrix represents the typical error variance, it does not correctly model the effect.

One approach to dealing with this problem would be to add a random walk state to the filter for each satellite tracked. However, for a dynamic user, there is not sufficient information to separate the SA from the vehicle motion effectively, nor is there any assurance that random walk (or any other one-state process) will properly model the SA process in effect at the moment.

Another method for dealing with this unknown signal dynamics is to include a "consider" state for each satellite in a Schmidt filter (Ref. 1, Chap. 9). The Schmidt filter accounts for the covariance of these additional states without trying to estimate the actual parameter values. This improves the overall state covariance estimate and leads to more realistic error bounds and better performance under SA. Of course, the Schmidt filter cannot remove the effect of SA; it does, however, account for it to within the bounds of our uncertain knowledge of SA.

Several methods are described in the literature that can be applied to correlated measurement errors for which the dynamic process governing the errors is known (cf. Refs. 1, 3, and 12). For example, an error that can be modeled by a first order Markov process with known variance and time constant can be readily accomodated in the filter. The key is to construct a new measurement that differences prior measurements to remove the correlated error. This results in modifications to the Kalman filter gain and covariance update equations, which are given in the references mentioned.

VI. GPS Filtering Examples

The following examples illustrate the set up and performance of a Kalman filter under a variety of conditions. All of the results were generated based on a simulation written in MATLAB® that includes the full primary GPS satellite constellation. The first case considered is a stationary buoy with no SA. The second is a vehicle traveling at constant velocity. The last two cases illustrate

the effects of unmodeled dynamics and correlated measurement errors on the filter performance.

A. Buoy Example

As a first example of the operation of a Kalman Filter for GPS navigation, we model a fixed buoy located near the surface of the Earth at 0° latitude and 0° longitude. The buoy is nominally not moving, so the stationary dynamic model is used. A relatively large dynamic uncertainty in each position component of $Q_p(i,i) = (10\text{ cm})^2$ over a 1-s interval is allowed to account for the possibility of random buoy motion on the water. The dynamic model for the clock is the second-order system described in Sec. IV.

Thus, the state is comprised of the three WGS-84 coordinates plus clock bias and drift components $\boldsymbol{x} = [x\ y\ z\ b\ f]^T$. The initial estimate of the state is

$$\hat{\boldsymbol{x}} = [6{,}377{,}000.0\text{ m} \quad 3{,}000.0\text{ m} \quad 4{,}000.0\text{ m} \quad 0.0\text{ m} \quad 0.0\text{ m/s}]^T$$

The diagonal elements of the initial covariance matrix are selected to reflect the uncertainty in the a priori state estimates. Generally these can be set very large, because after the first set of measurements is received, the uncertainty will be reduced to approximately the level of the single-point solution. One caveat is that if there are large differences between the initial uncertainties in the states, it can lead to numerical problems if the alternate form of Eq. (20) is used. For this example we use the following:

$$\boldsymbol{P}_0^- = \begin{bmatrix} 25\text{ km}^2 & & & & 0 \\ & 25\text{ km}^2 & & & \\ & & 25\text{ km}^2 & & \\ & & & 10^4\text{ km}^2 & \\ 0 & & & & \left(c\cdot 10^{-6}\,\dfrac{\text{km}}{\text{s}}\right)^2 \end{bmatrix}$$

The receiver takes measurements to all GPS satellites at an elevation above 10 deg, at intervals of 1 s. Each pseudorange measurement is assumed to have a variance $R = 36\text{ m}^2$.

Figure 5 presents the estimation errors for the $\boldsymbol{x}$ position and clock bias states over a 20 s simulation run. The graphs show the actual error in the estimate as well as the $\pm 1 - \sigma$ bounds computed from the diagonals of the filter covariance matrix. (The initial a priori covariance is off the scale.) This clearly illustrates the convergence of the filter. As each set of measurements is incorporated into the filter, the state uncertainty is decreased by an amount related to the a priori covariance, the measurement variance, and the measurement geometry. When the state is projected ahead to the next measurement epoch, the uncertainty increases because of the limitations of our knowledge of the governing dynamics.

After only about five epochs, the Kalman filter reaches the almost steady-state condition in which the amount of information gained in the measurement step is equal to the loss of information in the projection step. If the satellite geometry

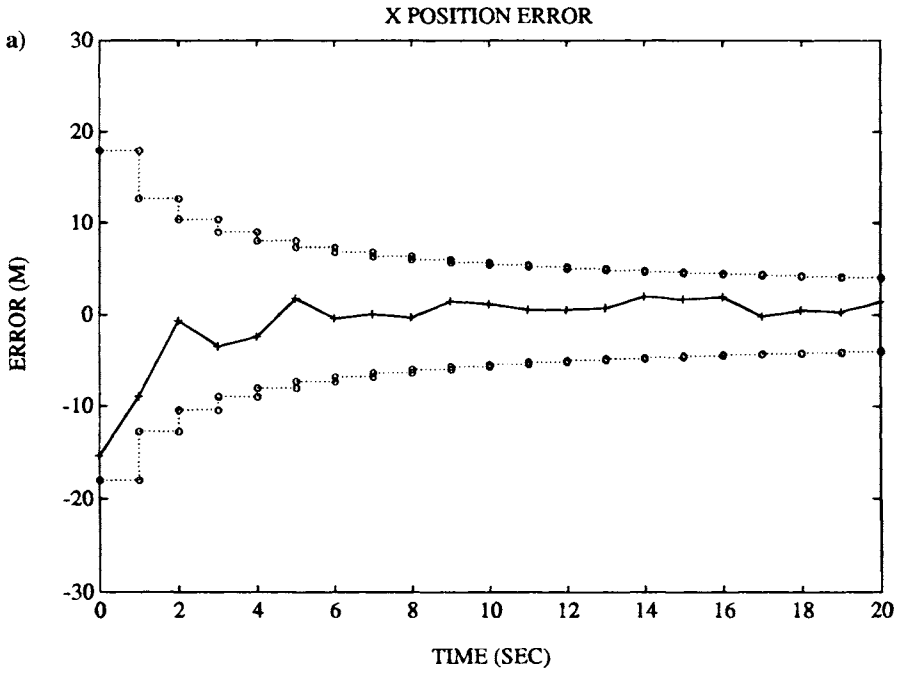

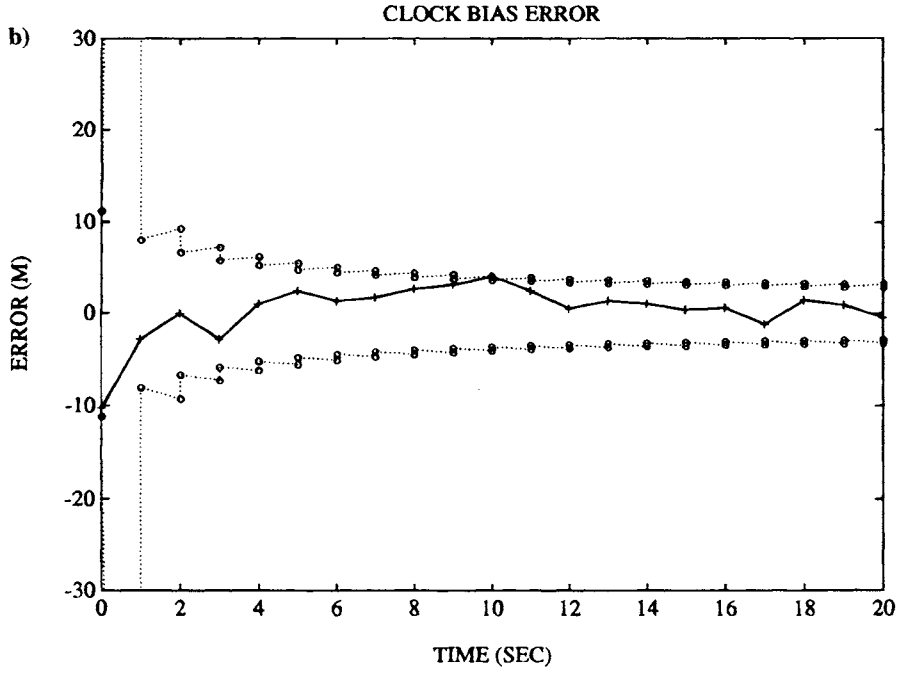

Fig. 5 Kalman filter estimation errors for buoy example. In both graphs the solid line with the "+" symbols represents the actual error. The dotted lines with the "o" symbols represent the filter computed $1 - \sigma$ bounds both before and after the measurement update; a) x position estimation error; b) clock bias estimation error.

remains fairly consistent, this condition will continue. If the geometry degrades or if measurements are missed, the uncertainty will grow at a rate determined by the process noise matrix.

For comparison with the Kalman filter results, Fig. 6 shows the errors in the z position and clock bias point solutions utilizing the same measurement data. Note that although the filter solution uncertainty was reduced to less than 5 m within 20 s, the point solution accuracy does not improve. In this static example, the point solution could be averaged to form an improved estimate that would be at least as accurate as the filter solution.

This example shows good performance of a Kalman filter for GPS navigation solutions because it employs accurate models for both the observations and the observer dynamics. In the next two examples, we look at what happens if these rules are violated.

B. Low Dynamics

The next example is for a user traveling along the Earth surface at 100 m/s in the direction due North from 0° latitude, 0° longitude. The position and velocity components of the state are implemented in WGS-84 coordinates, with the full state given by, $\boldsymbol{x}_L \equiv [x\ y\ z \mid \dot{x}\ \dot{y}\ \dot{z} \mid b\ f]^T$.

The process model given in Eq. (17) is used in the filter to propagate the state and covariance between measurement epochs. The discrete process noise matrix for a 1-s measurement interval is assumed to be diagonal with uncertainty for the velocity states set to $(1\text{ cm/s})^2$, and $(10\text{ cm})^2$ for the position states.

The initial estimate of the state is

$$\hat{\boldsymbol{x}} = [6{,}377{,}000.0\text{ m} \quad 3{,}000.0\text{ m} \quad 4{,}000.0\text{ m} \quad 0.0\text{ m/s} \quad 0.0\text{ m/s} \quad 0.0\text{ m/s} \quad 0.0\text{ m} \quad 0.0\text{ m/s}]^T$$

The diagonal elements of the initial covariance matrix for the position states are each set to 25 km^2; for the velocity states to 1 km^2/s^2; for the clock bias state to 10^4 km^2; and for the clock drift state to $(c \cdot 10^{-6})^2$ km^2/s^2. The receiver takes measurements to all GPS satellites above an elevation of 10 deg at intervals of 1 s. Each pseudorange measurement is assumed to have a variance $R = 36$ m^2.

Figure 7 shows the filter estimation error for each of the position and clock bias states. The results are similar to the buoy case in that the filter estimates the trajectory accurately, and the $\pm 1 - \sigma$ uncertainty bounds it computes are reasonable. (In all graphs, the solid line with the "+" symbols represents the actual error. The dotted lines with the "o" symbols represent the filter computed $1 - \sigma$ bounds both before and after each measurement update.)

C. Unmodeled Dynamics

The next step is to introduce unmodeled dynamics. Figure 8 shows the trajectory for a vehicle traveling at a speed of 100 m/s in a 5 km radius circle. Thus, the acceleration is quite mild at 2 m/s^2. The same models were used as in the previous example except that the discrete process noise values were increased to $(1\text{ m/s})^2$ for each of the velocity states.

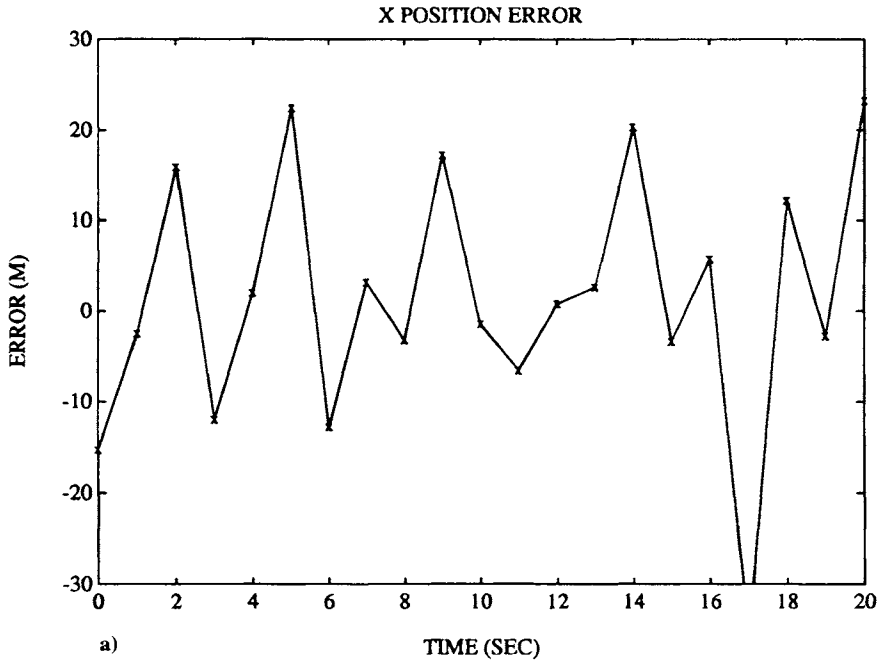

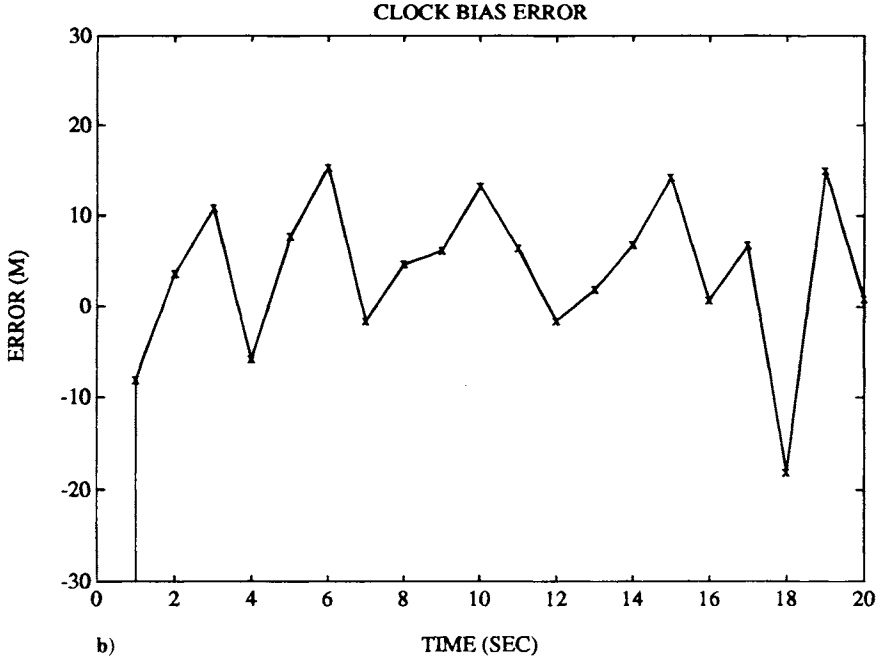

Fig. 6 Point solution estimation errors for buoy example.

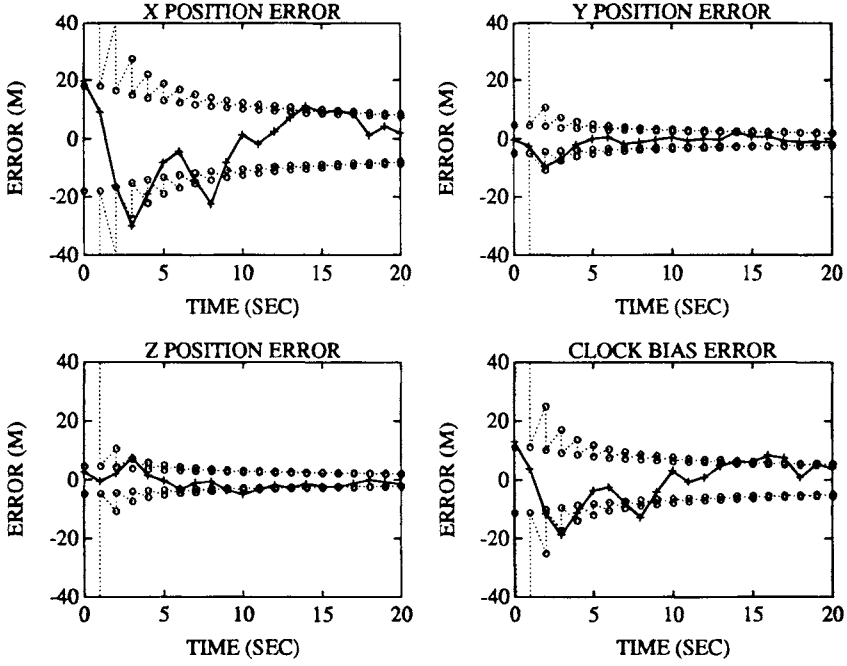

Fig. 7 Kalman filter estimation errors for constant velocity vehicle.

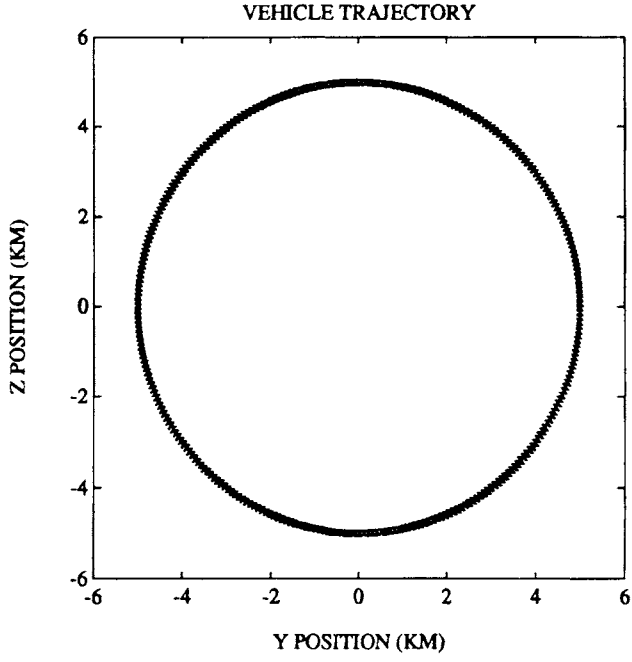

Fig. 8 True *Y–Z* trajectory for vehicle traveling in a circle at a speed of 100 m/s.

The filter results are shown in Fig. 9. Unlike the previous examples, the position and velocity estimation errors for the Y and Z components have a correlated nature that is not reflected in the filter computed covariance bounds. This illustrates an important limitation of the Kalman filter—it can only work as well as its models. Of course, in this particular case, it would be possible to augment the dynamic model to include acceleration states that would lead to improved performance.

D. Correlated Measurement Errors

As described in Chapter 17 of this volume SA introduces highly correlated errors into the GPS measurements. The figures in Chapter 17 illustrate a variety of observed and simulated SA error profiles. For this example, the model described in Chapter 17, Sec. II was used to generate simulated SA errors for a single satellite. An error profile was created for each GPS satellite, and the buoy filter example was re-run. The only change made to the filter parameters was to increase the measurement variance to $(35\ \text{m})^2$ corresponding to the variance of the actual errors (note that this is not a Schmidt filter). Recall, however, that the filter assumes that the measurement errors are uncorrelated between epochs, which is clearly not the case with SA. Figures 10 and 11 illustrate the filtered and point solution results obtained. Note that in both cases, the solution wanders, following the wandering SA profiles. The filtered solution is smoother, but not more accurate than the point solution.

VII. Summary

This chapter has presented mathematical models for each of the basic GPS measurement types. Pseudoranges were used to form a single point position and clock bias solution. This solution depends only on observations from a single measurement epoch. To improve the navigation accuracy, we must include knowledge of the vehicle dynamics. The extended Kalman filter is an approach commonly used in GPS receivers and data-processing packages. Dynamic models for a stationary, low dynamic, and high dynamic user were given, as well as a useful model for a typical receiver clock. Examples were shown of the performance of the filter as compared to the least squares solution under various conditions, and the consequences of mismodeled dynamics and measurements were described.

In addition to stand-alone navigation, Kalman filtering plays an important role in other GPS applications. Several of the chapters in the companion volume describe models and results obtained for diverse applications such as orbit determination, and aircraft approach and landing. The key to success with this approach is an accurate model of the dynamics and the measurement processes.

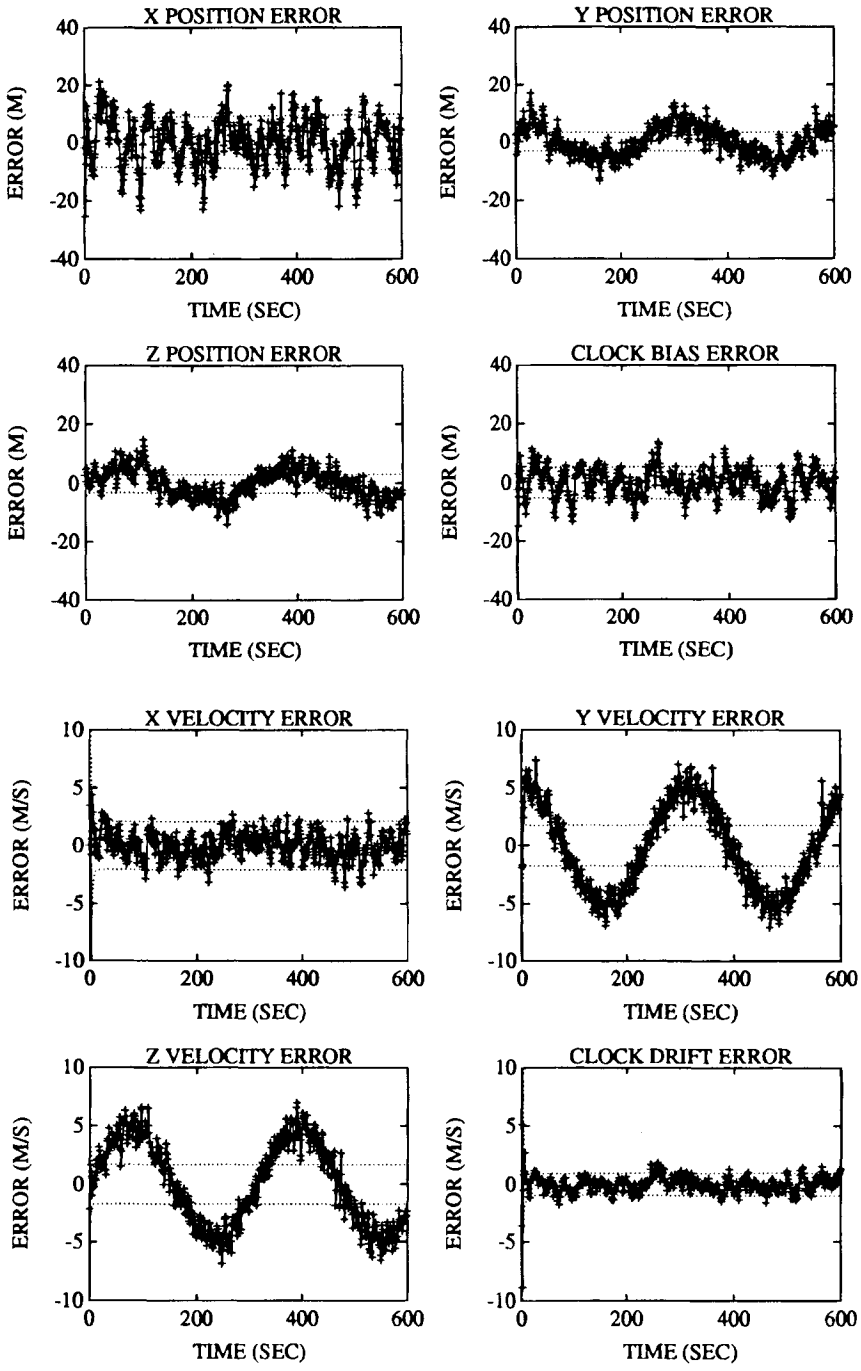

Fig. 9 Kalman filter position, velocity and clock estimation errors for vehicle traveling in a circle. The solid line with the "+" symbols represents the actual error. The dotted lines represent the filter computed $1-\sigma$ bounds after each measurement update.

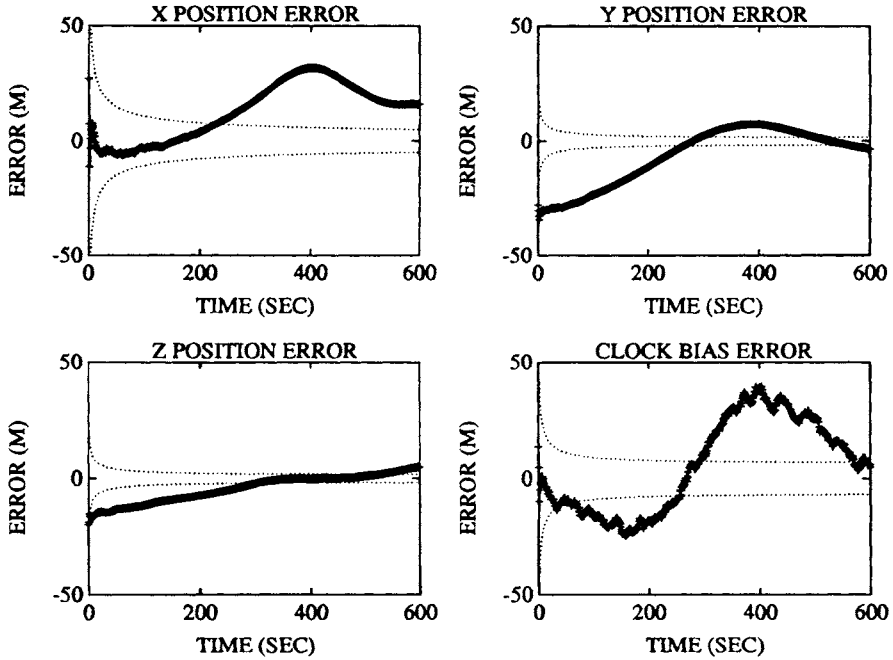

Fig. 10 Kalman filter estimation errors for buoy with SA pseudorange errors. The solid line with the "+" symbols represents the actual error. The dotted lines represent the filter computed $1 - \sigma$ bounds after each measurement update. In this case, the filter bounds are clearly not meaningful.

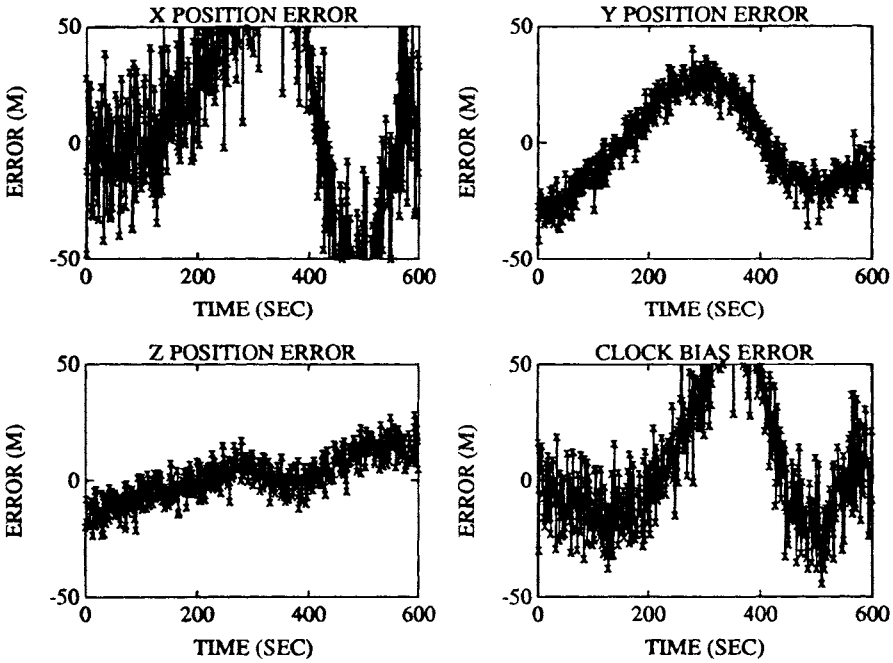

Fig. 11 Point solution estimation errors for buoy with SA pseudorange errors. The solid line with the "+" symbols represents the actual error. The dotted lines represent the filter computed $1 - \sigma$ bounds after each measurement update. In this case, the filter bounds are clearly not meaningful.

References

[1]Brown, R. G., and Hwang, P. Y. C., *Introduction to Random Signals and Applied Kalman Filtering,* 2nd ed., Wiley, New York, 1992.

[2]Gelb, A. (ed.), *Applied Optimal Estimation,* MIT Press, Cambridge, MA, 1984.

[3]Bryson, A. E., and Ho, Y. C., *Applied Optimal Control,* Hemisphere, New York, 1975.

[4]Maybeck, P. S., *Stochastic Models, Estimation and Control,* Vol. 1, Academic Press, New York, 1979.

[5]Wells, D. E., et al., *Guide to GPS Positioning,* Canadian GPS Associates, 1986.

[6]Hatch, R., "The Synergism of GPS Code and Carrier Measurements," *Proceedings of the Third International Symposium on Satellite Doppler Positioning,* (New Mexico State University), Feb. 8–12, 1982, pp. 1213–1231.

[7]Hwang, P. Y. C., and Brown, R. G., "GPS Navigation: Combining Pseudorange with Continuous Carrier Phase Using a Kalman Filter," *Proceedings of ION GPS-89,* (Colorado Springs, CO), Institute of Navigation, Washington, DC, Sept. 27–29, 1989, pp. 185–190.

[8]Anon., ICD-GPS-200, IRN-200B-PR-00J, Rev.B-PR, July 1992.

[9]Golub, G. H., and Van Loan, C. F., *Matrix Computations,* Johns Hopkins University Press, Baltimore, MD, 1989.

[10]Van Dierendonck, A. J., McGraw, J. B., and Brown, R. G., "Relationship Between Allan Variances and Kalman Filter Parameters," *Proceedings of the 16th Annual Precise Time and Time Interval (PTTI) Applications and Planning Meeting,* NASA Goddard Space Flight Center, Nov., 1984, pp. 273–293.

[11]Minkler, G., and Minkler, J., *Theory and Application of Kalman Filtering,* Magellan Book Company, 1993.

[12]Kailath, T. (ed.), *Linear Least-Squares Estimation,* Dowden, Hutchinson & Ross, 1977.

[13]Bierman, G. J., *Factorization Methods for Discrete Sequential Estimation,* Academic Press, Orlando, FL, 1977.

Chapter 10

GPS Operational Control Segment

Sherman G. Francisco*
IBM Federal Systems Company, Bethesda, Maryland 20817

THE GPS user solution is based on Space Vehicle (SV) orbit and time scale information contained in the navigation data sets generated by the operational control segment (OCS).[1] The space assets of GPS are managed and supported by this dedicated ground-based segment, which consists of *L*-band facilities to continually track the GPS radio frequency navigation signals, a digital computer network to process scientific and system control data, dedicated *S*-band facilities to conduct duplex information transfer sessions with each individual space vehicle, dedicated secure communications datalinks to couple the globally distributed ground assets into one integrated real-time global system, and a personnel system located at the principal ground facility where dedicated members of the United States Air Force operate the complex system. Functions allocated to this segment of GPS include the operational responsibility to perform the following:

1) Control and maintain the status, health, and configuration of the SV Constellation.

2) Support the user segment with precision predictions of ephemeris and time scale calibration data. Prepare and upload the formatted navigation message data sets to the SV for subsequent metered retransmission to the user community.

3) Monitor the quality of navigation and time transfer services as provided to the end users.

4) Support system interfaces to associated services (i.e., United States Naval Observatory).

5) Manage and schedule the ground assets of the control segment.

This chapter provides a summary description of the present OCS, which includes both the manned master control station (MCS) facility located at Falcon Air Force Base and the automated globally distributed radio frequency station assets deployed to control and continually monitor each satellite of the space vehicle constellation. System architecture, satellite contact coverage, measurement data correction, estimation, and prediction are addressed in this chapter.

*Senior Technical Staff Member.

Figure 1 illustrates the components of this segment and the major system interfaces, including those to other GPS segments and to associated support services.

This OCS architecture provides the GPS operating agency the means for self-sufficient support of the navigation mission once operational space vehicles are stabilized on orbit, and the OCS facilities have ample resources to handle the fully populated constellation supplemented with additional on-orbit spare satellites. External operational interfaces are implemented to the Air Force Satellite Control Facility (AFSCF), to the United States Naval Observatory (USNO), and to the Defense Mapping Agency (DMA) for the respective data exchange functions of SV hand-over in their assigned orbit plane, of coordinating the universal coordinated time (UTC) absolute time scale (which is not visible to GPS instrumentation), and of providing Earth orientation data relative to the existing standard international conventions for inertially fixed coordinate systems. These external support dependencies are strategic in nature because the primary GPS services can autonomously continue service within the established system performance specification for many weeks. Less formal system interfaces also exist to import from the Jet Propulsion Laboratory (JPL) the predicted Sun–Moon position data, to exchange pertinent information with associated user data services, and to support the initial prelaunch activities at Cape Canaveral.

Both the operational procedures and the equipment configuration have been designed to ensure continuous GPS system services. Although the GPS user community is buffered by the distributed store-and-forward data concept implemented in GPS satellite memory, the OCS is designed so that single failures on the ground can be accommodated without disrupting the time-critical functions allocated to this segment. Redundancy of all critical equipment is provided, and

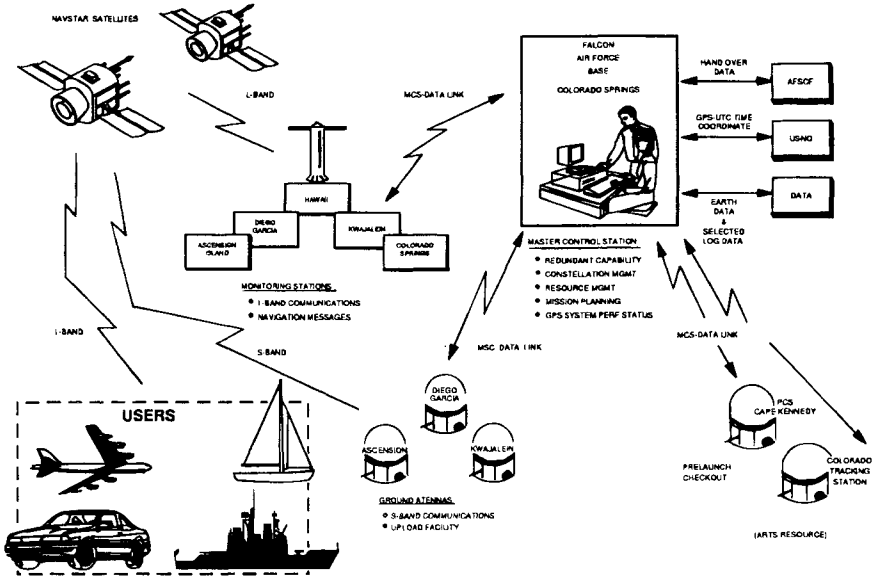

Fig. 1 Operational control segment configuration.

nonreal-time support tasks such as the numerically intensive integration of future reference orbits are identified and judiciously scheduled at OCS convenience on the standby system assets so as to make efficient use of the overall facility investment while meeting the critical data preparation needs. This conservative design philosophy extends to providing database redundancy and to the protection of vital information from contamination. High availability architectural features are cooperatively incorporated in both hardware and software to tolerate single equipment failures, to facilitate equipment reconfiguration and maintenance actions, and to perform (if necessary) process initialization/restart functions without residual corruption of either the database values or of the critical estimation process. Stringent consistency checks are applied to the measurement data, to the estimation process, and to the OCS products generated for internal and for export use. The OCS navigation service product integrity is thus maintained in the presence of normally encountered implementation imperfections.

The robust, underlying GPS service integrity concept of allocating tactical autonomy to each space vehicle and of implementing end-to-end error detection and fail-safe interlocks in the OCS protocols associated with data movement make possible fault-tolerant operational procedures that ensure dataset consistency at the satellite. The occasional OCS process adjustments and equipment reconfigurations encountered during continuous operations are formulated so as to be transparent to users who properly adhere to the total content of the navigation message and the application constraints as documented in the ICD-GPS-200[2] documentation.

Thus, the OCS provides high-integrity navigation data sets at the SV memory. Data errors occurring on the SV–user link are correctable using codes that originated at the ground OCS MCS. Although improbable, an unpredictable flaw in the timing of the GPS signal structure as generated by the SV has occasionally occurred on Block I satellites. The OCS detects and records such events, but has no practical means to provide a service alarm in a timely (10 s) manner. The defensive concept of receiver autonomous integrity monitor (RAIM) has evolved within the community for the user to identify any such SV signal inconsistencies based on the inherent information redundancy of the fully populated constellation. For critical applications such as precision aviation approach navigation, real-time communications can augment the basic GPS service by disseminating both the current status of service and differential corrections to the predictions for each satellite. Such feed-forward error correction overcomes the practical limits of precision time scale and orbit prediction in the baseline GPS concept, but at a cost of service vulnerability.

As space technology continues to advance, some OCS functions of the base system level concept may be reallocated to future space vehicles so as to reduce tactical dependencies on ground assets. Estimation of navigation data (such as SV clock correction term estimation) could be improved by the availability of satellite-to-satellite cross-link measurement capabilities, which makes the on-board refinement of navigation data possible.[3] The precision ranging service from these unaided SVs would also be improved[4] with the potential of a continuously available user range error (URE) of 2 m enabled by the reduced delay in providing precise relative clock corrections to the user sets.

The Consolidated Space Operation Center (CSOC) is located at Falcon Air Force Base (Fig. 2) near Colorado Springs, Colorado. Here the MCS for GPS

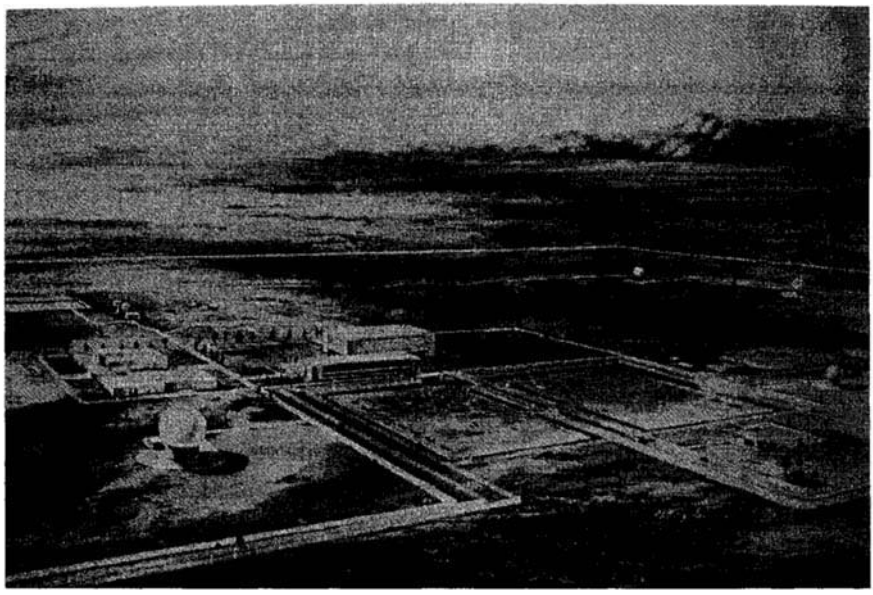

Fig. 2 Consolidated space operations center.

resides and operates 24 hours a day with a dedicated United States Air Force staff. They are responsible for the SV constellation and operate the ground support processing that generates the fresh navigation data uploads.

This facility is the overall operations center for GPS with operational responsibility for all OCS functions including navigation information processing, satellite data upload, vehicle command and control, and overall system management. Full responsibility of each on-orbit SV commences once the normal Earth-oriented attitude stabilization is established which enables *L*-band tracking, an operational capability unique to the GPS control segment (CS). Monitoring the performance of the numerous GPS services and system components by OCS is an essential element of system availability and service quality assurance.

Visibility of the GPS signal structure is provided to the OCS by the five monitor stations (MS). These are remote, unmanned* GPS assets used to passively track the continuous navigation ranging signals of the entire satellite constellation and to acquire the digital data transmitted on *L*-band by each SV. Both the upload message generation and the GPS service quality monitoring are based on analysis of these tracking data.

Another type of unmanned OCS radio frequency asset is the ground antenna (GA), a full-duplex *S*-band communications facility that has dedicated command and control sessions with a single SV at a time. Interactive burst-communication sessions are periodically established for navigation data upload, satellite command, and telemetry reception that are essential to constellation operations and navigation service support. *S*-band ranging services are not available. Both types

*On-call maintenance provided by the host site.

of these distributed GPS radio frequency facilities include the functionality to tolerate automatically short disruption of communications with no induced flaw in service and to support remote reconfiguration with diagnostics conducted from the MCS. Location of these radio frequency facilities has been a programmatic compromise between radio frequency contact utility to the GPS mission and the availability of adequate secure physical facilities with on-call technical support.

I. Monitor Stations

Navigation signal visibility is provided to the MCS by the globally distributed unmanned monitor stations. The GPS monitor stations are radio frequency-passive facilities that receive the same signal structure as the user community. Some low-rate telemetry unique to the instantaneous SV state is of operational interest to the OCS. These stations track the apparent pseudoranges and carrier phase between SV–MS pairs and also collect the transmitted navigation messages for two operationally routine purposes:

1) The pseudorange and carrier phase histories are required to derive precisely and provide the GPS user with ephemerous and clock calibration data for each SV.

2) Both the pseudorange histories and the broadcast navigation data are required to monitor the services as provided to the user community.

Note that the technical performance required of OCS monitor stations must exceed that of the conventional high-precision user set for two fundamental reasons:

1) The OCS task of prediction is more demanding of data quality than is the deterministic end user's current position solution. Both the state separation process encountered in estimating current nonorthogonal system states and the time projection process encountered in predicting future SV states are extremely sensitive to noise, bias, and systematic errors in the measurements. Monitor station measurement errors are magnified in their propagation to become user input error components.

2) The MCS must maintain clear, detailed signal visibility and cope with abnormal signal structures both to permit initial SV process alignments and to support overall system diagnostics. The user has no need to deal with out-of-specification signals or malfunctioning system elements.

The GPS is committed to the operational requirement of global continuous navigation service, and monitoring the system service implies that each satellite's signal should be continuously monitored for pseudorange accuracy compliance, message content, and signal health. The ground projected latitude of block II and later satellites will never exceed the orbit inclination angle of 55 deg; therefore, near-equatorial sites that can track the complete 110-deg groundtrack latitude band are the most desirable MS locations for contact efficiency. Although observations from a spread of latitudes is beneficial to geopotential and force anomaly modeling, covariance error analysis shows that they are not critical to observe the GPS states. Scientific modeling efforts external to the operational program are adequate support to achieve the system performance requirements.

Colorado Springs, Ascension Island, Diego Garcia, Kwajalein, and Hawaii have been chosen as the OCS monitor station sites that best meet the overall OCS requirements, and the precise coordinates of the antenna phase center were

accurately determined in the WGS84 coordinate system through special surveys and custom off-line tracking data reductions. Figure 3 illustrates the resulting track coverages provided by this selection of monitor station sites for SV lines of sight that are above the horizontal by a practical 5-deg elevation angle at the receiving antenna. This selection of sites achieves a 95.87 % average coverage for the baseline constellation with only five monitor stations. Contact statistics with each of the operational ground tracks is different, varying from 93.63 to 100% of the ground track. Because of the latitude of Colorado Springs, a slight gap in signal monitoring (not navigation service) does occur for satellites when ground tracks are over the open ocean west of southern South America, which is apparent in Fig. 3. A limited *L*-band capability is also implemented in the eastern launch site at Cape Canaveral for the OCS to verify segment compatibility prior to satellite launch, but use of this facility does not close the slight operational coverage gap.

Regions of tracking coverage overlap (simultaneous *L*-band contact with the same SV by two monitor stations) are very important in establishing a robust GPS estimation process. Observed residuals in pseudorange measurements must be allocated to probable errors in time and in SV position by the action of the Kalman filter estimator. Solution for the states of an isolated satellite and of the monitor stations is quite fragile because of the extensive linear relationships that prevail in pseudorange-based measurement systems and to the effects of accumulated model uncertainty (process noise) when marginal measurement geometry exists to distinguish the error source. Common view strengthens any solution by enabling direct time transfer between MS sites. Fortunately, the extreme situation of sporadic track contact only occurs during system development (and possibly during recovery from an improbable loss of the OCS database). Although it was deemed impractical at the time of initial OCS development to

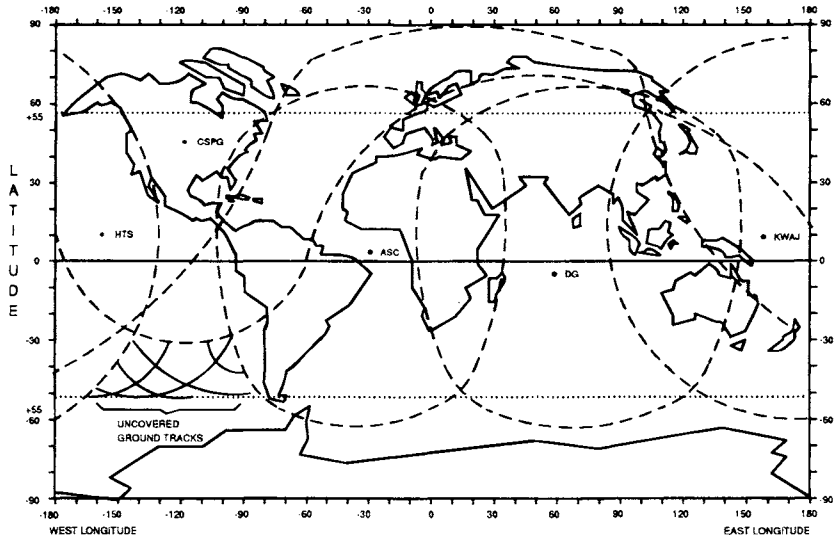

Fig. 3 Monitor station tracking coverage.

implement the total GPS state solution in one large filter formulation so as to fully exploit the available measurement geometry (space and time), near optimum performance has been practically achieved at a much lower computer burden by partitioning the constellation and adhering to the following important system design choices that have been found very beneficial in stabilizing the estimation process and achieve a robust solution within estimation filter partitions, or subsets of states.

1) Select the SVs for inclusion in each partition so as to maintain (near) continuous time transfer between monitor stations within each partition through common-view SV observations. This strategy is made possible by the existence of significant regions of tracking coverage overlap provided by the MS site selection, thus greatly strengthening the GPS system solution by effectively decoupling the MS time and the SV state components of pseudorange errors.

2) Adopt the same SV-signal instance for sampling the common view measurements of a common-view sample set to establish cleanly one satellite state for each common view sample set. This strategy, which effectively decouples satellite velocity states, is achieved in the OCS monitor stations by basing the pseudorange measurement instant on the waveform epoch in the received signal structure. Utilization of this sample time convention reduces the terms in the measurement model, and this choice is essential if corrections for selective availability are to be made with precision.

3) Eliminate the interchannel measurement biases that disrupt the clean separation of system ground states. This reduces the true number of time states and is achieved by the OCS monitor station architecture practice of using, whenever possible, the same physical hardware for common MS functions (i.e., downconverter, station time reference).

Thus, the objective of achieving the full GPS performance potential strongly drove both the selection of MS sites and the detailed receiver equipment architecture. The above design guidance, which greatly influences MS implementation, was formulated through extensive error analysis and simulation efforts at the GPS system level, and these advanced principals have been verified through a decade of stable estimator performance. Even in a partitioned estimator solution, exploiting the common-view information potential is possible through advantageous selection of the MS sites, prudent selection of the SV members within a partition, and the adoption of common-view measurement time tagging (adopting the specific source SV code epoch for sampling). This practice of simultaneous measurement instances for a SV significantly stabilized the partitioned estimator formulation and reduced estimation process sensitivity to systematic error stresses. Errors in position and time are more decoupled, which significantly reduces the degree of error source aliasing. Estimation of the individual satellite trajectories is then numerically solid because the large off-diagonal covariances characteristic of weak geometry are avoided. The relatively large clock process noise levels are less coupled into the position solution, and once the MS time-transfer network closes through common-view measurements, robust estimator performance is established. This strategy has had the effect of immediately stabilizing the relative monitor station time scales for each partition.

Obviously, the precision of knowledge estimated by the CS at the beginning of the prediction period must be an order of magnitude better in quality than

the end-ranging service specification after a possibly long prediction interval. Prediction magnifies any errors existing at the beginning of the interval, and so errors in MS measurements affect the user solution more than do the errors in user set measurements. Similarly, the measurements to substantiate system performance metrics must be substantially better than the specified ranging service requirement to be a reliable performance indicator.

Two distinct categories of tracking performance requirements exist. The precision range data, which are used to estimate clock and SV trajectory states, must be free of significant error. Systematic errors are especially damaging because they are not countered by averaging the abundant measurement data, and their presence can cause significant spatial biases in the resulting navigation service product. The OCS allocated processes of separating states and of predicting ahead in time greatly amplifies the size of error to the user. Therefore, systematic errors, such as the effects of multipath interference, must be carefully controlled. The ranging measurement data used by the estimation filters is restricted by the OCS operational procedures to track elevation angles of 15 deg or greater above the horizon so as to avoid significant multipath effects and to eliminate the relatively large, uncorrectable measurement errors that could result from excessively long propagation paths in the troposphere. Exceptional multipath rejection ratio characteristics and phase center stability are still required above this mask angle, but this can be achieved with the simplicity of a single-beam antenna that precludes the problem of antenna channel bias. In contrast, measurement data to support navigation service monitoring and subsequent user process emulation for service verification need only be consistent in quality with that of baseline user practice, which is a relaxation from the accuracy required for the OCS estimation data acquisition. Tracking performance monitoring must, however, extend down to 5-deg elevation angle to achieve coverage with a practical number of MS sites while providing range data better than the baseline user requirement and with acceptable bit error rates.

These OCS L-band tracking requirements imposed a formidable antenna design problem. Master station design practice is based on the philosophy that the raw data acquisition performance of an operational system should be consistent, when practical, with the achievable state of the art so as to assure clear visibility of data anomalies for fault analysis. Design studies and then chamber testing of the actual antennas indicate that a phase stability of plus or minus two centimeters is achievable on both L_1 and L_2 without spatial calibration. This uncertainty is consistent with the assessed level of error in the measurement model components.

Thus, a single, unsteered beam fulfilling both the navigation service monitoring and the precision range tracking requirements on both L_1 and L_2 frequencies is implemented at each MS site, and multiple radio frequency channels with resulting equipment duplication and the introduction of interchannel bias problems were avoided. Vega Precision Laboratories provided the high-performance design and developed the production MS antennas (Fig. 4). A shaded, bent turnstile is used to receive dual-frequency, right-hand circularly polarized signal transmission. The conical ground plane with annular chokes at the base produces the specified performance with 14-dB multipath rejection ratio for signal paths above 15-deg elevation angle. The design is optimized for L_2 to compensate for the difference in SV signal transmission strengths. The antenna design contains the low noise

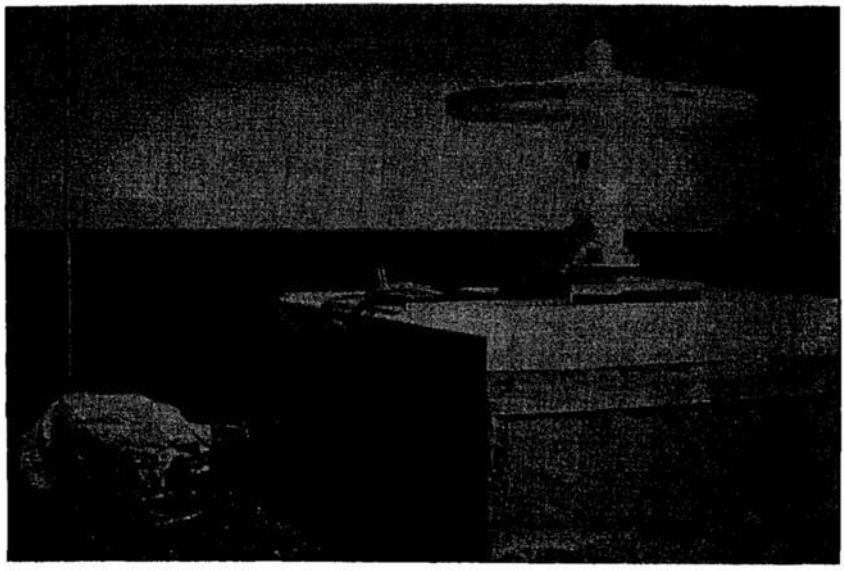

Fig. 4 Monitor station antenna.

amplifier in the pedestal base, as is shown at the Ascension monitor station installation. (An external heated radome with heating is installed at the CSOC location to handle the Colorado winter climate.)

In operational practice, the CS experiences a measurement update innovation level of 2–4 cm for (carrier-aided) 15-min smoothed measurements during normal steady-state operation for each MS. Because this is achieved with estimation filter tuning optimized for the multiday prediction interval performance that demands the use of low but realistic process noise values, the data acquisition and measurement strategy and implementations are verified in practice.

The *L*-band receivers for the CS must have other additional functionality not found in conventional user sets. They must work with signals not in compliance with the operational specification. Initial acquisition of a new satellite cannot be dependent upon the complex signal alignment promised the user, and no correct prompting is assured. The MS receiver must accommodate and detect abnormal signal structures that naturally occur prior to completion of the navigation payload alignment or when a related equipment fault is experienced. Good visibility of the signal structure is retained by the specialized OCS MS receiver design, and the capability for a technical specialist at the MCS to assist in the initial alignment or SV diagnostic process is provided.

For normal tracking, the OCS simultaneously tracks multiple SVs on both *L*-band frequencies to permit correction of the ionospheric delay. Contact scheduling for each MS is based on the requirements for each MS to track all visible satellites above the estimator data criterion of 15-deg elevation angle, and to track continually each SV of the constellation by some MS, if anywhere visible to the OCS. This strategy maximizes the common-view contacts and provides the long track histories for carrier-aided smoothing to support the estimation

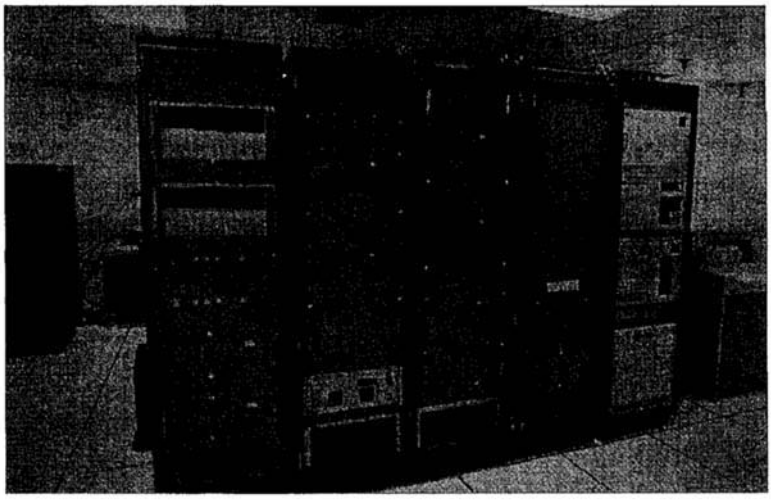

Fig. 5 Monitor station equipment.

process. It also maintains maximum signal monitor contact with each SV. Adequate channel assets are provided in each monitor station to meet this schedule criteria, to provide an active spare channel, and to include a calibration channel programmed to cycle through all the channels. This innovation permits the MCS to sense and correct for any residual interchannel biases in the receiver correlator instrumentation. All modes of track acquisition can be accomplished so that the operator can verify *L*-band support of the numerous user strategies and that reliable SV contact in unusual adverse conditions is possible.

The specialized monitor station receiver equipment was developed by Stanford Telecommunications, Inc. and provide accurate multisatellite range data with minimum interchannel biases. The circa 1978 technology, as shown in Fig. 5, provides data of unprecedented quality to support the precision estimation of clock and ephemeris parameters, and measurement performance is comparable to the best of today's receivers. The internal clock circuits and the two down converters are common to all channels, so that any common bias can be absorbed within the estimated monitor station clock states. Critical cables are trimmed to consistent lengths in order to match delay and drift affects. Pseudorange and accumulated delta range measurements are obtained each 1.5 s on the exact received *X*-1 epoch for both the L_1 and the L_2 signals.[5] This selection meeting the objective of SV-referenced sampling is convenient to the designer, and the high sample rate captures the information content of the noisy pseudorange measurements. The resulting signal visibility not dependent upon SV alignment is essential to support SV diagnostics and the MS–MCS communications is adequate to return all the data to the MCS. Thermal noise for P-code tracking under the worse specification signal conditions is approximately 2.5 m, one sigma, for pseudorange and less than 0.7 cm, one sigma, for accumulated delta range (ADR). These measurements, the received navigation message, and signal-

to-noise power data observations are formatted by the receiver and then transferred to the local digital processor for message handling at this autonomous facility.

A test and calibration signal generator, which provides remote station diagnostic capability, is also controlled by this processor. These test signals can be configured and routed to the LNA, down-converter, or correlator by an MCS ground controller. This capability permits precise station-ready verification and is used to support local maintenance whenever a service call is made.

Frequency Electronic, Inc. (FEI) developed the monitor station frequency standard rack, which establishes the precision reference for pseudorange measurements. Although ultrastable atomic time scales at each MS are not critical to GPS navigation mission once a major portion of the constellation is up, this equipment was important to the development program. Two cesium atomic frequency standards are installed at each unmanned monitor station to permit functional substitution of the hot spare from the MCS. These Hewlett Packard 50-61A Options 4 Standards were modified to provide remote indication of clock parameters considered characteristic of atomic standard health. Phase comparison is instrumented in the FEI design so that the MCS can maintain a current frequency calibration of the backup unit and transfer the timescale to the redundant unit with no further time scale calibration. Remote fault sensing with the option of automatic switchover is provided. The battery-powered backup units have been designed for high availability in unmanned applications. They are fully integrated with the overall MS asset monitoring control structure.

Advanced time subsystems are being introduced to give better support to the time transfer community. This extension is intended to improve the coupling of GPS atomic time and the official USNO reference. Support of local time users can be integrated into the local monitor station reference, which is more current than that available from the SVs.

Remote indicating sensors of barometric pressure, temperature and dew point are included in each MS to permit approximate correction for tropospheric delay. The dew-point sensor at unmanned sites has been undependable, and often a default value is substituted to accommodate sensor malfunction.

Tracking orders and equipment configuration commands are received from the MCS over dedicated, secure communication channels. Measurements and status data are forwarded to the MCS over the same duplex channel, which utilizes commercially developed SDLC protocol to provide error detection and block data retransmission features transparent to the application software. Buffer time of 5 min is provided to accommodate communication equipment reconfiguring or other short service outages without loss of data.

II. Master Control Station

The master control station consists of the processing complex and controller facilities necessary to manage completely the operational GPS space assets and to produce the navigation message. Figure 6 provides an overview of the major functions and the flow of information types throughout OCS. Communications and remote processing can be tested remotely and initialized from the MCS to recover from a fault or extended outage of any remote unmanned facilities. The navigation mission requires upload availability of 98% (not to be confused with

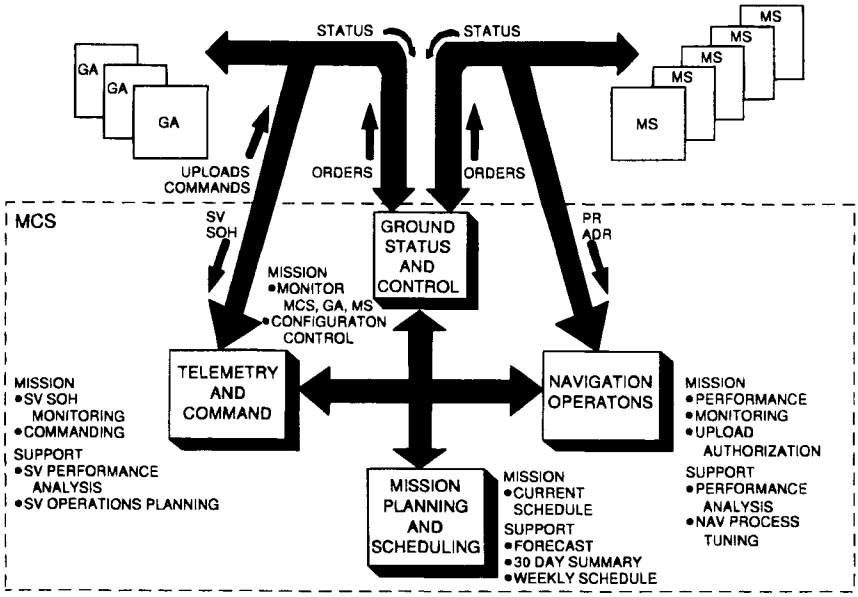

Fig. 6 Operations overview.

navigation service availability), so redundancy is provided for all mission critical equipment. Dual processors, communications controllers, and peripherals are configured to permit processing of the on-line navigation processing and satellite control functions with either processor unit. Many other GPS functions required to maintain the operation are deferrable for short periods of time when necessary to accommodate peak computation loads, fault recovery, and maintenance. Real-time communications are critical, and the OCS has implemented remote initialization and synchronization control from the MCS as well as the diagnostic capabilities to control remotely both digital and analog line looping features. Data Products New England implemented line and service management features of the MCS communications subsystem, which facilitate maintaining communications services. Loop back of the equipment and the control of the communications net is facilitated by the flexibility of this communications interface. All communications with the MCS are encrypted for integrity to prevent spoofing of the system.

Personnel at the MCS control all navigation, processor, constellation, and OCS assets and are responsible for the overall GPS integrity. This requires the establishment of the procedures and efficient access to critical mission data. The MCS provides many identical work consoles initially developed by the Sanders Corporation; each having a keyboard, two-color displays, and a hard copy unit. Air Force controllers are on duty during a full shift. Each shift is under the direction of a senior duty officer, who has overall shift responsibility. This officer is aided by a ground controller, SV engineer, navigation specialist, and multiple pass controllers. The ground controller is responsible for the ground equipment and communications, while the SV engineer is responsible for the overall satellite

status and the resolution of problems concerning the SV. The navigation specialist is responsible for the overall navigation mission performance and manages the generation of upload messages. Prime responsibility for the satellite upload transaction, TT&C, and other satellite contacts rests with the pass controllers. Each operator can sign on at any of the consoles; giving his identity, function, and required passwords. The software then configures the display and interface options for that console to meet the specific requirements of the mission function authorized during the sign-on.

The MCS navigation process must generate predicted clock time scale and ephemeris on which to base the data in the navigation message, which is then stored and forwarded to the user by the satellite. Figure 7 illustrates the complex system information flow that is the basis of the GPS concept and integrates the segments to provide the GPS navigation service. As an illustration of the intertwined dependencies within GPS, consider that the pseudorandom radio frequency signal originating at the SV is tracked by the C Segment from which the navigation message is generated and returned to the SV for dissemination to the user, and also back to the CS for verification of the total system performance. The scientific navigation processing that generates the data for the formatted navigation message from measurements acquired by the MS is detailed in a subsequent section of this chapter.

III. Ground Antenna

Navigation message uploads, SV commands, and telemetry data are communicated via *S*-band sessions between a specific SV and one ground antenna (GA) as scheduled by a pass controller. Such information must be communicated to the SV constellation by the network of globally distributed, unmanned ground antenna facilities. Figure 8 illustrates the contact opportunities provided by the chosen GA sites of Ascension Island, Diego Garcia, and Kwajalein. The regions

	INPUT	FUNCTION	PRODUCT
SPACE	NAVIGATION MESSAGE COMMANDS	PROVIDE ATOMIC TIME SCALE GENERATE PSEUDORANGE SIGNALS STORE AND FORWARD NAVIGATION MESSAGES	PSEUDORANDOM RF SIGNAL NAVIGATION MESSAGE TELEMETRY
CONTROL	PSEUDORANDOM RF SIGNAL TELEMETRY UTC	CALIBRATE TIME SCALE, PREDICT EPHEMERIS MANAGE SPACE ASSETS	NAVIGATION MESSAGE COMMANDS
USER	PSEUDORANDOM RF SIGNAL NAVIGATION MESSAGE	SOLVE NAVIGATION EQUATIONS	POSITION VELOCITY TIME

Fig. 7 System information flow.

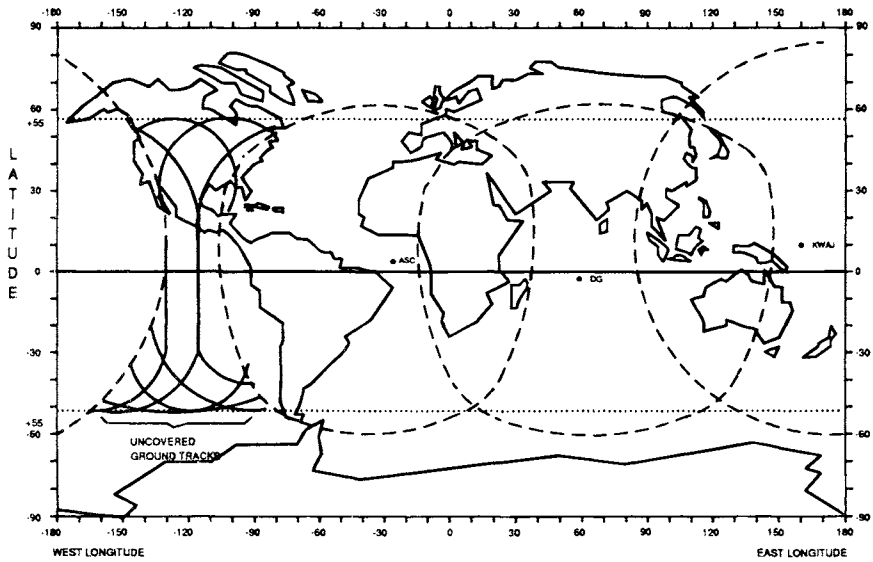

Fig. 8 Ground antenna contact window.

of coverage provide scheduling flexibility to best meet the overall MCS contact requirements. A fourth GA facility owned by GPS is located at the Eastern Launch Site, but is not depicted for coverage because radio frequency transmissions are severely restricted at launch sites, and the prime intent of this equipment is to support segment compatibility verification during prelaunch operations. In the event of a system emergency involving a SV in this contact gap, interoperability with an automated remote tracking station (ARTS) at the Falcon AFB is possible on an emergency basis to provide critical *S*-band services.

The dedicated GA installations developed by the Harris Corporation consist of a Scientific Atlanta 10-m *S*-band antenna and extensive Harris electronic equipment assembled in two rack groups according to function. Figure 9 shows the installation of the rack group containing the radio frequency exciter, high-power transmitter, receiver, and the servodrive equipment. Site selection was influenced by the location of existing remote tracking stations and with an objective of establishing the best overall space-tracking capability. Extensive remote readiness testing, fault alarms, and diagnostic features are incorporated to ensure equipment integrity and to support the on-call site maintenance. On-line equipment safety provisions respond to local sensor inputs to protect the GPS assets from thermal or power anomalies, even if communications with the MCS are disrupted. Command, telemetry, and navigation upload traffic is handled by these GA installations. Tracking orders, equipment configuration commands, and data are received over secured, dedicated duplex communications channels. The local GA processors store this transaction information on disks prior to SV contact, which minimizes operational sensitivity to communications anomalies. The command and upload protocol can be automatically maintained by the GA equipment in accordance with a programmable contact protocol decision tree

Chapter 11

GPS Error Analysis

Bradford W. Parkinson*
Stanford University, Stanford, California 94305

I. Introduction

ALTHOUGH the Global Positioning System (GPS) is clearly the most accurate worldwide navigation system yet developed, it still can exhibit significant errors. By understanding these errors, the user can both hope to reduce them and to understand the limitations of the GPS system. This section of the book should help develop that understanding. This chapter provides both an overview of the sources of error and a detailed analysis of the general error equations. It also presents a standard table of errors that should help clarify the impacts of variations in the specific error magnitudes. Later chapters delve into the expected ranges of these errors.

This development assumes that we are dealing with state-of-the-art receiver technology. In general, this requires a six-channel, continuous tracking implementation. Receivers with fewer channels will probably give a significantly degraded performance. In fact, a number of implementation compromises can produce receiver errors that are greater than those presented here.

This chapter first develops the general error equations and then illustrates how the dilution of precision (DOP) caused by satellite geometry can seriously degrade results. Finally, the error budget is summarized.[1]

II. Fundamental Error Equation

A. Overview of Development

As explained in introductory chapters, a GPS receiver fundamentally measures a quantity called pseudorange ρ, which is a raw, one-way range measurement corrupted by a user clock bias.[2] Using either models or measurements, ρ can be corrected for atmospheric and other effects to produce corrected pseudorange ρ_c. With an approximate user location, the receiver can then process these corrected pseudoranges (to four or more satellites) to determine location in a convenient coordinate system. (Various manufacturers have implemented the "anywhere"

*Professor, Department of Aeronautics and Astronautics; Director of Stanford GPS Program.

fix, which can start from any location. Such techniques are beyond this text and are not a part of error analysis.) This calculation is developed in this chapter.

For GPS, the underlying coordinate system is currently the 1984 World Geodetic System (WGS-84), which is an accepted worldwide geodetic coordinate system. It is expected that this will be replaced with a more accurate version as satellite geodesy improves. It is usual and convenient for the receiver to perform initial calculations in an Earth-centered, Earth-fixed (ECEF) Cartesian coordinate system. These coordinates can then be converted to any other required reference. For *error analysis,* it is usual to consider a local coordinate frame centered at the user and oriented East, North, and Up. This is convenient because many users have differing sensitivities to vertical errors and horizontal errors.

B. Derivation of the Fundamental Error Equation

This section develops the GPS error equation, beginning with the fundamental measurements and proceeding through analysis of the effects of various error sources. It lays the groundwork for the essential understanding of the dilution of precision (DOP) concept.

1. *Ideal Measurement*

The "true" or ideal measurement is the GPS signal arrival time. This is equal to the signal transmission time delayed by the vacuum transit time and corrected for the true additional delays caused by the ionosphere and troposphere:

$$t_A = t_T + D/c + T + I \tag{1}$$

where t_A = true arrival time (s); t_T = true transmit time (s); D = true range (m); c = vacuum speed of light (m/s); T = true tropospheric delay (s); and I = true ionospheric delay (s).

2. *Measured Arrival Time*

The measured arrival time reflects the user's clock bias and other measurement errors:

$$t_{Au} = t_A + b_u + v \tag{2}$$

where t_{Au} = arrival time measured by the user (s); b_u = user clock bias estimate (s); and v = receiver noise, multipath, interchannel error (different for each satellite (s)).

3. *Satellite Transmission Time*

The satellite clock correction transmitted by the satellite can also be in error (the dominant error may be due to selective availability SA):

$$t_{Ts} = t_T + B \tag{3}$$

where t_{Ts} = value of transmission time in the current satellite message (s); and B = true error in satellite's transmission time (includes SA).

4. True Range

The true range is the absolute value of the vector difference between the true satellite position and the true user position:

$$D = |\bar{r}_s - \bar{r}_u| = \bar{\mathbf{l}}_s \cdot [\bar{r}_s - \bar{r}_u] \tag{4}$$

where $\bar{r}_s$ = true satellite position; $\bar{r}_u$ = true user position; and $\bar{\mathbf{l}}_s$ = true unit vector from user to satellite.

The right-hand expression in Eq. (4), which uses the vector dot product, is a convenient way to calculate the range in the later user equation. In this calculation, the *estimated* user position can be used to find the unit vector from user to satellite. This unit vector need not be exact. Even *errors* of *several hundred meters* in user or satellite location have a very small effect on the dot product that uses this unit vector. Such a position error would produce angular errors of a few arc-seconds (about 10^{-5} rad) in the unit vector. Because the dot product *error* would be proportional to the cosine of this angle, it is of the order (angle)^2/2 or about $10^{-10}/2$ times the range. Because the range is 2×10^7 m, the effect would be less than 1 mm.

5. Pseudorange

The user receiver actually "measures" the "pseudorange" ρ, given by the following:

$$\rho = c \cdot (t_{Au} - t_{Ts}) \tag{5}$$

This is called the pseudorange because it is linearly a function of the range to the satellite, but it is also corrupted by the user's clock bias, which must be estimated and removed. In addition, it must be corrected for the estimated satellite time bias and for variations in the speed of transmission.

Substituting Eqs. (3), (2), and (1) into Eq. (5) gives the following result:

$$\rho = D + c \cdot (b_u - B) + c \cdot (T + I + v) \tag{6}$$

Using Eq. (4) in this expression gives the following:

$$\rho = \bar{\mathbf{l}}_s \cdot [\bar{r}_s - \bar{r}_u] + c \cdot (b_u - B) + c \cdot (T + I + v) \tag{7}$$

To account for the estimated value ($\hat{}$) and the estimate error (Δ), each of the above terms is to be broken into two parts as follows:

$\bar{r}_s = \hat{\bar{r}}_s - \Delta\bar{r}_s$, where $\hat{\bar{r}}_s$ = satellite position reported in the transmitted message (m)

$\bar{r}_u = \hat{\bar{r}}_u - \Delta\bar{r}_u$, where $\hat{\bar{r}}_u$ = user estimated position (m)

$\bar{\mathbf{l}}_s = \hat{\bar{\mathbf{l}}}_s - \Delta\bar{\mathbf{l}}_s$, where $\hat{\bar{\mathbf{l}}}_s$ = unit vector from user to the satellite estimated from $\hat{\bar{r}}_s$ and $\hat{\bar{r}}_u$

$b_u = \hat{b}_u - \Delta b_u$, where $\hat{b}_u$ = user clock bias estimate common to a set of simultaneous measurements (s)

$B = \hat{B} - \Delta B - S$, where $\hat{B}$ = satellite transmitted clock bias (s)

ΔB = the "natural" satellite clock error; that is, the error in control system prediction (s)

S = error in transmit time due to SA (s)
$T = \hat{T} - \Delta T$ $\hat{T}$ = estimated (or modeled) tropospheric delay (s)
$I = \hat{I} - \Delta I$ $\hat{I}$ = estimated (or modeled) ionospheric delay (s)

Equation (7) can then be modified to account for the estimated values:

$$\rho_j = (\hat{\bar{1}}_{sj} - \Delta\bar{1}_{sj})\cdot(\hat{\bar{r}}_{sj} - \Delta\bar{r}_{sj} - \hat{\bar{r}}_u + \Delta\bar{r}_u) + c\cdot(\hat{b}_u - \Delta b_u - \hat{B}_j + \Delta B_j + S_j) + c\cdot(\hat{I}_j - \Delta I_j + \hat{T}_j - \Delta T_j + v_j) \tag{8}$$

where the j subscript is the satellite number and has been added to point out quantities unique to each satellite.

In preparation for conversion to matrix form, Eq. (8) can be rewritten as follows:

$$\underbrace{\hat{\bar{1}}_{sj}\bullet\hat{\bar{r}}_u}_{(b)} - \underbrace{c\cdot\hat{b}_u}_{(a)} - \underbrace{\hat{\bar{1}}_{sj}\bullet\Delta\bar{r}_u}_{(d)} + \underbrace{c\cdot\Delta b_u}_{(d)} = \underbrace{\hat{\bar{1}}_{sj}\bullet\hat{\bar{r}}_{sj}}_{(b)} - \rho_j + c\cdot[\hat{I}_j + \hat{T}_j - \hat{B}_j]$$

$$+ \underbrace{-\hat{\bar{1}}_{sj}\bullet\Delta\bar{r}_{sj} - \Delta\bar{1}_{sj}\bullet(\hat{\bar{r}}_{sj} - \hat{\bar{r}}_u) + c\cdot(\Delta B_j + S_j) - c\cdot(\Delta I_j + \Delta T_j) + c\cdot v_j}_{(c)}$$

$$+ \text{higher order terms} \tag{9}$$

The large dots represent the dot product. Note that the terms underlined as (a) are the user's position and clock errors to be solved, the terms (b) are estimated or measured by the user, and the terms (c) are unknown errors that produce the solution errors given by (d). The right-hand portion of (b) includes ρ_{cj}, or corrected pseudorange, as: $\rho_{cj} = \rho_j - c\cdot[\hat{I}_j + \hat{T}_j - \hat{B}_j]$. This variable is used below.

Next, define the following matrices for K satellites in view (note that $K = 4$ is normally the minimum number of measurements):

$$\mathbf{G}_{K\times 4} \triangleq \begin{bmatrix} \hat{\bar{1}}_{s1}^T & 1 \\ \hat{\bar{1}}_{s2}^T & 1 \\ \vdots & \vdots \\ \hat{\bar{1}}_{sK}^T & 1 \end{bmatrix} \qquad \mathbf{A}_{K\times 3K} \triangleq \begin{bmatrix} \hat{\bar{1}}_{s1}^T & & & 0 \\ & \hat{\bar{1}}_{s2}^T & & \\ & & \ddots & \\ 0 & & & \hat{\bar{1}}_{sK}^T \end{bmatrix}$$

$$\hat{\bar{x}}_{4\times 1} \triangleq \begin{bmatrix} \hat{\bar{r}}_u \\ -c\cdot\hat{b}_u \end{bmatrix} \qquad \Delta\bar{x}_{4\times 1} \triangleq \begin{bmatrix} \Delta\bar{r}_u \\ -c\cdot\Delta b_u \end{bmatrix} \qquad \bar{R}_{3K\times 1} \triangleq \begin{bmatrix} \hat{\bar{r}}_{s1} \\ \hat{\bar{r}}_{s2} \\ \vdots \\ \hat{\bar{r}}_{sK} \end{bmatrix}$$

$$\Delta\bar{R}_{3K\times 1} \triangleq \begin{bmatrix} \Delta\bar{r}_{s1} \\ \Delta\bar{r}_{s2} \\ \vdots \\ \Delta\bar{r}_{sK} \end{bmatrix}, \qquad -\hat{\bar{\rho}}_{cK\times 1} \triangleq \begin{bmatrix} -\rho_1 + c\cdot(\hat{I}_1 + \hat{T}_1 - \hat{B}_1) \\ -\rho_2 + c\cdot(\hat{I}_2 + \hat{T}_2 - \hat{B}_2) \\ \vdots \\ -\rho_K + c\cdot(\hat{I}_K + \hat{T}_K - \hat{B}_K) \end{bmatrix} = \begin{bmatrix} -\rho_{c1} \\ -\rho_{c2} \\ \vdots \\ -\rho_{cK} \end{bmatrix}$$

$$\epsilon_{K\times 3K} \triangleq \begin{bmatrix} \Delta\bar{1}_1^T & & 0 \\ & \Delta\bar{1}_2^T & \\ & & \ddots \\ 0 & & \Delta\bar{1}_K^T \end{bmatrix}, \qquad \bar{\bar{P}}_{3K\times 1} \triangleq \begin{bmatrix} \bar{r}_u \\ \bar{r}_u \\ \vdots \\ \bar{r}_u \end{bmatrix}$$

and $\Delta\bar{B}$, $\bar{S}$, $\Delta\bar{I}$, $\Delta\bar{T}$, $\bar{v}$ are all obvious. The error in the unit vector to the satellite is $\Delta\bar{1}_j$. The matrix transpose is a convenient matrix notation for the dot product.

Equation (8) then becomes the following (neglecting higher-order terms):

$$\mathbf{G}\cdot\hat{\bar{x}} - \mathbf{G}\cdot\Delta\bar{x} = \mathbf{A}\cdot\bar{\bar{R}} - \hat{\bar{\rho}}_c - \mathbf{A}\cdot\Delta\bar{\bar{R}} + c \cdot(\Delta\bar{B} + \bar{S} - \Delta\bar{I} - \Delta\bar{T} + \bar{v}) + \epsilon\cdot(\bar{\bar{R}} - \bar{\bar{P}}) \tag{10}$$

The user does not know the last terms of Eq. (10), which are the errors, and calculates position based on the following:

$$\mathbf{G}\cdot\hat{\bar{x}} = \mathbf{A}\cdot\bar{\bar{R}} - \hat{\bar{\rho}}_c$$

to find the following for $K = 4$:

$$\hat{\bar{x}} = \mathbf{G}^{-1}(\mathbf{A}\cdot\bar{\bar{R}} - \hat{\bar{\rho}}_c) \tag{11a}$$

and the following for $K > 4$:

$$\hat{\bar{x}} = (\mathbf{G}^T\mathbf{G})^{-1}\mathbf{G}^T(\mathbf{A}\cdot\bar{\bar{R}} - \hat{\bar{\rho}}_c) \tag{11b}$$

using the generalized matrix inverse (or pseudoinverse) of $\mathbf{G}$.

These are the fundamental position calculations. Note that $\mathbf{G}$, the geometry matrix, is constructed from the set of approximate directions to the satellites, as is the matrix $\mathbf{A}$. The vector $\bar{\bar{R}}$ is constructed from the location of the satellites that has been transmitted and $\hat{\bar{\rho}}_c$ is the corrected pseudorange to each satellite.

Inserting Eq. (11a) back into Eq. (10) cancels appropriate terms and leaves the fundamental error equation*:

$$\mathbf{G}\cdot\Delta\bar{x} = c\cdot(-\Delta\bar{B} - \bar{S} + \Delta\bar{I} + \Delta\bar{T} - \bar{v}) - \epsilon\cdot(\bar{\bar{R}} - \bar{\bar{P}}) + \mathbf{A}\cdot\Delta\bar{\bar{R}} \equiv \Delta\bar{\rho} \tag{12}$$

Thus, the right-hand side consists of all the ranging and calculation errors expressed in meters as we have defined them. Distance and time can be equated by recalling that light travels one meter in about three ns.

* The situation for the generalized inverse, Eq. (11b), is somewhat more complicated and is not presented here. The same expression for $\Delta\bar{\bar{x}}$ is obtained. The same generalized development can then be used.

$$\text{for } K = 4, \qquad \Delta\bar{x} = \mathbf{G}^{-1}\Delta\bar{\rho}_c \tag{13a}$$

$$\text{for } K > 4, \qquad \Delta\bar{x} = (\mathbf{G}^T\mathbf{G})^{-1}\mathbf{G}^T\Delta\bar{\rho}_c \tag{13b}$$

where $\Delta\bar{x}$ is the positioning error in meters.

III. Geometric Dilution of Precision

It is intuitively obvious that satellite geometry can affect the accuracy of Eq. (13). This section develops the quantitative tools to understand the "dilution" of precision caused by various satellite geometrical configurations.

A. Derivation of the Geometric Dilution of Precision Equation

Now the well-known geometric dilution of precision (GDOP) equation can be easily derived. The covariance of position (m) is calculated as follows:

$$\text{cov(position)} = E(\Delta\bar{x}\cdot\Delta\bar{x}^T) = (\mathbf{G}^T\mathbf{G})^{-1}\mathbf{G}^T\cdot E[(\Delta\bar{\rho}\cdot\Delta\bar{\rho}^T)]\cdot\mathbf{G}(\mathbf{G}^T\mathbf{G})^{-1},\ K > 4 \tag{14a}$$

$$\text{cov(position)} = \mathbf{G}^{-1}\cdot E[\Delta\bar{\rho}\cdot\Delta\bar{\rho}^T]\cdot\mathbf{G}^{-T},\ K = 4 \tag{14b}$$

where E is the expectation operator. Because the $\mathbf{G}$ matrix does not have a random component, it has been brought outside the expectation operation.

If all ranging errors have the same variance $[\sigma_R^2]$ (m^2) and are uncorrelated zero mean ($E[\Delta\rho_i\Delta\rho_j] = 0, i \neq j$), then the expectation in Eqs. (14a and 14b) becomes $\sigma_R^2 \cdot U$, where U is the 4×4 identity matrix. Then both Eqs. (14) collapse to the following:

$$\text{cov(position)} = \sigma_R^2\cdot[\mathbf{G}^T\mathbf{G}]^{-1}$$

Therefore, $[\mathbf{G}^T\mathbf{G}]^{-1}$ is the matrix of multipliers of *ranging* variance to give *position* variance. It is known as the GDOP or geometric dilution of precision matrix. If the position coordinates are the ordered right-hand set, east, north and up, then the *square root* of the ordered diagonal terms from the upper left are: east DOP, north DOP, vertical DOP, and time DOP. Note that σ_R^2 is expressed in m^2 rather than s^2.

cov(Position) =

$$\sigma_R^2(\text{m}^2)\begin{bmatrix} (\text{East DOP})^2 & & \text{covariance terms} & \\ & (\text{North DOP})^2 & & \\ & & (\text{Vertical DOP})^2 & \\ \text{covariance terms} & & & (\text{Time DOP})^2 \end{bmatrix}$$

The scalar GDOP is defined to be the square root of the trace of the GDOP matrix. Also HDOP (horizontal) = $\sqrt{(\text{NorthDOP})^2 + (\text{EastDOP})^2}$, and PDOP-(position) = $\sqrt{(\text{HDOP})^2 + (\text{VDOP})^2}$.

For satellites constrained to be above a minimum elevation angle* (greater than 0 deg), the best GDOP for $K = 4$ is obtained when one satellite is overhead and the other three are equally spaced at the minimum elevation angles around the horizon. In later chapters, we explore the power of pseudolites that provide ranging signals *transmitted from the ground.* These have negative elevation angles for an aircraft and can significantly improve geometry.

B. Power of the GDOP Concept

The concept of GDOP is a powerful tool for GPS. All receivers use some algorithm based on GDOP to select the best set of satellites to track among the group of up to 11 satellites in view. *Positioning* accuracy can then be estimated as the *ranging* accuracy multiplied by a dilution factor. This dilution factor (DOP) depends solely on geometry.

Typically, variations in geometry are far greater than variations in ranging accuracy for the nominal satellite constellation. The GDOP concept also quantizes the effect when the nominal satellites are not in view. Examples include local terrain shading, satellite outages, and user shading caused by vehicle extensions such as aircraft wings, etc. During these circumstances, the GDOP calculation for those satellites still being tracked will give the multiplier on ranging accuracies to yield positioning accuracies.

C. Example Calculations

To gain insight into the GDOP concept, some sample calculations are useful. They reveal the tradeoff of accuracy with satellite location. We define satellite direction as azimuth (Az-measured 360 deg clockwise from true north) and elevation (E-measured up from local horizontal—0–90 deg). This can be translated into the east, north, up coordinate frame, and the G matrix becomes:

$$\begin{bmatrix} (\cos(E_1)*\sin(Az_1)) & (\cos(E_1)*\cos(Az_1)) & \sin(E_1) & 1 \\ (\cos(E_2)*\sin(Az_2)) & (\cos(E_2)*\cos(Az_2)) & \sin(E_2) & 1 \\ (\cos(E_3)*\sin(Az_3)) & (\cos(E_3)*\cos(Az_3)) & \sin(E_3) & 1 \\ (\cos(E_4)*\sin(Az_4)) & (\cos(E_4)*\cos(Az_4)) & \sin(E_4) & 1 \end{bmatrix}$$

Using only satellites as ranging sources, the best accuracy† is found with three satellites equally spaced on the horizon, at minimum elevation angle, and one satellite directly overhead (See Table 1).

* Elevation angle is the angle of the satellite above the local horizontal.

† Note that the lower satellite elevation angles tend to have the greater *ranging errors.* The statement is that this configuration offers the best *geometry.* Usually geometry has a larger effect on accuracy than ranging errors.

Table 1 Satellite location

	Sat 1	Sat 2	Sat 3	Sat 4
Elevation, deg	5	5	5	90
Azimuth, deg	0	120	240	0

The following example, for 5-deg minimum satellite elevation, illustrates the technique. Using the best satellite geometry previously described, and the formulas for GDOP we get the following:

$$\mathbf{G} = \begin{bmatrix} 0.000 & 0.996 & 0.087 & 1.000 \\ 0.863 & -0.498 & 0.087 & 1.000 \\ -0.863 & -0.498 & 0.087 & 1.000 \\ 0.000 & 0.000 & 1.000 & 1.000 \end{bmatrix}$$

Recall that the position and time solution ($\mathbf{x}$) is simply given by $\mathbf{G}^{-1}$ (for the four-measurement case*) times the column of corrected pseudoranges ρ_c. $\mathbf{G}$ inverse for the above $\mathbf{G}$ is listed below. Note that each of the first three rows sums to exactly zero. This implies that any common bias in ranging measurements will not affect the position solution. Note also that the last row sums to one. This is the row that gives the time solution (or bias in the local clock). This implies that any common error shows up solely as an error in the local clock. To see these two results, simply multiply on the right by a column whose elements are all the same value. These two results are always true. They arise from inverting the $\mathbf{G}$ matrix, which always has a constant last column of ones.

$$\mathbf{G}^{-1} = \begin{bmatrix} 0.000 & 0.580 & -0.580 & 0.000 \\ 0.670 & -0.335 & -0.335 & 0.000 \\ -0.365 & -0.365 & -0.365 & 1.095 \\ 0.365 & 0.365 & 0.365 & -0.095 \end{bmatrix}$$

The GDOP matrix for this example $(\mathbf{G}^T\mathbf{G})^{-1}$ is shown below. Note that, in this case, all off-diagonal terms are zero except for those correlating vertical errors and time. This correlation is negative, which implies that the errors tend to have opposite signs. In general, large correlations will be found between vertical errors and timing errors, and in general, off-diagonal terms will not be zero.

* For a greater number of satellites, $\mathbf{G}^{-1}$ is replaced with $(\mathbf{G}^T\mathbf{G})^{-1}\mathbf{G}^T$.

$$(\mathbf{G}^T\mathbf{G})^{-1} = \begin{bmatrix} 0.672 & 0.000 & 0.000 & 0.000 \\ 0.000 & 0.672 & 0.000 & 0.000 \\ 0.000 & 0.000 & 1.600 & -0.505 \\ 0.000 & 0.000 & -0.505 & 0.409 \end{bmatrix}$$

Listed below are the results of taking the square roots of appropriate diagonal terms of the GDOP matrix above:

HDOP (horizontal DOP) = 1.16 TDOP (time DOP) = 0.64

VDOP (vertical DOP) = 1.26 GDOP = 1.83

PDOP (position DOP) = 1.72

A PDOP of 1.72 is very good. In fact, it is the optimum for four satellites with a minimum elevation angle of 5 deg. A more representative median (50th percentile) worldwide result for PDOP is about 2.5. With all satellites of a 24-satellite constellation available, PDOP numbers as high as six or seven will be found. Thus, geometry can affect the results by a factor of as much as five or more.

D. Impact of Elevation Angle on GDOP

Figure 1 illustrates the impact of satellite position on DOP.[3,4] Maintaining the same symmetric spacing in azimuth, the minimum elevation angle is varied, including negative angles that could only be achieved with Earth-based transmitters (pseudolites).

The HDOP is quite flat over the whole range, which reflects the optimum azimuthal configuration. Satellites more concentrated in one-half of the sky than the other would cause greater variation in these results. Another interesting conclusion is that the lower elevation angles are of significant help for the vertical position.

Fig. 1 Dilution of position values for symmetric satellites at various elevation angles above the horizon. The minimum GDOP is at −19.5 deg (i.e., below the local horizontal). This corresponds to locating four transmitters at the apexes of a regular tetrahedron.

IV. Ranging Errors

A. Six Classes of Errors

Ranging errors are grouped into the six following classes:

1) *Ephemeris data*—Errors in the transmitted location of the satellite
2) *Satellite clock*—Errors in the transmitted clock, including SA
3) *Ionosphere*—Errors in the corrections of pseudorange caused by ionospheric effects
4) *Troposphere*—Errors in the corrections of pseudorange caused by tropospheric effects
5) *Multipath*—Errors caused by reflected signals entering the receiver antenna
6) *Receiver*—Errors in the receiver's measurement of range caused by thermal noise, software accuracy, and interchannel biases

Each class is briefly discussed in the following sections. Representative values for these errors are used to construct an error table in a later section of this chapter. A more complete discussion of individual error sources can be found in succeeding chapters.

B. Ephemeris Errors

Ephemeris errors result when the GPS message does not transmit the correct satellite location. It is typical that the radial component of this error is the smallest: the tangential and cross-track errors may be larger by an order of magnitude. Fortunately, the larger components do not affect ranging accuracy to the same degree. This can be seen in the fundamental error Eq. (12). The $\Delta\overline{R}$ represents each satellite position error, but when dot-multiplied by the unit satellite direction vector (in the A matrix), only the projection of satellite positioning error along the line of sight creates a ranging error.

Because satellite errors reflect a position prediction, they tend to grow with time from the last control station upload. It is possible that a portion of the deliberate SA error is added to the ephemeris as well. However, the predictions are long smooth arcs, so all errors in the ephemeris tend to be slowly changing with time. Therefore, their utility in SA is quite limited.

As reported during phase one, (Bowen, 1986) in 1984,[5] *for predictions of up to 24 hours, the rms ranging error attributable to ephemeris was 2.1 m.* These errors were closely correlated with the satellite clock, as we would expect. Note that these errors are the same for both the P- and C/A-codes (see Chapter 16 of this volume for a more detailed discussion of ephemeris and clock errors).

C. Satellite Clock Errors

Fundamental to GPS is the one-way ranging that ultimately depends on satellite clock predictability. These satellite clock errors affect both the C/A- and P-code users in the same way. The error effect can be seen in the fundamental error Eq. (11) as ΔB. This effect is also independent of satellite direction, which is important when the technique of differential corrections is used. All differential stations and users measure an identical satellite clock error.

A major source of apparent clock error is SA, which is varied so as to be unpredictable over periods longer than about 10 minutes. The rms value of SA

is typically about 20 m in ranging, but this can change after providing appropriate notice, depending on need. The U.S. Air Force has guaranteed that the two-dimensional rms (2 DRMS) positioning error (approximately 90th percentile) will be kept to less than 100 m. This is now a matter of U.S. federal policy and can only be changed by order of the President of the United States.

More interesting is the underlying accuracy of the system with SA off. The ability to predict clock behavior is a measure of clock quality. GPS uses atomic clocks (cesium and rubidium oscillators),[1] which have stabilities of about 1 part in 10^{13} over a day. If a clock can be predicted to this accuracy, its error in a day ($\sim 10^5$ s) will be about 10^{-8} s or about 3.5 m. The experience reported in 1984 was 4.1 m for 24-hour predictions. *Because the standard deviations of these errors were reported to grow quadratically with time, an average error of 1–2 m for 12-hour updates is the normal expectation.*

D. Ionosphere Errors

Because of free electrons in the ionosphere, GPS signals do not travel at the vacuum speed of light as they transit this region. The modulation on the signal is *delayed* in proportion to the number of free electrons encountered and is also (to first order) proportional to the inverse of the carrier frequency squared ($1/f^2$). The phase of the radio frequency carrier is *advanced* by the same amount because of these effects. Carrier-smoothed receivers should take this into account in the design of their filters. The ionosphere is usually reasonably well-behaved and stable in the temperate zones; near the equator or magnetic poles it can fluctuate considerably. An in-depth discussion of this can be found in Chapter 12, this volume.

All users will correct the raw pseudoranges for the ionospheric delay. The simplest correction will use an internal diurnal model of these delays. The parameters can be updated using information in the GPS communications message (although the accuracy of these updates is not yet clearly established). *The effective accuracy of this modeling is about 2–5 m in ranging for users in the temperate zones.*

A second technique for *dual-frequency P-code* receivers is to measure the signal at both frequencies and directly solve for the delay. The difference between L_1 and L_2 arrival times allows a direct algebraic solution. *This dual-frequency technique should provide 1–2 m of ranging accuracy, due to the ionosphere, for a well-calibrated receiver.*

A third technique is to rely on a near real-time update. An example would be the proposed Wide Area Differential GPS system (WADGPS). *This should also produce corrections with accuracies of 1–2 m or better in the temperate zones of the world.*

E. Troposphere Errors

Another deviation from the vacuum speed of light is caused by the troposphere. Variations in temperature, pressure, and humidity all contribute to variations in the speed of light of radio waves. Both the code and carrier will have the same delays. This is described further in the chapter devoted to these effects, Chapter

13 of this volume. *For most users and circumstances, a simple model should be effectively accurate to about 1 m or better.*

F. Multipath Errors

Multipath is the error caused by reflected signals entering the front end of the receiver and masking the real correlation peak. These effects tend to be more pronounced in a static receiver near large reflecting surfaces, where 15 m or more in ranging error can be found in extreme cases. Monitor or reference stations require special care in siting to avoid unacceptable errors. The first line of defense is to use the combination of antenna cut-off angle and antenna location that minimizes this problem. A second approach is to use so-called "narrow correlator" receivers which tend to minimize the impact of multipath on range tracking accuracies. *With proper siting and antenna selection, the net impact to a moving user should be less than 1 m under most circumstances.* See Chapter 14 of this volume for further discussion of multipath errors.

G. Receiver Errors

Initially most GPS commercial receivers were sequential in that one or two tracking channels shared the burden of locking on to four or more satellites. With modern chip technology, it is common to place three or more tracking channels on a single inexpensive chip. As the size and cost have shrunk, techniques have improved and five- or six-channel receivers are common. Most modern receivers use reconstructed carrier to aid the code tracking loops. This produces a precision of better than 0.3 m. Interchannel bias is minimized with digital sampling and all-digital designs.

The limited precision of the receiver software also contributed to errors in earlier designs, which relied on 8-bit microprocessors. With ranges to the satellites of over 20 million meters, a precision of $1{:}10^{10}$ or better was required. Modern microprocessors now provide such precision along with the co-requisite calculation speeds. *The net result is that the receiver should contribute less than 0.5 ms error in bias and less than 0.2 m in noise.* Further information on receiver errors is available in Chapters 3, 7, 8, and 9 of this volume.

V. Standard Error Tables

These overview discussions on error sources and magnitudes, as well as the effects of satellite geometry, can be summarized with the following error tables. Each error is described as a bias (persistence of minutes or more) and a random effect that is, in effect "white" noise and exhibits little correlation between samples of range. The total error in each category is found as the root sum square (rss) of these two components.

Each *component* of error is assumed to be statistically uncorrelated with all others, so they are combined as an rss as well. The receiver is assumed to filter the measurements so that about 16 samples are effectively averaged reducing the random content by the square root of 16. Of course, averaging cannot improve the bias-type errors.

Finally, each satellite error is assumed to be uncorrelated and of zero mean, so the application of HDOP and VDOP are justified as the last step. Despite these limiting assumptions, the resulting error model has proved to be surprisingly valid. Of course, the assumptions on uncorrelated errors is almost always violated to some degree. For example, if the estimate of zenith ionosphere delay is in error, a proportional error is induced in all measurements through the obliquity calculation. Clearly, such an error would be correlated. These and other correlations have not caused serious problems in the use of this model.

A. Error Table without SA: Normal Operation for C/A Code

Table 2 assumes that SA is not operating. Consequently, the residual satellite clock error, at 2.1 m, is not the dominant error; in fact, the largest error is expected to be the mismodeling of the ionosphere, at 4.0 m. Thus, the worldwide civilian positioning error for GPS is potentially about 10 m (horizontal), as shown in Table 2.

B. Error Table with SA

A second example shows the impact of SA on these errors. Because the deliberately mismodeled clock so dominates the ranging error, all other effects could be safely ignored in the error budget. The results of Table 3 have been repeatedly corroborated by actual measurements. Note that SA is listed as a bias because it cannot be averaged to zero with a 1 s (or less) filter. Selective availability is expected to be zero mean, but only when averaged over many hours or perhaps days. Of course, such averaging is not practical for a dynamic user who only sees the satellite for a portion of the orbit. If differential corrections are used,

Table 2 Standard error model—no SA

	One-sigma error, m		
Error source	Bias	Random	Total
Ephemeris data	2.1	0.0	2.1
Satellite clock	2.0	0.7	2.1
Ionosphere	4.0	0.5	4.0
Troposphere	0.5	0.5	0.7
Multipath	1.0	1.0	1.4
Receiver measurement	0.5	0.2	0.5
User equivalent range error (UERE), rms[a]	5.1	1.4	5.3
Filtered UERE, rms	5.1	0.4	5.1
Vertical one-sigma errors—VDOP= 2.5			**12.8**
Horizontal one-sigma errors—HDOP= 2.0			**10.2**

[a]This is the statistical ranging error (one-sigma) that represents the total of all contributing sources. The dominant error is usually the ionosphere. A horizontal error of 10 m (one-sigma) is the expected performance for the temperate latitudes using civilian (C/A-code) receivers.

Table 3 SA error model

	One-sigma error, m		
Error source	Bias	Random	Total
Ephemeris data	2.1	0.0	2.1
Satellite clock	20.0	0.7	20.0
Ionosphere	4.0	0.5	4.0
Troposphere	0.5	0.5	0.7
Multipath	1.0	1.0	1.4
Receiver measurement	0.5	0.2	0.5
UERE, rms	20.5	1.4	20.6
Filtered UERE, rms	20.5	0.4	20.5
Vertical one-sigma errors—VDOP= 2.5			**51.4**
Horizontal one-sigma errors—HDOP= 2.0			**41.1**

they will eliminate the SA error entirely (if corrections are passed at a sufficiently high data rate) as discussed in Chapter 21, this volume.

The 41-m horizontal error is a one-sigma (σ) result; under the existing agreement between the U.S. Department of Transportation (DOT) and the U.S. Department of Defense (DOD), the 2 DRMS horizontal error is to be less than 100 m. The impact on the vertical error is probably greater, because the VDOP value usually exceeds the HDOP value.

C. Error Table for Precise Positioning Service (PPS Dual-Frequency P/Y Code)

The errors for dual-frequency P/Y code are similar to those above except that SA errors are eliminated because the authorized user can decode the magnitude as part of a classified message. An expected horizontal error is less than 10 m. The ionosphere error is reduced to 1-m bias and about 0.7 m of noise by the dual-frequency measurement. The dominant sources are the satellite ephemeris and clocks. This is illustrated in Table 4.

VI. Summary

Excluding the deliberate degradation of SA, the dominant error source for satellite ranging with single frequency receivers is usually the ionosphere. It is on the order of four meters, depending on the quality of the single-frequency model. For dual-frequency (P/Y-code) receivers (which eliminate SA) the Standard Error Model of Table 1 has one principal change (in addition to the elimination of the SA error). The ionospheric error is reduced from four meters to about one meter.

Greater variations in the errors are due to geometry, which are quantified as dilutions of precision or DOPs. While geometric dilutions of 2.5 are about the worldwide average, this factor can range up to 10 or more with poor satellite geometry. Reduced satellite availability (and consequent increases in DOP) could

Table 4 Precise error model, dual-frequency, P/Y code

	One-sigma error, m		
Error source	Bias	Random	Total
Ephemeris data	2.1	0.0	2.1
Satellite clock	2.0	0.7	2.1
Ionosphere	1.0	0.7	1.2
Troposphere	0.5	0.5	0.7
Multipath	1.0	1.0	1.4
Receiver measurement	0.5	0.2	0.5
UERE, rms	3.3	1.5	3.6
Filtered UERE, rms	3.3	0.4	3.3
Vertical one-sigma errors—VDOP= 2.5			**8.3**
Horizontal one-sigma errors—HDOP= 2.0			**6.6**

be caused by satellite outages, local terrain masking, or user antenna tilting (for example due to aircraft banking). Typical normal accuracy (one-sigma) for well-designed civil equipment under nominal operating conditions *with SA off* should be about 10 m horizontal and 13 m vertical.

References

[1]Martin, E. H., "GPS User Equipment Error Models," *Global Positioning System Papers,* Vol. I, Institute of Navigation, Washington, DC, 1980, pp. 109–118.

[2]Milliken, R. J., and Zollar, C. J., "Principle of Operation of NAVSTAR and System Characteristics," *Global Positioning System Papers,* Vol. I, Institute of Navigation, Washington, DC, 1980, pp. 3–14.

[3]Copps, E. M., "An Aspect of the Role of the Clock in a GPS Receiver," *Global Positioning System Papers,* Vol. III, Institute of Navigation, Washington, DC, 1986.

[4]Massat, P., and Rudnick, K., "Geometric Formulas for Dilution of Precision Calculations," *Navigation,* Vol. 37, No. 4, 1990–1991.

[5]Bowen, R., et al., "GPS Control System Accuracies," *Global Positioning System Papers,* Vol. III, Institute of Navigation, Washington, DC, 1986, pp. 241–247.

Chapter 12

Ionospheric Effects on GPS

J. A. Klobuchar*
Hanscom Air Force Base, Massachusetts 01731

I. Introduction

THE ionosphere is an important source of range and range-rate errors for users of the global positioning system (GPS) satellites who require high-accuracy measurements. At times, the range errors of the troposphere and the ionosphere can be comparable, but the variability of the Earth's ionosphere is much larger than that of the troposphere, and it is more difficult to model. The ionospheric range error can vary from only a few meters, to many tens of meters at the zenith, whereas the tropospheric range error at the zenith is generally between two to three meters. Fortunately, the ionosphere is a dispersive medium; that is, the refractive index is a function of the operating frequency, and two-frequency GPS users can take advantage of this property of the ionosphere to measure and correct for the first-order ionospheric range and range-rate effects directly. Unlike the troposphere, the ionosphere can change rapidly in absolute value. Although the range error of the troposphere generally does not change by more than $\pm 10\%$, even over long periods of time, the ionosphere frequently changes by at least one order of magnitude during the course of each day. The major effects the ionosphere can have on GPS are the following: 1) group delay of the signal modulation, or absolute range error; 2) carrier phase advance, or relative range error; 3) Doppler shift, or range-rate errors; 4) Faraday rotation of linearly polarized signals; 5) refraction or bending of the radio wave; 6) distortion of pulse waveforms; 7) signal amplitude fading or amplitude scintillation; and 8) phase scintillations.

In order to understand the reasons for these potential effects on GPS performance, a brief description of the major characteristics of the ionosphere is necessary.

II. Characteristics of the Ionosphere

To first order, the ionosphere is formed by the ultraviolet (uv) ionizing radiation from the Sun. Different regions of the ionosphere are produced by different

*Geophysics Directorate, Ionospheric Effects Division, Phillips Laboratory.

chemical species. The ionosphere is a weakly ionized plasma, or gas, which can affect radiowave propagation in various ways. The electron and ion densities are assumed to be equal in the ionosphere, and the density of the ions is much less than 1% of the neutral density at all heights. When the ionosphere was first discovered, the original regions were named with the alphabetic letters E and F, for electric and field,[1] with the thought that regions of less density, and earlier letters of the alphabet, would eventually be found at lower heights. Today we know that the ionosphere is composed of the D, E, F1, and F2 regions, named in order of increasing height. Figure 1 illustrates the different regions and their electron densities in the ionosphere. The D, E, and F1 regions are closely tied to the uv ionizing daytime radiation from the sun, and are not present at night. The F2 region is present at night, but it is lower in density and generally has its maximum density at a greater height during the night, as compared with daytime.

The various regions of the ionosphere are produced by different wavelengths of radiation from the sun, with the harder solar radiation, namely x rays, penetrating farther into the neutral atmosphere, and the less intense uv radiation being stopped at greater heights where they produce ionization. Much early work was done by Chapman[2] in developing the mathematics of the production of ionization of the atmosphere.

Because the neutral atmosphere is approximately in diffusive equilibrium, the scale height of each neutral atomic and modecular species falls off exponentially with increasing height above the Earth's surface. Thus, the total neutral density is mostly composed of the heavier, molecular species at lower heights, and of the lighter, atomic species at greater heights. Above approximately 180 km, electron diffusion becomes important, and electrons generated by solar uv emissions are free to move to greater heights following the Earth's magnetic lines of force. Additional changes in electron density above approximately 180 km are produced by electric fields that cause electrons to move in a direction perpendicular to the magnetic lines of force, while neutral winds can cause electrons to

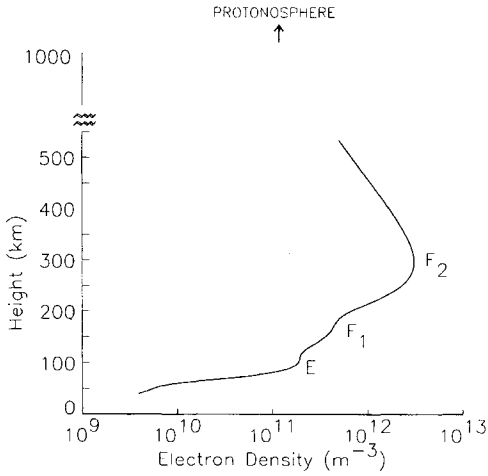

Fig. 1 Electron density of the different regions of the ionosphere vs height for daytime conditions.

flow either up or down the Earth's magnetic field lines, further complicating the specification of electron density at any given height above where diffusion becomes important.

The chemistry of the F2 region is predominately attributable to the ionization of atomic oxygen, whereas the electrons at great heights are attributable to ionized hydrogen gas. The scale height of each species is: $H = kt/mg$, where k is Boltzmann's constant, T is the absolute temperature, m is the mass of the species, and g is the acceleration of gravity.

The scale height of each species is inversely proportional to its atomic weight; thus, the scale height of the electrons associated with H^+ is 16 times greater than that of the electrons due to O^+ ions. Charge neutrality generally is assumed to be the case in the ionosphere, thus the number of electrons always is equal to the number of ions. The scale height of the F2 region is typically 60 km, while that of the protonosphere is over 1,000 km. Thus, although the electron density of the protonosphere is small, the number of electrons does not fall off very fast with increasing height. Therefore, the number of electrons in the protonosphere can be an important fraction of the total, especially during the nighttime periods when the electron density of the F2 region is small, as it normally is during the nighttime.

The parameter of the ionosphere that produces most of the effects on GPS signals is the total number of electrons in the ionosphere. This integrated number of electrons, commonly called the total electron content (TEC), is expressed as the number of electrons in a vertical column having a 1-m^2 cross section, and extending all the way from the GPS satellite to the observer. Details of the behavior of the TEC of the Earth's ionosphere are given in Sec. V of this chapter.

The electron density of the F2 region is not only the highest of the various regions, producing the greatest potential effects on many radiowave systems, but is the most highly variable, safely keeping many ionospheric researchers employed to understand better and be able to predict the physics of its detailed behavior. The major characteristics and importance of each region of the ionosphere for potential effects on GPS signals are summarized as follows (note that heights given are only approximate):

1) D region, 50–90 km: This region, produced by ionization of several molecular species from hard x rays and solar Lyman α radiation, causes absorption of radio signals at frequencies up to the low vhf band, and has no measurable effect on GPS frequencies.

2) E Region, 90–140 km: The normal E region, produced by solar soft x rays, has a minimal effect on GPS. An intense E region, with irregular structure, produced by solar particle precipitation in the auroral region, might cause minor scintillation effects. Sporadic E, still of unknown origin, is very thin and also has a negligible effect at GPS frequencies.

3) F1, 140–210 km: The normal F1 region, combined with the E region, can account for up to 10% of the ionospheric time delay encountered by GPS. Diffusion is not important at F1 region heights, and, as with the normal E region, it has a highly predictable density from known solar emissions. The F1 region is produced through ionization of molecular species, and its electron density nicely merges into the bottomside of the F2 region.

4) F2, 210–1,000 km: The F2 region is the most dense and also has the highest variability, causing most of the potential effects on GPS receiving systems. The height of the peak of the electron density of the F2 region generally varies from 250 to 400 km, but it can be even much higher or somewhat lower under extreme conditions. The F2 region is produced mainly from ionization of atomic oxygen, which is the principal constituent of the neutral atmosphere at those heights. The F2, and to some extent the F1, regions, cause most of the problems for radiowave propagation at GPS frequencies.

5) $H^+ > 1{,}000$ km: The protonosphere, is a region of ionized hydrogen, with a lesser contribution from helium gas. It is of low density, but extends out to approximately the orbital height of GPS satellites. It can be a significant source of unknown electron density and consequent variability of time delay for GPS users. Estimates of the contribution of the protonosphere vary from 10% of the total ionospheric time delay during daytime hours, when the electron density of the F2 region is highest, to approximately 50% during the nighttime, when the F2 region density is low. The electron content of the protonosphere does not change by a large amount during the day, but is depleted during major magnetic storms and can take several days to recover to prestorm values.

III. Refractive Index of the Ionosphere

In order to quantify the propagation effects on a radio wave traveling through the ionosphere, the refractive index of the medium must be specified. The refractive index of the ionosphere, n, has been derived by Appleton and Hartree,[1] and it can be expressed as

$$n^2 = 1 - \frac{X}{1 - iZ - \dfrac{{Y^2}_T}{2(1 - X - iZ)} \pm \left[\dfrac{{Y^4}_T}{4(1 - X - iZ)^2} + {Y^2}_L\right]^{1/2}} \tag{1}$$

where $X = Ne^2/\epsilon_o m\omega^2 = f_n^2/f^2$, $Y_L = eB_L/m\omega$, $= f_H \cos\theta/f$, $Y_T = eB_T/m\omega = f_H \sin\theta/f$, $Z = \nu/\omega$, $w = 2\pi f$, where f is the system operating frequency, in Hz and

e = electron charge, -1.602×10^{-19} coulomb
ϵ = permittivity of free space, $= 8.854 \times 10^{-12}$ farad/m
m = rest mass of a electron, $= 9.107 \times 10^{-31}$ kg
θ = the angle of the ray with respect to the Earth's magnetic field
ν = the electron-neutral collision frequency
f_H = the electron gyro frequency

The electron gyro frequency f_H is typically 1.5 MHz; the plasma frequency f_N rarely exceeds 20 MHz; and the collision frequency, f_ν, is approximately 10^4 Hz. Thus, to an accuracy of better than 1%, the refractive index of the ionospheric is given by the following:

$$n = 1 - (X/2) \tag{2}$$

The ionospheric refractive index is the basis for the effects on GPS signals described later, and the first-order form is sufficient for most purposes. Higher-order corrections are described in Sec. IV.D.

IV. Major Effects on Global Positioning Systems Caused by the Ionosphere

Knowing the refractive index of the ionosphere it is possible to derive the group delay or absolute range error; the carrier phase advance or relative range error; and the Doppler shift or range-rate error. It is also possible to calculate the potential effects of Faraday rotation and refraction, or bending, of the radio wave. The distortion of pulse waveforms is described briefly. Finally, the effects of signal fading, or amplitude scintillation, and phase scintillations are described. All of these effects are produced because the refractive index of the ionosphere differs from unity.

A. Ionospheric Group Delay—Absolute Range Error

1. *Single-Frequency Group Delay*

The group delay of the ionosphere produces range errors, which can be expressed either in units of distance, or in units of time delay, to GPS users. This group delay can be determined by

$$\Delta t = \frac{1}{c}\int (1 - n)\mathrm{d}l \tag{3}$$

or

$$\Delta r = \int (1 - n)\mathrm{d}l \tag{4}$$

At L-band the first-order refractive index is, $n = 1 - X/2$, where

$$X = \frac{40.3}{f^2}\int N\mathrm{d}l$$

and the ionospheric group delay is

$$\Delta t = \frac{40.3}{cf^2}\int N\mathrm{d}l, \ldots, \text{seconds} \tag{5}$$

The quantity $\int N\mathrm{d}l$ is the TEC, in el/m^2, integrated along the path from observer to each GPS satellite. The temporal and spatial variations of TEC, which are responsible for the variability of ionospheric time delay to GPS users, are described in Sec. V.

2. *Dual-Frequency Group Delay*

By measuring the group path delay independently at the two, widely spaced GPS frequencies, $L_2 = f_2$ and $L_1 = f_1$, the TEC along the path from satellite to receiver can be measured directly. A dual-frequency GPS receiver measures the difference in ionospheric time delay at $L_2 - L_1$, referred to as $\delta(\Delta t)$. From Eq. (5), we obtain

$$\delta(\Delta t) = (40.3/c) \times \text{TEC} \times [(1/f_2^2) - (1/f_1^2)] = \Delta t_1[(f_1^2 - f_2^2)/f_2^2] \tag{6}$$

or

$$\Delta t_1 = [f_2^2/(f_1^2 - f_2^2) \times \delta(\Delta t)] \tag{7}$$

where Δt_1 is the ionospheric time delay at L_1.

The value $\delta(\Delta t)$ is obtained from the difference of the simultaneous measurements of the total range, including ionospheric time delay, at the two frequencies f_1 and f_2, because the geometric distance is, of course, the same at all frequencies. The quantity, is $[f_2^2/(f_2^2 - f_2^2)]$ is called the ionospheric scaling factor. For the GPS pair of frequencies, this factor is 1.546.

If the two GPS frequencies had been chosen to be too closely spaced, the differential ionospheric time delay between them would have been very small and would have been masked by the receiving system noise. A wider frequency separation between L_1 and L_2 would have made the measurement capability of absolute ionospheric range error more precise, but probably would have required two separate transmitting and receiving antennas, and more elaborate transmitter and receiver designs. The frequency separation between L_1 and L_2, giving an ionospheric scaling factor of 1.546, is a reasonable compromise between system hardware design and absolute ionospheric range error/time delay requirements. Although Δt_1 is 1.546 times the difference between the two, relatively noisy, pseudorange measurements this differential time delay can be averaged over many samples, and, hence, can be measured to subnanosecond accuracy. The limitations in measuring absolute differential pseudoranges are mostly caused by multipath and lack of a precise knowledge of the differential pseudorange as transmitted from each GPS satellite.

B. Ionospheric Carrier Phase Advance

1. *Single-Frequency Ionospheric Carrier Phase Advance*

The carrier phase advance, as compared with the received carrier phase in the absence of an ionosphere, can be expressed as

$$\Delta\phi = \frac{1}{\lambda}\int (1 + n)\, \mathrm{d}l, \ldots, \text{cycles, or wavelengths} \tag{8}$$

or

$$\Delta\phi = \frac{f}{2c}\int X\mathrm{d}l = \frac{40.3}{cf}\int N\mathrm{d}l = \frac{1.34 \times 10^{-7}}{f}\int N\mathrm{d}l, \ldots, \text{cycles} \tag{9}$$

Remember that $v_g v_\phi = c^2$, where v_g, v_ϕ are the group and phase velocities, respectively. Although the carrier phase travels faster than the velocity of light, it carries no information, and thus, communication does not occur faster than the velocity of light.

2. *Differential Carrier Phase Advance*

As a radio signal traverses the ionosphere, the phase of the carrier of the radio frequency transmission is advanced from its velocity in free space. In practice, the amount of this phase advance cannot be measured readily on a single frequency

unless both the transmitter and the receiver have exceptional oscillator stability and the satellite orbital characteristics are extremely well known. Usually two, coherently derived, frequencies are required for this measurement. In the case of the GPS satellites, the L_1 and L_2 transmitted carriers are phase coherent, both being derived from a common 10.23 MHz oscillator. The differential carrier phase shift (δ_ϕ) between the two frequencies then can be measured. That differential measurement is related to TEC by

$$\Delta\delta_\phi = [(1.34 \times 10^{-7})/f_L \times [(m^2 - 1)/m^2]/\text{TEC}, \ldots, \text{cycles} \qquad (10)$$

where $m = f_1/f_2$. The GPS system uses differential carrier phase to correct automatically for range-rate errors in its system. Differential carrier phase also provides a very precise measure of changes in relative TEC during a satellite pass, but, because of the unknown number of differential cycles of phase, absolute TEC values must be obtained from the differential group delay measurement.

3. Relationship Between Carrier Phase Advance and Group Delay

The relationship between group delay and carrier phase is simply

$$\Delta\phi = -f\Delta t \qquad (11)$$

or, for every cycle of carrier phase advance, there are

$$1/f, \ldots, \text{seconds} \qquad (12)$$

of time delay. In the case of GPS at L_1, one cycle of carrier phase advance is equivalent to 0.635 ns of group delay. The minus sign in Eq. (11) is meant to indicate that the differential code group delay and the differential carrier phase advance move in opposite directions. We must be careful to note this when using carrier-aided code tracking, if the ionosphere changes significantly during the observation period. It is also possible to measure *relative* ionospheric changes using the L_1 C/A code minus L_1 carrier phase during a pass.

4. Useful Numbers for GPS Are Shown in Table 1.

C. Higher-Order Ionospheric Effects

Because we are concerned here only with radiowave propagation at GPS frequencies, the terms X, Y_T, Y_L, and Z in Eq. (1) are all much less than one. Thus, the refractive index of the ionosphere at GPS frequencies, as given by Brunner and Gu,[3] neglecting those terms whose magnitude is less than 10^{-9}, can be expressed as

$$n = 1 - (X/2) \pm (XY/2)\cos\theta - (X^2/8) \qquad (13)$$

As Eq. (13) illustrates, the terms contributing to the refractive index of the ionosphere are A: 1, the free-space velocity; B: $(X/2)$, the first-order, or $(1/f^2)$ term; C: $(XY/2)\cos\theta$, the second-order, or $(1/f^3)$, term; and D: $(X^2/8)$, the third-order, or $(1/f^4)$ term where f is the GPS operating frequency. X and Y are defined in Sec. III. Using the Brunner and Gu[3] derivation, the magnitudes

Table 1 Relationships between the various global positioning system first-order measured parameters and total electron content of Earth's ionosphere

L_2–L_1, differential group delay
360 deg, or 151.098 ns of delay, measured at L_1, or 97.75 ns of differential delay; i.e., 1 code chip
360 deg = 278.83×10^{16} (el/m^2); 1 deg = 0.7745×10^{16} (el/m^2)
1 ns of differential code delay
= 2.852×10^{16} (el/m^2)
= 1.546 ns of delay at L_1
= 0.464 m of range error at L_1
1 ns of delay, measured at L_1
= 1.8476×10^{16} (el/m^2)
= 0.300 m of range error at L_1
1 cycle, or 1 wavelength, 19.04 cm, of carrier phase advance at L_1 = 1.173×10^{16} (el/m^2)
1 m of range error:
measured at L_1 = 6.15×10^{16} (el/m^2)
measured at L_2 = 3.73×10^{16} (el/m^2)
1 TEC unit [1×10^{16} (el/m^2)]
= 0.351 ns of differential delay
= 0.542 ns of delay at L_1
= 0.163 m of range error at L_1
= 0.853 cycles of phase advance at L_1

L_2–L_1 differential carrier phase advance, measured at L_2	
1 deg = 6.456×10^{13} (el/m^2)	
0.1 rad = 3.699×10^{14} (el/m^2)	
360 deg = 2.324×10^{16} (el/m^2)	
To convert differential carrier phase advance (measured at L_2) to an equivalent single frequency phase change at a specified frequency.	
Frequency	Multiply GPS differential carrier phase by
244 MHz	12.81
1 GHz	3.125

of the higher-order terms at GPS frequencies, for maximum worldwide ionospheric conditions, are $B \approx 2 \times 10^{-4}$; $C \approx 2 \times 10^{-7}$; and $D \approx 2 \times 10^{-8}$.

The ratios of the higher-order terms, C and D, to the first order term, B, again under these worst case ionospheric conditions, is $C/B \approx 10^{-3}$; and $D/B \approx 10^{-4}$.

Thus, these higher-order terms are much less than 1% of the first-order term at GPS frequencies, even for the extremely high value of $f_n = 25$ MHz used for the maximum ionospheric plasma frequency, and for the GPS L_2 frequency used in the computation. For a more typical ionospheric maximum plasma frequency of, say, 12 MHz, and for GPS L_1 users, the higher-order terms in ionospheric refraction are even much less than those given here. Thus, within better than 0.1% accuracy, even during worst case ionospheric conditions, the ionospheric refractive index at GPS frequencies can be expressed simply as

$$n = 1 - (X/2) \tag{14}$$

During times of high TEC, the first-order range error can be a few hundred meters. At these times, higher-order ionospheric effects can be several tens of centimeters of range error, which represent large errors in geodetic measurements. Brunner and Gu[3] have used the full form of the refractive index given in Eq. (1) to calculate the residual range error from the first-order form for refractive index. Their model also includes the geomagnetic field, and the effects of ray bending at both the GPS frequencies, L_1 and L_2. They claim that their improved form of dual-frequency ionospheric correction eliminates the ionospheric higher-order effects to better than 1 mm residual range error. However, in order to achieve this order of ionospheric error correction, they require knowledge of the actual maximum electron density, N_m, an ionospheric electron density profile shape factor they call η, and the average value of the longitudinal component of the Earth's magnetic field along the ray path, $\overline{B(\cos\theta)}$. In a practical case, these parameters are not easy to estimate.

Bassiri and Hajj[4] have done similar work on higher-order ionospheric range errors for GPS. They find the magnitudes of the second- and third-order terms at L_1 to be $\sim$ 1.6 cm and $\sim$ 0.9 mm, respectively, for a TEC of 10^{18} (el/m^2). Rather that requiring a knowledge of the electron density profile shape, as is the case with Brunner and Gu,[3] they use a constant ionospheric shape factor of 0.66, and they assume a constant height for the maximum of the electron density profile. Their form of higher-order ionospheric corrections are not as good as those claimed by Brunner and Gu,[3] but they are much easier to implement, and, in the practical case of actual ionospheric data required, may result in corrections of the same magnitude. GPS users who require ionospheric corrections to centimeter or millimeter accuracy should refer to the works of Brunner and Gu[3] and Bassiri and Hajj[4] for additional details.

D. Obtaining Absolute Total Electron Content from Dual-Frequency GPS Measurements

1. Removing Multipath Effects

If both the differential carrier phase and the differential group delay are measured with a dual-frequency GPS receiver, the user easily can obtain both the absolute TEC and its rate of change. Jorgensen,[5] first showed that the differential group delay could be used to fix the differential carrier phase to an absolute scale after a satellite pass, thus obtaining the best of both measurements; namely, the absolute scale obtained from the differential group delay and the precision of the differential carrier phase. Hatch[6] suggested that combining GPS carrier with code measurements results in better absolute and relative positioning. Because the differential carrier phase is much less sensitive to multipath, the final result, providing there are no unresolved carrier cycle slips during the pass, is a precise, smooth rendition of absolute TEC over an entire pass. The ratio of multipath effects on the rf carrier, as compared with multipath observed on the P-code modulation, is proportional to their respective wavelengths. That is, multipath on the L_2 carrier is 120 times smaller than on the 10.23 MHz modulation.

Figure 2 shows a typical pass of a GPS satellite. The top panel is the L_1 carrier signal strength divided by the receiver noise, on a linear amplitude scale. The middle panel shows the relative differential carrier phase on a relative scale.

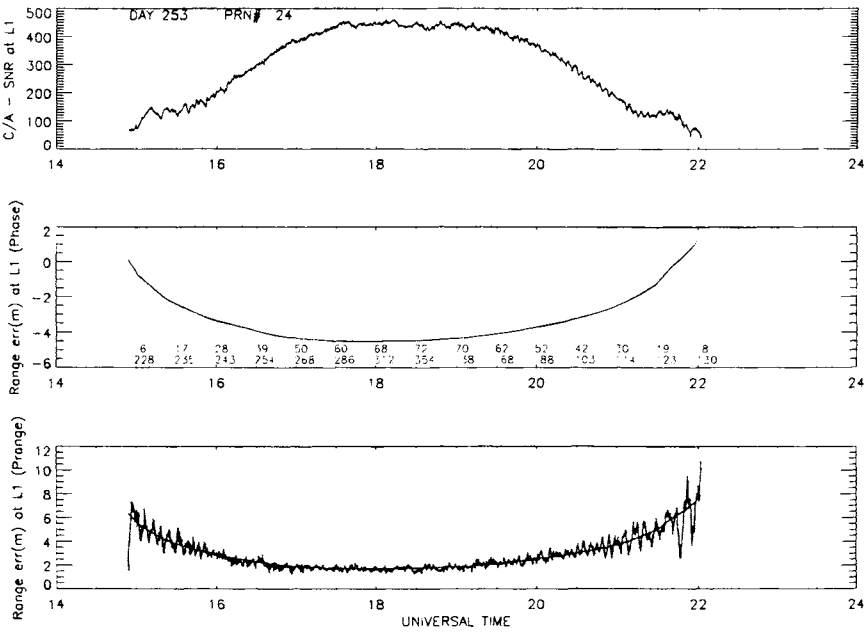

Fig. 2 Recording of a typical global positioning system pass, showing the carrier-assisted relative signal-to-noise ratio at L_1 (top panel), relative range error computed from the differential carrier phase (middle panel), and absolute rate error computed from the differential *P*-code group delay (bottom panel).

Normally the differential carrier phase is set at zero relative range error at the beginning of each pass. Elevation and azimuth values are printed in the middle panel, just under the relative differential phase record. The bottom panel shows the absolute ionospheric range error, in meters, obtained from differential group delay. Note the large multipath effects in the differential group delay, especially at both ends of the pass. The fact that the differential group variations are attributable to multipath effects becomes obvious if two, or more, successive days of passes are plotted to the same scale. The individual multipath variations agree exactly with a time shift corresponding to the sidereal difference in the time of passage of the GPS satellite along the same track over successive days.

The bottom portion of Fig. 2 also shows the differential carrier phase, now translated to an absolute scale. The process of converting the differential carrier phase to an absolute scale, by fitting to the absolute differential group delay, is done over the higher-elevation portions of each pass, when multipath is generally smallest. Multipath may not be a zero mean process and may not necessarily average out if the fitting procedure were done over the entire pass, or even worse, if the fitting were done only over the low-elevation portions of a pass.

After the differential carrier phase is converted to an absolute scale by fitting it to the differential group delay curve over the desirable, low multipath, portion of each pass, the differential group delay data are simply discarded, because they have done their task. The final TEC values are precise, accurate, and without

multipath, unless the multipath environment is really terrible, in which case a small, residual amount of multipath can even be seen in the differential carrier phase.

If a user requires absolute TEC measurements soon after acquisition of each GPS satellite at a low-elevation angle, the fitting of the differential carrier phase to the differential group delay must be done for only a few minutes of data, usually where multipath on the differential group is large. There are several, relatively straightforward, schemes for removing multipath at low-elevation angles. One is to use a high-gain, directional antenna that has smaller multipath effects. An antenna with a large ground plane also can attenuate multipath reflections. Another method is to take advantage of the fact that the orbit of each GPS satellite repeats in its ground track over successive days, thereby giving the stationary user nearly the same multipath conditions. Suitable matching and filtering techniques can be employed to use the multipath for preceeding days to remove its effects in near real time. The user must take care to see that the day-to-day differences in multipath for each GPS satellite really are the same. GPS antennas deployed in locations where the multipath effects may change from day to day, such as near automobile parking lots or aircraft terminals, may not be suitable for this procedure.

2. *Automated Ionospheric Range and Range-Rate Error Corrections*

In using an operational dual-frequency GPS receiver, all the processes described above are done automatically and are transparent to the user. If the ionospheric first-order range and range-rate error corrections are done for each satellite soon after each satellite is acquired, it is likely that only the differential group delay is used to obtain an absolute range error correction. However, the process of determining an absolute ionospheric correction by using both the differential carrier phase and the differential group delay, with an improving fit of the phase data to the group delay data as more data are acquired, could be used routinely.

E. Ionospheric Doppler Shift/Range-Rate Errors

Because frequency is simply the time derivative of phase, an additional contribution to geometric Doppler shift results because of changing TEC. This additional frequency shift is generally small compared with the normal geometric Doppler shift, but can be computed by

$$\Delta f = (\mathrm{d}n/\mathrm{d}t) = [(1.34 \times 10^{-7})/f]\,(\mathrm{d}/\mathrm{d}t)\ \mathrm{TEC}, \ldots, \mathrm{Hz} \qquad (15)$$

For high-orbit satellites, such as the GPS satellites, where the apparent satellite motion across the sky is slow, the diurnal changes in TEC are generally greater than the geometric ones. An upper limit to the rate of change of TEC, for a stationary user, is approximately 0.1×10^{16} (el/m^2) per second. This value yields an additional frequency shift of 0.085 Hz at L_1, which would not be significant compared with a typical required receiver carrier tracking loop bandwidth of at least a few Hz. The value of 0.085 Hz at L_1 corresponds to 1.6 cm/s of range-rate error.

Ionospheric range-rate or Doppler shift errors are attributable to the time rate of change of the electron content of the ionosphere, as seen by the observing

system. The range-rate error depends upon the diurnal rate of change of the electron content of the ionosphere, the structure of any large-scale irregularities that may exist in the region, and the motion of any vehicle. For instance, a GPS satellite moving up from the horizon will usually encounter fewer electrons as it rises in elevation, simply because of the decrease of the signal path length in the ionosphere. An observer in a high-velocity aircraft, or even more so, in a low-orbit spacecraft, generally will encounter geometric changes far greater than the temporal rate of change of electron content in the ionosphere.

For the slowly moving GPS satellites, the satellite motion, diurnal changes in the ionosphere, and observer platform motion, all contribute to ionospheric range-rate errors. It is difficult to model the relatively high day-to-day variability of range-rate changes attributed to the ionosphere even for a fixed observer because of the large variability in the day-to-day ionospheric rates of change. Thus, for ionospheric range-rate errors, corrections through the use of an ionospheric model, particularly one with a simple representation of diurnal ionospheric changes, such as that in the single-frequency GPS user ionospheric algorithm, are not recommended. The dual-frequency GPS user can, of course, automatically correct for both the first-order range and range-rate ionospheric errors.

F. Faraday Rotation

1. *Amount of Faraday Rotation*

When a linearly polarized radio wave traverses the ionosphere, the wave undergoes rotation of the plane of this linear polarization. At frequencies of approximately 100 MHz, and higher, the amount of this polarization rotation can be described by

$$\Omega = \frac{k}{f^2} \int B \cos\theta \, N dl, \ldots, \text{radians} \tag{16}$$

where the quantity inside the integral is the product of electron density times the longitudinal component of the Earth's magnetic field, integrated along the radio wavepath. Many ionospheric workers have used this effect to make measurements of the TEC of the ionosphere.

Because the longitudinal magnetic field intensity, $B \cos\theta$, changes much slower with height than the electron density of the ionosphere, Eq. (16) can be rewritten as

$$\text{TEC} = (\Omega f^2 / k B_L) \tag{17}$$

where $B_L = \overline{B \cos(\theta)}$ is taken at a mean ionospheric height, usually near 400 km, $k = 2.36 \times 10^{-5}$, and TEC is simply $\int N dl$.

Generally, the equivalent vertical TEC is determined by dividing the slant TEC by the secant of the zenith angle at a mean ionospheric height. The equivalent vertical TEC is the one most often used for comparison purposes among sets of TEC data, because these different slant TEC values cannot easily be directly compared. Much of the TEC data available today from stations throughout the world, used in model construction and testing, are from Faraday rotation measurements from vhf telemetry signals of opportunity from various geostationary satellites.

For satellite navigation and communication designers, the Faraday polarization rotation effect is a nuisance. If a linearly polarized wave is transmitted from a satellite to an observer on, or near, the surface of the Earth, the amount of polarization rotation may be nearly an odd integral multiple of 90 deg, thereby giving no signal on the receiver's linearly polarized antenna, unless the user is careful to realign the antenna polarization for maximum receiver signal. The Faraday rotation problem is overcome by the use of circular polarization of the correct sense at both the satellite and at the user's receiver.

2. *Faraday Rotation Effects on Global Positioning Systems*

GPS signals are transmitted with right-hand circular polarization; thus, Faraday rotation is not a problem with GPS users. The optimum receiving antenna for GPS users also would be one of right-hand circular polarization, to ensure that the receiving antenna polarization matches the characteristics of the received signal. However, it is impossible to design a nearly omnidirectional GPS receiving antenna having circular polarization over most of the entire sky. If a GPS user uses a linearly polarized antenna, the loss will be 3dB, because only one-half of the potential signal energy is being received. Thus, the optimum receiving antenna will exhibit right-hand circular polarization over as much of the sky as possible. Generally the mobile user finds it difficult to utilize circular polarization, because of the continual vehicle directional changes; thus, the user settles for nearly linear polarization. The up to 3-dB loss between transmitted circular polarization and receiver nearly linear polarization is a necessary price GPS users pay for antenna maneuverability and simplicity. The transmitted signal levels from the GPS satellites were designed to provide adequate signal strength for users with linearly polarized antennas.

Had the GPS satellites been transmitting linearly polarized radio waves, the polarization rotation, viewing satellites in various directions from a northern midlatitude station, could be up to 90 deg. For values of polarization rotation near 90 deg, signal loss for two, cross-aligned, linearly polarized antennas can be in excess of 30 dB. Thus, circular polarization was wisely chosen for use on GPS.

G. Angular Refraction

The refractive index of the Earth's ionosphere is responsible for the bending of radio waves from a straight line geometric path between satellite and ground. Normally, for GPS users, the small bending of radio waves is not a problem. The angular refraction, or bending, produces an apparent higher elevation angle than the geometric elevation. Millman and Reinsmith[7] have derived expressions relating the refraction to the resultant angular bending. Perhaps the easiest expressions to use, as given by Millman and Reinsmith,[7] relate the ionospheric range error to angular refraction. This expression is:

$$\Delta E = \{(R + r_0 \sin E_0)\,(r_0 \cos E_0)/[h_i(2r_0 + h_i) + (r_0^2 \sin^2 E_0)] \times (\Delta R/R)\} \quad (18)$$

where E_0 is the apparent elevation angle; R is the apparent range; ΔR is computed from, $\Delta R = (40.3/f^2) \times \text{TEC}$; r_0 is the Earth's radius; and h_i is the height of the centroid of the TEC distribution, generally taken to be between 300 and 400 km.

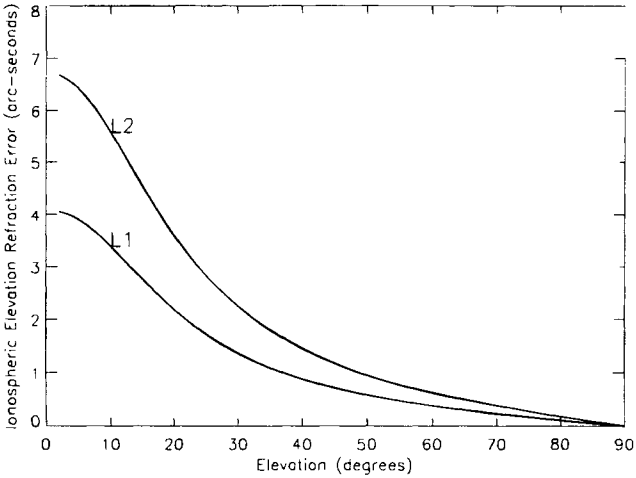

Fig. 3 Ionospheric refraction vs elevation for both L_1 and L_2.

Typical values of elevation refraction error for GPS at L_1 and at L_2, for a TEC of 10^{18} (el/m^2) column are given in Fig. 3.

The refraction, or radio wave bending illustrated in Fig. 3, is generally not a problem for GPS, because the user does not attempt to use GPS satellites at elevation angles lower than approximately 5 deg, due to other effects at low elevation angles, including antenna multipath, and tropospheric delay effects that increase greatly at low elevation angles. Errors in the azimuth of GPS radio signals transmitted through the ionosphere also can occur. They depend upon azimuthal gradients in TEC that generally are smaller than vertical gradients, and they can be neglected in most practical cases.

H. Distortion of Pulse Waveforms

Two characteristics of the ionosphere can produce distortion of pulses of rf energy propagated through it. The GPS signals consist of spread spectrum pseudorandom noise, having bandwidths of approximately 2 MHz and 20 MHz for the C/A and the P codes, respectively. The ionosphere can produce dispersion of the spread spectrum signals from GPS, but this effect is very small. The dispersion, or differential time delay caused by the normal ionosphere, as derived by Millman,[8] produces a difference in pulse arrival time across a bandwidth, Δf, of

$$\Delta t = [(80.6 \times \Delta f)/cf^3] \times \text{TEC}, \ldots, \text{seconds} \qquad (19)$$

where c is the velocity of light in m/s, f and Δf are expressed in Hz, and TEC is in el/m^2 column. The dispersive term for pulse distortion is thus proportional to TEC. When the difference in group delay time across the bandwidth of the pulse is the same magnitude as the width of the pulse, it will be significantly disturbed by the ionosphere. The dispersion across the 20-MHz GPS bandwidth is normally small and can be ignored.

Chapter 13

Tropospheric Effects on GPS

J. J. Spilker Jr.*
Stanford Telecom, Sunnyvale, California 94089

I. Tropospheric Effects

A. Introduction

THIS chapter discusses the effects of the troposphere on the GPS *L*-band signals and the resulting effect on GPS positioning. The specific effects discussed include tropospheric attenuation, scintillation, and delay. To be precise, the term tropospheric used in this chapter is somewhat of a misnomer because roughly 25% of the delay effect is caused by atmospheric gases above the troposphere, specifically gases in the tropopause and stratosphere as shown in Fig. 1. The troposphere produces attenuation effects that are generally below 0.5 dB and delay effects on the order of 2–25 m. These effects vary with elevation angle because lower elevation angles produce a longer path length through the troposphere and also vary with the detailed atmospheric gas density profile vs altitude.

1. Atmospheric Constituents and Profile

The atmosphere consists of dry gases and water vapor. The wet and dry constituents of the atmosphere affect the propagation delay of the radio frequency signals quite differently, and these constituents have different pressure profiles. Water vapor is confined to the troposphere and generally exists only below altitudes of 12 km above sea level, and most of the water vapor is below 4 km. Water vapor density varies widely with position and time and is much more difficult to predict than the dry atmosphere. For example, significant changes in water vapor can occur over tens of km and hours of time. Fortunately, however, water vapor effects represent only a relatively small fraction (roughly 1/10) of the total. Because the water vapor content is highly nonuniform, a total average fractional volume is not a very meaningful method of description of the water vapor content. Instead, a measure of water vapor often employed is the total amount of water in a vertical column of air one square cm in area:

*Ph.D., Chairman of the Board.

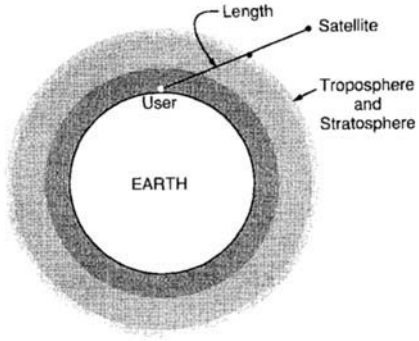

Fig. 1 Propagation of the GPS signal through the troposphere and stratosphere produces attenuation, delay and scintillation effects. The tropopause is the boundary between the troposphere and the higher altitude stratosphere.

$$W = \int_0^\infty \rho_w(h)\mathrm{d}h \text{ g}$$

where $\rho_w(h)$ is the water vapor density in g/cm^3. The total integrated water content W can vary enormously with position and ranges from 0.01 to 7.5 g, from the polar region to the tropics.

On the other hand, the dry atmosphere is relatively uniform in its constituents. Typical dry gas constituents have molar weights and fractional densities,* as shown in Table 1. At the GPS frequencies, oxygen is the dominant source of attenuation.

Table 1 Molar weights and approximate fractional volumes[a] of the major constituents of dry air[1]

Constituent	Molar weight, kg/kmol	Fractional volume unitless
N_2	28.0134	0.78084
O_2	31.9988	0.209476
Ar	39.948	0.00934
CO_2	44.00995	0.000314
Ne	20.183	0.00001818
He	4.0026	0.00000524
Kr	83.30	0.00000114
X_e	131.30	0.000000087

[a]For reference, at sea level and at 100% humidity, the water vapor occupies roughly 1.7% by volume, but note that percent humidity varies considerably with both time and position.[2]

* The fractional volume of CO_2 is the only major constituent of dry air that shows a significant variation, and it shows an annual variation of 6 ppm out of approximately 300 ppm and is increasing at a rate of 1.7 ppm/year.[3] However, for our purposes, these effects are negligible.

The temperature profile of a highly simplified model of the atmosphere in Fig. 2 shows that the temperature generally decreases with altitude at a constant lapse rate of -5 to -7°C per km of altitude increase from sea level up to the tropopause. At higher latitudes in winter and at nighttime, there is sometimes a temperature inversion layer in the 0.5–2 km region before the constant lapse rate of the troposphere begins. The tropopause is a region of approximately constant temperature and has an altitude of 8–12 km in the winter, or 10–12 km during the summer. The height of the tropopause has a downward slope from the equator toward the poles, and there is a small discontinuity in the tropopause height just above and below the equator. In the tropopause, the temperature rate of change decreases to zero. In the lower stratosphere (just above the tropopause), the rate of change of temperature gradually reverses to a slight $+1$°C to 2°C/km, and this relatively slow, nonuniform increase continues through the stratosphere up to an altitude of approximately 50 km. At this altitude, the stratopause, the temperature rate begins to reverse, and the temperature is roughly 0°C.[3,4] In the region directly above the stratopause; namely, the mesosphere, the temperature again decreases until it reaches approximately -90°C at the mesopause, which has a height of approximately 90 km. However, the atmospheric pressure in the mesosphere is so small (0.02–1 mb) as to be inconsequential for purposes here.

The atmospheric pressure at sea level is roughly 1013 mb and decreases with altitude to approximately 200–350 mb at the tropopause at the pole, and 70–150

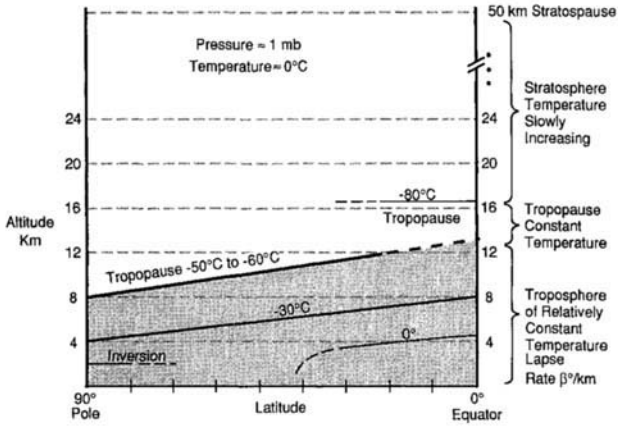

Fig. 2 Simplified model of the isothermal lines during the winter. Below the tropopause, the isotherms are approximately equally spaced at a temperature lapse rate of approximately 5–7°C/km decrease in temperature for every km of altitude increase. At the tropopause, the temperature lapse rate equals zero and then gradually reverses to a small rate of increase of approximately 1°–2°C/km in the stratosphere. Note that the height of the tropopause is roughly 4–8 km lower at the pole than near the equator. Thus, the tropopause has a downward slope toward the poles. During the summer, the tropopause is approximately 2 km higher in altitude at the poles but remains in the range of 17 km at the equator. At the polar regions, there is also an arctic temperature inversion at approximately 2 km, where the temperature lapse rate reverses.[3,4]

mb at the equator. Pressure decreases further to only 30 mb at approximately an altitude of 24 km at the pole and is only 1 mb at the stratopause. One atmosphere of pressure is defined as 1013.25 mb. The water vapor content lies primarily in the region below 4 km.

B. Atmospheric Attenuation

Atmospheric attenuation in the 1–2 GHz frequency band is dominated by oxygen attenuation, but even this effect normally is small. The attenuation is on the order of 0.035 dB for a satellite at zenith.[5,6] However, it can be ten times larger (in dB) at low elevation angles. The effects of water vapor, rain, and nitrogen attenuation at frequencies in the GPS frequency bands are negligible.[3]

Oxygen attenuation $A(E)$ in dB for the 1.5 GHz frequency range is approximately 0.035 dB at zenith ($E = 90$ deg) and varies with elevation angle E in proportion to the tropospheric path length L (obliquity factor or mapping function). If the troposphere is modeled by a simple uniform spherical shell of height h_m above the Earth, as shown in Fig. 3, then the length of the path L varies with elevation angle E, as shown in the fig. Thus, $A(E)$ has the following approximate value:

$$A(E) \cong \frac{2A(90\text{ deg})(1 + a/2)}{\sin E + \sqrt{\sin^2 E + 2a + a^2}} \cong \begin{cases} \dfrac{2A(90\text{ deg})}{\sin E + 0.043}\ \text{dB for small } E \text{ but } > 3\text{ deg} \\ \dfrac{A(90\text{ deg})}{\sin E}\ \text{dB for } E > 10\text{ deg} \end{cases} \tag{1}$$

where $a = h_m/R_e << 1$ and h_o is the equivalent height for oxygen $h_m = 6$ km, and R_e is the Earth radius $R_e \cong 6378$ km.[7]

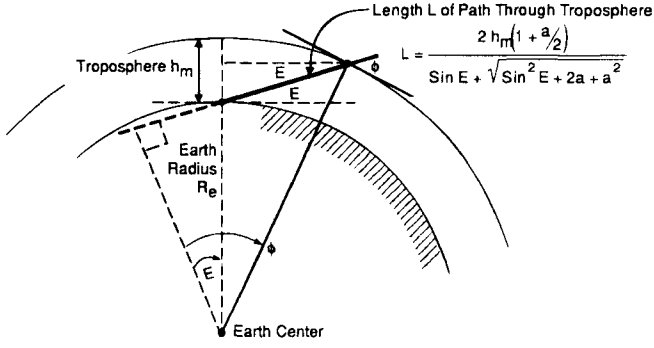

Fig. 3 Path length L through a uniform shell troposphere at elevation angle E where $\cos E = (1 + a)\cos\phi$ where $a \triangleq h_m/R_e$.

The attenuation of Eq. (1) is plotted in Fig. 4 for elevation angles $E > 3$ deg. This expression for $A(E)$ has assumed a spherical troposphere symmetrical in azimuth and uniform in density up to the equivalent height h_o. Note, if the troposphere were simply a planar layer with thickness h over a flat Earth, the length would simply be $h_o csc\ E$. Near the horizon; e.g., below 3 deg, the uniform spherical model of Fig. 3 is no longer accurate, and neither Eq. (1) nor Fig. 4 should be used. The complexity of the atmosphere at low elevation angles is discussed later in this chapter. Nonetheless, note from Fig. 4 that the attenuation at 5 deg elevation angles is 0.38 dB, which is approximately ten times the zenith attenuation of 0.035 dB.

The mapping or obliquity function [i.e., the ratio $A(E)/A(90\ \text{deg})$] at low elevation angles for the troposphere is significantly larger than that for the ionosphere (10 compared to 3) because the troposphere extends down to the surface of the Earth. Thus, at low elevation angles, the ray path to the satellite penetrates the lower troposphere in a more nearly horizontal direction than it does at the ionosphere, which exists only above approximately 60 km. In practice, we should avoid using GPS satellites below approximately 5-deg elevation not only because of the lower signal levels associated with tropospheric attenuation, but because of larger uncertainties in tropospheric and ionospheric delay and greater scintillation effects caused by both the troposphere and the ionosphere (discussed later in this chapter and discussed in the previous chapter for the ionosphere). Furthermore, potential signal multipath, refraction, and receiving antenna gain roll-off effects may be magnified at low elevation angles.

C. Rainfall Attenuation

For a frequency of 2 GHz, the attenuation even for dense, 100 mm/h rainfall, is less than 0.01 dB/km; thus, it has a very small effect. Rainfall attenuation below 2 GHz is even less; thus, rain attenuation is of little consequence in the frequency bands of interest for GPS, 1.57542 GHz and 1.2276 GHz.[5]

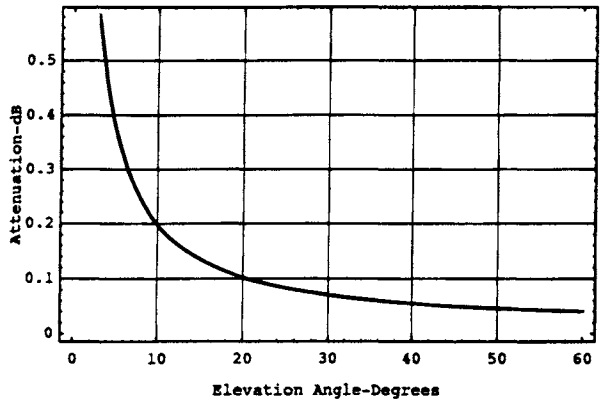

Fig. 4 Atmospheric attenuation vs elevation in degrees. Near the horizon at $E \leq 3$ deg, the model is no longer accurate.

D. Tropospheric Scintillation

Tropospheric scintillation is caused by irregularities and turbulence in the atmospheric refractive index primarily in the first few kilometers above the ground. The satellite–Earth propagation link through the troposphere is affected by a combination of random absorption and scattering from a continuum of signal paths that, in turn, cause random amplitude and phase scintillations in the received waveform. The scintillation effect varies with time and is dependent upon frequency, elevation angle, and weather conditions, especially dense clouds. At elevation angles above 10 deg, the predominant effect is forward scattering caused by atmospheric turbulence. At GPS frequencies, these effects are generally relatively small except for a small fraction of the time and at low elevation angles.

A received carrier from a satellite generally has the form $A(t)\sin(\omega t + \phi)$. Define the scintillation intensity $x(t)$ as the log of the amplitude ratio $A(t)/\overline{A(t)}$:

$$x(t) = 20 \log_{10}[A(t)/\overline{A(t)}] \text{ dB} \tag{2}$$

where $\overline{A(t)}$ is the mean (short-term) amplitude of the signal. The probability density of $x(t)$ in dB in the short term is Gaussian and has variance σ_x^2 (see Boithias,[5] Ippolito,[8] and Moulsey and Vilar[9]). Thus, $A(t)$ has lognormal statistics. Experimental measurements of received carrier amplitude[8,9] have shown that the statistics of amplitude scintillation $A(t)$, although well represented by a lognormal distribution (Gaussian in dB representation with rms value σ_x) in the short term are not truly stationary and, over a longer observation interval, have significant fluctuations in the σ_x parameter with time caused, for example, by changes in weather. The appearance of large irregularly shaped cumulus clouds in the satellite–user path can change the value of σ_x. In observations taken while a large cumulus cloud passed through the antenna beam, the value of σ_x increased by a factor of six (see Ippolito[8]), although when scaled to L-band these effects are still small.

Moulsey and Vilar[9] represent $A(t)$ with a conditional lognormal distribution. Thus the probability of $x(t)$ conditional on a given σ_x is then normal with a variance σ_x^2 and is then as follows:

$$p(x|\sigma_x) = \frac{1}{\sigma_x\sqrt{2\pi}} \exp - \left(\frac{x^2}{2\sigma_x^2}\right) \tag{3}$$

The rms value σ_x in dB is itself a random variable with a mean σ_m, and its long-term fluctuations have a probability density that is also lognormal:

$$p(\sigma_x) = \frac{1}{\sigma_\sigma\sigma_x\sqrt{2\pi}} \exp - \left[\frac{(\log \sigma_x - \log \sigma_m)^2}{2\sigma_\sigma^2}\right] \tag{4}$$

where σ_σ^2 is the variance of this distribution. Thus $p(x|\sigma_x)$ can be viewed as a short-term statistic wherein σ_x itself has a distribution for the long term. The rms value of x in the long term is defined as σ_{xm}, which can be evaluated using $p(x) = \int p(x|\sigma_x)p(\sigma_x)d\sigma_x$ and found to be $\sigma_{xm} = \sigma_m \exp(\sigma_\sigma^2/4)$ dB.

For a value $\sigma_\sigma = 1$, which seems to match measurements by Moulsey and Vilar,[9] the value of $\sigma_{xm} = 1.28\,\sigma_m$. The interpretation of this result is that although the long-term mean value of σ_x is σ_m, and σ_m may be small; e.g., on the order

of 0.259 dB, the variance $\sigma_\sigma^2 = 1$ can lead to momentary periods of much larger scintillation.

The CCIR (1982) has given an expression for the long-term mean value of σ_x, namely, σ_m. For small antennas such as omnidirectional GPS antennas, the CCIR expression for the long-term rms amplitude scintillation varies with frequency and elevation angle as follows:

$$\sigma_m = 0.025 f^{7/12} (\csc E)^{-0.85} \text{ dB} \tag{5}$$

where f is in GHz, and the elevation angle is E. (Larger antennas, not of importance for most GPS applications, produce an antenna averaging effect that decreases the value of σ_m). For $L_1 = 1.57542$ GHz we have the following:

$$\sigma_m = 0.0326 (\csc E)^{-0.85} \text{ dB} \tag{5a}$$

and $\sigma_m = 0.259$ dB at $E = 5$ deg. Over the long term, the value of σ_x can vary substantially. If the mean σ_m of σ_x is taken as $\sigma_m = 0.259$ corresponding to the (worst case) 5 deg elevation angle for the CCIR model, and $\sigma_m = 0.081$ dB for 20-deg elevation angle, the cumulative distribution of σ_x is then as shown in Fig. 5. Thus, roughly 10% of the time the rms scintillation σ_x has a value of 0.9 dB and 0.3 dB for these two elevation angles, respectively, for this model. Thus, for low elevation angles and small fractions of time, tropospheric scintillation can be significant, but otherwise it is quite small.

II. Tropospheric Delay

The signal received from a GPS satellite is refracted by the atmosphere as it travels to the user on or near the Earth's surface. The atmospheric refraction causes a delay that depends upon the actual path (slightly curved) of the ray and

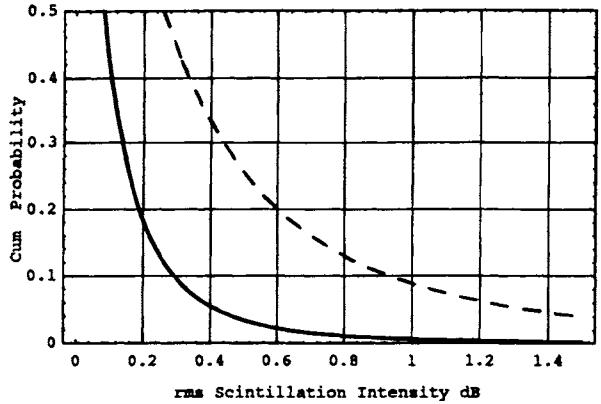

Fig. 5 Cumulative probability for the rms tropospheric scintillation σ_x dB. For this example, the mean value of $\sigma_m = 0.259$ dB for small 5 deg elevation angles (dashed curve) and $\sigma_m = 0.081$ dB for 20 deg elevation angle solid curve. For this lognormal model and a cumulative probability of 10%, the rms scintillation intensity σ_x is equal to 0.9 dB and 0.3 dB, respectively, for 5-deg and 20-deg elevation angles.

the refractive index of the gases along that path. For an atmosphere symmetric in azimuth about the user antenna, the delay depends only upon the vertical profile of the atmosphere and the elevation angle to the satellite.

A. Path Length and Delay

There are two major delay effects of the troposphere. The first and larger effect is a dry atmosphere excess delay caused primarily by N_2 and O_2. The dry atmosphere zenith excess delay corresponds to approximately 2.3 m and varies with local temperature and atmospheric pressure in a reasonably predictable manner.* The dry atmosphere effect varies by less than 1% in a few hours. The second effect—the wet atmosphere or water vapor effect—is generally smaller, 1–80 cm at zenith; i.e., perhaps $^1/_{10}$ the size of the dry atmosphere delay effect, but it varies markedly, 10–20%, in a few hours and is less predictable even with surface humidity measurements. Dual frequency 22, 31 GHz radiometer measurements can be made to make more precise predictions, but these measurements are fairly complicated and not feasible for most navigation applications.

The tropospheric delay is caused by the larger refractive index n ($n > 1$) of atmospheric gases than that of free space ($n = 1$), which causes the speed of light (group velocity) in the medium to decrease below its free space value c. Thus, a ray with an infinitesimal path length ds that travels through a medium with a refractive index n has a time delay $d\tau = n\, ds/c$ and has an equivalent distance $c\, d\tau = n\, ds$. In this section, delays are measured in meters rather than time, and the c is omitted after this paragraph. The difference between the actual total path delay $S = c\tau = \int n(s) \times 10^{-6}\, ds$ and the geometrical path distance S_g is the excess tropospheric delay Δ. The difference between the actual refractive index and unity is of the order of magnitude of $n-1 \cong 2.7 \times 10^{-4}$ at sea level and varies with altitude, latitude, and various meteorological conditions.

At the L-band frequencies of GPS signals, the refractive index is essentially constant with frequency, and hence, is nondispersive; i.e., $dn/df = 0$, and thus, the group velocity and phase velocity are the same. As shown in the previous chapter, this equivalence is not true in the ionosphere.

The spatially varying refractive index causes the signal path to have a slight curvature with respect to the geometric straight line path. Thus, the actual satellite-to-user path is a slightly curved path, as shown in Fig. 6 where the path curvature has been greatly exaggerated for clarity. The total length of the actual path from P_1 to P_2 in m is as follows:

$$S = \int_{\text{Actual}} ds \tag{6}$$

and is clearly longer than the straight line geometric path S_g (at elevation angles less than 90 deg) that the ray would take in a vacuum. However, it is well known from Fermat's principle[5,10] that the actual ray path is that path which minimizes the total delay from P_1 to P_2 (omitting c from $c\tau$ from now on):

* In the frequency range below 15 GHz, both the wet and dry components have an effect. At optical frequencies, the whole effect is attributable to the dry component.

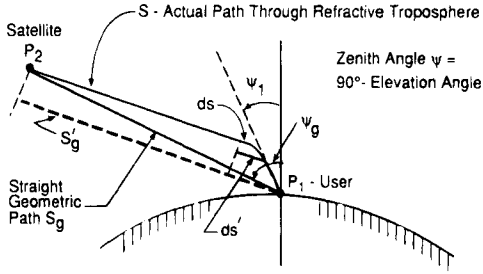

Fig. 6 Actual slightly curved path S and straight geometric paths through the refractive atmosphere. The difference in the actual path distance vs the geometric path distance is $\Delta_g \triangleq S - S_g \cong S - S_g'$ where $\Delta_g \triangleq \int ds - \int ds'$.

$$\tau = \int_{\text{Actual}} n(s)\, ds \tag{7}$$

The actual (curved) path from P_1 proceeds along a path which is initially closer to the zenith so that it passes through the region of high dielectric constant more rapidly. Thus, the actual curved path length S is longer than the straight line geometric path length (a rectilinear chord) S_g in m:

$$S_g \triangleq \int_{\text{geo}} ds \quad \text{and} \quad \tau_{\text{geo}} = \int_{\text{geo}} n(s)\, ds \tag{8}$$

although it is shorter in time delay. The notation τ_{geo} represents the path delay which would be accumulated along the geometric rectilinear chord. The integral path notation geo defines the geometric straight line path. That is, delay τ is shorter than the delay τ_{geo} of the straight line path. The quantity of primary interest is the excess delay caused by the atmosphere $\Delta = \tau - S_g$. The difference between the length of the actual curved path and the straight line path is typically quite small $S - S_g < 0.1$ m[11] except at low elevation angles.

If point s along the ray path is expressed in polar coordinates, then $s = re^{j\phi}$ (two dimensions), where the center of the coordinate system is at the Earth center, then the total delay [Eq. (7)], can be written as follows:

$$\tau = \int_{\text{Actual}} n(s)\, ds = \int_{\text{Actual}} n(r, \phi)\sqrt{1 + (r\phi')^2}\, dr \tag{9}$$

where $ds = dr\sqrt{1 + (r\phi')^2}$ and $\phi' \triangleq d\phi/dr$ for the path. Assume that $n(r,\phi) = n(r)$; i.e., the troposphere is spherically symmetric about the Earth's center. Fermat's principle and the calculus of variations then gives a minimum τ for the path and results in the following relationship:

$$\frac{n(r)r^2\phi'(r)}{\sqrt{1 + (r\phi')^2}} = \text{constant, or } n(r)r \sin \psi(r) = n(0)R_e \sin \psi(0) = \text{constant} \tag{10}$$

which is Snell's Law, and where $\psi(r)$ is the angle between the Earth's center radial vector at (r,ϕ), and the path tangent at height h above the Earth (see Fig.

7). At the user point P_1 on the Earth's surface, the radial distance $r = R_e$, the Earth radius, and the angle $\psi(0)$ is the zenith angle at the user $\psi(0) = 90$ deg $- E$, where E is the elevation angle. Another method of arriving at the same result is to assume a concentric set of spherical shells of height Δr and constant refractive index n_i, as shown in Fig. 7. Thus, we have Snell's law for spherical shells as follows:

$$r_i n_i \sin \psi_i = r_1 n_1 \sin \psi_1 = n(0) R_e \sin \psi(0) = \text{constant} \tag{10a}$$

In summary, the curved path, although physically slightly longer, has a slightly shorter total delay than would a path traveling in a straight line through the troposphere. Thus, the difference between the actual curved delay and straight line geometric distance (rectilinear chord) is as follows:

$$\Delta = \tau - S_g = \int_{\text{Actual}} n(s)\, ds - \int_{\text{geo}} ds \tag{11}$$

The second integral is the delay for the straight line (neglecting relativity) path that the ray would take in a vacuum. This difference can be rewritten as follows:

$$\Delta = \int_{\text{Actual}} (n - 1)\, ds + \left[\int_{\text{Actual}} ds - \int_{\text{geo}} ds \right] = \int_{\text{Actual}} (n - 1)\, ds + \Delta_g \tag{12}$$

where the second term in brackets Δ_g is the difference between the curved and

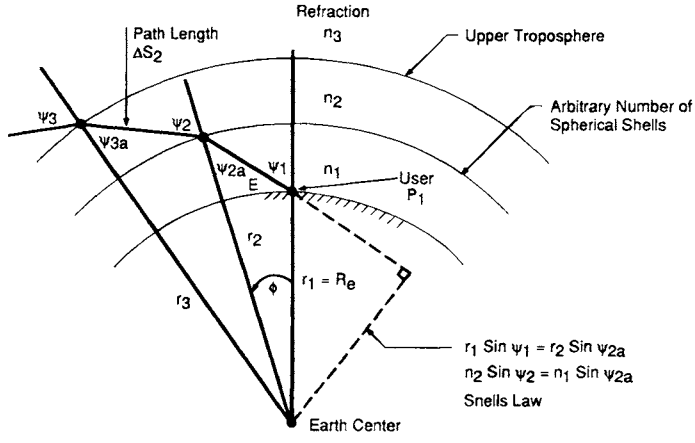

Fig. 7 Diagram of a ray path through sequential spherical shells of uniform refractive index n_i with base shell radi r_i and heights $h_i = r_i - R_e$, respectively. Snells law for spherical shells is $r_1 n_1 \sin \psi_1 = r_2 n_2 \sin \psi_2$. For planar boundaries Snells law has the familar form $n_2 \sin \psi_2 = n_1 \sin \psi_{2a}$. The same relationships hold for an arbitrary number of uniform shells of width Δr. The length of each path within a shell of infinitesimal width dh is related to the shell width by the ratio

$$ds/da = R_e(1 + a\, n(a))/(2a\, n(a) + a^2 n^2(a) + \sin^2 E)^{1/2}$$

where $a \triangleq h/R_e$, $n(a)$ is the refractive index; and a is the normalized height.

free-space paths $S - S_g \triangleq \Delta_g$. Ray-tracing calculations comparing excess delay Δ for a straight line path vs. a curved path from Snell's law have been calculated by Janes et al.[7] for the U.S. Standard atmosphere for various latitudes and elevation angles. The error caused by the neglect of path curvature is less than 3 mm for $E \geq 20$ deg; 2 cm for $E = 10$ deg; and increases to 17 cm at $E = 5$ deg (primarily from dry gases). The initial elevation angle difference between the straight line path and the curved path is on the order of seconds of arc, except for low elevation angles. The actual difference between the actual zenith angle $\psi(0)$ and the geometric straight line zenith angle ψ_g is difficult to compute (we must integrate $\int \tan \psi \, dn/n = \psi_g - \psi(0)$). However, a loose upper bound is easily obtained as follows:

$$\Delta\psi = \psi_g - \psi(0) < N(0) \times 10^{-6} \tan \psi(0) \tag{13}$$

by integrating over a single shell of constant refractive index $N(0)$ (see also Ref. 9). A more precise formula (radio ranging standard formula) from Saastamoinan[11] *is as follows:*

$$\Delta\psi \text{ in seconds of arc} \cong \frac{16.0 \tan \psi_g}{T}\left(P + \frac{4800e}{T}\right) - 0.07(\tan^3 \psi_g + \tan \psi_g)\left(\frac{P}{1000}\right) \tag{14}$$

where P and e are the atmosphere pressure and the partial pressure of water vapor in millibars, respectively, and T is the absolute temperature in °Kelvin. The quantity $\Delta\psi$ is the angle of refraction. The angle $\Delta\psi$ is generally quite small, generally $\Delta\psi < 0.1$ deg.

In general, the estimation models for the actual troposphere excess delay from point P_1 to point P_2 is as follows:

$$\Delta = (10^{-6}) \int_{\text{Actual}} N ds + \Delta_g \tag{15}$$

where the refractivity $N \triangleq (n - 1) \times 10^6$ has both dry and wet terms. The excess delay Δ can be approximated as the sum of wet and dry delay effects in a simplified form similar to the following:

$$\Delta = [\Delta_{zd} m_d(E) + \Delta_{zw} m_w(E)] \tag{16}$$

where Δ represents the excess tropospheric delay; Δ_{zd} represents the dry zenith delay; Δ_{zw} represents the wet zenith delay; and $m_d(E)$ and $m_w(E)$ are the dry and wet mapping functions (obliquity factor) that magnify the tropospheric delay as the elevation angle E decreases. In general, $m_d(E)$ and $m_w(E)$ are really functions of the atmospheric profile as well as E. However, expressing them as a function of E alone is a useful approximation.

To analyze Δ further, it is first necessary to investigate the refractivity profiles of the troposphere with altitude. These results can then be employed to compute the zenith delay terms Δ_{zd} and Δ_{zw}. Finally, models can be developed for the mapping functions $m_d(E)$ and $m_w(E)$. We must be careful to understand exactly

what is meant by the wet and dry terms because the actual path of the ray is dependent on all contributions to the index of refraction. As shown below, it is often convenient to break up the excess delay into a hydrostatic component Δ_h, which is dependent only upon the total pressure (and not the mix ratio of dry and wet air) and a wet component Δ_w.

B. Tropospheric Refraction Versus Pressure and Temperature

The general empirical expression for refractivity of nonideal gases including water vapor to be used here is as follows (see Davis et al.[1] and Thayer[12]).

$$\begin{aligned} N = (n-1)10^6 &= k_1(P_d/T)Z_d^{-1} + k_2(e/T)Z_w^{-1} + k_3(e/T^2)Z_w^{-1} \\ &= 77.604(P_d/T)Z_d^{-1} + 64.79(e/T)Z_w^{-1} + 377600(e/T^2)Z_w^{-1} \\ &= 77.604(P_d/T)Z_d^{-1} + (e/TZ_w)(64.79 + 377600/T) \end{aligned} \tag{17}$$

where P_d and e are the partial pressure of dry air and partial pressure of water vapor both in millibars; T is the temperature in °Kelvin; and the compressibility Z factors correct for the small departures of the moist atmosphere from an ideal gas. Ideal gases obey the relationship $PV = RT$; nonideal gases operate as $PV = ZRT$ where R is the universal gas constant. The experimentally derived values used here are: $k_1 = 77.604 \pm 0.0124$; $k_2 = 64.79 \pm 10$; $k_3 = 377600 \pm 3000$. See Table 2 for various values of k_i.

The inverse compressibility expressions are as follows[1]:

$$\begin{aligned} Z_d^{-1} &= 1 + P_d[57.97 \times 10^{-8}(1 + 0.52/T) - 9.4611 \times 10^{-4}\, T_c/T^2] \\ Z_w^{-1} &= 1 + 1650\,(e/T^3)[1 - 0.01317T_c + 1.75 \times 10^{-4}T_c^2 + 1.44 \times 10^{-6}T_c^3] \end{aligned} \tag{18}$$

where T_c is temperature in °Celsius; T is in °Kelvin; and P_d is the dry pressure in millibars. The molar weight of dry air is $M_d = 28.9644$ kg/kmol, and for water $M_w = 18.0152$ kg/kmol. The ratio $M_w/M_d = 0.621977$.

The task at hand is to define models for the pressure and temperature vs. altitude that will yield models for N vs altitude h using Eqs. (17) and (18). The first term in Eq. (17) is referred to as the dry term, and the second two terms as the wet terms. Typically, the dry term represents perhaps 90% of the total effect and is relatively well predicted by surface pressure measurements. The wet terms, although small, are not easily predicted, and the water vapor effects vary considerably with position, elevation angle, and time. The pressure P and density ρ for the dry and wet air are related by the gas law as follows:

$$P_d = \rho_d \frac{R}{M_d} TZ_d, \qquad P_w = e = \rho_w \frac{R}{M_w} TZ_w \tag{19}$$

where ρ_d and ρ_w are the dry and wet densities, respectively.

Thus, the refractivity N can be expressed in terms of the densities by substituting Eq. (19) into the first two terms of Eq. (17) as follows:

$$\begin{aligned} N &= k_1 \frac{R\rho_d}{M_d} + k_2 \frac{R\rho_w}{M_w} + k_3 \frac{e}{T^2} Z_w^{-1} \\ &= k_1 \frac{R\rho}{M_d} + \left(k_2 - k_1 \frac{M_w}{M_d}\right) \frac{e}{T} Z_w^{-1} + k_3(e/T^2)Z_w^{-1} \end{aligned}$$

Table 2 Constants used in the refraction Eq. (17) by various sources for microwave frequencies. In this chapter, the Thayer values are employed.

Source	k_1(°K/mb)	k_2(°K/mb)	k_3(°K²/mb)
Thayer[12] (with Davis et al.,[1] uncertainty)	77.604 ± .014	64.79 ± 10	377600 ± 3000
Hill,[13] theoretical	——	98 ± 1	358300 ± 300
Birmbaum and Chatterjee,[14] measurements	——	71.4 ± 5.8	374700 ± 2900
Boudouris,[15] measurements	——	72 ± 11	375000 ± 3000

$$= (77.604 \pm 0.014)\,\rho \frac{R}{M_d} + k_2' \frac{e}{T} Z_w^{-1} + k_3 \frac{e}{T^2} Z_w^{-1}$$

$$= 22.276\,\rho + (16.5 \pm 10) \frac{e}{T} Z_w^{-1} + 377600 \frac{e}{T^2} Z_w^{-1} \qquad (20a)$$

where $\rho = \rho_d + \rho_w$ is the total mass density, $k_2' = k_2 - k_1 M_w/M_d$; and, of course, both the ρ_d, ρ_w densities and T vary with height h. Note that there is considerable uncertainty in the coefficient of the $(e/T)Z_w^{-1}$ term.[1] The uncertainty in the k_1 term is ±0.018%. Note that the first term in Eq. (20a) is dependent only on the total density ρ and is independent of the fractional water vapor content. The first term in the last version of Eq. (20) is termed the hydrostatic component. Total pressure is related to total density through the hydrostatic equation $dP/dh = -\rho(h)\,g(h)$, where $g(h)$ is the acceleration of gravity at the receiver antenna that also has a variation with height (only small variation for the relatively short range of heights for the troposphere). Generally $g(h)$ has very little variation with h, and a good approximation is obtained by replacing $g(h)$ by its weighted mean value over the range of integration $g_m = [\int \rho(h) g(h) dh]/[\int \rho(h) dh]$.

For this reason, we rewrite Eq. (20a) as the sum of hydrostatic and wet refractivity:

$$N = N_h + N_w \qquad (20b)$$

where the hydrostatic refractivity is $N_h = (k_1 R/M_d)\,\rho = 22.276\,\rho$, and the wet refractivity is as follows:

$$N_w = \left[k_2 - k_1 \frac{M_w}{M_d}\right] \frac{e}{T} Z_w^{-1} + k_3 \frac{e}{T^2} Z_w^{-1}$$

The hydrostatic refractivity is sometimes referred to as the dry refractivity and differs only by the Z_d^{-1} coefficient.

1. Temperature, Pressure, Refraction Index Models

The variation of the refractivity of the atmosphere vs altitude is exceedingly complex, and the models for refractive index are in the end based on fitting coefficients to match extensive sets of measured data. Nevertheless, it is instructive to review fundamental thermodynamics and ideal gas laws because some of the more complex models bear a close resemblance to these idealized models.

a. Troposphere–ideal gas models—adiabatic process. First consider an atmosphere of a single ideal gas with a pressure vs. altitude $P(h)$. At the lower altitudes within the troposphere, there is continual upward and downward motion of the air masses. Assume as an approximation that the process is assumed to be reversible and adiabatic (no heat entering or leaving the process). Also, assume that the gases are ideal* $PV = RT$. For an ideal gas with constant pressure heat capacity C_p and constant volume heat capacity C_v where $C_p = C_v + R$, a reversible adiabatic process with no heat transfer yields the following:

$$C_v\, dT + P\, dV = 0 \tag{21a}$$

Because $P = RT/V$ and $R/C_v = \gamma - 1$ where $C_p/C_v = \gamma$ is defined as the ratio of heat capacities. By using $PV = RT$ and $R/C_v = \gamma - 1$, Eq. (21a) becomes the differential equations that follow:

$$dT/T = -R/V\, dV = -(\gamma - 1)\, dV/V, \quad \text{or} \quad dT/T = [(\gamma - 1)/\gamma]\, dP/P \tag{21b}$$

Equation (21b) has the following solutions:

$$\left(\frac{T_2}{T_1}\right) = \left(\frac{V_1}{V_2}\right)^{\gamma - 1}, \quad \text{and} \quad \left(\frac{T_2}{T_1}\right) = \left(\frac{P_2}{P_1}\right)^{(\gamma - 1)/\gamma} \tag{21c}$$

For a diatomic gas such as O_2, the heat capacity ratio changes slowly with temperature and has an approximate value of $\gamma = 1.4$. For polyatomic gases such as H_2O and CO_2, the value of γ is usually less than 1.3. Define the gas density as $\rho = M/V$, where M is the molar mass, and V is the volume. The hydrostatic relationship for the pressure P is dependent on the height h of the air column. For a differential air column of height dh the hydrostatic pressure increases by $(\rho dh)g\, dP$ at the bottom of the differential element compared to the top by the differential weight of the air per unit area:

$$dP = -\rho(h)g(h)\, dh = -\frac{Mg}{V}\, dh, \quad \text{and} \quad \frac{dP}{P} = \frac{-Mg}{RT}\, dh \tag{22}$$

Assume now that the acceleration of gravity g is constant. Thus, using Eqs. (21) and (22), we have the following:

$$\frac{dT}{T} = \left(\frac{\gamma - 1}{\gamma}\right)\frac{dP}{P} = -\left(\frac{\gamma - 1}{\gamma}\right)\left(\frac{Mg}{RT}\right) dh, \quad \text{or}$$
$$\frac{dT}{dh} = -\left(\frac{\gamma - 1}{\gamma}\right)\frac{Mg}{R} \cong \text{constant} = \beta \tag{23}$$

if γ is also constant with h over the region of interest. For $\gamma = 1.4$, the rate of change of temperature with altitude is then as follows:

* Note that real gases do not strictly obey the ideal gas law, and the van der Waals equation $[P + (a/v^2)]\,(v - b) = RT$ is a more accurate representation.[16] In this chapter, the effects of nonideal gases are taken into account by the compressibility factors Z_d and Z_w for the dry gases and water vapor.

$$\beta = -34.0866(\gamma - 1)/\gamma = -9.74 \text{ deg/km} \quad \text{for} \quad \gamma = 1.4$$

$$M = M_d = 28.9644$$

$$\beta = -7.87 \text{ deg/km} \quad \text{for} \quad \gamma = 1.3$$

Thus, the adiabatic assumption with constant C_v, C_p leads to a constant lapse rate $dT/dh = \beta = -[(\gamma - 1)/\gamma]$ Mg/R. See Table 3 for example measured values of β, which are on the order of $(-6 \pm 0.5$ deg)/km, and other useful physical constants.

For nitrogen/oxygen atmosphere with $\gamma = 1.4$, the pressure then varies with altitude h as follows:

$$P = P_0\left(1 + \frac{\beta h}{T_0}\right)^{\gamma/(\gamma-1)} = P_0\left(1 + \frac{\beta h}{T_0}\right)^{1.4/(1.4-1)} = P_0\left(1 + \frac{\beta h}{T_0}\right)^{3.5} \tag{24}$$

where the ratio of heat capacities for diatomic gases is $\gamma = 1.4$, and T_0 is the temperature at sea level. The typical observed values of β are negative at approximately -5 to -7°C/km in the troposphere. For $\gamma = 1.3$, the exponent would be 4.33. Measurements give a ratio γ of heat capacitances, which corresponds to a somewhat higher exponent of $\gamma/(\gamma - 1) = 5.17$.[17]

We can also simply assume at the outset that the temperature has a constant lapse rate without the adiabatic assumption; i.e., $T = T_0 + \beta h$, where β is expressed in units of deg/km. Then, from the hydrostatic equation, we can integrate $dP/P = -(Mg/RT)\, dh$ for constant g over the range of heights $h = (0,h)$ to obtain the following:

$$\int_{P_0}^{P} \frac{dP}{P} = \frac{-Mg}{R} \int_0^h \left(\frac{dh}{T_0 + \beta h}\right) \quad \text{yields} \quad P = P_0\left(\frac{T_0 + \beta h}{T_0}\right)^{-Mg/R\beta} \tag{25}$$

where the surface pressure $P = P_0$ at $h = 0$. Thus, because $N_h \sim P_d/T$, the hydrostatic refractivity N_h can be written in terms of the surface value of hydrostatic refractivity N_{do} with a power law dependence on h as follows:

$$N_h = N_{h0}\left(\frac{T_0 + \beta h}{T_0}\right)^{\mu} \tag{26}$$

where $\mu \triangleq (-Mg/R\beta) - 1$. Thus, the exponent depends on the lapse rate β. If $\beta = -6.81$°C/km, then the exponent $-Mg/R\beta - 1 = 4.0$, a value shown later to be used by Hopfield[18,19] in a two quartic model of the troposphere pressure variation vs. altitude. Other more complex models[11,20] also use a power law model but only for the troposphere, not the stratosphere. (Note that at an altitude $h = -T_0/\beta$, the temperature would have fallen to absolute zero in this model if β remained constant for all h.) The rate of change of N_h at $h = 0$ for this model is then obtained by differentiating Eq. (26) to obtain the following[21]:

$$dN_n/dh = \beta\mu N_{h0}/T_0 = \frac{-N_{h0}Mg}{RT_0}\left(1 + \frac{R\beta}{Mg}\right) \quad \text{at} \quad h = 0$$

See Table 3 for typical values of dN_h/dh (shown as dN/dh).

Table 3 Thermodynamic constants and typical values of refraction variables and height of tropopause[1,11,17]

Typical measured values of tropopause height and lapse rates

Location	Location, north latitude	Tropopause, h_T km	Lapse rate, β °K/km
Onsala, South Sweden	57°	10.5	−5.7
Ettelsburg, Germany	51°	9.6	−5.7
Haystack, East Massachusetts	43°	13.6	−5.6
Owens Valley, Southern California	37°	12.8	−5.6
Fort Davis, Southwest Texas	31°	13.4	−6.3

Typical values of key parameters at surface and tropopause (models 1,2,3)[20]

Zone	Radius, km	P_0 *mb*	T, °K	$(n-1)$ 10^6	$-(dN/dh)$ 10^6/km	β, °K/km
Tropical	6360 + 0	1010.60	299.85	265.72	24.82	−6.06
Tropical	6360 + 16.8	98.03	198.00	39.06	5.525	
Temperate	6380 + 0	1015.00	285.08	280.87	27.28	−6.45
Temperate	6380 + 10.4	245.33	218.00	88.78	11.28	
Arctic	6400 + 0	1020.00	252.50	318.67	56.96	−6.525
Arctic	6400 + 8.8	303.56	223.60	107.39	13.33	

g_m = weighted mean gravitational constant = $[\int \rho(h) g(h) dh]/[\int \rho(h) dh]$ = $9.8062(1 - 0.0026 \cos 2\lambda - 0.00031\,\bar{h}) ms^{-2}$ where $\bar{h}$ is the effective height above sea level of the center of gravity of the atmospheric column. Saastamoinen[20] has shown that $\bar{h} \cong 7.3 + 0.9\,h_0$ km where h_0 is the user height and λ is the user latitude.

g_{eff} = effective gravitational constant = $9.784\,(1 - 0.0026 \cos 2\lambda - 0.00028 h_0) ms^{-2}$ is the effective value of g for this $\bar{h}$. λ is the user latitude and h_0 is the user height.

1 atmosphere = 1013.25 millibars

M_d = mean molar mass of dry air 28.9644 kg/kmol

M_W = molar mass of water = 18.0152 kg/mol

1 kJ = 10^3 kg m^2/s^2 = 10^{10} erg

R = universal gas constant 8.31434 kJ/(kmol · °K)

$$\frac{M_d g}{R} = \frac{(28.9644)(9.784)}{8.314} \frac{°K}{km} = 34.0866 \frac{°K}{km}.$$ For dry air at sea level $h = 0$ and λ = 45 deg.

0°C = 273.16°K

Key:

C_v, diatomic gas Heat capacity, constant volume ≈ (5/2)R at room temperature.

C_p, diatomic gas Heat capacity, constant pressure ≈ (7/2)R; $C_p = C_v + 1$.

b. Stratosphere—isothermal model of pressure vs altitude. At higher altitudes from the top of the troposphere (termed the tropopause), at altitude h_T ($h_T \cong$ 12 km), and throughout the stratosphere to the stratopause, a constant temperature (isothermal) condition can be used as an approximation. Except in the tropospause itself, the temperature is not truly constant but varies more slowly than in the troposphere. For a region of ideal gases of constant temperature, the eq. $dP/P = (Mg/RT)\,dh$ can be integrated easily because T is a constant. This isothermal (constant temperature) condition leads to the exponential barometric height equation for pressure at altitudes above h_T:

$$P = P_0 \exp\left[\frac{-Mg(h - h_T)}{RT_T}\right] \tag{27}$$

where R is the universal gas constant, 8.31434 kJ/(kmol · °K); g is the effective Earth's free fall acceleration in the stratosphere; P_T is the pressure at the tropopause; T_T is the temperature at the tropopause; and M is the molar mass of the air ($M \approx M_d$ in the stratosphere) (see Table 3). Thus, for the isothermal model, pressure decreases exponentially with height.

2. *Zenith Delay for Dry Gases—Hydrostatic Component*

The exact variation of the refractive index vs altitude is critical if we need to determine the excess tropospheric delay vs elevation angle, especially at the lower elevation angles (large zenith angles). However, for a satellite at the user's zenith, the hydrostatic gas effect of the atmosphere is independent of the shape of the profile with height and the dry air/water vapor mix ratio. The differential dry delay error at zenith Δ_{dz} (for no water vapor) from Eq. (17) is as follows:

$$d\Delta_{dz} = N_d(h) \times 10^{-6}\,dh \quad \text{where} \quad N_d(h) = 77.624\,P_d/T \tag{28}$$

where $N_d(h)$ is the dry refractivity as a function of altitude h. In this analysis, it is more useful to work with the total hydrostatic delay (which is primarily the dry delay component) where the total hydrostatic refractivity from Eq. (20) is $N_h(h) = 22.276\,\rho(h)$, and the zenith hydrostatic delay is $\Delta_{hz} = 22.276 \int \rho(h)dh$. Note that the surface pressure P_0 is related to the density ρ by the hydrostatic equation $P_0 = \int \rho(h)g(h)dh \cong g_{\text{eff}} \int \rho(h)dh$ where $g_{\text{eff}} = \int \rho(h)g(h)dh / \int \rho(h)dh$ is the effective gravitational constant and is approximated in Table 3. Thus, the zenith excess hydrostatic delay [see Eq. (20)] is as follows:

$$\Delta_{hz} = 22.276 \times 10^{-3}\,P_0/g_{\text{eff}} = 2.2768 \times 10^{-3} P_0/G \text{ m} \tag{29}$$

where we define $G \triangleq (1 - 0.002626 \cos 2\lambda - 0.00028h_0) = g_{\text{eff}}/9.784$, and P_0 is in millibars.

Water vapor does not conform to the hydrostatic equation because water vapor is subject to myriad effects including condensation and has wide variations in concentration unlike the dry gases that are uniformly mixed. Thus, there is no simple, highly accurate estimate of the wet delay related to the surface vapor pressure. The use of water vapor radiometers is generally impractical for most GPS applications; however, where they are available, Elgered[3] has developed expressions to estimate delay from these measurements to within a few mm for zenith delay.

III. Empirical Models of the Troposphere

A. Saastamoinen Total Delay Model

In a series of papers in 1972 and 1973, Saastamoinen[11,20] presented one of the first models of the refraction of the troposphere that estimates delay vs elevation angle E. In this model, the dry pressure is modeled using the constant lapse rate model for the troposphere and an isothermal model above the tropopause. The vertical gradient of temperature is $T = T_0 + \beta(r - r_0)$, and the resulting pressure profile is $P = P_0(T/T_0)^{-Mg/R\beta}$ where r is the radius from the Earth center ($r = R_e + h$) and r_0 is the user radius (usually $r_0 = R_e$, the Earth radius), and T_0 is the user temperature. The radius r ranges in value from r_0 to r_T which represents the radius to the tropopause. The corresponding dry refractivity, as discussed previously, is then $n - 1 = (n_0 - 1)(T/T_0)^{\mu}$ where $\mu = -M/R\beta - 1$ is a constant exponent [see Eq. (26)]. Using the isothermal model Eq. (27) above the tropopause, the pressure drops exponentially from its initial value at the tropopause P_T:

$$P = P_T \exp\left[-\frac{gM}{RT_T}(h - h_T)\right]$$

where the subscript T refers to the values at the tropopause.

The wet refraction is dependent on the partial pressure e, which decreases in somewhat the same way as total pressure in the troposphere Eq. (25) although much more rapidly. Saastamoinen[11,20] uses an exponent four times as large as in Eq. (25) to account for this difference, $e = e_0(T/T_0)^{-4gM/R\beta}$.

Saastamoinen[11,20] described both a precision model and a standard model for the tropospheric delay. Only the standard model is given here, and its delay correction for radio frequency ranging for elevation angles $E \geq 10$ deg is as follows[11,20]:

$$\Delta = 0.002277\,(1 + D)\sec\psi_0\left[P_0 + \left(\frac{1255}{T_0} + 0.005\right)e_0 - B\tan^2\psi_0\right] + \delta_R \text{ m} \quad (30)$$

where Δ is the delay correction in meters; P_0, e_0 are in millibars; and T_0 is in °K. The correction terms B and δ_R are given in Table 4 for various user heights h. The apparent zenith angle $\psi_0 = 90$ deg $- E$. The value of D in Eq. (30) is $D = 0.0026\cos 2\phi + 0.00028h$, where ϕ is the local latitude, and h is the station height in km.

B. Hopfield Two Quartic Model

Hopfield[18,19,21] has developed a dual quartic zenith model of the refraction, different quartics for the dry and wet atmospheric profiles. Black[22,23] has extended this zenith model to add the elevation angle mapping function, as shown in a later paragraph.

Figure 8 shows an example of the measured variation in the vertical integrated index of refractivity, the zenith excess delay.[18] As can be seen, the dry component is on the order of 2.3 m and has a relatively small variation, whereas the wet

Table 4 Correction terms for Saastamoinen's[11,20] standard model, Eq. (30)

	Apparent zenith	Station height above sea level							
	Angle	0 km	0.5 km	1 km	1.5 km	2 km	3 km	4 km	5 km
	60 deg 00 min,	+0.003	+0.003	+0.002	+0.002	+0.002	+0.002	+0.001	+0.001
	66 deg 00 min,	+0.006	+0.006	+0.005	+0.005	+0.004	+0.003	+0.003	+0.002
	70 deg 00 min,	+0.012	+0.011	+0.010	+0.009	+0.008	+0.006	+0.005	+0.004
	73 deg 00 min,	+0.020	+0.018	+0.017	+0.015	+0.013	+0.011	+0.009	+0.007
	75 deg 00 min,	+0.031	+0.028	+0.025	+0.023	+0.021	+0.017	+0.014	+0.011
δ_R, m	76 deg 00 min,	+0.039	+0.035	+0.032	+0.029	+0.026	+0.021	+0.017	+0.014
	77 deg 00 min,	+0.050	+0.045	+0.041	+0.037	+0.033	+0.027	+0.022	+0.018
	78 deg 00 min,	+0.065	+0.059	+0.054	+0.049	+0.044	+0.036	+0.030	+0.024
	78 deg 30 min,	+0.075	+0.068	+0.062	+0.056	+0.051	+0.042	+0.034	+0.028
	79 deg 00 min,	+0.087	+0.079	+0.072	+0.065	+0.059	+0.049	+0.040	+0.033
	79 deg 30 min,	+0.102	+0.093	+0.085	+0.077	+0.070	+0.058	+0.047	+0.039
	79 deg 45 min,	+0.111	+0.101	+0.092	+0.083	+0.076	+0.063	+0.052	+0.043
	80 deg 00 min,	+0.121	+0.110	+0.100	+0.091	+0.083	+0.068	+0.056	+0.047
B mb		1.156	1.079	1.006	0.938	0.874	0.757	0.654	0.563

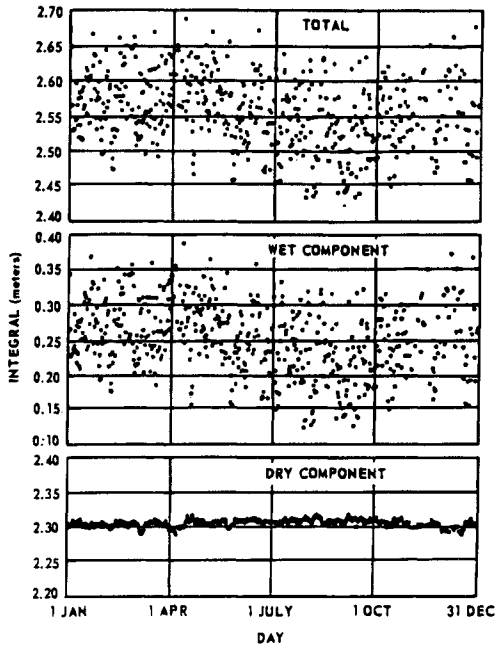

Fig. 8 Vertical integral of refractivity at Pago Pago, Samoa during 1967, balloon data from Hopfield.[18]

component is on the order of 0.25 m but varies ± 40%. Note that the scales used in all three plots are the same 5 cm/division. In data taken overland or in cold climates, the wet component is often much lower, ranging from 0 to 0.1 m.

The two-quartic model for the refractive index vs altitude h is similar in form to that of Eq. (26). Each fourth power term represents the dry and wet refractive indices as follows:

$$N_d(h) = N_{d0}\left(1 - \frac{h}{h_d}\right)^4 \quad \text{for} \quad h \leq h_d = 43 \text{ km} \tag{31a}$$

and

$$N_w(h) = N_{w0}\left(1 - \frac{h}{h_w}\right)^4 \quad \text{for} \quad h \leq h_w = 12 \text{ km} \tag{31b}$$

where N_{d0} and N_{w0} are the respective dry and wet refractive indexes at the surface, and h is the altitude. The zenith delay is then obtained by integrating Eq. (31) as follows:

$$\Delta = 10^{-6}\int_0^{h_d} N_{d0}\left(1 - \frac{h}{h_d}\right)^4 dh + 10^{-6}\int_0^{h_w} N_{w0}\left(1 - \frac{h}{h_w}\right)^4 dh$$

$$= \frac{10^{-6}}{5}[N_{d0}h_d + N_{w0}h_w] = \Delta_d + \Delta_w \tag{32a}$$

Note that h_d and h_w refer to height above the surface level where the surface refractivities N_{d0} and N_{w0} are measured. This quartic relationship is taken from the constant lapse rate model in Eq. (25), which gives an exponent $-(Mg/R\beta) - 1$. As mentioned earlier, this exponent becomes 4 at a lapse rate $\beta = -6.81$°K/km. Hopfield[18,19,21] chose the 4th power for ease of calculation and as a good approximation to the observations, and integrate along the satellite to user ray path for the wet atmosphere (troposphere only) to $h_w = 12$ km and the dry atmosphere to approximately $h_d = 43$ km to cover the troposphere and stratosphere. The values of h_d and h_w are determined by best fit to experimental measurements. As shown earlier in Eq. (29), the zenith integral of dry (really hydrostatic delay) tropospheric delay is equal to a constant times the surface pressure:

$$\Delta_d = kP_0 \tag{32b}$$

where $k = (77.6\ R/g) \times 10^{-9}$ in cgs units (Ref. 19).

C. Black and Eisner (B&E) Model

Black and Eisner[23] began with a model for excess delay for paths from point P_1 to P_2 at various elevation angles, as follows:

$$\Delta = 10^{-6}\int_{P_1}^{P_2} [N_d(s) + N_w(s)]\, ds \tag{33}$$

where the refraction equation is a simplified version of Eq. (17); namely, $N_d = 77.6\ P/T$ (see Eq. 32), and $N_w = 3.73 \times 10^5\ (e/T^2)$. For a straight geometric line path that neglects ray-bending effects at elevation angle E, the differential ds has been shown [simplified version of Eq. (1) for small a] to be $ds = dh/\sqrt{1 - [\cos E/(1 + a)]^2}$, and the excess delay becomes as follows:

$$\Delta = 10^{-6} \int_0^{h_d} \frac{(N_d(h) + N_w(h))\, dh}{\sqrt{1 - [\cos E/(1 + a)]^2}} \tag{34}$$

where the $h_d = 45$ km; $a \triangleq h/R_e$, and N_w is nonzero only for $h < h_w = 13$ km.

Figure 9 shows the Haystack observatory measurements (in summer) of the profile of water vapor density vs height. Note the very substantial 1σ variation of the water vapor density measurements. The expression for delay error Δ, Eq. (34), is now approximated by the product of the zenith delay and a mapping function $m(E)$. The zenith delay approximation is based on numerical integration of a quartic dry term modeled after Hopfield[18,19,21] and a wet term that is exponential with saturated conditions at the surface and models measured profiles similar to Fig. 9.

The B&E delay error[23] is thus approximated by the following:

$$\Delta = (\Delta_{dz} + \Delta_{wz})\, m(E, T) \tag{35}$$

where B&E use a single mapping function (as opposed to separate mapping functions for wet and dry). The mapping $m(E,T)$ is a function of both the elevation E and has the following small temperature dependence:

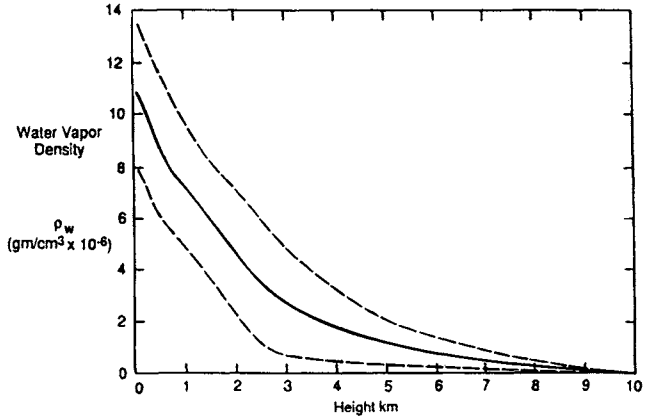

Fig. 9 Mean profile of water vapor density ρ_w taken from 45 radiosonde measurements at Haystack Observatory in August 1973. The dashed lines depict the 1 σ standard deviation. "The profile approximates an exponential dependence with a scale height of 2.2 km although the high part decreases more slowly than an exponential."[23,24]

$$m(E, T) = 1/\sqrt{1 - ((\cos E)/(1 + X_{dw} h_d/R_e))^2} \tag{36}$$

where X_{dw} in general varies with temperature.

For elevation angles in the range 7 deg $< E \leq 90$ deg and surface temperatures in the region $-30°C < T_0 < 40°C$, the value of X_{dw} is in the range, $0.00088 \leq X_{d_w} h_d/R_e \leq 0.001$. Thus, B&E approximate $m(E,T) \cong m(E)$

$$m(E) = 1/\sqrt{1 - ((\cos E)/(1 + 0.001))^2} = 1.001/\sqrt{(.001)^2 + 0.002 + \sin^2 E} \tag{37}$$

Compared with the results for more exact models also developed by Black and Eisner[23] this approximate model showed an error of approximately 7 cm at 7-deg elevation angle and 1 cm at 13-deg elevation angle.

D. Water Vapor Zenith Delay Model—Berman

Berman[25] has developed a simple model for water vapor zenith delay based on the correlation between the dry gas and water vapor delay for day and night measurements at Edwards Air Force Base, CA. Thus, if we can estimate the dry zenith delay from surface pressure measurements and estimate the surface wet and dry refractivities, we can then estimate the wet zenith delay as some fraction of that delay. The Berman model[25] gives the ratio of zenith excess delays for wet and dry components, $\tau_w/\tau_d = k N_{\omega 0}/N_{d0}$, as proportional to the ratio of wet and dry surface refractive indexes where the empirically determined scale factor is as follows:

$$k = \begin{cases} 0.2896 & \text{day} \\ 0.3773 & \text{night} \\ 0.3224 & \text{mixed day/night} \end{cases}$$

Note that this empirical result was obtained in a relatively dry region of California.

E. Davis, Chao, and Marini Mapping Functions

As discussed earlier, the mapping function attempts to relate accurately the actual excess path delay $\Delta(E)$ as a function of elevation angle and meteorological conditions to the zenith excess delay Δ_z. The mapping function can be used in conjunction with other models for the zenith delay (e.g., Davis et al.[1] and Hopfield[18]). For elevation angles near 90 deg (the zenith), clearly, a simple $1/\sin E$ approximation is generally sufficient. However, at lower elevation angles, the nonuniform and finite width spherical shell model troposphere make this simple model inadequate.

Marini[26] described a continued fraction version of the mapping function as follows:

$$m(E) = \cfrac{1}{\sin E + \cfrac{a}{\sin E + \cfrac{b}{\sin E + \cfrac{c}{\sin E + \cdots\cdots}}}} \tag{38}$$

where the *a, b, c.*, . . . are constants. Chao[27] employed a model of this form for the excess delay Δ that utilizes separate mapping functions for the wet and dry components. These mapping functions are of the same form as the continued fraction representation except that only the first two terms are used and the second sin E has been replaced by tan E so as to make $m(90 \text{ deg}) = 1$. The specific dry and wet mapping functions used by Chao are as follows:

$$m_d(E) = \frac{1}{\sin E + \dfrac{0.00143}{\tan E + 0.0445}}$$

$$m_w(E) = \frac{1}{\sin E + \dfrac{0.00035}{\tan E + 0.017}} \tag{39}$$

Davis[1] has developed a more sophisticated function for the dry (hydrostatic) mapping function wherein the coefficients *a, b,* and *c* are dependent on surface pressures, temperature, lapse rates, and tropospheric height h_T. This representation has been compared with ray-tracing results and found to be accurate to within about 2.5 cm even at elevation angles as low as 5 deg. This model is termed the Davis Cfa 2.2 mapping function and is as follows:

$$m(E) = \cfrac{1}{\sin E + \cfrac{a}{\tan E + \cfrac{b}{\tan E + c}}} \tag{40}$$

where *a, b,* and *c* are dependent upon measurements or estimates[1]:

$$\begin{aligned} a = 0.001185[&1 + 0.6071 \times 10^{-4}(P_0 - 1000) - 0.1471 \times 10^{-3}\, e_0 \\ &+ 0.3072 \times 10^{-2}(T_0 - 20) + 0.1965 \times 10^{-1}(\beta + 6.5) \\ &- 0.5645 \times 10^{-2}(h_T - 11.231)] \end{aligned} \tag{40a}$$

$$\begin{aligned} b = 0.001144[&1 + 0.1164 \times 10^{-4}(P_0 - 1000) - 0.2795 \times 10^{-3}\, e_0 \\ &+ 0.3109 \times 10^{-2}(T_0 - 20) + 0.3038 \times 10^{-1}(\beta + 6.5) \\ &- 0.1217 \times 10^{-1}(h_T - 11.231)] \end{aligned}$$

$$c = -0.0090$$

and β is the tropospheric temperature lapse rate in °C/km; h_T is the height of the tropopause in km; T_0 is the surface temperature in °C; and P_0 is the surface pressure in mb.

F. Altshuler and Kalaghan Delay Model

This tropospheric excess delay model[28] is easy to use and that can either use monthly average refractivity values or can be updated with real-time corrections. The model, hereafter called the A&K model (note that there is an errata sheet in the published report for this model), consists of empirical expressions for

tropospheric range error corrections suitable for GPS users, based upon worldwide statistics of surface refractivity. The model requires that the user input the elevation angle, height above the surface, and the surface refractivity, if known. If the user cannot measure the actual surface refractivity, the A&K model has an expression for the average surface refractivity as a function of height above sea level, latitude, and season of the year. The A&K model also contains a term for off-zenith angle correction, valid down to a viewing angle of 3-deg elevation angle. The A&K model has the following form:

$$\Delta(E, h, N_s) = 2.29286\, m(E)H(h)F(h, N_s) \qquad \text{feet}$$
$$= (0.3048)(2.29286)\, m(E)H(h)F(h, N_s) \qquad \text{meter} \qquad (41)$$

where $m(E)$ is the A&K mapping function, and H is a function of the user's height (note that one foot is exactly 0.3048m). The function F depends on both the user's height and the surface refractivity N_s. The factors are chosen to be of polynomial form to simplify computation:

$$m(E) = \{(0.1556 + 138.8926/E - 105.0574/E^2 + 31.5070/E^3) + [1.000 + 1.0 \times 10^{-4}(E - 30.00)^2]\}/2.29286 \qquad (41a)$$

where E is in deg. [The factor 2.29286 has been broken out from the mapping function in the original A&K formulation, so that $m(90\text{ deg}) = 1$.] The function $H(h)$ is as follows:

$$H(h) = [(0.00970 - 2.08809(h + 8.6286)^{-1} + 122.73592(h + 8.6286)^{-2} - 703.82166(h + 8.6286)^{-3}] \qquad (41b)$$

where h is in thousands of feet. The third function $F(h,N_s)$ is as follows:

$$F(h, N_s) = 3.28084\left[\frac{6.81758}{h + 3.28084} + 0.30480(h + 3.28084) + 0.00423\, N_s - 1.33333\right][1 - 1.41723 \times 10^{-6}(N_s - 315.000)] \qquad (41c)$$

The surface refractivity N_s, if not known, can be estimated as follows:

$$N_s = \alpha_0 + \alpha_1 h' + \alpha_2\phi + \alpha_3 h' s^2 + \alpha_4\phi s^2 + \alpha_5 h' c + \alpha_6\phi\lambda c \qquad (41d)$$

where ϕ is the latitude in degrees, and h' is the height of the surface above sea level in feet. The constants α_i and c are as follows: $\alpha_0 = 369.03$; $\alpha_1 = -0.01553$; $\alpha_2 = -0.92442$; $\alpha_3 = -0.0016$; $\alpha_4 = -0.19361$; $\alpha_5 = 0.00063$; $\alpha_6 = -0.05958$; $s = \sin(\pi M/12)$; and $c = \cos(\pi M/12)$. The value M (month) varies with the season: $M = 1.5$ winter; 4.5 spring; 7.5 summer; and 10.5 fall. The average global surface refractivity[28] is $\bar{N} = 324.8$, and the standard deviation is $\sigma_N = 30.1$.

Altshuler and Kalaghan[28] have estimated errors in their tropospheric range error model to be approximately 3.7% if the surface refractivity is known, and 6% if it is not known. If only a global average surface refractivity of 324.8 N units is used, they estimate the standard error of their model to be approximately 8%.

G. Ray Tracing and Simplified Models

For some purposes, a much simpler model of the tropospheric delay is all that is required. Typical troposphere delays vs elevation angle for a user at sea level have been computed by Janes et al.[7] by ray tracing for U.S. Standard Atmosphere and are shown in Table 5. Notice that the total delay at zenith ranges from a low of 2.316 m at latitude 75°N in January to a high of 2.576 m at 30°N in July. Shown in the lower portion of Table 5, the dry atmosphere delay ranged from 2.297 m in July at 60°N to a high of 2.328 m in January at 30°N for a 3-cm variation. The wet delay at zenith varied from a low of 0.015 m in January at 75°N to a high of 0.263 m in July at 30°N for a 24.8-cm variation. Notice that the ratio of 5-deg elevation angle delay to 90-deg elevation angle delay is fairly constant ranging from 10.183 to 10.231 at 75°N but that at the midlatitude of 30–45°, the ratio ranges only from 10.187 to 10.201 for only a 0.14% variation. Note the ratio $\Delta_w(90°)$ to $\Delta(90°)$ of wet delay to total delay is approximately 7% in summer in the midlatitudes (45–75°) but is only 0.6–2% in the winter.

If a simple model for sea level delay is employed, the excess delay could be modeled as follows:

$$\Delta = 2.47/(\sin E + 0.0121) \tag{42}$$

which gives a value at zenith of 2.44 that is the average value for users in Table 3 at 30°N, 45°N, 60°N, and gives a mapping function value of approximately 10.2 at a 5-deg elevation angle.

Figure 10 shows this simplified mapping function

$$m(E) = 1.0121/(\sin E + 0.0121)$$

and the mapping functions of Black and Eisner[23]

$$m(E) = 1/\sqrt{1 - (\cos E/1.001)^2},$$

and Altshuler and Kalaghan[28]. They are relatively close to one another on the graph.

If we assume that refractivity varies as $(1 - h/h_d)^4 = (1 - .023h)^4$ for h in km and a scale height $h_d = 43$ km, then the zenith delay for a user at altitude h is computed as follows:

$$\Delta(h) = N_s \int_h^{h_d} (1 - h/h_d)^4 \, dh = \Delta(0)(1 - h/h_d)^5 \tag{43}$$

As an alternative approach, an exponential profile can be employed to give the following simplified model:

$$\Delta(h) = 2.47\, e^{-0.133h}/(\sin E + 0.0121) \tag{44}$$

so that the zenith delay decreases to $e^{-0.133h} = 0.393$ of the sea level value at $h = 7$ km altitude.

H. Lanyi Mapping Function and GPS Control Segment Delay Estimate

Lanyi[29,30] has published one of the more precise but complex estimates of the tropospheric delay vs elevation angle where excess delay is of the form

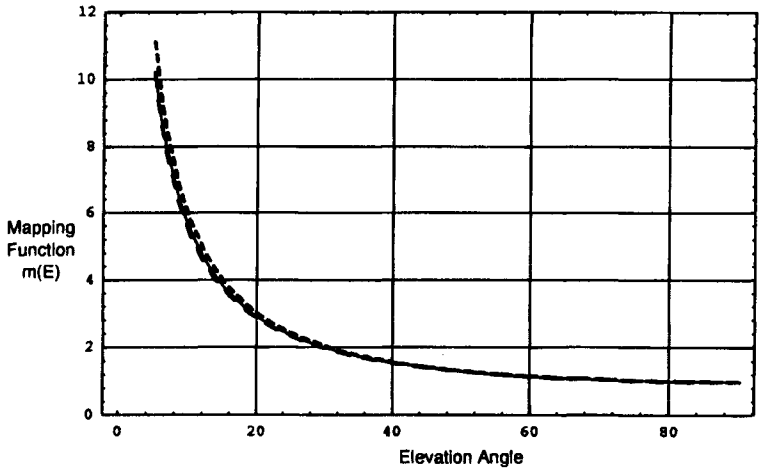

Fig. 10 Mapping functions of the simplified model (dashed), the B&E[23] (fine solid line) model, and the A&K[28] model (fine dashed line) for the range of E 5 $< E \leq$ 90 deg. The values of m(5 deg) are 10.1969, 10.218, and 11.114 for the simplified model, Eq. (44) the B&E model, and the A&K model, respectively.

$$\Delta(E) = F(E)/\sin E \qquad E > 5°$$

where

$$F(E) = \Delta_d F_d(E) + \Delta_w F_w(E) + (\Delta_d^2/D)F_{b1}(E) + (2\Delta_d\Delta_w/D)F_{b2}(E) + \Delta_w^2/D)F_{b3}(E) + (\Delta_d^3/\Delta^2)F_b4(E).$$

The terms Δ_w and Δ_d are the wet and dry zenith delays, respectively, D is a scale height $\approx$8.567 km, and the F_{b1}, F_{b2}, F_{b3}, F_{b4}, are various complicated mapping functions. Suffice it to say that special cases of the Lanyi mapping function yield approximations to the Saastamoinen and Black mapping functions.

The GPS Control Segment also employs a model for tropospheric excess delay to correct the smoothed pseudoranges. The overall equation for tropospheric delay is[31]:

$$\Delta(E) = \frac{(0.02312)P_s[\mathrm{T} - 4.11 + 5(r_m - r_a)/148.98]}{T\sqrt{1 - \left[\dfrac{r_a \cos E}{r_m + (1 - C)(r_d - r_m)}\right]^2}} + \frac{(0.0746)eh[1 + 5(r_m - r_a/h]}{T^2\sqrt{1 - \left[\dfrac{r_a \cos E}{r_{m+}(1 - C)h}\right]^2}} \qquad E > 5°$$

where P_s = monitor station barometric pressure converted to kilopascals, T = monitor station measured temperature converted to Kelvin, r_m = radial distance

Table 5 Troposphere delay (wet + dry component) in meters vs elevation angle in degrees, latitude, and season developed by ray tracing the U.S. Standard Atmosphere; also shown in the lower portion of the table is the individual wet and dry delay components (using results from Janes et al.[7])

Elevation angle E	15°N annual avg.	30°N July	30°N Jan.	45°N July	45°N Jan.	60°N July	60°N Jan.	75°N July	75°N Jan.
5 deg	26.088	26.279	25.06	25.365	24.239	24.781	23.853	24.409	23.694
10 deg	14.237	14.341	13.689	13.854	13.234	13.352	13.002	13.338	12.911
20 deg	7.416	7.47	7.132	7.219	6.893	7.05	6.769	6.95	6.719
90 deg = zenith	2.558	2.576	2.46	2.49	2.378	2.431	2.334	2.397	2.316
Ratio, Δ(5 deg)/ Δ(90 deg)	10.199	10.201	10.187	10.187	10.193	10.194	10.220	10.183	10.231
Ratio, Δ_w(90 deg)/ Δ(90 deg)	0.0958	0.1020	0.0537	0.0731	0.0240	0.0551	0.0124	0.0405	0.0065

Elevation angle	Dry/wet excess delay, m: Annual	30°N latitude July	30°N latitude Jan.	45°N latitude July	45°N latitude Jan.	60°N latitude July	60°N latitude Jan.	75°N latitude July	75°N latitude Jan.
90 deg	2.313/.245	2.313/.263	2.328/.132	2.308/.182	2.321/.057	2.297/.134	2.305/.029	2.300/.097	2.301/.015
20 deg	6.702/.714	6.703/.767	6.747/.385	6.688/.531	6.727/.166	6.658/.392	6.683/.086	6.667/.283	6.674/.045
10 deg	12.841/1.396	12.842/1.499	12.936/.753	12.817/1.037	12.910/.324	12.766/.766	12.835/.167	12.786/.552	12.823/.088
5 deg	23.381/2.707	23.379/2.900	23.600/1.460	23.356/2.009	23.612/.627	23.300/1.481	23.530/.323	23.341/1.068	23.523/.171

from the Earth's center to the meterorological sensors, r_a = radial distance from the Earth's center to the monitor station antenna, r_d = tropospheric dry radius, E = satellite elevation, h = wet height of troposphere, e = estimate of the partial water vapor pressure, C = assumed integration constant = 0.85 when $E > 5.0°$.[31]

I. Model Comparisons

Janes et al.[7] have done an extensive comparison of the various models described in the previous paragraphs. A few words of summary are appropriate here. For the zenith delay, both the Saastamoinen and Hopfield models in Refs. 11 and 18–21 gave results for the dry component that were within several mm of the ray trace delay as computed for the U.S. Standard Atmosphere (Table 5). Even at a 5-deg elevation angle, the Hopfield model was within 5 cm, whereas the two-layer model[11,20] gave more accurate results to within 6 mm. At zenith, the water vapor component for the standard model[11,20] gave results mostly within 30 mm, whereas the model errors[18,19,21] were within 20 mm.

Janes also compared the mapping function error $\delta m(E)$ scaled by the total zenith delay; namely, $\delta m(E)\Delta_z$. For the total delay at the 20-deg elevation angle, the Saastamoinen and Black and Eisner models of Refs. 11, 20, and 23 gave results within 8 mm. These errors rose to approximately 50 mm at 10 deg elevation. At 5-deg elevation angle the result[23] was still within 10 cm, whereas the standard model[11,20] produced errors of 1.2 m. For the dry gas component the Davis mapping function was the most accurate, yielding errors of less than 6 cm at 5-deg elevation angle.

J. Tropospheric Delay Errors and GPS Positioning

Errors in the estimates of the tropospheric delay have some amount of cancellation relative to GPS positioning because of the correlation in the errors for different satellites. Clearly, a constant bias for four pseudoranges to four different satellites would not affect position errors at all but would cause a user clock time bias error. As we have seen, the significant tropospheric errors are likely to be those from satellites at low elevation angles. If, as an example, four satellites at low elevation angle all have an identical error bias in the troposphere delay, and a satellite at zenith has no delay bias error, the bias error in the horizontal plane position estimate cancels out, but an altitude error remains.

One of the primary contributors to horizontal position error, in addition to lower elevation angle prediction of the dry tropospheric delay (with satellites of different elevation angles) is the variation in wet low elevation angle errors for satellites at substantially different azimuths. At 5-deg elevation angle, the wet troposphere can contribute widely varying delay errors (relative to the total wet delay contribution $\approx$ 25 cm). The water vapor zenith correction can also change significantly 2 cm with a 10-km horizontal displacement, or in a few hours of time passage, and these can be magnified by the mapping function at low elevation angles E. Water vapor zenith delay changes of 3 cm have been observed in one hour.[3] There is also no way to predict the wet delay correction change with the azimuth. It is expected, however, that the dry component of delay error would be highly correlated with azimuth; only the wet component is expected to decorrelate in any significant way with azimuth.

References

[1]Davis, J. L., et al., "Geodesy by Radio Interferometry: Effects of Atmospheric Modeling Errors on Estimates of Baseline Length," *Radio Science,* Vol. 20, 1985.

[2]NOAA, "U.S. Standard Atmosphere, 1976," NOAA-S/T76-1562, National Technical Information Service, U.S. Dept. of Commerce, Springfield, VA, 1976.

[3]Elgered, G., "Tropospheric Radio Path Delay," edited by M. A. Jansse, *Atmospheric Remote Sensing by Microwave Radiometry,* Wiley, New York, 1993.

[4]Smith, D. G., (ed.), The Cambridge Encyclopedic of Earth Sciences, Cambridge University Press, New York, 1981.

[5]Boithias, L., *Radio Wave Propagation,* McGraw Hill, New York, 1982.

[6]Spilker, J. J., Jr., "Digital Communications by Satellite," Prentice Hall, Englewood Cliffs, NJ, 1977, 1995.

[7]Janes, H. W., Langley, R. B., and Newby, S. P., "Analysis of Tropospheric Delay Prediction Models," *Bulletin Géodésiqué,* Vol. 65, 1991.

[8]Ippolito, L. J., Jr., *Radio Wave Propagation in Satellite Communications,* Van Nostrand, New York, 1986.

[9]Moulsley, T. J., and Vilar, E. "Experimental and Theoretical Statistics of Microwave Amplitude Scintillation on Satellite Downlinks," *IEEE Trans. Antennas and Propagation,* Vol. AP-30, pp. 1099–1106, Nov. 1982.

[10]Sears, F. W., *Optics,* Addison-Wesley, Reading, MA, 1949.

[11]Saastamoinen, J., "Contribution to the Theory of Atmospheric Refraction, *Bulletin Géodésiqué,* Vol. 105, Sept. 1972, Vol. 106, Dec. 1972, Vol. 107, March 1973.

[12]Thayer, G. D., "An Improved Equation for the Radio Refractive Index of Air," *Radio Science,* Vol. 9, 1974.

[13]Hill, R. J., Lawrence, R. S., and Priestly, J. T., "Theoretical and Calculated Aspects of the Radio Refractive Index of Water Vapor," *Radio Science,* Vol. 17, pp. 1251–1257, 1982.

[14]Birmbaum, G., and Chatterjee, S. K., "The Dielectric Constant of Water Vapor in the Microwave Region," *Journal of Applied Physics,* Vol. 23, 1952.

[15]Boudouris, G., "On the Index of Retraction of Air, the Absorption and Dispersion of Centimeter Waves by Gases," *Journal of Research of the National Bureau of Standards,* 1963.

[16]Sears, F. W., *Thermodynamics, The Kinetic Theory of Gases, and Statistical Mechanics,* Addison-Wesley, Reading, MA, 1953.

[17]Abbott, M. M., and Van Ness, H. C., *Thermodynamics,* McGraw Hill, New York, 1989.

[18]Hopfield, H. S., "Tropospheric Effect on Electromagnetically Measured Range: Prediction from Surface Weather Data," Applied Physics Laboratory, Johns Hopkins University, Baltimore, MD, July 1970.

[19]Hopfield, H. S., "Tropospheric Range Error Parameters—Further Studies," Applied Physics Laboratory, Johns Hopkins University, Baltimore, MD, June 1972.

[20]Saastamoinen, J., "Atmospheric Correction for the Troposphere and Stratosphere in Radio Ranging of Satellites," Geophysical Monograph 15, American Geophysical Union, Washington, DC, 1972.

[21]Hopfield, H. S., "Two Quartic Tropospheric Refractivity Profile for Correcting Satellite Data," *Journal of Geophysical Research,* April 1969.

[22]Black, H. D., "An Easily Implemented Algorithm for the Tropospheric Range Correction," *Journal of Geophysical Research,* Vol. 38, No. 4, 1978, pp. 1825–1828.

[23]Black, H. D., and Eisner A., "Correcting Satellite Doppler Data for Tropospheric Effects," *Journal of Geophysical Research,* Vol. 89, 1984.

[24]Moran, J. M., and Rosen, B. R., "The Estimation of the Propagation Delay Through the Troposphere from Microwave Radiometer Data," *Radio Interferometry Techniques for Geodesy,* NASA Conf. Publ. 2125, 1979.

[25]Berman, A. L., "The Prediction of Zenith Refraction from Surface Measurements of Meteorological Parameters," JPL TR-32-1602 California Institute of Technology, Jet Propulsion Laboratory, Pasadena, CA, 1976.

[26]Marini, J. W., "Correction of Satellite Tracking Data for an Arbitrary Tropospheric Profile," *Radio Science,* Vol. 7, 1972.

[27]Chao, C. C., "The Tropospheric Calibration Model for Mariner Mars, 1971," JPL TR 32-1587, Jet Propulsion Laboratory, Pasadena, CA, March 1974.

[28]Altshuler, E. E., and Kalaghan, P. M., "Tropospheric Range Error Corrections for the NAVSTAR System," Microwave Physics Laboratory, Air Force Cambridge Research Laboratories, April 1974.

[29]Lanyi, G., "Tropospheric Delay Effects in Radio Interferometry," Telecommunications and Data Acquisition Progress Rep., Jet Propulsion Lab, Pasadena, CA, April–June 1984.

[30]Sovers, O. J., and Lanyi, G. E., "Evaluation of Current Tropospheric Mapping Functions by Deep Space Network Very Long Baseline Interferometry," The Telecommunications and Data Acquisition Progress Rep. 42–119, Jet Propulsion Laboratory, Pasadena, CA, Nov. 1994.

[31]Master Control Station Kalman Filter–Mission Support Study Guide, 2nd ed. Oct. 1993.

Bibliography

Brunner, F. K., ed., "Atmospheric Effects on Geodetic Space Measurements," Monograph 12, School of Surveying, University of New South Wales, Kinsington, NSW, Australia, 1988.

Hendy, M. R., and Brunner, F. K., "Modeling the Zenith Wet Component of the Tropospheric Path Delay for Microwaves," *Australian Journal of Geodesy, Photogrammetry & Surveying,* Dec. 1990.

Chapter 14

Multipath Effects

Michael S. Braasch*
Ohio University, Athens, Ohio 45701

I. Introduction

THE Global Positioning System (GPS) has been shown to be capable of supporting a wide variety of exciting applications. In addition to the usual functions of position, velocity, and time determination, it is also possible to perform attitude and heading determination of dynamic platforms, measurement of flexing in large space structures, and to provide precision approach and landing guidance. The later applications require high accuracy in real time. However, these technologies face a major stumbling block. It is the effect of multipath. Multipath is the phenomenon whereby a signal arrives at a receiver via multiple paths attributable to reflection and diffraction. Multipath represents the dominant error source in satellite-based precision guidance systems.

Multipath has been cited as a major error source both in differential satellite systems as well as interferometry.[1,2] Multipath distorts the signal modulation and degrades accuracy in conventional and differential systems. Multipath also distorts the phase of the carrier, and hence degrades the accuracy of the interferometric systems. Furthermore, because interferometric systems often employ pseudorange measurements for initialization (ambiguity resolution) purposes, multipath contamination of the pseudorange can increase the time required for initialization.

For standard code-based differential systems, signal degradation attributable to multipath can be severe. This stems from the fact that multipath is a highly localized phenomenon. Multipath sources that affect the ground reference station receiver do not necessarily cause errors in the mobile receiver. Likewise, multipath sources that affect the mobile receiver do not necessarily affect the ground reference station.

Multipath effects in pseudorandom noise (PRN) ranging have been studied since the early 1970s. Hagerman[3] derived relationships involving multipath and PRN code-tracking error. This fundamental work formed the basis for the analysis of GPS code and carrier multipath errors during the field tests at the Yuma Proving Ground (YPG).[4] In the early 1980s, the effect of multipath on short

* Assistant Professor, Department of Electrical and Computer Engineering.

baseline interferometry was studied at the Massachusetts Institute of Technology[5,6] and at the Charles Stark Draper Laboratory.[7] The studies concluded that the effects of multipath (in this differential carrier-phase tracking system) could be reduced to a few centimeters of error over short baselines if the signals could be averaged over a period of an hour or more. Bletzacker[8] also considered multipath errors in geodetic applications. Performance improvements were obtained by mounting the antenna on rf-absorbing material, thereby improving the characteristics of the antenna pattern. Tranquilla and Carr[9] confirmed this by collecting data in stressful environments using a geodetic antenna with and without an rf-absorbing ground plane.

Falkenberg et al.[10] and Lachapelle et al.[1] describe marine differential GPS experiments in which multipath was mitigated through the use of rf-absorbing ground planes and filtering schemes. Evans[11] demonstrated multipath effects on ionospherically corrected code and carrier measurements from a geodetic GPS receiver. Georgiadou and Kleusberg[12] considered multiple reflections and showed that multipath on short baselines could be detected using dual-frequency measurements. Abidin[13] examined the effects of multipath in dual-frequency-measurement-based ambiguity resolution.

The effect of multipath on ionospheric measurements using GPS was presented by Bishop et al.[14] Their work verified the theoretical multipath relations derived by Hagerman[3] and considered various mitigation schemes for static applications. Sennott and Pietraszewski[15] and Sennot and Spalding[16] have developed state variable models for the estimation and mitigation of multipath in differential GPS ground reference stations.

Van Nee[17] has shown that code-phase multipath error traces tend not to be zero mean and can have periods on the order of an hour. This contradicts the popular notion that code-phase multipath can be eliminated in static applications simply through averaging. Van Nee[18,19] has shown that an exception to this rule occurs when a coherent delay–lock-loop (DLL) receiver is used and the rate-of-change of the multipath relative phase is large compared to the tracking loop bandwidth.

Much of this chapter is based upon Braasch,[20] which examined the characteristics of multipath error in the precision approach and landing environment.

II. Signal and Multipath Error Models

Fundamental to the understanding of the effects of multipath in any given environment is an understanding of PRN ranging receivers and how multipath distortion results in ranging errors. This section derives closed form expressions for code-phase and carrier-phase multipath errors resulting from a single multipath ray entering a stationary receiver. Although most multipath scenarios involve multiple rays, much insight results from the analysis of the single-ray case. It also serves as the starting point from which the multiple-ray case can be considered. The analysis considers the two most prevalent types of receivers: the coherent delay–lock-loop (DLL) and the noncoherent DLL. This section extends the theoretical developments documented by Hagerman[3] to include consideration of code multipath error spectra. It should be noted that although the derivations

follow the signal flow of analog receivers, the results are exactly the same for modern digital architectures.

A. Pseudorandom Noise Modulated Signal Description

The signal broadcast from the satellite in a PRN ranging system may be expressed as follows:

$$s_1(t) = A \cos[\omega_o t + p(t)\pi/2] \tag{1}$$

where $0.5*A^2$ is the average signal power into the receiver, ω_o is the frequency of the received signal in radians per second (carrier frequency plus Doppler shift), and $P(t)$ is the PRN code (either $+1$ or -1).

Note that the actual GPS signal is considerably more complicated. The GPS carrier is modulated by two PRN codes (the coarse/acquisition (C/A) code and the precision (P) code) in addition to navigation data. For the present purpose of multipath analysis, however, the model given by Eq. (1) is adequate. By applying trigonometric identities, Eq. (1) may be rewritten as follows:

$$\hat{s}_1(t) = -Ap(t)\sin(\omega_o t) \tag{2}$$

Once inside the receiver, multipath is characterized by four parameters (all of which are relative to the direct signal): 1) amplitude; 2) time delay; 3) phase; 4) phase rate of change. For the present discussion, a stable multipath scenario is assumed; thus, the relative phase rate of change is assumed to be zero. Relative phase of the multipath is a function of the relative time delay and the reflection coefficient of the reflecting object. If the received signal is composed of the direct signal plus a single multipath ray, it may be expressed as follows:

$$s_{1m}(t) = \hat{s}_1(t) + \alpha\hat{s}_1(t + \delta) \tag{3}$$

where α is the multipath relative amplitude and δ is the multipath relative time delay (note: must be negative given the convention used in the equation).

Note that the relative phase of the multipath is not shown. Substitution of Eq. (2) into Eq. (3) and inclusion of relative phase yields the following:

$$s_{1m}(t) = -Ap(t)\sin(\omega_o t) - \alpha Ap(t + \delta)\sin(\omega_o t + \theta_m) \tag{4}$$

where θ_m is the multipath relative phase.

B. Coherent Pseudorandom Noise Receiver

This section derives expressions for the coherent DLL discriminator curve in the absence and presence of multipath. Also derived is the expression for the composite phase of the multipath corrupted signal as it is tracked by the carrier-tracking loop.

1. Coherent Delay Lock Loop Discriminator Curve in the Absence of Multipath

Following the usual signal flow in an analog receiver, the incoming signal $S_1(t)$ is mixed with early and late versions of the PRN code modulated onto a local oscillator frequency:

$$s_E(t) = -p(t + \tau - \tau_d)\sin(\omega_l t + \theta) \tag{5}$$

$$s_L(t) = -p(t + \tau + \tau_d)\sin(\omega_l t + \theta) \tag{6}$$

where τ is the DLL tracking error, τ_d is the time advance of the early code or the time delay of the late code (relative to the on-time code), θ is the tracking error of the phase lock loop (PLL), and ω_l is the local oscillator frequency in rad/s.

The signals output from the mixers are passed through bandpass filters (BPF). It is assumed that the passband of the BPFs is narrow enough to reject the sum-frequency terms. The filters also serve to complete the correlation process. The bars shown over the quantities in Eqs. (7) and (8) denote the operation of the BPFs. The output of the filters is as follows:

$$\overline{s_1(t)s_E(t)} = 1/2\, AR(\tau - \tau_d)\cos(\omega_1 t - \theta) \tag{7}$$

$$\overline{s_1(t)s_L(t)} = 1/2\, AR(\tau + \tau_d)\cos(\omega_1 t - \theta) \tag{8}$$

where ω_1 is the difference-frequency ($\omega_1 = \omega_o - \omega_l$) and $R(\tau)$ is the correlation function of the PRN code.

A sufficient approximation of the PRN code correlation function is given by the following:

$$\begin{aligned} R(\tau) &= 1 - \frac{|\tau|}{T}, & |\tau| \le T \\ &= 0, & |\tau| > T \end{aligned} \tag{9}$$

where T is the PRN code bit period (note: a PRN code bit is also known as a "chip." Accordingly, the PRN code bit-rate is also known as the "chipping-rate").

Correlation sidelobes are ignored, and infinite bandwidth is assumed. The finite bandwidth of the BPFs distorts the shape of the PRN code bits and results in a smoothing of the correlation function.[23] Comparison of the results of this analysis (Sec. II. B.) with those obtained when smoothing the correlation function[24] reveals that the smoothing slightly reduces the maximum range error due to a given set of multipath parameters. As a result, Eq. (9) yields slightly conservative results.

The signals out of the BPFs are thus the early and late correlator functions at the intermediate frequency (IF). Low-pass filters can be used to remove the IF term leaving the baseband signal. Assuming a PLL carrier-phase tracking error of zero ($\theta = 0$) then yields the following:

$$\overline{s_1(t)s_E(t)} = 1/2\, AR(\tau - \tau_d) \tag{10}$$

$$\overline{s_1(t)s_L(t)} = 1/2\, AR(\tau + \tau_d) \tag{11}$$

Finally, the discriminator function is formed, for example, by differencing the outputs of the LPFs. The normalized form of the discriminator function is as follows:

$$D_c(\tau) = R(\tau + \tau_d) - R(\tau - \tau_d) \tag{12}$$

where the subscript c denotes coherent DLL operation.

Note that the DLL tracks the peak of the correlation function by tracking the zero-crossing of the discriminator function since both occur for $\tau = 0$. As derived in the next section, multipath distorts the discriminator curve so that the zero-crossing occurs for some non-zero τ. Thus, the τ corresponding to the zero-crossing is the DLL tracking error caused by the multipath. Note that although τ is an error in correlation, ranging is a time-domain function. An error in correlation corresponds to an equal but opposite error in timing. Thus, the ranging error is given by the opposite of the DLL tracking error.

2. *Coherent Delay Lock Loop Discriminator Curve in the Presence of Multipath*

In the presence of multipath, the incoming signal is given by Eq. (4). In the case of the coherent DLL, the early and late codes are modulated onto a local oscillator frequency, which is phase-locked to the incoming signal. However, the incoming signal has been perturbed because of the presence of the multipath. Thus, the PLL tracks the phase of the composite signal and not that of the direct signal. The early and late signals are now given by the following:

$$s_{Em}(t) = -p(t + \tau - \tau_d)\sin(\omega_I t + \theta_c + \theta) \tag{13}$$

$$s_{Lm}(t) = -p(t + \tau + \tau_d)\sin(\omega_I t + \theta_c + \theta) \tag{14}$$

where θ_c is the composite phase of the direct plus multipath signal and θ is the PLL carrier-phase tracking error of the composite signal.

The relations governing the composite phase of the direct plus multipath signal are derived in the next section. The outputs of the mixers are given by multiplying Eq. (4) by Eqs. (13) and (14).

Passing the output of the mixers through the BPFs completes the correlation process and removes the sum frequency terms. Low-pass filters then allow only the baseband signals to pass, yielding the following:

$$\overline{s_{1m}(t)s_{Em}(t)} = 1/2\, AR(\tau - \tau_d)\cos(-\theta_c - \theta) + 1/2\, \alpha AR(\tau - \tau_d - \delta)\cos(\theta_m - \theta_c - \theta) \tag{15}$$

$$\overline{s_{1m}(t)s_{Lm}(t)} = 1/2\, AR(\tau + \tau_d)\cos(-\theta_c - \theta) + 1/2\, \alpha AR(\tau + \tau_d - \delta)\cos(\theta_m - \theta_c - \theta) \tag{16}$$

Assuming a PLL tracking error of zero and taking advantage of the fact that the cosine is an even function yields the following:

$$\overline{s_{1m}(t)s_{Em}(t)} = 1/2\, AR(\tau - \tau_d)\cos(\theta_c) + 1/2\, \alpha AR(\tau - \tau_d - \delta)\cos(\theta_m - \theta_c) \tag{17}$$

$$\overline{s_{1m}(t)s_{Lm}(t)} = 1/2\, AR(\tau + \tau_d)\cos(\theta_c) + 1/2\, \alpha AR(\tau + \tau_d - \delta)\cos(\theta_m - \theta_c) \tag{18}$$

Again, the discriminator function is formed by differencing the outputs of the LPFs. The normalized form of the discriminator function is as follows:

$$\begin{aligned} D_{cm}(\tau) &= R(\tau + \tau_d)\cos(\theta_c) + \alpha R(\tau + \tau_d - \delta)\cos(\theta_m - \theta_c) \\ &\quad - R(\tau - \tau_d)\cos(\theta_c) - \alpha R(\tau - \tau_d - \delta)\cos(\theta_m - \theta_c) \\ &= [R(\tau + \tau_d) - R(\tau - \tau_d)]\cos(\theta_c) \\ &\quad + \alpha[R(\tau + \tau_d - \delta) - R(\tau - \tau_d - \delta)]\cos(\theta_m - \theta_c) \end{aligned} \tag{19}$$

where the subscript *cm* denotes coherent DLL operation in the presence of multipath.

3. *Carrier Phase Lock Loop Operation in the Presence of Multipath*

Prior to entering the PLL, the incoming signal is mixed with the on-time code modulated onto the local oscillator frequency. The incoming signal in the presence of a single multipath ray was given by Eq. (4). The on-time signal generated by the receiver is given by the following.

$$s_{Om}(t) = -p(t + \tau)\sin(\omega_I t + \theta_c + \theta) \tag{20}$$

After mixing the two signals and passing through a BPF, we achieve the following;

$$\begin{aligned} \overline{s_{1m}(t)s_{Om}(t)} &= 1/2\, AR(\tau)\cos((\omega_o - \omega_I)t - \theta_c - \theta) \\ &\quad + 1/2\, \alpha AR(\tau - \delta)\cos((\omega_o - \omega_I)t + \theta_m - \theta_c - \theta) \end{aligned} \tag{21}$$

Assuming perfect carrier PLL tracking of the composite signal ($\theta = 0$) and substituting $\omega_1 = \omega_o - \omega_I$, Eq. (21) becomes the following:

$$\begin{aligned} \overline{s_{1m}(t)s_{Om}(t)} &= 1/2\, AR(\tau)\cos(\omega_1 t - \theta_c) \\ &\quad + 1/2\, \alpha AR(\tau - \delta)\cos(\omega_1 t + \theta_m - \theta_c) \end{aligned} \tag{22}$$

Using the trigonometric identity for the cosine of a sum gives the following:

$$\begin{aligned} \overline{s_{1m}(t)s_{Om}(t)} &= 1/2\, AR(\tau)[\cos(\omega_1 t)\cos(\theta_c) + \sin(\omega_1 t)\sin(\theta_c)] \\ &\quad + 1/2\, \alpha AR(\tau - \delta)[\cos(\omega_1 t)\cos(\theta_c - \theta_m) + \sin(\omega_1 t)\sin(\theta_c - \theta_m)] \end{aligned} \tag{23}$$

Grouping the cosine and sine terms leads to the following:

$$\begin{aligned} \overline{s_{1m}(t)s_{Om}(t)} &= 1/2\, A[R(\tau)\cos(\theta_c) \\ &\quad + \alpha R(\tau - \delta)\cos(\theta_c - \theta_m)]\cos(\omega_1 t) + 1/2\, A[R(\tau)\sin(\theta_c) \\ &\quad + \alpha R(\tau - \delta)\sin(\theta_c - \theta_m)]\sin(\omega_1 t) \end{aligned} \tag{24}$$

The PLL tracks the composite signal so that the coefficient of the $\sin(\omega_1 t)$ term is nulled:

$$R(\tau)\sin(\theta_c) + \alpha R(\tau - \delta)\sin(\theta_c - \theta_m) = 0 \tag{25}$$

a. Region I: Absolute value of the DLL tracking error less than one chip. In this region, the correlation function $R(\tau)$ is nonzero. After making trigonometric substitutions and rearranging, Eq. (25) may be rewritten as follows:

$$\tan(\theta_c) = \sin(\theta_c)/\cos(\theta_c)$$
$$= \alpha R(\tau - \delta)\sin(\theta_m)/[R(\tau) + \alpha R(\tau - \delta)\cos(\theta_m)] \quad (26)$$

For region I operation, then, the composite phase of the signal entering the PLL is given by the arctangent of the right-hand side of Eq. (26). The interdependency of the code- and carrier-tracking loops may also be observed in Eq. (26) by noting the presence of the code-correlation function.

Assuming that the multipath strength is always less than or equal to the direct, it can be shown that the carrier-phase error can be no more than 90 deg. At the GPS L_1 band (1575.42 MHz), this corresponds approximately to 4.8 cm. As shown later, code-phase errors can exceed 100 m. Carrier-phase tracking, thus, yields relatively multipath-free measurements.

b. Region II: Absolute value of the DLL tracking error greater than or equal to one chip. In this region, $R(\tau)$ is approximately zero. Although this is not strictly true, it is a reasonable approximation in light of its proximity to zero relative to the peak value of the correlation function. Using this assumption, Eq. (25) simplifies to the following:

$$\alpha R(\tau - \delta)\sin(\theta_c - \theta_m) = 0 \quad (27)$$

therefore

$$\theta_c = \theta_m + 2\pi N \quad (28)$$

For region II operation, then, the composite phase of the signal entering the PLL is simply the multipath phase relative to the direct signal. The direct signal phase is taken to be zero. Conceptually, region II operation involves the DLL tracking the multipath rather than the direct signal. In either operating region, then, the multipath-induced carrier-phase measurement error is given by θ_c.

C. Noncoherent Pseudorandom Noise Receiver

This section details expressions for the noncoherent DLL discriminator curve in the absence and presence of multipath. Because it can be shown that the PLL carrier-phase error attributable to multipath has the same form as for the coherent receiver architecture, the derivation is not given here.

1. Noncoherent Delay Lock Loop Discriminator Curve in the Absence of Multipath

The signal flow for the noncoherent DLL is similar to that of the coherent DLL except the outputs of the early and late correlators (mixers plus bandpass filters) are squared prior to being low-pass filtered and differenced. The signals entering the LPFs are given by squaring the expressions in Eqs. (7) and (8):

$$\{\overline{s_1(t)s_E(t)}\}^2 = 1/4\, A^2R^2(\tau - \tau_d)\cos^2(\omega_1 t - \theta) \tag{29}$$

$$\{\overline{s_1(t)s_L(t)}\}^2 = 1/4\, A^2R^2(\tau + \tau_d)\cos^2(\omega_1 t - \theta) \tag{30}$$

Note that because the early and late signals are being generated noncoherently, θ is simply the phase offset of the frequency tracking loop. After Eqs. (29) and (30) have been expanded, the LPFs reject the double-frequency terms leaving the following:

$$\{\overline{s_1(t)s_E(t)}\}^2 = 1/8\, A^2R^2(\tau - \tau_d) \tag{31}$$

$$\{\overline{s_1(t)s_L(t)}\}^2 = 1/8\, A^2R^2(\tau + \tau_d) \tag{32}$$

Again, the discriminator function is formed by differencing the outputs of the LPFs. Thus, the normalized form of the noncoherent discriminator function is as follows:

$$D_n(\tau) = R^2(\tau + \tau_d) - R^2(\tau - \tau_d) \tag{33}$$

where the subscript n denotes noncoherent DLL operation.

2. *Noncoherent Delay Lock Loop Discriminator Curve in the Presence of Multipath*

Following a procedure similar to that for the analysis of the coherent DLL, the normalized form of the noncoherent discriminator function is given by the following:

$$D_{nm}(\tau) = R^2(\tau + \tau_d) - R^2(\tau - \tau_d) + \alpha^2[R^2(\tau + \tau_d - \delta) - R^2(\tau - \tau_d - \delta)]$$
$$+ 2\alpha\cos(\theta_m)[R(\tau + \tau_d)R(\tau + \tau_d - \delta) - R,(\tau - \tau_d)R(\tau - \tau_d - \delta)] \tag{34}$$

where the subscript nm denotes noncoherent DLL operation in the presence of a single multipath ray.

D. Simulation Results

Having derived the multipath error equations, simulations allow for the quantification of the error encountered under various multipath conditions.

1. *C/A Code*

The pseudorange error envelope as a function of relative multipath amplitude and delay is given in Fig. 1 for the standard coherent DLL. Note that the standard separation of 1 PRN bit period between the early and late correlators is assumed. In the figure, the relative multipath amplitude is constant and the upper curve represents error attributable to a multipath ray that is in phase with the direct signal. The bottom curve represents the out-of-phase case. It is important to remember that the relative phase of the multipath signal is a function of the electromagnetic properties of the reflecting object in addition to the path length difference. A multipath signal with a given delay can, therefore, take an arbitrary relative phase depending upon the reflector. Examination of the plot reveals that even for a weak multipath signal (−20 dB), the peak error is 15 m. It is also

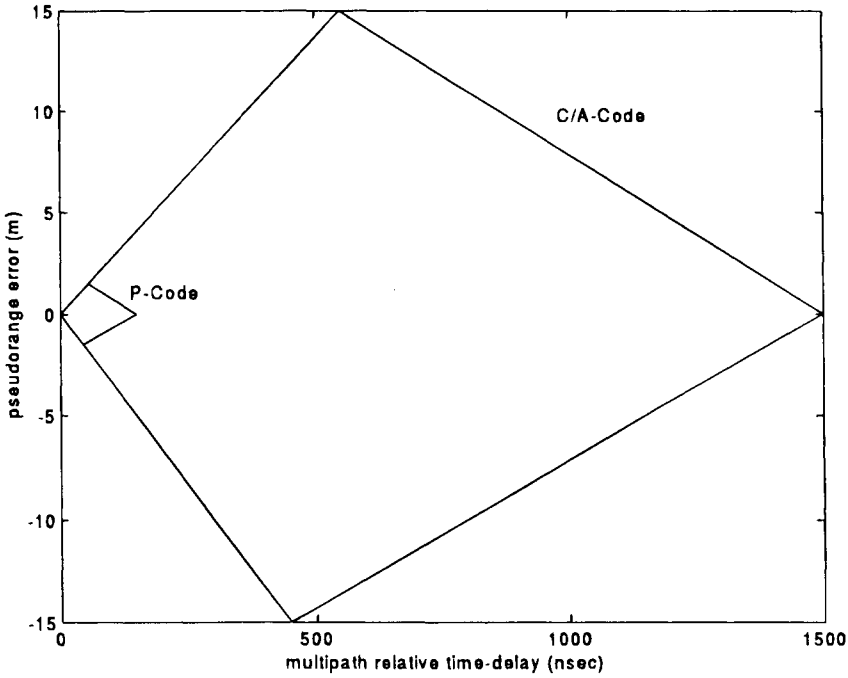

Fig. 1 C/A-code and P-code multipath error envelopes for relative multipath amplitude set at −20 dB.

important to note that the error drops to zero at a delay of 1466 ns (1.5 chips). Furthermore, as shown in Refs. 19 and 20, the error increases when the multipath relative strength increases. Assuming an environment in which the multipath signal strength never exceeds that of the direct, the peak multipath error equals one-half of a chip length.[3] Although not shown, the error envelope for the noncoherent DLL is exactly the same as for the coherent DLL. Their behavior within the envelope is different, however, as is shown later in the plots of average error.

It is important to note that, in reality, multipath signals that are delayed by more than 1.5 chips can induce some error. Recall that in the derivation of the multipath error equations, the sidelobes of the correlation function were ignored. This was not a problem for analyzing multipath with relative time delays of less than 1.5 chips. However, for longer delay multipath, the correlation sidelobes provide the mechanism for interference with the direct signal. The small magnitude of these sidelobes relative to the main lobe means that long delay multipath signals will be attenuated about 24 dB in the correlation process. Although weak, this kind of multipath can induce error on the order of several meters.

For a better understanding of the behavior of the error curve within the envelope, Figs. 2 and 3 show C/A-code pseudorange error over a small range of time delay for different relative multipath amplitudes. For these examples, the multipath relative phase was assumed to be strictly a function of relative path delay. When

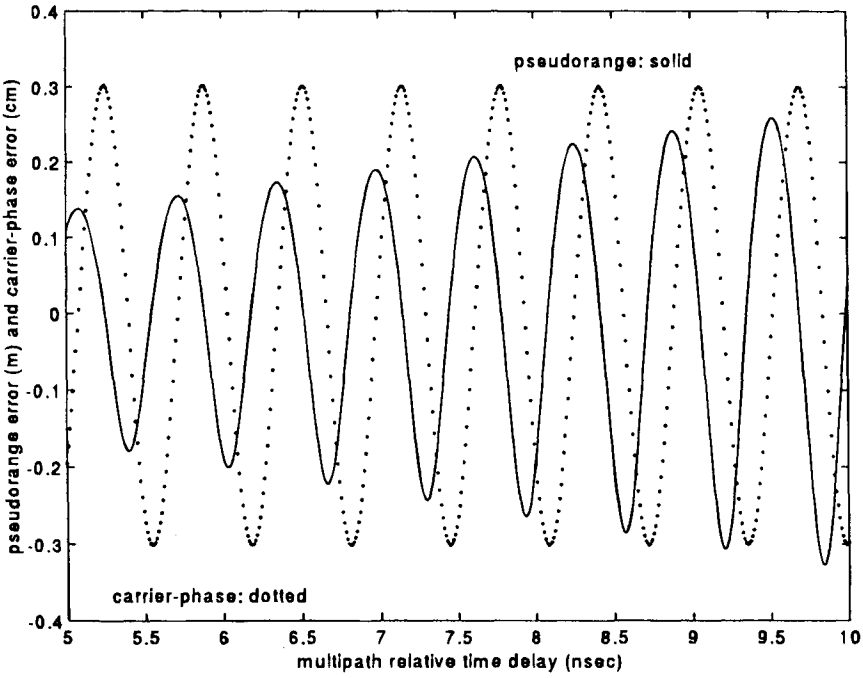

Fig. 2 C/A-code and carrier-phase multipath error for relative multipath amplitude set at −20 dB. Relative phase was calculated strictly from relative path delay.

the relative multipath amplitude is small, the error varies sinusoidally as a function of relative path delay and thus is narrow band. When the relative amplitude is large, however, the error is not sinusoidal and, in fact, it contains sharp discontinuities. In this case, the error signal is wide band.[20,21] This disproves the popular myth that every peak in a multipath error spectrum corresponds to a separate multipath ray. The nonsinusoidal behavior is a result of nonlinearities in the receiver architecture. The effects reach further than simply causing an increased error signal bandwidth. As was first shown by Hagerman[3] and later by Van Nee[17] and Braasch and Van Graas,[21] the error signal is not zero-mean. In situations where the multipath relative phase is fluctuating (nonzero relative phase rate-of-change), the errors will not average out to zero.

Plots of average error vs time delay are given in Fig. 4. Because relative-phase is a complex function of the electromagnetic properties of the reflecting object in addition to the time delay, errors may be computed by holding relative amplitude and phase constant, and varying the time delay. For each of the plots shown, error was averaged over 10 relative-phase values evenly spaced between 0 and 180 deg. As can be seen in the plots, not only are the error traces nonzero mean, the average value can easily be several meters. For example, a relative multipath amplitude of −8 dB yields a peak average error of 8 m for the coherent DLL.

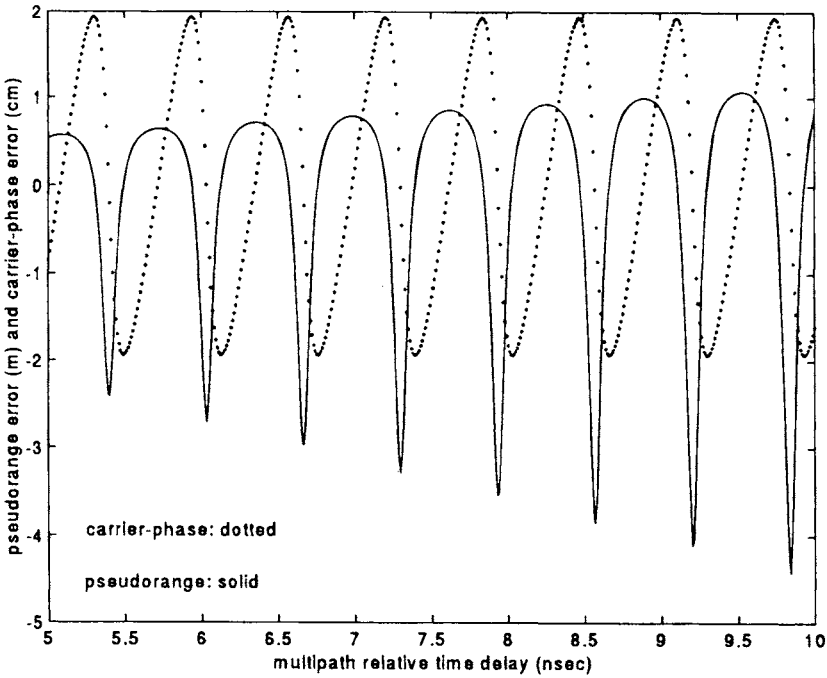

Fig. 3 C/A-code and carrier-phase multipath error for relative multipath amplitude set at −4.4 dB. Relative phase was calculated strictly from relative path delay.

2. *P Code*

The P code is the second PRN code modulated onto the GPS carrier. Although it was made available to the public during the satellite constellation buildup, DOD policy dictates that this code be encrypted (forming the so-called Y code) so as to be accessible only by authorized users. For those users having access to it, however, considerable multipath reduction or rejection is gained. Because the P code (10.23 MHz) is modulated at a rate ten times higher than the C/A code (1.023 MHz), its chips are thus one-tenth the length. The P code, therefore, is much less sensitive because it is affected only by multipath with relative time delays less than 1.5 times its own chip. Instantaneous and average multipath error curves for the P code have exactly the same shape as for the C/A code. In fact, the only difference is the scale factor of 10. The results for the P code may be obtained from Figs. 2–4 simply by dividing the C/A-code pseudorange numbers on both axes by 10. The P-code error envelope is given in Fig. 1.

3. *Carrier Phase*

As mentioned earlier, carrier-phase multipath errors typically are on the order of centimeters. This is illustrated in Figs. 2 and 3. Carrier-phase errors are shown with the corresponding pseudorange errors. It is interesting to note that, as the

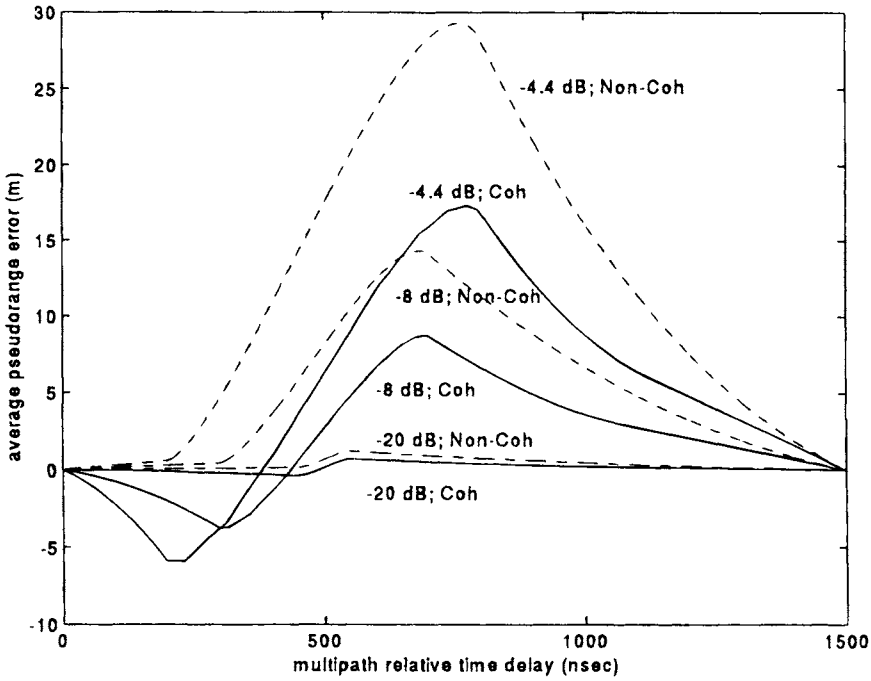

Fig. 4 C/A-code average multipath error. Curves are given for relative multipath amplitudes of −4.4 dB, −8 dB, and −20 dB for both coherent and noncoherent DLLs. For a given time delay for each of the curves, error was averaged over ten relative-phase values evenly spaced between 0 and 180 deg.

theory would predict, the pseudorange errors peak when the carrier-phase errors are zero and vice versa.

III. Aggravation and Mitigation

In the previous section, the basic relationships governing the response of the receiver to multipath were derived. Multipath was parameterized in terms of amplitude, time delay, phase, and phase-rate relative to the direct signal. As was shown, multipath error is proportional to the relative strength of the multipath signal and nonlinearly dependent upon time-delay and phase. The time-delay of a given multipath signal is entirely dependent upon the geometry of the environment in which the receiver is located. The amplitude and phase, however, are dependent upon both the environment and the characteristics of the user's antenna.

A. Antenna Considerations

In Sec. II, the relationships governing the response of the receiver to multipath were derived. Multipath was parameterized in terms of amplitude, time delay, phase and phase-rate relative to the direct signal. Prior to arriving at the receiver

tracking loops, multipath must pass through the antenna. Realizable antennas (as opposed to theoretical isotropic radiators) do not receive signals equally from all directions. In fact, partial multipath rejection is built in to some antenna designs by shaping the gain pattern. Because most multipath arrives from angles near the horizon, multipath may be reduced by shaping the pattern to have low gain in these directions. However, extensive shaping of the pattern requires either a large aperture or multiple elements and signal processing. This might be feasible for the reference station in a differential system. However, this is not possible for highly dynamic platforms (i.e., aircraft), which require compact antennas and virtually omnidirectional gain.

Additional multipath attenuation by the antenna results from polarization discrimination. The direct GPS signal incident on the antenna is right-hand circularly polarized. In general, a single reflection from a planar surface will be left-hand elliptically polarized if the angle of incidence is less than the Brewster angle.[22] An ideal GPS antenna would completely reject all signals that are left-hand circularly polarized. In reality, total rejection is not obtained, but attenuation on the order of 10 dB is typical. The situation deteriorates further when we consider reflectors with nonsmooth surfaces. Reflections from very rough surfaces have random polarization characteristics. As a result, typically only 3 dB of attenuation can be achieved.

Having determined the multipath rejection properties of the antenna itself, the issue of antenna siting can be addressed. The multipath error equations (discussed in Sec. II) along with the antenna characteristics (just described) give general guidance regarding the siting of ground reference stations. To minimize the effects of multipath, the antenna should be located as far away from other objects as possible and/or should be located in such a way that multipath arrives from directions in which the antenna has low gain.

Locating the antenna away from objects minimizes signal blockage and reduces the strength of multipath signals. Mere distance, however, does not guarantee multipath error immunity. One of the great GPS multipath myths is the following (C/A-code processing assumed): GPS receivers reject multipath signals that arrive more than 1.5 chips (440 m or 1466 ns) after the direct signal; therefore, objects greater than 440 m from the receiver are not of concern. The error in this statement stems from a misinterpretation of the concept of multipath delay. As shown in sec. II, the 1.5 chips delay is a delay of the multipath *relative to the direct signal.* As was shown in Braasch,[20] the relative delay of the multipath is a function of receiver-to-object distance *and* proximity of the object to the satellite-to-receiver line-of-sight. The closer an object is to the line-of-sight, the greater the receiver-to-object distance can be while still yielding a relative multipath delay of less than 1.5 chips. The conclusion, then, is that increased receiver-to-object distance only guarantees a weakening of the multipath signal.

Maximization of the receiver-to-object distance was the first general siting guideline mentioned above. The second considered the gain pattern of the antenna. Multipath mitigation can be maximized if the antenna is located so that multipath arrives from directions in which the antenna has low gain. Multipath usually arrives from angles near the horizon and below. Multipath mitigation, then, is achieved by using an antenna with low gain in these directions.

B. Receiver Design

As demonstrated in Sec. II, multipath error is highly dependent upon receiver architecture. The following sections expand upon this.

1. Coherent vs Noncoherent Delay Lock Loop Architectures

As the plots in Sec. II demonstrate, for a given set of multipath parameters, average multipath error is smaller for a coherent DLL than for a noncoherent DLL. Furthermore, van Nee[19] has shown that when the relative phase rate-of-change of the multipath is large compared to the code tracking loop bandwidth, the coherent DLL error does average to zero. The primary disadvantage of the coherent DLL is a matter of robustness and not multipath. A coherent DLL will be disrupted by cycle slips, whereas a noncoherent DLL will continue to function independently of the carrier-phase tracking loop.

2. C/A Code with Narrow Correlator Spacing

Fenton et al.[23] and Van Dierendonck et al.[24] describe a patented development in GPS receiver design that lessens the effect of multipath by narrowing the spacing of the early and late correlators in a noncoherent DLL. By using a small portion of the correlation function (around the peak) to form the discriminator, maximum multipath error is reduced by a factor of 10 and multipath with relative delays of approximately 1 chip or greater is rejected entirely (0.1 chip correlator spacing). Braasch[26] and Van Nee[18] showed that the narrow correlator concept applies to the coherent DLL also. Meehan and Young[25] describe variations of the narrow correlator concept which benefit carrier-phase measurements as well as code measurements.

3. P Code

As discussed in Sec. II the P-code multipath performance is far superior to C/A-code tracking. For a given set of multipath parameters, peak error on the C/A code is 10 times larger than on the P code. When access is available, P code is clearly the choice when multipath is considered. It is important to note, however, that the 10:1 multipath error reduction applies to the maximum error and not necessarily the instantaneous error. This is illustrated in Fig. 1 where a relative multipath amplitude of -20 dB has been simulated. Note that for short delay multipath, the P-code and C/A-code multipath error envelopes coincide. Thus, for multipath in this region, the P code will not necessarily perform an order of magnitude better than the C/A code.

IV. Multipath Data Collection

In many instances it is desirable to evaluate the multipath in a given environment. This is particularly true in the siting of a ground reference station. Thus, the situation arises that GPS data are to be collected, and the multipath component of the error is to be isolated. Note that a truth reference system is not useful in this case. A truth reference system allows for the determination of the total system error. However, in this case only the multipath component of the error is desired.

The GPS signal itself may be exploited to isolate the combination of code multipath plus receiver error[4,11]. The GPS code and carrier-phase (integrated Doppler) measurements may be expressed as follows:[26]

$$\rho_{\text{code}} = D + c(b_u - B) + c(T + I + M_{\text{code}} + \text{HW} + \nu_{\text{code}}) + \text{URE} + \text{SA} + \text{MEAS}_{\text{code}} \tag{35}$$

$$\rho_{\text{phase}} = D + c(b_u - B) + c(T - I + M_{\text{phase}} + \text{HW} + \nu_{\text{phase}}) + \text{URE} + \text{SA} + \text{MEAS}_{\text{phase}} + \Delta \tag{36}$$

where

B = satellite clock offset from system time
b_u = receiver clock offset from system time
c = speed of light, m/s
D = true line-of-sight range from the satellite to the user in meters
HW = receiver hardware delay, s
I = apparent change in signal path delay due to propagation through the ionosphere, s
M = apparent change in signal path delay due to specular (i.e., nondiffuse) multipath, s
MEAS = receiver measurement (tracking) errors
SA = (selective availability) range error due to the intentional degradation of the satellite clock and orbit information by the DOD (used for security purposes), m
T = apparent change in signal path delay due to propagation through the troposphere, s
URE = (user range error) range error due to satellite clock and orbit uncertainty, m
ν = apparent change in signal path delay due to a combination of receiver noise and diffuse multipath, s
Δ = range difference between the code and integrated Doppler measurements due to an integer wavelength ambiguity, m
ρ_{code} = code measurement (pseudorange), m
ρ_{phase} = carrier-phase (integrated Doppler) measurement, m

Diffuse multipath arises from reflection and diffraction from a group of electrically small objects. Each of these objects individually produces a negligible multipath field, but the sum effect can be on the order of receiver noise values. This effect is lumped in with receiver noise because it is generally uncorrelated over time, and therefore noise-like in behavior. Note that the ionosphere term is equal in magnitude but opposite in sign for the two measurements. More detailed information on the effects of the ionosphere can be found in Chapter 12, this volume. The integer wavelength ambiguity arises in the carrier measurement because the basic measurement is that of integrated Doppler (change-of-range relative to the start of signal tracking). For the moment, consider the observable obtained by differencing the code and carrier-phase measurements:

$$\rho_{\text{code}} - \rho_{\text{phase}} = 2I + \text{MEAS}_{\text{code}} - \text{MEAS}_{\text{phase}} + \nu_{\text{code}} - \nu_{\text{phase}} + M_{\text{code}} - M_{\text{phase}} - \Delta \tag{37}$$

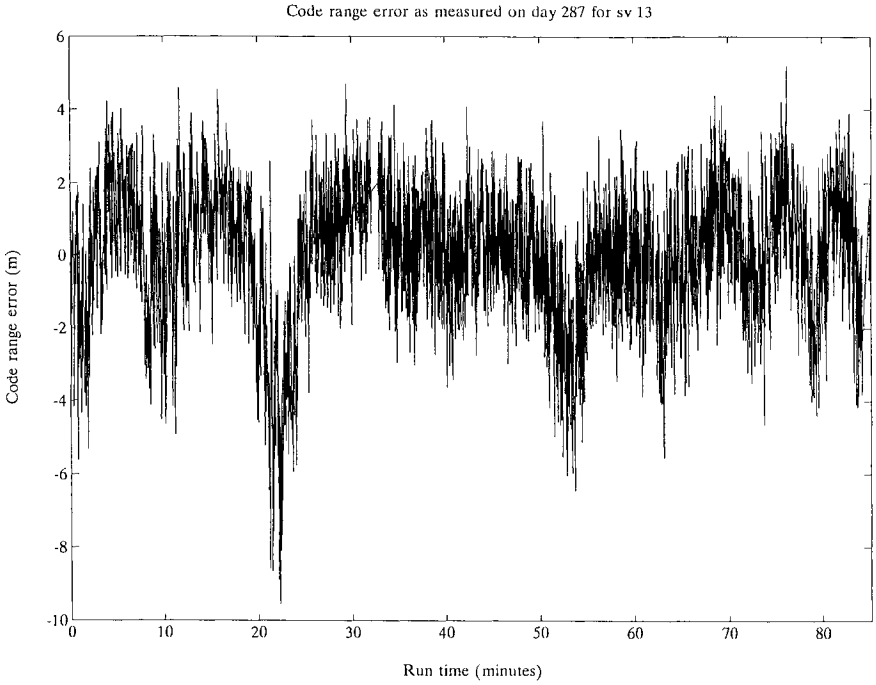

Fig. 5 Ohio University hangar test. Data were collected using an Ashtech 3DF receiver approximately 4 m from the hangar (which is approximately 10 m tall). Note that the curve shows the combined effects of multipath and receiver noise.

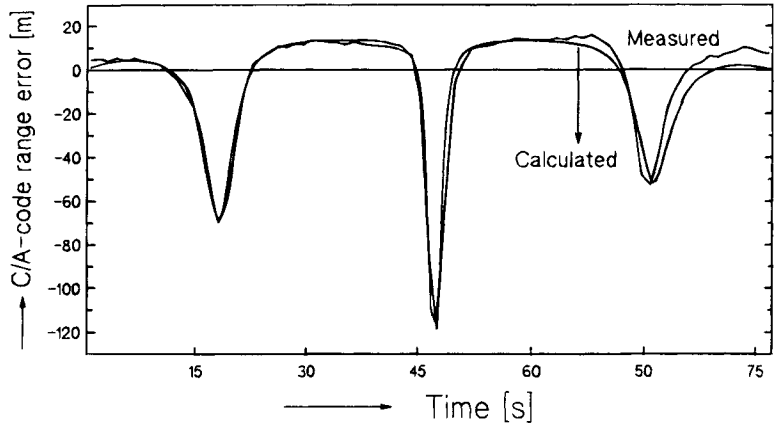

Fig. 6 Delft University electrical engineering building test. Data were collected using a Trimble 4000SST receiver approximately 30 m from the building (which is approximately 100 m tall). The curve labeled "calculated" is the result of fitting a model based on theory described in Sec. II. Reprinted from Van Nee (1992) with permission from R. van Nee and the Delft University of Technology.

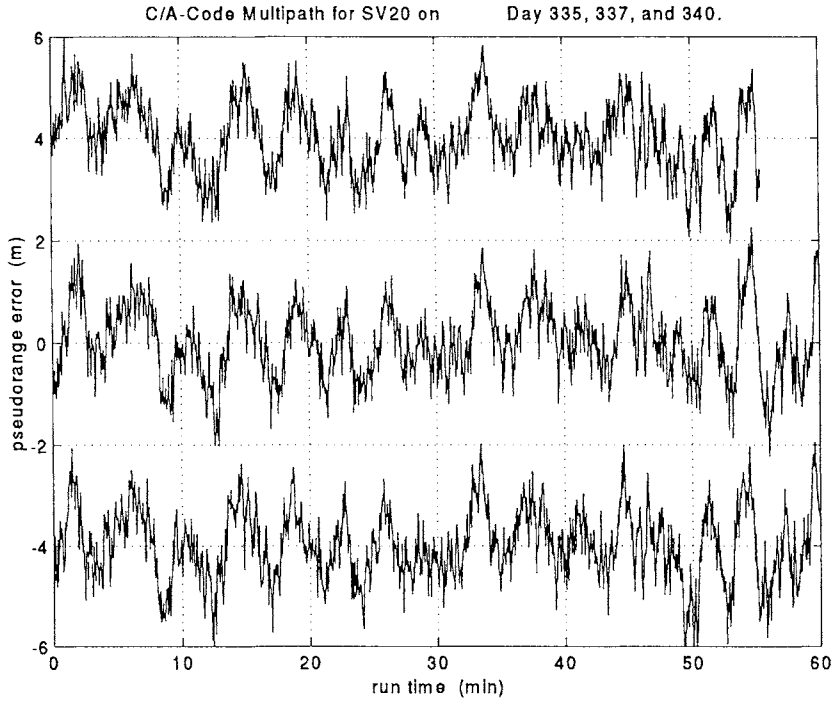

Fig. 7 Day-to-day repeatability of C/A-code multipath. Curves show pseudorange multipath error for three days. The data from day 235 have been offset in amplitude by +4 m and in time by 0 min; data from day 237 have been offset in amplitude by 0 m and in time by 8 min; and data from Day 240 have been offset in amplitude by −4 m and in time by 20 min. Data were collected using a Turborogue receiver on the roof of the University of Colorado, Boulder, Engineering Center.

Phase measurement errors, phase noise, and multipath typically are negligible.[27,28] The usual application of this process involves differencing code and carrier data collected over a given period of time. The integer ambiguity may, thus, be removed by subtracting out the bias. What remains is a combination of multipath, receiver code measurement error, noise, and an ionospheric term:

$$(\rho_{\text{code}} - \rho_{\text{phase}})_{\text{adj}} = 2I + \text{MEAS}_{\text{code}} + \nu_{\text{code}} + M_{\text{code}} \tag{38}$$

Receiver code measurement errors typically result from dynamics-induced tracking loop lags.[29] Although these are usually correlated over time, receiver noise is not, and therefore it may be reduced through filtering. The filtering scheme smooths the code against the carrier measurements. Typical implementations are the Hatch filter[30] and the complementary Kalman filter.[31] The remaining term besides multipath is then the effect due to the ionosphere. However, measurements from two different carrier frequencies can be used to eliminate the ionospheric term. For those users with single-frequency receivers, the effect of the ionosphere is typically a long-term drift, which can easily be distinguished from the higher-frequency multipath errors.

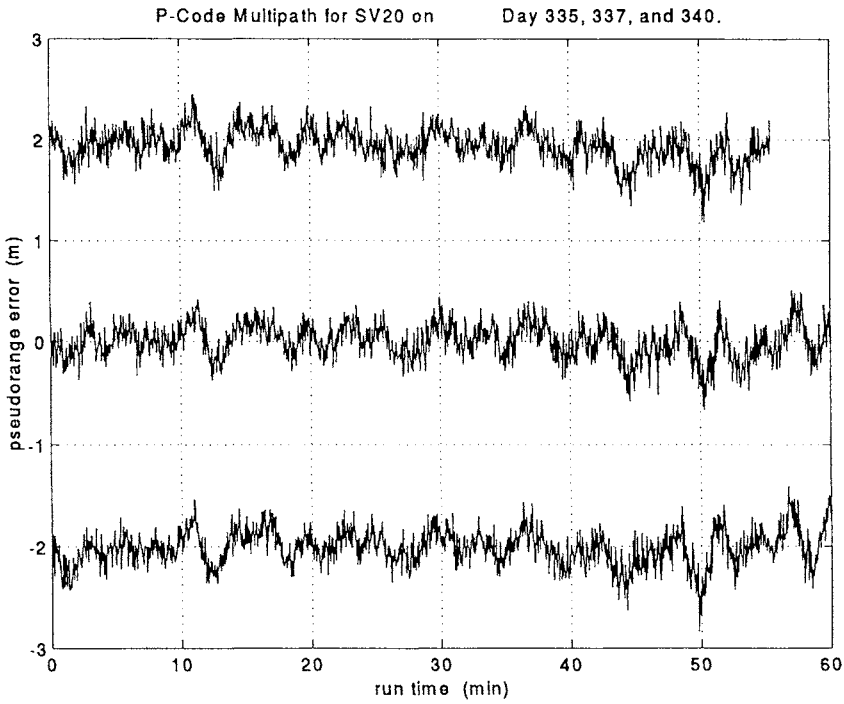

Fig. 8 Day-to-day repeatability of P-code multipath. Curves show pseudorange multipath error for three days. The data from Day 235 have been offset in amplitude by +2 m and in time by 0 min; data from Day 237 have been offset in amplitude by 0 m and in time by 8 min; and data from Day 240 have been offset in amplitude by −2 m and in time by 20 min. Data were collected using a Turborogue receiver on the roof of the University of Colorado, Boulder, Engineering Center.

As a result, the differencing of code and carrier measurements allows for the isolation of pseudorange multipath and receiver code measurement errors. The magnitude and behavior of receiver code measurement errors is, quite obviously, receiver dependent. However, it must be taken into consideration when analyzing the data. Test results indicate that receiver code measurement errors can be on the order of one meter.

For static data collection efforts, the repeating pattern of the satellite orbits can be exploited to gain confidence in the multipath analysis. The question often arises as to whether a given set of error data is truly multipath or not. The answer lies in collecting data on successive days. If, for instance, data are collected from satellite 20 on Wednesday between 2:00 p.m. and 3:00 p.m., data from the same satellite should be collected during the same time on Thursday. Because the satellite orbits the Earth twice every sidereal day (23 h 56 min), it returns to the same location four minutes earlier each day. Thus, errors thought to be multipath can be checked for repeatability. Any residual noise errors and the like will not repeat from day to day. However, because the same antenna, object, and satellite positions are being used, the multipath data should repeat. In this way, confidence

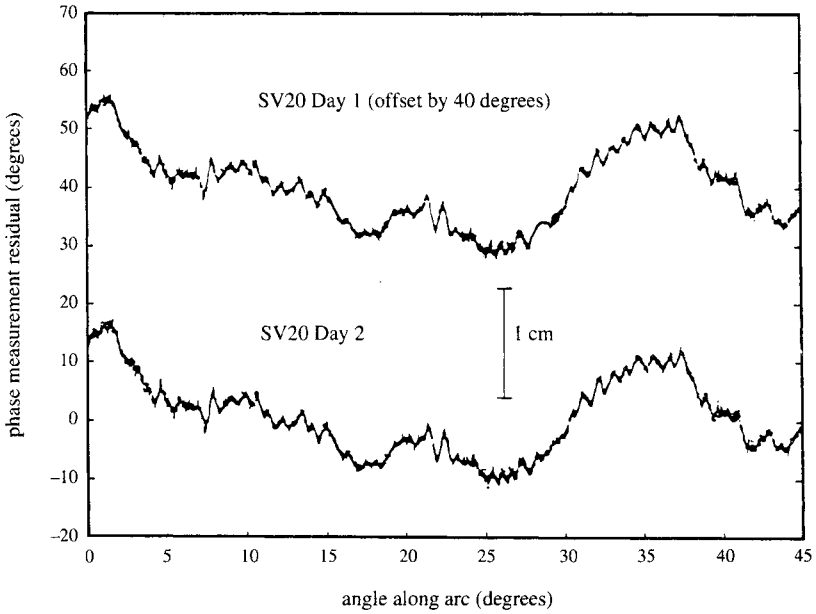

Fig. 9 Carrier-phase multipath error. Data was collected using a Trimble Navigation TANS-based GPS receiver. Multipath was induced by mounting a rectangular sheet metal reflector near one of the interferometer antennas. Reprinted from Cohen (1992) with permission.

can be gained that a set of error data is truly due to multipath. Obviously, this method assumes that the multipath comes from stationary objects.

Examples of GPS code multipath errors are given in Figs. 5–8. For the data shown in Fig. 5, a GPS antenna was placed approximately 4 m in front of a hangar door at the Ohio University airport.[32] In this case, the measurements were not filtered, and thus the graph shows a combination of multipath and receiver noise on the code measurements. The low-frequency trend shows the oscillating error attributable to the phase variation of the multipath. The trend is much clearer in fig. 6. These data were collected by the Electrical Engineering Department at the Delft University of Technology in Delft, The Netherlands.[18] A GPS antenna was placed approximately 30 m away from the Delft University Electrical Engineering building. The building is approximately 100 m high and 70 m wide. This figure illustrates several points about multipath error. First, it is highly nonsinusoidal. This verifies the earlier claim and is a direct result of the nonlinearities in the receiver architecture. Second, the maximum error is −120 m, thus verifying the assertion that code multipath errors can be extremely large. Finally, using the equations described in Sec. II, a model was fit to the data with the assumption that there were two major reflectors. Time delays were calculated from the geometry of the test set-up. The other parameters were adjusted to achieve a good fit. The results show clearly that the theoretical equations are good descriptions of actual multipath error.

Figures 7 and 8 illustrate C/A-code and P-code multipath day-to-day repeatability. The data sets were collected on DOY 335, 337, and 340 of 1993 (Dec. 1, 3, 6) on the roof of the Engineering Center at the University of Colorado, Boulder. Each of the three days of data for each code has been offset from each other for visual clarity (4 m for the C/A code, 2 m for the P code). The lower frequency oscillations due to multipath are apparent as well as the day-to-day repeatability. Sample correlation coefficients between data sets are on the order of 0.50–0.60.

Figure 9 illustrates carrier-phase multipath and its repeatability in a controlled environment. These data were collected at Stanford University using a short baseline GPS interferometer.[33] A metal sheet was intentionally placed near one antenna to induce multipath. The carrier-phase residuals clearly demonstrate the presence of multipath.

Acknowledgments

The author gratefully acknowledges the assistance of the Delft University of Technology, Faculty of Electrical Engineering, Telecommunications and Traffic-Control Systems Group (Delft, The Netherlands). In particular, the help of Edward Breeuwer, Richard van Nee, and Durk van Willigen was invaluable. Penina Axelrad and Christopher Comp of the Colorado Center for Astrodynamics Research, University of Colorado, Boulder, are thanked for their comments on the manuscript and for the collection of the C/A-code and P-code multipath data. Clark Cohen, Department of Aeronautics and Astronautics, Stanford University is thanked for the provision of the carrier-phase multipath error plot.

References

[1]Lachapelle, G., Falkenberg, W., Neufeldt, D., and Keilland, P., "Marine DGPS Using Code and Carrier in a Multipath Environment," *Proceedings of ION GPS-89,* Colorado Springs, CO, Sept. 1989, Institute of Navigation, Washington, DC, pp. 343–347.

[2]Cohen, C., and Parkinson, B., "Mitigating Multipath Error in GPS-Based Attitude Determination," *Guidance and Control 1991,* Vol. 74, *Advances in the Astronautical Sciences,* edited by R. Culp and J. McQuerry, American Astronautical Society, 1991, pp. 53–68.

[3]Hagerman, L., "Effects of Multipath on Coherent and Noncoherent PRN Ranging Receiver," Aerospace Rep. TOR-0073(3020-03)-3, Development Planning Division, The Aerospace Corporation, May 15, 1973.

[4]General Dynamics, Electronics Division, "Final User Field Test Report for the NAVSTAR Global Positioning System Phase I, Major Field Test Objective No. 17: Environmental Effects, Multipath Rejection," Rept. GPS-GD-025-C-US-7008, San Diego, CA, March 28.

[5]Counselman, C., and Gourevitch, S., "Miniature Interferometer Terminals for Earth Surveying: Ambiguity and Multipath with Global Positioning System," *IEEE Transactions on Geoscience and Remote Sensing,* Vol. GE-19, No. 4, 1981, pp. 244–252.

[6]Counselman, C., "Miniature Interferometer Terminals for Earth Surveying (MITES): Geodetic Results and Multipath Effects," Digest of the International Geoscience and Remote Sensing Symposium, Washington, DC, June 1981, Institute of Electrical and Electronics Engineers, New York, pp. 219–224.

[7]Greenspan, R., Ng, A., Przyjemski, J., and Veale, J., "Accuracy of Relative Positioning by Interferometry with Reconstructed Carrier GPS: Experimental Results," *Proceedings of the Third International Geodetic Symposium on Satellite Doppler Positioning,* New Mexico State University, Las Cruces, NM, Feb. 1982, pp. 1177–1195.

[8]Bletzacker, F., "Reduction of Multipath Contamination in a Geodetic GPS Receiver," Proceedings of the First International Symposium on Precise Positioning with the Global Positioning System, U.S. Department of Commerce, National Oceanic and Atmospheric Administration, Rockville, MD, April 1985, pp. 413–422.

[9]Tranquilla, J., and Carr, J., "GPS Multipath Field Observations at Land and Water Sites," *Navigation,* Vol. 37, No. 4, 1990–1991, pp. 393–414.

[10]Falkenberg, W., Kielland, P., and Lachapelle, G., "GPS Differential Positioning Technologies for Hydrographic Surveying," Record of the Position, Location, and Navigation Symposium, PLANS, Orlando, FL, Institute of Electrical and Electronics Engineers, New York, Dec. 1988, pp. 310–317.

[11]Evans, A., "Comparison of GPS Pseudorange and Biased Doppler Range Measurements to Demonstrate Signal Multipath Effects," Proceedings of the International Telemetering Conference, Las Vegas, NV, Instrument Society of America, Research Triangle Park, NC, Oct. 1986, pp. 795–801.

[12]Georgiadou, Y., and Kleusberg, A., "On Carrier Signal Multipath Effects in Relative GPS Positioning," Manuscripta Geodaetica, Vol. 13, 1988, pp. 172–179.

[13]Abidin, H., "Extrawidelaning for 'On the Fly' Ambiguity Resolution: Simulation of Multipath Effects," *Proceedings of ION GPS-90,* Colorado Springs, CO, Institute of Navigation, Washington, DC, Sept. 19–20, 1990, pp. 525–533.

[14]Bishop, G., Klobuchar, J., and Doherty, P., "Multipath Effects on the Determination of Absolute Ionospheric Time Delay From GPS Signals," *Radio Science,* Vol. 20, No. 3, 1985, pp. 388–396.

[15]Sennott, J., and Pietraszewski, D., "Experimental Measurement and Characterization of Ionospheric and Multipath Errors in Differential GPS," *Navigation,* Vol. 34, No. 2, 1987, pp. 160–173.

[16]Sennott, J., and Spalding J., "Multipath Sensitivity and Carrier Slip Tolerance of an Integrated Doppler DGPS Navigation Algorithm," Record of the Position Location and Navigation Symposium (PLANS), Las Vegas, NV, Institute of Electrical and Electronics Engineers, New York, March 1990, pp. 638–644.

[17]van Nee, R., "Multipath Effects on GPS Code Phase Measurements," *Proceedings of ION GPS-91,* Albuquerque, NM, Institute of Navigation, Washington, DC, Sept. 1991, pp. 915–924.

[18]van Nee, R., "GPS Multipath and Satellite Interference," *Proceedings of the Forty-eighth Annual Meeting of the Institute of Navigation,* Institute of Navigation, June 1992, Washington DC, pp. 167–177.

[19]van Nee, R.,"Spread Spectrum Code and Carrier Synchronization Errors Caused by Multipath and Interference," *IEEE Transactions on Aerospace and Electronic Systems,* Vol. 29, No. 4, 1993, pp. 1359–1365.

[20]Braasch, M., "On the Characterization of Multipath in Satellite-Based Precision Approach and Landing Systems," Ph.D. Dissertation, Department of Electrical and Computer Engineering, Ohio University, Athens, OH, June 1992.

[21]Braasch, M., and van Graas, F., "Mitigation of Multipath in DGPS Ground Reference Stations," *Proceedings of the ION National Technical Meeting,* San Diego, CA, Institute of Navigation, Washington, DC, Jan. 1992, pp. 105–114.

[22]Balanis, C., *Advanced Engineering Electromagnetics,* Wiley, New York, 1989, pp. 185–196.

[23]Fenton, P. et al., "Novatel's GPS Receiver: The High Performance OEM Sensor of the Future," *Proceedings of ION GPS-91,* Albuquerque, NM, Institute of Navigation, Washington, DC, Sept. 1991, pp. 49–58.

[24]Van Dierendonck, A., Fenton, P., and Ford, T., "Theory and Performance of Narrow Correlator Spacing in a GPS Receiver," *Navigation,* Vol. 39, No. 3, 1992, pp. 265–283.

[25]Meehan, T., and Young, L., "On-Receiver Signal Processing for GPS Multipath Reduction," Proceedings of the 6th International Geodetic Symposium on Satellite Positioning, Columbus, OH, Defense Mapping Agency and the Ohio State University, Columbus, OH, March 1992, pp. 200–208.

[26]Braasch, M., "A Signal Model for GPS," *Navigation,* Vol. 37, No. 4, 1990–1991, pp. 363–377.

[27]Ferguson, K., et al., "Three-Dimensional Attitude Determination with the Ashtech 3DF 24-Channel GPS Measurement System," *Proceedings of the ION National Technical Meeting,* Phoenix, AR, Institute of Navigation, Washington, DC, Jan. 1991.

[28]Braasch, M., and van Graas, F., "Guidance Accuracy Considerations for Real-Time GPS Interferometry," *Proceedings of ION GPS-91,* Albuquerque, NM, Institute of Navigation, Washington, DC, Sept. 1991, pp. 373–386.

[29]Braasch, M., "Isolation of GPS Multipath and Receiver Tracking Errors," *Proceedings of the ION National Technical Meeting,* San Diego, CA, Institute of Navigation, Washington, DC, Jan. 1994, pp. 511–521.

[30]Hatch, R., "The Synergism of GPS Code and Carrier Measurements," *Proceedings* of the Third International Geodetic Symposium on Satellite Doppler Positioning, New Mexico State University, Las Cruces, NM, Feb. 1982, pp. 1213–1231.

[31]van Graas, F., and Braasch, M., "GPS Interferometric Attitude and Heading Determination: Initial Flight Test Results," *Navigation,* Vol. 38, No. 4, 1991–1992, pp. 297–316.

[32]Breeuwer, E., "Modeling and Measuring GPS Multipath Effects," Master's Thesis, Faculty of Electrical Engineering, Delft University of Technology, Delft, The Netherlands, Jan. 1992.

[33]Cohen, C., "Attitude Determination Using GPS," Ph.D. Dissertation, Department of Aeronautics and Astronautics, Stanford University, Stanford, CA, Dec. 1992.

Chapter 15

Foliage Attenuation for Land Mobile Users

J. J. Spilker Jr.*
Stanford Telecom, Sunnyvale, California 94089

I. Introduction

LAND mobile users are expected to be one of the largest categories of GPS users, and it is important to examine the specific GPS propagation issues for this environment. It has already been shown that the optimum geometric dilution of precision (GDOP) is provided when several of the GPS satellites are at low elevation angle near the horizon. However, the land mobile user environment differs from that of aircraft in flight or ships at sea in that the user driving along a road or freeway is often subject to shadowing, diffraction, and scattering of the satellite signal by trees, utility poles, buildings, or hills. These effects are accentuated by the need for operation at low elevation angles for at least some of the GPS satellites. In addition, the requirement for receiver simplicity, and the need to track several satellites widely spaced in angle simultaneously, generally dictates the use of an omnidirectional or hemispherical antenna. Thus, while receiving the direct line-of-sight ray from the satellite, the user has little means to discriminate against multipath signals scattered from ground reflections, tree limbs and foliage, or other scattering elements. In addition, the direct ray may itself be attenuated by tree foliage.

This chapter describes and models the statistics of the signal environment for the rural land mobile user where tree foliage often shadows the user. The statistical models are then compared with measured data for *L*-band signals at various elevation angles. Both stationary and mobile users are considered.

The satellite-to-land mobile user links can be categorized in one of three forms: 1) line of sight, unshadowed; 2) shadowed by trees or foliage; and 3) completely obstructed where the link is totally blocked by hills or other major obstructions (see Fig. 1).

The unshadowed link is characterized by a link where there is a clear line of sight to the satellite, but there can also be a scattered and/or specular multipath component in addition to the line-of-sight link. The multipath component can be caused by ground reflections. The unshadowed link can be modeled as the sum

* Ph.D., Chairman of the Board.

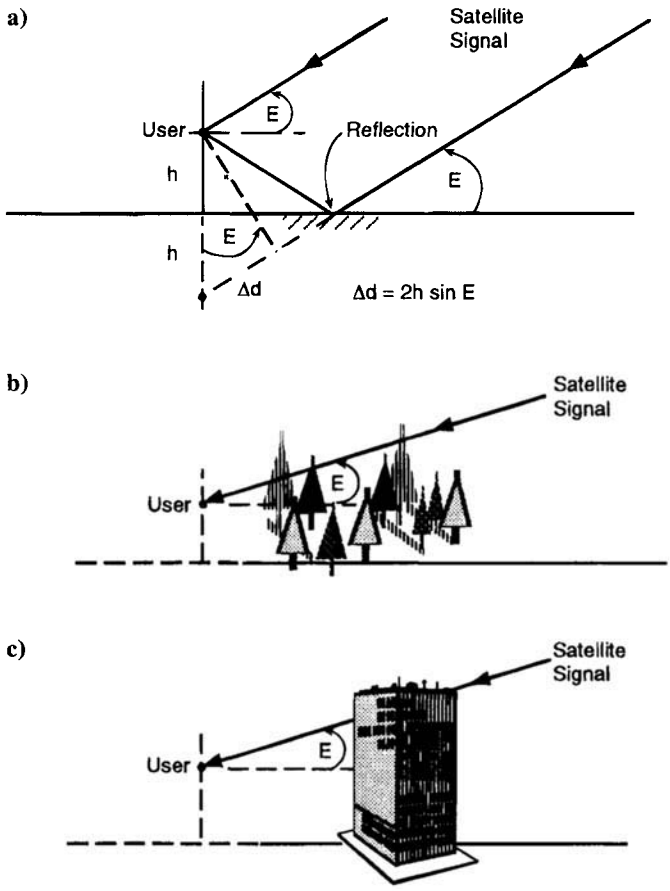

Fig. 1 Different types of links experienced by a mobile user, or fixed user on the ground: a) unshadowed link with multipath reflection a distance *h* below the user and satellites at elevation angle *E*; b) link partially shadowed by trees, telephone poles; c) link completely shadowed by buildings, hills, or other obstructions.

of a fixed line-of-sight signal plus a Rayleigh scattered term. The sum of these two components has a distribution alternatively known as a Rician or a Nakagami–Rice distribution.[1]

Partially shadowed links have a randomly attenuated direct link in addition to the scattered component. The attenuation generally is caused by individual trees, utility poles, clusters of trees, or forests along a roadway. The shadowed signal is sometimes modeled by assuming a lognormal distribution for the direct ray. The sum of direct and scattered components has a Rician distribution for any given amplitude direct ray; i.e., the conditional distribution for a given line-of-sight signal amplitude is Rician. The resulting distribution, obtained by averaging over the lognormal direct ray, is known as the Loo distribution.[2]

The completely obstructed link may be blocked by hills or large man-made structures and has no useful signal component at all over a substantial period of time.

Discussion in this chapter is limited to the shadowed/unshadowed environment common along road/highways in the rural or suburban environment. Typically, a vehicle moves from the shadowed environment where forests are adjacent to the roadway to regions of relatively open space with line-of-sight propagation and then back to the shadowed region. In a given region, there is a certain fraction of time S that a mobile user is in the shadowed region, and during the remaining fraction of time $1-S$ the user is in the unshadowed region.

The channel model employed in this chapter assumes that the received signal $S_r(t)$ has the form

$$S_r(t) = \alpha(t)s(t - \tau) + \Sigma\beta_i(t)s(t - \tau - \Delta\tau_i) \tag{1}$$

where $\alpha(t)$ represents the random path attenuation caused by the foliage, τ is the delay of the direct line-of-sight satellite user path, and $\beta_i(t)$ represents the random attenuation of the scattered components with additional delay $\Delta\tau_i$. For purposes of this chapter, the delays $\Delta\tau_i$ of the scattered components are considered negligible compared to the inverse bandwidth of the signal. Thus, the channel considered here is strictly limited to the flat fading channel; i.e., the signal spectrum is unchanged by the fading except for a random amplitude. Larger multipath delays; for example, as experienced by an aircraft in flight with sea surface reflections, could produce frequency selective fading. Multipath channels where the delays are not negligible are considered in another chapter.

The discussion that follows first treats the stationary user and views the various GPS satellites through individual trees or groves of trees at different elevation angles. The remainder of the chapter emphasizes mobile users where the link is varying fairly rapidly with time as the vehicle moves past trees and other short duration obstructions.

II. Attenuation of an Individual Tree or Forest of Trees—Stationary User

Consider first the attenuation caused by an individual tree where a GPS satellite is viewed by a stationary user at an elevation angle E deg. Goldhirsh and Vogel[1,3] have published measurements of attenuation of an individual tree vs. elevation angle. The approximate geometry of the tree and the relative position of the receiver are shown in Fig. 2. These measurements were taken at 870 MHz, but the results can be translated to L-band after being scaled up to 1.575 GHz using the following relationship:

$$\begin{aligned} &\text{Attenuation } (f) \sim \sqrt{f} \\ &\text{Attenuation (1.575 GHz) dB} \approx \sqrt{\frac{1575 \text{ MHz}}{870 \text{ MHz}}} \text{ Attenuation (870 MHz) dB} \end{aligned} \tag{2}$$

where the attenuation in dB is scaled by $\sqrt{1575/870} = 1.345$. That is, foliage attenuation varies approximately as the square root of frequency.*

*The square root relationship is only a rough approximation. In the frequency range 800 MHz to 2 GHz the rms error has been estimated[1] at 6%.

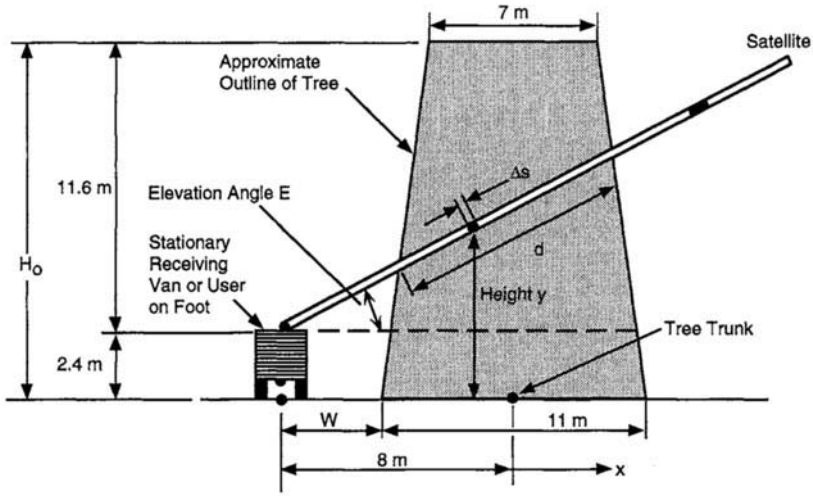

Fig. 2 Simplified geometric configuration of a single callery pear tree vs elevation angle in measurements made by Goldhirsh and Vogel[3] as viewed by a stationary user. The origin of the *x, y* coordinates used in the text is the base of the tree trunk.

It has also been shown that the attenuation of a tree in full foliage is roughly 35% greater in dB than that of a deciduous tree without foliage. Thus, the bulk of a tree's attenuation is clearly caused by the wood tree limbs, branches, and trunk rather than by the leaves.

Foliage attenuation is often characterized as attenuation in dB/m of foliage penetration. As shown later, these numbers of attenuation per meter tend to vary widely depending on the type of tree and the height of the ray relative to the top of the tree because the foliage density varies with height. The attenuation also varies with the distance of the tree from the user. Fresnel diffraction analyses have been used to explain the average decrease of attenuation with increasing distance of the receiver to the tree.[4]

As an attempt to obtain a simple purely empirical geometric interpretation of the foliage attenuation refer to Fig. 2 again. Consider a ray path through a nonuniform density foliage slab where for each incremental distance Δs along the ray path has some random value of attenuation in dB/m. The mean attenuation coefficient at that position depends on various parameters, such as type of tree, density of trees, position relative to center, and base of tree. The total attenuation then depends on the distance W from the receiver to the edge of the trees, the elevation angle to the satellite, and the geometric extent of the foliage. In effect, we consider the trees to be a slab of foliage with nonuniform attenuation where the attenuation density in dB/m varies with position. The quantity H_o is the height of the foliage slab representing the tree or trees. It is assumed that $A_d(x, y)$ represents the mean attenuation density vs position, and the actual attenuation is either 0 or k_o depending on whether that position in space has foliage or not. The probability of the incremental ray being attenuated at that position cell is p, and all cells are independent. Thus, the mean attenuation for that incremental

cell of length Δs is pk_o where k_o varies with position relative to the base of each tree.

It should be emphasized that this representation is only a simple empirical model which we can attempt to fit to the measured data and compare with measured data. If we use the model for attenuation just discussed and we use the law of large numbers for a large number of independent attenuation cells of length Δs, the total path attenuation in dB approximately follows a normal distribution. The distribution of received signal level in absolute terms then follows a lognormal distribution. We return to this distribution later.

We can easily show that the total distance d through the foliage of the model of Fig. 2 does not change substantially as we vary the elevation angle from 0 to 45 deg; d remains at approximately 10 m. Consequently, a uniform attenuation density foliage slab model would show little variation in total attenuation with elevation angle. However, the attenuation measured by Ref. 1 varies considerably from approximately 9.5 dB at 40 deg to approximately 19 dB at 20 deg elevation angle (measured numbers are scaled up to 1.545 GHz). Thus, the attenuation density in dB/m obviously must vary substantially with position relative to this base of the tree if the attenuation vs elevation angle of the model is to match the measurement. That variation is consistent with what we might expect from a simple observation of the wood portion of a typical tree, which has a greater wood density near the base of the trunk.

We have selected an empirical attenuation density profile (in dB/m) that varies with position relative to the base of the tree's center (the trunk), which seems to match fairly well-measured data for the tree of Fig. 2. This attenuation profile is shown in Fig. 3 for this given tree and tree–user distance. The mean attenuation density in dB/m of this empirical model varies as follows:

$$A_d(x, y) = (1 - y/14)^2(1 - |x|/5.5)\text{K dB/m} \tag{3}$$

This attenuation density profile can be integrated along the path s through the tree at a given elevation angle E to obtain the total attenuation $A_T(E)$ where the following obtains:

$$A_T(E) = \int_{\text{path}} A_d(x, y)\, \mathrm{d}s \tag{4}$$

Assume a rectangular tree of 14-m height, 11-m width, a trunk 8 m away from the receiver, and the receiver 2.4 m above ground (see Fig. 2). The mean total attenuation A_T is then

$$A_T(E) \cong \frac{K \sec(E)}{5.5}\left[\int_{2.5}^{8}(1 - y/14)^2(x - 25)\mathrm{d}x + \int_{8}^{13.5}(1 - y/14)^2(13.5 - x)\mathrm{d}x\right] \tag{5}$$

where $y = 2.4 + x \tan E$. Thus,

$$\begin{aligned} A_T(E) &\approx K[3.78 \sec E - 5.21 \sec E \tan E + 1.937 \sec E \tan^2 E] \\ &\cong K[3.726 - 0.0670\, E] \text{ for a least mean square fit} \\ &\cong 24.6 - 0.442\ \text{E}. \end{aligned}$$

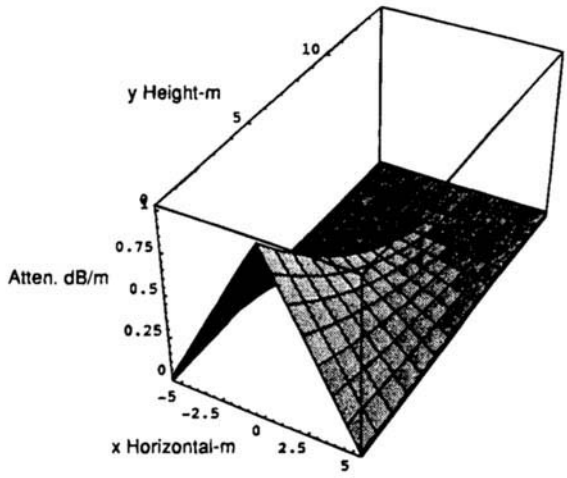

Fig. 3 Simplified mean normalized attenuation density profile of a tree in dB/m that has been adjusted to match measured variation of total attenuation with elevation angle for a callery pear tree of 14-m height and 11-m width at the base. The height is the height above the ground level. The zero point on the x width scale represents the trunk of the tree.

The calculated value of $A_T(E)$ vs elevation angle is shown in Fig. 4 as the dashed curve where K has been selected for a good match to measured data. Also shown in the figure are the measured points from Goldhirsh and Vogel[1] (which have been scaled up to 1.525 from 870 MHz by a factor of 1.345). The solid curve represents the Goldhirsh and Vogel empirical model:

$$A_T(E) = 25.8 - 0.47\,E \tag{6}$$

which is rather close, as can be seen, to the measured points and the linear best fit result using the geometric model of Fig. 2. We can conclude that the attenuation density is clearly not uniform with position, and the empirical model of Fig. 2, at least for this example, gives a good match for the limited range of elevation data available (between 12 and 30 deg).

Other data have been gathered for various types of trees, as shown in Table 1. The table shows measured tree attenuation for various types of trees at 870 MHz. As discussed earlier, in this frequency region, tree foliage attenuation varies approximately as the square root of frequency; i.e., $\sqrt{f_{LI}/870\ \text{MHz}}$ and results are scaled to 1.575 GHz in terms of increased dB/m attenuation. Trees with full foliage have approximately 1.35 times the attenuation in dB/m compared to attenuation for deciduous trees bare of foliage. Note that some trees have as much as 3–4 dB/m of attenuation at 1.5 GHz. Elevation angle information was not available for these measurements. Note also the substantial difference in two attenuation measurements made for pin oak. The measurements were made at two different locations. Thus, we should expect a wide variation in the data from tree to tree, and the data are primarily useful in a statistical sense.

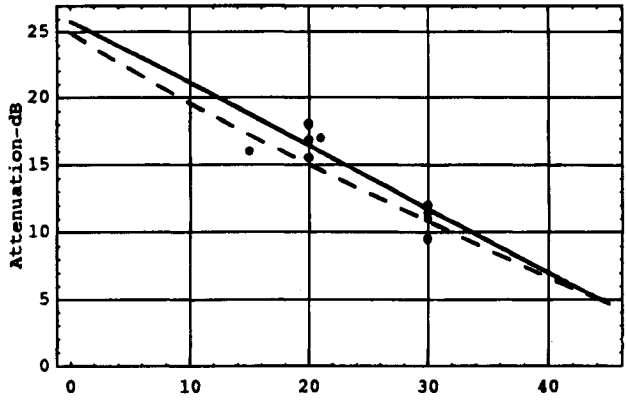

Fig. 4 Measured and approximate attenuation scaled to 1.575 GHz for a callery pear tree of 14-m in height with a base width of 11 m corresponding to Fig. 2. The measured points are shown, the solid curve is the empirical model from Ref. 3, and the dashed curve is the resulting curve from the simple physical model of Fig. 2.

Next, consider the attenuation through a grove of trees, as shown in Fig. 5 where the user–satellite path travels a distance d through the grove. The CCIR[5] has developed an approximate model for mobile user path loss vs the ray foliage penetration distance d of Fig. 5. The CCIR modified exponential decay model gives a path loss $L = \alpha d$ where $\alpha = 1.33 f^{0.284} d^{-0.412}$ dB/m for $14 < d < 400$ m and $\alpha = 0.45 f^{0.284}$ for $0 < d < 14m$ and frequency f in GHz. This model* gives less than a linear dependence over d, which compensates for the Fresnel diffraction effect that gives a decreased attenuation effect with larger user–tree grove distances.[5,6]

A. Foliage Attenuation—Mobile User

Next consider a user who is mobile rather than stationary; i.e., the user is moving rapidly past trees and open spaces alongside the roadway. If these trees and open spaces pass by relatively rapidly compared to the GPS receiver closed loop bandwidth and databit interval of 20 ms = 1/50 bps, then the mean attenuation statistic is more useful than the attenuation of each individual tree.

An empirical model[7] for the fade depth attenuation in dB at 1.5 GHz vs elevation angle E for driving along forested roadways in Maryland is given by the following:

$$F(P, E) = -[a_0 + a_1 E + a_2 E^2] \ln P + bE + c \text{ dB} \tag{7}$$

where P is the percentage of time this fade depth F is exceeded (P = 1–20%); $a_0 = 3.44$; $a_1 = 0.0975$; $a_2 = -0.002$; $b = -0.443$, $c = 34.76$, and E is the elevation angle in degrees to the satellite. A graph of this empirical relationship over the region 20 deg $< E <$ 60 deg for P = 1%, and P = 10% is shown in Fig. 6.

*Note that this CCIR model does not deal with specifics such as the type of foliage, or the distance from user to the grove of trees.

Table 1 Single tree attenuations at f = 870 MHz and attenuation coefficient scaled dB/m for 1.5 GHz (scale factor of 1.35)[7]

	Attenuation dB—870 MHz		Attenuation coefficient dB/m—870 MHz		Attenuation coefficient dB/m—1.575 GHz	
Tree type	Largest	Average	Largest	Average	Largest	Average
Burr oak	13.9	11.1	1.0	0.8	1.3	1.1
Callery pear	18.4	10.6	1.7	1.0	2.2	1.3
Holly	19.9	12.1	2.3	1.2	3.0	1.6
Norway maple	10.8	10.0	3.5	3.2	4.6	4.2
Pin oak	8.4	6.3	0.85	0.6	1.1	0.8
Pin oak	18.4	13.1	1.85	1.3	2.4	1.7
Pine cone	17.2	15.4	1.3	1.1	1.7	1.5
Sassafras	16.1	9.8	3.2	1.9	4.2	2.5
Scotch pine	7.7	6.6	0.9	0.7	1.2	0.9
White pine	12.1	10.6	1.5	1.2	2.0	1.6
Overall average	14.3	10.6	1.8	1.3	2.4	1.7

The empirical Eq. (7) for fade depth statistics can be rewritten in terms of the probability of a fade level being exceeded as a function of fade level for various elevation angles. This probability is as follows:

$$P(F, E) = \exp[(-17380 + 500F + 221.5E)/(-1720 - 48.75E + E^2)] \quad (8)$$

for $1 < P < 20\%$ and 20 deg $< E >$ 60 deg. The probability of fade exceedance is shown in Fig. 7 for elevation angles of 20, 30, 40, 50, and 60 deg along these forested roadways in Maryland.

B. Probability Distribution Models for Foliage Attenuation—Mobile User

The probability distribution for fading along roadways has one of two different types of models, shadowed or unshadowed. For the unshadowed model, we

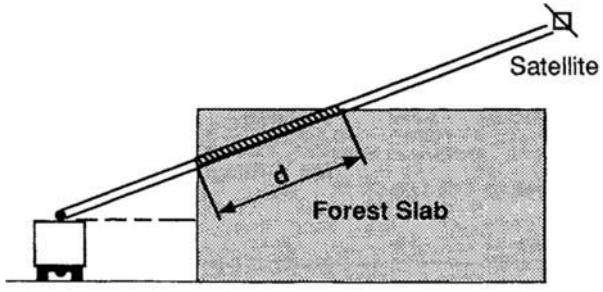

Fig. 5 Model of forest next to roadway. The vegetative path length is d meters.

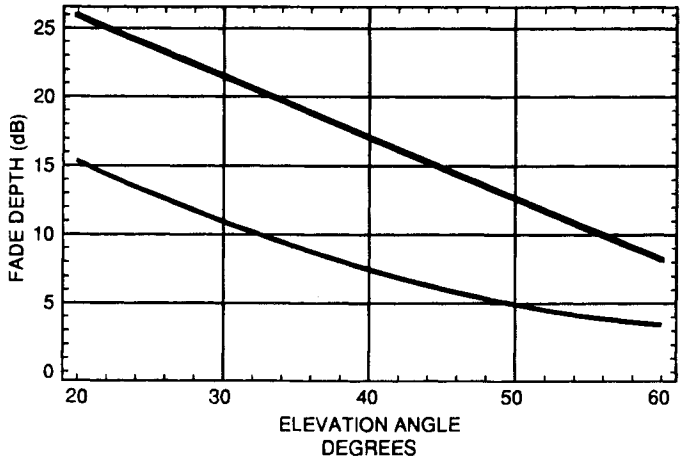

Fig. 6 Fade depth statistics in dB vs elevation angle E in degrees for L-band satellite to mobile users along a forested roadway. The two curves are for 1% (upper heavy curve) and 10% (light curve) probability that the fade is no more than the value shown.

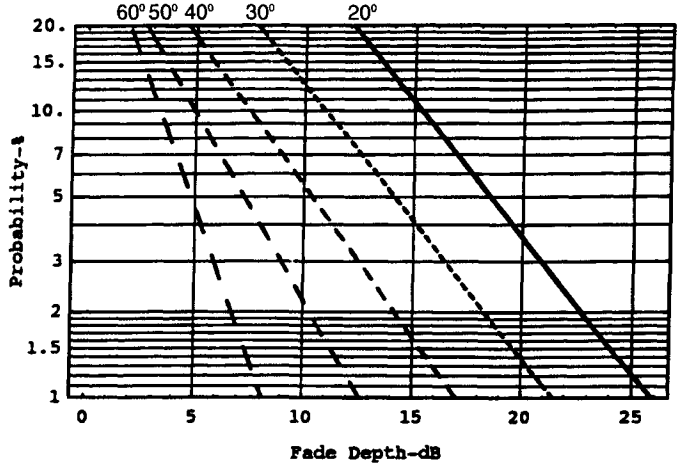

Fig. 7 Probability of fade depth being exceeded vs fade depth for various elevation angles: 20 deg, 30 deg, 40 deg, 50 deg, 60 deg. The solid curve is for an elevation angle of 20 deg, and the curves to the left are for progressively higher elevation angles in 10-deg increments. These empirical data correspond to measurements at L-band taken along forested roadways in Maryland. (data from Ref. 7)

assume that the received signal energy consists of the sum of 1) direct ray (constant amplitude); and 2) Rayleigh scattered signals. The received signal then has the following form:

$$\begin{aligned} r &= a\cos(\omega_o t + \phi) + \omega\cos(\omega_o t + \theta) \\ &= x_c \cos\omega_o t + x_s \sin\omega_o t \end{aligned} \tag{9}$$

where ω has a Rayleigh distribution with mean square value σ^2 and a is the direct ray signal amplitude. The sum of these two has a Nakagami–Rice distribution for the envelope $z = \sqrt{x_c^2 + x_s^2}$ of the in-phase and quadrature signal components. The probability density of the unshadowed envelope is then as follows:

$$p_u(z) = \frac{z}{\sigma^2}\exp\left[\frac{-z^2 + a^2}{2\sigma^2}\right] I_o\left(\frac{za}{\sigma}\right) \tag{10}$$

where the normalized line-of-sight signal power is $P_s = a^2/2$, and the power in the Rayleigh scattered signal is $P_R = \sigma^2$, and $I_o(\,)$ is the modified Bessel function of zero order. If the direct line-of-sight a^2 term decreases to zero, we are left with the Rayleigh signal.

In the shadowed environment, we use a distribution proposed by Loo[2] in which the conditional probability density of the total received signal for a given direct signal level a; namely $p(z|a)$, is given by the Nakagami–Rice distribution, and the probability density of the a direct ray $p(a)$ component is lognormal. The lognormal density is given by the following:

$$p(a) = \frac{1}{\sigma_o a\sqrt{2\pi}}\exp\left[\frac{-(\ell n\, a - \mu)^2}{2\sigma_o^2}\right] \tag{11}$$

as shown in Fig. 8. In essence, the lognormal distribution is the same as a Gaussian

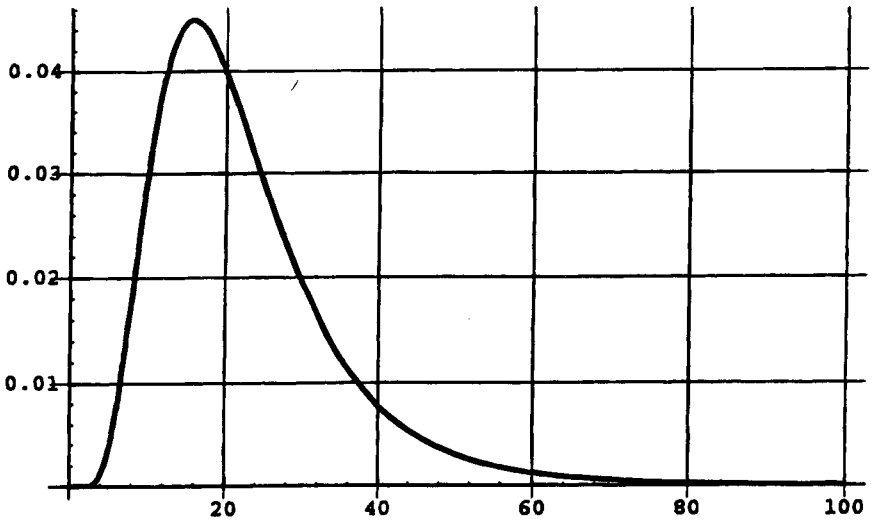

Fig. 8 Probability density functions of the lognormal distribution function for mean $\mu = 3$, and $\sigma_o = 0.5$.

density function where the variable is attenuation or signal level expressed in dB (except for a scale factor to account for the difference between $\log_{10}$ and ℓn).

The shadowed density function formulated by Loo[2] is then the convolution of the Rice and lognormal densities:

$$p_s(z) = \int p(z \mid a)p(a)\, da \tag{12}$$

Barts and Stutzman[6] have taken this problem a step further by assigning a probability S that the user is shadowed in the course of travel down a road. During the shadowed condition, the probability density is $p_s(z)$. The signal level has an unshadowed probability density $p_u(z)$ for the remaining fraction $1 - S$ of the time. The composite signal probability density is then as follows:

$$p_c(z) = Sp_s(z) + (1 - S)p_u(z) \tag{13}$$

The coefficients of these probability densities can be fit to measured data to give reasonably good models for the measurements.

The Loo probability density from Eq. (12) is as follows:

$$p_s(z) = \frac{2z}{\alpha\sigma\sqrt{2\pi}} \int_0^\infty \frac{1}{a} I_o\left(\frac{2za}{\alpha}\right) \exp\left[\frac{-(ln\ a - \mu)^2}{2\sigma^2} - \frac{a^2 + z^2}{\sigma}\right] da \tag{14}$$

where α is the Rayleigh parameter; and μ, σ are the lognormal mean and sigma. This density is rather cumbersome to use. Barts and Stutzman[6] have suggested an approximation to the Loo density for the envelope of the shadowed signal. Their power–law approximation to the shadowed propagation fade distribution is then as follows:

$$P_s(F) \cong \left(\frac{50 - F}{V_1}\right)^{V_2} \tag{15}$$

where

$$V_1 = -0.275\, \overline{K} + 0.723\mu + 0.336\sigma + 56.979$$

$$V_2 = [-0.006\, \overline{K} - 0.008\mu + 0.013\sigma + 0.121]^{-1}$$

where in the expression all parameters $\overline{K}$, μ, σ are expressed in dB, and $P_s(F)$ is the probability that the fade F in dB is exceeded. We have defined $\overline{K} = 10 \log(1/\alpha)$ dB.

A similar approximation was given for the unshadowed Ricean distribution:

$$p_u(z) = p_{\text{Rice}}(z) = \frac{2z}{\beta} \exp\left[\frac{-(z^2 + a^2)}{\beta}\right] I_o\left(\frac{2za}{\beta}\right) \tag{16}$$

where B is the mean square value of the Ricean distribution of r; and C is the amplitude of the direct component. Define $K = 10 \log(a^2/\beta)$ dB. The approximation of Barts and Stutzman[6] is as follows:

$$P_u(F) \cong \exp\left[\frac{-(F + u_1)}{u_2}\right] \tag{17}$$

where

$$u_1 = 0.01K^2 - 0.378K + 3.98$$

$$u_2 = 331.35\ K^{-2.29}$$

and $P_u(F)$ is the probability or fraction of time that a given fade depth F in dB is exceeded.

III. Measured Models—Satellite Attenuation Data

Fade statistics for mobile users in suburban, rural/forested, rural/farmland, mountainous terrain, and tree-lined roads have been measured by a number of investigators. A set of data taken at the moderately low elevation angle of 19 deg is shown for a variety of environments in Fig. 9. Note again that for GPS applications, we generally want access to satellites at low elevation angles for low GDOP, as well as access to a satellite at zenith. As can be seen, fades of 8 dB or more are possible for a reasonable fraction ($\approx$10%) of the time in suburban areas. Fades of 20 dB or more are encountered 1% of the time for suburban and rural forested regions at this low 19-deg elevation angle. It should also be pointed out that there can be a rapid spatial fluctuation in the fading. The deeper fades generally have considerable variation ($\approx$5 dB) for movements of the receiver as small as 2 m for forested roadways.

At higher elevation angles where line-of-sight propagation (unshadowed) is maintained, the attenuation (caused by multipath scattering) is significantly less.

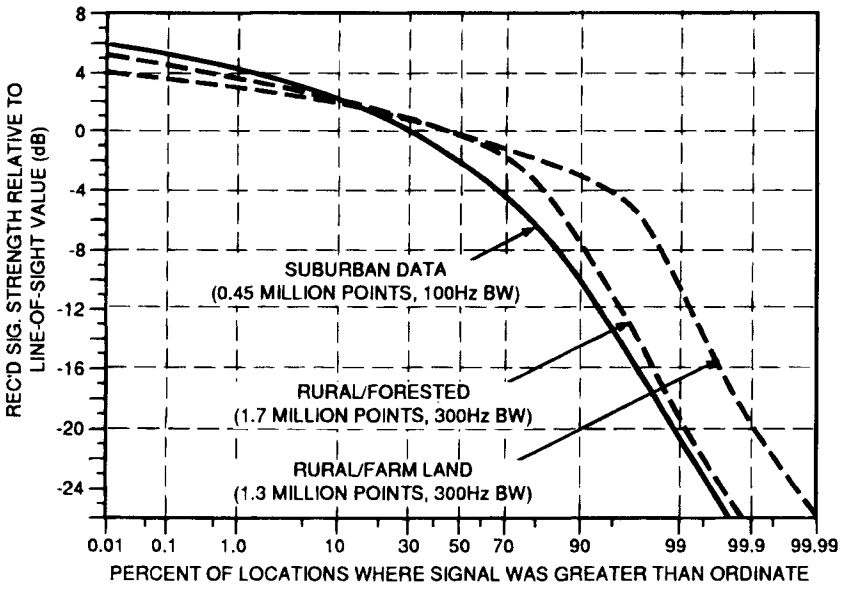

Fig. 9 Measurements of *L*-band propagation statistics for mobile users on land for various environments at an elevation angle of 19°. These plots are based on data from Kent.[8]

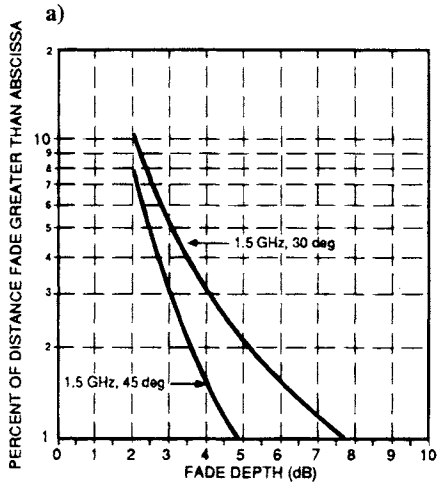

Best power curve fit cumulative fade distributions for line-of-sight configurations in mountainous terrain. The cumulative fade distribution probability P for this power law approximation is of the form

$$P = aF^{-b}$$

where F is the fade in dB and where a, b are

	E	
	30°	45°
a	33.19	39.95
b	1.710	2.321

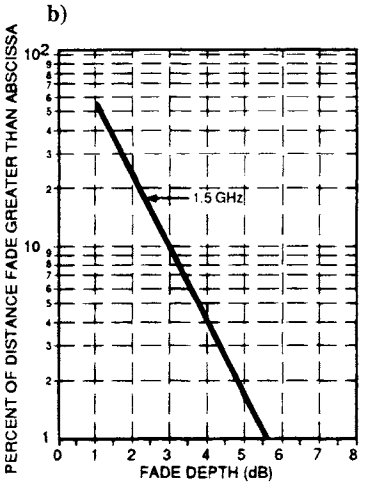

Best exponential fit cumulative fade distributions for line-of-sight configurations on tree-lined roads. The best exponential fit is of the form

$$P = u \exp(-vF)$$

where

$u = 125.6$

$v = 1.116$

are the best u, v values for moderately high elevation angles when averaged over measurements at E = 30°, 45°, 60°

Fig. 10 Unshadowed line-of-sight measurements of *L*-band fade distributions for mobile users on land for various environments and elevation angles. Multipath reflections cause the fading: a) line-of-sight model for mountainous terrain; b) line-of-sight for tree-lined roads. These plots are based on data from Goldhirsh and Vogel.[14]

Figure 10 shows best fit empirical cures at the GPS L_1 frequency 1.5 GHz. The 1% fade depth was about 5 dB for either tree-lined roads or mountainous terrain (with an elevation angle of 45 deg).

A. Measured Fading for Tree-lined Roads—Mobile Users

Numerous measurements have been made worldwide on fading depth as a function of elevation angle as a vehicle is driven around various tree-lined roads. Figure 11 shows a summary of a selected set of these measurements. These measurements include the following:

1) Bundrock and Harvey,[9] Melbourne, Australia—1.55 GHz tree-lined road with 85% tree incidence

2) Butterworth and Mott,[10] Ottawa, Canada—1.5 GHz, 19 deg elevation angle, rural, forested, hilly terrain with immature timber with occasional cleared areas, two-lane road with good shoulders

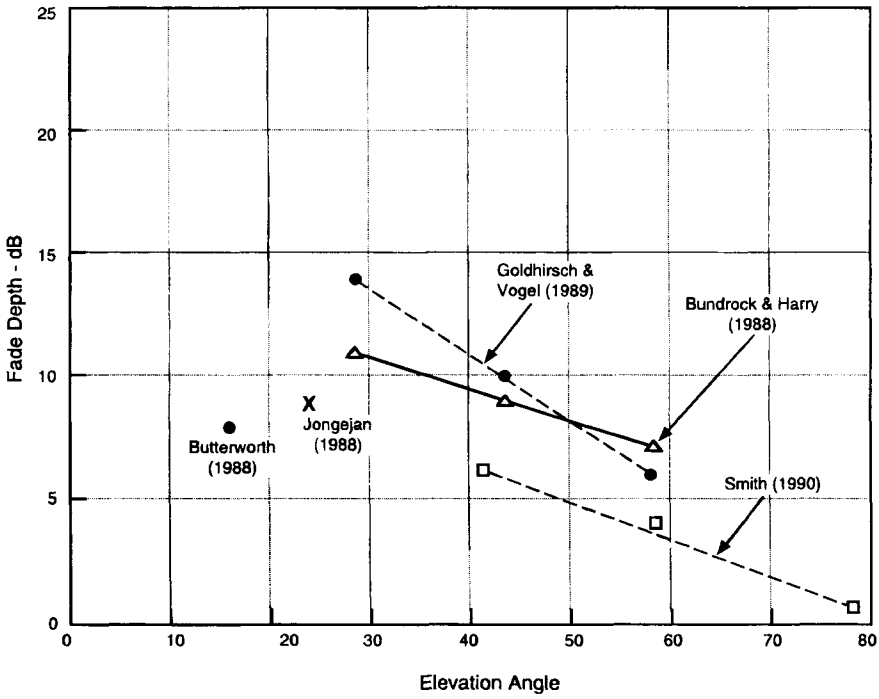

Fig. 11 Summary of various measurements of fading depth for tree-lined roads for 10% probability of the fade level being exceeded.

3) Jongejans et al.,[11] Belgium, 1.5 GHz—hilly Ardennes with roadside lined with bare trees in winter

4) Smith et al.,[12] England—rural, tree-shadowed environment with trees with full leaf cover, *L*-band

5) Goldhirsh and Vogel[3]—forested roads in Maryland, two- and four-lane highways

In general, the 1% fade points are substantially higher by as much as a factor of two in the dB fade level; i.e., a 10 dB fade for 10% might increase to 20 dB for the 1% mark.

These measured data were generally taken with circularly polarized signals of narrow bandwidth. Reference 13 showed that measurements made in a pine forest for vertical and horizontal polarization showed little difference between the two polarizations and concluded that that type of forest at least is approximately an isotropic medium.

References

[1]Goldhirsh, J., and Vogel, W. J., "Propagation Effects for Land Mobile Satellite System: Overview of Experimental and Modeling Results," NASA Ref. Pub. 1274, Feb. 1992.

[2]Loo, C., "A Statistical Model for a Land Mobile-Satellite Link," *IEEE Transactions on Vehicular Technology,* Aug. 1985.

[3]Goldhirsh, J., and Vogel, W. J., "Mobile Satellite System Fade Statistics for Shadowing and Multipath from Roadside Trace at UHF and L-Band," *IEEE Transactions on Antenna and Propagation,* April 1989.

[4]Yoshikawa, M., and Kagohara, M., "Propagation Characteristics in Land Mobile Satellite Systems," Thirty-Ninth Annual IEEE Vehicular Technical Conference, May 1989.

[5]CCIR Study Group 1990–1994, "Impact of Propagation Impairments on the Design of LED Mobile Satellite System Providing Personal Communication," CCIR, U.S. WP-8D-14 (Rev. 2), October 1992.

[6]Barts, R. M., and Stutzman, W. L., "Modeling and Simulation of Mobile Satellite Propagation," *IEEE Antenna and Propagation,* April 1992.

[7]Goldhirsh, J., and Vogel, W. J., "Mobile Satellite System Propagation Measurements at L-Band Using MARECS B2," IEEE Trans-Antenna and Propagation, February 1990.

[8]Kent, J. D. B., "A Land Mobile Satellite Data System," International Mobile Satellite Conference, Ottawa, 1990.

[9]Bundrock, A., and Harvey, R., "Propagation Measurements for an Australian Land Mobile-Satellite System," *Proceedings of Mobile Satellite Conference,* 1988.

[10]Butterworth, J. S., and Mott, E. E., "Characterization of Propagation Effects for Land Mobile Satellite Services," International Conference Satellite System for Mobile Communication and Navigation, June 1983.

[11]Jongejans, A. A., et al., "PROSAT—Phase I Report," European Space Agency TR, ISA, STR-216, May 1986.

[12]Smith, H., et al., "Assessment of the Channel Offered by a High Elevation Satellite Orbit to Mobiles in Europe," IEEE Conference on Radio Receiver and Associated Systems, July 1990.

[13]Ulaby, F. T., et al., "Measuring the Propagation Propagation Properties of a Forest Canopy Using Polarimetric Scattermeter," *IEEE Transactions on Antenna and Propagation,* Feb., 1990.

[14]Goldhirsh, J., and Vogel, W. J., "An Overview of Results Derived from Mobile-Satellite Propagation Experiments," Inter. Mobile Satellite Conference, Ottawa, 1990.

Chapter 16

Ephemeris and Clock Navigation Message Accuracy

J. F. Zumberge* and W. I. Bertiger†
Jet Propulsion Laboratory, California Institute of Technology, Pasadena, California 91109

IN this chapter, we discuss the accuracy of the ephemeris and clock corrections contained in the Global Positioning System (GPS) navigation message. We first provide a brief description of how the Control Segment generates these quantities. Next, we compare them with results from precise (non-real-time) solutions of satellite parameters derived from the simultaneous analysis of data from a globally distributed network of GPS receivers. Finally, we cast these accuracies into the form of a user equivalent range error.

I. Control Segment Generation of Predicted Ephemerides and Clock Corrections

One of the primary purposes of the Control Segment (Chapter 10, this volume) is to generate predicted satellite ephemerides and clock corrections, which are regularly uploaded to the satellites. The predictions are then included as part of the 50-b/s 1,500-bit navigation message (Chapter 4, this volume) that modulates the transmitted GPS signal. Ground receivers then use the predictions for real-time estimates of satellite coordinates and clock corrections.

Data used for the predictions are acquired from receivers situated at precisely known locations in Hawaii, Colorado, Ascension Island in the Atlantic Ocean, Diego Garcia in the northern Indian Ocean, and Kwajalein in the western Pacific. The distribution in longitude of these sites (Table 1) is reasonably uniform, allowing continuous tracking of all GPS spacecraft. The sites at Ascension, Diego Garcia, and Kwajalein are capable of transmitting computed navigation message updates to the satellites. Receivers at all stations use cesium oscillators for time stability, and measure dual-frequency phase and pseudorange. Meteorological data are acquired at each station and used to aid in estimation of troposphere

*Member Technical Staff, Satellite Geodesy and Geodynamics Systems Group, Tracking Systems and Applications Section.

†Member Technical Staff, Earth Orbiting Systems Group, Tracking Systems and Applications Section.

Table 1 Tracking stations used by the Control Segment and approximate locations

Site	Latitude	Longitude
Hawaii	21°N	158°W
Colorado Springs[a]	39°N	105°W
Ascension Island[b]	8°S	14°W
Diego Garcia[b]	7°S	72°E
Kwajalein[b]	9°N	168°E

[a]Master Control Station.
[b]Can transmit to GPS satellites.

delay. All data are regularly transmitted to the Master Control Station in Colorado Springs.

Only the P-code pseudorange measurements are used as data in the parameter estimation scheme, which is based on a Kalman filter. Estimated satellite parameters include epoch-state position and velocity, solar radiation pressure coefficients, clock bias, drift, and drift rate. Station parameters include similar clock quantities and troposheric delay. The terrestrial coordinate system and gravity field are 1984 World Geodetic System (WGS-84). The reference time is an average of monitor station clocks and a subset of GPS clocks.

Data going back 4 weeks are used to estimate reference satellite trajectories, which are then used to propagate satellite positions and clock corrections into the future. The first 28 h of prediction are divided into overlapping 4-h fit intervals separated by 1 h. The fit results for each such interval are cast in the format of the navigation message (through a fitting procedure), and are uploaded into the satellites once a day, more frequently if required to meet a 10-m user-equivalent range error specification. The daily upload is based on a data window that closed 45 min prior to the upload.[1–3]

Given the daily upload, the satellite broadcasts satellite positions and clock corrections contained in the appropriate 4-h interval. Although predictions beyond 28 h are also uploaded, they are normally not used, because the next day's upload overwrites them with results derived from more current data.

II. Accuracy of the Navigation Message

This section assesses the accuracy of the information broadcast in the navigation message. The "truth cases" to which the navigation messages are compared are daily GPS solutions, from the Jet Propulsion Laboratory (JPL), of satellite positions and clock corrections. First we describe the daily JPL solutions, including estimates of their accuracies. Next, based on the period 1993 July 4–Oct. 22, we compare these daily solutions with their counterparts from the navigation message. Of course, it must be remembered that one of the key differences between the GPS Control Segment solutions and the truth model is that the GPS solutions are predictions of the future based on past data, whereas the "truth" solutions are based on after-the-fact, postfit smoothed estimates.

A. Global Network GPS Analysis at the Jet Propulsion Laboratory

Since June 1992, analysts at the JPL have regularly reduced GPS data from a globally distributed network of 20–40 precision P-code GPS receivers using the GIPSY/OASIS-II software.[4,5] Shown in Fig. 1 are locations of the sites as of fall 1993. In addition to dense coverage in North America and Europe, there is also reasonable coverage elsewhere, including eight sites in the Southern hemisphere.

Receivers at these sites make measurements of the carrier phase and pseudorange observables on both the L_1 and L_2 bands from GPS satellites, at 30-s data intervals. Data are analyzed daily in 30-h batches, centered on GPS noon. The 6-h overlap centered at each GPS midnight allows for consistency checks between solutions from adjacent days. Prior to parameter estimation, data are edited using the TurboEdit alogrithm[6] and decimated to a 10-min interval.

The model used in the analysis corrects for ionospheric delay (through the formation of the ionosphere-free linear combination of phase and pseudorange observables), tropospheric delay (by stochastic estimation of the wet component at each receiver site), transmitter and receiver phase center offsets, Earth orientation (through explicit estimation of pole position and length of day), solid Earth tides, and relativistic effects. Transmitter and receiver clock corrections are estimated as independent parameters at each sample time. [In the case of selective availability (SA)-affected transmitters, this accounts for the dithering of GPS clocks.] The reference clock is a hydrogen maser driving one of the receivers. Satellite parameters include epoch-state position and velocity, and solar radiation pressure; the latter is estimated stochastically. The Earth-fixed reference frame is defined by adopting fixed locations for eight of the receivers, as specified in the international terrestrial reference frame, ITRF-91.[7,8] The carrier phase biases are estimated as piecewise-constant, real-valued parameters.

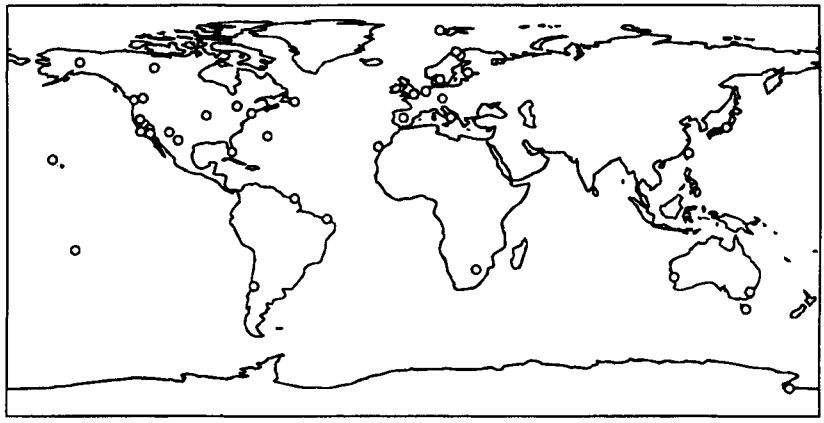

Fig. 1 Global distribution of GPS tracking receivers in the International GPS Service for Geodynamics, fall 1993. In addition to dense coverage in North America and Europe, there is also reasonable coverage elsewhere, including eight sites in the southern hemisphere.

B. Accuracy of the Precise Solution

One assessment of orbit quality from the precise solutions can be made by looking at the continuity of results from adjacent days. For example, the solution for Oct. 7 uses data from 2100 h on Oct. 6 to 0300 h on Oct. 8. Similarly, the solution for Oct. 6 uses data from 2100 h on Oct. 5 to 0300 h on Oct. 7. The difference between these solutions in the position of satellite PRN 12 within ± 3 h of midnight between Oct. 6 and 7 is shown in Fig. 2. The rms variation over the 6-h period is 12 cm, 22 cm, and 25 cm for the radial, cross-track, and along-track components, respectively.

A number of other groups estimate satellite parameters from the same data, using independent software, thus allowing a separate assessment of orbit quality. Shown in Fig. 3 is the comparison of the JPL's orbit solution for PRN12 on Oct. 7, 1993 with that determined by the Center for Orbit Determination in Europe (CODE) at the University of Berne, Switzerland.[9] The vertical scale is the same as that in Fig. 2. The rms difference over the day between the solutions is 7 cm for the radial component, 5 cm for the cross-track, and 9 cm for the along-track. For other days and satellites, this agreement is generally within 20 cm for all components. Comparisons with results from other analysis centers show comparable agreement. To summarize, the precise orbit solutions are typically accurate to 5–30 cm rms, depending on the component and other factors.

A comparison similar to that shown in Fig. 2 is shown for a transmitter clock in Fig. 4. Plotted there is the difference between the Oct. 6 and Oct. 7 solution for the PRN13 clock. The rms difference over the 6-h period is 0.22 ns, of which a portion is attributable to a 0.18-ns bias. This few-tenths-ns rms difference is typical for other satellites and days.

The reference for the precise clock solutions is the maser-based receiver at Algonquin Park, Canada, maintained by the Geodetic Survey Division of Canada's Department of Energy, Mines and Resources. This clock is adjusted periodically,

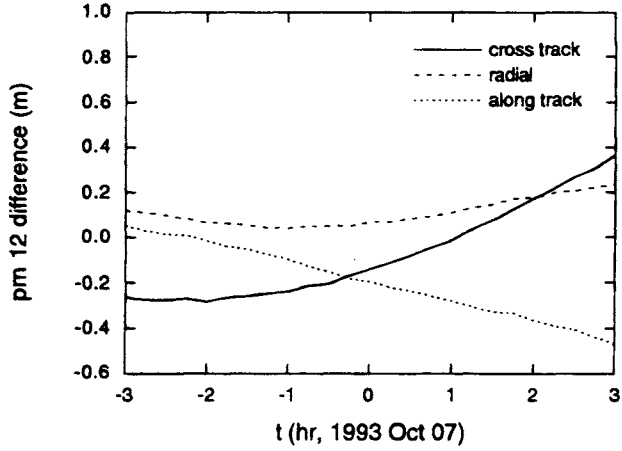

Fig. 2 Difference near the midnight boundary between the JPL's precise solutions of Oct. 6, 1993 and Oct. 7. The rms differences are 0.12 m, 0.22 m, and 0.25 m in the radial, cross-track, and along-track components.

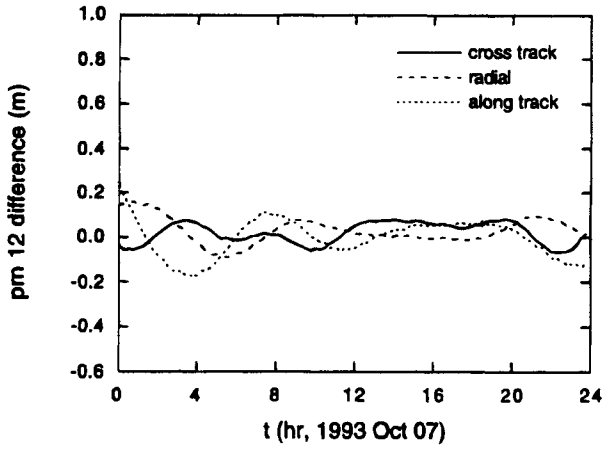

Fig. 3 Comparison of the precise solution from the JPL with that from the CODE (University of Berne), for PRN 12 on Oct. 7, 1993. The rms values over the day (which include both the bias and the variation) are 0.07 m for the radial component, 0.05 m for the cross-track, and 0.09 m for the along-track. The agreement between the JPL and CODE for this satellite and day is somewhat better than typical. However, for other satellites and days the agreement is, with few exceptions, at least as good as a few tens of centimeters.

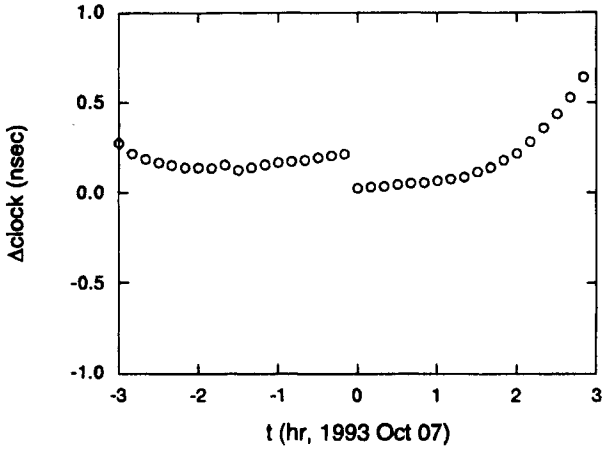

Fig. 4 Difference in the clock solution for PRN 13 from the Oct. 6, 1993 solution and the Oct. 7, 1993 solution. The rms value over the 6-h overlap is 0.22 ns (of which a portion is attributable to a 0.18-ns bias).

and is believed accurate with respect to GPS time to within a few hundred ns, with drift magnitudes of no more than a few tens of ns per day.[10] Of course, biases and drifts in the reference clock will be masked in a comparison such as Fig. 4, but would appear in a comparison between the navigation message and the precise solutions.

C. Comparison of Precise Orbits with Broadcast Ephemerides

Fig. 5 shows the position difference between the JPL precise solution and the broadcast orbit for satellite PRN 12 on Oct. 7, 1993. The interval between updated navigation messages typically is one hour. The satellite and day are the same as in Figs. 2 and 3, although the vertical scale is 10 times larger. The rms values over the day are 0.56 m for the radial component, 1.67 m for the cross-track, and 2.67 m for the along-track.

Similar calculations have been made for all satellites and days over the period July 1, 1993 through Oct. 22, 1993 (a total of 2490 satellite days). For the given satellite and day, the rms difference over the day between the broadcast ephemeris and the precise solution is computed, for each of the three components. The results are summarized in Fig. 6.

Figure 6 contains three histograms, one for each of the position difference components. The median values in the above distributions are 1.3 m for the radial component, 3.6 for the cross-track, and 4.7 m for the along-track. Thus, half of the satellites and days over the ~4-month period had a daily rms agreement between the navigation message and the precise solution of less than 1.3 m in the radial component.

The reference frame ITRF-91 used for the precise solutions differs from the 1984 World Geodetic System (WGS-84) used by the broadcast ephemeris. To test how much this reference-frame difference contributes to the observed

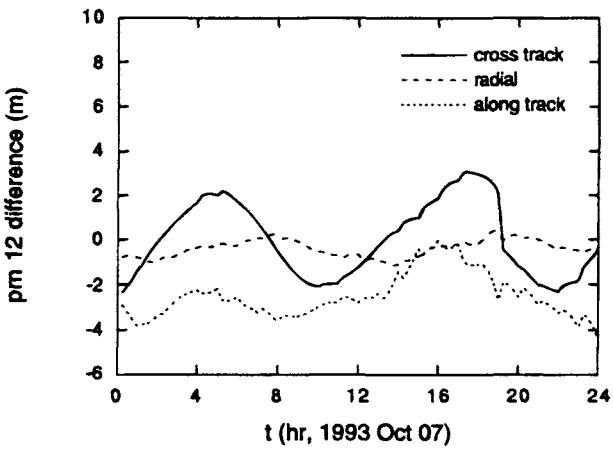

Fig. 5 Comparison of the GPS broadcast ephemeris in the navigation message with the JPL's precise solution, for PRN 12 on Oct. 7, 1993. The rms values over the day are 0.56 m for the radial component, 1.67 m for the cross-track, and 2.67 m for the along-track. The vertical scale is 10× that of Figs. 2 and 3.

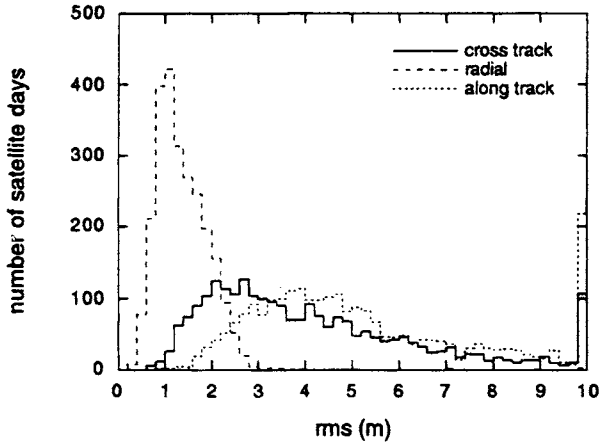

Fig. 6 Comparison of the GPS broadcast ephemeris with precise orbital solutions for the period July 4, 1993 through Oct. 22, 1993. An "event" in one of the three histograms corresponds to a single satellite on a single day (as in Fig. 5). For the given satellite and day, the rms difference over the day between the broadcast ephemeris and the precise solution is computed, for each of the three components. The median values in the above distributions are 1.3 m for the radial component, 3.6 m for the cross-track, and 4.7 m for the along-track. If a daily seven-parameter transformation is applied to align the navigation message reference frame with that of the precise solution, the medians are marginally reduced to 1.2 m, 3.2 m, and 4.5 m.

difference in ephemerides, consider the 7-parameter transformation defined by $x' = (1 + \epsilon)\, x + T + \Theta\, x$, where T is a translation vector, ϵ a scale factor, and

$$\Theta \equiv \begin{pmatrix} 0 & \theta_z & \theta_y \\ \theta_z & 0 & -\theta_x \\ -\theta_y & \theta_x & 0 \end{pmatrix}$$

is a rotation matrix. The difference between x and x' can be thought of as arising from 1) a shift or translation T; 2) a change in orientation, characterized by Θ; and 3) an overall expansion or contraction, characterized by ϵ.

The calculations that resulted in Fig. 6 were repeated, but each day a transformation was applied to all coordinates in the broadcast message. The parameters were chosen to minimize $\Sigma_{pct}\,[\Delta^2_{pct}]$ where $\Delta_{pct} \equiv X_{pct} - x'_{pct}$ is the difference at time t between the precise orbit (X_{pct}) and the transformed broadcast orbit (x'_{pct}) for PRN p and Cartesian component c.

The median values of the daily rms differences in the radial, cross-track, and along-track components are reduced to 1.2 m, 3.2 m, and 4.5 m, respectively, from the values corresponding to Fig. 6. The values of the transformation parameters are given in Table 2, and Fig. 7 shows the daily values of the scale factor.

There are two known effects which would contribute to the scale factor parameter ϵ. The first is that the precise orbits refer to the spacecraft center

Table 2 Parameters in the transformation from the broadcast ephemeris reference frame to that of the precise orbits, based on 120 daily transformations[a]

Parameter	Average	Standard deviation
T_x (cm)	-4.0 ± 2.3	24.7
T_y (cm)	6.3 ± 1.8	19.6
T_z (cm)	-4.6 ± 3.3	36.3
ϵ (ppb)	-12.7 ± 0.2	2.2
θ_x (nrad)	-7.9 ± 3.2	34.9
θ_y (nrad)	-6.8 ± 3.3	35.9
θ_z (nrad)	-125.5 ± 4.3	47.2

[a]The uncertainties in the average values are based on observed daily fluctuations, shown in the third column, divided by $\sqrt{120}$. The most significant parameters are the -12.7×10^{-9} scale factor and the -125.5-nrad rotation around the z-axis.

of mass, whereas the broadcast orbits refer to the spacecraft antenna phase center. Because these points are separated by 0.9519 m, mostly in the radial direction, we could expect a contribution of about $0.9519/(26.55 \times 10^6) \approx +35.9$ ppb to ϵ in the broadcast-to-precise transformation.

Second, the broadcast orbits use the WGS-84 gravity field, with GM = 3.986005×10^5 km^3 s^{-2}, compared with the JGM2 value (Nerem et al.) of 3.986004415×10^5 km^3 s^{-2} used in the precise solutions. Because the radius varies with $(GM)^{1/3}$, we would expect a contribution to ϵ of $-1/3$ $(3.986005 - 3.986004415)/3.986004415 \approx -48.9$ ppb. (The larger value of WGS-84 would put the satellite out further, requiring a negative value of ϵ to bring it into agreement with the precise orbit.) The sum of these expectations, -13.1 ppb, is remarkably close to the observed value of -12.7 ppb in Table 2.

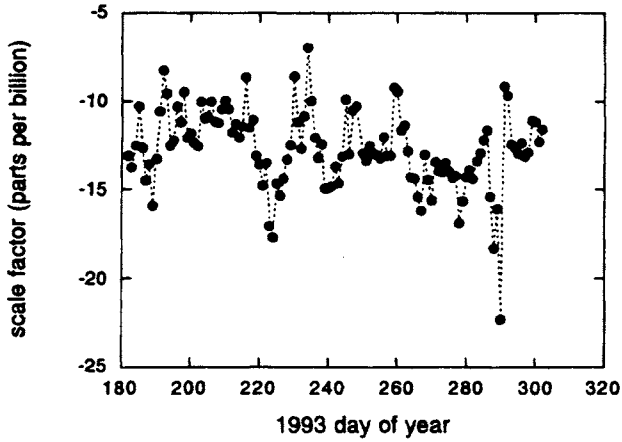

Fig. 7 Scale factor in the transformation from the WGS-84 reference frame to the International Terrestrial Reference Frame. The average value is -12.7 ± 0.2 parts per billion, which corresponds to about -30 cm in the radial direction.

Note that we could use the values in Table 2 to transform WGS-84 coordinates of terrestrial sites to the ITRF-91 reference frame (at epoch midway between July 1 and Oct. 22, 1993), except that ϵ should be taken as $(-12.7 - 35.9)$ ppb $= -48.6$ ppb.

The differences between the precise and broadcast orbits are significantly larger than the accuracies of the precise solutions, as estimated in the previous section. This is not surprising, as the broadcast solutions are, by necessity, the result of an extrapolation in time from hours-old data. The precise solutions, on the other hand, do not have such a real-time constraint. It should also be mentioned that the intentional degradation of broadcast ephemeris quality, one speculated aspect of selectve availability (SA), has not been observed.

D. Comparison of Precise Clocks with Broadcast Clocks

Shown in Fig. 8 are the the clock corrections for PRN 13 on Oct. 7, 1993, as determined by the JPL's precise solution (solid squares) and that from the navigation message (open circles). The interval between points is 30 min. (Points whose estimated uncertainty—"formal error"—exceeds 10 ns in the precise solution are not considered.) The difference between the navigation message and the precise solution is shown in Fig. 9, where the discontinuities in the former are clearly evident.

The GPS satellites on this day can be grouped into two classes depending on the variation over the day in the difference between the precise and broadcast clocks. Figures 9 and 10 contain satellites in the group for which this scatter is of the order of 10 ns. Of the five satellites in this group, three are Block I (PRNs 3, 12, and 13) and two are Block II (PRNs 15 and 20). Note that the time series in Figs. 9 and 10 are reasonably smooth with time.

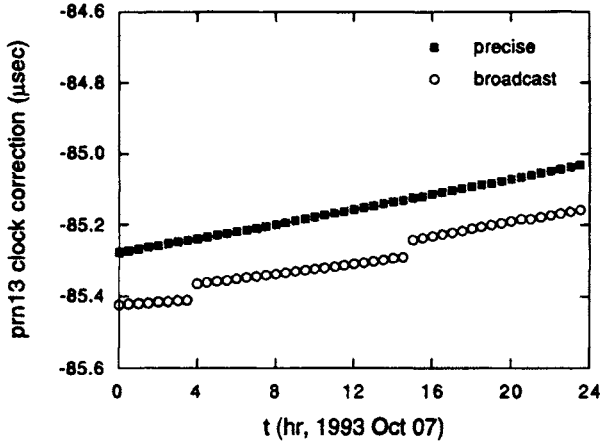

Fig. 8 Clock correction for PRN 13 broadcast in the navigation message (open circles) and determined in JPL's precise solution (solid squares). The precise solution uses a maser-based GPS receiver as its reference. The solid squares describe a slope of about 250 ns/day.

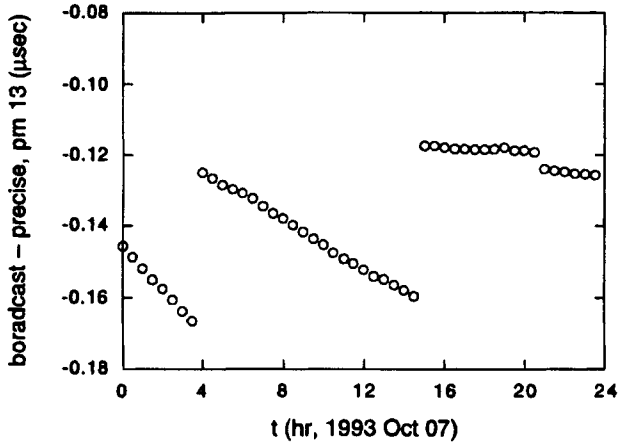

Fig. 9 Difference in the broadcast and precise clock corrections for PRN 13. The discontinuities are attributable to new broadcast messages, as indicated in Fig. 8.

The second class consists of satellites for which the difference is much noisier. All satellites in this group are Block II, and are shown in Fig. 11 as a function of time, together with the histogram that indicates the distribution of the differences. The standard deviation of the distribution is about 80 ns.

The clock dithering component of SA is clearly evident in this second class and absent from the first class. Note that the biases of the distributions in Figs. 9–11 are all about −120 ns, and thus, represent a constant difference between the GPS reference time and that of the precise solution. This could be entirely attributable to the maser-based reference clock used for the latter.

Similar analyses of GPS clocks were made for all satellites and days from July 4, 1993 through Oct. 22, 1993. For each day and satellite, any linear trend in the difference between the precise solution and the broadcast clock over the day was removed. The standard deviation over the day of the detrended difference has been calculated. The distribution of daily standard deviations is shown in Fig. 12. The median of the lower distribution is 4.5 ns, which represents the nonsystematic component of the broadcast clock error for satellites not affected by clock dithering. The median of the upper distribution is 79.9 ns; this quantifies the effect of clock dithering.

A second, systematic component of clock error arises because of differences among satellites each day in the linear trends. (The *average* trend parameters arise from the difference between GPS system time and the time of the Algonquin maser reference; such a difference is not included here because it will have essentially no effect on user position.) Based on the variations in trend parameters among the non-SA satellites over each day, the median value of this systematic component, over all days in the period being studied, has been calculated to be 10.3 ns. The total clock error for non-SA satellites is thus $(4.5^2 + 10.3^2)^{1/2}$ ns $\approx$ 11.2 ns. For satellites affected by clock dithering it is $(79.9^2 + 10.3^2)^{1/2}$ ns $\approx$ 80.6 ns.

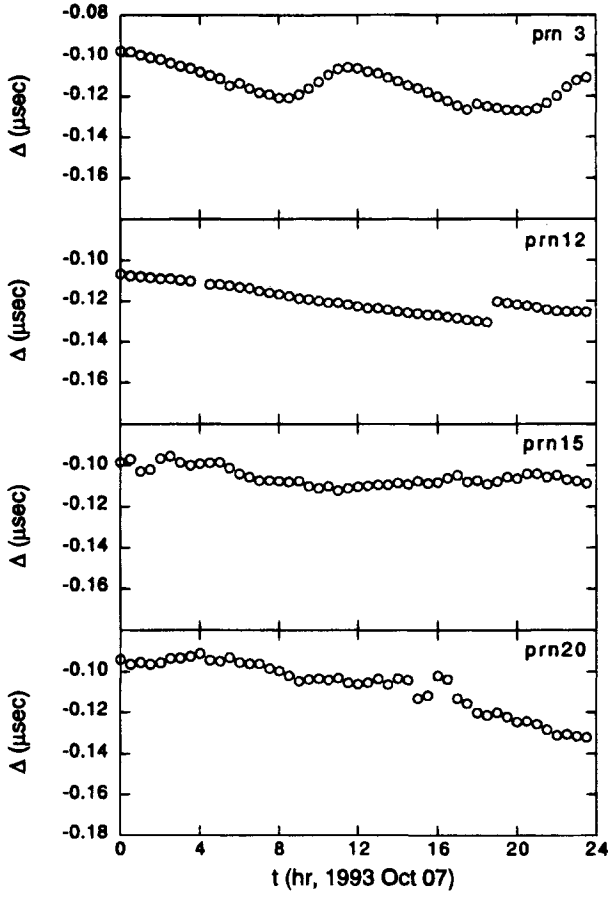

Fig. 10 Difference in the GPS broadcast and precise clock corrections, Δ, for two Block-I spacecraft (PRNs 3 and 12) and two Block-II spacecraft (PRNs 15 and 20). Full scale on each plot is 100 ns. The bias of about −120 ns in all of these (as well as that for PRN 13 in Fig. 9) represents a constant difference between GPS reference time and that of the precise solution.

E. Summary and Discussion

Table 3 compares these results with a prediction[11] of how well the GPS Control Segment would be able to predict clock corrections and GPS ephemerides. The prediction is reasonably consistent with the comparisons between the navigation message and the JPL precise solution, as discussed in this section.

A distribution of differences can be divided into two components: an average (bias) and deviation about that average. Our rms values for orbits include both. Our rms values for orbits include both of these components. Because the transformation from WGS-84 to ITRF will absorb most of the biases, and because the remaining rms values are not reduced much (see Sec. II.C) follow-

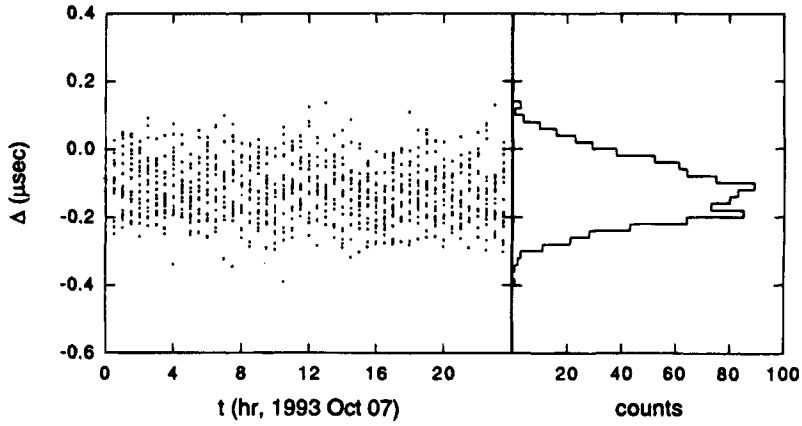

Fig. 11 The effects of clock dithering in SA are shown here, which includes all satellites not shown in Figs. 9 or 10. The distribution of Δ (right) has a standard deviation of about 80 ns and a mean of about −120 ns. (The mean is about the same as those in in Figs. 9 and 10.)

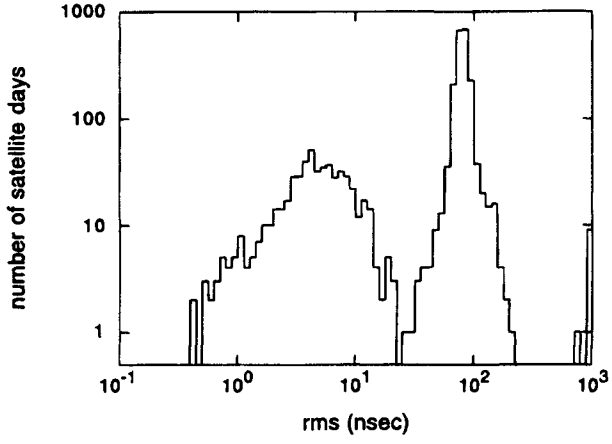

Fig. 12 Comparison of broadcast clock solution with precise solution, for each day and satellite during the period July 4, 1993 through Oct. 22, 1993. The bimodal distribution arises from the effects of clock dithering as part of SA. (There are also a handful of satellites and days when there was rather poor agreement between the precise solution and the broadcast clock.) The median value of the lower distribution (clock dithering presumably not in effect, rms de-trended difference over the day between precise solution and broadcast clock less than 25 ns) is 4.5 ns. The median value of the upper distribution is 79.9 ns.

Table 3 GPS Control Segment performance, predicted and observed

Parameter	Prediction	Observed
Radial (σ_r)	0.8 m	1.2 m
Cross-track ($\sigma_\dagger$)	3.0 m	3.2 m
Along-track (σ_a)	6.3 m	4.5 m
Clock (no SA) (σ_t)	7.7 ns	11.2 ns
Clock (with SA)	—	80.6 ns

ing the transformation, the dominant component is the deviation and not the bias.

The radial uncertainty, just over a meter, is about a factor of 3–4 less than the cross- and along-track uncertainties. This occurs because the range measurement is more sensitive to changes in the radial dimension than to the other dimensions (see Appendix).

We can cast the performances from Table 3 into a user equivalent range error $\sigma_u : \sigma_u^2 = k_r\sigma_r^2 + c^2\sigma_t^2 + k_\rho\rho_{rt}\sigma_r c\sigma_t + k_{\dagger a}(\sigma_\dagger^2 + \sigma_a^2)$. Here, ρ_{rt} is the correlation coefficient between the radial and clock errors; c is the speed of light; and $\sigma_\dagger$, σ_a are the cross- and along-track errors. For a satellite at zenith, an error in the radial component maps directly into σ_u (this is always true for the clock error), while cross- and along-track errors do not affect the user range. We expect nominally, then, that $k_r = 1$, $k_\rho = 2$, and $k_{\dagger a} = 0$. We show in the Appendix that $k_r \approx 0.959$, $k_\rho \approx 1.959$, and $k_{\dagger a} \approx 0.0204$ account for the average geometry in the relationship between satellite and user positions.

It is expected that the correlation between radial and clock errors is small, in which case $|\rho_{rt}| << 1$. For completeness, however, we indicate in Table 4 the contributions to σ_u over the range of possible correlations, that is $\rho_{rt} = 0, \pm 1$.

When SA clock dithering is not in effect, the contributions to σ_u from the ephemeris and clock errors are of the same order, and result in $\sigma_u \approx 3$–4 m. The more usual circumstance, however, has clock dithering in effect, in which case the dominant contribution to σ_u is from the 80-ns noise in the broadcast clock, resulting in $\sigma_u \approx 24$ m.

Appendix: User Equivalent Range Error

Choose a spherical coordinate system with origin at the center of the Earth. Suppose a satellite has the following Cartesian coordinates:

Table 4 User equivalent range error (meters)

					σ_u		
	σ_r	$c\sigma_t$	$\sqrt{(2\sigma_r c\sigma_t)}$	$\sqrt{[k_{\dagger a}(\sigma_\dagger^2 + \sigma_a^2)]}$	$\rho_{rt} = -1$	$\rho_{rt} = 0$	$\rho_{rt} = +1$
No SA	1.2	1.3	1.8	0.8	0.7	1.9	2.6
With SA	1.2	24.0	7.6	0.8	22.8	24.0	25.1

$$\begin{pmatrix} X \\ Y \\ Z \end{pmatrix} = \begin{pmatrix} r \sin\Theta \cos\Phi \\ r \sin\Theta \sin\Phi \\ r \cos\Theta \end{pmatrix}$$

and an observer on the Earth has the following Cartesian coordinates:

$$\begin{pmatrix} x \\ y \\ z \end{pmatrix} = \begin{pmatrix} r_e \sin\theta \cos\phi \\ r_e \sin\theta \sin\phi \\ r_e \cos\theta \end{pmatrix}$$

where $r_e \approx 6370$ km, and $r \approx 26{,}550$ km. We use θ and Θ to indicate polar angle, and ϕ and Φ to indicate azimuth.

The user range is $u = \sqrt{(X-x)^2 + (Y-y)^2 + (Z-z)^2} = u(r, \Theta,\Phi,r_e,\theta,\phi)$. Choose the orientation of the axes so that 1) the z-axis intersects the satellite ($\Theta = 0$, nominally); and 2) an increase in Θ at $\Phi = 0$ corresponds to the direction of the resultant of the cross- and along-track uncertainties in the satellite position. (We assume that errors in different orbit components are not correlated.) Then, the user equivalent range error is as follows:

$$\sigma_u^2 = c^2\sigma_t^2 + \left(\frac{\partial u}{\partial r}\right)^2 \sigma_r^2 + 2\frac{\partial u}{\partial r}\rho_{rt}\,\sigma_r c\,\sigma_t + \left(\frac{\partial u}{r\partial\Theta}\right)^2 (\sigma_\dagger^2 + \sigma_a^2)$$

(Note that, at $\Theta = \Phi = 0$, we have $\partial u/\partial X = \partial u/r\partial\Theta$.) Differentiations of $u(r,\Theta,\Phi,r_e,\theta,\phi)$ evaluated at $\Theta = 0$ give the following:

$$\frac{\partial u}{\partial r} = \frac{r - r_e\cos\theta}{\sqrt{r^2 + r_e^2 - 2\,r\,r_e\cos\theta}}, \qquad \left(\frac{\partial u}{\partial r}\right)^2 = \frac{(r - r_e\cos\theta)^2}{r^2 + r_e^2 - 2\,r\,r_e\cos\theta}$$

and

$$\left(\frac{\partial u}{r\partial\Theta}\right)^2 = \frac{r_e^2\sin^2\theta\cos^2\phi}{r^2 + r_e^2 - 2\,r\,r_e\cos\theta}$$

If we assume uniform distribution of positions on the Earth, then we have $p(\theta,\phi)\,d\theta\,d\phi \propto \sin\theta\,d\theta\,d\phi$ as the joint probability distribution of θ and ϕ, for θ less than its maximum value of $\theta_{\max} = \cos^{-1}(r_e/r) \approx 76$ deg. If we average $\partial u/\partial r$, $(\partial u/\partial r)^2$, and $(\partial u/r\partial\Theta)^2$ over $0 \le \theta \le \theta_{\max}$ and $0 \le \phi \le 2\pi$ with this distribution as the weighing function, we obtain $\sigma_u^2 \approx 0.959\,\sigma_r^2 + c^2\,\sigma_t^2 + 1.959\,\rho_{rt}\,\sigma_r\,c\,\sigma_t + 0.0204\,(\sigma_\dagger^2 + \sigma_a^2)$.

References

[1]Shank, C., and Smetek, R., personal communication.

[2]Brown, K. R., Jr., "Characterizations of OCS Kalman Filter Errors," *Proceedings of ION GPS-91,* ION, Washington, DC, Sept. 1991.

[3]Bowen, R., Swanson, P. L., Winn, F. B., Rhodus, N. W., and Feess, W. A., "Global Positioning System Operational Control System Accuracies," *Navigation,* Vol. 32, No. 2, 1985.

[4]Webb, F. H., and Zumberge, J. F., (eds.). "*An Introduction to GIPSY/OASIS II,*" JPL Course Notes, Boulder, CO, JPL D-11088, July 1993.

[5]Wu, S. C., et al., Topex/Poseidon Project: Global Positioning System (GPS) Precision Orbit Determination (POD) Software Design, JPL D-7275, March 1990.

[6]Blewitt, G., "An Automatic Editing Algorithm for GPS Data," *Geophysical Research Letters*, Vol. 17, No. 3, 1990, pp. 199–202.

[7]Boucher, C., Altamimi, Z., Duhem, L., "*ITRF-91 and Its Associated Velocity Field,*" IERS TN 12, Observatoire de Paris, Oct. 1992.

[8]Blewitt, G., Heflin, M. B., Webb, F. H., Lindqwister, U. J., and Malla, R. P., "Global Coordinates with Centimeter Accuracy in the International Terrestrial Reference Frame using GPS," *Geophysical Research Letters,* Vol. 19, No. 9, 1992, pp. 853–856.

[9]Rothacher, M., Beutler, G., Gurtner, W., Brockmann, E., and Mervart, L., "Bernese GPS Software Version 3.4," Documentation May 1993, Druckerei der Universitaet Bern, Bern, Germany, May 1993.

[10]Kouba, J., and Tetreault, P., "International GPS Service for Geodynamics (IGS)," Natural Resource, Canada, Analysis Reports available every week from the IGS Central Bureau at the JPL (access, for example, with lynx http://igscb.jpl.nasa.gov/).

[11]Rusell, S. S., and Schaibly, J. H., "Control Segment and User Performance," *Global Positioning System, Papers published in Navigation, 1980,* The Institute of Navigation, Washington, DC, 1980.

[12]Wells, D., et al., *Guide to GPS Positioning,* Canadian GPS Associates, Fredericton, New Brunswick, Canada, 1986.

Chapter 17

Selective Availability

Frank van Graas* and Michael S. Braasch†
Ohio University, Athens, Ohio 45701

I. Goals and History

SELECTIVE availability (SA) is the intentional degradation of the Global Positioning System (GPS) signal with the objective to deny full position and velocity accuracy to unauthorized users. Selective availability is part of the Standard Positioning Service (SPS), which was formally implemented on 25 March 1990. Although there have been limited periods of time during which the levels of SA were fairly benign, the GPS policy[1] continues to state the following:

> SPS is planned to provide, on a daily basis, the capability to obtain horizontal positioning accuracy within 100 meters (2 drms, 95 percent probability) and 300 meters (99.99 percent probability), vertical positioning accuracy within 140 meters (95 percent probability), and timing accuracy within 340 ns (95 percent probability).

Clearly, this policy indicates that SA will be active, because the performance of GPS without SA would be in the 20-m range for horizontal positioning accuracy (95%).

SA was not part of the experimental design of GPS. However, initial testing of the Coarse/Acquisition (C/A) code during the 1970s revealed accuracies that were much better than anticipated. The C/A code provided 20–30 m position accuracies rather than the predicted accuracy of no better than 100 m.[2] This prompted the DOD to degrade intentionally the accuracy available to unauthorized users. Initially, the level of SA was set at 500 m (95%), but this was changed to 100 m (95%) in 1983. This level of accuracy was chosen because it is comparable with that provided by an on-airport VHF omnidirectional range (VOR) during the nonprecision approach phase of flight.

II. Implementation

The GPS position solution is obtained by solving a set of four or more pseudorange equations (i = 1 through the number of measurements)

*Associate Professor, Department of Electrical and Computer Engineering.
†Assistant Professor, Department of Electrical and Computer Engineering.

$$\rho_i = \sqrt{(X - X_i)^2 + (Y - Y_i)^2 + (Z - Z_i)^2} + (\Delta t_{RCVR} - \Delta t_{sv_i})c \qquad (1)$$

where the unknowns are the receiver position X, Y, Z and the receiver clock with respect to GPS time, Δt_{RCVR}. Propagation delays and other error sources are omitted from Eq. (1). The following parameters are required to solve for the receiver position and clock offset:

ρ_i	measured pseudorange
(X_i, Y_i, Z_i)	satellite position for satellite number i
Δt_{sv_i}	satellite clock offset for satellite i with respect to GPS time

The satellite positions and clock offsets are calculated from the navigation data transmitted by the satellites. Two different methods can be used to deny the full GPS accuracy: 1) manipulation of the navigation message orbit data, also referred to as the ϵ-process; and 2) manipulation of the satellite clock frequency, also referred to as the δ-process or clock dither. Manipulation of the navigation orbit data degrades the accuracy of the calculated satellite positions and results in slowly varying user position errors (periods on the order of hours). Note that the actual satellite orbits are not affected, only the parameters describing the satellite orbits are corrupted. Clock dither, on the other hand, involves the manipulation of the satellite clock itself. This results in fairly rapid errors on the pseudorange measurements with periods on the order of minutes. Because the actual satellite clock is manipulated, clock dither affects both the C/A code and the P code, as well as the integrated Doppler shift measurements.

Although position errors are specified in the GPS policy statement (see previous section), no information is provided with respect to the power spectral density of SA. Therefore, GPS receiver and system designers should anticipate a wide range of possibilities. The next section characterizes SA based on collected data.

III. Characterization of Selective Availability

The SPS provides information on the effects of SA in terms of position and time accuracies, which are summarized in Table 1. Also listed in Table 1 are the corresponding accuracies without SA, which were obtained from the U.S. Naval Observatory Bulletin Board.[3] The bulletin board also provided that frequency stability with SA would be on the order of 1 part in 10^{10}, whereas in the absence of SA, the frequency stability is on the order of 1 part in 10^{12}.

It should be noted that Table 1 provides position and timing accuracies only. No information is provided on the dynamics of the errors. The only way to

Table 1 Standard positioning service position and timing accuracies with and without selective availability

Parameter	With SA	Without SA
Horizontal position	100 m (95%) 300 m (99.99%)	20 m (95%)
Vertical position	140 m (95%)	30 m (95%)
Time	340 ns (95%)	40 ns

determine the dynamics of SA is through actual data collection. Figure 1 represents typical horizontal positioning accuracies of the GPS SPS with and without SA. Without SA, the horizontal position errors are fairly constant over periods on the order of tens of minutes. Position changes without SA are mostly caused by slowly changing propagation delays and satellite clock and ephemeris errors. With SA, the horizontal position "wanders around" within a circle with a radius of approximately 100 m. Successive position errors become uncorrelated after a period of approximately 2–5 min. Similar performance characteristics can be found for vertical positioning and for time transfer.

Although the characterization of SA in the position domain provides helpful information, several shortcomings of just a position domain characterization are quickly recognized.

1) SA is generated in each satellite and seems to be uncorrelated between satellites,[4] which means that the effect on the position accuracy depends on the satellite geometry.

2) The SPS policy assumes that at least 21 satellites are operational; therefore, additional satellite failures could produce larger than normal position errors.

3) No information is provided on velocity and acceleration errors.

4) Differential positioning accuracies are difficult to analyze with only position domain information. These depend on the acceleration of SA, processing time, and the latency of the data link.

5) No information is provided on the power spectral density of SA, which makes it difficult to simulate SA for receiver design and performance analysis purposes.

Because of these shortcomings, a complete analysis of SA-induced errors must start in the range measurement domain. Next, the range domain errors can be converted into positioning and timing errors depending on the application. Figure 2 shows representative, measured SA errors in the range domain. The SA error consists of the sum of a bias component (epsilon error) and a rapidly varying

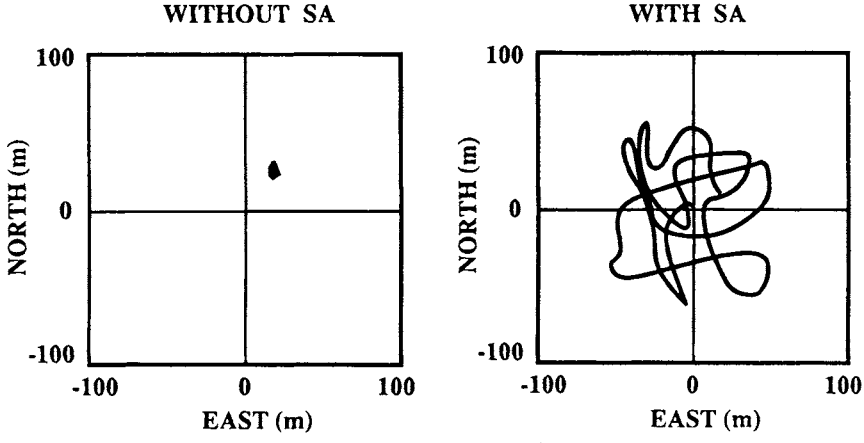

Fig. 1 Horizontal positioning errors with and without selective availability for data collected during a 1-h period.

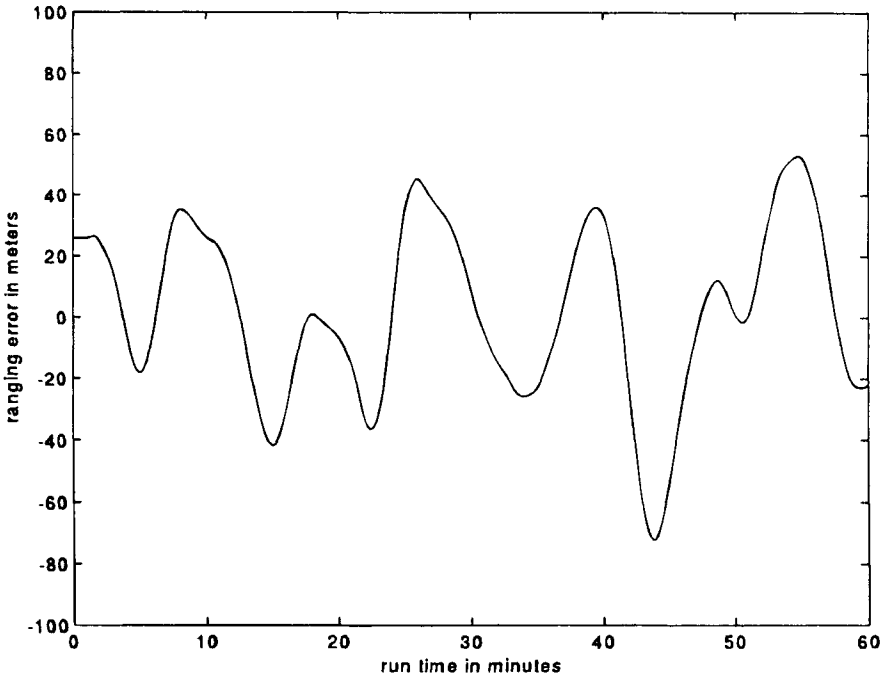

Fig. 2 Representative, measured range selective availability errors.

component (clock dither). The period of the oscillations is on the order of 2–5 min, while the standard deviation is approximately 23 m.

A first-order analysis of SA-induced ranging errors would start with the determination of the one-sigma range, velocity, and acceleration errors. Table 2 provides typical numbers resulting from such an analysis for two cases.[5] Case 1 refers to data collected from PRN 14 on day 124 of 1989, while case 2 represents data collected from both PRN 2 and 14 on day 259 of 1989. The user range accuracies (URA) were set to 32 and 64 m, respectively. The data without SA were collected from PRN 6 (a Block I satellite), while its URA was set to 2–4 m. Kremer et al.[5] gives detailed description of the data-processing techniques used. For both cases, the correlation time of the SA errors was on the order of 180 s. The range biases could either be caused by slow clock dither or by epsilon error.

Table 2 Example of measured line-of-sight range, velocity, and acceleration with and without selective availability

Parameter	One-sigma range	One-sigma velocity	One-sigma acceleration	Range bias
Without SA	1–1.5 m	0.0055 m/s	0.4 mm/s^2	0 m
With SA (case 1)	29 m	0.12 m/s	2 mm/s^2	74 m
With SA (case 2)	38–57 m	0.21 m/s	3.5 mm/s^2	−61–38 m

Further characterization of SA usually focuses on the clock dither. Epsilon errors are effectively simulated by adding random biases to the satellite orbit data. It should be noted, however, that SA could consist of either clock dither or epsilon errors, or both. RTCA, Inc. (formerly known as the Radio Technical Commission for Aeronautics), for instance, simulates epsilon error by adding random biases chosen from a Gaussian distribution with zero mean and a standard deviation of 23 m to the satellite range measurements. These biases are held constant during each GPS receiver test. Methods for identifying the epsilon and dither components of SA can be found in Ref. 6. Epsilon error may be found by comparing the orbits obtained from the broadcast ephemeris and from the postfit precise ephemeris. Dither is obtained by processing the corrections generated in a differential ground reference station.

The next step in the characterization of SA would be to determine the actual power spectral density (PSD) of the signal. This involves the postulation of a model for SA, which then can be used to generate statistically equivalent SA. The first SA model was derived by Matchett in 1985.[7] This model was not derived from actual data, but was deduced from a sample probability distribution curve. The GPS Joint Program Office (JPO) generated SA samples and then computed the distribution curve from these samples. A second-order Gauss–Markov process was postulated, and the coefficients were adjusted until its distribution curve matched the one provided by the JPO. A second-order Gauss–Markov process has also been adopted by Special Committee 159 of RTCA for the purpose of simulating SA errors.[8] The first models obtained from actual SA data were time series models derived by Braasch in 1989 using system identification theory.[9] The resulting models were autoregressive moving average (ARMA) models. Later, Chou implemented a second-order Gauss–Markov process based on measured SA data.[10] At the same time, Chou also provided the formulation for a recursive autoregressive model.[11] Other models of interest were published by Lear et al., who presented several time series and analytical models, also based on measured SA data.[12] Four of the above models are discussed in the following sections. These are the second-order Gauss–Markov model, an autoregressive (AR) model, an analytic model, and a recursive AR model (lattice filter). It should be noted that all of these models simulate clock dither only.

A. Second-Order Gauss–Markov Model

The second-order Gauss–Markov model implementation follows the description provided in Ref. 8. The continuous time model of a second-order Gauss–Markov process is given by the following:

$$\ddot{x}_p + 2\beta\omega_0\dot{x}_p + \omega_0^2 x_p = c \times w \tag{2}$$

where ω_0 = natural frequency; β = damping factor < 1; w = white Gaussian noise; and power spectral density = 1.

The continuous time model given by Eq. (2) can be expressed in the form of a state-space equation:

$$\begin{bmatrix} \dot{x}_p \\ \dot{x}_v \end{bmatrix} = \begin{bmatrix} 0 & 1 \\ -\omega_0^2 & -2\beta\omega_0 \end{bmatrix} \begin{bmatrix} x_p \\ x_v \end{bmatrix} + \begin{bmatrix} 0 \\ c \end{bmatrix} w \tag{3}$$

where $\dot{x}_v = \dot{x}_p$. The corresponding discrete-time state-space equation is then given by the following:

$$\begin{bmatrix} x_p \\ x_v \end{bmatrix}_{i+1} = \begin{bmatrix} \phi_{11} & \phi_{12} \\ \phi_{21} & \phi_{22} \end{bmatrix} \begin{bmatrix} x_p \\ x_v \end{bmatrix}_i + \begin{bmatrix} u_{11} & u_{12} \\ 0 & u_{22} \end{bmatrix} \begin{bmatrix} w_1 \\ w_2 \end{bmatrix}_i \tag{4}$$

where w_1 and w_2 are white Gaussian noise processes with zero mean and unit variance. The elements of the discrete-time state transition matrix are as follows:

$$\begin{aligned} \phi_{11} &= e^{-\beta\omega_0\Delta T}[\cos(\omega_1\Delta T) + \beta(\omega_0/\omega_1)\sin(\omega_1\Delta T)] \\ \phi_{12} &= (1/\omega_1)e^{-\beta\omega_0\Delta T}[\sin(\omega_1\Delta T)] \\ \phi_{21} &= -\omega_0^2\phi_{12} \\ \phi_{22} &= e^{-\beta\omega_0\Delta T}[\cos(\omega_1\Delta T) - \beta(\omega_0/\omega_1)\sin(\omega_1\Delta T)] \end{aligned} \tag{5}$$

where ΔT is in units of seconds.

The error covariance matrix of the white noise is as follows:

$$\begin{bmatrix} Q_{11} & Q_{12} \\ Q_{21} & Q_{22} \end{bmatrix} = \begin{bmatrix} u_{11} & u_{12} \\ 0 & u_{22} \end{bmatrix} \begin{bmatrix} u_{11} & 0 \\ u_{12} & u_{22} \end{bmatrix} \tag{6}$$

in such a way that

$$u_{11} = \sqrt{Q_{11} - Q_{12}^2/Q_{22}} \qquad u_{12} = Q_{12}/\sqrt{Q_{22}} \qquad u_{22} = \sqrt{Q_{22}} \tag{7}$$

The elements of the covariance matrix Q are as follows:

$$\begin{aligned} Q_{11} &= \frac{c^2}{4\beta\omega_0^3}\left[1 - \frac{\omega_0^2}{\omega_1^2}e^{-2\beta\omega_0\Delta T}\left(1 - \beta^2\cos(2\omega_1\Delta T) + \beta\frac{\omega_1}{\omega_0}\sin(2\omega_1\Delta T)\right)\right] \\ Q_{12} &= Q_{21} = \frac{c^2}{4\omega_1^2}[e^{-2\beta\omega_0\Delta T}(1 - \cos(2\omega_1\Delta T))] \\ Q_{22} &= \frac{c^2}{4\beta\omega_0}\left[1 - \frac{\omega_0^2}{\omega_1^2}e^{-2\beta\omega_0\Delta T}\left(1 - \beta^2\cos(2\omega_1\Delta T) - \beta\frac{\omega_1}{\omega_0}\sin(2\omega_1\Delta T)\right)\right] \end{aligned} \tag{8}$$

where

$$\omega_0 = \frac{\sigma_v}{\sigma_x} \qquad c^2 = 4\beta\frac{\sigma_v^3}{\sigma_x} \qquad \omega_1 = \frac{\sigma_v}{\sigma_x}\sqrt{1 - \beta^2} \tag{9}$$

$$\text{time constant: } \tau_d = \frac{1}{\beta}\frac{\sigma_x}{\sigma_v} = \frac{1}{\beta}\frac{1}{\omega_0}$$

$$\text{range sigma: } \sigma_x = \sqrt{\frac{c^2}{4\beta\omega_0^3}} \tag{10}$$

$$\text{velocity sigma: } \sigma_v = \sqrt{\frac{c^2}{4\beta\omega_0}}$$

The power spectral density function specified by RTCA for the above model is given by the following:

$$S(\omega) = c^2/(\omega^4 + \omega_0^4)\ \text{m}^2/(\text{rad/s}) \tag{11}$$

where ω is the frequency in rad/s.

The power spectral density is factored into right-half plane and left-half plane components:

$$S(\omega) = c/[\omega^2 - (2/\sqrt{2})(\omega_0\omega) + \omega_0^2]\ c/[\omega^2 + (2/\sqrt{2})\ (\omega_0\omega) + \omega_0^2] \tag{12}$$

Next, a second-order Gauss–Markov process is created by passing zero mean, unit variance, white Gaussian noise through the filter given by the left-half plane component of the power spectral density. The corresponding realization of the second-order Gauss–Markov process in the time domain is given by Eq. (2), see Ref. 13. From Eq. (2), it is found that the damping factor is given by the following:

$$\beta = 1/\sqrt{2} \tag{13}$$

For simulation purposes, RTCA has proposed the following parameters:

$$\begin{aligned} \omega_0 &= 0.012\ \text{rad/s} \\ c^2 &= 0.002585\ \text{m}^2 \end{aligned} \tag{14}$$

The model then results in the following:

$$\sigma_p = \sqrt{\frac{0.002585}{4\dfrac{1}{\sqrt{2}}0.012^3}} = 23\ \text{m}$$

$$\sigma_v = \sqrt{\frac{0.002585}{4\dfrac{1}{\sqrt{2}}0.012}} = 0.28\ \text{m/s} \tag{15}$$

$$\tau = \sqrt{2}\frac{23}{0.28} = 118\ \text{s}$$

The process outlined in the preceding equations is to be generated for each satellite. The error x_p is the second-order Gauss–Markov process to be added to the "perfect" pseudorange. The error x_v is the first-order Gauss–Markov process to be added to the instantaneous "perfect" pseudorange rate. Initialization of x_p is Gaussian with σ_p, initialization of x_v is Gaussian with σ_v.

For an update period of 1 s, the matrices in Eq. (4) become the following:

$$\Phi = \begin{bmatrix} \phi_{11} & \phi_{12} \\ \phi_{21} & \phi_{22} \end{bmatrix} = \begin{bmatrix} 0.9999284 & 0.9915387 \\ -0.0001428 & 0.9831014 \end{bmatrix}$$
$$U = \begin{bmatrix} u_{11} & u_{12} \\ 0 & u_{22} \end{bmatrix} = \begin{bmatrix} 0.0146771 & 0.0252060 \\ 0 & 0.0504133 \end{bmatrix} \tag{16}$$

Figure 3 shows typical results for the second-order Gauss–Markov model. The range SA is slightly noisier than the actual range SA (see Fig. 2). The range rate SA is adequate for simulation purposes, but it is much noisier than actual range rate SA.

B. Autoregressive Model

This section follows the material presented in Ref. 6. In general, time series models are based on the assumption that the data of interest can be modeled as the output of a linear system (pole-zero filter) driven by Gaussian white noise. Conceptually, the derivation of a time series SA model can be thought of as a two-step process. The first step is to send the SA data through a filter and adjust the poles and zeros, or equivalently, the filter coefficients, in such a way that the output is Gaussian white noise with minimum variance (the output is referred

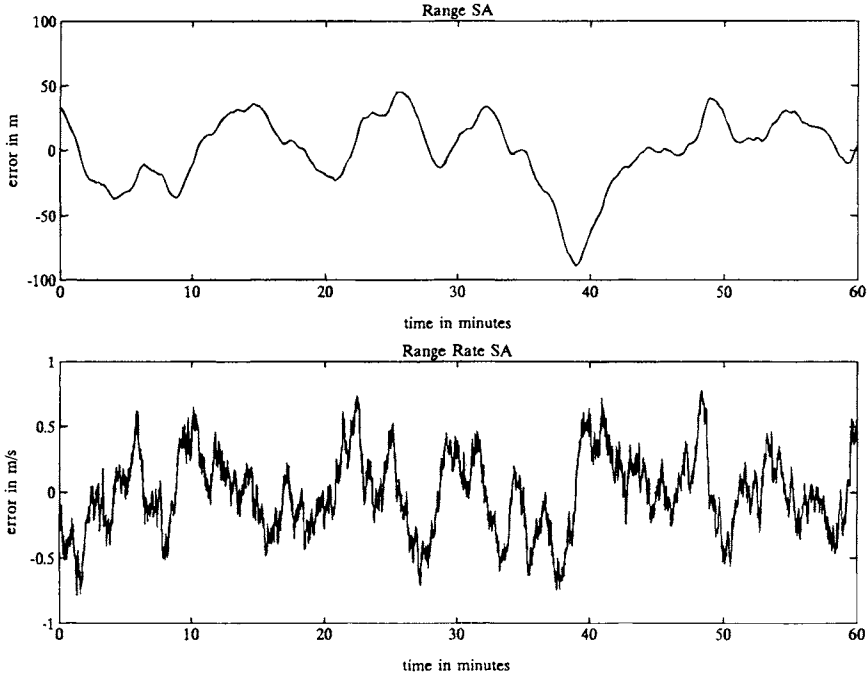

Fig. 3 Selective availability range and range rate errors generated by the second-order Gauss–Markov model.

to as residuals). The second step is to compute the inverse of the filter determined in the first step. Model identification is now complete.[6] Statistically equivalent SA data can then be generated by driving the inverse filter with Gaussian noise, whose variance is equivalent to that of the residuals in the first step. This process is illustrated in Fig. 4. Kelly provides and excellent overview of time series model identification and its application to the problem of microwave landing system (MLS) signal modeling.[14]

Three decisions are inherent in the procedure described in the preceding paragraph. The first is the choice of model (filter) type. Three are possible: 1) a pole-zero filter giving rise to an ARMA model; 2) an all-pole filter yielding an AR model; and 3) an all-zero filter yielding a moving average (MA) model. The second decision is the choice of model order. For example, if an AR model is chosen, how many poles will be used? The third decision is related to the first two and involves determining if a given residual sequence is white.

Because the primary goal is to derive an accurate SA-only model, an AR model type is chosen. This is because ARMA and MA models tend to be noisy. In fact, Braasch[9] concluded that an ARMA model was the best type for the combination of SA and receiver noise. An AR model of order p [referred to as an AR(p)] is defined as follows[15]:

$$x(n) = -\sum_{k=1}^{p} a(k)\, x(n-k) + e(n) \tag{17}$$

where x is the model output; n is the time index; $a(k)$ is the kth filter coefficient;

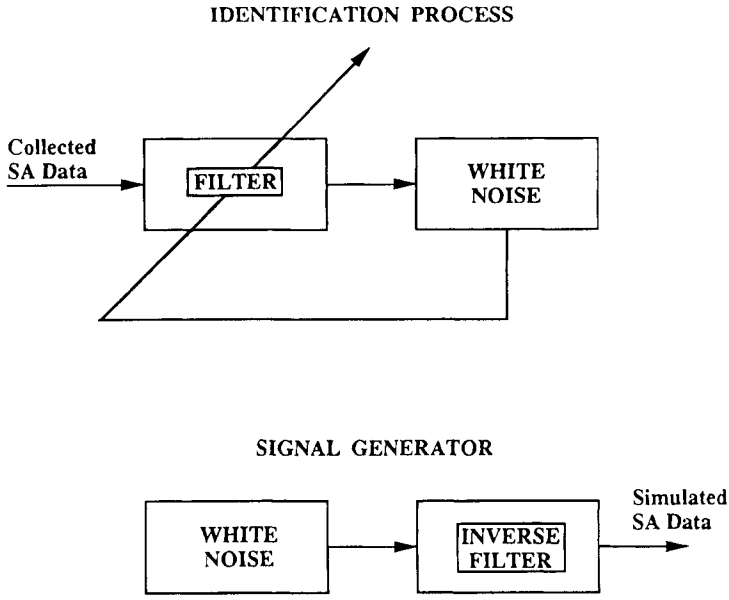

Fig. 4 Characterization of selective availability using system identification theory.

and e is the input Gaussian white noise. Note that SA models derived from data will operate at the same rate as the data collection rate.

Once having made the decision to use an AR model type, the rest of the process involves finding the optimum model order and coefficients (pole locations). For a given model order, many methods exist for optimizing the coefficients.[15–17] The one chosen is the modified covariance or forward–backward method. The second name stems from the fact that the optimization criterion is the minimization of forward and backward prediction errors. As shown later, this method performs quite well with SA data.

Several methods exist for model order selection. The majority of these have been developed for extremely short data records. The main issue is that we want to derive a model for the underlying statistical process that gave rise to the data. When model orders are selected that are too high (i.e., approaching the number of data points in the sample), the result is a "fit" of the sample data record rather than the underlying statistical process. The model order selection method used in this study is known as the Principle of Parsimony—the simplest acceptable model is the one chosen. An acceptable model is the inverse of the filter that outputs white noise when driven with SA. Note that if the model order is too low, the residuals will not be white, although the coefficients have been optimized.

The model identification, therefore, proceeds as follows. For a given sample of SA data, the coefficient is optimized for a first-order filter, and the residuals

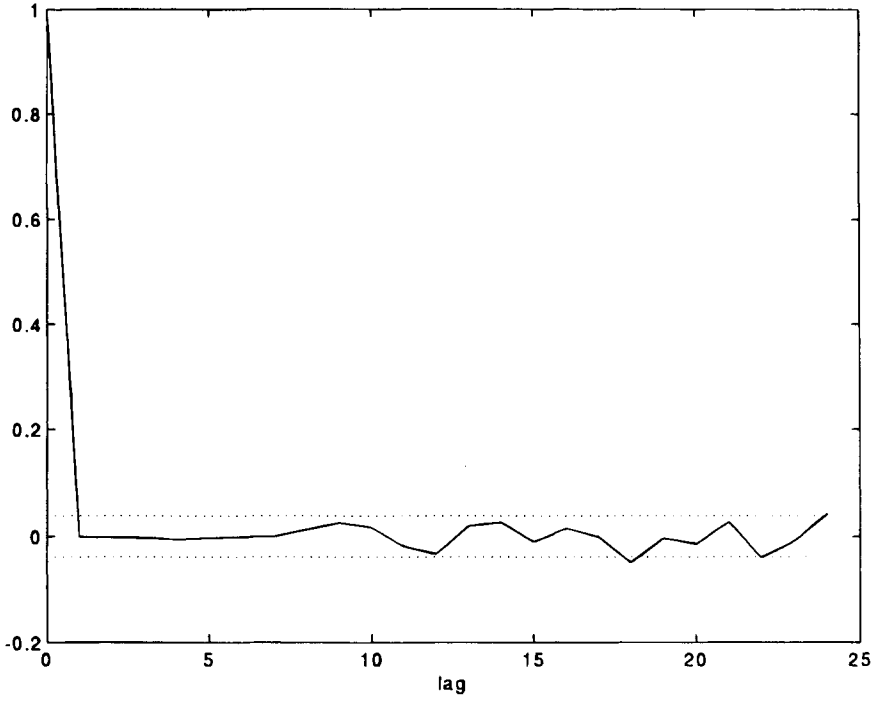

Fig. 5 Autocorrelation function of residuals for satellite 28.

are examined. If they are not white, then the coefficients for a second-order filter are optimized, and the residuals are examined again. The process is repeated until the model order and optimum coefficients are found for which the residuals are white. This process was performed for a variety of SA data sets. Depending upon the data set, models of either 9 or 11 coefficients were derived.

The method for determining whiteness involves examination of the autocorrelation function. An example is given in Fig. 5 where the autocorrelation function is plotted for the residuals from the SA data of satellite 28. Ideally, the autocorrelation function of white noise has a spike at lag zero and is zero everywhere else. However, this can be obtained only for infinite length sequences. As a result some minor "sidelobes" will occur at lags other than zero for white noise sequences that are finite. The dotted lines in the figure represent the 99% confidence intervals for the sidelobes. As can be seen in the plot, the sidelobes lie inside the confidence intervals for the most part, and thus the model is acceptable.

Further validation of the model can be performed by generating some waveforms and comparing the PSDs of the generated and collected data. An example is shown in Figs. 6 and 7. Figure 6 shows the waveform generated by the SA model derived from the SV 28 data. Note that if we compare the waveform to that of the collected data (Fig. 2), they are not the same; however, they are statistically equivalent. That is, the periods and amplitudes of the generated data are the same as for the collected data. This is better illustrated in Fig. 7 where the PSDs of the two waveforms are plotted. The lower line represents the collected

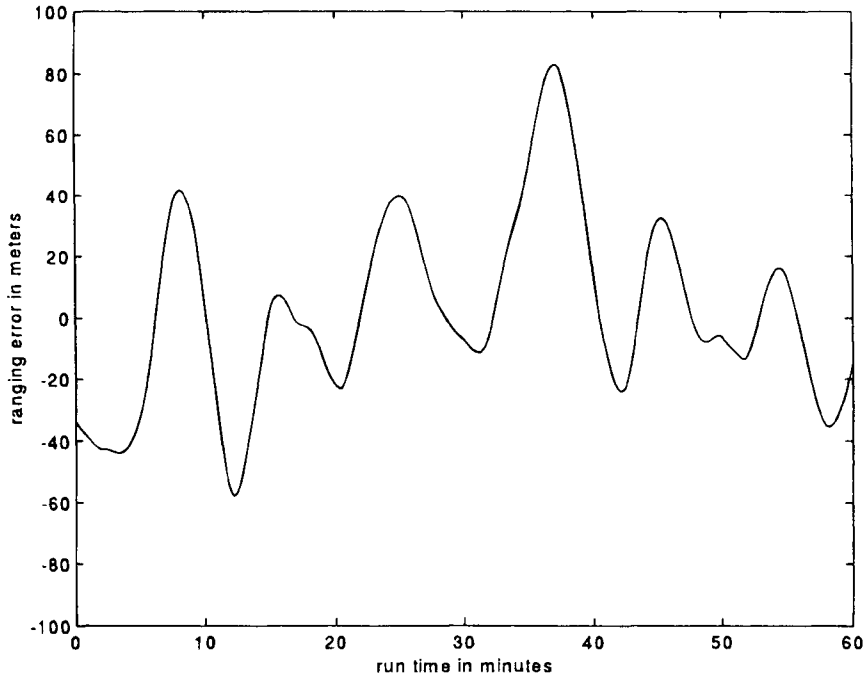

Fig. 6 Example selective availability model output for satellite 28.

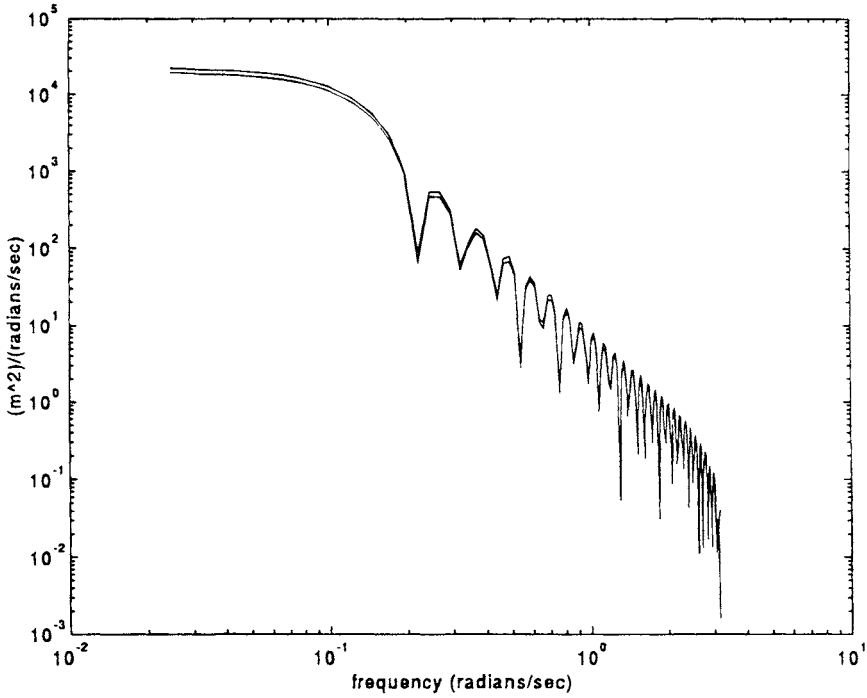

Fig. 7 Power spectral density functions of modeled and measured selective availability for satellite 28.

data, and the upper line represents the generated waveform. Power spectral density comparisons were performed on all of the models derived from the data. In each case, the result was similar to that shown here.

A final step in model validation concerns the power in the residuals. Recall that in step one of the model derivation process, the goal was to find a filter that output white noise (residuals) with minimum variance when driven with SA. The need for minimum variance is important from both a theoretical and practical viewpoint. Theoretically, having residuals with minimum variance means that the filter has been optimized and embodies the structure (i.e., correlation or information) of the SA. Kelly[14] refers to this as the filter "explaining" the data. However, from a practical viewpoint, minimum variance is also required. This is particularly true when trying to model random, yet smooth, waveforms such as SA.

Figures 8 and 9 illustrate the success of the AR model type in this respect. The residuals plotted in Fig. 8 have a standard deviation of 4.12 mm (4.12×10^{-3} m). Because this represents the amplitude of the noise driving the model [see Eq. (17)], it follows that any noise-like behavior in the generated SA waveforms will be negligible. This is verified in Fig. 9, which shows the smooth waveform of the generated SA over a short time interval.

A typical set of AR coefficients and the variance of the white noise input for

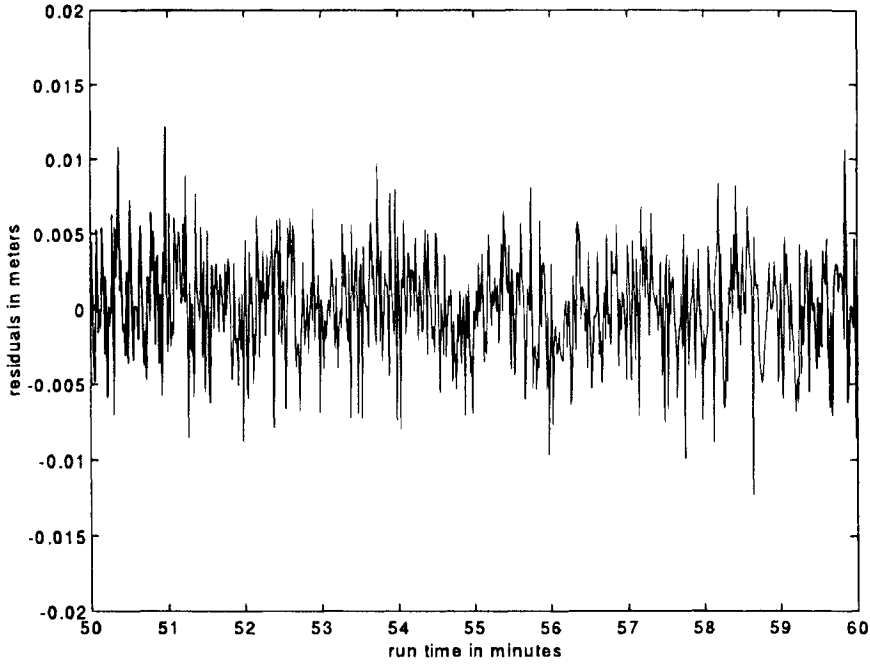

Fig. 8 Residuals for satellite 28.

data collected at a one-second update rate are given below:

$$
\begin{aligned}
a(1) &= -1.36192741558063 \\
a(2) &= -0.15866710938728 \\
a(3) &= +0.13545921610672 \\
a(4) &= +0.21501267664869 \\
a(5) &= +0.30061078095966 \\
a(6) &= -0.12390183286070 \\
a(7) &= +0.10063573000351 \\
a(8) &= +0.02694677520401 \\
a(9) &= -0.12898590228866 \\
a(10) &= +0.05083106570666 \\
a(11) &= -0.05600186282898
\end{aligned}
$$

$$\sigma_e^2 = 1.6993 \times 10^{-5}\ (\mathrm{m}^2)$$

where σ_e^2 is the variance of the Gaussian white noise input. These particular coefficients were derived from data collected from SV 28 during the first week of December 1992. Data from other satellites were found to produce similar results. The seemingly excessive number of significant figures are required to ensure filter stability.

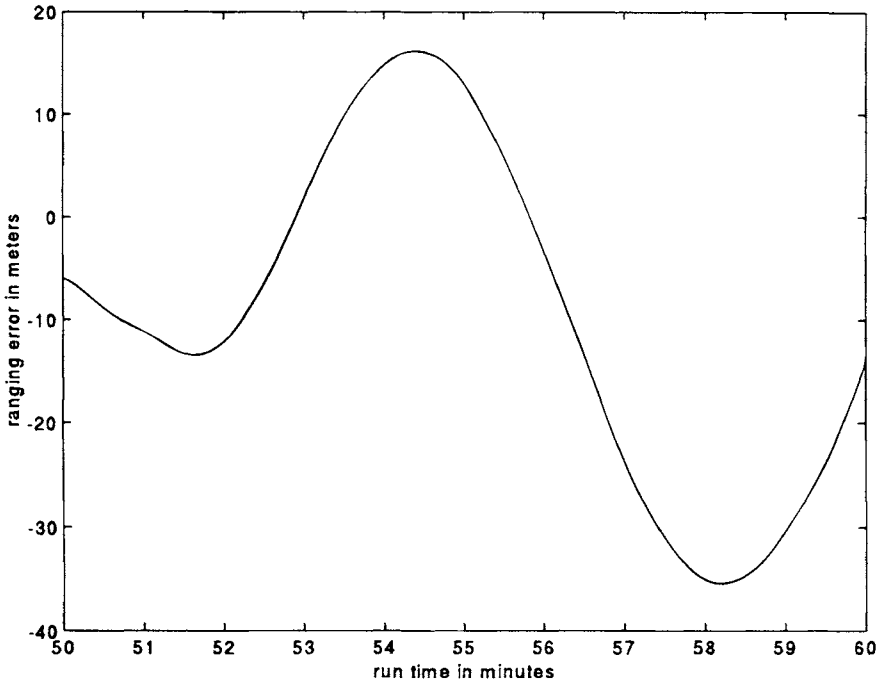

Fig. 9 Modeled selective availability for satellite 28—expanded scale.

C. Analytic Model

Lear et al. present several time series and analytical models in their 1992 paper.[12] Only one of the analytical models is discussed here because of its uniqueness. The term *analytic model* refers to "a piecewise smooth differentiable stochastic process with randomness appearing through the coefficients or model parameters".[12] These parameters are kept constant for randomly selected time intervals. The Rater analytic SA model was developed by observing data from satellite 19 on day 71 of 1992. Using low-noise integrated Doppler shift measurements and ionospheric corrections, the observed raw range was differenced twice. Data differenced once provided smooth pseudorange rate data, while the data differenced twice provided noisy pseudorange acceleration data. Rater observed that the second differences resemble connected ramps of varying slopes. This would imply that the third derivative (jerk) would consist of random steps. The third difference was too noisy, however, to show this behavior.

The Rater analytic SA model uses two randomly selected time intervals from uniform distributions. A constant jerk value is calculated for each time interval based on the length of the interval. The jerk is then integrated three times to obtain the range domain errors. Next, two of these waveforms (independently generated) are added together to obtain the range SA. In detail, the Rater model proceeds as follows:

1) Generate $x_1(t)$: Select the time duration T_1 of x_1 from a uniform distribution (100,700 s). Next, select the time constant τ_1 from a uniform distribution (0,

$T_1/2$ s) where τ is the period of time during which the jerk level is zero. This period is preceded by a jerk level of $+A_1$ and followed by a jerk level of $-A_1$. The jerk level A_1 is calculated from the following:

$$A_1 = -\ddot{x}_1(0)(2T_1 + \tau_1)/T_1(T_1 + \tau_1) \tag{18}$$

where $x_1(0) = \dot{x}_1(0) = 0$, and $\ddot{x}(0) = 4$ mm/s^2

The following jerk profile is generated:

Time interval	Jerk level
$0 < t \leq (T_1 - \tau_1)/2$	$+A_1$
$(T_1 - \tau_1)/2 < t \leq (T_1 + \tau_1)/2$	0
$(T_1 + \tau_1)/2 < t \leq T_1$	$-A_1$

The jerk profile is integrated three times to obtain $x_1(t)$.

2) Generate $x_2(t)$: Same as the generation of $x_1(t)$, but use new random numbers for T_2 and T_2 and choose $\ddot{x}_2(0) = -\ddot{x}_1(0)$.

3) Add the two processes $x(t) = x_1(t) + x_2(t)$.

The heart of this model lies in the basic waveform obtained after integrating the jerk profile three times. The result is a Gaussian-like pulse that is entirely non-negative or nonpositive depending upon the sign of $\ddot{x}_1(0)$. Then $x_1(t)$ consists of a series of positive pulses with random lengths and amplitudes, and $s_2(t)$ is a series of negative pulses. Finally, the sum of $x_1(t)$ and $x_2(t)$ results in a SA-like waveform.

Figure 10 shows a typical output of the Rater analytic SA model. As noted by the author of the model, a direct analytic relationship between the choice of parameters and the sigma of the process does not exist.[12] Nevertheless, the model seems to generate representative SA data. In addition, the model generates smooth range rate data, which is not the case for the previous two models.

D. Recursive Autoregressive Model (Lattice Filter)

A recursive AR model allows for the estimation of the AR model coefficients in real time, rather than in (off-line) batch processing. In principle, this would allow the AR model to predict ahead, once the model has "learned" the coefficients. The degradation of the accuracy of the predictions depends on the correlation time of the data. Highly correlated data would allow the AR model to predict ahead for longer periods of time than in the case of data that exhibit a low serial correlation. A recursive least squares (LS) lattice filter was first used by Chou in 1990.[11] The results presented by Chou were very promising, but they have not been repeated with the same level of success for other sets of data (see also Ref. 18). However, the use of a recursive AR model shows significant accuracy improvements in the prediction of the waveform when significant SA accelerations are presents. In the absence of significant SA accelerations, the recursive AR model does not offer any improvement over a simple linear extrapolation.

The LS lattice algorithm lends itself best to the real-time estimation of the AR coefficients because of the inherent stability offered by the lattice structure.[19] Following Refs. 16 and 19, the steps needed to implement the LS lattice filter are given below. The reader is referred to Ref. 19 for a detailed description of LS lattice filters.

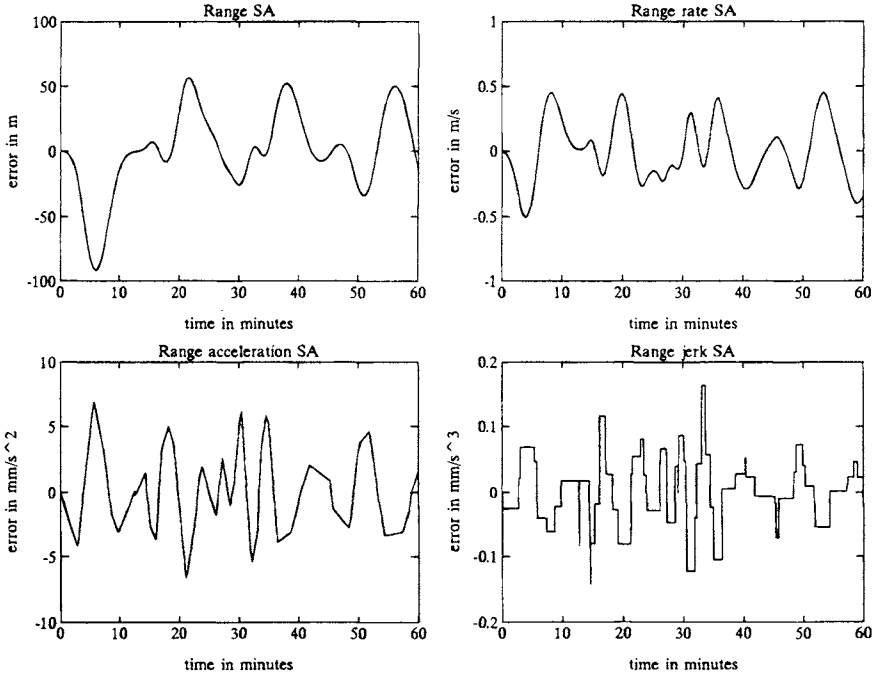

Fig. 10 Typical output of the Rater analytic selective availability model.

Initialization (δ is the steady-state squared prediction error; e.g., $\delta = 10^{-5}$):

$$e_m^b(0) = \Delta_m(0) = 0$$
$$\gamma_m(0) = 1 \qquad (0 \leq m \leq N)$$
$$\epsilon_m^f(0) = \epsilon_m^b(0) = \delta$$

For $n = 1$ to $n =$ final *do* (n is the current time index; x is the collected SA data)

$$e_0^b(n) = e_0^f(n) = x(n)$$
$$\epsilon_0^b(n) = \epsilon_0^f(n) = \epsilon_0^f(n-1) + x^2(n)$$
$$\gamma_0(n) = 1$$

For $0 \leq m \leq N-1$ *do* (N is the model order)

The AR filter coefficients are calculated from

$$\Delta_{m+1}(n) = \Delta_{m+1}(n-1) + [e_m^b(n-1)e_m^f(n)/\gamma_m(n-1)]$$
$$e_{m+1}^f(n) = e_m^f(n) - [\Delta_{m+1}(n)e_m^b(n-1)/\epsilon_m^b(n-1)]$$
$$e_{m+1}^b(n) = e_m^b(n-1) - [\Delta_{m+1}(n)e_m^f(n)/\epsilon_m^f(n)]$$

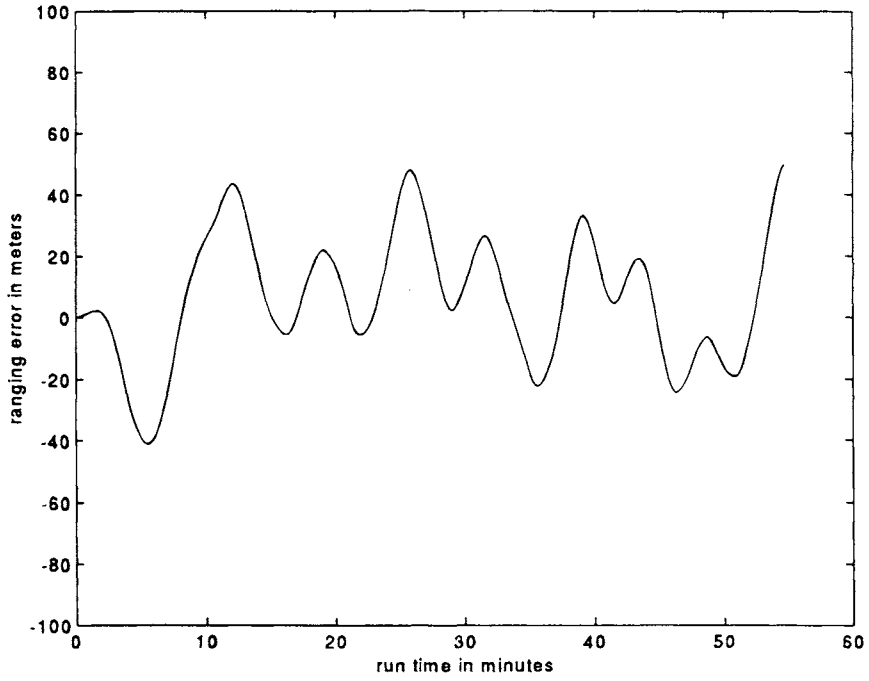

Fig. 11 Selective availability data used to "train" the least squares lattice filter.

$$\epsilon^f_{m+1}(n) = \epsilon^f_m(n) - [\Delta^2_{m+1}(n)/\epsilon^b_m(n-1)]$$

$$\epsilon^b_{m+1}(n) = \epsilon^b_m(n-1) - [\Delta^2_{m+1}(n)/\epsilon^f_m(n)]$$

$$\gamma_{m+1}(n-1) = \gamma_m(n-1) - \{[e^b_m(n-1)]^2/\epsilon^b_m(n-1)\}$$

The reflection coefficient is calculated from

$$k_{m+1}(n) = \Delta_{m+1}(n)/[\epsilon^b_m(n-1)\,\epsilon^f_m(n)]^{1/2}$$

For $1 \leq i \leq m-1$ *do*

$$\alpha_m(i) = \alpha_{m-1}(i) - k^b_{m+1}\alpha_{m-1}(m-i)$$

End (*i do* loop)

$$\alpha_m(m) = k^b_{m+1}(n)$$

End (*m do* loop)

For $1 \leq i \leq N$ *do*

$$a_i(n) = \alpha_N(i)$$

End (*i do* loop)

End (*n do* loop)

The coefficients and parameters used in the LS lattice filter are summarized below:

$e_m^b(n)$ = the backward prediction error for order m at time equals n
$e_m^f(n)$ = the forward prediction error for order m at time equals n
$\Delta_m(n)$ = the partial correlation coefficient between the forward and backward prediction errors for order m at time equals n
$\gamma_m(n)$ = the angle parameter for order m at time equals n
$\epsilon_m^f(n)$ = the squared forward prediction error for order m at time equals n
$\epsilon_m^b(n)$ = the squared backward prediction error for order m at time equals n
δ = the steady-state squared prediction error
$x(n)$ = the collected SA data at time equals n
n = the current time index
N = AR model order
m = model order index (0 through $N-1$)
$k_m(n)$ = the reflection coefficient for order m at time equals n
$\alpha_m(i)$ = the ith prediction coefficient for order m
$a_i(n)$ = the ith AR filter coefficient at time equals n

As an example of the usefulness of the LS lattice filter, an 11th-order filter was "trained" with almost 1 h of simulated SA data generated with the model

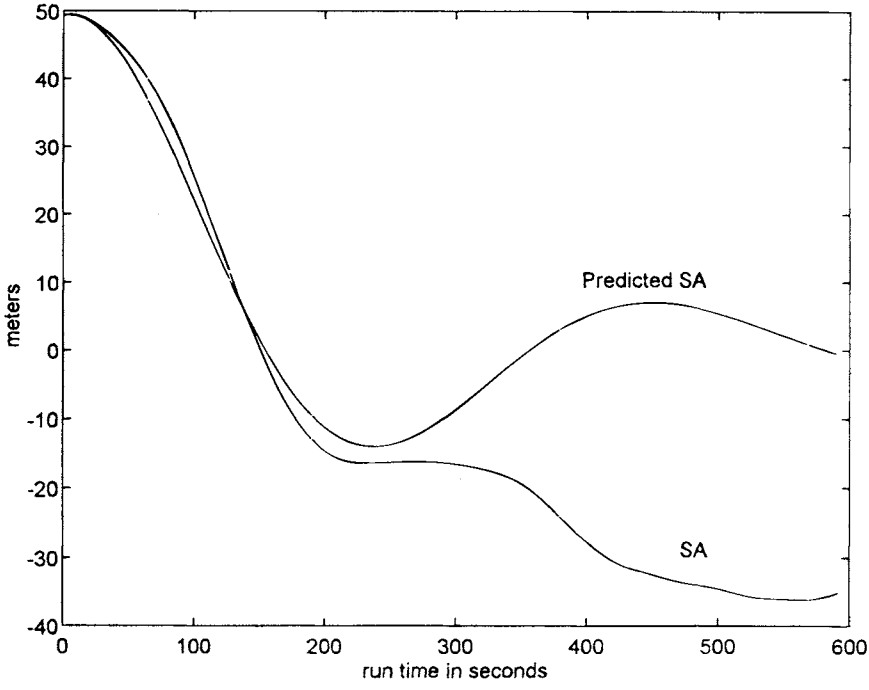

Fig. 12 Comparison of actual selective availability error and selective availability error predicted by the least squares lattice filter.

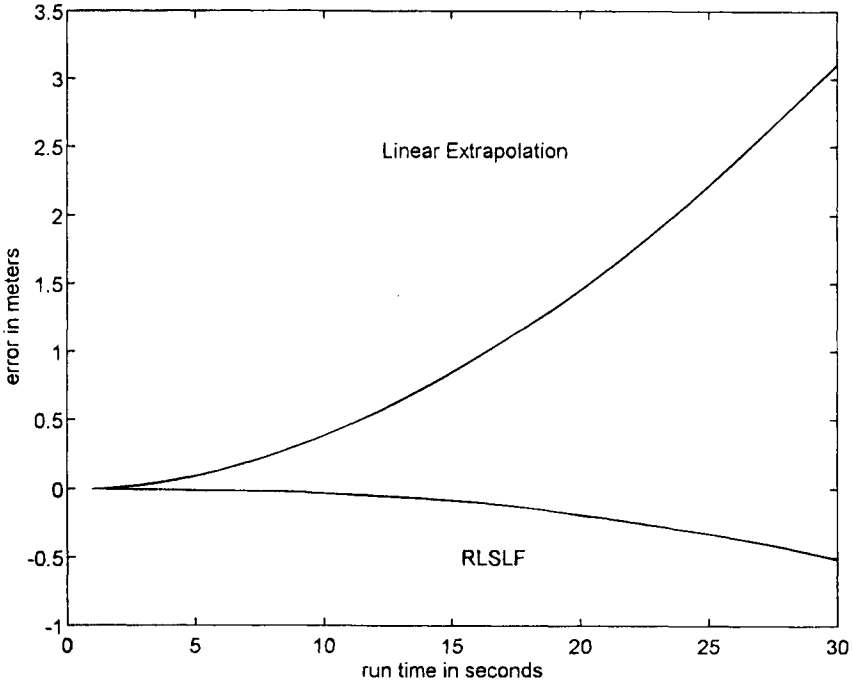

Fig. 13 Comparison of least square lattice filter prediction error and linear prediction error.

described in Sec. III. B., as shown in Fig. 11. At the end of the training period, the SA waveform was just starting to turn around from a positive slope to a negative slope. Figure 12 shows the predicted SA generated by the LS lattice filter, as well as the actual SA. During the first 3 min of the prediction interval, the predicted SA matches the actual SA to within 5 m. For periods of time longer than 3 min, the predicted values go to zero. This is consistent with the anticipated performance: the data can be predicted for a period of time on the order of the correlation time of the data. If a linear extrapolation is used instead of the LS lattice filter, the results are much worse, as illustrated in Fig. 13. After a period of 30 s, the linear extrapolation error is approximately 3 m, while the LS lattice filter prediction error is only -0.5 m. The opposite sign of the prediction errors is caused by the change in the slope of the SA data at the end of the training period. For this particular example, the LS lattice filter order was chosen to best match the SA data. Performance could be degraded if the filter is not adequately matched to the data. It should be noted that in the absence of significant SA acceleration, the performance of the linear extrapolator is statistically similar to the performance of the lattice filter.

E. Selective Availability Model Summary

Three different SA models are presented in this section. The highlights of each of the models are summarized as follows:

1. *Second-Order Gauss–Markov Model*

This model generates both range and range rate errors. It has been adopted by RTCA for GPS receiver-testing purposes. The main disadvantage of the model is that both the range and the range rate SA are noisier than that observed from actual satellite measurements.

2. *Autoregressive Model*

This model only generates range errors. Statistically, this is a very powerful model that is closely matched to measured SA data.

3. *Analytic Model*

This model generates both range and range rate errors. It also closely matches measured SA data. The range rate data represent the measured data better than those generated by the second-order Gauss–Markov model. The main disadvantage of this model is that there is not a direct relation between the choice of the model parameters and the output data. Noise levels must be set empirically.

Because the actual SA algorithms are not known, it is recommended, when required during GPS systems design and performance evaluations, to simulate the effect of SA using a variety of different models.

References

[1]Anon., "1992 Federal Radionavigation Plan," U.S. Department of Transportation and U.S. Department of Defense, Washington, DC, Rep. DOT-VNTSC-RSPA-92-2/DOD-4650.5, Jan. 1993.

[2]Georgiadou, Y., and Doucet, K. D., "The Issue of Selective Availability," *GPS World,* Sept.–Oct. 1990, pp. 53–56.

[3]United States Naval Observatory Electronic Bulletin Board, U.S. Coast Guard, Telephone (703) 866-3890, Aug. 29, 1990.

[4]Misra, P., Bayliss, E., LaFrey, R., and Pratt, M., "Integrated Use of GPS and GLONASS in Civil Aviation Navigation I: Coverage & Data Models," *Proceedings of the ION GPS-90,* Colorado Springs, CO, Institute of Navigation, Washington, DC, Sept. 1990, pp. 425–435.

[5]Kremer, G. T., Kalafus, R. M., Loomis, P. V. W., and Reynolds, J. C., "The Effect of Selective Availability on Differential GPS Corrections," *Navigation,* Vol. 37, No. 1, Spring 1990, pp. 39–52.

[6]Braasch, M. S., Fink, A., and Duffus, K., "Improved Modeling of GPS Selective Availability," *Proceedings of the ION National Technical Meeting,* San Francisco, CA, Institute of Navigation, Washington, DC, Jan. 20–22, 1993, pp. 121–130.

[7]Matchett, G., "Stochastic Simulation of GPS Selective Availability Errors," TM, FAA Contr. DTRS-57-83-C-00077, June 1985.

[8]Studenny, J., "Simulation of a Second-Order Gauss–Markov Process," RTCA Paper 148-93/SC159-424, March 17, 1993.

[9]Braasch, M. S., "A Signal Model for the NAVSTAR Global Positioning System," *Navigation,* Vol. 37, No. 4, Winter 1990–1991, pp. 363–377.

[10]Chou, H., "An Anti-SA Filter for Non-Differential GPS Users," *Proceedings of ION GPS-90,* Colorado Springs, CO, Institute of Navigation, Washington, DC, Sept. 19–21, 1990, pp. 535–542.

[11]Chou, H., "A Robust Filter for DGPS Users," *Proceedings of ION GPS-90,* Colorado Springs, CO, Institute of Navigation, Washington, DC, Sept. 19–21, 1990, pp. 607–612.

[12]Lear, W., Montez, M., Rater, L., and Zyla, L., "The Effect of Selective Availability on Orbit Space Vehicles Equipped with SPS GPS Receivers," *Proceedings of ION GPS-92,* Albuquerque, NM, Institute of Navigation, Washington, DC, Sept. 16–18, 1992, pp. 825–840.

[13]Åström, K., and Wittenmark, B., *Computer Controlled Systems—Theory and Design,* Prentice-Hall, Englewood Cliffs, NJ, 1984, pp. 146–151.

[14]Kelly, R. J., "MLS System Error Model Identification and Synthesis," *IEEE Transactions on Aerospace and Electronic Systems,* Vol. 28, No. 1, Jan. 1992, pp. 164–173.

[15]Marple, S. L., Jr., *Digital Spectral Analysis with Applications,* Prentice-Hall, Englewood Cliffs, NJ, 1988, pp. 172–260.

[16]Kay, S., *Modern Spectral Estimation: Theory and Application,* Prentice-Hall, Englewood Cliffs, NJ, 1987, pp. 106–270.

[17]Ljung, L., *System Identification—Theory for the User,* Prentice-Hall, Englewood Cliffs, NJ, 1987, pp. 169–207.

[18]Chou, H., "An Adaptive Correction Technique For Differential Global Positioning System," Ph.D. Dissertation, W. W. Hansen Experimental Physics Laboratory, Gravity Probe B Program, Stanford Univ., (SUDAAR 613), Stanford, CA, June 1991, pp. 59–82.

[19]Alexander, S. T., *Adaptive Signal Processing—Theory and Applications,* Springer-Verlag, New York, 1986, pp. 34–152.

Chapter 18

Introduction to Relativistic Effects on the Global Positioning System

N. Ashby*
University of Colorado, Boulder, Colorado 80309
and
J. J. Spilker Jr.†
Stanford Telecom, Sunnyvale, California 94089

I. Introduction

A. Objectives

THE GPS is one of the first operational systems, outside of particle accelerators, that has important effects from relativity. The reasons for this are threefold. The GPS satellites have a large velocity, there is a non-negligible gravitational potential difference between that of the satellites and that of the users (usually at or near the Earth's surface), and there are significant Earth rotation effects. These effects of themselves are not necessarily important, clearly, there are other operational satellite systems. However, when coupled with the fact that GPS satellites carry precision atomic frequency standards, that pseudorange measurements can be made to accuracies in the nanosecond range, and that carrier-phase measurements are made to the centimeter level, relativistic effects can, indeed, be significant and must be taken into account (see also Chapter 3, this volume, and Ref. 1).

For a fixed user at sea level on the Earth's surface, there are three primary consequences of relativity effects (see Table 1):

1) There is a fixed frequency offset in the satellite's clock rate when observed from Earth. Most of the effect is purposely removed by slightly offsetting the satellite clocks in frequency prior to launch, the so-called "factory offset" of the clock.

2) The slight eccentricity of each satellite orbit causes an additional periodic clock error effect that varies with the satellite's position in its orbit plane.

*Professor of Physics.

†Ph.D., Chairman of the Board.

Table 1 List of key relativistic effects on GPS

- **Fixed user on the geoid**

  Constant frequency offset (factory offset)

  The net effect of relativity for a zero eccentricity GPS satellite is a combination of effects caused by the satellite's velocity and the Earth's gravitational field, including its quadrupole field. This effect produces a small fixed frequency offset of received signal frequency relative to the satellite transmitted frequency in addition to the classical Doppler shift. This effect is compensated by a prelaunch factory offset in the satellite clock.

  Sinusoidal delay perturbation caused by the eccentricity of the satellite orbit.

  Sagnac delay caused by the Earth's rotation during the time of transit of the satellite signal to the ground user.

- **Moving user or user above the geoid**

  In addition to the above effects, there are effects caused by the user velocity and height of the user above the geoid. Some of these effects can cancel or partially cancel in position estimation. These effects can be significant if the user is another satellite in orbit.

- **Secondary effects**

  There are a host of secondary effects discussed briefly in this chapter that are smaller than the accuracy level required by most users. These include:

  Tidal potential effects on clocks

  The user is on or near the rotating Earth, which in turn, is revolving about the sun with its gravitational field. However, both the satellite and user are in orbit about the sun at approximately the same position so much of this effect cancels.

  Nonspherical gravity potential

  The Earth's gravity potential is slightly nonspherical primarily because of the ellipsoidal shape of the Earth, which causes a currently nonmodeled quadrupole field effect on GPS satellite clocks.

  Shapiro delay

  The Shapiro delay is caused by variations in the apparent velocity of light because of the Earth's gravitational field. Approximate values of the Shapiro delay are calculated and shown to be small.

  Lense-Thirring effect–frame dragging

  This effect is caused by the rotation of the Earth's mass on its axis. This effect, a so-called frame-dragging effect, slightly modifies the solutions to the field equations and generates a slightly different metric with a term related to the Earth's angular momentum, but its effects are negligible for our purposes here.

3) There is also an effect (Sagnac delay) caused by the Earth's rotation during the time of transit of the satellite signal from satellite to ground.

Moving users on or near the Earth's surface or fixed users at an altitude above or below the geoid* may have to make additional corrections caused by their velocity and height above the ground. Satellite users in low-Earth orbit (LEO), geostationary-Earth-orbit (GEO), or other orbit altitudes have additional corrections that may be necessary depending upon the accuracy required. Clearly, the

* The geoid is an equipotential surface that differs slightly from the ellipsoidal model of the Earth by geoid undulations. The gravity potential W is the sum of both a gravitational potential Φ and a centrifugal potential $V = -{}^1/_2\,\omega^2(x^2 + y^2)$ and is also affected by nonuniformity in the Earth's density, and topography (see Sec. 3.1).

Table 2 Objectives of the chapter

- Introduce special and general relativistic effects. For the GPS, most of the significant general relativity effects can be shown from the principle of equivalence, and flat or nearly flat space models are adequate.
- Define the appropriate invariant equations, the metric tensors, and show their application to translational linear motion at constant velocity, rotating coordinates, spherically symmetric and cylindrically symmetric gravitational fields with and without coordinate system rotation.
- Compute the relativistic effects on GPS pseudorange and Doppler frequency measurements on both fixed and moving users, including users in orbit. Discuss effects on the calculation of user position, velocity, and time transfer estimates. Compute both primary and secondary effects.

impact of these relativistic effects can differ depending upon the objective and precision desired; e.g., for GPS and differential GPS (DGPS) position estimates, some common error relativistic effects cancel; whereas, for time transfer, they may not.

This chapter's objective is to describe for the reader the detailed effects of relativity for GPS users, and is summarized in Table 2. For an extensive treatment of relativity, the reader is referred to the texts in the References at the end of the chapter. In this chapter, the effects of the Earth's atmosphere are ignored. These effects have been discussed in Chapters 12 and 13, this volume, and are assumed to have been taken into account already.

B. Statement of the GPS Problem

As already discussed in detail in previous chapters, the GPS receiver makes two types of measurements on the received signal, pseudorange and carrier-phase/Doppler frequency measurements. In this chapter, we focus only on relativistic effects and assume that perfect atomic frequency standards are employed both for the satellite clock and the user clock. We ignore all other error sources covered in other chapters. Ideal atomic clocks moving with the user and satellite are sometimes referred to as *standard clocks.* For our purposes, it is assumed that the satellite transmits coded electromagnetic pulses at time instants as determined by this perfect satellite clock* and transmits these pulses at a precisely determined frequency f_o (see Fig. 1.). The satellite-generated coded pulse—really a sequence of pulses—carry embedded in the code the precise satellite clock time at the precise time of transmission of this coded pulse. The GPS receiver is also assumed to have a perfect atomic clock and measures the time of reception of the satellite-coded pulse waveform and decodes the satellite's clock time word. The receiver then simply subtracts the satellite clock time number (at the time of transmission) from the user clock time number at the time of reception. Corrections must be applied to account for the fact that the user undoubtedly

*The GPS clocks prior to launch are set to run at GPS time—an atomic standard time—with a factory offset for relativity. While in orbit, the satellite clocks are periodically corrected by the GPS Control Segment (CS) to match GPS time with both "paper" and, less frequently, physical clock corrections (see Chapters 4 and 10, this volume).

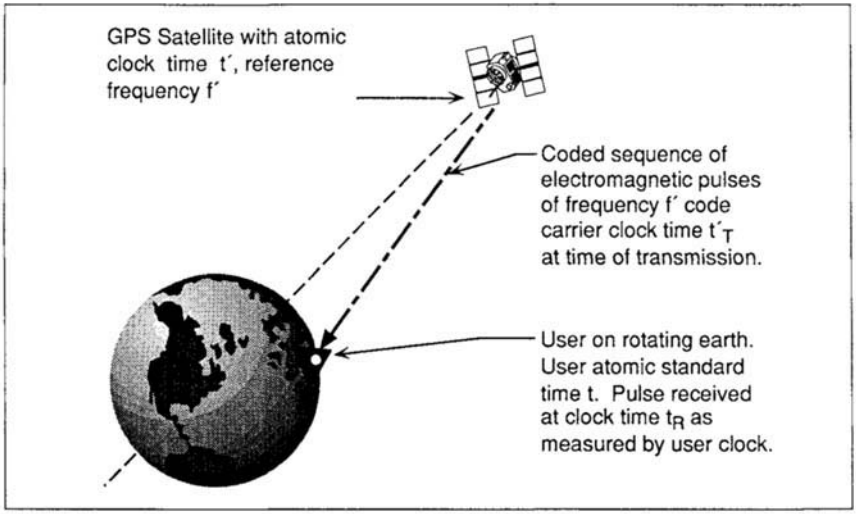

Fig. 1 The GPS relativistic problem. The GPS satellite is assumed to carry a noise-free atomic frequency standard and produces a clock time t' carried on the satellite. The satellite transmits a coded sequence of electromagnetic pulses of frequency f'. The coded pulse sequence represents a number t'_T, which is the satellite standard clock time at the beginning of the coded pulse *transmission*. The GPS user receiver for this example also carries a perfect atomic frequency standard and produces time t. The receiver measures the time of *reception* t_R and then subtracts $t_R - t'_T$ to give pseudorange. The receiver moves during propagation of the signal. The receiver also measures the frequency of the received electromagnetic pulses and compares it with the frequency of its own coordinate clock to measure frequency shift.

has moved during the time of transit, because either the user is on the rotating Earth, in an aircraft slightly above the Earth's surface, or perhaps in another satellite in low-Earth orbit. Finally, the user also compares the satellite frequency and phase changes with its own clock to compute range rate and accumulated delta range (ADR), a carrier-phase measurement. In both instances, pseudorange and carrier frequency are affected by various relativistic effects. The problem is to account for motional Doppler shifts, gravitational frequency shifts, and propagation delays so the user can accurately determine his or her position and time.

The importance of relativistic effects for GPS, and especially for GPS time transfer, is heightened by the fact that today's atomic time standards carried in the GPS satellites and used on the ground are so precise. Today's clocks exhibit long-term Allan variance stability levels (see Chapter 4, this volume) on the order of 10^{-14}, and even better stability is possible for clocks on the ground.

Simultaneity is a crucial concept in the GPS. For users to determine position and time, atomic clocks in the satellites should be synchronized. For users to rendezvous successfully after traversing different paths with different speeds through different gravitational fields, their clocks must be synchronized, and their positions must be accurately determined. When coordinate reference frames are

inertial, as in special relativity, the usual Einstein synchronization procedures may be employed.* However, typical users are moving over the rotating Earth and are in the Earth's gravitational field, giving rise to noninertial effects. Proper time elapsed on standard clocks depends upon the clocks' history, and the Einstein procedure is not sufficiently accurate. Instead, we use the concept of a *global coordinate time* wherein there is a hypothetical network of clocks synchronized in an underlying Earth–centered-inertial frame (ECI frame) and running at a rate consistent with atomic time standards on the geoid of the rotating Earth.[2] The definition of simultaneity employed is that of *coordinate simultaneity*,[3] namely, two events with space–time coordinates $\{t_1, x_1, y_1, z_1\}$ and $\{t_2, x_2, y_2, z_2\}$ are simultaneous in the given reference frame if $t_1 = t_2$.

In this chapter, standard time refers to *International Atomic Time* (TAI).†[4] Strictly speaking, GPS time is a coordinate time with rate determined by an independent composite set of clocks (see Chapter 10, this volume) which is indirectly coupled to TAI and Universal Coordinated Time (UTC) (with its leap seconds) through UTC–GPS corrections (see Chapter 4, this volume). Synchronization is achieved by methods discussed in this chapter.

II. Introduction to the Elementary Principles of Relativity

The mathematics of general relativity are extremely complex. However, for this treatment of the relativistic effects on GPS, only a small fraction of the theory is required, and even in this fraction, many simplifications can be made, because the gravitational fields (of the Earth) are relatively weak, and the velocities of the satellites and users are small compared to the velocity of light c. As a result, the curved spaces of general relativity are nearly flat.

Although much of the discussion of the relativistic effects of GPS involves either rotation of the Earth or satellites in orbit, and gravitational fields with some nonuniformity, we stress the admonition of Misner et al.[5] that "physics is simple when analyzed locally. Don't try to describe motion relative to far away objects." Physics is always and everywhere locally Lorentzian (has a local inertial frame). Thus, we begin the discussion by reviewing Euclidean geometry and inertial frames and then introduce the concepts of special relativity, the principle of equivalence and metric tensors. Metric tensors and their associated scalar intervals are the key tools that allow us to define the geometry of the space and interpret the consequences of the theory.

A. Euclidean Geometry and Newtonian Physics

In this section, we begin by considering families of inertial coordinate systems each moving at constant velocity (no acceleration) with respect to the others. To be called *inertial,* a coordinate system must satisfy the properties[6] of Table 3.

*Simultaneity can be defined self-consistently for a homogeneous, isotropic inertial frame; if light pulses emitted from two points, A and B, in the frame arrive at the midpoint of A and B at the same time, then the transmit events are simultaneous.

†TAI is a coordinate time scale, defined in a geocentric reference frame with the SI second as scale unit as realized on the rotating geoid. It can be extended to a fixed or moving point in the vicinity of the Earth with sufficient accuracy at the present state of the art by the application of first-order corrections of the General Theory of Relativity; i.e., corrections arising from differences in the gravitational potential and differences of speed, in addition to the rotation of the Earth.

Table 3 Required properties of an inertial coordinate system and related definitions

Event

An event marks an action that takes place at a point in space–time. Events are denoted by ϵ_1, ϵ_2, etc. for this chapter.

Observation by an inertial observer

An observer assigns to an event ϵ, the coordinates x, y, z of the location of the occurrence and the time t read by a clock in that coordinate frame located *exactly* at the position of that event for that frame.

World-line

A world-line is the path taken by a particle or light ray in four-dimensional space–time. The world-line is a line for which $\boldsymbol{x}$ is given as a function of t.

Inertial coordinate frame

The coordinate system must satisfy the three properties:

1) The distance between point P_1 at (x_1, y_1, z_1) and point P_2 at (x_2, y_2, z_2) is a constant independent of time.
2) The clocks that sit at every grid point in the coordinate frame are all synchronized, all run at the same rate, and provide a *coordinate time* for that coordinate frame, the same as proper time measured by synchronized standard clocks. *Proper time* is time measured on a single arbitrarily moving standard clock.
3) The geometry of space at any fixed instant of time is Euclidean, a flat space. Acceleration and gravitational fields violate property 2, except for a very localized region of space.

Much of our analysis focuses on these very localized regions of inertial space that apply to the GPS. Consider two coordinate systems S and S', where S' is moving at constant velocity v in the x direction relative to S, as shown in Fig. 2.

In standard Euclidean geometry, the *Galilean transformation* between coordinates for these Cartesian coordinate systems is as follows:

$$\begin{aligned} x' &= x - vt \\ y' &= y \\ z' &= z \\ t' &= t \end{aligned} \tag{1}$$

The very thought that t and t' could be different is not even considered in

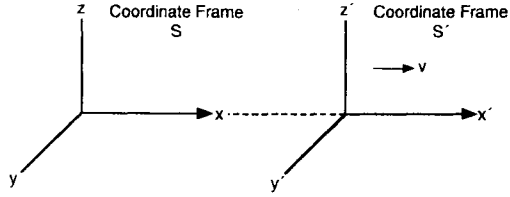

Fig. 2 Two (nonaccelerating) inertial coordinate frames S and S'. Coordinate frame S' is moving in such a way that $x' = x - vt$ where the origins of both frames are coincident at $t = t' = 0$.

Newtonian physics, and there is no constraint on velocity relative to the speed of light. In these Euclidean coordinate systems, the invariant differential interval between two events is the differential distance, given by the following

$$\begin{aligned} d\sigma^2 &= dx^2 + dy^2 + dz^2 && \text{Cartesian coordinates} \\ &= dr^2 + r^2 d\phi^2 + dz^2 && \text{cylindrical coordinates} \\ &= dr^2 + r^2(d\theta^2 + \sin^2\phi\, d\phi^2) && \text{spherical coordinates} \end{aligned} \tag{2}$$

The *spatial metric* in Cartesian coordinates can be written as

$$d\sigma^2 = dx^2 + dy^2 + dz^2 = \rho_{ik} dx^i dx^k = \delta_{ik} dx^i dx^k$$

where ρ_{ik} written in matrix form is the following diagonal matrix:

$$\|\rho_{ik}\| = \begin{bmatrix} 1 & 0 & 0 \\ 0 & 1 & 0 \\ 0 & 0 & 1 \end{bmatrix}$$

See Table 4 for an explanation of the Einstein summation convention. Thus, a differential distance between any two points in Euclidean space is the same regardless of the chosen coordinate system; it is a scalar. This space is a perfectly flat space. The deficiency in this Galilean system is that it makes no allowance for the fundamental fact that the speed of light is a constant c in all inertial frames, nor that time measures could be different in different coordinate frames; i.e., t and t' can be different.

In special and general relativity where there are coordinate systems with different velocities, rotational effects, and gravitational effects, the three-dimensional spatial metric does not suffice. Instead, we deal with a four-dimensional space–time coordinate frame, and the *scalar interval* is of the form, $ds^2 = g_{\alpha\beta} dx^\alpha dx^\beta$ where the individual $g_{\alpha\beta}$ terms can be functions of position and time; i.e., $g_{\alpha\beta}(x^\alpha)$. The set of elements $g_{\alpha\beta}$ together form a *covariant tensor* $g_{\alpha\beta}$ of rank 2. The tensor is symmetric; i.e., $g_{\alpha\beta} = g_{\beta\alpha}$. This *metric tensor* defines the geometry (differential geometry) of the space.* In general, the space–time coordinates are not flat. However, with the GPS and the users in relatively close proximity to the Earth, $r < 40{,}000$ km, the spatial coordinates are very nearly flat.

The fundamental basis for special relativity and its *Lorentz transformation* are contained in Einstein's postulates relating to the constancy of the speed of light in all inertial frames shown in Table 5.

B. Space–Time Coordinates and the Lorentz Transformation

Let us begin by considering four-dimensional space–time coordinates. This coordinate system may be envisioned as a standard Cartesian coordinate system filled with precision standard clocks at every point in the coordinate grid (see

*Any symmetric covariant tensor field of rank 2 defines a metric. A manifold with an applicable metric is termed a Riemanian manifold.[7] The concept of a differentiable manifold is abstract; however, it can be described roughly as an n-dimensional space that can be covered by one or more open neighborhoods, each of which has a coordinate system. Pairs of these coordinate systems are related to each other by differentiable coordinate transformations. A smooth surface in three-dimensional Euclidian space is a simple example of a differentiable manifold.[8]

Table 4. General expressions for distance in three-dimensional space and four-dimensional space–time

We introduce a set of three-dimensional spatial coordinates $\{x, y, z\} = \{x^1, x^2, x^3\}$ in frame S and a new set of coordinates $\{x'^1, x'^2, x'^3\}$ in frame S' where $x = x^1(x'^1, x'^2, x'^3)$, $y = x^2(x'^1, x'^2, x'^3)$, $z = x^3(x'^1, x'^2, x'^3)$. A coordinate differential $dx = dx^1$ is related to coordinate differentials dx'^i by the following:

$$dx = dx^1 = \frac{\partial x}{\partial x'^1}dx'^1 + \frac{\partial x}{\partial x'^2}dx'^2 + \frac{\partial x}{\partial x'^3}dx'^3 = \sum_i \frac{\partial x}{\partial x'^i}dx'^i = \frac{\partial x^1}{\partial x'^i}dx'^i$$

Einstein's summation convention is used, where two repeated indices—one subscript and one superscript—automatically imply a summation over the range of the indices. Latin indices range from 1 to 3, while Greek indices range from 0 to 3. Thus, $a_i b^i$ is shorthand for $a_1 b^1 + a_2 b^2 + a_3 b^3$.
Similarly, the differentials for dy and dz may be written in the following compact form:

$$dx^j = \sum_i \frac{\partial x^j}{\partial x'^i}dx'^i = \frac{\partial x^j}{\partial x'^i}dx'^i$$

Quantities that transform under a change of coordinates according to such a rule: $V^j = \partial x^j/\partial x'^i\, V'^i$ are termed *contravariant vectors*. (In three-dimensional Euclidean space, the distinction between contravariant and covariant vectors is not as significant as it is in general space-time.)

The invariant distance measure is as follows:

$$ds^2 = dx^2 + dy^2 + dz^2 = \delta_{ij}dx^i dx^j = \delta_{ij}\frac{\partial x^i}{\partial x'^m}\frac{\partial x^j}{\partial x'^n}dx'^m dx'^n$$

$$= g'_{mn}(x'^1, x'^2, x'^3)dx'^m dx'^n$$

where the *metric tensor* in the new coordinate system $\{x'^1, x'^2, x'^3\}$ is the following:

$$g'_{mn} = \delta_{ij}\frac{\partial x^i}{\partial x'^m}\frac{\partial x^j}{\partial x'^n} = \left[\frac{\partial x}{\partial x'^m}\frac{\partial x}{\partial x'^n} + \frac{\partial y}{\partial x'^m}\frac{\partial y}{\partial x'^n} + \frac{\partial z}{\partial x'^m}\frac{\partial z}{\partial x'^n}\right]$$

The three-dimensional distance measure, thus, simplifies to $ds^2 = g'_{ij}dx'^i dx'^j$. The three-dimensional metric tensor g'_{ij} in an arbitrary coordinate system has nine components but only six are independent because $g'_{ij} = g'_{ji}$.

The metric tensor generalizes to four-dimensional spacetime using the coordinate x^0 for ct where t is the time for that coordinate system, and the spatial coordinates are $\{x^1, x^2, x^3\}$. Then a general *line element* in four dimensions is written

$$ds^2 = g_{\alpha\beta}dx^\alpha dx^\beta$$

The particular dependence of $g_{\alpha\beta}$ on space–time is determined by the physical situation (see Table 10).

In special and general relativity, the increment of *proper time* $d\tau$ elapsed on a standard clock that moves along the space–time path dx^α is just $d\tau = |ds|/c$. Thus, if a clock does not move, $dx^\alpha = 0$ for $\alpha = 1, 2, 3$, and then $d\tau^2 = ds^2/c^2 = g_{00}(dx^0)^2/c^2$, and the proper time elapsed on the clock is $\sqrt{|g_{00}|}\,dt$.

Table 5 Einstein's two postulates[9]

Postulate 1: The Principle of Relativity

"No inertial system is preferred. The equations expressing the laws of physics have the same form in all inertial systems."

Postulate 2: The Principle of the Constancy of the Speed of Light

"The speed of light is a universal constant independent of the state of motion of the source. Any light ray moves in the inertial system of coordinates with constant velocity, c, whether the ray is emitted by a stationary or by a moving source."[10]

Of course, the speed of light c refers to the speed of light in a vacuum. Obviously, the speed of light decreases in a dielectic medium such as air or glass fiber.

Ref. 11). Second, define *events*; for example, a light pulse transmission as, say, ϵ_1, not only by the place of occurrence x, y, z, but also by the time t in that coordinate system at which the event took place. Thus, an event ϵ_1 is labeled in an inertial (nonaccelerating, gravity-free) coordinate frame S as $\epsilon_1(t_1, x_1, y_1, z_1)$ and in coordinate frame S' by $\epsilon_1(t_1', x_1', y_1', z_1')$ where the clock time is labeled by the time on the clock that is *exactly* at the same location in each coordinate system as the event. The two coordinate frames S and S' are generally in relative motion to one another. Each frame must have its own set of measuring rods and synchronized clocks at rest in that frame. An "observer" is a shorthand way of speaking of the whole ensemble of clocks and measuring rods associated with one coordinate frame, and an observation is the operation of labeling each event with the position coordinates and clock time at that event. It is critical that the clock time label be that associated with the exact position of that event, not a clock time at some distant point. An observation is *not* the act of looking at some clock distant from the event, and attempts to do so will often lead to error and sometimes leads to so-called paradoxes.

1. *Time Dilation*

Consider next two inertial coordinate frames, as shown in Fig. 3, where the origin of the S' frame moves with respect to reference frame S along the x-axis at velocity v, i.e., $dx/dt = v$. At time $t = 0 = t'$, the origins coincide. Consider an event ϵ_A wherein a light flash is emitted at the origin of both coordinate frames; i.e., ϵ_A ($t = 0$, $x = 0$, $y = 0$, $z = 0$), ϵ_A ($t' = 0$, $x' = 0$, $y' = 0$, $z' = 0$). Event B is the reception of the flash after reflection from a mirror or other reflector at position $y = \Delta L = y'$. (Symmetry considerations imply that the two observers agree on lengths oriented perpendicular to the direction of relative motion.)

Note that the speed of light c is exactly the same in both frames, from Postulate 2 in Table 5. Assume that the reflecting mirror moves with the coordinate frame S' (or equivalently, that the light beam is angled in the S frame so that it returns to the origin of S'). The light pulse in frame S' travels exactly $2\Delta L$ meters, and hence event ϵ_B in S' has coordinates ($t' = 2\Delta L/c$, $x' = 0$, $y' = 0$, $z' = 0$). Thus, the coordinate changes between the two events in S' are $\Delta t' = 2\ \Delta L/c$, $\Delta x' = 0$, $\Delta y' = 0$, $\Delta z' = 0$.

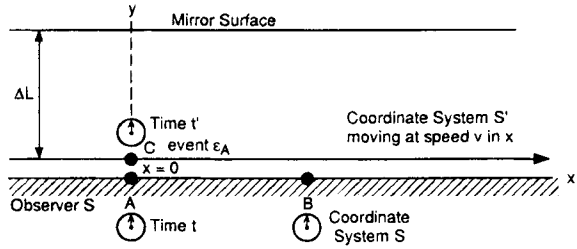

(a) Configuration of the two coordinate systems. S' is moving at speed v to the right with respect to System S. A and B are two synchronized clocks at rest in S.

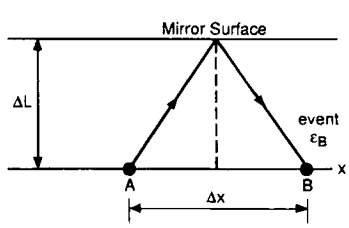

(b) Light pulse transmission as observed in System S. The time between transmission and reception is t_B-t_A = Δt.

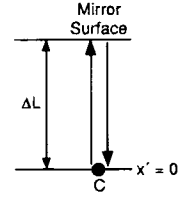

(c) Light pulse transmission in System S'. The time between transmission and reception in frame S' is t'$_B$-t'$_A$ = Δt'.

Fig. 3 Example of light pulse transmission in two coordinate frames S and S'. The light pulse is transmitted, event ϵ_A, at position A in frame S and at position C in frame S', which is exactly coincident with A at the time of event ϵ_A. The pulse is received, event ϵ_B, at the same location C in frame S' and at a displaced point B in frame S where $\Delta x = v\Delta t$.

In coordinate frame S, on the other hand, the light pulse arrives, event ϵ_B, at the following time:

$$t = \Delta t = 2\sqrt{(\Delta L)^2 + (\Delta x/2)^2}/c \tag{3}$$

where $\Delta x = v\Delta t$, and $x = \Delta x$, $y = 0 = z$. Thus, in S, event ϵ_B has coordinates $t = \Delta t, x = v\Delta t$, $y = 0$, $z = 0$. The coordinate changes between the two events are, therefore, (Δt, $\Delta x = v\Delta t$, $\Delta y = 0$, $\Delta z = 0$). Because $\Delta x = v\Delta t$, we can solve Eq. (3) for Δt to obtain the following:

$$\Delta t = \frac{2\Delta L/c}{\sqrt{1 - (v/c)^2}} \tag{4}$$

The ratio of the two time intervals is as follows:

$$\frac{\Delta t}{\Delta t'} = \frac{1}{\sqrt{1 - (v/c)^2}} = \frac{1}{\sqrt{1 - \beta^2}} \triangleq \gamma \geq 1 \tag{5}$$

where γ is the *time dilation* factor, and $\beta \triangleq v/c$ is the normalized speed, with $v = |v|$. Thus, the laboratory reference frame clock accumulates a larger clock count between the same two events than the clock in the moving coordinate

system S', and hence, the moving clock seems to be running at a lower frequency clock rate than the laboratory clock. *Moving clocks run slow when compared with a sequence of synchronized clocks at rest.* Of course, if the experiment were reversed so that the light pulse returned to the origin of S, then $\Delta x = 0$, the clock at A in S is moving at velocity $-v$ with respect to S', and it would seem that the S frame clock is running slow.

For the two events ϵ_A, ϵ_B discussed here, the clock in S' moves uniformly from ϵ_A to ϵ_B, and in S', the events occur at the same position in space. Whenever it is possible to introduce a uniformly moving clock whose world line intersects two events, an inertial frame can be constructed with this clock as reference, in which the spatial separation between the events is zero. The space–time separation between the events is then *timelike*, and the proper time elapsed on the clock is a measure of this separation. We can then show that, in general, the space–time separation between events $\Delta s^2 = -(c\Delta t)^2 + \Delta x^2 + \Delta y^2 + \Delta z^2$ is a scalar quantity having the same value in all inertial frames. Indeed, in the present case in S' $-(c\Delta t')^2 + (\Delta x')^2 + (\Delta y')^2 + (\Delta z')^2 = -(c\Delta t')^2 = -4(\Delta L)^2$, while from Eq. (4) in S, $-(c\Delta t)^2 + (\Delta x)^2 + (\Delta y)^2 + (\Delta z)^2 = (c\Delta t)^2(1 - v^2c^2) = [-4(\Delta L)^2/(1 - \beta^2)]\,(1 - \beta^2) = -4(\Delta L)^2$. Thus, because v no longer appears, Δs^2 is an invariant quantity independent of the coordinate frame.

In differential form* we write the following:

$$ds^2 = -c^2dt^2 + dx^2 + dy^2 + dz^2 \tag{6}$$

This invariant is termed the space–time interval for the *Lorentz space* (inertial space). Notice that if the clock is fixed in the reference frame; i.e., $dx = dy = dz = 0$, then $dt = d\tau$, and dt is equal to proper time. Thus, a fixed (standard) clock in the coordinate system carries proper time (see Table 1). *Proper time* is the time carried by a clock that is transported along a world line in space–time through the events. Figure 4 shows a world-line description of the light pulse transmission. A *world line* is the path taken by a particle or light ray in space–time.

The expression for the invariant ds^2 contains one form of the metric tensor and can be written for this inertial space as the following quadratic form†:

$$ds^2 = \sum_{\alpha}^{3}\sum_{\beta}^{3} g_{\alpha\beta}\,dx^{\alpha}\,dx^{\beta} = g_{\alpha\beta}\,dx^{\alpha}\,dx^{\beta} \tag{7}$$

For inertial space (Minkowski space), the metric tensor in Cartesian coordinates can be written in matrix form as follows:

*Note that many texts use simplifying normalizing notations so that c does not appear, and some use $ds^2 = -dt^2 + (dx^2 + dy^2 + dz^2)/c^2$ and express the line element in time dimensions. In this chapter, ds has the dimensions of meters.

†The metric tensor $g_{\alpha\beta}$ is a tensor of rank 2 that carries out an operation $\boldsymbol{g}(d\boldsymbol{x}, d\boldsymbol{x}) = g_{\alpha\beta}\,dx^{\alpha}dx^{\beta}$ on any two vectors inserted and computes a scalar that has certain invariant properties under coordinate transformation. For more detail refer to Refs. 5, 8, 12, 13. We are using Einstein notation and automatically sum over any index that appears as both a subscript and superscript.

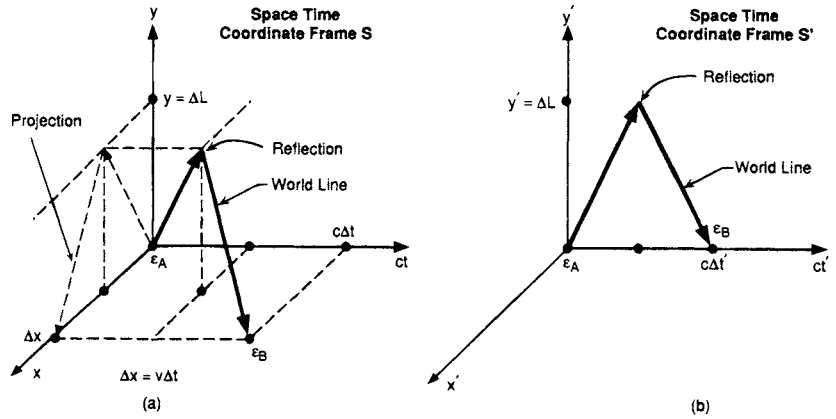

Fig. 4 Space–time coordinate frame world lines in coordinate frames S and S' showing events ϵ_A and ϵ_B. Coordinate frame S' is moving in the x direction with respect to coordinate frame S at speed v. A light pulse is transmitted, event ϵ_A, when the origins at time $t = 0 = t'$ at the origin of S and S'. The pulse is reflected at $y = \Delta L$ and returned to $y = 0$; $y' = 0$, event ϵ_B.

$$\|g_{\alpha\beta}\| = \|\eta_{\alpha\beta}\| \triangleq \begin{bmatrix} -1 & 0 & 0 & 0 \\ 0 & 1 & 0 & 0 \\ 0 & 0 & 1 & 0 \\ 0 & 0 & 0 & 1 \end{bmatrix}$$

where $\eta_{\alpha\beta}$ is defined as the metric tensor for *Minkowski space* and is one form of the generalized Kronecker delta. This scalar invariant, or line element, can also be written in cylindrical and spherical coordinates as follows:

$$ds^2 = -c^2dt^2 + dr^2 + r^2d\phi^2 + dz^2$$

$$ds^2 = -c^2dt^2 + dr^2 + r^2(d\theta^2 + \sin^2 d\phi^2) \tag{8}$$

The line element for any path in space–time is invariant under coordinate transformations between inertial frames. Along the path of a photon, the line element or invariant distance measure, $ds^2 = 0$. Notice that because for photon travel $ds^2 = 0$, the line element yields the result $c^2dt^2 = dx^2 + dy^2 + dz^2$, which is an expression of the constancy of the speed of light in all inertial frames.*

2. *Geodesics*

A geodesic is the path in space–time that a body takes when it is free from nongravitational forces. In the flat space of special relativity, inertial space, the body moves with uniform speed along a straight line. In more general spaces,

*Note that in three dimensions x, y, t, this equation $c^2\,dt^2 = dx^2 + dy^2$ can be visualized as a cone in three dimensions, sometimes referred to as a light cone. Physical objects must travel inside the light cone, and light rays travel on the surface of the cone.

the geodesics* are extremal paths. For physical particles, a geodesic ordinarily corresponds to the shortest path. For light rays, the geodesics have zero space–time length and are termed null geodesics. In general, in a gravity field, the geodesics are curved, at least slightly, in space.

3. *Transformations Between Inertial Frames*

Consider an inertial system S with $ds^2 = -c^2dt^2 + dx^2 + dy^2 + dz^2$. This space–time interval is not form-invariant under Galilean coordinate transformations, because if we apply Eqs. (1) to transform ds^2, we obtain

$$ds^2 = -(cdt')^2(1 - \beta^2) + 2\beta dx' cdt' + dx'^2 + dy'^2 + dz'^2,$$

which is not of the same form as Eq. (6). However, because it is a quadratic form in the primed coordinate increments, by performing additional linear transformations of x' and t' it is possible to reduce this expression to the appropriate form $-(cdt')^2 + dx'^2 + dy'^2 + dz'^2$.

Let us, instead, begin by assuming that x and ct are linear combinations of x' and ct'. For the event ϵ_B of Fig. 3, $x' = 0$, while $ct = \gamma ct'$, and $x = vt = \gamma\beta ct'$. This set of relationships is enough to determine two of the four needed coefficients. Then, for an arbitrary event we must have the following:

$$ct = \gamma ct' + Ax' \tag{9}$$

$$x = Bx' + \gamma\beta ct' \tag{10}$$

where A and B are constants that remain to be computed. Consider events at the origin of S, at $x = 0$. These must occur at $x' = -vt'$, so from Eq. (10) $0 = B(-vt') + \gamma\beta ct'$, which gives $B = \gamma$. Invariance of the speed of light implies that if $x' = ct'$, then $x = ct$. That is, the position of a light pulse transmitted from the origins at the moment they coincide must move with speed c in both coordinate systems. Then, substituting $x' = ct'$ in Eqs. (9) and (10) we must have $x = \gamma ct' + \gamma\beta ct' = ct = \gamma ct' + Act'$.

This equation can only be satisfied if $A = \gamma\beta$. The resulting transformations, the so-called Lorentz transformations, can be written as follows:

$$ct = \gamma(ct' + \beta x')$$

$$x = \gamma(x' + \beta ct') \tag{11}$$

There are many other ways of deriving the Lorentz transformations. Another method is to assume the transformations between coordinates of S' and S are linear, then impose the requirement that ds^2 must have the same form in the two frames. This yields Eqs. (11) after some algebra.

Compare Eq. (11) with the Galilean transformation where we would have $x = x' + vt'$ and $t = t'$. First-order corrections enter in the time transformation; second-order corrections enter through the factor γ.

*A geodesic is a curve for which the integral $\int ds$ is an extremum; the curve has zero geodesic curvature.[11]

4. *Velocity Addition*

Consider a double transformation of velocities where there are three inertial coordinate systems: S_a, S_b, S_c, as shown in Fig. 5. The coordinate frame S_b moves at velocity v_b with respect to S_a, and S_c moves at velocity v_c with respect to S_b. The velocities would, of course, simply add in a Galilean transform with S_c moving with respect to S_a with velocity $v_b + v_c$. Let the three sets of coordinates be $\{ct_a, x_a, y_a, z_a\}$, $\{ct_b, x_b, y_b, z_b\}$, and $\{ct_c, x_c, y_c, z_c\}$.

Using the Lorentz transformation (11), we can write the following:

$$\begin{aligned} x_a &= \gamma_b(x_b + v_b t_b) = \gamma_b[\gamma_c x_c + \gamma_c v_c t_c] + \gamma_b v_b[\gamma_c t_c + v_c \gamma_c x_c] \\ &= \gamma_b\gamma_c[x_c + v_c t_c + v_b t_c + v_c v_b x_c] = \gamma_b\gamma_c[x_c(1 + v_b v_c) + (v_b + v_c)t_c] \\ &= \gamma_b\gamma_c(1 + v_b v_c)\left[x_c + \left(\frac{v_b + v_c}{1 + v_b v_c}\right)t_c\right] \end{aligned} \tag{12}$$

where $\gamma_b = 1/\sqrt{1 - \beta_b^2}$, and $\beta_b \triangleq v_b/c$, etc. Thus, the effective velocity of S_c with respect to S_a in the x direction is as follows:

$$v_{\text{eff}} = \frac{v_b + v_c}{1 + v_b v_c} \quad \text{and} \quad \gamma_{\text{eff}} \triangleq 1/\sqrt{1 - (v_{\text{eff}}/c)^2} = \gamma_b\gamma_c(1 + v_b v_c) \tag{13}$$

Thus, $v_{\text{eff}} \leq c$. This result is generalized in Table 6.

It is important to point out that this velocity addition applies equally when a coordinate system S_b, moving with respect to S_a, has a moving transmitter on it. That is, the transmitter is moving with respect to S_b at velocity v_c and is observed by S_a. We cannot simply use the Galilean velocity addition formulas except as an approximation for small v/c. Tables 7 and 8 summarize the four-velocity and four- momentum characteristics in inertial space. Table 9 summarizes the definition and symbols used herein.

5. *Light Pulse Time Delay*

Now we consider how different observers, in relative motion, view the propagation of a light pulse from one point to another. This can be approached quite generally from the Lorentz transformations, Eq. (11). Referring to Fig. 6a, the event ϵ_1 is the transmission of a light pulse, viewed in the S' frame, from the point $(x' = -L'\cos\theta', y' = L'\sin\theta', z' = 0)$ at the time $ct' = 0$. The light pulse propagates with speed c to the origin of S', at $x' = y' = z' = 0$, where it

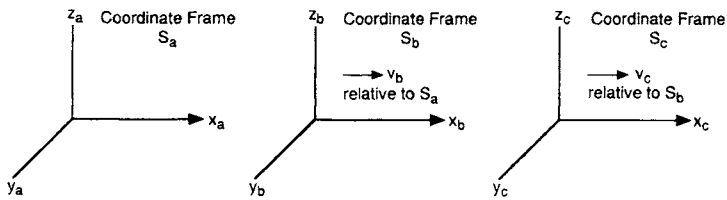

Fig. 5 Three coordinate frames S_a, S_b, S_c where S_b moves at velocity v_b with respect to S_a, and S_c moves at velocity v_c relative to S_b, both in the x direction.

Table 6 General Lorentz velocity addition transformation

Consider a particle in an inertial frame S' that moves at velocity $u'_x = \frac{dx'}{dt'}$, $u'_y = \frac{dy'}{dt'}$, $u'_z = \frac{dz'}{dt'}$, i.e., $\boldsymbol{u}' = (u'_x, u'_y, u'_z)$ with respect to S. Frame S' again moves at velocity v in the x direction with respect to S. The velocity of that particle in the S frame is then obtained from the following differentials:

$$dx = \gamma(dx' + vdt') = \gamma(u'_x dt' + vdt') = \gamma dt'(u'_x + v)$$

$$dy = dy' = u'_y dt'$$

$$dz = dz' = u'_z dt'$$

$$dt = \gamma(dt' + vdx'/c^2) = \gamma(dt' + vu'_x dt'/c^2) = \gamma dt'(1 + u'_x v/c^2)$$

Thus, the velocity as measured in the S frame is $\boldsymbol{u} = (u_x, u_y, u_z)$ is as follows:

$$u_x = \frac{dx}{dt} = \frac{u'_x + v}{(1 + u'_x v)}$$

$$u_y = \frac{dy}{dt} = u'_y/\gamma(1 + u'_x v/c^2)$$

$$u_z = \frac{dz}{dt} = u'_z/\gamma(1 + u'_x v/c^2)$$

This expression generalizes the velocity addition formula.

arrives at the time $t' = L'/c$. The coordinate intervals along the path in frame S' are $c\Delta t' = L'$, $\Delta x' = L' \cos\theta'$, $\Delta y' = -L' \sin\theta'$, and $\Delta z' = 0$.

Figure 6b shows how the path of the light looks in frame S. Because the Lorentz transformations are linear, coordinate intervals along the light path can be calculated by taking differences in Eq. (11):

$$c\Delta t = \gamma(c\Delta t' + (v/c)\Delta x') \tag{14}$$

$$\Delta x = \gamma(\Delta x' + (v/c)c\Delta t') \tag{15}$$

and $\Delta y = \Delta y'$. The last term $\gamma v\Delta x'/c$ in Eq. (14) is an extra delay caused by the distance traveled by S' during the time of transit.

Consider, for example, the special case $\theta' = 0$. The rod of length L' in S' is laid out parallel to the direction of relative motion and, therefore, to S appears to be shorter, by the Lorentz contraction, so $L = L'\sqrt{1 - \beta^2}$. Light propagates toward the front of the rod, which moves away with speed v. The relative speed with which the light catches up to the front of the rod is $c-v$, so the propagation time in S is as follows:

$$\Delta t = \frac{L'\sqrt{1 - \beta^2}}{c-v} = \frac{\gamma L'(1 - \beta^2)}{c(1 - \beta)} = \gamma\Delta t'\left(1 + \frac{v}{c}\right) \tag{16}$$

On the other hand, this result follows directly from the transformation (14), for substituting $\Delta x' = c\Delta t'$ into Eq. (14):

Table 7 Four-velocity and its space–time invariant

A *four-velocity vector* in a local inertial frame is defined by its components:

$$\boldsymbol{u} = \{u^0, u^1, u^2, u^3\} = \left\{\frac{dx^0}{d\tau}, \frac{dx^1}{d\tau}, \frac{dx^2}{d\tau}, \frac{dx^3}{d\tau}\right\} = \left\{\frac{cdt}{d\tau}, \frac{dx}{d\tau}, \frac{dy}{d\tau}, \frac{dz}{d\tau}\right\}$$

where $d\tau$ is the proper time on a hypothetical clock carried along with the particle. $d\tau$ is a scalar invariant, $d\tau = |ds|/c$ along the particle's path. If the particle velocity has magnitude v_p, then

$$d\tau = \sqrt{1 - v_p^2/c^2}\, dt = dt/\gamma(v_p)$$

where

$$v_p^2 = (v_p^1)^2 + (v_p^2)^2 + (v_p^3)^2 \quad \text{and} \quad \gamma(v_p) = (1 - v_p^2/c^2)^{-1/2}$$

In another frame S', the four-velocity vector will have components $u'^{\alpha} = dx'^{\alpha}/d\tau$, and under a Lorentz transformation such as Eq. (11) the four-velocity components transform as a contravariant vector (see Table 4):

$$u^{\beta} = \frac{\partial x^{\beta}}{\partial x'^{\alpha}} u'^{\alpha} \quad \text{or} \quad u^0 = \gamma(v)(u'^0 + vu'^1/c),\ u^1 = \gamma[v](u'^1 + vu'^0/c),\ u^2 = u'^2,\ u^3 = u'^3$$

where $\gamma(v)$ is the time dilation factor of the Lorentz transformation.

Operating on two four-velocity vectors with the metric tensor yields a scalar; e.g.,

$$\boldsymbol{g(u, v)} = g_{\alpha\beta}u^{\alpha}u^{\beta} = -u^0v^0 + u^1v^1 + u^2v^2 + u^3v^3$$

where for any inertial frame with Cartesian coordinates the metric tensor $g_{\alpha\beta} = \eta_{\alpha\beta}$, where $\eta_{\alpha\beta}$ has been defined earlier. The first term with a minus sign arising from η_{00} corresponds to the time variable term in the invariant interval, (6), while the other three terms correspond to the spatial variables. The quantity $\boldsymbol{g(u, u)}$ is invariant under any Lorentz transformation:

$$\boldsymbol{g(u, u)} = -(u^0)^2 + (u^1)^2 + (u^2)^2 + (u^3)^2 = -\gamma[v_p]^2c^2 + \gamma[v_p]^2v_p^2 = -c^2$$

because $\gamma(v_p) = (1 - v_p^2/c^2)^{-1/2}$.

$$c\Delta t = \gamma(c\Delta t' + (v/c)c\Delta t') = \gamma c\Delta t'(1 + v/c) \tag{17}$$

In the more general case where the length L' is oriented at a nonzero angle to the x,x'-axes, then $\Delta x' = L' \cos\theta'$, and the Lorentz transformation gives the following:

$$c\Delta t = \gamma c\Delta t' + \gamma(v/c)L' \cos\theta' \tag{18}$$

and the extra time delay is $\gamma vL' \cos\theta'/c$. That is, the correction is proportional to the projection of the vector $\boldsymbol{x}'$ on the x-axis. This correction term can, therefore, be written $\gamma\boldsymbol{v} \cdot \boldsymbol{x}'/c$. The correction survives even if second-order effects such as Lorentz contraction are neglected. As shown later, an analogous effect occurs with movement of the Earth's surface where the delay corresponds to a projection of the light pulse position on the equatorial plane.

6. *Drag Effect–Light Velocity in a Moving Dielectric*

Einstein's velocity addition formula also applies to the computation of the velocity of light traveling in a moving dielectric. Consider a dielectric with a

Table 8 Four-momentum for particles and photons

The *four-momentum* of a particle with rest mass m and velocity $\boldsymbol{v} = \{v^1, v^2, v^3\}$ and $v = |\boldsymbol{v}|$ is equal to

$$\boldsymbol{p} = \{p^0, p^1, p^2, p^3\} = \{E/c, p^1, p^2, p^3\} = m\boldsymbol{u}$$

where $\boldsymbol{u}$ is the four-velocity and where $p^0 = E/c = m\gamma c = mc/\sqrt{1 - v^2/c^2} \approx mc + 1/2\, mc(v/c)^2$ for small v, and where $p^1 = m\gamma v^1$, $p^2 = m\gamma v^2$, $p^3 = m\gamma v^3$.

For the four-momentum vector $\boldsymbol{p}$, the quantity $\boldsymbol{g}(\boldsymbol{p}, \boldsymbol{p})$ is invariant under Lorentz transformation:

$$\mathbf{g(p, p)} = -E^2/c^2 + (p^1)^2 + (p^2)^2 + (p^3)^2 = \boldsymbol{g}(m\boldsymbol{u}, m\boldsymbol{u}) = m^2\boldsymbol{g}(\boldsymbol{u}, \boldsymbol{u}) = -m^2c^2$$

and is proportional to the squared mass of the particle.

A photon has zero rest mass. Along the path of a photon $ds^2 = 0$; there is no frame S for which a photon is at rest. A photon carries energy and momentum described by its four-momentum vector $\boldsymbol{p} = \{E/c, p^1, p^2, p^3\}$. For a photon $\boldsymbol{g}(\boldsymbol{p}, \boldsymbol{p}) = 0$ and $E^2/c^2 = (p^1)^2 + (p^2)^2 + (p^3)^2$. Energy E and frequency f are related by $E = hf$, where $h = 6.6256 \times 10^{-34}$ Js is Planck's constant. More generally, if the wave number four-vector for photons is $\boldsymbol{k} = \{k^0, k^1, k^2, k^3\} = \{2\pi f/c, k^1, k^2, k^3\}$ then the four-momentum and wave number four-vector are related by $\boldsymbol{p} = h\boldsymbol{k}/2\pi$. Then the Lorentz transformation describes the Doppler shift formula for photons. For example, if in frame S', for which the Lorentz transformations to frame S are given by Eq. (11), a photon has frequency f' and propagates parallel to the x'-axis, then the x'-component of the wave vector is $k'^1 = 2\pi f'/c$, and the frequency f of the photon in S is given by the Lorentz transformation:

$$2\pi f/c = \gamma(2\pi f'/c + \beta 2\pi f'/c) \quad \text{or} \quad f = \gamma(1 + \beta)f' = \sqrt{\frac{1 + \beta}{1 - \beta}}\, f'$$

Table 9 Key definitions for GPS relativistic effects

x^α	four-vector space–time coordinates $\{x^0, x^1, x^2, x^3\}$, where x^0 is time expressed in meters, $x^0 = ct$
$\boldsymbol{e}_0, \boldsymbol{e}_1, \boldsymbol{e}_2, \boldsymbol{e}_3$	basis vectors
$\boldsymbol{x}$	$x^0\boldsymbol{e}_0 + x^1\boldsymbol{e}_1 + x^2\boldsymbol{e}_2 + x^3\boldsymbol{e}_3$ or $\{x^0, x^1, x^2, x^3\}$
$\boldsymbol{u}$	four-vector velocity (space–time) $\{u^0, u^1, u^2, u^3\}$, $\boldsymbol{u} = d\boldsymbol{x}/d\tau$ m/s
$\boldsymbol{a} = d\boldsymbol{u}/d\tau$	four-acceleration in m/s^2
$c\Delta t$	observed time interval, in meters, measured by clocks at rest in the observer's coordinate frame
β	normalized speed v/c
γ	Lorentz time dilation $\gamma = (1 - \beta^2)^{-1/2} = dt/d\tau$ for inertial frames
τ	proper time is the time measured by a perfect clock moving arbitrarily (measured in seconds)
$\boldsymbol{g} = g_{\alpha\beta}$	metric tensor
ds^2	infinitesimal metric line element $ds^2 = \Sigma\Sigma g_{\alpha\beta}dx^\alpha dx^\beta = g_{\alpha\beta}dx^\alpha dx^\beta$
E	energy
$\boldsymbol{p}$	four-momentum of a photon of energy $E = -\boldsymbol{p}\cdot\boldsymbol{u}$
S	inertial coordinate frame
$\mathfrak{S}$	general accelerating, gravitational coordinate frame

Chapter 19

Joint Program Office Test Results

Leonard Kruczynski*
Ashtech, Sunnyvale, California 94088

I. Introduction

FAVORABLE test results can have a tremendous positive influence on the survivability of a program. This is especially true in the early stages of a program and when a program faces stiff budget battles. A 1979 Comptroller General's report to the Congress was titled "The NAVSTAR Global Positioning System: A Program with Many Uncertainties." The Global Positioning System (GPS) was in a particularly vulnerable position. Two prior reviews by the Comptroller General had made recommendations about the program that, although agreed to by the Department of Defense, had not been implemented. The majority of the questions revolved around funding, schedules, and estimated cost savings. Chapter 4 of the report, however, gave grudging credit to the test results that had been made available. As of October 1978, test data showed that navigation accuracies were better than expected. The favorable test results were one of the bright spots in the Comptroller General's report and undoubtedly contributed to the program's continuation.

In this chapter, we review some of the details of the Joint Program Office (JPO) testing program with an emphasis on the tests conducted at the U.S. Army Yuma Proving Ground (YPG), Arizona. During phase I, Yuma was the site of the majority of tests conducted to support the Concept Validation Phase of GPS. Tests were also conducted by the Navy near San Diego. In phase II, testing expanded worldwide, but YPG remained the heart of JPO testing. U.S. military testers took the GPS receivers to many sites around the world. NATO personnel, an integral part of the JPO, tested GPS equipment in their own countries. Agencies such as the Department of Transportation also conducted tests in support of phase II. The phase III approval carried requirements for equipment modification. Tests continued into phase III at Yuma to validate the modifications that had been made to the equipment.

When not in conflict with GPS user equipment (UE) testing, the JPO supported tests at Yuma that expanded the horizons of GPS. Real-time differential tests were

* Ph.D.

conducted as early as 1979. The experiences using the ground transmitters (GT) at Yuma provide much information to those who would use pseudolites. Detailed and rigorous testing on the F-4 weapon delivery platform provided proof of the potential weapon delivery accuracy. The results of the F-4 tests became a benchmark for future weapons delivery tests. When selective availability (SA) and antispoofing (AS) were tested early in the program, the YPG GTs were used because Block I satellites cannot implement clock dither or AS. The JPO-developed test capability proved to be a highly valuable resource in the development of GPS.

II. U.S. Army Yuma Proving Ground (YPG)

The U.S. Army Yuma Proving Ground (YPG) is the Army's only general purpose proving ground located in desert terrain (Fig. 1). Located about 25 miles from the city of Yuma, Arizona, YPG covers an area of about 1,400 square miles or 870,000 acres. Originally activated in 1943, the Yuma Test Branch's mission was to test bridges, boats, vehicles, and well-drilling equipment. In 1962, what was then Yuma Test Station was assigned to the U.S. Army Material Development Command and was placed under the immediate control of the U.S. Army Test and Evaluation Command (TECOM). The name was changed to Yuma Proving Ground in 1963 and finally to U.S. Army Yuma Proving Ground in 1973. In 1974, YPG was designated a DoD major test facility partly because of the selection of YPG as the primary test site for GPS user equipment.

Yuma Proving Ground's missions include testing tube artillery systems, aircraft armament systems, air delivery systems, and air movable equipment. The missions also include planning, conduct, and reporting of the results of desert environmental

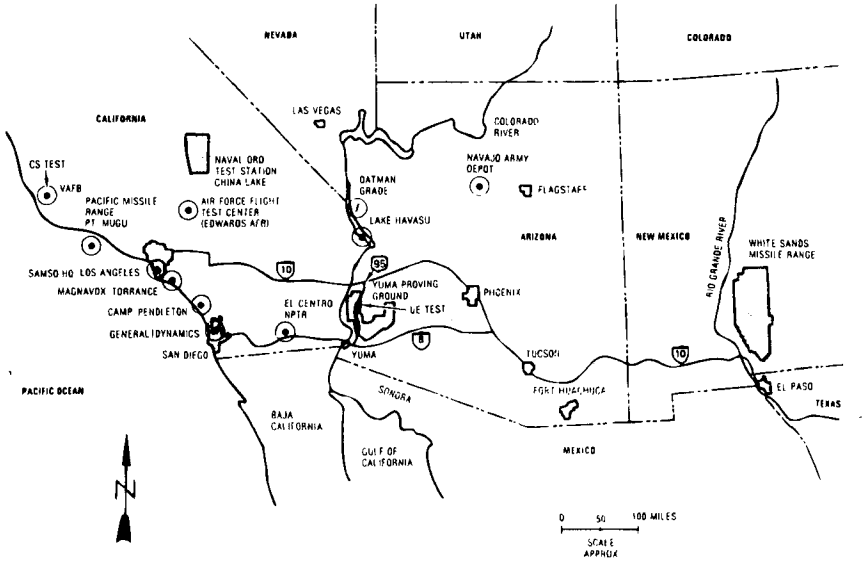

Fig. 1 GPS test locations.

tests of all classes of materiel. The M-1 Abrams tank was a heavy user of the range during the time of GPS testing.

III. Reasons for Selection of Yuma Proving Ground

Yuma Proving Ground has a climate characterized by clear skies, with an average visibility of 25 miles and only three and one-half inches of rain per year. With the extensive real estate and restricted air space, uninterrupted testing can be almost guaranteed. YPG had embarked on a program to use lasers to track artillery shells. The range proposed to use the laser trackers to determine truth trajectories for GPS tests.

IV. Lasers

A total of six lasers were eventually installed at YPG. Figure 2 shows the location of the six lasers and the area of the range covered by at least two lasers. Four lasers were in the southern half of the range and two in the northern half. The tracking lasers are Neodymium YAG lasers built by Sylvania Electronics. The system is designated PATS for precision automated tracking system. The specified radiated power is 50 mJ per pulse, which is automatically attenuated to eye safe levels by measuring the return signal level. Beam divergence, as used in eye safety tests, is less than 2 mrad. Eye protection is required when closer than 2 km to an operating laser.

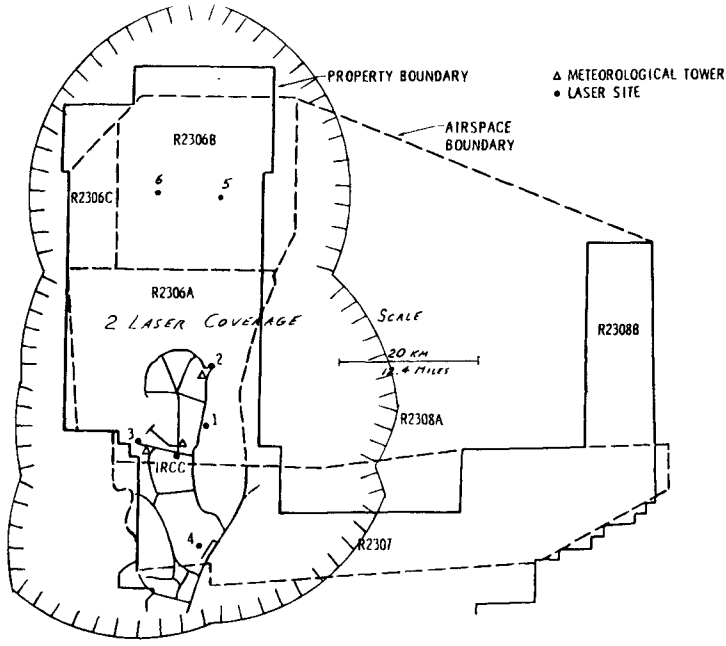

Fig. 2 Yuma Proving Ground area with laser coverage.

Each tracker takes range, azimuth, and elevation measurements at a 100-Hz rate. Specification accuracy for the range measurements is 0.5 m rms from 200 m to 10 km and 1 m rms from 10 km to 30 km. Azimuth and elevation measurement accuracy is 0.1 mrad in each axis. Every fifth measurement is transmitted from the laser site to the Range Operations Center (ROC). No smoothing or editing is performed on the measurements at the laser except to aid in target tracking by the laser. The transmitted measurement is selected only to synchronize the measurements so that a measurement is available on an even second as given by IRIG time. At the laser site, the measurements are recorded at a 100-Hz rate. This field tape is used only for fault isolation. No processing is done on the 100-Hz measurements.

Prior to and immediately following each mission, the laser takes measurements to a series of short targets circling the laser. Typically, there are eight short range targets roughly 1 km from the laser. The short range calibrations are processed by the ROC to provide corrections to tilt (two terms), azimuth, elevation, and range terms.

Each laser also has eight long-range targets at ranges from 1 km to 30 km. The primary use for the long-range calibrations is to determine range bias. Long-range calibrations normally are accomplished monthly or upon request.

"Dump cals" is a third type of calibration for the lasers. To do a dump cal, the laser housing is rotated in elevation through 180 deg, and the short-range targets are tracked. Dump cals are accomplished after maintenance and upon request.

V. Range Space

The Cibola Range covers a ground area approximately 50 km $\times$ 100 km and extends to 25 km altitude. Most of the tests were conducted in the southern half of the range. A hilly ridge separates the southern half from the northern half. Two lasers were installed in North Cibola to support aircraft testing that required the entire range. The difficult logistics involved in supporting North Cibola resulted in low utilization of North Cibola. However South Cibola was more than adequate for the majority of testing that had to be accomplished.

Ground vehicle testing was conducted on the dynamometer course. Vehicles on the dynamometer course were tracked by a single laser. Also, the location of the GTs on hills allowed the vehicles to track pseudolite signals when necessary.

VI. Joint Program Office Operating Location

The official presence of the JPO at YPG was the operating location, OL-AA. The operating location normally consisted of Air Force officers and enlisted personnel, civilians assigned by YPG Materiel Test Directorate, military assigned by YPG, Aerospace Corporation personnel, and other agency representation depending on needs. Defense Mapping Agency maintained a slot at OL-AA for several years. General Dynamics Electronics Division and later General Dynamics Services Company provided operations and maintenance support for the operating location.

VII. Satellite Constellation for Test Support

GPS orbital parameters had to satisfy several requirements. High-altitude orbits were desired for survivability and to reduce the number of satellites needed for global coverage. A high inclination was needed to provide coverage in polar areas. A 12-h orbit was selected because it allowed each satellite to be visible over the continental U.S. at least once per day. Twenty-four-hour orbits would not have this feature. In addition, satellites in 24-h orbits were farther from the users, thus requiring greater transmitted power. A critical criterion to support testing was to require that a test window, and preferably an identical test window, exist at a single test site each day. For phase I, the GPS constellation was set up to optimize coverage for testing at YPG.

It is easier to explain GPS test window behavior by assuming that the test site is on the equator and that, on the first day of testing, the satellite passes directly overhead. The requirement for constellation repeatability is that on the next day of testing, the satellite must again be directly overhead. We can further assume that the satellite is crossing the equator in the northerly direction, making this point the ascending node of the orbit.

After two orbits, the satellite will again be at the ascending node over the equator. The key is to require that two orbits of the satellite take the same amount of time as the test site takes to move back under the satellite. Satellites move in space independently of the Earth's rotation. To require that the position of the satellite relative to the ground location repeat requires planning. The two orbits must take 23 hours, 56 minutes and 4 seconds because that is how long it takes the Earth's rotation to bring the test site back to the satellite's ascending node. If this timing is not satisfied, then the location of the satellite with respect to the test site will drift daily, eventually resulting in the lack of a test window at the test site. It is this requirement that gives rise to the 4-min regression of the test window each day.

Had the Earth been perfectly round, the test window would repeat not only in character but also time of day each year. However, the Earth is oblate and the satellite is perturbed. The result is an approximate 50-min shift in the test window each year. This phenomenon helps explain why the GPS test window at Yuma moves from night in the summer of one year to daytime in the summer of a later year.

VIII. Control Segment Responsiveness to Testing Needs

The Control Segment that existed for the testing through phase II consisted of a Master Control Station (MCS) at Vandenberg Air Force Base, California, and monitor stations in Alaska, Hawaii, and Guam. Vandenberg was the launch site for the Block I satellites. The configuration of the monitor stations was especially beneficial to testing at Yuma. The satellites have an eastward motion, so they were generally visible to at least one of the monitor stations prior to rising at Yuma. The MCS was able to upload a satellite either prior to or shortly after the satellite rose at Yuma. By avoiding the use of day-old data, the space and control segment errors seen by receivers under test were minimized.

IX. Trajectory Determination at YPG

A. Real-Time Estimate

The workhorse trajectory at YPG is the real-time estimate (RTE), a position and velocity solution obtained from a single laser. The lasers transmit range, azimuth, and elevation measurements at a 20-Hz rate via microwave links to the ROC. In the ROC, the measurements are preprocessed by a PDP 11/35 and sent to a SEL 32/77 for real-time processing. In the SEL, the measurements are processed first at the incoming 20-Hz rate (every 50 ms) and then at a 5-Hz rate (every 200 ms). The 200-ms task takes every fourth 50 ms measurement on the even 0.2 s, as given by IRIG time.

In the 50-ms task, the measurements are processed using a QD filter with a memory parameter equal to six. Measurement residuals are calculated by subtracting the measurement predicted using a second-order formula from the actual measurements. The output of the 50-ms task is range, azimuth, elevation, and first and second rates of change of range, azimuth, and elevation.

The 200-ms task selects every fourth 50-ms output. Calibration factors obtained from premission tests are now applied. The measurements are then transformed from laser-centered range, azimuth, and elevation to IRCC-centered Cartesian coordinates. The IRCC is the Inverted Range Control Center and is located in the middle of the southern part of the YPG test range. These measurements are processed in the 200-ms task with a QD filter with a memory parameter of 10. QD processing in the 200-ms task is similar to the 50-ms task, except the state consists of IRCC East, North, and Vertical components instead of range, azimuth, and elevation used in the 50-ms task. Following the 200-ms QD, the software attempts to determine which retroreflector is being tracked.

To provide continuous track at all attitudes, most aircraft have two retroreflectors. A retroreflector is an array of corner cubes that reflect light in the direction from which the light comes. A retro mounted on top of the aircraft is needed to maintain track when the aircraft banks. The bottom-mounted retro is the real-time estimate solution point. If the software determines that the upper retro is being tracked by the laser, then lever arm corrections are made to move the solution to the lower retro point.

Retro identification and lever arm adjustment are normally accomplished using one of two methods. If no inertial data are available, a wind–velocity algorithm is used to estimate the attitude of the aircraft. Look angles from the laser to the target are computed and are used to determine which retro is being tracked. In the second method, attitude data from GPS user equipment can be used to provide aircraft attitude information for the look angle computation.

There is a range of look angles for which there is a high degree of uncertainty as to which retro is being tracked. Should the look angles fall into this range, the validity flag for the laser's trajectory estimate is lowered. The laser validity flag can also be lowered if measurements are outside statistical bounds.

If a laser is declared valid, then the solution is a candidate for the RTE. The RTE is the truth trajectory for evaluation of GPS UE. Typically, it is the solution determined by the laser closest to the target if the laser's solution has been declared valid. There is an optional composite laser solution that can be used as the RTE. The composite is a weighted average of the valid laser solutions.

Weighting is a function of range to the target. The closer the laser is to the target, the higher the weighting given the laser solution. There is a maximum gain that can be given any laser.

B. Best Estimate of Trajectory

In critical cases, it is possible to compute a best estimate of trajectory (BET), which considers multiple laser inputs. When requested, BETs are computed postprocessed. The quality of the RTE was sufficient for most tests and BETs were computed sparingly.

C. Validation of Truth Trajectory Accuracy

Performance evaluation of GPS UE must be made using a trajectory estimate that is more accurate than the GPS equipment being tested. Laser tracker specifications indicate that the YPG capabilities were within the requirements to evaluate GPS equipment. To support YPG's ongoing program to improve laser accuracy, validation tests were conducted using the Texas Instruments five-channel phase I High Dynamics User Equipment (HDUE). The HDUE was integrated with a Honeywell inertial measuring unit and installed on a Convair 880. The equipment was operated in a differential navigation mode to remove Space and Control Segment errors. The conclusions reached during the various validation tests was that the RTE was accurate to within 3 m throughout the range, with better accuracy in areas of optimal laser coverage.

Velocity accuracy of the lasers was shown to be about 0.2–0.3 m/s. This is on the order of GPS accuracy, especially when aided by inertial sensors. Evaluation of GPS velocity accuracy using the RTE-computed velocities had to be considered only in the sense of bounding the errors. The source of the velocity error could have been the laser as well as the UE.

D. Ground Truth

Early in the GPS program, it was evident that the accuracy performance of user equipment would vary from day to day, depending on the behavior of the satellites and the ability of the Control Segment to predict satellite orbital and clock behavior. Ionospheric delays can vary considerably over time. Tropospheric delay, although it is a smaller contributor to navigation error, might also be different from one test time to the next. However, it was incumbent on the government to evaluate the performance of the various manufacturers fairly, regardless of the performance of the Space and Control Segments and regardless of atmospheric activity. The solution was to compare the error in the positions calculated by the UE to a "ground truth."

Ground truth is the absolute error in the solutions computed by a "perfect" receiver. The development specification for the IRCC defined ground truth as "a direct real-time estimate of the expected error in an IRCC located user's computation of position and time." It was expected that all receivers under test on the range would see virtually identical errors. Thus, if ground truth was 15 m East of the surveyed location and if the receiver under test was also 15 m East, then the receiver was deemed to have perfect accuracy performance.

To create ground truths, the Magnavox phase I X-set receiver in the IRCC was used. The IRCC was located in the center of the southern part of the YPG test range (Fig. 2). The topography was flat with virtually no blockages except by IRCC equipment itself, such as the lightning rod. To minimize clock errors, a cesium frequency standard was connected to the X-set.

Ground truths were computed by the IRCC computer using measurements from the X-set. The measurements were adjusted by removing estimated range and satellite clock behavior using the satellite navigation data and the IRCC's true position, by using L_1-L_2 data to remove ionospheric delay, and by using locally collected meteorological data to remove tropospheric delays. Receiver clock offsets and drift were removed by using the clock synchronization navigation solution. If the satellite data are accurate, if L_1-L_2 measurements allow complete removal of ionospheric delays, if the tropospheric delays are correctly modeled, if the receiver clock algorithm is accurate, and if other error sources such as multipath and receiver noise are zero, then the corrected pseudorange will be zero. Based on the evaluation of all error sources, corrected pseudorange measurements greater than 1–2 m were most likely caused by satellite navigation data inaccuracies.

The clock synchronization navigation solution was a two-state Kalman filter. Receiver clock offset and drift were the two states. Corrected pseudoranges were input to the Kalman filter and the output was processed until the filter was in steady state. Values for the clock offset could vary wildly on a point-by-point basis, especially if different satellites were used to provide the input data. However, rapidly changing values for the clock offset are neither an accurate depiction of true clock behavior, nor are they desirable for the calculation of position ground truths. The IRCC assumed the clock filter to be in steady state when the best estimate of receiver time was fairly constant, when the average of the pseudorange residuals from all the satellites was zero, and when the differences between the pseudorange residuals of the satellites tended to be constant.

The ground truth navigation solution was calculated using a five-state Kalman filter. The first three states were the three-dimensional position and the other two states were the receiver clock offset and drift as they would be calculated by a navigating receiver. The Kalman filter was tuned to provide an explicit solution with each new set of measurements but with a small amount of filtering to reduce noise.

Ground truths were presented as errors in solutions. To use the ground truth, the receiver under test had to use the same constellation for positioning as was used by the IRCC. Initially, this was no problem because the constellation was limited. Four satellites were launched from February 1978 to December 1978. The fifth and sixth successful launches occurred in 1980. The seventh satellite was launched in 1983. The ground truth computation was modified to allow for the best five GDOP constellations. With five satellites available, only five four-satellite constellation selections are possible. With six satellites, up to 15 different four-satellite constellations are possible. However, many constellations would have geometries beyond acceptable limits.

The IRCC performed the additional function of controlling the ground transmitters (GTs). Using ground transmitters requires that the phase of each GT be accurately synchronized. The GTs themselves did not have atomic clocks.

Table 1 Phase I major field test objectives

Navigation accuracy	Threat performance
Position accuracy	Jamming resistance
Velocity accuracy	Denial of accuracy
Effects of dynamics on accuracy	
	Environmental effects
Demonstrations of military value	Propeller and rotor modulation
Precision weapon delivery	Foliage attenuation
Landing approach	Multipath rejection
Rendezvous	Ionospheric and tropospheric correction
Photomapping	
Nap-of-Earth operations	System characteristics
Static positions	Satellite and clock and ephemeris accuracy
Combined operations	Acquisition and reacquisition time
Crosscountry	Time transfer
Shipboard operations	Signal levels and signal structure

X. Phase I Tests (1972–1979)

After passing DSARC I in December 1973, GPS entered the concept validation phase of development. The major field test objectives for phase I are identified in Table 1. The user equipment tested at YPG included receivers from Magnavox under contract to General Dynamics, Collins, and Texas Instruments. Table 2 lists the basic characteristics of user equipment tested as part of the concept validation phase. User sets were mounted in specially instrumented pallets on several vehicles, such as those listed in Table 3.

XI. Ground Transmitters

Testing GPS at YPG began on March 15, 1977. At that time, there were no satellites in orbit. Instead, four ground transmitters, or pseudolites, were used to transmit a satellite-like signal to provide a simulated constellation. The locations of the ground transmitters are identified in Fig. 3 as IRGT-21 through IRGT-24. The pseudolites transmitted an L_1 signal modulated with C/A and P-codes. The data transmitted was a unique message because it is impossible to model the dynamics of a receiver on the ground in a Keplerian formulation. The pseudolites did not transmit an L_2 signal because ionospheric delay was not an issue. PRN codes from 33 to 36 inclusive have been reserved for GTs.

The four GTs and the IRCC comprised the inverted range (IR). The IR was used in the early days of GPS testing when no satellites were available and later to supplement inadequate coverage, for special tests such as SA/AS, and for real-time differential tests. When four GTs were used, even the best geometry has poor vertical dilution of precision (VDOP) performance. When operating in a hybrid mode, one satellite and three GTs provide an optimal geometry. As more satellites became available, it was advantageous to minimize the use of GTs, even at the expense of larger dilutions of precision (DOPs).

Table 2 Characteristics of concept validation phase user equipment

User equipment	Frequency	Code	Number of channels	Integrated with inertial	Contractor
X	L_1 and L_2	P and C/A	4	Yes or No	General Dynamics/ Magnavox
Y	L_1 and L_2	P and C/A	1	Yes or No	General Dynamics/ Magnavox
Z	L_1	C/A	1	No	General Dynamics/ Magnavox
General development model (GDM)	L_1 and L_2	P and C/A	5	Yes	Collins
High dynamics user equipment (HDUE)	L_1 and L_2	P and C/A	5	No	Texas Instruments
Manpack (MP)	L_1 and L_2	P and C/A	1	No	General Dynamics/ Magnavox
Manpack/ vehicular equipment (MVUE)	L_1 and L_2	P and C/A	1	No	Texas Instruments

When four pseudolites were used, the DOPs on the range varied significantly and rapidly. Typical horizontal dilutions of precision (HDOPs) at 20,000 ft above the range changed from 2 to 20 in 8 miles. Thus, an aircraft flying at 300 kt would pass through this range of HDOPs in 90 s. VDOPs had several singularities existing over the course. The character of the DOP contours changed when three GTs were used in conjunction with one satellite, but steep gradients were still present.

The IRCC controlled the transmitted power of the GTs during operation. Each pseudolite was equipped with a remotely controlled programmable attenuator. Maintaining proper power levels was necessary to prevent the GT from jamming the receiver. Power levels were adjusted based on the distance between the receiver and the GT. Multiple aircraft tests were not conducted. Power adjustments were especially critical when the receiver lost lock on a satellite because the receiver would switch to C/A code, which was much more susceptible to jamming than the P-code.

When operating in a hybrid mode, the IRCC had to offset the GT clocks and synchronize them to GPS satellite time. The IRCC attempted to keep the GT clocks accurate to within one ns. The IRCC monitored the GT signals and used a uhf radio control system to control the GTs. The pseudolite clocks were driven by temperature stabilized precision oscillators, which were kept in thermal canisters buried six feet under ground at each pseudolite site.

When satellites were used in conjunction with GTs, the aircraft required two antennas; one antenna on the top and a second antenna on the bottom of the aircraft. The upper antenna tracked satellites, while the lower antenna tracked

Table 3 Concept validation phase test vehicles

Vehicle type	GPS set type	Dynamic range
Mobile test van	XU	Static
Man	Manpack, MVUE	Low
Landing craft	XU, YU	Low
Frigate	XU, YU	Low
Armored personnel carrier	Manpack, MVUE	Low
M35 truck	XU, HDUE, Manpack, MVUE	Low to medium
Jeep	Manpack, MVUE	Low to medium
UH-1 helicopter	XU, YU, Manpack, HDUE, MVUE	Medium
C-141 aircraft	XU, XA, YU, YA, GDM, Z, HDUE	High
P3 aircraft	XU, XA, YU, YA, Z	High
F4 aircraft	XA	Very high

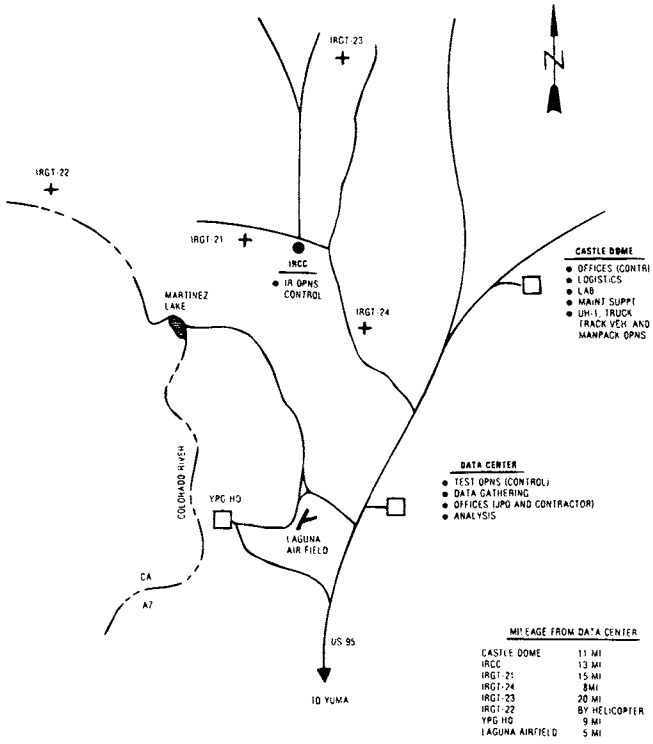

Fig. 3 GPS test area at Yuma Proving Ground showing ground transmitter locations.

the GTs. The phase I UE were designed with two antenna ports. The dual-antenna design also minimized dropouts of GPS satellites during maneuvers. The phase I equipment used inertial attitude data from an external sensor to determine which antenna should be used to track a specific satellite.

The pseudolites on the IR served their assigned purpose of helping to discover and solve user equipment design problems when satellites were not available. Later in the test program, GTs were used to test selective availability and anti-spoofing performance because the Block I satellites did not have SA/AS capabilities. GTs were also used as the data link in real-time differential tests. The experience with GTs has proved valuable to groups investigating the use of pseudolites such as the Range Applications JPO at Eglin Air Force Base.

Phase I test results were excellent. Figure 4 summarizes the performance of the various equipment tested during the conduct of the phase I program. Three-dimensional position errors at the 90% confidence level ranged from about 35 m for the single-frequency Z-set to 15 m for the multichannel, dual-frequency receivers.

Precise statistical values for weapon delivery performance are classified. However, the JPO often presents graphic depictions of the accuracy of weapon delivery. The results from tests have often been displayed relative to the cupola in the center of the Pentagon or relative to a typical suspension bridge.

XII. Navy Testing for Phase I

The U.S. Navy conducted several tests in support of phase I. Most of the tests were conducted in the waters near San Diego. Figure 5 shows the ground track

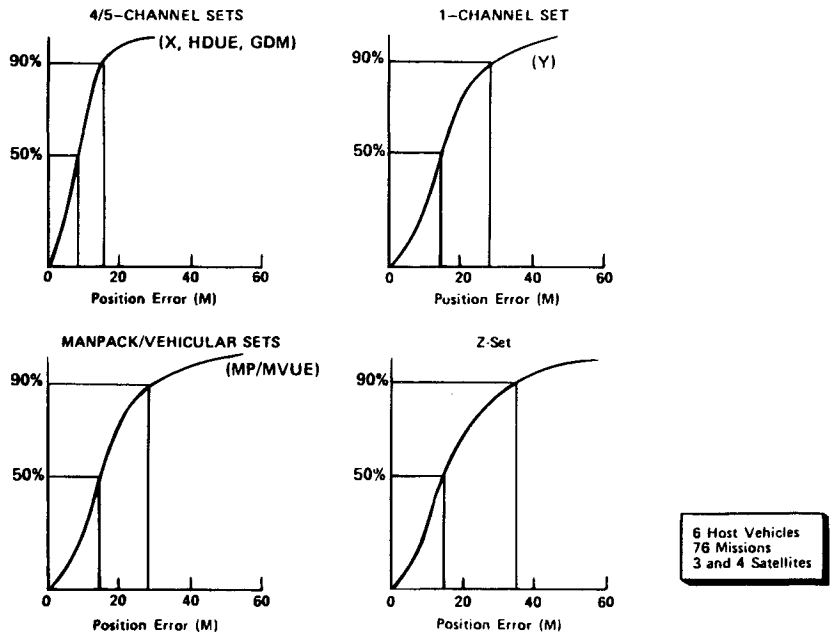

Fig. 4 Phase I results.

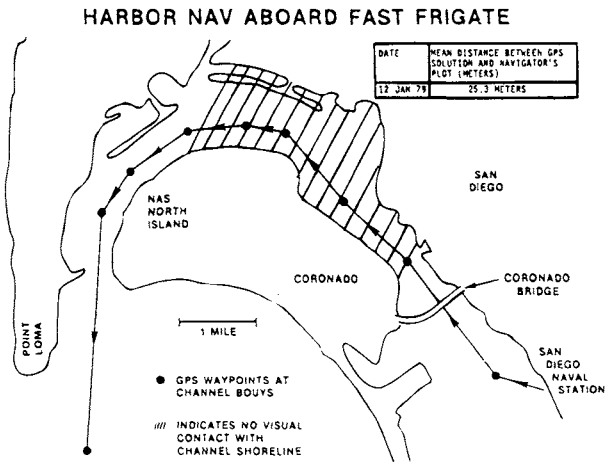

Fig. 5 Navigation aboard a fast frigate in San Diego harbor.

of a fast frigate test in San Diego harbor. The hatched area was fogged in during the test. No laser-accuracy truth solution was available for this test. However, the average difference between the navigator's plot and the GPS solution was about 25 m.

Several Navy tests were aimed at identifying and characterizing multipath effects. Dockside testing was accomplished using a Navy landing craft and a fast frigate. Tests were conducted on two subsequent days for each of the craft using P-code receivers. Signal strength fading and pseudorange errors were analyzed to determine multipath effects. Although frequency standard instabilities made the analysis difficult, the tests identified peak-to-peak pseudorange oscillations of 4–5 m caused by multipath.

XIII. Tests Between Phase I and Phase II (1979–1982)

A. Weapons Delivery

Weapons delivery tests continued while YPG awaited the start of phase II. A Navy F-4 was equipped with a Magnavox phase I X-set and integrated with an IMU. Considerable work was done to tune the pilot's display to inform the pilot better about steering information. The software accounted for aircraft attitude, bomb location, ejection velocities, bomb dynamics, ejection velocities, winds estimates, and so forth. The statistical results are classified, but it was not unusual for the inert bomb to hit the stake used to mark the surveyed target point.

B. Differential Tests

Differential GPS was an integral part of range operations from the beginning. Ground truth was based on the concepts behind differential GPS; that is, the removal of errors common to all users in the vicinity. But differential was not limited to simply laying a ground truth plot over a UE error plot. In 1979, a

real-time differential system was established to allow the Air Force to conduct flights to validate the performance of the YPG trajectory estimate.

The Texas Instruments HDUE was a five-channel receiver. In normal operation, four channels tracked satellites on L_1 and the fifth channel sequenced through the satellites on L_2. This allowed the receiver to make real-time ionospheric delay measurements.

To modify the HDUE for real-time differential operation, the fifth receiver channel was used to receive the differential corrections transmitted by a GT. The software was modified to allow proper decoding of the GTs data. At first look this may seem to have the effect of removing the capability to compute ionospheric delay. In reality, the differential message transmitted to the HDUE was computed based on a no-ionosphere position computation, in effect, accounting for ionospheric effects.

Tests of the real-time differential HDUE began on December 13, 1979 at YPG on board a UH-1H helicopter. The initial series of tests clearly demonstrated that nondifferential horizontal errors of approximately 20 m are reduced to 5 m or less upon application of the differential correction.

Table 4 is a summary of horizontal and vertical accuracies reported during a series of differential GPS tests in January 1980. Subsequent analysis of the data showed that the processing was flawed and that actual achieved accuracy was better than indicated in the table. The detailed data analysis determined that the processing had not accounted for the lever arm between the retroreflector and the antenna.

The HDUE in differential mode proved to be very accurate. Range validation tests conducted to test the accuracy of the lasers used the HDUE in differential mode. The tester had become the tested.

The early tests with differential mode were accomplished with the corrections transmitted in terms of adjustments to the position solution. As more satellites were launched and it became impossible to count on the receivers using the same constellation, the HDUE differential mode and the IRCC/GT differential message were modified. The IRCC now transmitted corrections to the individual satellite measurements. The HDUE, after receiving and decoding those corrections, applied them as ionospheric delay estimates to the individual pseudoranges. Tests

Table 4 Differential test summaries, m

Date		Mean	Root sum square	Standard deviation	CEP/ probable error
9 Jan 1980	Horizontal	4.2	4.7	2.1	3.8
	Vertical	−5.2	5.5	1.9	5.2
10 Jan 1980	Horizontal	5.0	5.3	1.8	5.0
	Vertical	3.9	4.5	2.2	4.0
11 Jan 1980	Horizontal	3.8	3.8	0.8	3.7
	Vertical	1.4	2.0	1.5	1.5
16 Jan 1980	Horizontal	3.6	3.8	1.5	3.4
	Vertical	2.1	2.6	1.5	2.1

using the measurement correction method began in 1984, with accuracy results similar to previous differential tests. The system again demonstrated its accuracy by identifying an out-of-calibration laser.

XIV. Phase II: Full-Scale Engineering Development Tests (1982–1985)

Phase II, full-scale engineering development testing of GPS UE began in 1982. Two contractors, Rockwell-Collins and Magnavox, had been selected to compete in the phase II program.

In the concept validation phase, it was appropriate and acceptable to tune equipment to specific situations. Satellite selection algorithms and acquisition techniques were not an issue during phase I. Indeed, with the lack of satellites, it would have been difficult to test such requirements. Environmental requirements for the equipment were also secondary considerations in phase I. In phase II, however, the equipment was to be integrated into several host vehicles and the integrations were to be representative of production requirements. Several other applications of GPS were to be tested, especially those related to the integration into complex avionics systems. Phase II test objectives included the following:

1) Verify reaction time, time to first fix, time to subsequent fix, and reacquisition time.
2) Verify static and dynamic position and velocity accuracies.
3) Evaluate IMU/INS alignment and gyro damping capabilities.
4) Determine susceptibility to electronic warfare and nuclear threats.
5) Evaluate precision weapons delivery using GPS bombing mechanization.

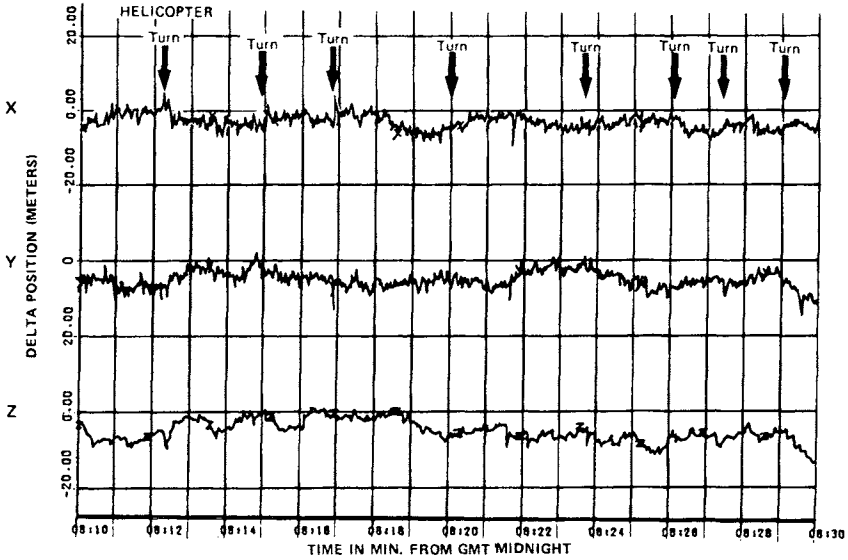

Fig. 6 Example of global positioning system position errors (UH-60 two-channel set).

Table 5 Summary of position accuracy for phase II tests

Vehicle	Spherical error probable, 3D, 50%
A-6	6 m
B-52	9 m
SSN (submarine)	12 m
F-16	13 m
Manpack/vehicular	12 m
UH-60 helicopter	12 m
CV (aircraft carrier)	16 m

6) Determine mission performance improvement for aircraft landing approach, point-to-point and course navigation, rendezvous, ordnance delivery, and carrier-based aircraft alignment and gridlock.

7) Evaluate human factors design.

8) Evaluate reliability, availability, maintainability, and logistics supportability.

9) Identify and track deficiencies and improvements.

10) Evaluate the effects on performance caused by multipath from the surface of the water.

11) Evaluate the adequacy of specified military occupational specialties/skill levels and training.

12) Evaluate the effects on performance resulting from adverse environmental conditions to include RFI/EMI, temperature, humidity, altitude, and vibration.

13) Determine submarine antenna detectability.

14) Evaluate the effects of rotor blade modulation/multipath/masking on performance in an EW environment.

15) Determine ease of chemical, biological, and radiological decontamination.

A sample set of data from phase II testing is shown in Fig. 6. The data represent the East (X), North (Y), and Up (Z) errors in a two-channel GPS set flown on a UH-60 helicopter over the YPG range. A summary of the overall results of the phase II position accuracy tests for various host vehicles is shown in Table 5.

XV. Summary

In this chapter, we have highlighted only some of the massive amount of testing conducted on behalf of the GPS JPO. It will have been over 20 years from the date of the DoD directive that authorized GPS to the date of full operational capability. During that time, technology and politics progressed through several generations and mood swings. Keeping Congress and the public in favor of continued funding of an expensive program is a difficult task. GPS was successful in maintaining the needed funding partly because of the JPO's

ability to actually demonstrate capabilities of the system through a series of detailed and rigorous tests. Future users of GPS have a enormous database of information about the details of GPS on which to base decisions about equipment configuration and the appropriateness of application.

Bibliography

GPS User's Overview, Deputy for Space Navigation Systems, Navstar Global Positioning Joint Program Office, YEE-82-009A, Los Angeles, CA, Sept. 1984.

GPS User's Overview, Deputy for Space Navigation Systems, Navstar Global Positioning Joint Program Office, YEE-82-009B, Los Angeles, CA, Sept. 1986.

Henderson, D. W., and J. A. Strada, "NAVSTAR Field Test Results," Paper presented at the Institute of Navigation National Aerospace Symposium, Springfield, VA, March 6–8, 1979.

Kruczynski, L. R., "Truth Trajectory Estimation for Global Positioning User Equipment Tests," Paper presented at the International Telemetering Conference, San Diego, CA, Oct. 24–27, 1983.

Kruczynski, L. R., Abby, D. G., Porter, W. W., and Weston, E. T., "Global Positioning System Differential Navigation Tests at the Yuma Proving Ground."

Mai, R., "The QD Filter in YPG's Real Time Laser Display System," unpublished report by Yuma Proving Ground, June 1978.

"The NAVSTAR Global Positioning System: A Program with Many Uncertainties," Report of the Comptroller General to the Congress of the United States, Jan. 1979.

Teasley, S. P., Hoover, W. M., and Johnson, C. R., "Differential GPS Navigation," Texas Instruments, Inc., TR, 1981.

Weston, E. T., "Inverted Range Navigation Solutions," unpublished General Dynamics Electronics Div. Report, June 1981.

Chapter 20

Interference Effects and Mitigation Techniques

J. J. Spilker Jr.* and F. D. Natali†
Stanford Telecom, Sunnyvale, California 94089

I. Introduction

THE GPS navigation satellite system is designed to serve both military and commercial needs. Because of its military applications, the ability to tolerate significant amounts of interference and jamming was an important consideration in the design of the signal structure. The purpose of this chapter is to describe the effects of interference and to present some design guidelines and mitigation techniques to improve the tolerance to interference of commercial GPS receivers that operate on the C/A signal. The performance of the P(Y)-code signal in the presence of jamming is beyond the scope of this book.

The GPS frequency bands are protected by international and Federal Communication Commission (FCC) frequency assignments. Nonetheless, there is the chance of spurious unintentional interference and even intentional interference. Obviously, any radionavigation system can be disrupted by an interference of sufficiently high power, and the GPS is no exception. Of course, GPS has the obvious limitation that the signal power received has been attenuated by the path loss from the distant satellite. The GPS C/A and P signals are both spread-spectrum signals and, as such, are much less susceptible to interference than a narrow-band signal. For example, a sidetone ranging signal that consists of a pure carrier with tone modulation has a much greater susceptibility to interference. A tone interference could completely disrupt a sidetone- or Doppler-type positioning system if its power simply exceeded that of the desired ranging signal. Interference of even less power could cause significant errors. With the GPS, as described in Chapter 3, this volume, a received tone interference would have to be significantly greater in power than that of the received GPS signal in order to degrade performance appreciably. Thus, the GPS has several advantages over a conventional narrow-band navigation system with respect to purposeful or unintentional interference or disruption for the following reasons:

1) GPS signals, both C/A and P(Y) code, are spread-spectrum signals and permit well-designed receivers to tolerate significantly larger amounts of co-

*Ph.D., Chairman of the Board.

† Ph.D., Vice President, Chief Engineer.

channel or adjacent channel interference than can be tolerated by conventional narrowband signals.

2) The GPS position determination is relatively robust, because the system is generally overdetermined; i.e., there are often more satellites visible than the minimum number required for a solution. Furthermore data detection, which has a significantly higher threshold than the tracking functions, is not required continuously.

3) Special receiver design techniques, such as adaptive A/D converters, adaptive frequency notch filters, various types of adaptive delay lock loops (adaptive DLL), and adaptive nulling antennas can further improve receiver performance. An adaptive DLL detects the presence of interference and narrows the tracking loop bandwidth.

4) GPS receivers can be designed to detect interference levels strong enough to disrupt navigation, because the interfering signal must generally be large compared to the relatively stable thermal noise level. Once interference is detected, the receiver can take corrective action.

5) In addition, because the GPS signals are generated on a satellite at a considerable distance from Earth, the satellite signal sources are not easily disrupted by natural disasters. Ground-based transmitters, on the other hand, are sometimes disrupted by violent storms or earthquakes.

The GPS receivers can, by proper design, take maximum advantage of the GPS spread-spectrum signal characteristics. However, beyond a certain interference level, any radionavigation signal can be disrupted. In this situation, the GPS receiver can be designed to detect the presence of the interference and switch to the use of other sensors. This detection process can be similar to that employed in receiver autonomous integrity measurement (RAIM), as discussed in Chapter 5 of the companion volume. However, even in the rare instance when there are an insufficient number of satellites in view to employ RAIM, a high enough level of interference to disrupt GPS navigation can be reliably detected by a properly designed receiver interference detector or by discrete Fourier transform (DFT) processing, and the receiver can alert the operator to take corrective action. Interference mitigation techniques for GPS receivers include the following:

1) Use of adaptive array, multibeam, or adaptive nulling antennas. These techniques can be categorized as spatial signal processing.

2) Radio frequency/intermediate frequency (rf/IF) filtering to reduce adjacent channel and out-of-band interference.

3) Use of sufficient number of bits/sample and AGC to reduce nonlinear signal suppression effects. Adaptive A/D conversion can reduce constant envelope interference effects.

4) Adaptive filtering in the delay lock loop and phase lock tracking filters.

5) Use of the vector delay lock loop described in an earlier chapter on Signal Tracking Theory (Chapter 7, this volume).

6) Detection of interference followed by an appropriate change in the DLL signal processing and aiding from other sensors, such as inertial measurement units (IMUs).

7) Augmentation of the GPS by ground (pseudolite) and space-borne signal sources.

8) Use of Adaptive frequency notch filters to attenuate narrow-band interference.

A. Possible Sources of Interference

Possible sources of unintentional interference to GPS receivers are shown in Fig. 1. None of these is believed to be a real problem to the GPS, but we should be aware of them, nonetheless. Some of these have at times produced interference to GPS receivers. These include the following[1-3]:

1) Out-of-band interference caused by nearby transmitters coupled with inadequate rf filtering in the GPS receiver.

2) Harmonics or intermodulation products of various ground and airborne transmitters. For example, transmitters at 105.028 MHz, 225.06 MHz, 315.084 MHz, 525.14 MHz, and 787.71 MHz have harmonics (the 15th, 7th, 5th, 3rd, and 2nd respectively) that fall within the GPS L_1 frequency band. Normally these transmitters are sufficiently well filtered to avoid radiating interference.

3) Potential active or passive intermodulation products of signals or local oscillators on the same platform as the GPS navigation receiver or from other nearby platforms. We must ensure that these potential intermodulation products are adequately removed by filtering. For example, we must take care to prevent radiation of local oscillator or intermodulation products from an aircraft transmitter that might couple into a GPS receiver on that same aircraft.

4) Pulsed interference from radar signals in nearby frequency bands that are inadequately filtered.

5) Accidental transmission of signals in the wrong frequency band by experimenters.

B. Frequency Allocation in Adjacent and Subharmonic Bands

We first examine the frequency bands near the GPS frequency band and then other bands that could create harmonics or intermodulation products that fall within the GPS bands if the transmitters are improperly filtered. The frequency bands assigned to satellite radio navigation (GPS, GLONASS) are shown in

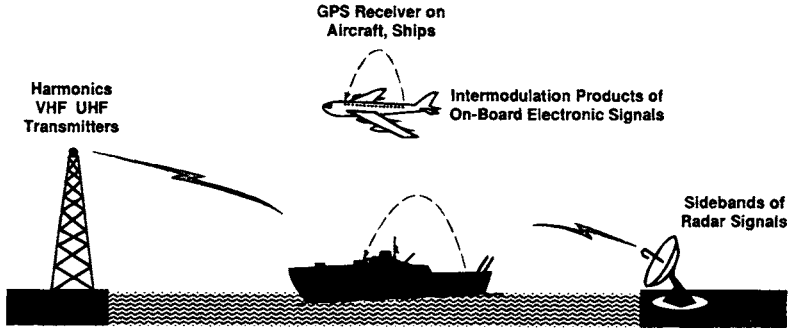

Fig. 1 Possible sources of unintentional interference caused by out-of-band emissions of other signal sources.

Table 1. Other bands in the vicinity of the L_2 signal are presently being considered as a second civil signal. The GPS C/A signal occupies approximately 2.5 MHz of bandwidth centered at 1575.42 MHz (the L_1 frequency).

Nearby bands are assigned for mobile, maritime, aeronautical, satellite communications and satellite-based cellular, as shown in Table 2. The frequency channel just below the GPS L_1 band is a satellite-to-ground link where the power levels received on Earth are expected to be relatively low. On the other hand, the 1610–1626.5 MHz band is a band reserved for hand-held transmitters to transmit to space for satellite-based cellular telephone. Both time division and code division multiple access (TDMA and CDMA) signals are licensed by the FCC for this band. The possible close proximity of these transmitters requires that the GPS receiver have adequate filtering to attenuate these transmissions, which are 34.58 MHz above the GPS L_1 center frequency and 24.58 MHz above the upper (10 MHz) edge of the GPS spectrum.

Another potential source of interference is from satellite communications uplinks at L-band in the 1626.5–1660.5 MHz bands (maritime satrom and aeronautical satrom). If these uplinks are on the same platform as the GPS receiver, there must be enough antenna separation and other isolation to prevent overload of the GPS low-noise amplifier (LNA). In addition one must avoid the effects of active or passive intermodulation products from either satellite communications (SATCOM) multicarriers or from local oscillators in close proximity to the GPS antenna or LNA.

Harmonics of improperly filtered TV channels also can be a potential source of interference in the vicinity of the TV transmission tower. The uhf TV transmission channels are spaced by 6 MHz and extend up to slightly over 800 MHz. Ultrahigh frequency military satellite communication takes place in the 240–400 MHz band with uplinks in the upper portion of the band, primarily in the 290–320 MHz band. Another possible source of interference is a harmonic (12th or 13th) of a VHF civil aviation air-to-ground link in the 118–136 MHz band.

II. Receiver Design for Tolerance to Interference

A. Receiver Systems

A simplified diagram of a GPS receiver that contains both spatial and signal processing for interference suppression is shown in Fig. 2. One or more antennas receive the GPS signal. This signal is rf filtered and downconverted to IF where it is amplified (with AGC) and then sampled and quantized. The quantized signal plus noise is then fed to the parallel code and carrier-tracking loops. All of these

Table 1 Radio navigation frequency bands

Frequency	Bandwidth
1.215–1.240 GHz	25 MHz
1.240–1.260 GHz	20 MHz
1.559–1.610 GHz	51 MHz

Table 2 Frequency bands assigned for mobile satellite communications and satellite-based cellular[a]

Frequency Band	Bandwidth	Usage
1.535–1.559 GHz	24 MHz	Several bands for satellite downlinks to mobile, marine, aeronautical users—space-to-ground
1.610–1.626.5 GHz	16.5 MHz	Uplink based from hand-held units Earth-to-space, satellite-based cellular
782–788 MHz 525 MHz	51 MHz	uhf television—6 MHz channels at 1/2 GPS L_1 frequency uhf television at 1/3 GPS L_1
1626.5–1660.5 MHz	34 MHz	Aeronautical satellite communications uplinks (possible intermodulation products)

[a]Also shown are subharmonic bands that would potentially cause interference if the transmitters are not operating properly.

elements are described in some detail in other chapters. In this chapter, we focus only on the possible effects of an interfering signal, be it broadband or narrowband.

1. Antenna and Adaptive Array Antennas

If only a single GPS antenna is employed, it often is a hemispherical antenna that typically has gain between 0 dB and +6 dB for much of the upper hemisphere. An example antenna pattern is shown in Fig. 3.

Note that at 5 deg elevation angle, the gain for this antenna has dropped to approximately −5 dB. However, as pointed out in the previous chapters, when the elevation angle drops below 5 deg, other effects, such as multipath, physical obstructions, and ionospheric/tropospheric delay uncertainty, may be the dominant error sources. In fact, it may be desirable to attenuate signals received below 5

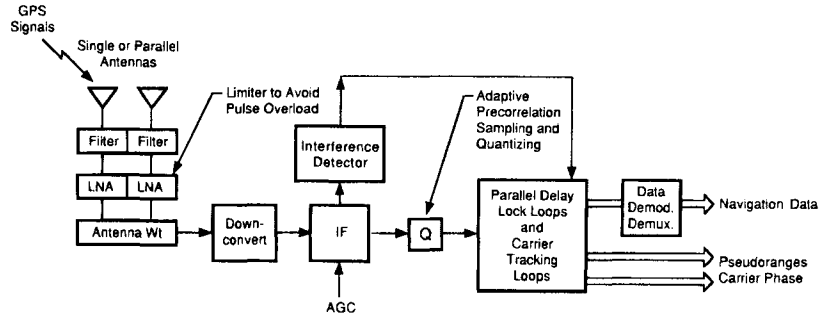

Fig. 2 Simplified diagram of a GPS receiver structure. An antenna array can perform spatial signal processing. An adaptive quantizer can be employed to suppress constant envelope interference. The DLL loop bandwidth can also be adapted. (The LNA is the low noise amplifier.)

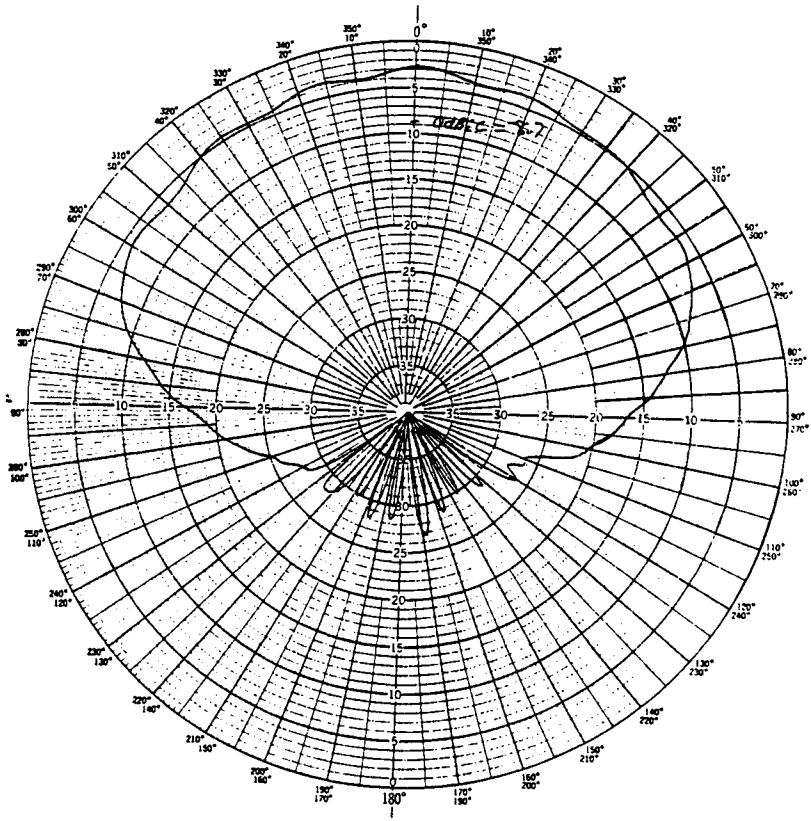

Fig. 3 Typical GPS antenna pattern at L_1 frequency in dB (the gain is 0 dBIC at −8.7 dB on the scale shown) (courtesy of Ball Aerospace).

deg in order to attenuate interfering signals and multipath that might come from the Earth's surface.

Although most GPS receivers employ only a single antenna, some receivers have more than one. For example, two antennas can be employed, one with maximum gain at zenith and another with larger gain at low elevation angles. Satellite receiver channels can be switched between them. Alternatively, a set of antennas can be operated as phased arrays to provide additional antenna gain in the directions to each of the satellites. We can also design an antenna array to null out a single source* of interference by adaptive weighting of multiple antennas, a form of spatial interference suppression. The adaptive nulling of an interfering signal can be performed using an adaptive algorithm very similar to that used in adaptive equalization. Section IV outlines some of the fundamentals of adaptive nulling.

* Multiple nulls can also be created for multiple interference sources as long as there is sufficient separation angle between the GPS satellite and the interference source, and there is a sufficient number of antenna elements.

A multiplicity of antennas can be used in an adaptive array, as shown in Fig. 4.[4,5] The interfering and the satellite signals generally have a significant angular separation if the interference source is on the Earth's surface. Thus, various least mean square and signal-to-noise enhancing adaptive array techniques can be used; e.g., the Applebaum array, to enhance the gain to desired signals and attenuate the interference. Many of these techniques require some knowledge of the signal and the arrival directions, although some adaptive nulling techniques require neither, as discussed in Sec. IV. Constraints can be placed on the adaptive weighting to provide significant gain in the upper hemisphere.

Figure 5 shows an antenna array configured with multiple-beam steering networks. The satellite angle of arrival relative to the user platform must be known to within the beamwidth of the antenna pattern. For fixed ground receiver applications, this information is generally known; for most mobile platforms, however, this operation can be complex.

1. Radio Frequency and Intermediate Frequecy Filtering

Several stages of rf and IF filtering are required. Radio frequency filtering is important to prevent out-of-band interference from causing nonlinear or saturation effects in the LNA and/or intermodulation or image problems in the downconverter mixers. Typically, the user receiver also provides some level of overload protection or limiting prior to the LNA to avoid saturation/burnout of the rf front end caused by high peak power pulses. The rf/IF filter–amplifier combination must be able to reject out-of-band interference and noise, suppress image signal response, prevent intermodulation and spurious effects in the IF amplification and sampling/quantizing operations, while not causing significant group delay variation over the desired signal bandwidth.

The bandwidth of the rf/IF filter for a C/A receiver might be set as wide as 20 MHz in order to get the greatest accuracy in a white thermal noise environment; whereas, this bandwidth could be set as small as 2 MHz (or even 1 MHz) in order to obtain the greater selectivity against out-of-band interference. Figure 6 shows five- and eight-pole Butterworth filter characteristics for bandwidths of

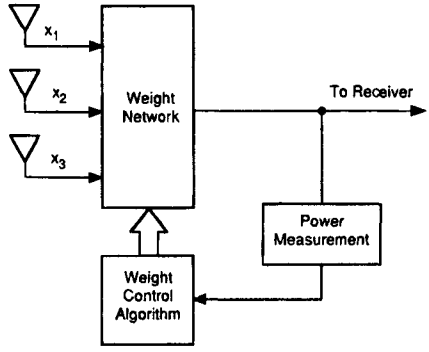

Fig. 4 Adaptive antenna array for nulling interfering signals. The adaptation algorithm can be set to minimize total power because, received power without interference is essentially constant thermal noise.

2 MHz and 20 MHz. Increasing the filter slope selectivity reduces interference effects but increases both the group delay and delay distortion. In summary, although the optimum C/A-code tracking accuracy in thermal noise is obtained by using the full 20 MHz bandwidth, interference rejection and other dynamic range effects may dictate a smaller rf/IF bandwidth.

The AGC sets the signal levels of the receiver so that the performance degradation of the quantizer is minimized. Short duration, high peak power pulses caused by radar sidebands, other pulse interference, or time-gated low duty factor GPS pseudolite transmissions are generally "peak clipped" (limited) or "blanked" (IF disabled for the length of the pulse). The IF or in-phase and quadrature (I,Q) baseband signal is then sampled and quantized. In the next section, the quantizer degradation caused by interference plus thermal noise is analyzed for various numbers of bits per sample and AGC levels. As is shown there, an interfering CW tone with some degree of coherence can cause a 1-bit quantizer to degrade substantially below the performance of that same quantizer with an equal power white thermal noise input. On the other hand, a well-designed multibit A/D converter can actually reduce interference effects for a constant envelope interference.

B. Quantizer Effects in the Presence of Interference

The GPS receiver processing system is assumed to be completely digital; thus, at some point, the received signal plus noise must be sampled and quantized. In this section, the received signal is assumed to contain the desired GPS satellite signal, receiver thermal noise, and an interfering signal. Two forms of the interfering signal are assumed: sinusoidal and Gaussian. A Gaussian interference simply

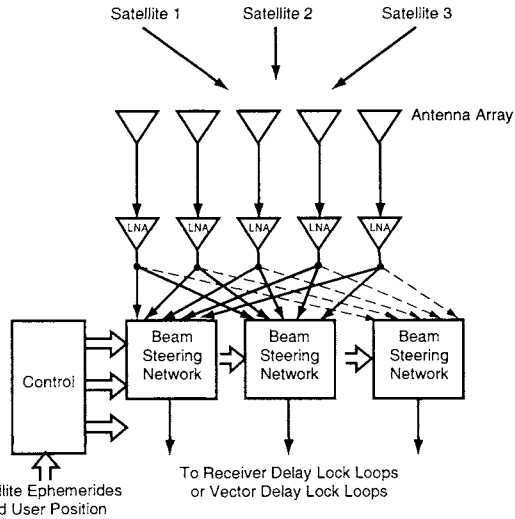

Fig. 5 Multibeam antenna array. This antenna array provides several separate beams, each pointing toward one of the GPS satellites. Approximate knowledge of the satellite angle of arrival is required for this antenna array.

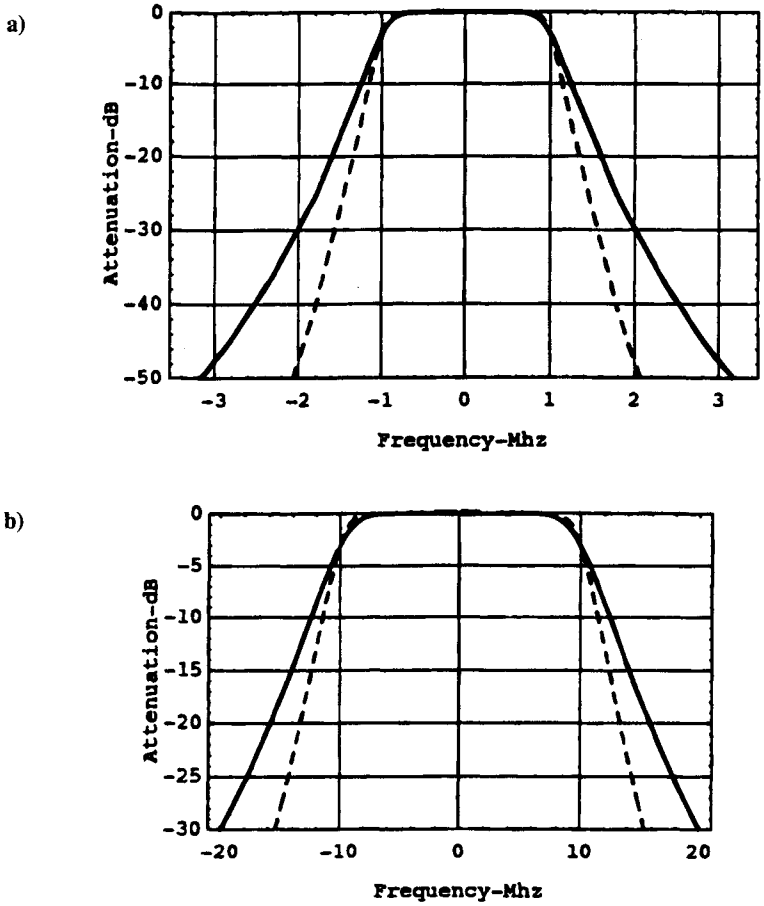

Fig. 6 Example of rf/IF filter frequency response (magnitude) characteristics for five-pole (solid) and eight-pole (dashed) Butterworth filters of 2 MHz and 20 MHz bandwidths.

adds to the Gaussian thermal noise although it may have a different bandwidth. A sinusoidal form of the interference can take on CW, narrowband, and wide bandwidth forms; e.g., an FM signal spread over 100 kHz or 2 MHz. The objective of this section is to analyze the signal-to-noise performance in the output of the quantizer–correlator relative to the input. A sinusoidal interference can have a severe impact on the receiver performance if a 1-bit quantizer is employed or if hard limiting occurs. On the other hand, a well-designed multibit A/D converter can actually suppress a constant envelope interference if the quantizing levels are properly set.

Before we proceed with the detailed discussion of quantizers, it is well to review some results for bandpass limiters. Recall that the GPS signal is a pseudonoise (PN) signal that is biphase modulated on a reference carrier. In a

receiver that employs a bandpass limiter,* it is well known that the output signal-to-interference ratio is degraded by 6 dB in the presence of strong sinusoidal interference with significant frequency offset. Frequency offset is defined with respect to the carrier center frequency. That is, the weaker signal is suppressed relative to the strong interference, so it is 6 dB weaker at the output of the bandpass limiter than at the input.[7] If the interference is at exactly the same frequency and in-phase with a desired binary phase-shift keyed (BPSK) PN signal, it can suppress the desired signal by much more than 6 dB and "capture" the receiver. If instead, the interference is a strong Gaussian signal, the suppression of the desired weaker signal by a bandpass hard limiter is $\pi/4$ or -1.05 dB. In this section, we analyze the effects of 1-, $1^1/_2$-, 2-, and 3-bit quantizers on the correlation performance of a receiver where the signal is received in the presence of various coherently modulated constant envelope interfering signals plus white Gaussian noise.

The GPS received signal power is assumed to range from -157 to -160 dBW for the C/A code for a 0 dB gain antenna. If the thermal noise density is -205.2 dBW/Hz, and a 2 MHz or 63 dB-Hz noise bandwidth is used, the total noise power is $P_n = -205.2 + 63 = -142.2$ dBW. The signal-to-noise ratio (SNR) then ranges from $P_s/P_n = \text{SNR} = -14.8$ dB to -17.8 dB for the C/A code. If a bandwidth of 10 MHz (or 70 dB) is used for higher accuracy, the SNR ranges between -21.8 dB to -24.8 dB. In the analyses that follow, a signal-to-thermal-noise ratio of -23 dB is assumed (the quantizer effects are not very sensitive to the SNR ratio in this range). The signal is assumed to be coherent with the receiver local oscillator so that all of the signal power passes through the in-phase channel; whereas, only half of the noise power is passed in the in-phase channel, the other half being in the quadrature channel. Thus, the ratio of signal amplitude level to rms noise level σ for this example is 1/10.

By way of reference it is well known[7] that the SNR degradation caused by a 1-bit quantizer (with high sampling rate) is a factor of $2/\pi$ or -1.96 dB for a signal plus large Gaussian noise (i.e., low SNR).† This degradation decreases to 0.5495 dB for a 2-bit quantizer for the best quantizer spacing relative to the noise level. For a 3-bit quantizer, the degradation decreases to 0.161 dB for optimum spacing.

Figure 7 shows the quantizer characteristic $Q(r)$ for 2- and 3-bit uniform quantizers where the quantizer interval is Δ, and the output levels are $\pm$ 1.5, $\pm$ 3.5. The quantizers considered here are all uniform quantizers with equal step sizes. Amoroso[8] shows that there is some advantage in interference suppression if nonuniform steps are employed on the output of a 2-bit quantizer, however, that benefit does not occur with thermal noise, and is not considered here.

1. *In-Phase and Quadrature (I,Q) Sampling and Quantizing*

In Fig. 8, it is assumed that the C/A signal from one satellite has been coherently downconverted to baseband along with Gaussian noise and sinewave interference.

*The bandpass limiter hard limits the envelope of the resultant and passes only the angular information.

†Note that 1-bit quantizing of each of the I and Q channels is not the same as bandpass limiting wherein a narrowband signal plus noise is hard limited and then bandpass filtered to pass frequency components only in the fundamental frequency zone to the output.

a)

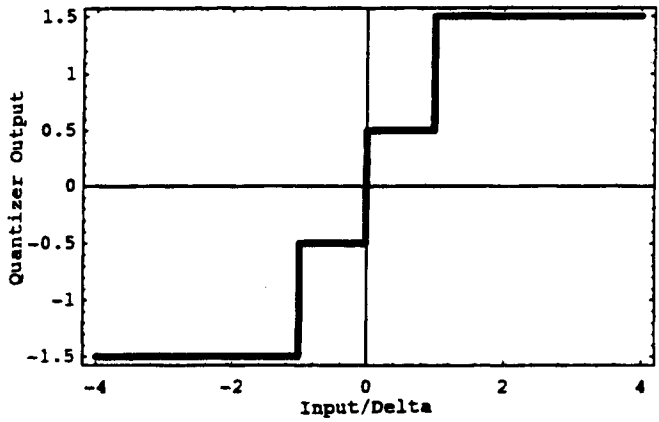

b)

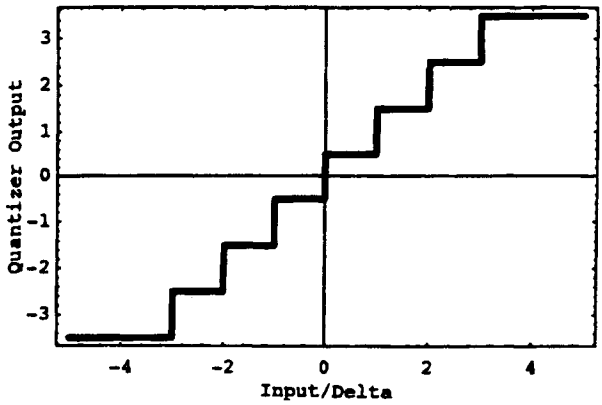

Fig. 7 Quantizer characteristic $Q(r)$ for 2- and 3-bit uniform symmetric quantizers with input quantizer interval Δ.

The interference can be received with or without uncorrelated PN modulation. Assume sufficiently wide bandwidth filters so that filter distortion effects are negligible (or that samples are taken with independent noise samples). The input $r(t)$ to the coherent channel quantizer is then $r(t) = A\ p(t) + K\ q(t) \cos \theta(t) + N_c(t)$, where A is the desired signal amplitude, $p(t)$ is the spreading code, the interference $I(t) = Kq(t) \cos \theta(t)$, and where the PN spreading codes $p(t)$ and $q(t)$ are both assumed to be ± 1. In this model, the interference modulation $q(t)$ may not be at the same rate as the PN code $p(t)$, and, in fact, $q(t)$ may not vary at all. If the interference has no PN modulation and is constant amplitude but offset in frequency by $f = \omega/2\pi$ the interference is $K \cos \omega t$. The bandlimited white noise $N_c(t)$ is assumed to have zero mean, variance σ^2, and Gaussian statistics. The quantizer output is defined as $Q_m[r(t)]$ where Q_m is an m-bit quantizer characteristic. The multiplier (correlator) output is then $c(t) = p(t)\ Q_m[r(t)]$ in the coherent channel.

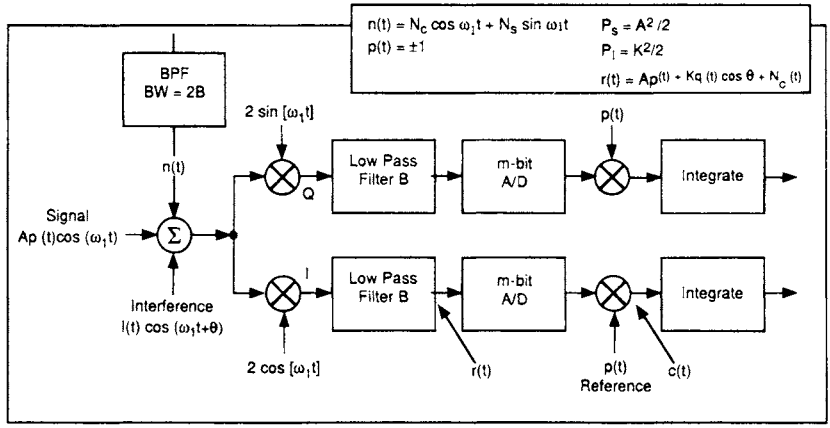

Fig. 8 Digital cross-correlation operation for an input of signal + noise + interference. An *m*-bit A/D converter is used prior to correlation.

The statistics of this multiplier output are examined in the next section. If the signal is sampled at a rate of $2B$ samples per second, the noise samples are independent, because the noise at baseband has bandwidth B. The objective is to compute the ratio of signal power in the correlator output to the variance in the correlator output and compare this ratio with the input signal-to-thermal-noise ratio and the ratio of input signal-to-noise plus interference.

The receiver noise at IF is represented as $n(t) = N_c \cos(\omega_i t + \theta) + N_s \sin(\omega_i t + \theta)$ where $n(t)$ has density N_o (one-sided), and the bandwidth at IF is 2B. The noise power in that bandwidth is $\sigma^2 = N_o 2B$ (see Fig. 9). The power in $n(t)$ is as follows:

$$E[n^2(t)] = E[N_c^2 \cos^2(\omega_i t + \theta) + N_s^2(t)\sin^2(\omega_i t + \theta)]$$

$$= E\left[\frac{N_c^2}{2} + \frac{N_s^2}{2}\right] = E[N_c^2] = \sigma^2 \tag{1}$$

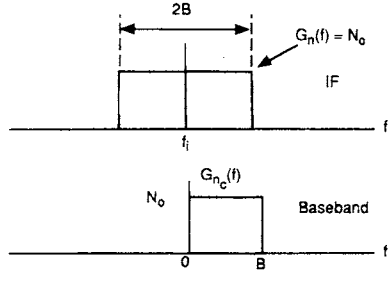

Fig. 9 Noise spectra at rf and at baseband. The baseband spectrum is one-sided.

because $N_c(t)$ and $N_s(t)$ are independent and of equal power, and θ is uniformly distributed; i.e., the variance of $N_c(t)$ is the same as that of $n(t)$. If the signal and noise are coherently mixed with the reference oscillator 2 cos $\omega_i t$, then the output of the in-phase channel for $\theta = 0$ is the product 2 cos $\omega_1 t$ $[Ap(t) \cos \omega_1 t + N_c(t) \cos \omega_1 t + N_s(t) \sin \omega_1 t]$. The low-pass component in this in-phase channel is $Ap(t) + N_c(t)$. If the signal power is P_s and the rf noise power is σ^2, then the SNR at the low-pass filter output of the in-phase channel is $A^2/E(N_c^2) = 2\,P_s/\sigma^2$, because $P_s = A^2/2$.

The interfering signal for this example is assumed to have amplitude K and rf power $P_I = K^2/2$. Consider, first, the example where the interference is in-phase with the signal. Other phases and frequencies are considered later for the more general interference model. The total input to the quantizer in the in-phase channel after downconversion is then $r(t) = Ap(t) + I(t) + n(t)$, where $p(t) = \pm 1$ with equal probability, $I(t) = K$, and $n(t)$ has variance σ. The resultant waveform $r(t)$ then has a probability density $\frac{1}{2}$ Normal $(\mu_+, \sigma) + \frac{1}{2}$ Normal (μ_-, σ), where $\mu_+ = K + A$, and $\mu_- = K - A$ are the mean values under these two conditions. The quantizer output $Q[r(t)]$ is then correlated with $p(t)$ to produce the multiplier (correlator) output $c(t)$; i.e.,

$$c(t) = p(t)Q[r(t)] = p(t)Q[Ap(t) + K + n(t)].$$

The correlator-output signal-to-noise ratio is

$$(\mathrm{SNR})_o = E[c(t)]^2/\{E[c^2(t)] - E[c(t)]^2\}.$$

The degradation in quantizer–correlator output SNR vs quantizer input signal-to-thermal-noise ratio* is, then, given by the ratio $R(K,\sigma,A,m,\Delta) = \mathrm{SNR}_o/(A^2/\sigma^2)$, where m is the number of bits in the quantizer, and Δ is the quantizer interval. Define a zero mean Gaussian or normal density function as follows:

$$p(x) = \frac{1}{\sigma\sqrt{2\pi}}\, e^{-(x^2/2\sigma^2)} \tag{2}$$

The error function is defined as follows:

$$\mathrm{Erf}(x) \triangleq \frac{2}{\sqrt{\pi}} \int_0^x e^{-t^2}\, dt, \quad \text{and} \quad \mathrm{Erf}(x_1, x_2) \triangleq \frac{2}{\sqrt{\pi}} \int_{x_1}^{x_2} e^{-t^2}\, dt \tag{3}$$

and the normal distribution function is

$$\Phi(y) = \int_{-\infty}^{y} p(x)\, dx$$

Thus, the error function and Gaussian distribution functions are related by the following:

$$\Phi(y) = \frac{1}{2}\,\{\mathrm{Erf}[y/(\sqrt{2}\,\sigma)] + 1\} \tag{4}$$

*Note that the quantizer input SNR is twice the rf input SNR for a coherent receiver. Note, also, that this degradation is not referenced to the ratio of input signal-to-noise plus interference.

and the probability of a random variable y being in the interval (y_1, y_2); namely, $p(y_1 < y < y_2)$, is as follows:

$$\Phi(y_2) - \Phi(y_1) = \frac{1}{2}\,\mathrm{Erf}[y_1/(\sqrt{2}\,\sigma),\quad y_2/(\sqrt{2}\,\sigma)] \tag{5}$$

Also, note that for small x, we have the following:

$$\mathrm{Erf}(x) \cong \frac{2}{\sqrt{\pi}}\left[x - \frac{x^3}{3} + 0(x^4)\right] \quad \text{for} \quad x << 1 \tag{6}$$

The expected value of the correlator output is the mean value of $Q[r]p$. For a 2-bit quantizer with output levels $\pm$ 1/2, $\pm$ 3/2, where $p(t) = \pm 1$ with equal probability and all levels normalized to $A = 1$ the expected value of the correlator output is† (see Appendix):

$$\begin{aligned}
E(c) = {} & \frac{1}{2}\left[P\left(Q = +\frac{1}{2}\,|p = 1\right) - P\left(Q = \frac{1}{2}\,|p = -1\right)\right]\frac{1}{2} \\
& + \frac{3}{2}\left[P\left(Q = +\frac{3}{2}\,|p = 1\right) - P\left(Q = \frac{3}{2}p|\, = -1\right)\right]\frac{1}{2} \\
& - \frac{1}{2}\left[P\left(Q = -\frac{1}{2}\,|p = 1\right) - P\left(Q = -\frac{1}{2}\,|p = -1\right)\right]\frac{1}{2} \\
& - \frac{3}{2}\left[P\left(Q = -\frac{3}{2}\,|p = 1\right) - P\left(Q = -\frac{3}{2}\,|p = -1\right)\right]\frac{1}{2}
\end{aligned}$$

This expression can be evaluated as follows:

$$\begin{aligned}
E(c) = {} & \frac{1}{8}\left\{\mathrm{Erf}\left[\frac{0 - (K+1)}{\sigma\sqrt{2}}, \frac{\Delta - (K+1)}{\sigma\sqrt{2}}\right]\right. \\
& \left. - \mathrm{Erf}\left[\frac{0 - (K-1)}{\sigma\sqrt{2}}, \frac{\Delta - (K-1)}{\sigma\sqrt{2}}\right]\right\} \\
& + \frac{3}{8}\left\{\mathrm{Erf}\left[\frac{\Delta - (K+1)}{\sigma\sqrt{2}}, \infty\right] - \mathrm{Erf}\left[\frac{\Delta - (K-1)}{\sigma\sqrt{2}}, \infty\right]\right\} \\
& - \frac{1}{8}\left\{\mathrm{Erf}\left[\frac{-\Delta - (K+1)}{\sigma\sqrt{2}}, \frac{0 - (K+1)}{\sigma\sqrt{2}}\right]\right. \\
& \left. - \mathrm{Erf}\left[\frac{-\Delta - (K-1)}{\sigma\sqrt{2}}, \frac{0 - (K-1)}{\sigma\sqrt{2}}\right]\right\}
\end{aligned}$$

† $P(Q = +1/2 \mid p = 1)$ is the conditional probability that $Q = +1/2$ given that the PN chip $p = 1$.

$$+\frac{3}{8}\left\{\mathrm{Erf}\left[-\infty, \frac{-\Delta-(K+1)}{\sigma\sqrt{2}}\right]-\mathrm{Erf}\left[-\infty, \frac{-\Delta-(K-1)}{\sigma\sqrt{2}}\right]\right\} \tag{7}$$

The variance of c can be computed in a similar manner by averaging the probabilities that c^2 takes on the values 1/4, 9/4. The variance of c for the 2-bit quantizer is, then, as follows:

$$\begin{aligned}\mathrm{var}(c) = &\left(\frac{1}{2}\right)^2\left[P\left(Q=+\frac{1}{2}\,|\,p=1\right)+P\left(Q=+\frac{1}{2}\,|\,p=1\right)\right]\frac{1}{2}\\ &+\left(\frac{3}{2}\right)^2\left[P\left(Q=+\frac{3}{2}\,|\,p=1\right)+P\left(Q=+\frac{3}{2}\,|\,p=-1\right)\right]\frac{1}{2}\\ &+\left(\frac{1}{2}\right)^2\left[P\left(Q=-\frac{1}{2}\,|\,p=1\right)+P\left(Q=-\frac{1}{2}\,|\,p=-1\right)\right]\frac{1}{2}\\ &+\left(\frac{3}{2}\right)^2\left[P\left(Q=-\frac{3}{2}\,|\,p=1\right)-P\left(Q=-\frac{3}{2}\,|\,p=-1\right)\right]\frac{1}{2}\end{aligned} \tag{8}$$

2. *One-Bit Quantizer—Quantizer–Correlator Degradation*

If the quantizer interval is set at $\Delta = 0$, the 2-bit quantizer of Fig. 7a degenerates to a 1-bit quantizer, and the output is then always $\pm 3/2$. Again consider a received input which consists of a unit amplitude biphase modulated signal plus a coherent interference of fixed amplitude K plus Gaussian noise of standard deviation σ. The probability density of the quantizer input given each of the two signs in the biphase modulation then appears as shown in Fig. 10. For this 1-bit quantizer, a coherently related interference of sufficient size can be shown to capture the receiver totally since the quantizer output then has almost no correlation with the input C/A–PN code $p(t)$.

Figure 11 shows the degradation in quantizer output SNR relative to quantizer input SNR plotted in dB for the signal level $Ap = \pm 1$, a noise level $\sigma = 10$, and interference amplitude K. Note that for small coherent interference amplitude $K = 0.1$, the degradation is 1.9548 dB, very close to the small SNR asymptotic value of $2/\pi$ (1.961 dB) for no interference. As the interference amplitude increases to 10, the degradation increases to approximately 6 dB. At larger interference levels for an interference amplitude level of approximately 25, the degradation rapidly increases to approximately 30 dB. This rapid quantizer–correlator degradation with interference levels not much greater than the receiver thermal noise level makes the use of 1-bit quantizing unacceptable if tolerance to coherent constant envelope interference is important. It can easily be seen that if there is no thermal noise, a coherent interference only slightly larger than the input signal amplitude completely suppresses the signal if a 1-bit quantizer is employed.

It is well known that BPSK PN signals are subject to stronger signal capture effects in a bandpass hard limiter, as shown in Fig. 12. A large interference,

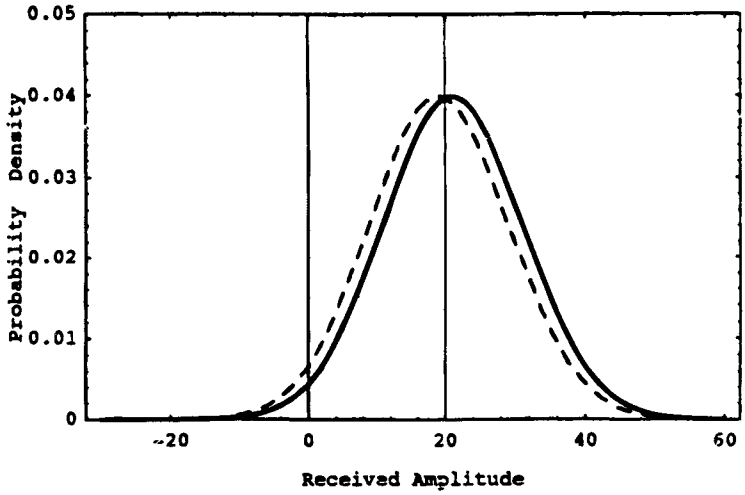

Fig. 10 Probability densities of the resultant of a biphase modulated unit amplitude signal plus coherent interference of level K plus thermal noise with $\sigma = 10$. This resultant signal is the input to a 1-bit quantizer for the two conditions $p = \pm 1$. In this example, $K = 20$, $\sigma = 10$, and $A = 1$. When the interference amplitude $K > \sigma$, the interference level carries the quantizer input to such a level that only very infrequent transitions are made, and the interference begins to capture the receiver totally.

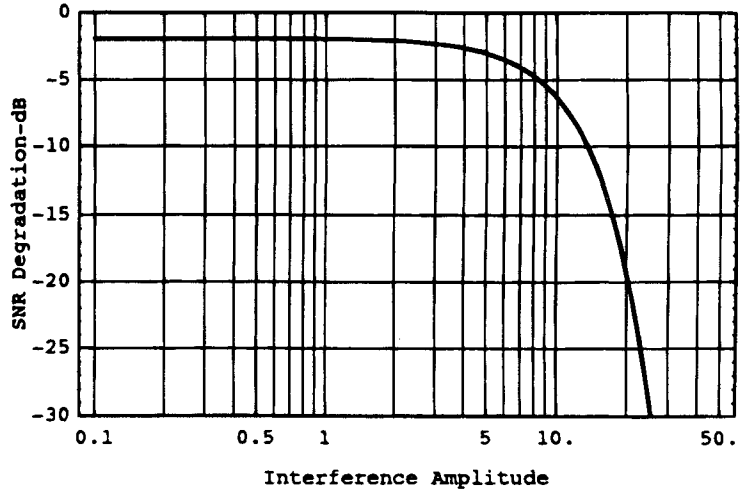

Fig. 11 Degradation in quantizer–correlator output SNR relative to quantizer input SNR caused by a 1-bit quantizer for coherent constant envelope interference of amplitude K relative to the signal amplitude. Gaussian noise is present with $\sigma = 10$. The SNR degradation is defined relative to the input signal to Gaussian noise ratio.

which is momentarily coherent with the signal for that time interval, completely suppresses the signal. Thus, we must avoid bandpass limiting in any GPS receiver with a potential for sinusoidal interference.* These effects with *I/Q* receiver 1-bit quantization are very similar to those studied by Baer[9] and Aein and Pickholtz.[10] The drastic suppression effects for a 1-bit *I,Q* quantizer however do not disappear with QPSK PN as they do with bandpass hard-limiter. The interference could be offset by 45 deg from the signal and would affect both *I* and *Q* channels equally.

The GPS C/A code, of course, only employs biphase modulation (the quadrature P(Y) code is not generally available to the civil user). Thus, the C/A receiver reference is also biphase modulated. The suppression effect of tone interference on the receiver, however, can be largely avoided through the use of quantizers with two, three, or more bits per sample, and an appropriate AGC, as shown below. Notice also that in the analysis of Fig. 10, the degradation has assumed that the interference is directly in-phase with the signal. If the interference is out of phase by some angle θ, the effective interference amplitude then becomes $K \cos \theta$ instead of K. However, it is clear that, in general, this effect simply means that the interference has to be slightly stronger, and, with θ slowly varying the signal, is suppressed periodically unless a multilevel quantizer is employed.

If the interference is offset in frequency by a large amount compared to the inverse of the averaging time; i.e., the data rate, then the mean and variance of $c(t)$ must be computed by averaging over θ in the $K \cos \theta$ term (with a uniform distribution of θ). This degradation is shown in Fig. 13. Note that for an interference amplitude of 20, the quantizer–correlator degradation is approximately 8.5 dB for the frequency offset interference vs 19 dB for the phase coherent interference, but the degradation is still increasing rapidly with increasing interference, and the 1-bit quantizer performance is unacceptable for this purpose.†

3. *Two-Bit Quantizing—Quantizer–Correlator Performance*

The performance of 2-bit quantizing is examined for PN signal plus noise alone, signal plus noise plus in-phase interference, and finally signal plus noise

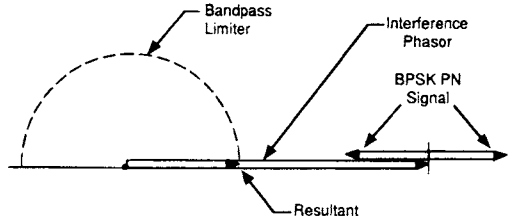

Fig. 12 Sum of BPSK PN signal and a coherent interference of larger amplitude. The resultant phasor is completely independent of the BPSK PN signal for this simple noise-free example, and the signal is completely suppressed. Note that noise is absent in this simple example.

*With QPSK PN, high-level sinusoidal interference would completely suppress only the in-phase term; i.e., half the signal power.

†One-bit quantizers are simple and lead to low-cost receivers, but their susceptibility to interference is a serious flaw for some applications.

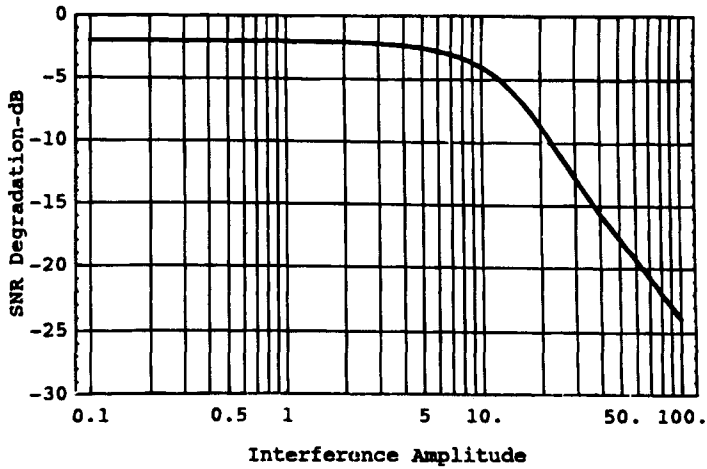

Fig. 13 Quantizer–correlator SNR degradation for a 1-bit quantizer with a frequency offset interfering sine wave $K \sin ax$ of amplitude shown. The signal is received with Gaussian noise ($\sigma = 10$) plus sinusoidal interference. For no interference the SNR degradation is $2/\pi$ or 1.961 dB. For large sinusoidal interference the degradation approaches 6 dB relative to the interference power level.

plus a sinusoidal interference which is offset in frequency from the signal center frequency. Clearly, in the limit for quantizer interval $\Delta = 0$ or ∞, the 2-bit quantizer is either always in saturation, or the received signal plus noise and interference never exceeds the first quantizer magnitude level Δ, and the 2-bit quantizer operates as a 1-bit quantizer. Figure 14 shows the output quantizer–correlator signal-to-noise performance degradation of a 2-bit quantizer relative to the quantizer input signal to thermal noise ratio (or to a receiver with an infinite number of quantizing intervals (linear)). The Gaussian noise has a $\sigma = 10$, and there is no interference. As shown in the figure, the minimum quantizer degradation for this case is 0.5415 dB and occurs at $\Delta = \sigma$. As the value of the input SNR declines to 0; i.e., infinite noise, the degradation increases only slightly to 0.5495 dB. Note that the degradation is still only 1 dB or less for quantizer interval variations of $\Delta = 0.4\,\sigma$ to $1.8\,\sigma$ corresponding to an AGC gain set error of approximately $\pm$ 7 dB.

If an interfering signal is present, and it has Gaussian amplitude statistics, the same result of Fig. 13 would also apply to the interfering signal problem. That is, set the AGC levels so that $\Delta = \sqrt{\sigma_n^2 + \sigma_I^2}$ where σ_n^2, σ_I^2 are the noise and interfering power levels, respectively.

Now consider a 2-bit quantizer that is employed with a signal in the presence of coherent interference of amplitude $I_c = K\cos\theta$ (for fixed θ) on the in-phase channel as well as Gaussian noise. The signal is of unit amplitude $Ap = \pm 1$, and the noise has rms value $\sigma = 10$. The quantizer interval is Δ. The quantizer–correlator SNR degradation above that of the quantizer input signal-to-thermal-noise ratio is shown in Fig. 15. Interference levels of $K = 0$, 10, 20, and 40 correspond to quantizer input interference-to-noise ratios of $-\infty$, 0, 6, and 12 dB,

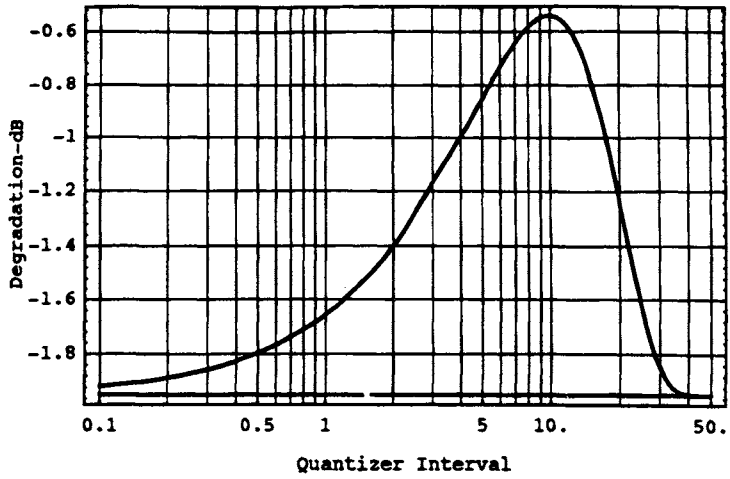

Fig. 14 Quantizer–correlator signal-to-noise degradation in dB for a 2-bit quantizer with normalized quantizer interval Δ for signal plus noise. The degradation is plotted vs quantizer interval Δ. The signal is of amplitude $Ap = \pm 1$, and the Gaussian noise has rms value $\sigma = 10$. There is no interference in this example.

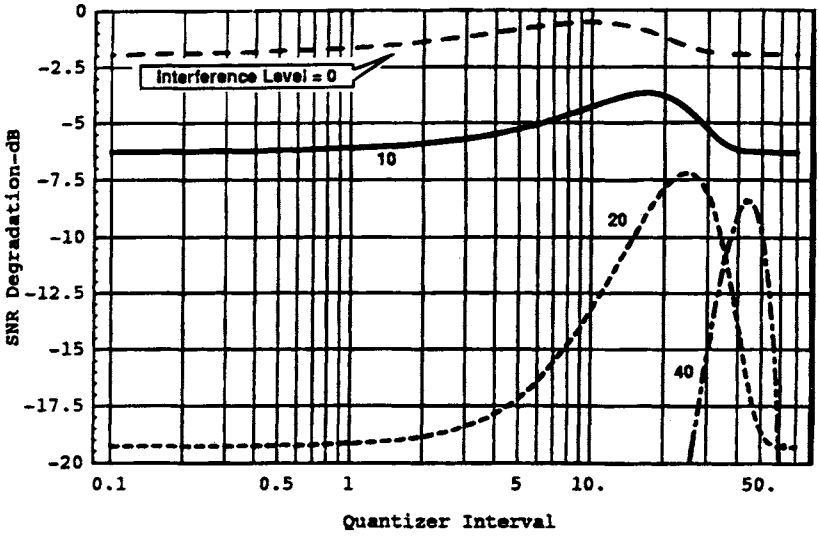

Fig. 15 Quantizer–correlator SNR degradation above that caused by noise alone for the 2-bit quantizer with coherent fixed interference levels of $K = 0$, 10, 20, and 40. If the quantizer was perfectly linear, the added degradation caused by interference would have been 0 dB, 3.0 dB, 7.0 dB, and 12.3 dB, respectively.

respectively. Notice that the range of good quantizer settings grows progressively narrower in percentage as the interference increases. Its width is approximately equal to the standard deviation of the noise. This result implies that the AGC level becomes more critical (when expressed in dB) as the interference level increases.

Note, however, that as the interference increases, the degradation does not increase proportionally with total noise plus interference power, as it would for Gaussian interference. It is clear from these results that the 2-bit quantizer interval Δ (or equivalently the AGC) can be set to attenuate the interference. Amoroso[8] pointed out that it is possible to design the quantizer to be adaptive so as to attenuate a sinusoidal interference. If the quantizer is set at the optimum level for large coherent interference, the input signal plus noise plus interference sits with a peak of the probability density near Δ (recall Fig. 10). Thus, the biphase modulated signal level toggles the magnitude both above and below the quantizer level Δ. In this case, a constant interference in the in-phase channel simply acts as a constant bias, and its effect to a large extent is canceled. Reference 8 showed that this effect can be enhanced by making the quantizer steps nonuniform, in the limit, the quantizer is a $1\frac{1}{2}$-bit null zone quantizer, as shown in Fig. 16. Clearly, in this example, the interference is almost completely canceled for a quantizer setting of $\Delta = K$ for large K.

As is evident from the curves of Figs. 14 and 15, the quantizer setting or AGC can be controlled to make it nearly equally probable to be in the two quantizer amplitude settings. The optimum quantizer setting in Fig. 15 is very close to $\Delta = \Delta_o \triangleq \sqrt{\sigma^2 + K^2}$. For example, at $K = 20$, the value of $\sqrt{10^2 + K^2} = 22.36$.

Note that the fact that the optimum quantizer setting results in equally probable output magnitudes makes it possible to build such an adaptive quantizer relatively easily. We simply have to count the number of occurrences in the two output magnitudes, and adapt the quantizer setting Δ so that they are equal.

Figure 17 shows the performance degradation for different AGC/quantizer settings for the 2-bit quantizer. Note that the optimum quantizer setting for this noise and interference, $\Delta \cong \sqrt{10^2 + K^2}$, gives a degradation that decreases to an

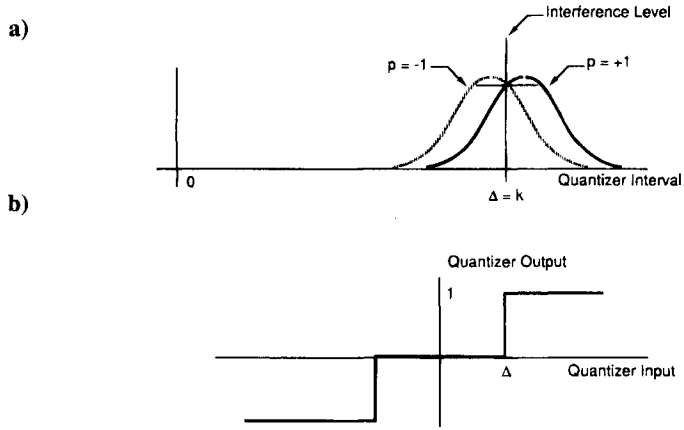

Fig. 16 Null zone quantizer setting with fixed large interference of amplitude K: a) quantizer input probability density; b) $1\frac{1}{2}$-bit, three-level quantizer with a null zone.

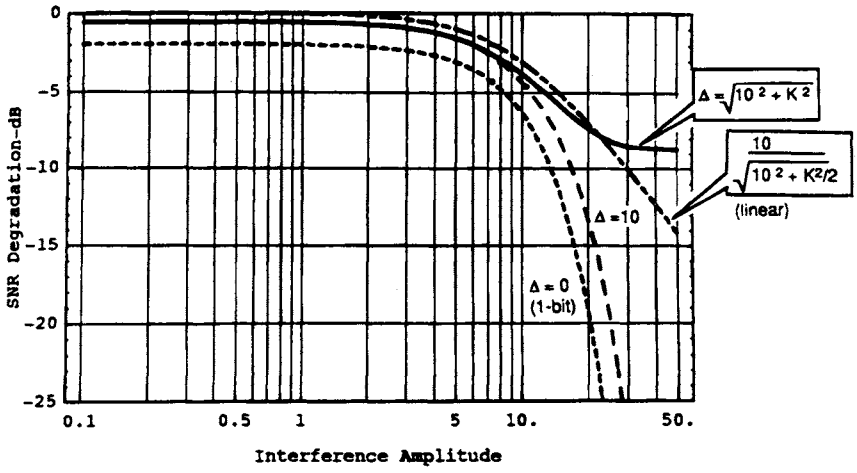

Fig. 17 Signal-to-noise ratio degradation for a 2-bit quantizer for quantizer intervals of $\Delta = \sqrt{10^2 + K^2} = \sigma_{\text{total}}$, $\Delta = 10$, and the 1-bit quantizer $\Delta = 0$. The linear reference degradation $10/\sqrt{10^2 + K^2/2}$ is shown as the alternate dash curve.

asymptote of approximately -9 dB. The reason for this behavior is that, as shown earlier in Fig. 5, a fixed interference level will still toggle the quantizer's output with the sum of random noise and signal. Thus, the interference effect itself is suppressed by the quantizer. Obviously, any time variation in the interference amplitude or phase would cause this interference nulling effect to be reduced, as shown below. As shown in Fig. 15, the minimum in quantizer degradation occurs in the region $\Delta = \Delta_0 \pm 10$. Although this result is for perfectly constant coherent interference, it is shown later that even with a sinusoidal offset interference, there is a definite performance improvement for an optimal quantizer compared to a linear quantizer.

A three-dimensional plot of the performance degradation vs both interference level and quantizer interval is shown in Fig. 18. As can be seen from the plot, there is a clearly defined ridge that optimizes the quantizing interval for any given interference level.

If the interference phase θ varies slowly with time relative to the databit rate, but the AGC maintains the quantizer level at a constant setting $\Delta = \sqrt{10^2 + K^2}$, then the quantizer output degradation varies slowly with phase offset (or time if the phase varies linearly with time), as shown in Fig. 19.

4. *Two-Bit Quantizer with Frequency Offset Interference*

Consider, now, an interference that is frequency offset from the center frequency of the PN signal. Assume that the frequency offset is large compared to the bit rate so that quantizer–correlator performance is determined by the time average of the interference in the in-phase channel ($K \cos \omega t$). Figure 20 shows the output degradation for values of $K = 10, 20, 40, 80$ relative to the signal amplitude of

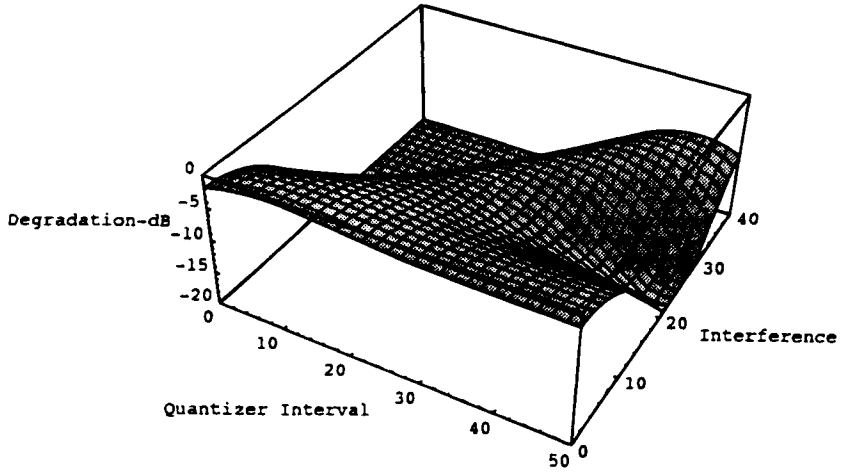

Fig. 18 Quantizer–correlator SNR degradation for the 2-bit quantizer vs both interference level and quantizer interval. The rms noise input is $\sigma = 10$.

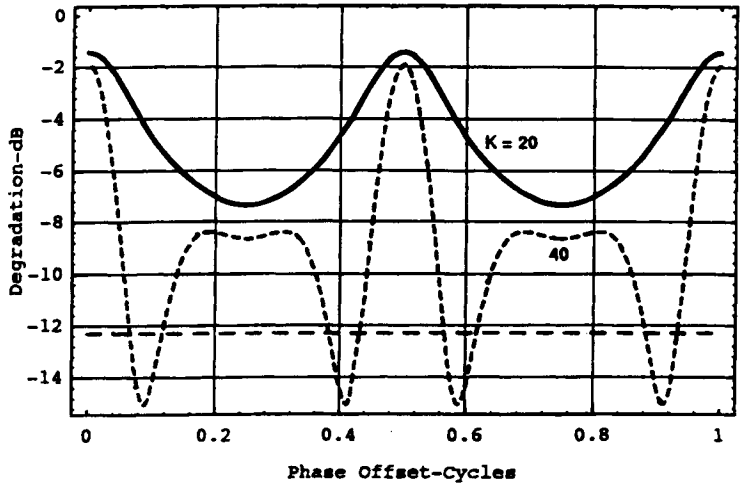

Fig. 19 Quantizer–correlator degradation for a setting of $\Delta = \sqrt{10^2 + K^2}$, with interference levels of $K = 20$ and 40. The horizontal dashed curve corresponds to the ideal quantizer degradation for $K = 40$ and a fixed phase offset $\theta = \pi/4$. The average degradation for this example with the linear quantizer would be 9.6 dB.

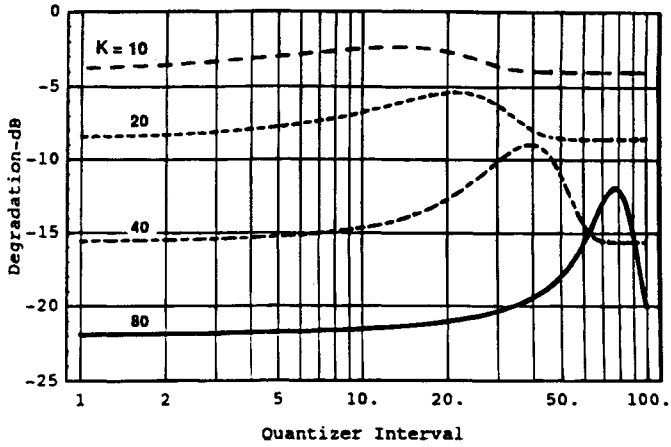

Fig. 20 Two-bit quantizer–correlator degradation in dB for four different values of the interference amplitude with frequency offset interference of the form $K \cos \omega t$. The results are given for $K = 10$, large dashes; $K = 20$, small dashes; $K = 40$, alternate dashes; and $K = 80$, solid curve.

unity and the rms noise $\sigma = 10$. The degradation in the quantizer–correlator output SNR relative to the quantizer input signal to thermal noise ratio varies with quantizer interval, as shown. Note that the optimum quantizer interval, again, has a value of $\Delta \cong \sqrt{\sigma^2 + K^2}$ and corresponds to roughly equal probable magnitude levels in the quantizer output during the interference peaks. Note, further, that the sinusoidal interference causes the quantizer output to have line components in its output. However, these components are spread by the cross-correlation operation with the C/A PN signal.

Figure 21 shows the quantizer–correlator output SNR degradation for the optimum quantizer spacing, $\Delta \cong \sqrt{\sigma^2 + K^2}$ with varying interference levels. Also shown in Fig. 21 is the degradation in quantizer output SNR relative to the quantizer input signal to thermal noise ratio that would be caused by the addition of the interference for a perfectly linear quantizer. Note that the output SNR for the quantizer correlator is improved over that of a perfectly linear quantizer–correlator for constant envelope interference above $K = 30$. At an interference level $K = 100$, the improvement is approximately 7 dB, as shown by the difference between the solid and large dashed curve. Note that the performance with a fixed amplitude interference of Fig. 17 has nearly reached an asymptote at $K = 100$; whereas, with a frequency offset, the performance degradation is still increasing in Fig. 21. Clearly, the optimum quantizer (adaptive AGC) has progressively greater performance compared to the linear quantizer as interference increases.

5. *Performance with Three-Bit Quantizing—Quantizer–Correlator Degradation*

Figure 22 shows the quantizer–correlator degradation for a 3-bit quantizer with a signal amplitude of $p = \pm 1$ and pure Gaussian noise with an rms value

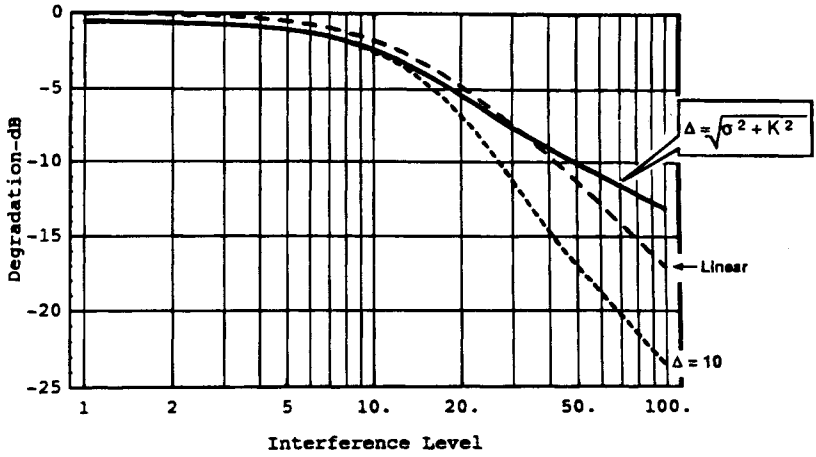

Fig. 21 Two-bit quantizer–correlator output degradation for frequency offset interference I = K cos ωt for various quantizer intervals. The solid curve represents near optimum performance with adaptive quantizer spacing $\Delta \cong \sqrt{\sigma^2 + K^2}$; the small dashed curve shows the performance with $\Delta = 10$ fixed at the optimum for no interference. The large dashed curve shows the degradation resulting from a perfectly linear quantizer and is of course equal, to the quantizer input signal to (noise + interference) power ratio.

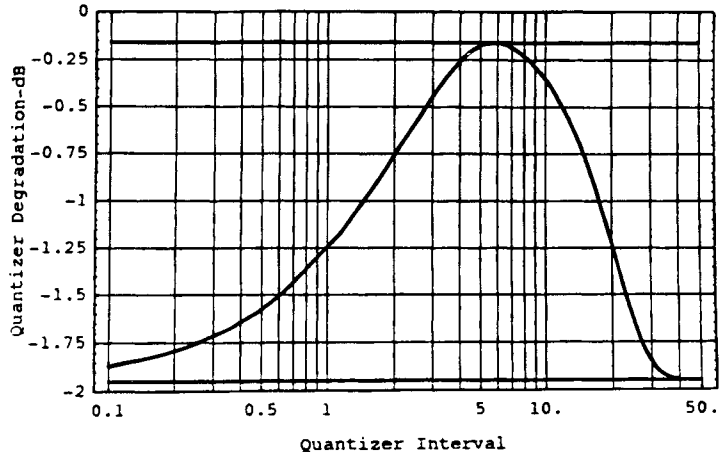

Fig. 22 Three-bit quantizer–correlator degradation in SNR for a signal level $p = \pm 1$, rms noise with $\sigma = 10$ and a quantizer interval Δ. The minimum occurs at $\Delta = 10/\sqrt{3} \approx 5.77$ and is ≤ 0.161 dB degradation. At $\Delta = 0$ or ∞ the degradation increases to -1.96 dB or $2/\pi$, the 1-bit quantizer result.

of $\sigma = 10$. There is no sinusoidal interference in this example. The minimum degradation occurs with a quantizer interval of $\Delta = \sigma/\sqrt{3}$ compared to $\Delta = \sigma$ for the 2-bit quantizer. The minimum degradation is 0.1613 dB vs 0.5415 dB for the 2-bit quantizer. Furthermore, for 3-bit quantization, the quantizing interval for less than 1 dB of degradation can range from $\Delta = 1.5$ to 18 or a 22 dB range. Thus, the AGC setting is considerably less sensitive than for the 2-bit quantizer, which has only a 13 dB range.

Figure 23 shows the cumulative normal probability distribution at the various quantizing intervals in terms of the magnitude probabilities. The probability of being in the magnitude interval 0 to Δ is 0.4363; Δ to 2Δ is 0.3155; 2Δ to $-\infty$ is 0.2482. Thus, the ratio of the probability of being in region 0 to Δ over that of being in Δ to 2Δ is 1.38, a little over unity. The quantizer AGC level, thus, can be set for both the 2-bit and 3-bit quantizers by properly balancing the counts in each magnitude bin (magnitude bits).

The additional quantizer–correlator output SNR degradation, beyond that of noise alone, caused by coherent interference of constant amplitude K is shown in Fig. 24 for $\sigma = 10$. The result for an ideal linear circuit is shown for comparsion. The flattening or double hump behavior appears because of the multiple quantizer magnitude levels in the 3-bit quantizer. Figure 25 gives the excess degradation for the four quantizing intervals $\Delta = \sqrt{\sigma^2 + K^2}/\sqrt{3}$, $\sqrt{\sigma^2 + K^2}$, a constant $\Delta = 10$, and the 1-bit quantizer $\Delta = 0$. For reference, the ratio of the degradation in the quantizer input SNR caused by interference; namely, $10/\sqrt{100 + K^2}$ is also shown. Again, the degradation for $\Delta = \sqrt{\sigma^2 + K^2} \approx K$ for $K >> 10$ is a special case for which the quantizing interval is almost squarely centered on the peak probability density of the interference plus noise amplitude. The degradation flattens to an asymptote at -9 dB for large K. This quantizer setting is not quite

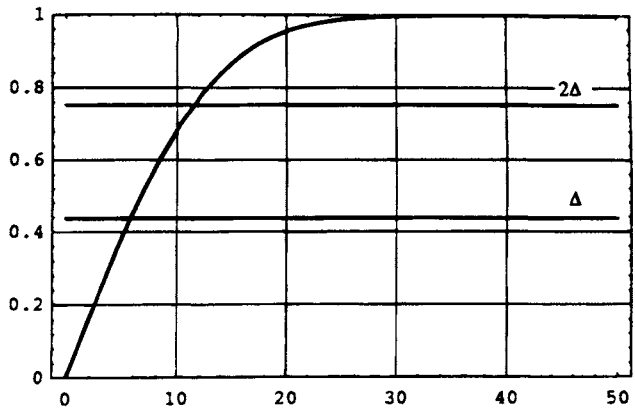

Fig. 23 Cumulative probability at the optimum quantizing interval $\Delta = 10/\sqrt{3}$, and 2Δ. Note that the ratio of the probability of being in the range 0–Δ is 0.44; whereas, the probability of being in the range Δ–2Δ is approximately 0.32. Thus, the ratio of the two probabilities can be used to set AGC level.

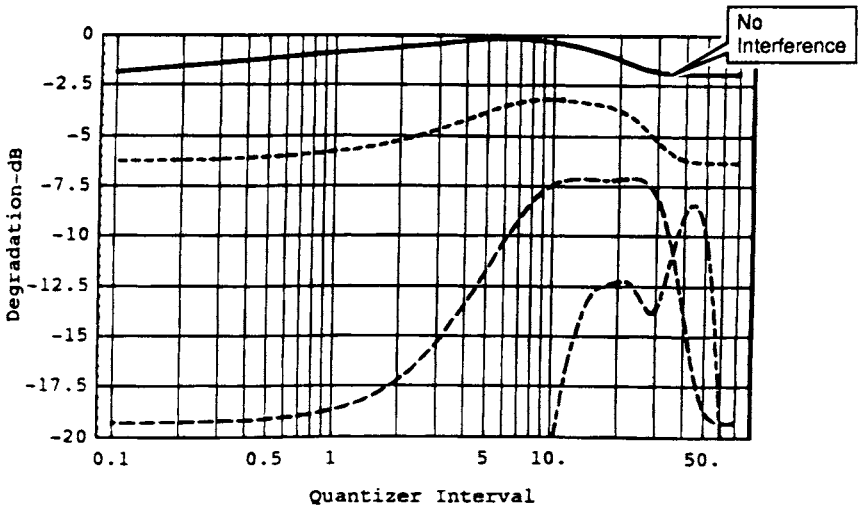

Fig. 24 Quantizer–correlator degradation for a 3-bit quantizer caused by fixed interference of amplitude $K = 0$, solid curve; $K = 10$, small dashes; $K = 20$, large dashes; and $K = 40$, alternate size dashes. The signal is $p = \pm 1$, and the noise has rms value $\sigma = 10$.

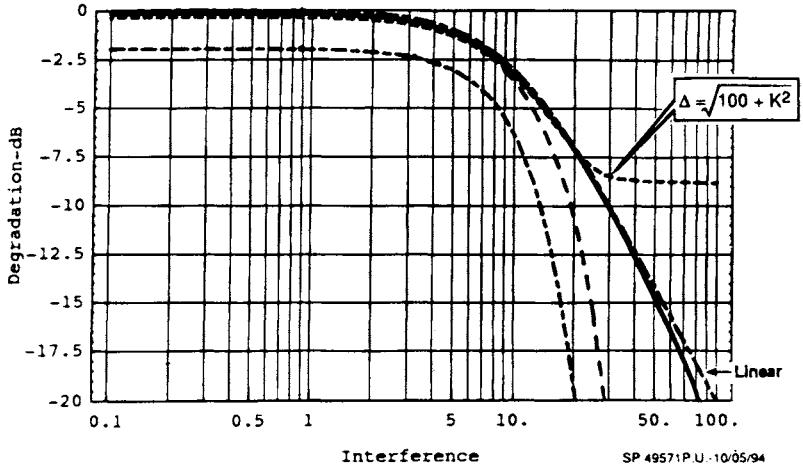

Fig. 25 Quantizer–correlator degradation for the 3-bit quantizer vs interference level for various quantizer intervals, $\Delta = \sqrt{100 + K^2} / \sqrt{3}$, solid curve; $\Delta = \sqrt{100 + K^2}$, small dash curve that levels off; $\Delta = 10$, large dashed curve. The small alternate dashed curve, the curve with the greatest degradation is the 1-bit quantizer $\Delta = 0$ for reference. A reference curve, $10/\sqrt{100 + K^2}$, the linear result, is also shown for reference with large alternate dashes.

as good for noise alone, as shown in Fig. 22. The degradation is about 0.35 dB for $\sigma = 10$, as compared to a minimum of 0.16 dB. The probability of being in the 0–Δ range increases with no interference to 0.6827, but the ratio of being in 0–Δ vs Δ–2Δ is approximately unity for high levels of interference. However, the 3-bit quantizer degradation caused by interference with amplitude $K = 10$ is nearly 11 dB less than that for a linear circuit.

Figure 26 shows the three-dimensional plot of degradation of the quantizer–correlator vs both quantizer level and interference amplitude. Again, there is a ridge of optimum quantizer level corresponding to $\Delta \cong \sqrt{K^2 + \sigma^2}$. However, with the 3-bit quantizer, there is a second ridge corresponding to the next quantizing level, and the 3-bit quantizer is not as sensitive to quantizer interval setting as is the two bit quantizer.

Figure 27 shows probability density superimposed on the quantizer intervals for $\Delta = \sqrt{100 + K^2/3}$, with $K = 20$, i.e., $\Delta = 12.9$, the optimum quantizer setting for noise alone. The recommended quantizer interval for interference plus noise would be $\Delta = 22.36$.

If the coherent interference phase is varied slowly compared to the data bit rate; namely, $I = K \sin \theta$, then the excess degradation for the 3-bit quantizer is as shown in Fig. 28 as a function of the phase. The degradation is given for $K = 20$ and 40. For reference, the peak degradation for the infinite level quantizer is shown as the horizontal dashed curve, and the average degradation is 6 dB above that.

6. *Three-Bit Quantizer with Frequency Offset Interference*

Consider next a frequency offset interference $K \cos \omega t$, where the offset frequency is larger than the databit rate by several times so that power averaging occurs. Figure 29 shows the quantizer–correlator degradation for values of interference $K = 10$,

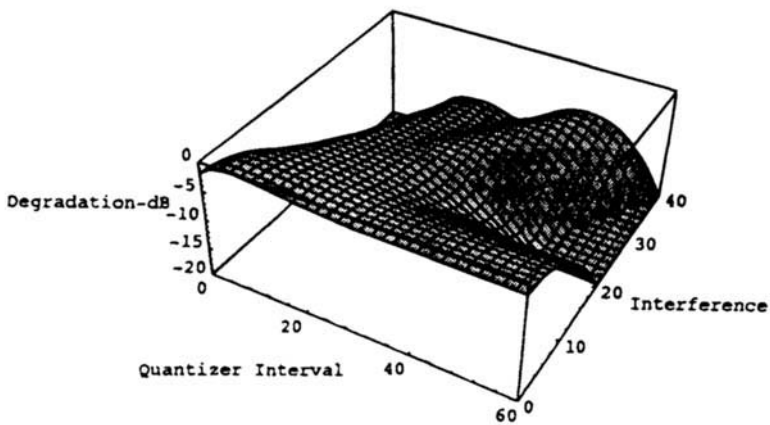

Fig. 26 Excess quantizer–correlator degradation for the 3-bit quantizer vs both quantizer interval and interference level.

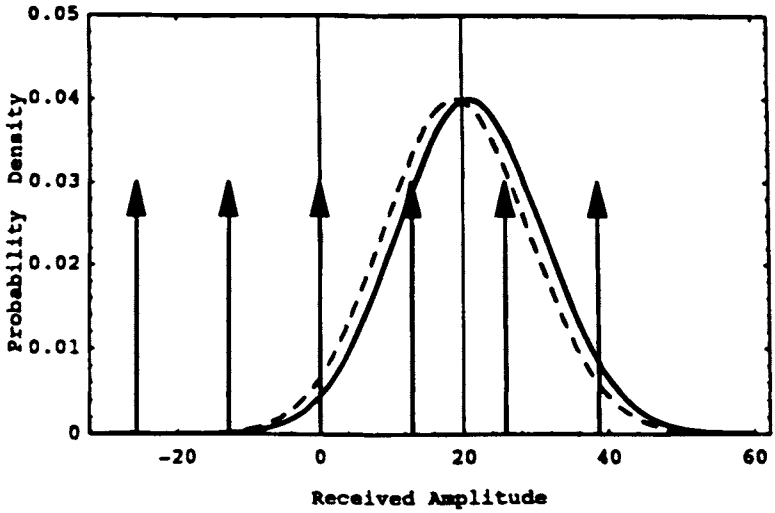

Fig. 27 Signal plus noise probability density and quantizer intervals for the 3-bit quantizer with $K = 20$ and a quantizer interval set by total power /3, i.e., $\Delta = \sqrt{100 + K^2}/\sqrt{3}$. The quantizer intervals are denoted by the arrows.

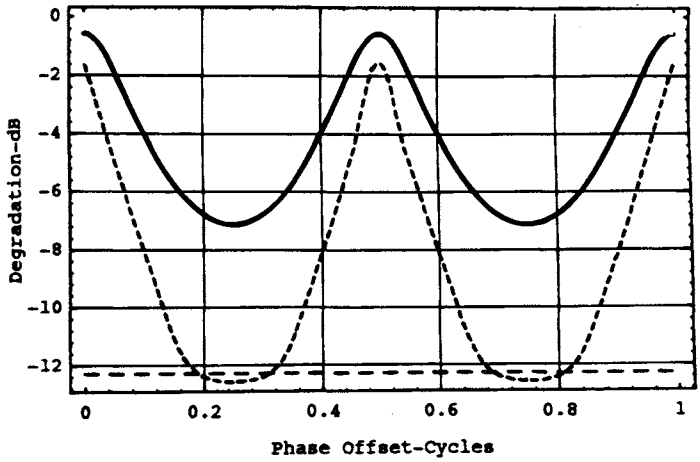

Fig. 28 Excess degradation in SNR for 3-bit quantizer for an interference $K = 20$ sin θ, solid curve i and $K = 40$ sin θ, small dashed curves. For reference, the peak degradation for an infinite level quantizer is shown as the horizontal dashed curve. The quantizer interval is $\sqrt{\sigma^2 + K^2}$.

AUTHOR INDEX

SUBJECT INDEX

D

F

Index Terms	Links		
G			
G-sensitivity	388		
Gabor bandwidth	110		
Gain	374		
Galilean transformation	635		
Galosi fields	57	113	
Gauss-Markov Theorem	194		
Gaussian density	249	340	578
GDOP derivation	179	475	
General relativity	637		
Generalized inverse matrix	196	296	
Geocentric latitude	139		
Geodesies	634		
Geoid the earth	152	662	
Geometric Dilution of Precision (GDOP)	16	474	
HDOP	245		
PDOP	474		
TDOP	245		
VDOP	245		
Geostationary satellite	197		
GIPSY/OASIS-II	587		
Global Navigation Satellite System (GLONASS)			
clocks	626		
time	631		
Global Positioning System (GPS)	3	29	
GPS clock correction data formats	132		
GPS ephemeris	135		
GPS Time	141		

M

S